Schriftenreihe

Siedlungswasserwirtschaft und Umwelt

Heft
36

RALPH SCHÖPKE

Filtration processes in nature and technology

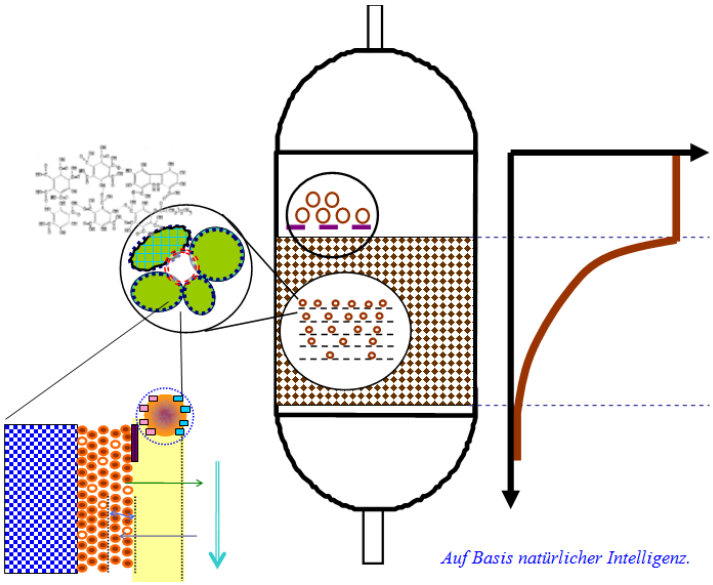

$$\dot{c} = \left(\frac{\partial}{\partial t} c\right)_L = -\mathrm{div}\left(\vec{v} \cdot c\right) + \mathrm{div}\left(D \cdot \mathrm{grad}(c)\right) + r$$

Cottbus 2025

Herausgeber: Dr.-Ing. Konrad Thürmer
Arbeitsgebiet Wassertechnik und Siedlungswasserbau
der Brandenburgischen Technischen Universität Cottbus-Senftenberg

ISBN 3-934294-43-X

Herausgeber: Dr.-Ing. Konrad Thürmer
Arbeitsgebiet Wassertechnik und Siedlungswasserbau
der Brandenburgischen Technischen Universität Cottbus-Senftenberg

Vertrieb: Eigenverlag des Arbeitsgebietes Wassertechnik und
Siedlungswasserbau der Brandenburgischen Technischen Universität
Cottbus - Senftenberg
Siemens-Halske-Ring 8
03046 Cottbus
Tel.: 0049-355-69-4303
Fax: 0049-355-69-3025
e-mail: konrad.thuermer@b-tu.de

Cottbus 2025

ISBN 3-934294-43-X

Inhalt

1 Introduction

Very similar processes take place in aquatic systems. Natural and technical reaction spaces differ in their different dimensions. Nature and technology cannot always be clearly distinguished from each other.

Here, joint description and design approaches are compiled for the processes in porous media flowing through between large-scale aquifers (aquifers GWL), technical filters up to membranes and on a wide scale. After many processes have been clarified down to the smallest detail, one is more inclined to be able to tackle a new problem by offsetting proven software solutions, whereby one runs the risk of losing the understanding of the process. This overview is intended to avoid this.

Scientists and engineers should have connections beyond their field of expertise to other scientists and their representatives, master the fundamentals of systems science, and keep an eye on the potential societal implications of their work. Since especially in the current phase the success of the competition, which must be strived for by all means, decides (almost) everything, it is worth remembering the further responsibility of scientists and engineers in the form of Hippocratic oaths for scientists and engineers.

- Hippocratic Oath for Natural Scientists (FÜRTH 1956, quoted in BRANDT 2015):

Since I am aware that my scientific knowledge has given me considerable power over the forces of nature, I pledge to use this knowledge and this power to the best of my knowledge and belief exclusively for the welfare of mankind and to abstain from any scientific activity which, as far as I am aware, is intended for harmful purposes.

- Hippocratic Oath for Engineers (Thring, M. W. 1973 quoted in BRANDT 2015):

In my work, I vow to strive for the following: the coexistence of all human beings in peace and human dignity, with everything that absolutely belongs to a fulfilled life, freed from fear, overexertion, ugliness, pollution and noise.

I would like to thank all those who have contributed to the creation of the empirical basis for this work, starting with the colleagues in the Water Treatment Process Group at VEB Prowa Cottbus, the staff of the Chairs of Water and Wastewater (names have changed several times - the old ones have remained) to the project sponsors and clients who financed many a project. This is not to be thanked to Bertelsmann's policy of the Entrepreneurial School, with its ruinous competition for third-party funding, which suppresses any long-term creative research work in connection with financial and personnel cuts (KREIß 2020).

2 Reactive compartments in Nature and Technology

2.1 Reaction compartments in Natural Scales

2.1.1 From the molecular scale to macroscopic scale

When considering the different systems, their scale size must be taken into account. Let's leave the Big Bang aside and start at the atomic level around 0.1 nm. Electromagnetic forces and quantum effects are mainly at work between atoms and molecules, leading to new bonds and configurations. On the smaller scales with increasing quantum effects, the thermodynamic approach becomes more and more complicated, although their conservation laws continue to apply statistically. This area is not relevant for water treatment.

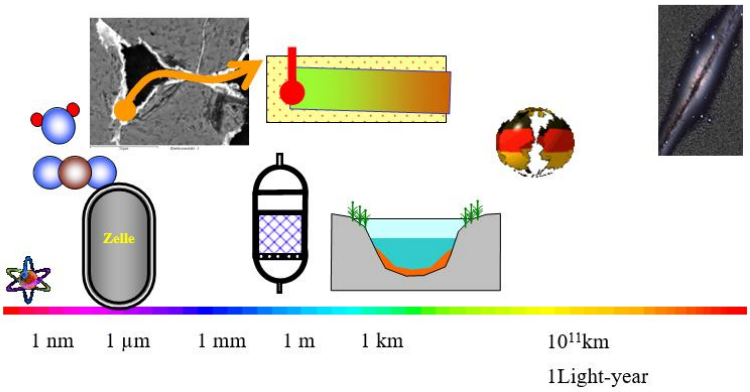

Fig. 2.1-1: Scale ranges between the molecular and global level.

The effects at the molecular level, such as rotation, oscillation, change of physicochemical bond states and diffusion, take place with changes in the energy and the state of order (entropy) of the particle collectives. This results in the system changes of energy and entropy typical of material turnover. In addition, there are chaotic systems whose *islands of stability* are the subject of our observations and whose *self-similarity* we encounter again and again during leaps in scale.

In more complex systems, such as microorganisms, the individual reaction pathways become increasingly unmanageable. Mass transport via diffusion is becoming increasingly important. For aggregated phases, a surface tension can be formulated. Attractive forces (adhesion) act between individual particles.

In the pore system of a filter (< 2 mm), convective mass transport also has an effect, which is accompanied by energy dissipation (internal friction, viscosity). Here, individual phases can be distinguished from each other by diffusion layers. This level is where the filtration processes in water treatment take place, but also in the aquifer.

Most water treatment plants are located on the next larger metre scale. Here, turbulence increasingly has an influence on flow and mass transport processes.

Even more confusing are processes in nature or those treatments that are designed to be close to nature and take place on scales from one meter to kilometers. Our climate models cover the entire Earth, although the scales below can usually only be taken into account in a highly simplified way, Tab. 2.1-1.

Tab. 2.1-1: Fundamentale Naturkonstanten.

Parameter	Symbol	Unit	Value
Speed of Light	c	m/s	$2{,}998 \cdot 10^{08}$
Planck's constant	h	J·s	$6{,}63 \cdot 10^{-34}$
dielectric constant	ε_0	$J^{-1}C^2m^{-1}$	$8{,}85 \cdot 10^{-12}$
gravitational acceleration	g	m/s^2	9,806

2.1.2 Relationships between molecular and macroscopic level

The relationship between the molecular and the macroscopic level is established by the definition of the mole, together with the corresponding mole concept. To do this, the properties of a system of particles are related to N0 = 6.02·10+23 particles (Avogadro constant), the mole. By definition, the mole is a counting quantity. The Avogadro constant was originally defined by the number of 12 g carbon ^{12C} and is now determined more and more precisely using different methods. The most important atomic/molecular constants are given by their molar equivalent, Tab. 2.1-2. This avoids calculating with very unwieldy small or large numbers.

In the SI system of units of measurement, the mole is only shown shortened to the amount of substance. You can specify water molecules but also the total number of the world's population in moles. 8 billion people correspond to $1.3 \cdot 10^{-14}$ mol or around 13 fmol.

Tab. 2.1-2: Conversions between the molecular level and macroscopic ratios. [1)] 0°C, 1 atm for an ideal gas.

Molecular level				Transition to the macroscopic level			
Description	symbol	Value	unit	Description	symbol	Value	unit
Chemistry object set	n		1	Avogadro constant	N_0	$6{,}02 \cdot 10^{+23}$	mol^{-1}
Particle mass		~	yg	Molar mass	M	~	g/mol
Particle volume		~	nm^3	Molar volume	V	22,414 [1)]	L/mol
Electron charge	e	$1{,}60 \cdot 10^{-19}$	As	Faraday constant	F	96485	As/mol
Boltzmann constant	k_B	$1{,}38 \cdot 10^{-23}$	J/K	Ideal gas constant	R	8,314	J/(K·mol)
Reaction energy		1	eV	Reaction energy	$\Delta_R U$	96,485	kJ/mol

The mass of a mole of particles is defined as molar mass [g/mol] defined as an equivalent of the atomic unit of mass [Da, Dalton] and is given in the periodic table (usually) to the right above the symbol. For a water molecule, its mass can be calculated, Eq.(2.1-1)

Tab. 2.1-3: Prefixes for units of measurement.

Prefix		log n		Prefix		log n
Deka	da	1		Dezi	d	-1
Hekto	h	2		Zenti	c	-2
Kilo	k	3		Milli	m	-3
Mega	M	6		Mikro	µ	-6
Giga	G	9		Nano	n	-9
Tera	T	12		Pico	p	-12
Peta	P	15		Femto	f	-15
Exa	E	18		Atto	a	-18
Zetta	Z	21		Zepto	z	-21
Yotta	Y	24		Yokto	y	-24

$$m(molecule\ of\ water) = \frac{M}{N_A} = \frac{18\ {}^{g}/_{mol}}{6{,}02 \cdot 10^{23}\ {}^{1}/_{mol}} \approx 3 \cdot 10^{-23} g = 30 yg \qquad (2.1\text{-}1)$$

Analogously, the respective molar volume results from the space required by a particle. The molar volume thus does not describe the actual particle volume and is dependent on the state of matter and the temperature-dependent state of motion of the phase under consideration. Since atoms and molecules are limited by their outer electrons with residence probabilities, their exact size is practically impossible. The space required by the molar volume of a particle oscillating in a crystal structure to the elastic collisions within a gas phase increases with temperature.

The molar volume of liquid water is calculated from the macroscopic quantities molar mass M and density ρ_{H2O}, Eq.(2.1-3).

$$V_{H2O} = \frac{M}{\rho_{H2O}} = \frac{18\ {}^{g}/_{mol}}{10^{6}\ {}^{g}/_{m^3}} = 18 \cdot 10^{-6}\ {}^{m^3}/_{mol} = 18\ {}^{mL}/_{mol} \qquad (2.1\text{-}2)$$

The corresponding molecular space requirement is obtained by dividing by the Avogadro constant N_0, Eq.(2.1-3).

$$V(Wassermolekül) = \frac{18 \cdot 10^{-3}\ {}^{L}/_{mol}}{6{,}02 \cdot 10^{23}\ {}^{1}/_{mol}} \approx 0{,}03 yL = 3 \cdot 10^{-29} m^3 = 0{,}03 nm^3 \qquad (2.1\text{-}3)$$

For ideal gases, their molar volume V is derived from the equation of state of ideal gases pressure(p)- and temperature(T)-dependent, Eq.(2.1-4) In the ideal gas theory, the Boltzmann constant represents the proportionality factor between the energy absorption of elastically colliding particles and the temperature. Their molar equivalent is the general gas constant of ideal gases R.

$$p \cdot V = n \cdot R \cdot T \qquad (2.1\text{-}4)$$

Under normal conditions, the ideal gas molecule has a space requirement of 36 nm^3, which corresponds to an edge length of 3.3 nm.

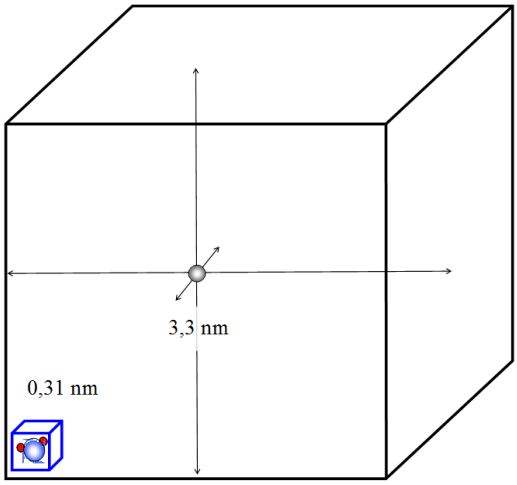

Fig. 2.12: Comparison of the space requirement of an ideal gas molecule under normal conditions with that of a liquid water molecule with indication of the edge length.

One mole of elementary charges is defined as the Faraday constant F. In this way, the material turnover of electrochemical reactions (electrolysis) is linked to the electricity demand. At a current of 1 ampere, 37.3 mmol/h electrons flow (≈ 10 µmol/s).

In the same way, the reaction energy U or enthalpy H, which are sometimes expressed in electron volts (eV), can also be converted into molar units. An electron volt is the energy that an electron absorbs when accelerating in the electric field of 1 Volt. The energy turnover of electron transitions can be converted into molar quantities, Eq.(2.1-5)

$$1\ eV \cdot N_0 = 1F \cdot V = 1As \cdot V \cdot 96485 mol^{-1} = 96{,}485\ \frac{kJ}{mol} \tag{2.1-5}$$

The molar free enthalpy for an absorption line with the wavelength λ_{max} is calculated using Planck's quantum of action h, Eq.(2.1-6).

$$\Delta G = h \cdot \nu \frac{c}{\lambda_{max}{}_{max}} \tag{2.1-6}$$

or using the usual units of measurement, Eq.(2.1-7).

$$\Delta G = 6{,}625 \cdot 10^{-34} \mathrm{Ws}^2\ \frac{2{,}998 \cdot 10^{8} \mathrm{m}}{10^{-9}\ \frac{\mathrm{m}}{\mathrm{nm}} \cdot \lambda_{max}\ \mathrm{s}} = \frac{1{,}986 \cdot 10^{-16}}{\frac{1}{\mathrm{nm}} \cdot \lambda_{max}} \mathrm{J} = \frac{1{,}196 \cdot 10^{5}}{\lambda_{max}}\ \frac{\mathrm{nm} \cdot \mathrm{kJ}}{\mathrm{mol}} \tag{2.1-7}$$

With 10^{20} eV or 16 J each, the most energetic extragalactic particles of cosmic rays reach us. This corresponds to 10^{22} kJ/mol or an equivalent molar mass around 107000 g/mol, i.e. the mass of a macromolecule or aggregate. Since these are mostly protons, the rest mass of 1 g/mol would still have to be subtracted from it.

2.2 Water-flowing reactive compartments

2.2.1 Flow through reaction spaces in mountain formations

BUSCH et al. (1993) distinguish the volumes available in fractured aquifers (mountains) for groundwater flow into primary and secondary cavities:

- Primary cavities:

P1 Porosity of Broken rock

P2 Inclusions in the formation of chemical and biogenic sediments

P3 Gas excretions from the magma during the eruption

- Secondary cavities

S1 joint system joint set

S2 Cavities, in fracture and fracture zones

S3 Solution cavities due to

  - dissolution of water-soluble minerals or
  - chemical weathering

S4 Secondary cavities caused by organisms and crystallization

The quality distribution in aquifers is determined by certain regional or site-specific factors, such as local geology, groundwater flow and genesis. The water quality is shaped by geological boundary conditions and their genesis. In the problem areas to be considered, stable flow patterns with associated property distributions usually formed over several years (to decades), Fig. 2.2-1 The porous aquifer have predominantly primary pore systems (P1 debris pore of solidified and unconsolidated sediments).

With groundwater recharge, as a balance of precipitation, evapotranspiration and surface runoff, the water flow begins along an imaginary streamline through the pore system towards the receiving water. The flow field (streamlined course of the velocity vectors in space) is determined by the hydraulic boundary conditions, such as the stanchion level heights (water levels) and the permeability.

In the upper part of the anthropogenic influenced area (aquifer, inner - dump), a groundwater lamella is formed, which is shaped by this nature and flows down to the opencast mining lake, Fig. 2.2-1. The groundwater flowing in from the outside (aquifer, outside) and from the floor (aquifer, lying) is of a different origin.

The cavity systems of fractured-rock aquifer are composed of all the primary and secondary cavities mentioned. The groundwater flows mainly along the fissures, FigFig. 2.22.

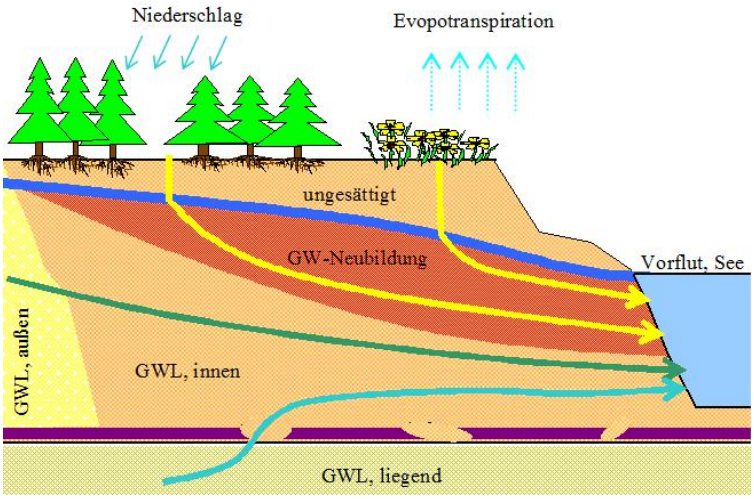

Fig. 2.2-1: Schematic section through an anthropogenically modified pore aquifer (mining dump) in the upstream of an opencast mining lake as an example of complex flow systems in pore aquifers.

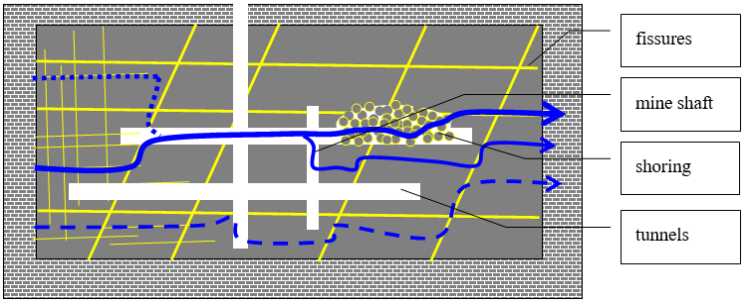

Fig. 2.22: Section through a fractured aquifer with mining relics (scheme).

In flooded mines, groundwater also preferentially flows through remaining sections, shafts and soft rock backfills (structures). Accordingly, flow distances and times vary greatly. Relatively stable current tube systems form in karst aquifers.

Bei Membranen ist der durchflossene Querschnitt im Verhältnis zur durchflossenen Wassersäule sehr groß. Prozesse auf der Membran und innerhalb der Membran lassen sich mit Einschränkungen auch als Filtration beschreiben.

2.2.2 Filtration as a flow through porous media

The term filtration is usually used for the separation of particles in equipment provided for this purpose (filters, sieves, ...). In contrast to sedimentation, the separated substances are retained in the direction of the flow and usually have to be removed there by regeneration. Sedimentation alone does not count as filtration.

Technical filters usually consist of a container filled with the filter materials (filter medium) through which the water to be treated is passed.

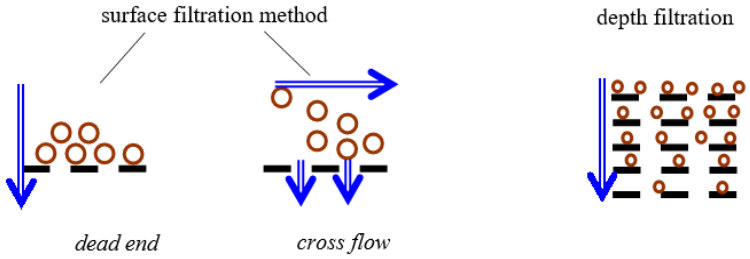

Fig. 2.23: General distinction between surface filtration and deepfiltration (GIMBEL & NAHRSTEDT 2004).

In surface filtration method the separated substances accumulate at the porous interface to the filter medium. In the process, a filter cake is formed from filtered substances, FigFig. 2.23 *Dead End*. In the *cross-flow* driving style, cake formation is largely avoided by removing part of the concentration of non-membrane-permeable substances, Fig. 2.23 *cross flow*.

In depth filtration, the colloidal or finely dispersed water constituents to be separated are retained inside, i.e. in the depth of a porous filter layer (also known as a room filter, GIMBEL & NAHRSTEDT 2004).

This particle separation takes place in sub-steps:

1. Transport of the particles inside the filter bulk from the suspension to the surface of the filter material or its loading layer until contact occurs. Various transport mechanisms are responsible for this.
2. Adhesion of the particles after contact, resulting in a stable, permanent deposit. Various adhesive mechanisms are responsible for this.

In addition,

3. biochemical reactions in the porous system cause further changes in their properties.

In a broader sense, all processes taking place in porous systems that flow through them are considered filtration processes. This opens up a common possibility of describing technical processes on the one hand and natural processes in the aquifer on the other. The process description is extended to all essential processes. As broad as the application of these processes is their description in the disciplines concerned, from chemical reaction engineering to water treatment and hydrogeology.

2.2.3 Dimensioning of porous reaction spaces (filters and aquifers)

The ones shown in Fig. 2.2-1 and Fig. 2.22 can be combined into characteristic current tubes, which are dimensioned like filters made of granular material, Tab. 2.2-1. Shown as a *black box*, the filter path describes the signal change between input and output function, or between inlet and outlet, Fig. 2.25.

The filter itself consists of the immobile solid and a mobile solution with the specific volume fraction nP(mobile). This mobile volume component reaches a maximum of the value of the porosity n_P Eq.(2.2-6) but is usually lower than that due to dead spaces or gas phase inclusions.

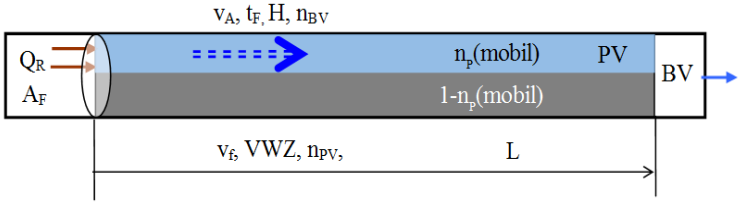

Fig. 2.24: Division of a horizontal current tube into an immobile and mobile volume fraction.

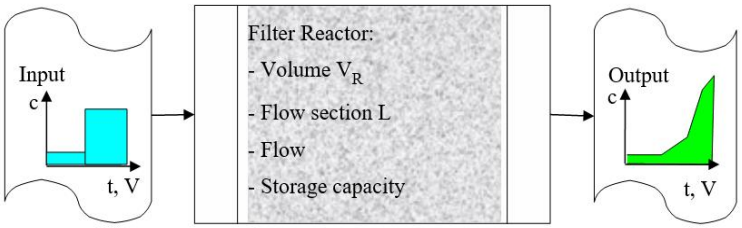

Fig. 2.25: *Black box* representation of a filter.

Tab. 2.2-1: Basic quantities of the reaction space flowing through in Fig. 2.25.

Parameter	Symbol	Units	Definition	Eq.
Length	L	m, dm		
Area of the flow cross-section	A_F	m^2, dm^2		
Reactor volume	V_R	m^3, dm^3	$V_R = A_F \cdot L$	(2.2-1)
Volume Flow, Flow	Q_R	m^3/s, m/h		
Filtration velocity	v_f	m/d, m/h	$v_f = \frac{Q_R}{A_F}$	(2.2-2)
space-time	t_F	d, h	$t_F = \frac{V_R}{Q_F} = \frac{L}{v_f}$	(2.2-3)
Water column flowing through	H	m	$H = \frac{1}{A_F}\int_{t0}^{t}(Q_R)\partial t = \int_{t0}^{t} v_f \partial t$	(2.2-4)

Technical filters are usually flowed vertically and aquifers horizontally, Fig. 2.26. The dimensioning of technical filters can be transferred to granular and non-cohesive sediments in the aquifer, Tab. 2.22.

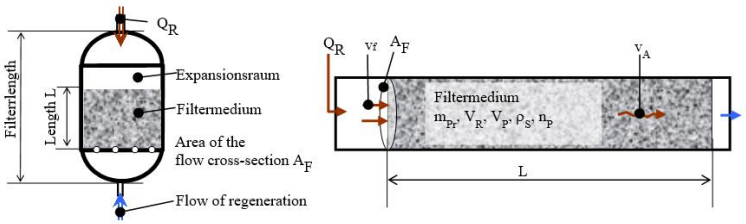

Fig. 2.26: Dimensioning of a downward-operated pressure filter (left) and a horizontally flowing power pipe in an aquifer (right).

Tab. 2.22: Basic quantities of the reaction chamber flowed through with a granular filter material, Fig. 2.26.

Parameter	Symbol	Units	Definition	Eq.
Pore volume or water volume	$V_P = V_W$	m^3, dm^3		
Solids (sample) mass	m_{Pr}	kg		
Bulk density	ρ_S	kg/dm^3	$\rho_S = \frac{m_{Pr}}{V_R}$	(2.2-5)
Pore volume	V_P	m^3, dm^3		
Porosity, specific pore volumen	n_P	1	$n_P = \frac{V_P}{V_R}$	(2.2-6)
Porosity of the particle	n_{PP}	1		
Distance velocity	v_A	m/d, m/h	$v_A = \frac{v_f}{n_P}$	(2.2-7)
residence time	VWZ	d, h	$VWZ = n_P \cdot t_F$	(2.2-8)
Solids (grain) density	ρ_{SS}	kg/dm^3	$\rho_{SS} = \frac{m_{Pr}}{V_R - V_P} = \frac{\rho_S}{(1 - n_P)}$	(2.2-9)
Phase Ratio	z	dm^3/kg	$z = \frac{V_W}{m_{Pr}} = \frac{n_P}{\rho_S}$	(2.2-10)
Interface between mobile and immobile phase (shear surface)	O_R	m^2		
Konzentration des Stoffes X	c_X	mmol/L		
Homogeneous reaction rate	r	mmol/(L·h)	$r(L, t.c_{X1}, ...)$	(2.2-11)
Amount of substance, cumulative material passage	n	mol, mmol	$n = \int_{t0}^{t} (c \cdot Q_R) \partial t$	(2.2-12)
Number of bed volumes flowed through	n_{BV}	1	für $BV = \frac{H}{L}$	(2.2-13)
Number of pore volumes flowed through	n_{PV}	1	für $PV = \frac{H}{n_P \cdot L}$	(2.2-14)

The reactor volume V_R is referred to as the filter bed volume BV. While the reaction sequence in the technical filter is often based on the number of bed volumes flowing through n_{BV} Eq.(2.2-13) geochemical simulation models refer to the number of pore volumes flowed through n_{PV}, Eq.(2.2-14) This results in different reference systems for the consideration of filtration processes:

- Flow-related approach:
  - The filtration velocity v_f Eq.(2.2-2) and the spacetime tF Eq.(2.2-3) refer to the total filter volume V_R and the total volume flow Q_R.
  - The distance velocity v_A Eq.(2.2-7) and the residence time VWZ Eq.(2.2-8) only take into account the pore volume n_P(mobile) flowing through it for the conversion.

- Integral approach:
  - The water column flowing through H Eq.(2.2-4) and the cumulative material passage Eq.(2.2-12) refer to the filter cross-section A_F and to the volume flowed through. The water exchange is determined by the number of bed volumes exchanged n_{BV} Eq.(2.2-13)).
  - When referring to the mobile solution phase, the pore volume PV Eq.(2.2-14) their exchanged number is counted as n_{PV} in the same way.
  - The reference to the solid mass is determined by the phase ratio z Eq.(2.2-10) which reduces the bulk density ρ_S Eq.(2.2-5) The phase ratio in filter mode then follows from Eq.(2.2-15).

$$z = \frac{V_W}{m_{Pr}} = \frac{H \cdot A_F}{\rho_S \cdot A_F \cdot L} = \frac{H}{\rho_S \cdot L} = \frac{\int_{t0}^{t} v_f \partial t}{\rho_S \cdot L} \tag{2.2-15}$$

Further compartmentalization and/or extension to multidimensional spaces can be carried out according to the same principles with corresponding computing capacity and with rapidly decreasing clarity.

2.2.4 Scale transitions of natural and technical reactors

Near-natural processes usually use the materials available at the respective location. The conditions explored usually determine the suitability of the location. In water treatment, narrowly classified chemically inert grains such as quartz sand/gravel, hydroanthracite, garnet sand, ilmenite, expanded clay, pumice and plastic granules are used as filter materials. Their treatment effect is caused by their pore system or active grain coatings that form. In addition, chemically active materials such as calcite, half-burnt dolomite, activated carbon and ion exchange resins are also used.

Tab. 2.2-3: Transition between natural and technical filtrations via granular media without the (bio-)chemical processes that take place in detail (u-unsaturated, g-saturated flow).

Infiltrationsverfahren	v_f Guideline values	Saturation	Evaporation/ rainfall	Kolmation	Infiltration areas
Processes					
Groundwater recharge	250 mm/a	u	Large	insignificant	Soils and biotopes
Soil filter for rainwater treatment	40 m/a	u / g	decreasing	increasing	natural soils, applied filter sand layers, vegetated and unvegetated
Low Groundwater recharge	0,5 m/d	u / g			
Groundwater flow	1 m/d	g	no	Porosity	
Slow sand filter with surface regeneration	10 m/d	g	unbedeutend	determining the procedure	
Rapid filters in water treatment	15 m/h	g	keine	*Depth filter*	Filter sands
Membrane Technology	20 mm/h	g	keine	*scaling*	Module

The complex processes can be reduced to a one-dimensional consideration of the reactive mass transport if there is a largely stationary flow field in which representative current tubes can be classified, Tab. 2.24.

With a high exchange rate of pore volume (water treatment filters, bank filtration and artificial groundwater recharge), relatively stable concentration profiles often form along the flow path. In contrast, when water bodies are displaced, complicated displacement fronts form between them, which migrate through the displaced filter area. In these cases (e.g. environmental and contaminated site problems), their pore volume is replaced only a few times. From the flow behavior determined in each case, adequate reactor models are selected for the description, chapter 3.2.

Tab. 2.24: Applications of filtration processes with reference to their process-determining processes.

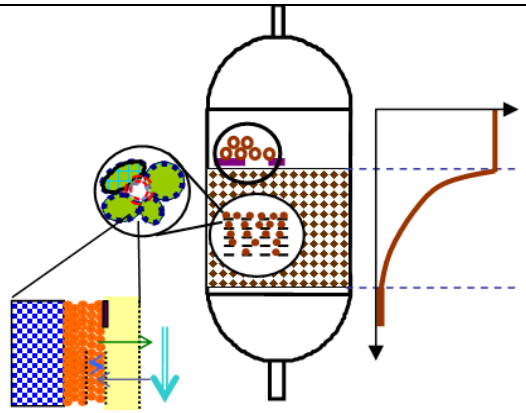	1. Technical filters: • Surface filtration, chapter 5.3, • Depth filtration, chapter 5.1, • Transport-controlled reactions at the phase interface, chapter 6.3.3, • Graindiffusion chapter • Steady-state concentration profiles, chapter 3.3.3.
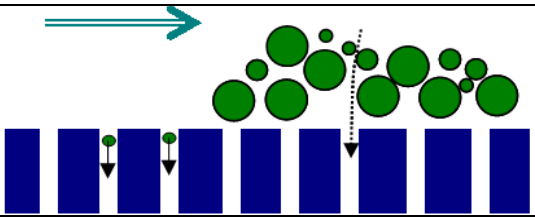	2. Membrane Technologies: • Surface filtration, chapter 5.3.

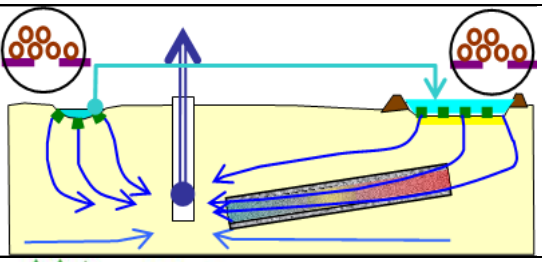	3. Artificial groundwater recharge and bank filtration: • Surface filtration, chapter 5.3 • Experiences with artificial groundwater recharge, chapter 10.4.1
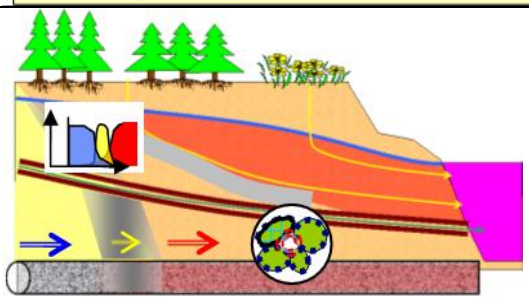	4. Contaminated sites in the pore aquifer as an opencast lignite mining dump: • Surface reactions and -equilibria, chapter 6.3 • Migration of concentration jumps, chapter 8.3.
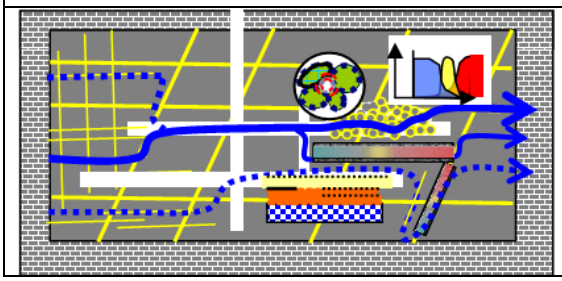	5. Fracture aquifer, flooded mine: • Transient communication with dead spaces chapter 8.3.4.

2.3 Thermodynamic basics

2.3.1 State Variables and mixed phases

The macroscopic properties of thermodynamic systems are described by state variables, which are linked to each other via state functions with state variables. A distinction is made between intensive and extensive state variables (system parameters).

- Extensive state variables change during a system division
- Intensive state variables do not change in a system division.

While in the geohydraulics of multiphase systems (BUSCH et al. 1993) DENSITY and concentrations are among the derived extensive system parameters, in chemical thermodynamics they belong to the intensive quantities. The state of mixing phases depends not only on temperature and pressure (intrinsic to the system) but also on their composition (intrinsic quantities). The parameters for describing the composition can be defined differently:

Extensive quantities are quantities of material, masses, etc.

- Intense quantities are obtained by dividing the proportion of a component by the total amount of the mixing phase. Depending on the choice of extensive reference values, mass or volume fractions or molar concentrations are obtained.

A state quantity y in a phase is described as a function of state variables, Eq.(2.3-1)

$$y = f(T, p, n_A, ...) \tag{2.3-1}$$

The changes describe the total differential of the function, Eq. (2.3-2)

$$d\,y = \left(\frac{\partial y}{\partial T}\right)_{p,ni} \cdot d\,T + \left(\frac{\partial y}{\partial p}\right)_{T,ni} \cdot d\,p + \sum_i \left(\frac{\partial y}{\partial n_i}\right)_{T,p,nj} \cdot d\,n_i \tag{2.3-2}$$

Partial molar quantities are the partial differentials of the state quantity of the respective amount of substance or concentration. The condition for a state variable is that all second mixed derivatives after the state variables are zero. Under isothermal-isobaric conditions, Eq.(2.3-3)

$$d\,y = \sum_i \left(\frac{\partial y}{\partial n_i}\right)_{T,p,nj} \cdot d\,n_i \;\text{ mit }\; \left(\frac{\partial^2 y}{\partial n_i \cdot \partial n_j}\right)_{T,p,i\neq j} = 0 \tag{2.3-3}$$

The thermodynamic state functions include enthalpy (h), entropy (s) and free enthalpy (g), as well as molar enthalpy (H), molar entropy (S) and molar gibbs enthalpy (G) in terms of substance quantity or reaction. The absolute magnitude of an object's energy cannot be given because not all components, including mass and dark energy, are quantifiable or unknown. Enthalpy, and the free enthalpy derived from it are only given as differences with respect to selected standard states, Eq.(2.3-4)

$$\begin{aligned} G &= H - T \cdot S \\ \partial G &= \partial H - T \cdot \partial S \end{aligned} \tag{2.3-4}$$

The derivatives of state variables according to the amount of substance result in the partial molar quantities Y, Eq.(2.3-5)

$$Y = \left(\frac{\partial y_j}{\partial n_i}\right)_{p,T,...} = f(c_i, c_j, p, T, ...) \tag{2.3-5}$$

The chemical potential μ is defined as the partial molar free enthalpy of a component and is related to the standard state μ^*, Eq.(2.3-6)

$$\mu_i = \mu_i^* + RT \cdot \ln(a_i) \tag{2.3-6}$$

In phase equilibrium, the chemical potentials in the phases are the same.

2.3.2 Reaction Stoichiometry

Every reaction of the starting materials A and B to the reaction products C and D can be expressed in the form of Eq.(2.3-7) or as Eq.(2.3-8) (Autorenkollektiv 1971),

$$|\nu_A|A + |\nu_B|B \rightarrow \nu_C C + \nu_D D \tag{2.3-7}$$

where the stoichiometric coefficients ν_A, ν_B of the starting materials are negatively defined and thus their substance sum results in zero, Eq.(2.3-8).

$$\nu_A A + \nu_B B + \nu_C C + \nu_D D = 0 \tag{2.3-8}$$

The macroscopic turnover of a reaction is indicated by the reaction run number ξ [mol, or mol/L], Eq.(2.3-9)

$$(\nu_1 X_1 + \nu_2 X_2 + \nu_3 X_3 + \nu_4 X_4 + ...) \cdot \xi = \xi \cdot \sum_i \nu_i X_i = 0 \tag{2.3-9}$$

Molar reaction sizes $\Delta_R Y$ are derived from the molar sizes of the reactants and the stoichiometry coefficients, Eq.(2.3-10)).

$$\Delta_R Y = \left(\frac{\partial y}{\partial \xi} \right) = \sum_i \nu_i Y_i \tag{2.3-10}$$

2.3.3 Chemical reactions and equilibria

2.3.3.1 Reaction rate and chemical equilibrium

The chemical potentials of the reactants make up the free enthalpy of the reaction, Eq.(2.3-11).

$$\Delta_R G = \nu_A \cdot \mu_A + \nu_B \cdot \mu_B + \nu_C \cdot \mu_C + \nu_D \cdot \mu_D \tag{2.3-11}$$

The energy level diagram Fig. 2.31 shows the difference between the initial and final products of a reaction. The reaction leads via an energetically higher activated complex. This energy barrier must be overcome in the event of a collision between the reaction partners before the transition complex disintegrates into the end products. The frequency of overcoming and thus the reaction rate depends on the energy distribution of the starting molecules at the reaction temperature, Eq. (2.3-12) and Fig. 2.31.

$$r = k \cdot e^{-\frac{E_A}{RT}} \cdot c_A^{\nu_A} \cdot c_B^{\nu_B} = k_{Temp\,0} \cdot \zeta_{Temp} \cdot c_A^{\nu_A} \cdot c_B^{\nu_B} \tag{2.3-12}$$

The reaction mechanisms of complex reactions can therefore usually be decomposed down to the more probable two-way interactions than elementary reactions. Irreversible reactions only take place in the direction of negative free enthalpy differences.

In chemical equilibrium, back and forth reactions take place at the same rates. The starting and end products are at the same energy level. The free enthalpy of reaction $\Delta_R G$ is therefore zero. By inserting Eq.(2.3-6) in Eq.(2.3-9) the law of mass action is derived, Eq.(2.3-13)

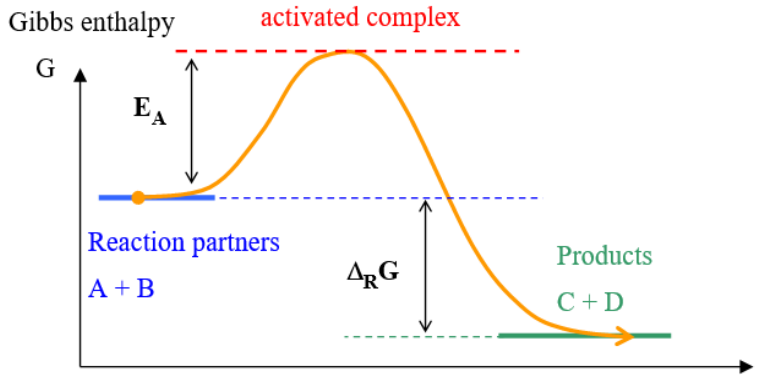

Fig. 2.31: Energy scheme of a chemical reaction ($\nu_i = 1$) with transition complex and the molar free enthalpy of the reaction $\Delta_R G$.

$$\Delta_R G = \nu_A \cdot \mu_A^* + \nu_B \cdot \mu_B^* + \nu_C \cdot \mu_C^* + \nu_D \cdot \mu_D^* + RT(\nu_A \ln(a_A) + \nu_B \ln(a_B) + \nu_C \ln(a_C) + \nu_D \ln(a_D)) \quad (2.3\text{-}13)$$

The sum of the standard chemical potentials is summarized in the free standard reaction enthalpy $\Delta_R G°$and the logarithms of the activity terms in the activity fraction, Eq.(2.3-14) The starting materials appear in the denominator because of their negative stoichiometry coefficients.

$$0 = \Delta_R G^0 + RT \cdot \ln\left(\prod_i \left(a_i^{\nu_i}\right)\right) = \Delta_R G^0 + RT \cdot \ln K \quad (2.3\text{-}14)$$

In chemical equilibrium, the fraction of activity corresponds to the general formulation of the law of mass action. The equilibrium constant is thermodynamically linked to the molar reaction enthalpy and entropy, Eq.(2.3-15)

$$\Delta_R G = \Delta_R G^0 + 2{,}303 \cdot RT \cdot \lg(K) = \Delta_R H - T \cdot \Delta_R S \quad (2.3\text{-}15)$$

From Eq.(2.3-14) follows the formulation of the equilibrium constant as a product of activity with the stoichiometry coefficients as exponents, or as a fraction of final and output components, Eq. (2.3-16)).

$$K = \prod_i a_i^{\nu_i} = \frac{a_C^{\nu_C} \cdot a_D^{\nu_D}}{a_A^{|\nu_A|} \cdot a_B^{|\nu_B|}} \quad (2.3\text{-}16)$$

2.3.3.2 Ion Activity Product IAP

The decadal logarithm of the break in activity, regardless of the equilibrium position, is also referred to as the Ion Activity Product IAP (PARKHURST & APPELO 1999), Eq.(2.3-17).

$$IAP = \frac{1}{\ln(10)} \sum_i \nu_i \cdot \ln(a_i) \quad (2.3\text{-}17)$$

Species that are in a pH or redox-dependent equilibrium (index j) are separated out as functions of their total concentrations. The equilibria are of type Eq.(2.3-18) or Eq.(2.3-19)).

$$XH \leftrightarrow X^- + H^+ \tag{2.3-18}$$

Protolysis equilibria are formed by H_2S, H_2CO_3, ... with the corresponding equilibrium-constants log(K) and pK.

$$X \leftrightarrow X^+ + e^- \tag{2.3-19}$$

From the reaction equation Eq.(2.3-17) separate pH and ORP dependent parameters follow, Eq.(2.3-20)).

$$\sum_i \nu_i \cdot \ln(X_i) + \nu_H \cdot H^+ + \nu_e \cdot e^- + \sum \nu_j \cdot f_j(pH, p\varepsilon, X_{TOT,j}) = 0 \tag{2.3-20}$$

On a redox equilibrium Eq.(2.3-19) for example, ferrous iron and ferrioc iron are linked. Often, however, only their sum c_{TOT} is known. According to the definitions of the pH and pε value for the ion activity product, the functions f_i and f_j, which contain the corresponding laws of mass action, follow from this.(2.3-21) to Eq.(2.3-24)).

$$IAP = \frac{1}{\ln(10)} \sum_i \nu_i \cdot \ln(a_i) - \nu_{pH} \cdot pH - \nu_\varepsilon \cdot p\varepsilon + \sum_j \nu_j \cdot \log f_j(a_{TOT,j}) \tag{2.3-21}$$

For i = X, or $f_i = f_{x-}$ of the protolysis equilibrium Eq.(2.3-18) follows Eq.(2.3-22)

$$f_{X^-}(a_{TOT,X}) = \frac{10^{pK-pH}}{(1+10^{pK-pH})} \cdot a_{TOT\_X} \tag{2.3-22}$$

and for j = X, or $f_j = f_{x+}$ of the redox equilibrium Eq.(2.3-19) follows Eq.(2.3-23)).

$$f_{X^+}(a_{TOT,X}) = \frac{10^{pK-p\varepsilon}}{(1+10^{pK-p\varepsilon})} \cdot c_{TOT,X} \tag{2.3-23}$$

Logarithmized follows Eq.(2.3-24) shown in Fig. 2.32.

$$\lg(a_{X-}) - \log(a_{TOT\_X}) = \log\left(\frac{10^{pK-pH}}{(1+10^{pK-pH})}\right) \text{ für pH und pε} \tag{2.3-24}$$

For

- pK-pH<<-1.5, species X has no influence on IAP and
- pK-pH >> 1.5, there is a linear influence of the total activity/concentration.

Valid for pH or pε.

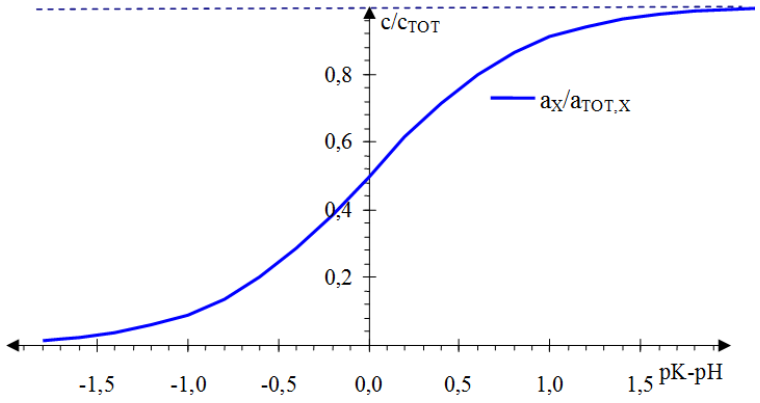

Fig. 2.32: Relationship between the differences (pK-pH) and (pK-pε).

2.3.3.3 Application of the total differential of the ion activity product IAP to error considerations

The influence of deviations in the input data is described by the total differential, Eq.(2.3-25),

$$\partial IAP = \frac{1}{\ln(10)} \sum_i \nu_i \cdot \frac{\partial a_i}{a_i} - \nu_{pH} \cdot \partial pH - \nu_\varepsilon \cdot \partial p\varepsilon + \sum_j \nu_j \cdot \frac{\partial a_{TOT,j}}{a_{TOT,j}} + \sum_j \nu_j \cdot \left(1 - \frac{1}{\left(1 + 10^{pK_l - pH|p\varepsilon}\right)}\right) \cdot \partial pH \,|\, p\varepsilon \tag{2.3-25}$$

whereby the pH|pε-dependent term is often either close to zero or close to one, depending on the milieu. The relative differences or errors [1, %] of the activities correspond to those of the concentrations, Eq.(2.3-26)).

$$\frac{\partial a_i}{a_i} \approx \frac{\partial c_i}{c_i} \tag{2.3-26}$$

To consider errors, the absolute values of the terms in the total differential are summed up (error propagation), Eq.(2.3-27)).

$$\Delta IAP = \frac{1}{\ln(10)} \sum_i |\nu_i| \cdot \frac{\Delta c_i}{c_i} + |\nu_{pH}| \cdot \Delta pH + |\nu_\varepsilon| \cdot \Delta p\varepsilon + \sum_j |\nu_j| \cdot \frac{\Delta c_{TOT,j}}{c_{TOT,j}} + \sum_j |\nu_j| \cdot \left(1 - \frac{1}{\left(1 + 10^{pK_l - pH|p\varepsilon}\right)}\right) \cdot \Delta pH \,|\, \Delta p\varepsilon \tag{2.3-27}$$

The relative (Δc/c) and absolute (ΔpH, Δpε) errors are always to be used positively.

2.3.4 Energetic size ranges

The (bio-)chemical reactions in the environment and nature take place in a broad energetic spectrum, Fig. 2.33.

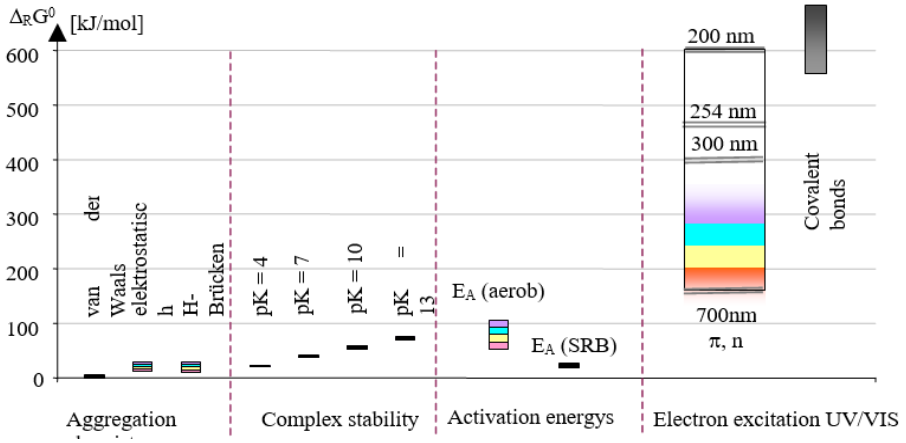

Fig. 2.33: Gibbs standard reaction enthalpies $\Delta_R G^0$ for different interactions and activation energies E_A compared to electromagnetic radiation (right).

The gibbs enthalpies of reactions lie in the following ranges:

- 2,5 kJ/mol: van-der-Waals-Kräfte in hydrophobic areas,
- 12-29 kJ/mol: electrostatic interactions of acid functions with complex-forming cations (Ca^{2+}, ...)
- 10-30 kJ/mol: Hydrogen bonds, mainly between hydroxyl groups
- Stability constants of complexes or associates (pK) can be converted into free standard enthalpies of formation, Eq.(2.3-28).

$$\Delta_R G^{\varnothing} \approx 5{,}61 \frac{\text{kJ}}{\text{mol}} \cdot \text{pK} \qquad (2.3\text{-}28)$$

- The microbiological activation energies E_A refer to the values listed in chapter 6.1.3.3 Temperature dependence of aerobic degradation processes (aerobic) and anaerobic sulfate reduction (SRB) described above.
- The energy of light quanta extends over the region of excitation of π and n-electrons.
- Covalent chemical bonds are only excited to fission from the vacuum UV ($\lambda < 200$ nm).
- Peak values are released during radioactive decay in the form of ionizing gamma radiation, ranging from tritium (1.8 GJ/mol) to radium and uranium-238 (around 450 GJ/mol) to plutonium (560 GJ/mol).

A high number of individual compounds between the macromolecules in aggregates results in an effectively high free bond enthalpy. LATTNER (2003), for example, demonstrates the stabilization of anionic macromolecules (alginate) by cations, Fig. 2.34. This mechanism stabilizes many organic and inorganic molecular associations and shapes their pH- and electrolyte-dependent mobility behavior.

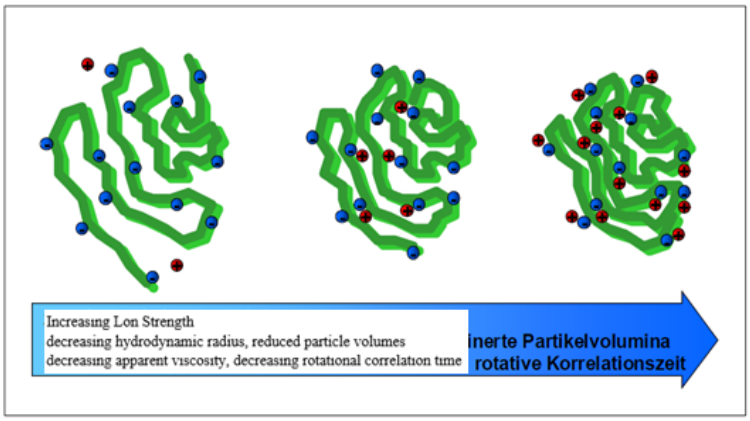

Fig. 2.34: Conformational change of a polymer as a function of the cation concentration; blue: carboxyl groups, red: cations (Li+) (Scheme according to LATTNER 2003).

2.3.5 Description of complex mixtures of substances (continuous thermodynamics)

2.3.5.1 Problem

Complex are multi-substance mixtures that contain a very large number of chemically similar components. Due to the large number of similar molecule species, it is difficult or practically impossible to determine them analytically, qualitatively or quantitatively. This is why they are also described as *substance continuums*. Variables used include the boiling temperature of hydrocarbons in petroleum distillation or the degree of polymerization in synthesis. Groups of substances with distinguishable properties can be grouped into pseudo-components. The concentration is usually determined by sum parameters, such as the DOC ... .

2.3.5.2 One-dimensional material distributions

One-dimensional material distributions are only distributed by a property parameter (x), Eq.(2.3-29)).

$$\partial c(x) = c_{TOT} \cdot f(x) \cdot \partial x \tag{2.3-29}$$

with

x = Distribution parameter (property) with $-\infty < x < +\infty$

c_{TOT} = Total concentration of the component

Here, the integral of the distribution function is defined by one over the definition range of x (e.g. Gaussian distribution), Eq.(2.3-30).

$$\int_{-\infty}^{+\infty} f(x) \cdot \partial x = 1 \tag{2.3-30}$$

The first derivative of the sum function describes the corresponding density distribution of the substances as a function of the selected parameter. The discretized density function is calculated from the difference coefficients of the sum function with a mostly unusual unit, Eq.(2.3-31).

$$\rho(x) = \frac{\Delta c}{\Delta x} \tag{2.3-31}$$

Often, properties are normally distributed around a fixed value xm with a standard deviation σ, Eq.(2.3-32),

$$\rho = \frac{\partial Y}{\partial x} = \frac{1}{\sigma \cdot \sqrt{2\pi}} \cdot \exp\left[-\frac{(x - x_m)^2}{2\sigma} \right] \tag{2.3-32}$$

or are composed of several normal distributions that can be separated as pseudocomponents. Partial molar quantities of substance distributions describe functional relationships. Partial (molar) quantities can also be determined for pseudocomponents, but with reference to their respective concentration basis (DOC, E_{254}, ...), Eq.(2.3-33).

$$Y = \left(\frac{\partial y}{\partial n_i} \right)_{p,T,\ldots} = \frac{1}{V} \left(\frac{\partial y}{\partial c_i} \right)_{p,T,\ldots} = \frac{1}{V} \left(\frac{\partial y}{c_{TOT} \cdot f(x) \cdot \partial x} \right)_{p,T,\ldots} \tag{2.3-33}$$

After multiplying by the volume V, a substance quantity equivalent of the pseudocomponent is obtained. This procedure can be transferred to multidimensional material distributions.

2.3.5.3 Set-theoretic prerequisites for the definition of pseudocomponents

Pseudo-components are subsets of a mixture of substances that meet specified criteria. Each unit of substance (molecule, ion, aggregate) can be regarded as an element of the amount of substance. The *set-theoretic mapping* of the mixture, or its fractions, to the set of natural numbers results in their extensive distribution function, i.e. the number of associated elements is assigned to each point in the multidimensional property space (SCHÖPKE 2007).

The set-theoretic prerequisites for pseudocomponents (Gemisch) are fulfilled if the entire definition range of a property can be divided into non-overlapping sections. For the classification of a mixture of substances into two pseudo-components, their intersection must always result in an empty set.

$$\begin{aligned} &\text{Gemisch} = A \cup B \\ &A \cap B = \varnothing \end{aligned} \tag{2.3-34}$$

This allows pseudo-components to be treated in the same way as homogeneous substances. For the (pseudo-) component i with its measured value y_i and its base concentration, Eq.(2.3-35)),

$$\partial y_i = \left(\frac{\partial y_i}{\partial n_i} \right) \cdot \frac{\partial n_i}{V} = Y_i \cdot \partial c_i \tag{2.3-35}$$

where c stands for the sum parameter used to quantify the pseudocomponent.

2.3.6 Properties of the flowing medium water

2.3.6.1 Density of water

The density of water depends on the temperature, pressure and composition of the water. In particular, the dissolved ingredients (salts and gases) cause density differences between mineralized and pure water. In the case of high-precision investigations, the isotopecompositionof the water, including the proportion of the heavy isotopes ^{18}O and ^{2}H (deuterium), must also be taken into account.

GRÖSCHKE (2007) researched the calculation of the density of pure, gas-free water ρ_0 for the following parameters:

- Air pressure p_0 = 1013,25 hPa
- Hydrostatic pressure p_h = 0 Pa and
- Salinity

Salinity SAL is the total mass of dissolved salts per unit mass of aqueous solution. According to Chen & Millero (1986, quoted in GRÖSCHKE 2007), the

Density ρ_W [g/cm³],

when specifying the

Temperature Temp [°C],

Pressure p_h [bar],

Salinity SAL [g/kg]

via polynomials of the nth degree, Eq.(2.2-1) to Eq.(2.2-3).

$$\rho_0 = \sum_{n=0}^{6} a_n \cdot Temp^n \tag{2.3-36}$$

$$\rho_W = \left(\rho_0 + SAL \cdot \sum_{n=0}^{2} \left(b_n \cdot Temp^n \right) \right) \cdot \left(1 - \frac{p_h}{K} \right)^{-1} + \Delta\rho_{Gas} \quad [g/cm^3] \tag{2.3-37}$$

$$K = \sum_{n=0}^{4} \left(c_n \cdot Temp^n \right) + \rho_h \cdot \sum_{n=0}^{2} \left(d_n \cdot Temp^n \right) + SAL \cdot \left(53{,}238 - 0{,}313 \cdot Temp + 0{,}005728 \cdot \rho_h \right) \quad [bar] \tag{2.3-38}$$

Mit den Koeffizienten wurde eine Excel-function für die Anwendung formuliert, Tab. 2.31.

Tab. 2.31: Coefficients for the Eq.(2.3-36) to Eq.(2.3-38). Further density calculations are provided by LERMAN et al. (1995).

Koeff.							
	0	1	2	3	4	5	6
a_n	0,9998395	$6{,}7914 \cdot 10^{-5}$	$-9{,}0894 \cdot 10^{-6}$	$1{,}0171 \cdot 10^{-7}$	$-1{,}2846 \cdot 10^{-9}$	$1{,}1592 \cdot 10^{-11}$	$-5{,}0125 \cdot 10^{-14}$
b_n	$8{,}181 \cdot 10^{-4}$	$-3{,}85 \cdot 10^{-6}$	$4{,}96 \cdot 10^{-8}$				
c_n	$1{,}965217 \cdot 10^{4}$	$1{,}48113 \cdot 10^{2}$	-2,293	$1{,}256 \cdot 10^{-2}$	$-4{,}18 \cdot 10^{-5}$		
d_n	3,2726	$-2{,}147 \cdot 10^{-4}$	$1{,}128 \cdot 10^{-4}$				
e_n	-68,0	18,209	-0,30866	$5{,}3445 \cdot 10^{-3}$	$-6{,}0721 \cdot 10^{-5}$	$3{,}1441 \cdot 10^{-7}$	
f_n	4,599	-0,1999	$2{,}79 \cdot 10^{-3}$				
g_n	0,3682	$-1{,}52 \cdot 10^{-2}$	$1{,}91 \cdot 10^{-4}$				
h_n	50,885	-0,38364	$8{,}7185 \cdot 10^{-3}$	$-1{,}2519 \cdot 10^{-4}$	$1{,}3488 \cdot 10^{-6}$	$-6{,}744 \cdot 10^{-9}$	
i_n	-0,1317	$2{,}732 \cdot 10^{-3}$	$-3{,}78 \cdot 10^{-5}$				
j_n	$-1{,}446 \cdot 10^{-2}$	$2{,}082 \cdot 10^{-4}$	$-3{,}83 \cdot 10^{-6}$				

2.3.6.2 Viscosity of water

Viscosity is a measure of the viscosity of a fluid. The greater the viscosity, the thicker (less flowable) the fluid; the lower the viscosity, the thinner (more flowable) it is, so it can flow faster under the same conditions. The temperature dependence for the dynamic viscosity η [Pa·s, kg/(m·s)] uses the WORCH (1993) in connection with the calculation of diffusion coefficients, Eq.(2.3-39).

$$\lg\left(\frac{\eta_{20}}{\eta}\right) = \frac{1{,}37023(\text{Temp} - 20°\text{C}) + 8{,}36 \cdot 10^{-4}(\text{Temp} - 20°\text{C})^2}{109°\text{C} + \text{Temp}} \qquad (2.3\text{-}39)$$

mit

$$\eta_{20} = 1{,}0019 \cdot 10^{-3}\,\text{Pa} \cdot \text{s}$$

The kinematic viscosity ν_X [m²/s] of a medium X is the quotient of the dynamic viscosity η_X and the fluid density ρ_X, Eq.(2.3-40)).

$$\nu_X = \frac{\eta_X}{\rho_X} \qquad (2.3\text{-}40)$$

The temperature dependence in the range (4°C < Temp < 30°C) is approximately linear, Eq.(2.3-41).

$$\frac{\nu_{20°\text{C}}}{\nu_{\text{Temp}}} \approx 0{,}5363 + 0{,}0238 \cdot \text{Temp} \qquad (2.3\text{-}41)$$

2.3.6.3 Molecular diffusion coefficients

For the estimation of mass transfers, knowledge of the molecular diffusion coefficient or constant is necessary. In aqueous media, the diffusioncoefficients of inorganic ions are in the order of 10^{-9} m²/s. WORCH (1993) compared a Wilke-Chang approach with data sets from the literature and found a correlation for low molecular weight organic

substances (56 g/mol < M < 407 g/mol), Eq.(2.3-42) This approach is probably also approximately applicable to higher molecular weight substances (>2000g/mol).

$$D_f = 3{,}595 \cdot 10^{-14} \cdot \frac{T}{\eta \cdot M^{0{,}53}} \left[m^2 s^{-1} \frac{Pa \cdot s (g/mol)^{0{,}53}}{K} \right] \tag{2.3-42}$$

With the temperature dependence for the dynamic viscosity η Eq.(2.3-39)).

SIRIPINYANOND et al. (2005) calculate the diffusion coefficients of humic aggregatesas a function of their hydrodynamic particle diameter d_K[nm], Eq.(2.3-43)).

$$D = \frac{k_B \cdot T}{3 \cdot \pi \cdot \eta \cdot d_K} \tag{2.3-43}$$

With the Boltzmann constant k_B (Tab. 2.1-2) and as a workingequation for 20° C Eq.(2.3-44)).

$$D_{20°C} = \frac{1{,}38 \cdot 10^{-23} \frac{kg \cdot m^2}{s^2 \cdot K} \cdot 293{,}15K}{3 \cdot \pi \cdot 1{,}0019 \cdot 10^{-3} \frac{kg}{s \cdot m} \cdot 10^{-9} m \frac{d_k}{nm}} = 4{,}286 \cdot 10^{-10} \frac{m^2}{s} \cdot \frac{1nm}{d_K} \tag{2.3-44}$$

Alternatively, BALCH & GUÉGUEN (2015) give the diffusion constant of humic and fulvic acids as a function of the molar mass for 25°C.(2.3-45)

$$D = 1{,}1 \cdot 10^{-7 \cdot} \frac{m^2}{mol} \cdot \left(\frac{M}{g/mol} \right)^{-0{,}81} \quad | r^2 = 0{,}78 \tag{2.3-45}$$

BUFFLE et al. (2007) compiled various computational approaches required for the three main types of chelating agents in aquatic systems and derived diffusion coefficients for inorganic ions:

- small ligands, Tab. 2.3-2,
- kolloid *partikles* or aggregates Eq.(2.3-46), and
- fulvischin and humin substances, BUFFLE et al. (2007).

$$D = 2{,}84 \cdot 10^{-9} \frac{m^2}{s} \cdot \left(\frac{M}{g/mol} \right)^{-1/3} \tag{2.3-46}$$

For various complexes with organic substances, including humic substances, even more complicated calculation methods are presented. When comparing the compiled diffusion coefficients, considerable differences are noticeable.

Tab. 2.3-2: Von BUFFLE et al. (2007) researched diffusion coefficients of hydrated inorganic cations and anions in water at T = 298.15 K and infinite dilution.

Kation	D	Kation	D	Anion	D	Anion	D
	10^{-10} m²/s		10^{-10} m²/s		10^{-10} m²/s		10^{-10} m²/s
H_3O^+	93,11	K^+	19,57	OH^-	52,7	PO_4^{3-}	6,1
Ag^+	16,48	La^+	6,19	$H_2AsO_4^-$	9,05	HPO_4^{2-}	7,59
Al^{3+}	5,41	Li^+	10,29	Br^-	20,8	$H_2PO_4^-$	9,59
Ba^{2+}	8,47	Mg^{2+}	7,06	CO_3^{2-}	9,2	HS^-	17,3
Be^{2+}	5,99	Mn^{2+}	7,12	HCO_3^-	11,9	SCN^-	17,58
Ca^{2+}	7,92	Na^+	13,34	Cl^-	20,3	SO_3^{2-}	9,59
Cd^{2+}	7,19	NH_4^+	19,57	ClO_4^-	17,92	HSO_3^-	13,31
Co^{2+}	7,32	Ni^{2+}	7,05	F^-	14,8	SO_4^{2-}	10,7
Cr^{3+}	5,95	Pb^{2+}	9,45	$Fe(CN)_6^{3-}$	8,96	HSO_4^-	13,3
Cs^{3+}	20,56	Tl^+	19,89	$Fe(CN)_6^{4-}$	7,35	$S_2O_3^{2-}$	11,32
Cu^{2+}	7,14	Tl^{3+}	6,1	I^-	20,45		
Fe^{2+}	7,19	Zn^{2+}	7,03	IO_3^-	10,78		
Fe^{3+}	6,04			MnO_4^-	16,32		
Hg^{2+}	8,47			NO_3^-	19,02		
Hg_2^{2+}	9,13						

2.3.6.4 Ionic strength and electrical conductivity

Polyvalently charged ions have a greater influence on the environmental properties of aqueous solutions. This takes into account the ionic strength I [mol/L], which is defined as the charge-weighted ion concentration, Eq.(2.3-47)).

$$I = 0{,}5 \cdot \sum \left(z_i^2 \cdot c_i \right) \tag{2.3-47}$$

with z_i= number of charges and c_i= concentration of ions.

Compared to the unweighted ion concentration, (mostly nonlinear) relationships are derived from the ionic strength, among other things, to electrical conductivity and activity constants. The experimentally determined conductivity LF (*electrical conductivity* EC) [mS/cm, mS/cm] captures the contributions of all ions moving in solution and is used as an orienting measure for the ion concentration and strength. In water chemistry, the measured value is converted to 25 °C. Due to the different equivalent conductivities of the individual ions, there is no simple relationship between the measured conductivity and the salinity of the solution.

3 Model Basics for Filter Reactors

3.1 Material balances

3.1.1 General balance equation for reactive mass transport

The filtration processes are described using the general balance equation, Eq.(3.1-1)

Change in concentration = Convection element + Diffusion element + Reaction element (3.1-1)

or as a partial differential equation, Eq.(3.1-2).

$$\dot{c} = \left(\frac{\partial}{\partial t} c\right)_L = -\mathrm{div}\left(\vec{v} \cdot c\right) + \mathrm{div}\left(D \cdot \mathrm{grad}(c)\right) + r(\vec{c}) \tag{3.1-2}$$

mit

$\vec{v}$ = Velocity Vector

D = Diffusion coefficient (vector)

r = Sources, sinks and reactions

The convection element balances the material flows via the divergence of the current vectors, in the three spatial dimensions and the concentration at the point (x, y, z) as a scalar quantity, Eq.(3.1-3)

$$\mathrm{div}\left(\vec{v} \cdot c\right) = \nabla\left(\vec{v} \cdot c\right) = \left(\frac{\partial\left(v_x \cdot c\right)}{\partial x} + \frac{\partial\left(v_y \cdot c\right)}{\partial y} + \frac{\partial\left(v_z \cdot c\right)}{\partial z}\right) \tag{3.1-3}$$

A positive divergence means a negative material balance, which is seen as a negative sign in Eq.(3.1-2)

Diffusion takes place in the direction of the decreasing concentration gradient. In multidimensional space, the concentration gradient represents a vector, Eq.(3.1-4)

$$\mathrm{grad}(c) = \left(\frac{\partial c}{\partial x}, \frac{\partial c}{\partial y}, \frac{\partial c}{\partial z}\right) \tag{3.1-4}$$

The gradient is the partial derivative of the concentration according to the spatial coordinates. The diffusive material flow results from the product with the direction-dependent diffusion coefficient. When balancing the diffusive material flows over the divergence, two negative signs (concentration gradient points against the direction of diffusion) cancel each other out, Eq.(3.1-2) Instead of diffusion, the term dispersion is used when looking at flow sections, which combines diffusion and convective remixing with the same formal description.

The source/sink term r(x, y, z, $\vec{c}$) contains reactions. The general balance equation Eq.(3.1-2) belongs to the linear inhomogeneous partial differential equationsystems. Under uniform flow and diffusion conditions, as in ideal filtration, it is reduced to a system of equations with constant constants and the source/sink term r(x, y, z,) describing the inhomogeneity $\vec{c}$ (KUNTZMANN 1970). Analytical solutions exist only for highly simplified special cases. By returning to analytical solution approaches, the application of numerical simulation methods is to be causality-related and the interpretation of measured values is to be simplified.

3.1.2 Multidimensional complex problems

With today's performance of computingtechnology, complex problems can be solved numerically. The temporal changes of a multidimensionalconcentration distribution are summarized in a partial differentialequationsystem in vector notation, Eq.(3.1-5).

$$\left(\dot{\vec{c}}\right)=\left(\frac{\partial}{\partial t}\vec{c}\right)_{x,y,z}=\vec{f}(x,y,z,t,...) \tag{3.1-5}$$

The temporal change of the three-dimensional concentration field, Eq.(3.1-6).

$$\vec{c}(x,y,z,t)=\vec{F}(x,y,z,t)=\int_{t=0}^{t}\iiint_{x,y,z}\vec{f}(x,y,z,...)\cdot\partial x\cdot\partial y\cdot\partial z\cdot\partial t \tag{3.1-6}$$

The numerical solution methods discretize the space through grids and translate the problem into difference equations that are integrated from an initial configuration in discrete time steps.

$$\vec{c}(x,y,z,t)=\vec{F}(x,y,z,t)=\sum_{t=0}^{t}\sum_{x,y,z}\vec{f}(x,y,z,...)\cdot\Delta x\cdot\Delta y\cdot\Delta z\cdot\Delta t \tag{3.1-7}$$

There are a large number of methods and computational implementations. The disadvantage of complex simulation calculations is their large amount of data in the solutions. Rows of scenarios with different boundary conditions and parameters can be calculated. The number of degrees of freedom grows into the unmanageable, as does the flood of data of the results. Individual scenarios differ only marginally. Ultimately, simulation results are evaluated again as original data from measurement series and causal relationships are even found. Examples of applications include the simulation of weather and climate phenomena, processes in aquatic systems or reactions in fluidized beds and combustion chambers.

3.1.3 An overview of the particulate solutions of the balance equation

For the consideration of reactions in the flowing pore solution in filters or aquifers, useful simplifying analytical partial solutions, so-called particulate solutions, can be found instead of sprawling numerics. Particulate solutions are usually contained in the special solutions and can often be found in them, Tab. 3.11. For a one-dimensional flow of flow length L, Eq.(3.1-2) to Eq.(3.1-8).

$$-\operatorname{div}\left(\vec{v}\cdot c\right)=-\frac{v_f}{n_P}\cdot\frac{\partial c}{\partial L} \tag{3.1-8}$$

For a one-dimensional filter flow (L, v_f) in a porous system with the distance velocity v_A Eq.(2.2-7) the partial differential equation of the second order with the axial diffusion coefficient D_L, Eq.(3.1-9).

$$\dot{c}=\left(\frac{\partial}{\partial t}c\right)_L=\frac{v_f}{n_P}\cdot\frac{\partial c}{\partial L}+\frac{\partial c}{\partial L}\left(D_L\cdot\frac{\partial c}{\partial L}(c)\right)+r(\vec{c})=v_A\cdot\frac{\partial c}{\partial L}+D_L\cdot\frac{\partial^2 c}{\partial L^2}+r(\vec{c}) \tag{3.1-9}$$

Reactions with the solid matrix can be defined from the extension to a diffusive interaction (D_y) perpendicular to the direction of flow with a source/sink.

If several substances reacting with each other are considered, the interaction of which is contained in the reaction term (source/sink), an inhomogeneous partial differential equation system is created, for which analytical solutions can only be found under further restrictions.

- Analytical solution for the non-reactive mass transport of a concentrationjump as an initialcondition at the inlet.

$$r = 0 \tag{3.1-10}$$

The solution is the dwell time spectrum, chapter 3.1.4. From this solution, or a discretization of the flow section, the various reactor models used in process engineering are derived, chapter 3.2.

For steady-state concentration profiles, Eq.(3.1-11) as a restriction, chapter 8.2.

$$\dot{c} = \left(\frac{\partial}{\partial t} c\right)_L = 0 = v_A \cdot \frac{\partial c}{\partial L} + D_L \cdot \frac{\partial^2 c}{\partial L^2} + r(c) \tag{3.1-11}$$

- If the mass transport takes place in chemical equilibrium with the stationary solid phase, the migrating transition fronts form.

Complex reaction mechanisms can also often be numerically simulated as transition fronts and their migration can be considered via the particulate solution of the residence time behavior, chapter 3.2 and chapter 8.3.3.

For this purpose, a three-dimensional, temporally homogeneous flow field is reduced to representative parallel current tubes, which individually describe mostly similar concentration curves at different temporal processes. For the one-dimensional numerical solution, the geochemical calculation program PHREEQC3 PARKHURST & APPELO (2013) or a newer version is recommended, pt. 3.3.1. This includes extensive basic data sets that simulate one-dimensional transport using a mixed cell approach (pt. 3.2.3) and programmable reaction kinetics. Expansion to up to three room dimensions is possible.

Tab. 3.11: Particular solutions with reference to the explanations.

Residence Time and Reactor Models	Explanation
	Residence time as a Non-Reactive Transport Problem $r(\vec{c}) = 0$, chapter 3.1.4
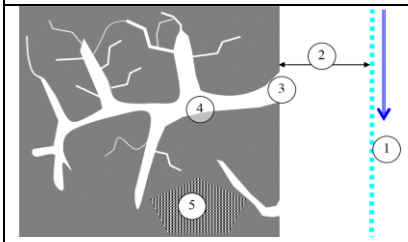	1 Advection on the shear surface v_A [m/s] Chapter 3.2 und Chapter 3.5 Diffusion by: 2 Prandl'sche boundary layer δ [µm] Chapter 3.6 3 Grain porosity, macro to micropores Chapter 4.1.3 4 Grain boundary diffusion chapter 3.7 5 Grain structures Chapter 4.2

Residence Time and Reactor Models	Explanation
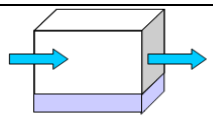	Zero Dimensional continuous reactor Residence Time: $r(\vec{c}) = 0$, Chapter 3.2.1
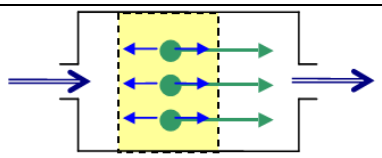	One-dimensional continuous flow tube Residence Time: $r(\vec{c}) = 0$, Chapter 3.2.2
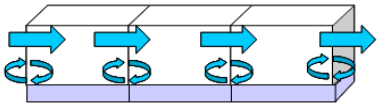	One-dimensional mixed cells Residence Time: $r(\vec{c}) = 0$, Chapter 3.2.3 Numerical simulation of one-dimensional reactive mass transport
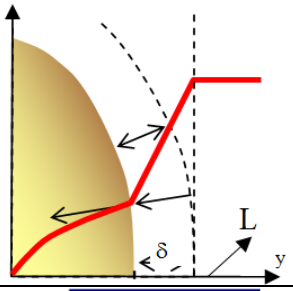	Transport-controlled mass transfer orthogonal to convective transport, $r_O(\vec{c}) = \frac{D_y}{\delta} \cdot (c_O - c)$, Chapter 3.6
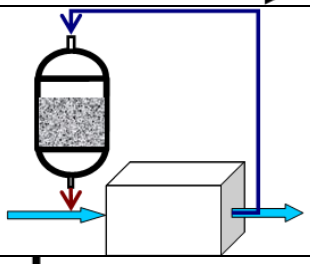	Continuous loop reactor with differential filter $r(\vec{c}) \neq 0$, Chapter 3.3.2
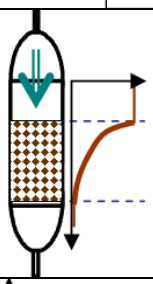	Steady-Stateone-dimensional concentration profiles $D_y \neq 0$, $r(\vec{c}) \neq 0$, $\dot{c} = \left(\frac{\partial}{\partial t} c\right)_L = 0$, Chapter 3.3.3
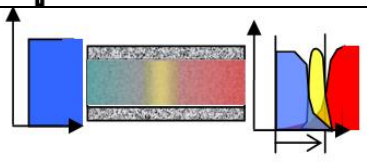	Retardation in chemical equilibrium, $D_L \rightarrow 0$, $\vec{c}_{Gl}$ Migration of ideal jumps of concentration, Chapter 8.3 Loading fronts in adsorption filters, Chapter 8.3.2.2
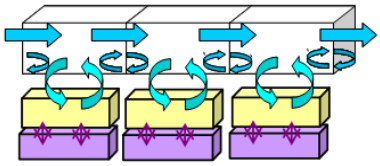	Diffusively coupled dead spaces as a dual-porosity model $D_y \neq 0$, Chapter **Fehler! Verweisquelle konnte nicht g efunden werden.**
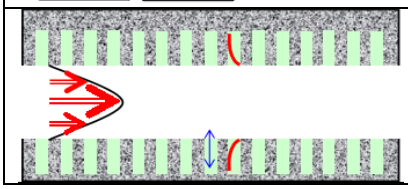	Penetration depth $\vec{c}_y(L,t)$ into diffusively coupled dead spaces $D_y \neq 0$, Chapter 8.3.4

Residence Time and Reactor Models	Explanation
Hydraulik	
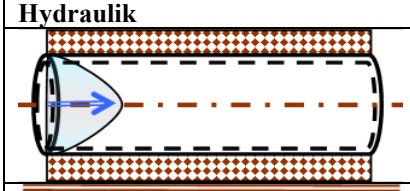	Hydraulics of laminar flow through pore channels, Chapter 3.5
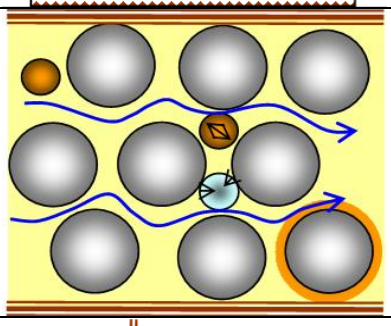	Hydraulics for reactions in the pore system through which the flow, Chapter 5.2
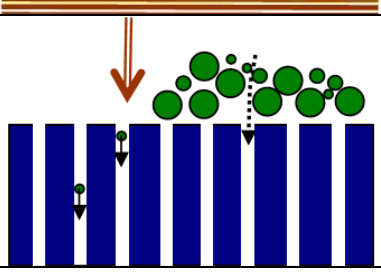	Hydraulics of the surface filtration layer (Sieve effects), Chapter 5.3
????	
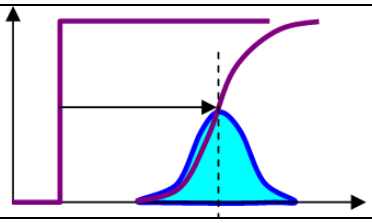	Residence time spectra as a particulate solution to the non-reactive transport problem, Chapter 3.1.4 and Chapter 9.7

3.1.4 Residence time spectra as tracer balances

The spacetime t_F Eq.(2.2-2) is a fictitious quantity that is calculated from the pore volume flowed through V_W and the volume flow Q_R. Taking into account a uniform pore volume, the mean residence time VWZ Eq.(2.2-8) as the expected value for the flow time through the filter. Transport and mixing processes (dispersion) take place in real filters and in the pore channel system, Eq.(3.1-2) The residence times of all particles that pass through the reactor form the residence time spectrum.

The residence time density function $\rho(t)$ gives the probability $\rho(t)\cdot\Delta t$ as a solid element in the range (t ... t+Δt), Eq.(3.1-12) The value of the (integral) residence time sum function F(t) represents the proportion of the volume elements that have left the reactor by time t after their addition at time zero, Eq.(3.1-12).

$$F(t)=\int_0^t \rho(t)\partial t \quad \text{bzw.} \quad \rho(t)=\frac{\partial F}{\partial t} \tag{3.1-12}$$

Both representations can be converted into each other by differentiation or integration.

Tracers are used to measure residence time functions, which are fed into the inlet current of the reactor in a certain way (entry signal, *input* function) and whose concentration is measured at the reactor outlet or another position of the reactor (exit signal, *output* function, Fig. 2.25).

Without a reaction link, Eq.(3.1-9) into a homogeneous differential equation with constant coefficients, which describes the residence time behavior, Eq.(3.1-13) By appropriately formulating the input function boundary conditions, the residence time behavior can be solved analytically, Fig. 3.11.

$$\dot{c} = v_A \cdot \frac{\partial c}{\partial L} + D_L \cdot \frac{\partial^2 c}{\partial L^2} \qquad (3.1\text{-}13)$$

➢ The jump function

At time $t = t_0$, the inlet current at L=0 with the concentration c_0 is replaced by an equal current with constant concentration c_1, which displaces the solution present in the reactor as a jump function (RAUSCH et al. 2002), Eq.(3.1-14).

$$c\ (t) = \begin{cases} c_0 \text{ für } t < t_0 \\ c_1 \text{ für } t \geq t_0 \end{cases} \qquad (3.1\text{-}14)$$

Alternatively, the tracer-containing current can be replaced by a tracer-free current.

➢ Impulse function

The momentum as *a Dirac function* δ represents the differentiated jump function in which the tracer is added in an infinitesimally short time, Eq.(3.1-15),

$$c(x, t=0) = \frac{\Delta n}{A_F} \cdot \delta(x) \qquad (3.1\text{-}15)$$

with Δn = the amount of *substance added in* the input.

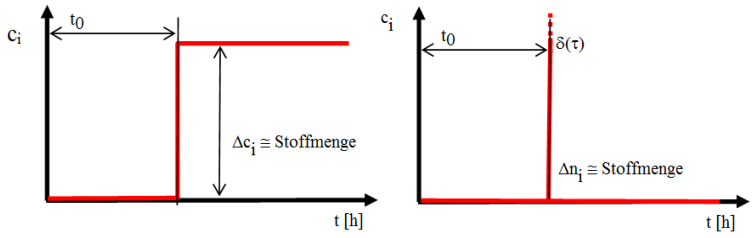

Fig. 3.11: Jump function (left) and the Dirac function (right).

$$(L=0, t=0) \Rightarrow t_0 = 0 \qquad (3.1\text{-}16)$$

Under the boundary condition Eq.(3.1-16) on the flow path the *input functions are converted* into Gaussian residence time distributions by t_{eff} with the variance σ^2, System-output Fig. 3.12.

From the *input* of the jump function with the initial condition Eq.(3.1-16) is followed by the integrated solution Eq.(3.1-17),

$$F(t) = c(L,t) = \frac{c_0}{2}\,\mathrm{erfc}\left(\frac{L - v_A \cdot t}{2\sqrt{D \cdot t}}\right) \tag{3.1-17}$$

with the Gaussian error integral Eq.(3.1-18).

$$\mathrm{erfc}(x) = 1 - \mathrm{erf}(x) = 1 - \frac{2}{\sqrt{\pi}}\int_0^x e^{-\xi^2}\,\partial\xi \tag{3.1-18}$$

The particular solution of the balance equation Eq.(3.1-9) for the empty conduit ($v_A = v_f$) describes Eq.(3.1-19) The time is determined by the flowing water column H Eq.(2.2-4) The residence time spectrum, considered according to the water column H flowing through it, is independent of filtration velocity and mathematically reversible, Eq.(3.1-19).

$$c(H_D, H) = \frac{c_0}{2}\,\mathrm{erfc}\left(\frac{L - H}{2 \cdot \sqrt{\frac{D \cdot H}{v_f}}}\right) \tag{3.1-19}$$

The one-dimensional solution for the Dirac function Eq.(3.1-15) at location L, also with the initial condition Eq.(3.1-16), Eq.(3.1-20)).

$$\rho(t) = c(L,t) = \frac{\Delta n}{2 \cdot A_F \cdot \sqrt{\pi \cdot D \cdot t}} \cdot \exp\left(\frac{(L - v_A \cdot t)^2}{4 \cdot D \cdot t}\right) \tag{3.1-20}$$

The integrated solution Eq.(3.1-20) is undefined for t = 0.

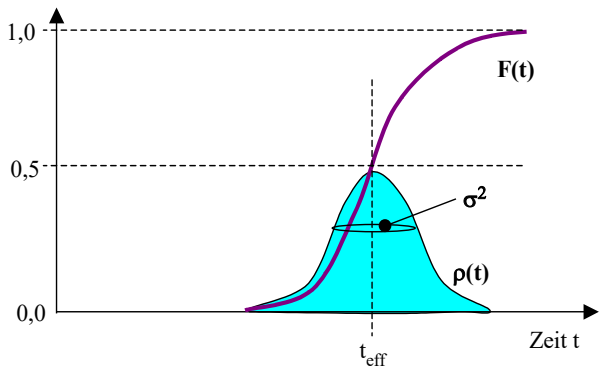

Fig. 3.12: Ideal residence time function of a tubular reactor with backmixing and its first discharge.

The two-dimensional case (x, y) of the propagation of a Dirac pulse in the x-direction is composed of the product of the solutions for propagation in both spatial directions with the longitudinal dispersions D_{xx} and D_{yy} (RAUSCH et al. 2002), Eq.(3.1-21).

$$c(x,y,t)=\frac{\Delta n}{A_F}\cdot\frac{1}{4\cdot\pi\cdot t\cdot\sqrt{D_{xx}D_{yy}}}\cdot\exp\left(-\frac{(x-v_A t)^2}{4D_{xx}}-\frac{y^2}{4D_{yy}}\right) \qquad (3.1\text{-}21)$$

For particulate solutions, Eq.(3.1-19) and Eq.(3.1-20) if the breakthrough and the longitudinal dispersion coefficients deviate from the theoretical assumptions. In this case, L is replaced by a measured or simulated breakthrough water column H_D, Eq.(3.1-22).

$$H_D=\frac{v_f}{n_P}\cdot t(\text{Durchbruch})\neq L \qquad (3.1\text{-}22)$$

Applications are used for the migration of response fronts, pt. 8.3 and their interpretation from measurement data pt. 9.7 Featured.

3.2 Residence Time and Mass Transport Behavior of Simple Reactor Models

3.2.1 Zero-dimensional stirred vessel

In process engineering, a distinction is made between two basic types of reactors (HAGEN 1993):

- continuous stirring vessel and
- Flow tube with diffuse remixing.

These can be further combined to form a stirring stage cascade or tube bundles. In the latter, the individual tubes can be described as both stirring stage cascades and flow-tubes. The ideal continuous stirring tank is completely mixed, Fig. 3.21.

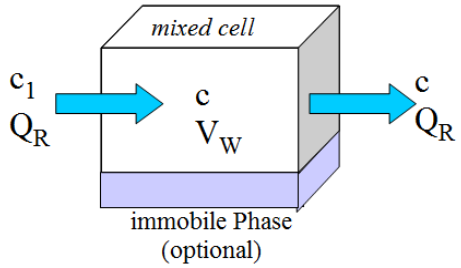

Fig. 3.21: Continuous stirred tank (*mixed cell*) with the solution volume (water) VW, the flow rate Q_R and the concentrations in the inlet c_1 and in the stirred tank c or in the effluent (see also Tab. 2.2-1 und Tab. 2.22).

The concentration is constant in time and place in the reactor and always corresponds to the outlet concentration. When using the jump function as *input*, the mass balance Eq.(3.2-1),

$$V_W\cdot\frac{\partial c}{\partial t}=Q_R\cdot c_1-Q_R\cdot c \qquad (3.2\text{-}1)$$

owhich is expressed over the space-time t_F Eq.(3.2-2),

$$\frac{\partial c}{\partial t} = \frac{(c_1 - c)}{t_F} \tag{3.2-2}$$

and integrated in the boundaries from t_0 to t, c(t), Eq.(3.2-3),

$$\int_{t0}^{t} \frac{\partial c}{\partial t} = \int_{c0}^{c} \frac{(c_1 - c)}{t_F} \tag{3.2-3}$$

with the initial concentration (t_0 => $c = c_0$, $c_1 = c_1$), c, starting from c_0, approaches exponentially to the inlet concentration c_1, Eq.(3.2-4).

$$c = c_0 + (c_1 - c_0) \cdot e^{-\frac{t}{t_F}} \tag{3.2-4}$$

3.2.2 One-dimensional flow tube

The ideal flow tube is characterized by plug flow, i.e. there is no mixing in the axial direction, Fig. 3.22 with $D_L = 0$. In contrast, complete mixing is assumed in the radial direction. The compositionof the reaction mixture, and consequently also the reaction rate, change over the length of the tube. The residence time is equal to the mean residence time for all particles ($D_L = 0$).

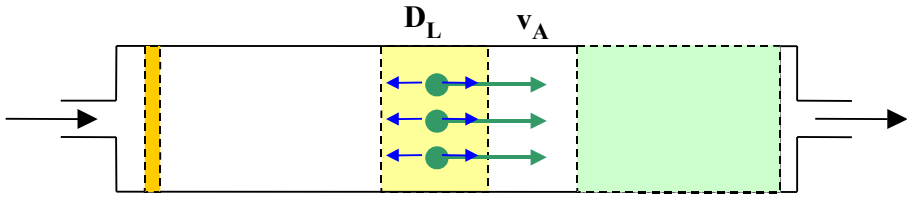

Fig. 3.22: Flow tube with backmixing and the distance velocity v_A and the axial (turbulent) diffusion coefficients D_L.

For real, i.e. aerodynamically non-ideal reactors, the simplifying assumptions formulated for ideal reactor basic types do not apply. If there are concentration gradients in the axial direction in a flow tube, diffuse material flows are formed, which compensate for concentration differences, Fig. 3.22. As a relationship between convective mass transport and axial mixing, the dimensionless Bodenstein number Bo was introduced (HAGEN 1993), Eq.(3.2-5) These describe the degree of remixing in the reactor. The peclet number Pe used for processes in the aquifer is defined analogously to Eq.(3.2-6).

$$Bo = \frac{\text{Konvektionsstrom}}{\text{axialer Diffusionsstrom}} = Pe \tag{3.2-5}$$

$$Bo = \frac{v_A \cdot L}{D_L} \tag{3.2-6}$$

The axial diffusion coefficient or effective mixing coefficient D_L is identical to diffusion constants in the general balance equation, Eq.(3.1-9) L characterizes the typical length scale of the transport phenomenon under consideration. A large number of floor blocks corresponds to a small axial diffusion coefficient and thus narrow residence time spectra.

On the boundary calculation

$Bo \rightarrow \infty, \quad D_L \rightarrow 0$ Ideal flow tube (no axial mixing),

$Bo \rightarrow 0, \quad D_L \rightarrow \infty$ Ideal stirring vessel (complete remixing)

a real reactor can be characterized by a floor stone number.

3.2.3 One- dimensional *mixed cell*s

The mass transport can also be described as a mixed cell cascade by a chain of mixing reactors, Fig. 3.21. PHREEQC solves the transport problem by a finite difference method with a distance-time discretization, in which a one-dimensional column is divided into ncell cells with the length Δx. The time steps result from the cell length and the distance velocity with the dimensioning Eq.(3.2-8) to Eq.(3.2-12) in Tab. 3.21.

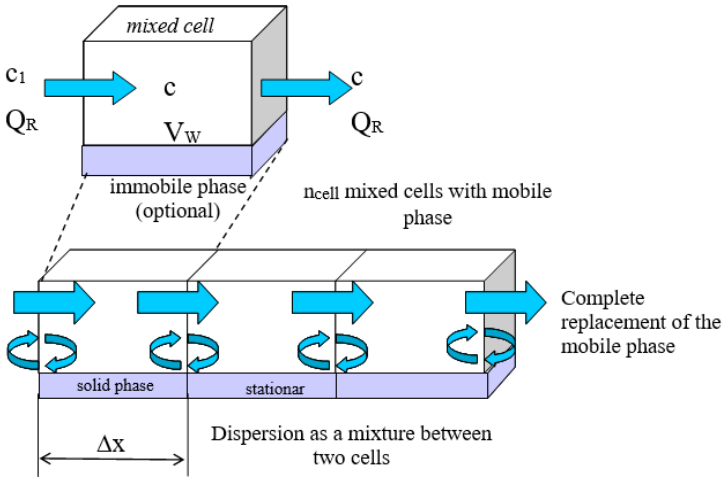

Fig. 3.23: Mixed cell *stirring stage model* composed of mixed reactors .

The *mixed cell* model differs from the dispersion model in its physical fundamentals, since according to the former, no mass transport against the convection current is possible in principle. The more stirring stages are connected in series, the closer the system comes to a tubular reactor with a plug flow character with the approximation Eq.(3.2-7)

$$\sigma_\theta^2 \approx \frac{1}{n_{cell}} \qquad (3.2\text{-}7)$$

Tab. 3.21: Sizing of mixd cells (see also Tab. 2.22).

Parameter	Symbol	Units	Definition	Eq.
Number of cells	n_{cell}	1		(3.2-8)
Flow Time	t_f	s		(3.2-9)
Cell Length	$\Delta x = L_{cell}$	m	$\Delta x = \frac{L}{n_{cell}}$	(3.2-10)
Time Step	$(\Delta t)_A = t_{cell}$	s	$(\Delta t)_A = \frac{\Delta x}{v_A}$	(3.2-11)
Number of transport steps	n_{shift}	1	$n_{shift} = \frac{v_A}{\Delta x} \cdot t$	(3.2-12)
reactor volume (BV), Eq.(2.2-13)	n_{BV}	1	$n_{BV} = \frac{v_A}{L} \cdot t$	(3.2-13)

PHREEQC describes the dispersion via the mixtures between neighboring cells. If the dispersion is low (Bo > 50), the equivalence Eq. exists between the model parameters of the dispersion and cell models Eq.(3.2-14) (GIMBEL et al. 1996).

$$n_{cell} \approx \frac{Bo}{2} \tag{3.2-14}$$

At lower cell counts ncell, this equivalence is only approximate. For $n_{cell} > 10$ (i.e. Bo > 20) there is already a mostly satisfactory agreement (HAGEN 1993). The *mixed cell* model should be preferred for the calculation of the reactor because of its easier handling.

3.3 Numerical Particular solutions of the balance equation

3.3.1 Geochemical simulation models PHREEQCx

3.3.1.1 Software

The *geochemical calculation programs* PHREEQCX, WHICH ARE AVAILABLE AS FREEWARE, enable the calculations of complex chemical equilibria and reaction systems with the annotations and cations dissolved in water. The temperature- and ion-strength-dependent equilibrium and kinetic parameters compiled in the associated (base) data sets can be extended as required. The program's own syntax is described in the respective *manual* .

The following were applied::

Version 2: PARKHURST & APPELO (1999),

Version 2: PARKHURST & APPELO (2006),

Version 3: PARKHURST & APPELO (2013).

Newer versions are no longer considered here.

For beginners, the *windows* version of PHREEQCx is also suitable(e.g. described in MERKEL & PLANER-FRIEDRICH 2002).

For routine use, spreadsheet programs were developed that control the corresponding batch (DOS) versions via macros. In addition, the source code is also published in C++, which eager programming freaks can integrate directly into their software.

3.3.1.2 Transport approach

The one-dimensional transport is represented by a stirring stage cascade (*mixed cells*) taking into account longitudinal dispersion, pt. 3.2.3. Furthermore, dead spaces and transport by diffusion can be included.

With each time step, the water of a cell is completely replaced, taking into account the criterion for numerical stability, Eq.(3.3-1).

$$(\Delta t)_D \le \frac{(\Delta x)^2}{3 \cdot D_L} \tag{3.3-1}$$

If the time steps for the dispersive transport become smaller than those for the transport, the calculation is carried out several times (mixrun) for a transport step, Eq.(3.3-2).

$$\text{mixrun} = \text{int}\left(\frac{3 \cdot \alpha_L}{\Delta x}\right) + 1 \tag{3.3-2}$$

The number of intermediate mixing steps allows only the use of discrete dispersives, Eq.(3.3-3).

$$\alpha_L = \text{mixrun} \cdot \frac{\Delta x}{3} \tag{3.3-3}$$

3.3.2 Continuous loop reactor with differential filter

The system under consideration consists of a mixed reactor with the flow Q_{MR} flow, from which a partial flow Q_R is (re)routed through a filter in the circuit and in which the concentration changes only by the small amount Δc , Fig. 3.31. The filter represents a differential filter layer under defined hydraulic conditions.

The material quantity balance n is composed of the individual sub-flows, Eq.(3.3-4).

$$\frac{\partial}{\partial t} n = \dot{n} = Q_{MR} \cdot c_0 + Q_R \cdot (c + \Delta c) - Q_R \cdot c - Q_{MR} \cdot c \tag{3.3-4}$$

The temporal change of the amount of substance n is normalized to the water volume V_W, Eq.(3.3-5).

$$\frac{\partial}{\partial t} \frac{n}{V_W} = \dot{c} = \frac{Q_{MR} \cdot c_0 + Q_R \cdot \Delta c - Q_{MR} \cdot c}{V_W} = \frac{Q_{MR}}{V_W} \cdot (c_0 - c) + \frac{Q_R}{V_W} \cdot \Delta c \tag{3.3-5}$$

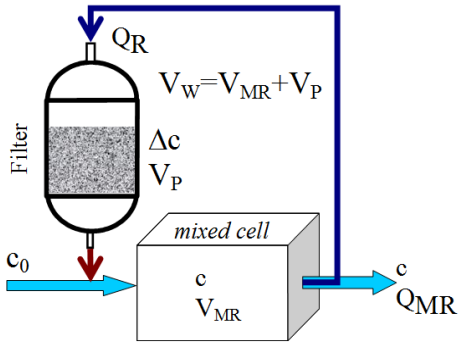

Fig. 3.31: Flow-through reactor with filter as differential reactor. The mobile (water) volume V_W is composed of the pore volume V_P and the remaining volume of the mixing reactor V_{MR}, according to the filter definitions chapter 0 together, Tab. 2.2-1 and Tab. 2.22.

The volume flow quotients are determined by the spacetimes of the system Eq.(3.3-6) or the residence time VWZ Eq.(2.2-8) ,

$$t_{MR} = \frac{V_W}{Q_R} \tag{3.3-6}$$

and inserted into the temporal change of concentration, Eq.(3.3-7).

$$\dot{c} = \frac{Q_{MR}}{Q_R} \cdot \frac{(c_0 - c)}{t_{MR}} + \frac{\Delta c}{t_{MR}} \tag{3.3-7}$$

In a differential filter circuit, the concentration difference Δc is approximately defined by the reaction rate in the filter $r_f(c)$, Eq.(3.3-8),

$$\Delta c \approx r_f(c) \cdot VWZ \tag{3.3-8}$$

from which follows Eq.(3.3-9).

$$\dot{c} = \frac{Q_{MR}}{Q_R} \cdot \frac{(c_0 - c)}{t_{MR}} + r_f(c) \cdot \frac{VWZ}{t_{MR}} \tag{3.3-9}$$

Two special cases are derived from this:

Special case $Q_{MR}=0$: Closed-loop reactor without flow

The change in concentration is delayed in time according to the residence time/space-time ratio, Eq.(3.3-10) The reciprocal value indicates the time spread.

$$\dot{c} = \frac{VWZ}{t_{MR}} \cdot r_f(c) \tag{3.3-10}$$

This makes it possible to investigate rapid reactions in the filter spread over time.

Special case of stationary operation: Chemostat

In stationary operation, a constant concentration c_{stat} is achieved, at which the mass exchange through the flow is equal to the change in substance through the reaction, Eq.(3.3-11).

$$c_{stat} = \frac{Q_R}{Q_{MR}} \cdot VWZ \cdot r_f(c_{stat}) + c_0 \tag{3.3-11}$$

Conversely, the reaction rate can be determined from the stationary concentration $c_{stat}$and the associated boundary conditions, Eq.(3.3-12).

$$r_f(c_{stat}) = \frac{Q_{MR}}{Q_R} \cdot \frac{(c_{stat} - c_0)}{VWZ} \tag{3.3-12}$$

This corresponds to the chemostat principle, which is often used to determine the turnover kinetics of microorganism suspensions.

3.3.3 Steady-State Concentration Profiles in Filters

Technical filtrations, such as flocculation, iron removal and manganese removal or adsorption filtration, usually take place under stationary boundary conditions. During a time-defined work phase, the concentration profile along the flow path is almost constant, FigFig. 3.32 and Eq.(3.3-13).

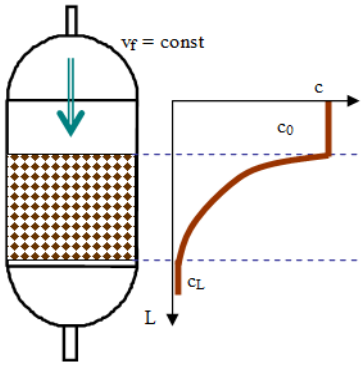

Fig. 3.32: Vertically flowed reactor (filter) with temporally stationary concentration profile.

$$\dot{c} = \left(\frac{\partial}{\partial t} c\right)_L = 0 = -\mathrm{div}\left(\vec{v} \cdot c\right) + \mathrm{div}\left(D \cdot \mathrm{grad}(c)\right) + r \tag{3.3-13}$$

And for the one-dimensional case of Eq.(3.3-14),

$$v_A \cdot \frac{\partial c}{\partial L} + D \cdot \frac{\partial^2 c}{\partial L^2} + r(c) = 0 \tag{3.3-14}$$

or

$$\frac{\partial^2 c}{\partial L^2} + \frac{v_A}{D} \cdot \frac{\partial c}{\partial L} = -\frac{r(c)}{D} \tag{3.3-15}$$

If the remixing (dispersion) is neglected, the diffusion element zero, Eq.(3.3-16):

$$\mathrm{div}(D \cdot \mathrm{grad}(c)) = 0 \tag{3.3-16}$$

following

$$\frac{\partial c}{\partial L} = -\frac{1}{v_A} r(c) \tag{3.3-17}$$

Eq.(3.3-17) forms the basis for the numerous design equations of depth (space) filtration.

3.3.4 The filtration parameter FP for dimensioning reactions on the grain surface

During filter passage, the reactions take place in the homogeneous solution (bulk) and at the phase interfaces. The reaction element r is therefore composed of the homogeneous reaction velocity r_h and the heterogeneous reaction velocity r_O at the phase interface O_{ges}. The heterogeneous reaction component is taken into account via the interface/solution volume ratio, Eq.(3.3-18)).

$$r = \frac{O_{ges}}{V_W} \cdot r_O(c) + r_h(c) \tag{3.3-18}$$

Taking into account the porosity n_P, Eq.(3.3-17) in Eq.(3.3-19) about.

$$\frac{\partial c}{\partial L} = -\frac{n_P}{v_f} \cdot \left(\frac{O_{ges}}{V_W} r_O(c) + r_h(c) \right) \tag{3.3-19}$$

At a constant filtration velocity, the reaction time is substituted by the flow path, Eq.(3.3-20),

$$\begin{aligned} v_f \cdot t &= n_P \cdot L \\ \partial t &= \frac{n_P}{v_f} \partial L \end{aligned} \tag{3.3-20}$$

and the homogeneous reaction in the pore solution is neglected, Eq.(3.3-21).

$$\frac{O_{ges}}{V_W} r_O >> r_h \tag{3.3-21}$$

The specific integration of Eq.(3.3-19) without homogeneous reaction from the initial to the effluent concentration, or their residence times, results in Eq.(3.3-22).

$$\int_{c_0}^{c} \frac{\partial c}{(r_O(c))} = \left[\int_0^t \frac{O_{ges}}{V_W} \cdot \partial t \right] = \frac{O_{ges}}{V_W} \cdot t \tag{3.3-22}$$

The left term of Eq.(3.3-22) contains the course of the reaction, including stoichiometry. The right term contains only the filtration dimensioning and is defined as filtration parameter FP, Eq.(3.3-23).

$$FP = \frac{O_{ges}}{V_W} t = \frac{O_{ges} \cdot n_P \cdot L}{V_W \cdot v_f} = \int_{c_0}^{c} \frac{\partial c}{r_O} \left[\frac{h}{m}\right] \tag{3.3-23}$$

FP contains the geometric boundary conditions of the filter with the reaction time. With the same filtration parameters, FP, different filter constructions and the same hydrochemical boundary conditions, the same effluent properties are to be expected. FP is suitable for comparing different filter geometries and operating modes. FP can be applied to stationary concentration profiles of flowing media via transformation, Eq.(3.3-24).

$$\begin{aligned} \partial c &= r_O \cdot \partial FP \\ r_O &= \frac{\partial c}{\partial FP} \end{aligned} \tag{3.3-24}$$

The ideal ball pouring over Eq.(3.4-12) is included in the definition of the filtration parameter, so that the calculation of FP can be done via the filter velocity v_f as well as via the space-time t_F, Eq.(3.3-25).

$$FP = \frac{6 \cdot (1 - n_P)}{d_w \cdot v_f} \cdot L = \frac{6 \cdot (1 - n_P)}{d_w \cdot n_P} \cdot t_F \tag{3.3-25}$$

The filtration parameter FP corresponds to the area under the function $-1/r_O$ as a function of the concentration c between the inlet concentration c_0 and the effluent concentration c_1, Fig. 3.33. The function $-1/r_O$ runs continuously for the ideal flow tube and represents a rectangle for a *mixed cell* and a rectangle function for *mixed cell* cascades. This allows changes in the nature of differently constructed reactors (L, d_W bzw. d_P, n_P, L, v_f) to be compared with each other. Process engineering uses an analog representation in which the reaction rate is balanced and the area indicates the space-time t_F.

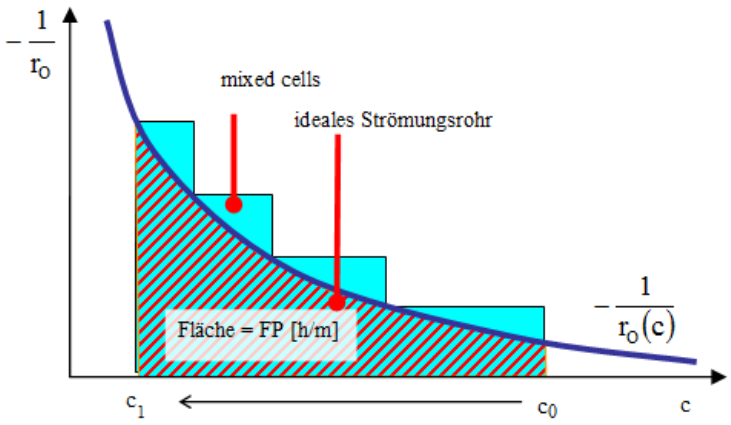

Fig. 3.33: Graphical illustration of the filtration parameter FP as an area under the integral of Eq.(3.3-22) or Eq.(3.3-23) for an ideal flow tube and a *mixed cell* cascade.

3.3.5 Dimensionless numbers

Dimensionless numbers do not have a unit and usually represent relationships between several values of a situation, whose units cancel each other out in the key figure definition. Dimensionless quantities play a major role in the theory of similarity, which is used in fluid mechanics and heat transfer, among other things. The theory of similarity makes it possible to describe the form of physical equations of dimensional quantities by means of dimensionless key figures. If A, B, C, and X are Dimensionless numbers, then the experimentally determined exponents α, β, γ are valid for a problem, which are determined via Eq.(3.3-26) give the dimensionless measure X.

$$X = A^{\alpha} \cdot B^{\beta} \cdot C^{\gamma} \cdot ... \tag{3.3-26}$$

The individual key figures conceal causal relationships, e.g. between different dimensions and/or material properties, and can also be understood as particulate solutions to complex relationships. All quantities defined in the key figure X behave similarly, i.e. a target variable can be roughly calculated from the remaining definition variables. An extensive catalogue of process engineering key figures includes, WETZLER (1985).

3.4 Idealized models for porous granular media

3.4.1 Geometry of the ideal sphere packing

3.4.1.1 Pore system and storage

Granular material can be described as a first approximation with bulkes of spheres of the same diameter with the particle diameter d_K, Tab. 3.4-1. The pore system of the grain structure contains barely passable constrictions between the spheres (two-dimensional) $d_{P,min}$ and cavities between the spatially arranged spheres (three-dimensional). The pore diameters between three spheres, as well as the spheres that find space in tetrahedral and octahedral gaps, represent the densest deposit, Fig. 3.41. From geometric considerations, the spherical diameters that fit exactly into these gaps can be specified, d_{TK} for a tetrahedral gap Eq.(3.4-1) or d_{OK} for an octahedron gap Eq. (3.4-2).

$$d_{TK} = \frac{1}{2} \cdot \left(\sqrt{6} - 2\right) \cdot d_w \approx 0{,}225 \cdot d_w \tag{3.4-1}$$

$$d_{OK} = \left(\sqrt{2} - 1\right) \cdot d_w \approx 0{,}414 \cdot d_w \tag{3.4-2}$$

The relative minimum of the pore channel diameter $d_{P,min}$ is defined as the diameter of the circle that can be inscribed between three (densest support) or four (loosest bearing) touching spheres in the central plane (BUSCH et al. 1993, Tab. 3.4-2). The gaps between several balls are usually larger in loose storage configurations. If you look at a longer flow path through the pore structure, you will most likely have to pass through a pore narrowing of three spheres touching each other. Thus, their diameter corresponds to the maximum size of a sphere $d_{P,min}$ for a continuous passage of the fill, Eq.(3.4-3) or for three-grain mixtures Eq.(3.4-4).

$$d_{P,min} = \frac{d_K}{\left(3 + 2 \cdot \sqrt{3}\right)} = 0{,}1547 \cdot d_K \tag{3.4-3}$$

The minimum pore channel diameters $d_{P,min}$ in a three-ball mixture were determined (Muckentaler 1989 cited in BUSCH et al. 1993) by statistical consideration, Eq.(3.4-4).

$$d_{P,min} = \frac{1}{\left(\frac{1}{d_1} + \frac{1}{d_2} + \frac{1}{d_3} + 2 \cdot \sqrt{\frac{1}{d_1 \cdot d_2} + \frac{1}{d_1 \cdot d_3} + \frac{1}{d_2 \cdot d_3}} \right)} \tag{3.4-4}$$

Tab. 3.4-1: Parameters of pore systems in ideal spherical fills. Locally used quantities are not listed in the symbol directory chapter 11.1.

Parameter	Symbol	Units	Definition	Eq.
Number (general)	N	1	(Local use)	
Ball diameter, grain diameter	d_K	mm		
effective grain diameter	d_w	mm		
Diameter of a cylinder pore	d_P	mm		(3.4-17)
Still passable pore narrowing	$d_{P,min}$	mm		(3.4-3)
Diameter of the tetrahedral gap	d_{TK}	mm	(Local use)	(3.4-1)
Diameter of the octahedron gap	d_{OK}	mm	(Local use)	(3.4-2)
Form Factor	f_O	1		(4.1-7)
Pore length	L_P	m		(3.4-19)
Detour factor, Tortuosity	f_L	1		(3.4-19)
Pore Flow Rate	v_P	m/h, m/s		(3.4-20)
Porosity	n_P	1, %		(2.2-6)
Surface (general)	O	m^2	(Local use)	
specific surface area of the fill	O_{sp}	m^2/kg		(3.4-10)
Surface/Reactor Volume Ratio	O_F	m^2/m^3, m^{-1}		(3.4-21)
Grain surface of a fill	O_R	m^2		Tab. 2.22
Grain (number) concentration	c_K	m^{-3},fmol/m^3	$c_K = \frac{N_K}{V_R}$	(3.4-13)

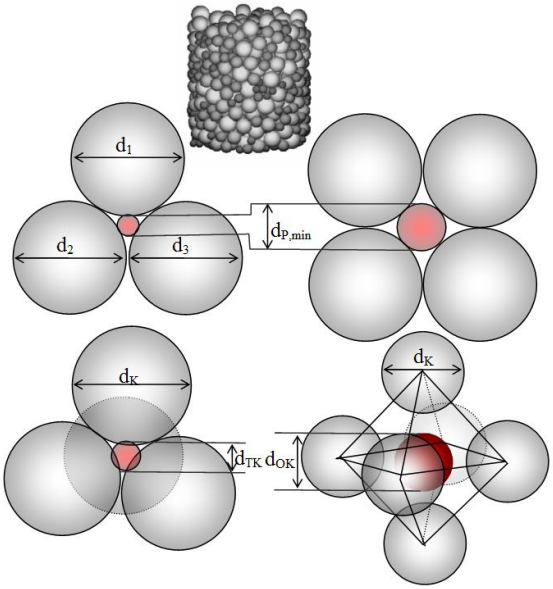

Fig. 3.41: Homogeneous storage of a spherical mixture with normally distributed spherical radii $d_{P,min}$ (top), minimum pore diameters $d_{P,min}$ between adjacent spheres of the same diameter (middle), as well as spheres in microstructure gaps (bottom: tetrahedral gap on the left, octahedron gap on the right).

The specification of the minimum pore channel diameter for polydisperse grain mixtures becomes more and more complex with the increasing number of diameters to be considered and also loses practical relevance. The one from Eq.(3.4-4) The minimum pore channel diameter derived as a special form for monodisperse fills equals Eq.(3.4-3)

The arrangement of the balls then also determines the porosity of the fill. This can be estimated for defined configurations between the single cubic and the densest bearing. At the same time, the pore diameter $d_{P,min}$ in the bulk changes with the porosity (Tab. 3.4-2).

Tab. 3.4-2: Porosities n_P and minimum pore diameters $d_{P,min}$ ideal ball fillings in different bearing forms (BUSCH et al. 1993).

Bulk density for $d_K = d_w$		n_P	$d_{P,min}$
Loosest packing	Simple cubic packing	0,476	$0,414 \cdot d_K$
Close packing	Hexagonal and Cubic close packing	0,259	$0,155 \cdot d_K$

Interpolate the transition area between the Close packing and Loosest packing Eq.(3.4-5) and Eq.(3.4-6),

$$\frac{d_{P,min}}{d_K} \approx -0,154 + 1,19 \cdot n_P \tag{3.4-5}$$

and approximation for $0,259 < n_P < 0,476$.

$$d_{P,min} \approx 0,45 \cdot \frac{n_P}{1 - n_P} \cdot d_K \tag{3.4-6}$$

3.4.1.2 Grain and pore surfaces

The grain surface is advantageously related to its particle volume. The diameter d_w of the ideal spherical fill, which is the same for all spheres, forms the same volume/surface ratio as the one determined from the grain distribution. In process engineering, this *grain diameter* d_w is also referred to as the Sauter diameter.

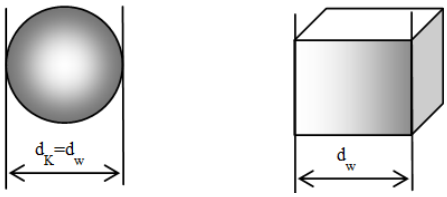

Fig. 3.42: Sphere and cube as elements of fills.

For an equal volume/surface ratio for spheres and cubes, there is the equivalence relationship Eq.(3.4-7).

$$\frac{V}{O} = \frac{(1-n_P)\cdot V_W}{n_P \cdot O} = \frac{\frac{\pi}{6}\cdot d_K^3}{\pi \cdot d_K^2} = \frac{d_K^3}{6 \cdot d_K^2} = \frac{d_K}{6} \tag{3.4-7}$$

For spherical and cube shapes, this is equal to the equivalent spherical diameter. The total surface area of a spherical fill O_R is calculated from the spherical surface and its particle number N in the fill, Eq.(3.4-8) and Eq.(3.4-9).

$$O_R = m_{Pr} \cdot O_{Sp} = N \cdot \pi \cdot d_w^2 \tag{3.4-8}$$

$$m_{Pr} = \rho_{SS} \cdot N \cdot \frac{\pi}{6} \cdot d_w^3 \tag{3.4-9}$$

This results in the specific interface O_{Sp}, Eq.(3.4-10),

$$O_{Sp} = \frac{6}{d_w \cdot \rho_{SS}} \qquad [m^2/kg] \tag{3.4-10}$$

and for the entire surface O_R, Eq.(3.4-11).

$$O_R = 6 \cdot \frac{(1-n_P)}{d_w} \cdot V_R \tag{3.4-11}$$

or in relation to the reactor volume Eq.(3.4-12).

$$O_F = \frac{O_R}{V_R} = \frac{6 \cdot (1-n_P)}{d_W} \qquad [m^2/m^3] \tag{3.4-12}$$

Geometrically, Eq.(3.4-10) Eq.(3.4-11) and Eq.(3.4-12) also for cubes with edge length d_w.

3.4.1.3 Grain concentration c_K

The grain concentration $c_K$in dicates the number of spheres in relation to the reactor volume, Eq.(3.4-13).

$$c_K = \frac{N_K}{V_R} = 6 \cdot \frac{(1 - n_P)}{\pi \cdot d_w^3} \qquad [1/m^3, fmol/m^3] \qquad (3.4\text{-}13)$$

A filter fill with d_W = 1 mm and n_P = 0.4 thus contains $c_K = 7{,}6 \cdot 10^8$ m^{-3} or 1.27 fmol/m^3 particles. The specifications as a number of particles or in moles are equally practical here.

3.4.2 Models of ideal sphere packing and tube bundle

The ideal homodisperse spherical packing is completely determined by its grain diameter d_K, the porosity n_P resulting from the storage density and the length of the layer, Fig. 3.43. The ratio of the spherical or pore surfaces (O_R) to the pore volume (V_W) corresponds to that of the real fill (equivalence criterion). Alternatively, the equivalence criterion can also be used to transform a bundle of cylindrical pore channels with a diameter of d_P, Eq.(3.4-17)

Beide Modellvorstellungen sind bei gleicher Porosität n_P im hydraulischen, wie im reaktionstechnischen Sinne äquivalent:

- The ideal spherical packing consists of spheres of equal diameters d_K.
- The tube bundle model consists of parallel flowing pipes (pore channels) of the same diameter d_P.

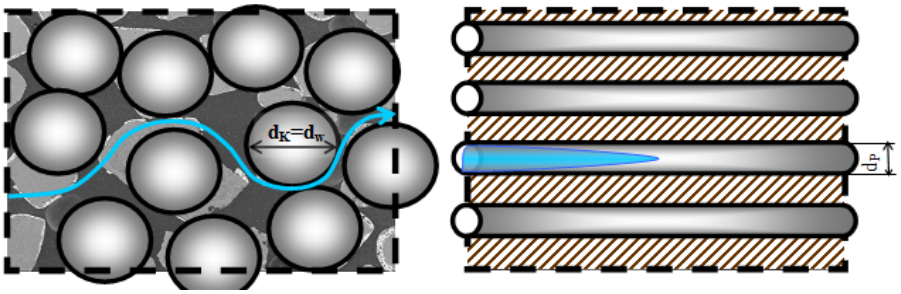

Fig. 3.43: Left: ideal sphere packing (left) with particle flow around and right: laminar flow-through bundle of cylindrical pores (tube bundle).

The ratio between the phase boundary or surface of a spherical packing (d_K) or a cylindrical pore bundle (number of pores N, d_P) is considered the equivalence criterion Eq.(3.4-14).

$$\frac{O}{V} = \frac{N \cdot \pi \cdot d_P \cdot L}{n_P \cdot V_R} = \frac{1}{n_P \cdot V_R} \frac{6 \cdot (1 - n_P) \cdot L}{d_w} \cdot A_F \qquad (3.4\text{-}14)$$

The number of pores N follows from the quotient of pore volume and the volume of each individual pore, Eq.(3.4-15).

$$N = \frac{n_P \cdot V_R}{\frac{\pi}{4} \cdot d_P^2 \cdot L} \tag{3.4-15}$$

After the onset of the pore number N, Eq.(3.4-16),

$$\frac{n_P \cdot V_R}{\frac{\pi}{4} \cdot d_P^2 \cdot L} \frac{\pi \cdot d_P \cdot L}{n_P \cdot V_R} = \frac{1}{n_P \cdot V_R} \frac{6 \cdot (1 - n_P) \cdot L}{d_w} \cdot A_F \tag{3.4-16}$$

and the relationship between the equivalent spherical diameter d_K and the diameter of the cylinder pore d_P Eq.(3.4-17).

$$d_P = \frac{2}{3} \cdot \frac{n_P}{(1 - n_P)} \cdot d_w \tag{3.4-17}$$

Alternatively, there is a relationship between the pore channel diameter and the phase-ratio Eq.(2.2-10) and the specific surface area Eq.(3.4-10), Eq.(3.4-18).

$$d_P = \frac{4 \cdot z}{O_{sp}} \tag{3.4-18}$$

The pore channel (L_P) winds through the solid matrix and is therefore longer than the filter layer L, by a factor of f_L Eq.(3.4-19).

$$L_P = f_L \cdot L \tag{3.4-19}$$

The detour factor f_L, also known as tortuosity, also increases the flowvelocity in the pore channel v_P, Eq.(3.4-20).

$$v_P = f_L \cdot v_A \tag{3.4-20}$$

For the surface-to-reactor volume ratio O_F Eq.(3.4-12) the equivalences Eq.(3.4-21).

$$O_F = \frac{O_R}{V_R} = \frac{4 \cdot n_P}{d_P} = \frac{6 \cdot (1 - n_P)}{d_W} \quad [m^2/m^3] \tag{3.4-21}$$

Filtration processes via granular media can be described either via an ideal sphere packing or a tube bundle.

3.5 Hydraulics of pore channels flowing through

3.5.1 Pipe Flow and Flow Condition

If we consider a cylinder pore with a developed tube flow as a partial cylinder with a radius of r ($0.5 \cdot d_P$) and the length L can be used to calculate the laminar pressure loss using the shear stresses and compressive forces (BOLLRICH 1989), Fig. 3.51.

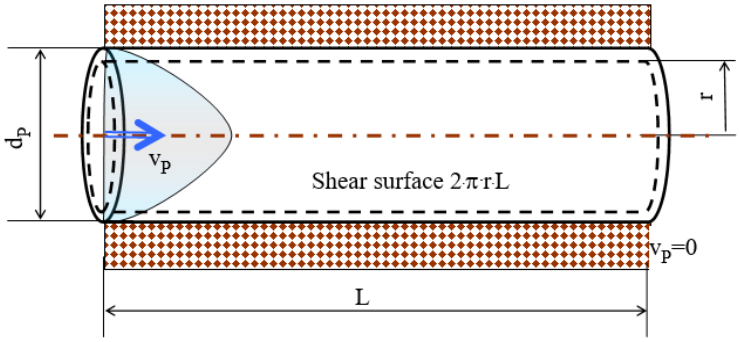

Fig. 3.51: Dimensioning of a cylindrical pore with laminar flow.

The pressure decreases linearly in the direction of flow, as the pressure drop caused by friction must be overcome. The flow state is characterized by the dimensionless Reynolds number Re, Eq.(3.5-1),

$$\mathrm{Re} = \frac{d \cdot v_f}{\nu} \tag{3.5-1}$$

with the characteristic length d and the kinematic viscosity ν. The definition of the characteristic length d can be done in different ways. For cylindrical pore channels (tubes), it corresponds to the pore channel diameter d_P, Eq.(3.5-2) This definition contradicts some differing definitions of other authors, but nevertheless allows the assessment of the flow state between laminar and turbulent.

$$\mathrm{Re} = \frac{d_P \cdot v_P}{\nu} \tag{3.5-2}$$

For sphere packings, the mean diameter of the pores flowing through is indirectly used as the characteristic length, analogous to the pore channel diameter Eq.(3.4-17) used, Eq.(3.5-3).

$$\mathrm{Re} = \frac{d_K \cdot v_f}{(1-n_P)\cdot \nu} \tag{3.5-3}$$

The strictly laminar flow range extends to Re ≤ 1-10 (DAVID 1998). This is followed by the transition to turbulent flow conditions.

VAUCK & MÜLLER (2000) derive the Reynolds number from the pore diameter d_P and the pore channel flow v_P and obtain Eq.(3.5-4).

$$\mathrm{Re} = \frac{2}{3} \cdot \frac{d_K \cdot v_f}{(1-n_P)\cdot \nu} \tag{3.5-4}$$

The transition to turbulent flow will take place there from Re > 20.

3.5.2 Laminar pore channel flow

3.5.2.1 Velocity Distribution in a Laminar Flow Pipe

In the case of stationary flow in a liquid cylinder, compressive force Δp Eq.(3.5-5) and frictional forces Eq.(3.5-6) against each other (BOLLRICH 1989), Eq.(3.5-7).

$$\Delta p \cdot A_F = \Delta p \cdot \pi \cdot r^2 \tag{3.5-5}$$

The frictional force is calculated by the shear stress τ and the dynamic viscosity η of the fluid over the tube radius, Eq.(3.5-6).

$$2 \cdot \pi \cdot r \cdot L \cdot \tau = 2 \cdot \pi \cdot r \cdot L \cdot \eta \cdot \frac{\partial v}{\partial r} \tag{3.5-6}$$

By equating the two forces Eq.(3.5-7) the integrated differential equation Eq.(3.5-8) in Fig. 3.51.

$$\Delta p \cdot \pi \cdot r^2 = 2 \cdot \pi \cdot r \cdot L \cdot \eta \cdot \frac{\partial v}{\partial r} \tag{3.5-7}$$

$$\int_{v_{max}}^{0} \partial v = \int_{r}^{d_P/2} \left(\frac{\Delta p}{2 \cdot L \cdot \eta} \cdot r \right) \partial r = \left(\frac{\Delta p}{4 \cdot L \cdot \eta} \right) \cdot \left(\frac{d_P^2}{4} - r^2 \right) \tag{3.5-8}$$

The maximum velocity is reached in the middle of the pipe r = 0, Eq.(3.5-9).

$$v_{max} = \left(\frac{\Delta p}{4 \cdot L \cdot \eta} \right) \cdot \left(\frac{d_P^2}{4} - 0^2 \right) \tag{3.5-9}$$

3.5.2.2 Pressure Loss Height and Filter Resistance in Laminar Flow

The average tube velocity v_A is $0.5 \cdot v_{max}$, Eq.(3.5-10).

$$v_f = \frac{\Delta p}{32 \cdot L \cdot \eta} \cdot d_P^2 \tag{3.5-10}$$

The pressure loss height Δh is calculated from the pressure loss, the fluid density ρ and the gravitational acceleration, Eq.(3.5-11) The prerequisite is that this is formed only by internal friction of the mobile phase without turbulence (Darcy area).

$$\Delta p = \rho \cdot g \cdot \Delta h = \frac{32 \cdot L \cdot \eta \cdot v_A}{d_P^2} \tag{3.5-11}$$

The pressure loss level (filter resistance) is given as Δh in natural systems and as filter resistance h_f in technical systems.(3.5-12).

$$h_f = \frac{32 \cdot \eta \cdot v_P \cdot L_P}{\rho \cdot g \cdot d_P^2} \tag{3.5-12}$$

The formulation of the filter resistance to filters flowing through is carried out taking into account the pore geometry (Fig. 3.43) by replacing d_P with Eq.(3.4-17) v_P by Eq.(3.4-20) and L_P by Eq.(3.4-19).

$$h_f = \frac{32 \cdot 9 \cdot \eta}{4 \cdot \rho \cdot g} \cdot \frac{(1 - n_P)}{n_P^3} \cdot \frac{v_f \cdot L}{d_w^2} = \frac{72 \cdot \eta}{\rho \cdot g} \cdot \frac{(1 - n_P)^2}{n_P^3} \cdot \frac{v_f \cdot L}{d_w^2} \tag{3.5-13}$$

In geohydraulics, the filter velocity v_f is linked to the potential gradient h_f/L via the permeability coefficient k_f, Eq.(3.5-14).

$$v_f = k_f \cdot \frac{h_f}{L} \tag{3.5-14}$$

The filter resistance of sphere packing (sand filters) is indirectly proportional to the permeability coefficient in the Darcy range, Eq.(3.5-15).

$$\frac{h_f}{v_f \cdot L} = \frac{1}{k_f} = 72 \cdot \frac{\nu}{g} \cdot \frac{f_L^2 (1-n_P)^2}{n_P^3} \frac{1}{d_w^2} \tag{3.5-15}$$

or

$$h_f = \frac{v_f \cdot L}{k_f} = \left(72 \frac{\nu}{g}\right) \cdot f_L^2 \cdot \frac{(1-n_P)^2}{n_P^3} \cdot \frac{v_f \cdot L}{d_w^2} \tag{3.5-16}$$

with

Temperature	Temp		°C	
gravitational acceleration	g	9,81	m/s^2	
Kinematic Viscosity	ν	$1{,}3 \cdot 10^{-6}$	m^2/s	at Temp = 10°C
Tortuosity	f_L	≈1,44		for ideal sphere packing

Eq. (3.5-16) is also known as the Karmann-Cozeny equation. Conversely, the permeability coefficient k_f, Eq.(3.5-17).

$$k_f = \frac{g \cdot d_w^2 \cdot n_P^3}{72 \cdot \nu \cdot f_L^2 (1-n_P)^2} \tag{3.5-17}$$

According to this, k_f can be derived from sieve lines. Compared to the empirical equations for k_f estimation from sieve curves, Eq.(3.5-17) the influence of porosity n_P, which plays a major role in determining permeability (e.g. through compaction during shaking or mineral dissolution/precipitation processes). For Temp = 10 °C, the working equation Eq.(3.5-18)).

$$k_{f10} = \frac{1}{\left(2{,}65 \cdot 10^{-3} \frac{mm^2 \cdot m}{m \cdot m/h}\right)} \cdot \frac{n_P^3}{f_L^2 (1-n_P)^2} \cdot d_w^2 = \frac{1}{\left(1{,}18 \cdot 10^{-3} \frac{mm^2 \cdot m}{m \cdot m/h}\right)} \cdot \frac{n_P}{f_L^2} \cdot d_P^2 \tag{3.5-18}$$

The calculation of the k_f over the effective diameter in Eq.(3.5-18) taking into account our own detour and tortuosities, the calculation listed in SZYMCZAK ET AL. (2009) in chapter 4.3.1, Eq.(4.3-8) identical.

3.5.3 Filter resistance for the entire Reynolds range

For the loss of pressure head of the filter flow in the entire Reynolds number range, GIMBEL & NAHRSTEDT (2004) give Eq.(3.5-19)).

$$\frac{h_f}{L} = k_1 \cdot \frac{\nu}{g} \cdot v_f \cdot \frac{(1-n_P)^2}{n_P^3} \cdot \frac{1}{d_w^2} + \frac{k_2}{g} \cdot v_f^2 \cdot \frac{(1-n_P)}{n_P^3} \cdot \frac{1}{d_w} \tag{3.5-19}$$

The term beginning with k_1 describes the laminar flow Eq. (3.5-15) The term beginning with k_2 thus represents the turbulent part of the pressure loss height, Tab. 3.5-1.

Tab. 3.5-1: Constants of different filter resistance approaches according to Eq.(3.5-19), GIMBEL & NAHRSTEDT (2004).

k_1	k_2	Filter	Flow	f_L	zitiert
64	0	Bundles of capillaries	laminary	/	KOZENY
180	0	Bulk layers	laminary	1,58	CARMANN
150	**1,75**	**Bulk layers**	**laminar, turbulent flow**	**1,44**	**ERGUN**
180	1,8	Air-flowed bulk layers	gesamter Re-Bereich	1,58	MACDONALD

The correspondence of the laminar term with Eq.(3.5-15) can be calculated via tortuosity f_L in Tab. 3.5-1.

$$f_L = \sqrt{\frac{k_1}{72}} \tag{3.5-20}$$

For the calculation of the filter resistance, the constants of Ergun are relevant. The tortuosity $f_L = 1.44$ is only slightly lower than calculated for the flow around spheres ($f_L = \pi/2 = 1.57$) and is therefore geometrically plausible.

3.6 Mass transfer controlled by transport at phase interfaces

3.6.1 Boundary layer diffusion

The transport-controlled mass transfer assumes that a stationary boundary film (δ) forms at the phase interface, which is overcome by diffusion (boundary layer diffusion), Fig. 3.61.

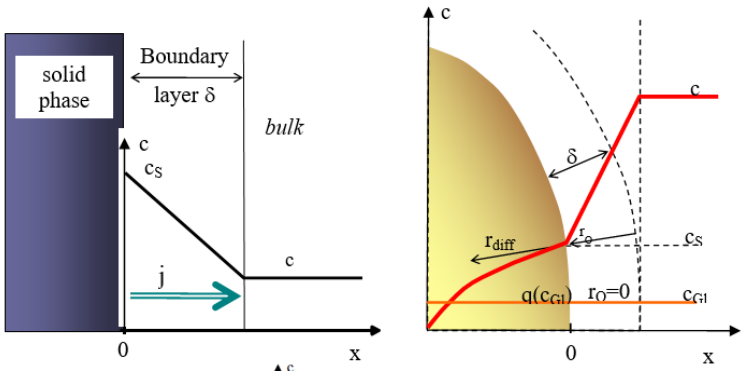

Fig. 3.61: Boundary layer diffusion with the surface concentration c_S (left) and double diffusion problem at a microporous adsorbent grain (right). x - spatial coordinate.

APPELO & POSTMA (1993) calculate the material flow j in the solution/precipitation of a mineral with the current mass m in the sample from a mass term (F) and concentration-specific (g) term, which can contain both transport and surface reactions, Eq.(3.6-1) This description can be extended to any surface reaction.

$$j = \frac{\partial n}{\partial t} = F(m) \cdot g(c) \tag{3.6-1}$$

The concentration-specific term g(c) follows from the 1. FICK'S LAW (SONTHEIMER et al. 1985), which describes the surface-normalized material flow over the product of the molecular diffusion coefficient D_f and the concentrationgradient in the boundary layer δ, Eq.(3.6-2).

$$g(c) = D_f \frac{c_S - c}{\delta} \tag{3.6-2}$$

The mass-specific term F(m*)* contains the relationship between mass and solid-phase boundary, which corresponds to the product of the specific surface O_{Sp} and the mass m_{Pr}, Eq.(3.6-3),

$$F(m) = O_{Sp} \cdot m_{Pr} \tag{3.6-3}$$

and together Eq.(3.6-4) yields.

$$r_O = \frac{D_f}{\delta}(c_S - c) \tag{3.6-4}$$

Used in Eq.(3.6-1) applies to the material flow j Eq.(3.6-5).

$$j = O_S \cdot m_{Pr} \cdot \frac{D_f}{\delta}(c_S - c) \tag{3.6-5}$$

The molecular diffusion coefficient and the boundary thickness are summarized in the mass transfer coefficient β, Eq.(3.6-6).

$$\beta = \frac{D_f}{\delta} \tag{3.6-6}$$

The one from Eq.(3.6-6) The following film thickness is fictitious and can even exceed the pore diameter mathematically at slow flow velocity.

3.6.2 Calculation of the mass transfer coefficient β over dimensionless quantities

The dimensionless mass transition is characterized by the Sherwood Sh number, Eq.(3.6-7).

$$Sh = \frac{\beta \cdot d}{D_f} = \frac{d}{\delta} \tag{3.6-7}$$

The boundary layer thickness δ is determined by the flow state, which is determined by the Reynolds number Eq.(3.5-3) A number of empirical approximations are available for the calculation of the Sherwood number, Tab. 3.61. The quotient of kinematic viscosity and the diffusion coefficient forms the Schmidt number Sc Eq.(3.6-8). In dilute aqueous solutions, the Schmidt number is between 2000 (10°C) and 1400 (25°C).

$$Sc = \frac{\nu}{D_f} \tag{3.6-8}$$

SONTHEIMER et al. (1985) cite relationships proposed by Williamson for low Reynolds numbers, Eq.(3.6-10) and Eq.(3.6-11).

WORCH (1993) compiles a series of empirical relationships for the calculation of the Sherwood number for the calculation of activated carbon breakthrough curves. In the field of technical filtration processes, which also includes grain carbon filtration, Eq.(3.6-12) and Eq.(3.6-13) almost identical Sherwod numbers. Ohashi et al. quoted in WORCH (1993) limit the mass transfer at very low flows to Sh ≥ 2. The investigations by PREUß (1999) showed lower values, Eq.(3.6-14).

VAUCK & MÜLLER (2000) give Eq.(3.6-15) and Eq.(3.6-16) for dissolving and precipitation processes in stirred tanks. The diameter of the stirring circuit is used as the characteristic length and the velocity of the stirring circumference as the flow velocity in the calculation of the Reynolds number.

For the application to filter processes and flows in the aquifer, SCHÖPKE (2007) summarized the empirical relationships Eq.(3.6-10) to Eq.(3.6-14) to the effective Sherwood number Sh_{eff}, Eq. (3.6-9) This compensates for discontinuitiesin calculations in different flow ranges, even if the validity limits are not always exactly adhered to, Fig. 3.62.

$$Sh_{eff} = \min\left(\max\left(Sh_{Ohashi}, Sh_{Preuß}\right), Sh_{Preuß}, Sh_{Preuß}\left(Re = 0{,}005\right)\right) \tag{3.6-9}$$

The lower limit was $Sh_{Preuß,0}$ (Re=0.005), only just below the flow range experimentally investigated by PREUß (1999). It would be desirable to have a function of the effective Sherwood number describing the entire Reynolds number range.

Tab. 3.61: Definitions of Sherwood Numbers for Different Processes in Aqueous Pore Solutions.

Definition	Operation range	Eq.
$Sh\left(\text{Williams a}\right) = 0{,}442 \cdot n_P \cdot Re^{0{,}69} \cdot Sc^{0{,}42}$	125 < Re <5000	(3.6-10)
$Sh\left(\text{Williams b}\right) = 2{,}4 \cdot n_P \cdot Re^{0{,}34} \cdot Sc^{0{,}42}$	0,08 < Re <125	(3.6-11)
$Sh\left(\text{Ohashi et al. a}\right) = 2 + 1{,}58 \cdot Re^{0{,}4} \cdot Sc^{1/3}$	0,001 < Re <5,8	(3.6-12)
$Sh\left(\text{Ohashi et al. b}\right) = 2 + 1{,}21 \cdot Re^{0{,}5} \cdot Sc^{1/3}$	5,8 < Re <500	(3.6-13)
$Sh\left(\text{Preuß}\right) = 2{,}01 \cdot n_P \cdot Re^{0{,}68} \cdot Sc^{0{,}42}$	0,008 < Re <0,05	(3.6-14)
$Sh = 2{,}0 + 0{,}95\,Re^{0{,}5} \cdot Sc^{0{,}33}$	countercurrent	(3.6-15)
$Sh = 0{,}5\,Re^{0{,}7} \cdot Sc^{0{,}33}$	stirred tank	(3.6-16)

From the Sherwood number, the mass transfer coefficient β is estimated, taking into account the characteristic length d_K in the grain structure, Eq.(3.6-17).

$$\beta = \frac{\frac{n_P}{1 - n_P} \cdot D_f}{d_K} Sh \tag{3.6-17}$$

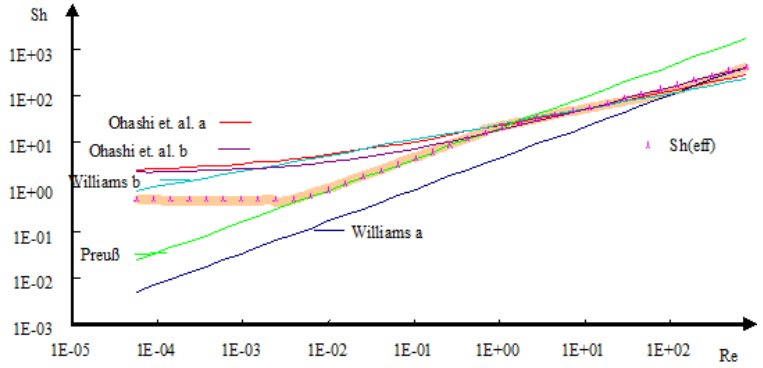

Fig. 3.62: Compilation of calculation approaches for the Sherwood number as a function of the Reynolds number and selection of Sh(eff).

3.7 Grain diffusion

3.7.1 Spherical pore (grain) diffusion in adsorption processes

Within the solid particles, diffusion processes dominate, which are composed of the free movement through the pore cavities (three-dimensional), the adsorbed substances on the inner surface (two-dimensional) and the matrix solid, or gel. WORCH (2004) derives pore diffusion from the molecular diffusion coefficient tortuosity of the pore system f_{LL}, Eq.(3.7-1).

$$D_P = \frac{D_f \cdot n_P}{f_{LL}} \tag{3.7-1}$$

Mackie (1955 quoted in STETTER, D. 2004) gives for the ratio of pore (grain) to film diffusion as a function of the internal grain porosity n_{PP} Eq.(3.7-2) .

$$D_P = \left(\frac{n_{PP}}{2 - n_{PP}} \right)^2 \cdot D_f \tag{3.7-2}$$

For the diffusive material flow j on the inner surfaces of spherical (activated carbon) particles with radius r, BAHR (2012) gives Eq.(3.7-3) .

$$j = O_F \cdot \rho_{SS} \cdot D_S \cdot \frac{\partial q}{\partial r} \qquad \left[m^2 \cdot \frac{kg}{m^3} \cdot \frac{m^2}{s} \cdot \frac{mol}{kg \cdot m} = \frac{mol}{s} \right] \tag{3.7-3}$$

The surface diffusion coefficient D_S summarizes different forms of diffusion. Taking into account the spherical symmetry, the surface diffusion model Eq.(3.7-4).

$$\frac{\partial q}{\partial t} = D_S \cdot \left(\frac{\partial^2 q}{\partial r^2} + \frac{2}{r} \cdot \frac{\partial q}{\partial r} \right) \qquad \left[\frac{m^2}{s} \left(\frac{mol}{kg \cdot m^2} + \frac{mol}{m \cdot kg \cdot m} \right) = \frac{mol}{kg \cdot s} \right] \tag{3.7-4}$$

Assuming a linear isotherm Eq.(6.5-16) in chapter 6.5.3, the surface diffusion coefficient D_S is approximately calculated from the pore diffusion coefficient, Eq.(3.7-5).

$$D_S = \frac{D_P}{\rho_{SS}} \cdot \frac{c_0}{q(c_0)} = \frac{K_d}{\rho_{SS}} \cdot D_P \tag{3.7-5}$$

For surface diffusion, the coefficient k_S is derived analogously to the mass transfer coefficient β [m/s], Eq.(3.7-6).

$$\frac{\partial q}{\partial t} = k_S \cdot \frac{O_F}{V_W}(q_S - q) \tag{3.7-6}$$

GLUECKAUF (quoted in WORCH 2004) formulated the relationships between surface diffusion and/or pore diffusion, Eq.(3.7-7).

$$k_S \cdot \frac{O_F}{V_W} = \frac{15 \cdot D_S}{r_K^2} = \frac{15 \cdot D_P \cdot c_0}{r_K^2 \cdot \rho_{SS} \cdot q(c_0)} \tag{3.7-7}$$

For ideal sphere packings, the insertion of Eq.(3.4-10) Eq.(2.2-6) and Eq.(3.4-8).

$$k_S = \frac{10 \cdot D_S \cdot n_P}{d_w \cdot (1 - n_P)} = \frac{10 \cdot D_P \cdot c_0 \cdot n_P}{d_w \cdot \rho_S \cdot q(c_0)} \tag{3.7-8}$$

Overall, there is a confusing number of descriptive approaches to describing grain diffusion.

3.7.2 Differentiation of grain and film diffusion via the dimensionless Biot-number

The Biot-number (assumption for pore diffusion model) is used to estimate the dominance of inner particle and film diffusion on the breakthrough behavior of adsorption filters. STETTER (2004) researched a biote number for the pore diffusion-model in cation exchangers with the diffusion coefficient $D_{P,i}$ for the diffusing component i, Eq.(3.7-9).

$$Bi_{P,i} = \frac{\beta_i \cdot d_w}{2 \cdot D_{P,i}} \tag{3.7-9}$$

BAHR (2012) extended the definition with the loading state $q_0(c_0)$ of the adsorption surface and the surface diffusion coefficient D_S, Eq.(3.7-10),

$$Bi = \frac{(1 - n_P) \cdot d_w \cdot c_0}{2 \cdot \rho_S \cdot q_0(c_0)} \cdot \frac{\beta}{D_S} \tag{3.7-10}$$

or simplified with the material density ρ_{SS}, Eq.(3.7-11).

$$Bi = \frac{\beta \cdot d_w}{2 \cdot D_S \cdot \rho_{SS}} \cdot \frac{c_0}{q(c_0)} \tag{3.7-11}$$

The exact distinction between dominant boundary layer and grain kinetics is given differently, Tab. 3.71.

Tab. 3.71: Dominant mass transfer mechanisms in adsorption filters via the Biot-number.

Zitat	Eq.	Filmdiffusion	...	Korndiffusion
Hand et al. 1984, quoted in BAHR (2012)	(3.7-11)	Bi <0,5	...	Bi > 30
Activated carbon filter (SONTHEIMER et al. (1985)	(3.7-11)	Bi <1,5	...	Bi > 50-100
Cation exchanger STETTER (2004)	(3.7-9)	Bi <5	...	Bi > 50

3.7.3 Empirical approaches to grain-reactions

Innerparticle diffusion usually limits the reaction kinetics in adsorption filters. Numerous empirical descriptive approaches have been developed for this purpose (HONG et al. 2018), whereby the influence of film kinetics was suppressed by intensive stirring in the batch approach.

The pseudo-first order describes the linear relationship between the absorbed amount of substance q [mg/g, mol/kg] and the adsorption rate with the first-order rate constant k_1 [1/s] and the maximum load q_e [mg/g, mol/kg], Eq.(3.7-12).

$$\frac{\partial q}{\partial t} = k_1 \cdot (q_e - q) \tag{3.7-12}$$

Since the average load of the particle is included in Eq.(3.7-12) the maximum load q_e is only loosely related to the equilibrium load. Integrated this results in an exponential approximation to q_e, Eq.(3.7-13).

$$\begin{aligned} q &= q_e \cdot [1 - \exp(-k_1 t)] \\ \ln(q_e - q) &= \ln q_e - k_1 t \end{aligned} \tag{3.7-13}$$

In some cases, a pseudo-second order with the second-order rate constant k_2 [g/(mg·s)], Eq.(3.7-14).

$$\frac{\partial q}{\partial t} = k_2 \cdot (q_e - q)^2 \tag{3.7-14}$$

This kinetic describes the approximation of an equilibrium state via a Monod/Langmuir-like term and can be linearized inversely, Eq.(3.7-15).

$$\begin{aligned} q &= \frac{k_2 \cdot q_e^2 t}{1 + k_2 q_e t} \\ \frac{t}{q} &= \frac{1}{k_2 q_e^2 t} + \frac{t}{q_e} \end{aligned} \tag{3.7-15}$$

Further empirical models were compiled by HONG et al. 2018).

3.8 Particle sedimentation

Sedimentation processes are usually of secondary importance in pore systems that flow through. The sedimentation of particles in solutions can be described analogously to the flow through the pore system. The gravity acting on the solid particles is compensated for by the frictional resistance of the water and the buoyancy force, so that solids sink to the ground at a constant velocity. For spherical particles that do not influence each other, the sedimentation velocity is calculated according to Stokes, Eq.(3.8-1).

$$v_{sed} = \frac{g}{18 \cdot \eta} (\rho_P - \rho_W) \cdot d_K^2 \tag{3.8-1}$$

mit

g Gravitational acceleration (9,81 m/s²)

η Dynamic viscosity

ρ_P, ρ_W Particle density (P), solution density (W)

d_K Particle diameter or d_w

or Eq.(3.8-2).

$$v_{sed} = 0{,}545 \cdot \frac{\nu_{20°C}}{\nu_{Temp}} \frac{(\rho_P - \rho_W)}{1\,kg/dm^3} \cdot \left(\frac{d}{1\,mm} \right)^2 \cdot \frac{m}{s} \tag{3.8-2}$$

For the sedimentation time of a sedimentation section L, this results in Eq.(3.8-3).

$$t_{Sed} = \frac{L}{v_{sed}} = 1{,}83 \cdot \frac{L}{\frac{\nu_{20°C}}{\nu_{Temp}} \frac{(\rho_P - \rho_W)}{1\,kg/dm^3} \cdot \left(\frac{d}{1\,mm} \right)^2} s \tag{3.8-3}$$

The temperature influence in the range of 4°C < temp < 30°C) can be approximated by the viscosity, Eq.(2.3-41).

When the volume fraction of the sedimenting substances can no longer be neglected, one speaks of hindered settling and the calculated sinking rate is calculated as a function of the volume fraction, as the solution fraction n_P [1] and the Reynolds number Eq.(3.5-1) Eq.(3.8-4).

$$\frac{v_{schw}}{v_{sed}} = (n_P)^{\alpha(Re)} \tag{3.8-4}$$

This Richardson-Zaki equation (DAVID et al. 2009) can be applied up to a particle concentrationof about 30 vol%, i.e. n_P > 70%. The required densities ρ_P of different minerals are given in Tab. 5.2-2.

$\alpha(Re_0) = 4{,}65$	für $Re_0 < 0{,}2$
$\alpha(Re_0) = 4{,}35 * Re_0^{-0{,}03}$	für $0{,}2 < Re_0 < 1$
$\alpha(Re_0) = 4{,}45 * Re_0^{-0{,}10}$	für $1 < Re_0 < 500$
$\alpha(Re_0) = 2{,}39$	für $Re_0 > 500$

4 Flow through porous media

4.1 Structure and properties of the solid matrix

4.1.1 Compartments of a granular solid matrix

The saturated porous medium consists primarily of a scaffolding, stationary solid phase (matrix) and the mobile and stationary phases filling the pore space. Matrix volume plus cavity volume form the reactor volume V_R. BUSCH et al. (1993) distinguish between single grain structures, honeycomb structures and flake structures. Pore aquifers and water treatment filters usually represent single-grain structures, Fig. 4.11. In a two-phase system of granular particles and the pore solution flowing through it, different compartments can be distinguished, FigFig. 4.12.

Biofilms and/or inorganic materials are often superimposed on the particle interfaces, which are assigned to the solid matrix as pore gel (f) in terms of flow technology. In terms of reactions, this pore gel represents a complex phase mixture. At the interfaces to the free pore space, water is solid in a layer around $\delta \approx 0.5$ µm ($5 \cdot 10^{-7}$ m, BUSCH et al. 1993). The adhesive or adsorption water levels out all minor roughness of the surface and can only be overcome by water constituents diffusively. The adsorption layer thickness decreases with increasing electrolyte concentration. At this transition to the flowing pore solution, known as the shear plane (g), the flow velocity is zero. The shear plane is applied as a specific surface O_{sp} [m^2/kg] to the mass of the solid matrix (or filter material) Eq.(3.4-10) or to the reactor volume O_F [m^2/m^3] Eq.(3.4-21) Tab. 2.22. The surface area available for adsorption processes with its electrical double layer is much larger by $\delta = 10$ nm (10^{-8} m) as the standard for adsorption equilibria (PARKHURST & APPELO 2006). The total intermediate grain or cavity volume n_P minus the volume of the adhesive water layer indicates the flow-effective porosity, i.e. the porosity available for hydraulic transport. The particles that build up the grain structure can have a complex internal pore system (h) with grain porosity n_{PP}, such as activated carbons and various adsorbents in water treatment, as well as coal, sandstone or pseudoparticles in aquifers, Tab. 2.22. Fine grain aggregates with a diffusively coupled inner pore system form pseudoparticles flowing around them.

In the case of grain sizes containing porous gas (unsaturated aquifer), a distinction is made between hysteres, spontaneously drainable and refillable porosity. There, the gravitationally influenced mass transport must also be taken into account. If there are also mobile liquid phases with different densities and surface tensions in the grain structure, one speaks of multiphase systems, which are not considered here.

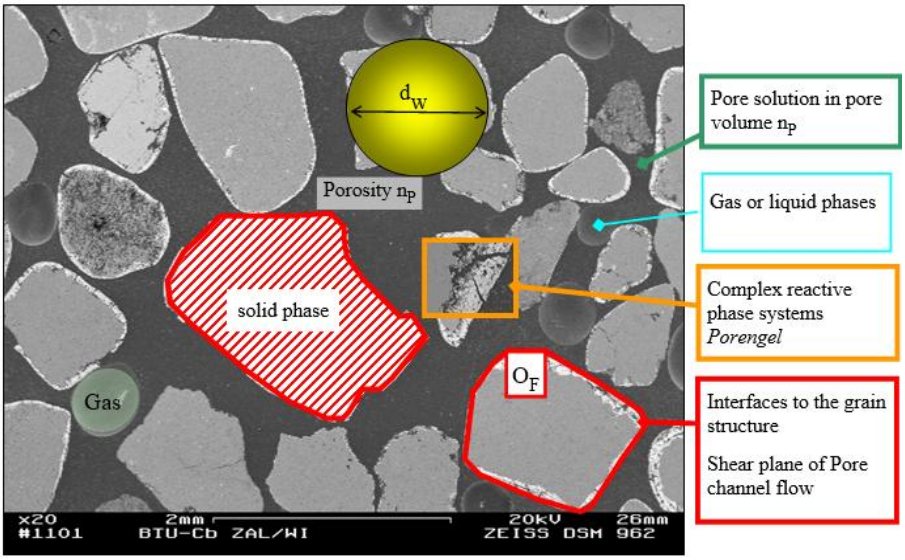

Fig. 4.11: Electron microscopic section through the pore system of an aquifer with different compartments and interfaces.

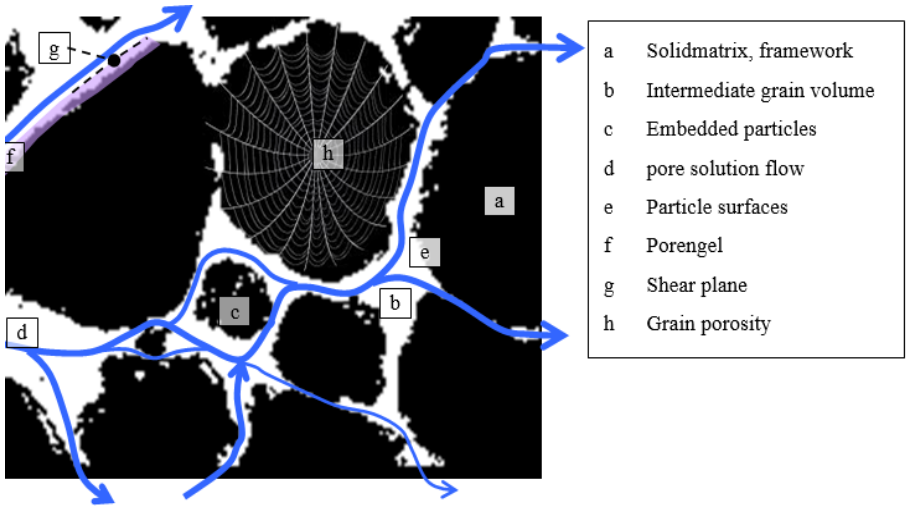

Fig. 4.12: Section through a saturated grain as a two-phase system. The main fraction of the solid matrix (a) forms a grain structure. Smaller particles (c) may be embedded in the spaces between the frameworks. The proportion of the intermediate grain volume (b) in the total volume is given by the porosity nP of the grain size Eq.(2.2-6) The pore solution flows through the free pore space (d).

Hydrogeology does not take into account the internal porosity of the solid matrix n_{PP} when specifying the total porosity n_P, as well as the flow-effective porosity n_f (effective porosity). The dewaterable porosity n_e indicates the hysteresis difference between water-saturated and drained material. This storage-usable porosity is included in the flow models of unstressed aquifers and is not considered here either.

For the quantitative determination of the different pore space fractions, laboratory methods (immersion weighing, helium pycnometry, mercury porosimetry, X-ray computed tomography) as well as field measurements (marking tests, borehole

geophysical measurements) are used. Each of these methods determines a precisely defined specific porosity percentage. The results are combined to form an overall picture in a correspondingly differentiated manner.

4.1.2 Particle size distribution and quantities derived from them

4.1.2.1 Particle size distribution oder Siebkurve

The sieving or slurry (chapter 9.8.1) are plotted as a cumulative relative sieve passage w(d) against the logarithm of the respective sieve width (sieve line, curve), Fig.4.1-3. In hydrogeology, the material d_K < 63 µm is often understood to be the undersize or fine-grain fraction UT (purple grain distribution). Bilek 2004) and Szymczak et al. (2009) refer to the fraction < 20 µm in dump aquifers as pellit.

From the particle size distribution curve, diameters d are read for specified sieve passes w[%], the percentile diameters $d_{x\%}$. The median grain size indicates the sieve diameter at the passage of 50%. From the arithmetic mean between 10% and 90% sieve passage, the average grain diameter d_m, Eq. (4.1-1) For narrowly classified bulks, this is assigned to the effective grain diameter d_w.

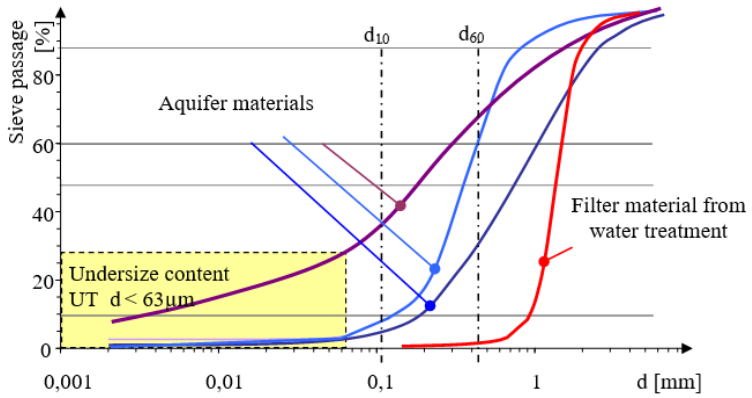

Fig. 4.13: Particle size distribution curves of different granular media with particle size distribution of the blown-offfine-grain fraction (UT63). The percentiles d_{10} and d_{60} for calculating the uniformity coefficient U Eq.(4.1-2) are drawn for the light blue curve.

$$d_m = \frac{d_{10} + d_{90}}{2} \tag{4.1-1}$$

The width of the distribution indicates uniformity coefficient U, Eq.(4.1-2).

$$U = \frac{d_{60}}{d_{10}} \tag{4.1-2}$$

SALEM (2001) use d_{90} for the deviating uniformity coefficient definition U_C, Eq.(4.1-3).

$$U_C = \frac{d_{90}}{d_{10}} = \frac{5}{2} \cdot U \tag{4.1-3}$$

Among the many other possible descriptions of the distribution width, the sorting S Eq.(4.1-4) and the skewness S_K Eq.(4.1-5).

Sorting S $$S = \sqrt{\frac{d_{75}}{d_{25}}} \approx U^{0,6745} \qquad \text{Eq.(4.1-20)} \tag{4.1-4}$$

Skewness S_K $$S_K = \frac{d_{25} + d_{75}}{d_{50}^2} \tag{4.1-5}$$

While the sorting of logarithmically normally distributed distributions depends only on their uniformity coefficient, the skewness depends on the mean grain diameter d_{50}, Fig. 4.14.

Only narrowly classified grain sizes (U < 1.5) should be used in water treatment. In the aquifer, the fine-grained particles can be transported by the water flow, which triggers suffosion, colmation or erosion phenomena. Soil scientists usually understand skeleton to mean the grain size range d_i > 2 mm, or their proportion w(d > 2 mm).

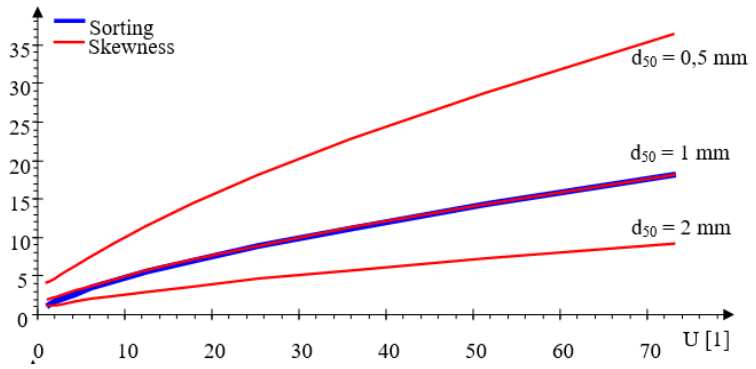

Fig. 4.14: Sorting and skewness of lognormal distributions as a function of their uniformity coefficient (example calculations according to chapter 4.1.2.3).

4.1.2.2 The surface equivalent sphere diameter d_K of particle size distribution

The surface equivalent sphere diameter d_K of an equivalent sphere packing is calculated using the integral Eq.(4.1-6) Assuming the same particle density, the equivalence criterion is met.

$$\frac{1}{d_K} = \int_{d\,min}^{d\,max} \frac{\partial w(d)}{d} \tag{4.1-6}$$

The discretized percentiles from the sieve and sludge analysis form support points for various numerical integration mFethods, chapter 9.8.2. The effective grain diameter d_w is then given taking into account the form factor f_O, Eq.(4.1-7) The deviation of the particles from the spherical or cube shape is described by the form factor f_O, Eq.(4.1-7) Tab. 3.4-1. Spheres and cubes with the diameter or edge length d_K have the same surface/volume ratios.

$$d_w = f_O \cdot d_K \tag{4.1-7}$$

4.1.2.3 Surface equivalent sphere diameters of different geometries

The relationship between particle volume and surface area results from the CAUCHY THEOREM, which states that the averaged area of the parallel projection in the plane (projection surface) of convex bodies always corresponds to a quarter of its surface. These methods are used, among other things, by particle counting devices. The sphericity (SPHT), represents the similarity of the particle shape to the sphere as a factor, Eq.(4.1-8) If the ball diameter is related to the particle volume Eq.(4.1-19)the sphericity is equal to the form factor f_O, Eq.(4.1-7).

$$SPHT = \left(\frac{d_V}{d_S}\right)^2 = f_O \tag{4.1-8}$$

Different particle geometries can be reduced to an equivalence diameter or an equivalent pore diameter using the equivalence criterion, Fig. 4.15.

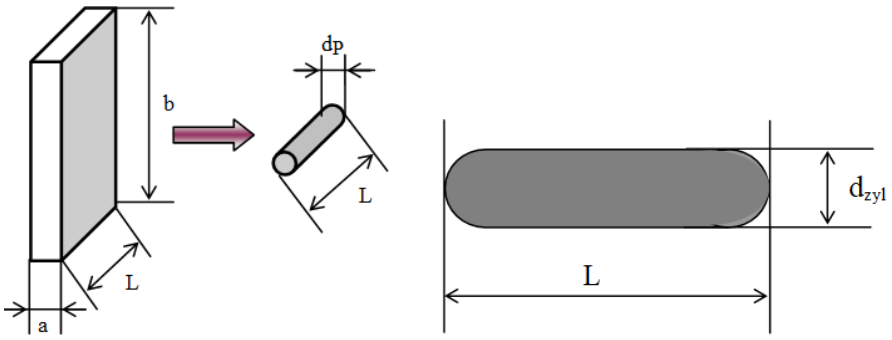

Fig. 4.15: Transformation of a cuboid fissure (column) into a current tube of equal length with a circular cross-section (left) and a rod-shaped bacillus to a spherical diameter d_w (right).

- Calculation of the equivalent (cylinder) pore diameter of a cuboid fracture, Eq.(4.1-9) to Eq.(4.1-12).

$$O = L \cdot (2a + 2b) = L \cdot \pi \cdot d_p \tag{4.1-9}$$

$$V_W = L \cdot a \cdot b = L \cdot \frac{\pi}{4} \cdot d_P^2 \tag{4.1-10}$$

This results in the transformation Eq.(4.1-12).

$$\frac{V_W}{O} = \frac{L \cdot a \cdot b}{L \cdot (2a + 2b)} = \frac{L \cdot \frac{\pi}{4} \cdot d_P^2}{L \cdot \pi \cdot d_P} = \frac{d_P}{4} \tag{4.1-11}$$

$$d_P = 2 \cdot \frac{a \cdot b}{(a + b)} \approx 2a \text{ für } a << b \tag{4.1-12}$$

- Calculation of the equivalent spherical diameter of a bacillus, Eq.(4.1-13) to Eq.(4.1-16).

The bacillus rods are compared with hemispherical cylinders at both ends, Fig. 4.15. The volume and surface area are composed of those of the ball and the cylinder shell, where the cylinder shell length Lzyl is calculated from the total length L minus the ball diameter d_{zyl}, Eq.(4.1-13).

$$L_{zyl} = L - d_{zyl} \tag{4.1-13}$$

About the volume/surface ratio,

$$\frac{V}{O} = \frac{\frac{\pi}{6}\cdot d_{zyl}^3 + \frac{\pi}{4}\cdot d_{zyl}^2\left(L - d_{zyl}\right)}{\pi\cdot d_{zyl}^2 + \pi\cdot d_{zyl}\cdot\left(L - d_{zyl}\right)} = \frac{d_w}{6} \tag{4.1-14}$$

$$\frac{\left(\frac{2}{12}\cdot d_{zyl} + \frac{3}{12}\left(L - d_{zyl}\right)\right)\cdot d_{zyl}^2}{\left(d_{zyl} + \left(L - d_{zyl}\right)\right)\cdot d_{zyl}} = \frac{d_w}{6} \tag{4.1-15}$$

follows for the surface equivalent sphere diameter d_w Eq.(4.1-16).

$$d_w = \frac{3}{2}\cdot\left(1 - \frac{d_{zyl}}{3\cdot L}\right)\cdot L \tag{4.1-16}$$

In the process engineering publications, there are other surface equivalent sphere diameter for geometric bodies.

In addition to the definition of an equal surface/particle volume ratio, the equivalent diameter of a fill is sometimes defined differently, Tab. 4.1-1.

Tab. 4.1-1: Equivalent *Diameter Definitions*.

Äquivalentdurchmesser	Definition	Eq.
Diameter of a sphere with the same projection surface A_{Pf}	$d_{Pf} = \sqrt{\frac{4\cdot A_{Pf}}{\pi}}$	(4.1-17)
Diameter of a sphere with the same cross-sectional area O	$d_O = \sqrt{\frac{O}{\pi}}$	(4.1-18)
Diameter of a sphere of equal volume V	$d_V = \sqrt[3]{\frac{6\cdot V}{\pi}}$	(4.1-19)

4.1.2.4 The logarithmically normally particle size distribution function

Most grain distributions can be composed of one, sometimes several normal distributions according to the logarithm of the diameter, Eq.(4.1-20),

$$w(d) = w\left(\lg(d_{50}), \lg(d)\right) = \operatorname{erfc}\left(\frac{\lg(d_{50}) - \lg(d)}{2\sigma}\right) \tag{4.1-20}$$

or formulated as an Excel function, Eq.(4.1-21) chapter 9.8.

$$w(d) = \text{NORM.VERT}(\lg(d_{50}); \lg(d); 0{,}651 \cdot \lg(U); \text{wahr}) \tag{4.1-21}$$

On the other hand, the adaptation to a sigmoid function with the parameter □ used by NOMURA et al. (2018), among others, is uncommon as an approximation of the Gaussian function, Eq.(4.1-22).

$$w(d) = \frac{1}{2} \tanh\left(\alpha \cdot \frac{d}{d_{50}}\right) + \frac{1}{2} \tag{4.1-22}$$

An empirical relationship can be established between the variance σ and the uniformity coefficient U by means of regression calculus, Eq.(4.1-23) and Fig. 4.16.

$$\begin{aligned} \sigma &= 0{,}2829 \cdot \ln(U) \\ &= 0{,}6514 \cdot \lg(U) \end{aligned} \tag{4.1-23}$$

Conversely, the percentile d(w) for the cumulative sieve passage w is calculated from the back transformation of Eq.(4.1-21) with the standard deviation σ calculated from the uniformity coefficient U and reference to d_{50}.

$$\log(d(w)) = \text{NORM.INV}(w; \log(d_{50}); \text{const\_10} \cdot \lg(U)) \tag{4.1-24}$$

In broad logarithmic grain distributions, the d_{50} differs from the arithmetically averaged d_m, Eq.(4.1-1) Hence derives the relation to uniformity coefficient, Eq.(4.1-25) and Tab. 4.12.

$$d_m = d_{50} \cdot 0{,}5 \cdot \left(10^{(\text{const\_10} \cdot \lg(U))} + 10^{(\text{const\_10} \cdot \lg(U))}\right) \tag{4.1-25}$$

Mit breiterer Verteilung (Ungleichförmigkeit U) nehmen die Oberfläche und auch der aus dem arithmetischen Mittel berechnete Korndurchmesser d_m zu und die Äquivalent-durchmessern d_K und d_w werden kleiner, Tab. 4.13.

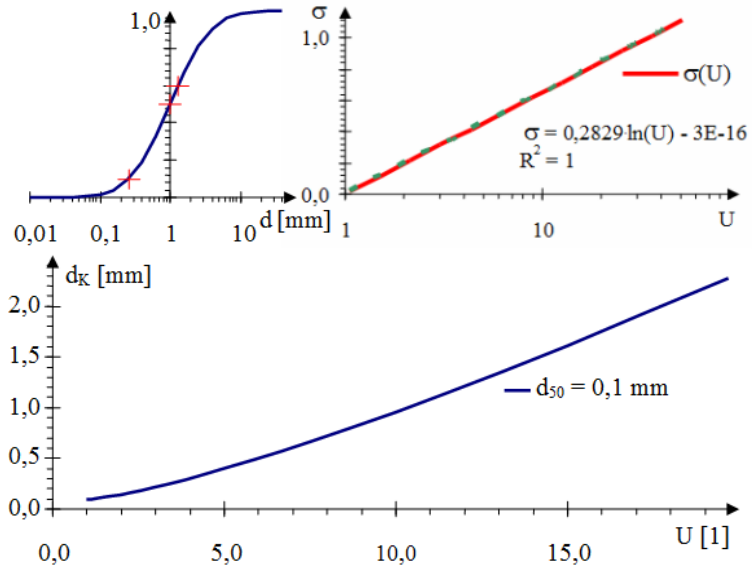

Fig. 4.16: Top: Logarithmic-normally distributed grain distribution with the percentiles for the determination of d_K and U (left) and the calculated relationship between variance and uniformity coefficient, Eq.(4.1-20) Below: Calculated average grain diameter d_K

according to Eq.(4.1-1) as a function of the uniformity coefficient U, starting from d_{50} = 0.1 mm.

Tab. 4.12: Theoretical relationship between the uniformity coefficient U and the resulting ratio between d_{50} and the mean grain diameter d_m.

σ	U	d_m/d_{50}	$\log(d_m/d_{50})$	σ	U	d_m/d_{50}	$\log(d_m/d_{50})$
1	1	1	1	1	1	1	1
0,02	1,06	1,00	0,0010	0,72	12,5	12,8	1,1068
0,12	1,50	1,14	0,0568	*0,82*	*17,8*	*20*	*1,3031*
0,22	2,14	1,51	0,1803	*0,92*	*25,4*	*32*	*1,4996*
0,32	3,05	2,21	0,3435	*1,02*	*36,2*	*50*	*1,6963*
0,42	4,34	3,36	0,5260	*1,12*	*51,5*	*78*	*1,8929*
0,52	6,18	5,21	0,7167	*1,22*	*73,4*	*123*	*2,0896*
0,62	8,80	8,15	0,9110	*1,32*	*104,5*	*193*	*2,2863*

Particle size distributions of granular filter media are determined by sieve and sludge analyses, whereby the blowdown portion is usually referred to as fine grain, Fig. 4.17, chapter 9.8. These fine-grained components are often attached to scaffold particles or aggregated in pseudoparticles, whereby their adsorption water layer of 0.5 µm is no longer negligible. This hydraulically ineffective grain fraction is not taken into account when determining the equivalent spherical diameter and its limit diameter UG = d_{min} [mm] is used as the lower limit for the integration Eq.(4.1-6) Especially in the case of wide grain distributions with a high fine-grain content, the choice of a suitable UG is not without problems.

4.1.2.5 Characterization of grain distributions over fractional dimensions

The natural and technically used porous media have fractal properties. Therefore, fractal theory can be used as a useful tool to describe its porosity and the apparent randomness of its geometric properties, PAVÓN-DOMÍNGUEZ & DÍAZ-JIMÉNEZ (2023).

The fractal dimension D as the main parameter of fractal analysis reflects the complexity of the pore structure. This indicates scale-related relationships between geometric quantities, such as particle surface O and particle volume V of a grain size distribution, Eq.(4.1-26).

$$O \approx \text{const} \cdot V^{D} \tag{4.1-26}$$

From Eq.(3.4-7) the fractal dimension $D_{O/V}$ can be derived for spheres in terms of their volume V or their equivalent diameter d_K, Eq.(4.1-27).

$$O = \frac{\pi \cdot d_K^2}{\frac{\pi}{6} \cdot d_K^3} \cdot V = 6 \cdot d_K^{2/3} \cdot V = 6 \cdot d_K^{2/3} \cdot \left(\frac{\pi}{6} \cdot d_K^3 \right) = \pi \cdot d_K^{\left(\frac{2}{3}+3\right)} = \pi \cdot d_K^{(D_{O/V}+3)} \tag{4.1-27}$$

For three-dimensional solids, $D_{O/V} = {}^2/_3$ in terms of volume. With regard to a characteristic length dK, the exponent DO/V+3 = ${}^{11}/_3$ applies, PAVÓN-DOMÍNGUEZ & DÍAZ-JIMÉNEZ (2023). For the consideration of size distributions of geometrically identical (similar) figures, Eq.(4.1-27) differentiated according to the dimension d_K, Eq.(4.1-28).

$$\frac{\partial}{\partial d_K} O = \pi \cdot \left(\frac{2}{3} + 3\right) \cdot d_K^{\left(\frac{2}{3}+3\right)-1} \tag{4.1-28}$$

Integrated via the size distribution of d_K, the fractal dimension becomes a function that often forms a constant in certain regions, which is then referred to as the fractional dimension of the distribution $D_{O/V}$, Eq.(4.1-29).

$$\ln(O) = \ln(\pi) + (D_{O/V} + 3) \cdot (d_K) \cdot \ln(d_K) \tag{4.1-29}$$

The fractional dimension corresponds to the rise of a logarithmic regression line according to the grain diameter d_K, Eq.(4.1-30),

$$\lg(O) = \text{const} + (D_{O/V} + 3) \cdot \lg(d_K) \tag{4.1-30}$$

or Eq.(4.1-31).

$$\frac{\partial \ln(O)}{\partial \ln(d_K)} = \frac{\partial \lg(O)}{\partial \lg(d_K)} = (D_{O/V} + 3) \tag{4.1-31}$$

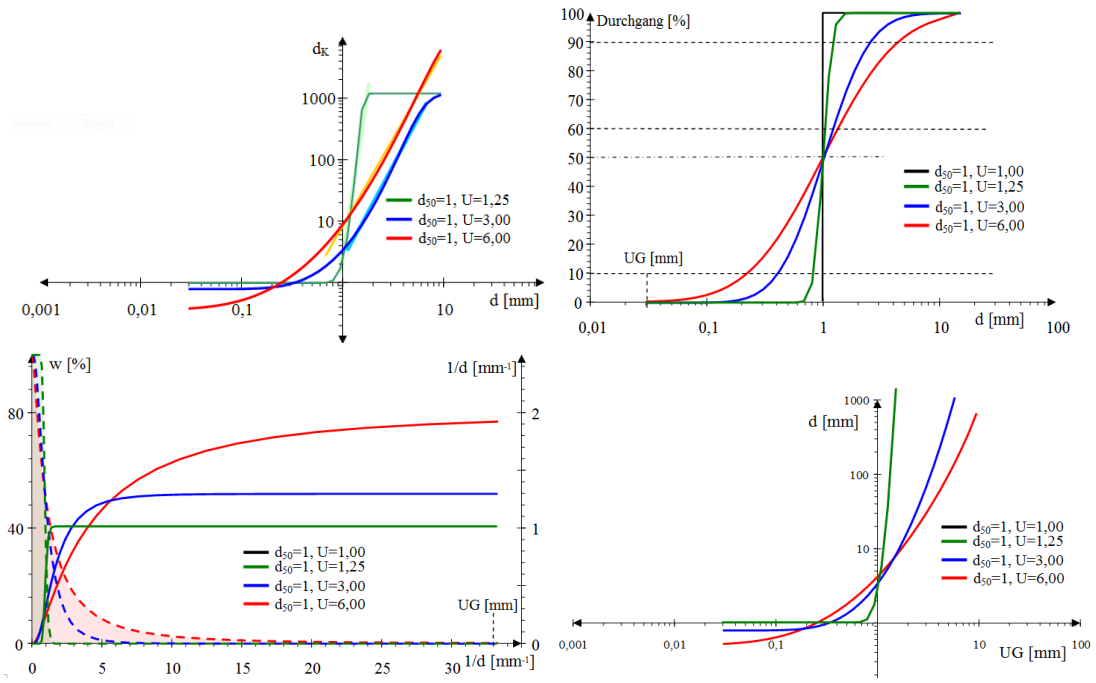

Fig. 4.17: Top left: Cumulative logarithmically normally distributed grain distributions. Top right: Representation according to 1/d (dashed) and up to the respective 1/d calculated as the lower limit UG surface equivalent sphere diameter. The surfaces under the passage curves U = 1.25 and U = 6 are highlighted in the same colour. Bottom left: Dependence of the surface equivalent sphere diameter on the lower limit UG. Bottom Right: Relationship between diameter and surface of the sieve passage. The regression line for determining the fractal dimension $D_{O/V}$ Eq.(4.1-30) are pale on the distribution curves, Tab. 4.13.

Tab. 4.13: Evaluation of according to Eq.(4.1-21) and Eq.(4.1-23) for d_{50} = 1.0 mm and various uniformity coefficients U calculated grain distributions with the corresponding mean grain diameters d_m, the equivalent diameters d_K, and the fractal dimension $D_{O/V}$ determined for the specified grain range.

U	UG	d_m	d_K	from	to	$D_{O/V}$	± σ	R^2
1	mm	mm	mm	mm		1		1
1,10	0,354	1,00	0,999	0,949	1,290	19,12	1,58	0,995
1,25	0,354	1,02	0,987	0,949	1,832	7,86	1,10	0,970
1,50	0,354	1,06	0,964	0,579	3,536	1,87	0,37	0,945
2,00	0,354	1,17	0,922	1,118	4,168	1,54	0,14	0,994
3,00	0,354	1,45	0,932	1,118	6,828	0,06	0,06	0,996
5,00	0,095	2,05	0,644	1,118	9,487	-0,79	0,04	0,997
6,00	0,095	2,34	0,616	0,683	9,487	-1,11	0,04	0,994
8,00	0,058	2,93	0,507	0,805	9,487	-1,31	0,02	0,997
10,00	0,035	3,49	0,417	0,805	9,487	-1,45	0,02	0,998

The fractional dimensions $D_{O/V}$ apply only to limited grain size ranges and decrease from the narrowly classified to the non-uniform ones. The d_K calculated from the surface function also indicates a fractional dimension, FigFig. 4.17. In the case of large screen diameters, this can take on high fictitious sizes due to the sharply falling surface-to-volume ratio with small residues. If the calculated d_K (d) becomes almost constant in the lower grain range, the UK subsize limit can be advantageously chosen in this range. The use of broken dimensions has not yet brought any practical advantages to filter technology.

4.1.3 The grain structure and texture

4.1.3.1 Texture

The storage of the particles that build up the grain structure and the resulting pore system are geometrically very complex. The arrangement or structure of the particles, crystal lattice, honeycomb or flake, is called the texture. Fillings of granular media that come close to ideal spherical fillings are usually compared to crystal lattices, and their pore geometries are derived from the hexagonal or cubic arrangement, chapter 3.4. In the case of high uniformity coefficient, small particles can occupy the pore spaces of the grain structure (Fig. 4.18 left) and thereby reduce the porosity nP. Stratified supports ensure anisotropy of the fills at horizontal flow (Fig. 4.18 right).

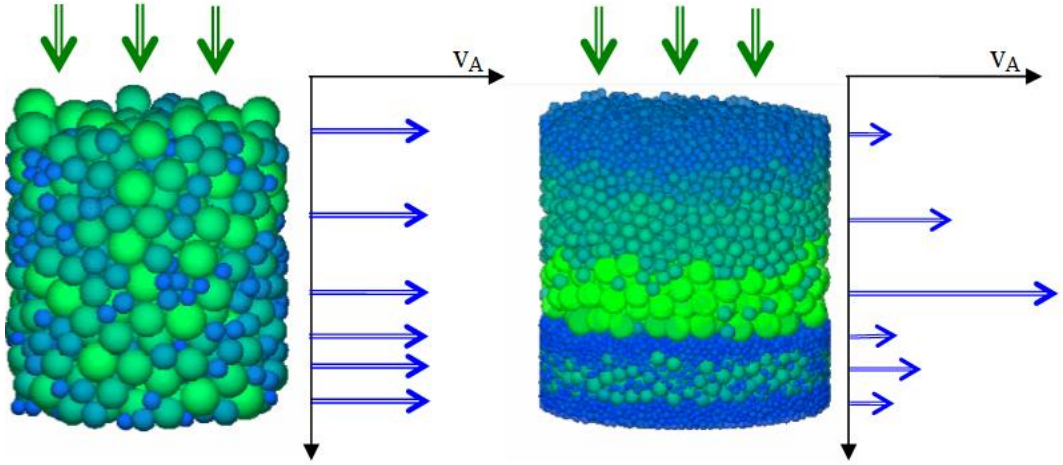

Fig. 4.18: Homogeneous storage (left) and anisotropically layered storage (right) of a mixture of normally distributed spherical radii, according to ENZMANN (2000). A position-dependent velocity profile is formed horizontally (right). Both fills are flowed through vertically homogeneously.

Stratified deposits form during filter flushing or sedimentation in the formation process of aquifers. Almost homogeneous deposits are created, for example, after intensive air/water flushing of filters or tipping of overburden. In addition to vertical anisometry, two-dimensional anisotropy is also important, especially in natural spaces.

4.1.3.2 Semi-empirical relationships for porosity and minimum pore channel diameter of unconsolidated rock

SALEM (2001) limited the porosity of logarithmically distributed particle size as a function of the grain diameter d_{50} [mm] and the uniformity coefficient by two relationships, Eq.(4.1-32).

$$\begin{aligned} \log\left(n_{P,max}\right) &= 1{,}62563 - 0{,}08653\cdot\log\left(d_{50}\right) - 0{,}03636\cdot\log\left(2{,}5\cdot U\right) \\ \log\left(n_{P,min}\right) &= 1{,}53902 - 0{,}18968\cdot\log\left(d_{50}\right) - 0{,}08201\cdot\log\left(2{,}5\cdot U\right) \end{aligned} \qquad (4.1\text{-}32)$$

The one from Eq.(4.1-32) the following porosity range is unsuitable for hydraulic calculations, Fig. 4.19.

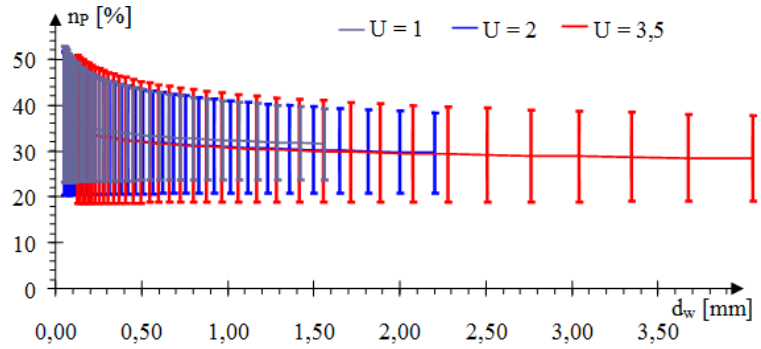

Fig. 4.19: Sample calculations by Eq.(4.1-32) for the relationship n_P (dw) and three uniformity coefficient. d_{50} follows after Eq.(4.1-25) from DW.

The DVGW-Arbeitsblatt W 210 (quoted in ENZMANN 2000) links porosity with a *fuzzy* depositional density and the uniformity coefficient U with the constants Tab. 4.11, Eq.(4.1-33).

$$n_p = a + b \cdot U^c \tag{4.1-33}$$

Tab. 4.11: Constants of the Eq. (4.1-33)

Storage density	a	b	c
loosely	0,300	0,146	-0,6636
medium	0,260	0,160	-0,6941
close	0,224	0,165	-0,5890

and the fuzzy information for the storage density:

- o 0,40 for backflushable quick filters
- o 0,30 for slow filters
- o 0,2 ...0,35 for aquifers

These guideline values are in the range of geometric calculations (BUSCH et al. 1993) or statistically generated spherical packings (ENZMANN 2000). The third-degree polynomial of lg(U) proposed by Fuchs et al. (2017) gives almost identical results to Eq.(4.1-33)).

By evaluating ideal grain distributions with different irregularities, BUSCH et al. (1993) indicate the minimum pore channel diameter as a function of the equivalent spherical diameter d_w, Eq.(4.1-34) and Fig. 4.110.

$$d_{P,min} \approx 0{,}44 \cdot \frac{n_P}{1 - n_P} \cdot d_w \tag{4.1-34}$$

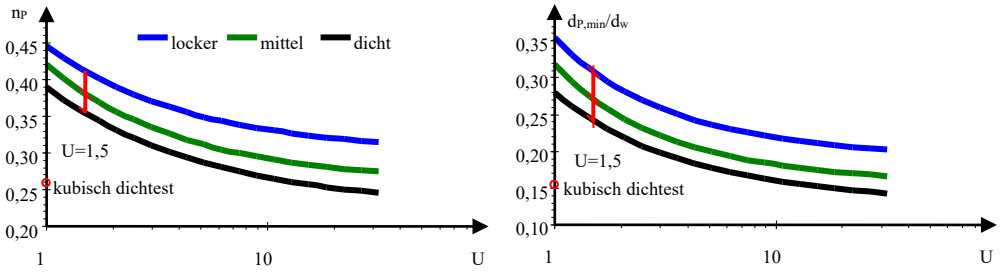

Fig. 4.110: Theoretical relationship between uniformity coefficient U and porosity n_P, as well as the minimum pore channel diameter $d_{P,min}$. The red vertical line marks filter fills with U = 1.5. The most densely dense bearing is shown as a red circle.

4.1.4 The *Porengel* as a small-scale complex mixing phase

Depending on the material, there are functional groups at the phase interface of the solid matrix that interact with the liquid phase, e.g. as adsorptionsites. These different phases with their interfaces, which are aggregated in the narrowest pore space via the solution phase and interact with each other, are combined into the *Porengel* as a separate phase.

This includes adsorbed phases and coatings made of biofilms, hydroxides, carbonates, sulphides, clay minerals and various organic substances (humic substances, EPS). Within the Porengel, chemical equilibrium constants can (apparently) deviate from their thermodynamically defined values. The cause can usually not be clearly clarified, so that these deviations must be measured and taken into account.

Primarily, the materials building up the pore structure in connection with the mobile media determine the developing Porengels. The solid framework with their surfaces primarily form the support, Fig. 4.111. Via very different mechanisms, the Porengel interacts with the pore solution, chapter 6.5, Fig. 6.51. Its description is therefore limited to special cases, chapter 10.4.

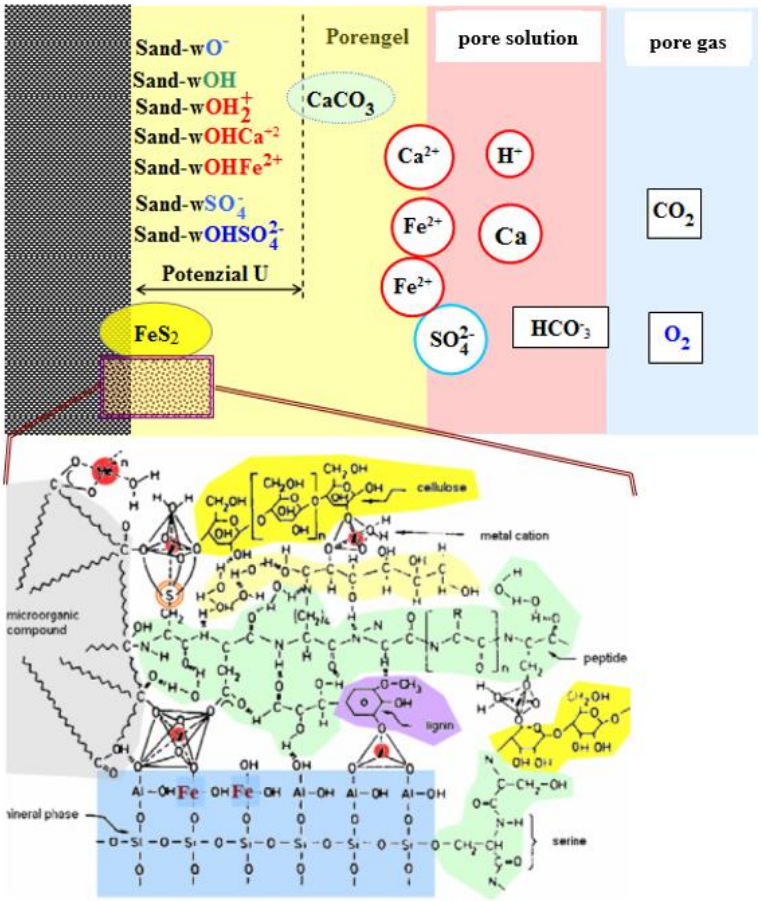

Fig. 4.111: Scheme of the complex composition and its interactions between Porengel and pore solution (SCHÖPKE et al. 2020) with addition of organic components (below: KOSOBUCKI & BUSZEWSKI 2014).

4.2 Real grain sizes

4.2.1 Evaluation standards

4.2.1.1 Fractal size distribution of surface area and porosity

In fills made of granular material, pore diameter, porosity and pore surface are important variables. All filtration-relevant processes have a scale-specific effect. The fractal distributions of porosity and surface area can be illustrated by determining the accessible volume or surface area for a sphere with varying diameter d.

For the diameter interval from the macroscopic to the molecular range, orienting distribution functions are postulated as a function of the diameter d via inscribed spheres/circles (SCHÖPKE & BALKE 2015), Fig. 4.21. These orienting distribution functions of the porosity n_P Eq.(4.2-2) or the surface O_F Eq.(4.2-1) are linked to flow and reaction processes, FigFig. 4.22.

$$n_P(d) = F_{PV}(d) = \int_0^{d_{max}} n_{Px}(d) \cdot \partial d \qquad d_{max} << \infty \tag{4.2-1}$$

$$O_F(d) = F_{OF}(d) = \int_0^{d_{max}} O_{Fx}(d) \cdot \partial d \tag{4.2-2}$$

Differentiated for the frequency distribution functions of the porosity $n_{Px}(d)$ Eq.(4.2-3) and the $O_{Fx}(d)$ Eq.(4.2-4).

$$n_{Px}(d) = \frac{\partial}{\partial d} F_{PV}(d) \tag{4.2-3}$$

$$O_{Fx}(d) = \frac{\partial}{\partial d} F_{OF}(d) \tag{4.2-4}$$

As long as no suitable measurement methods with specific software are used, these representations are mainly used to detect dominant scales in the pore system.

The flow sections in natural areas are usually heterogeneous in structure and contain areas that do not flow through or have little flow through - the dead spaces n_{Tot}. On a scale of meters to kilometers, these narrow the pore space through which they flow and are contained in the macroporosity n_{eff}, Fig. 4.22. No boundaries can be assigned to the dead spaces. The effective or usable porosity defined in the decimetre to metre range determined by pumping tests, together with smaller dead spaces and grain distributions, determines the flow behaviour around the well and is usually transferred to representative, larger areas of aquifers. This also explains the mostly lower effective porosities in the result of pumping tests compared to the n_P, chapter 9.8. The shear surface that determines the flow resistance is also in this range. In the case of fine-grained materials, the adsorption or adhesive water layer limits the flow-effective porosity. The model sizes of the equivalent spherical diameter d_w and the cylinder pore diameter are even larger than the still passable pore narrowing $d_{P,min}$, which estimates the theoretical sieve diameter of the fill, Eq.(3.4-3) chapter 3.4.1.

Diffusion through the flow-dependent *resting boundary layer* δ of the shear plane determines the diffusion to the stationary solid-phase particles with their internal grain

porosity, e.g. of activated carbon, macroporous ion exchangers or fine-grainaggregates. The pore radius distribution, and thus that of the inner pore volume and surface, is determined, among other things, by mercury intrusion porosimetry. The diameters of macro-, meso- and micropores also determine the accessibility of molecules of different sizes to the adsorption surface. The BET surface indicates the maximum surface area available for adsorption and is determined by the monomolecular nitrogen occupancy. At the grain boundary, the diameter and pore volume are reduced abruptly, which is associated with a jump to large surfaces in the case of porous particles.

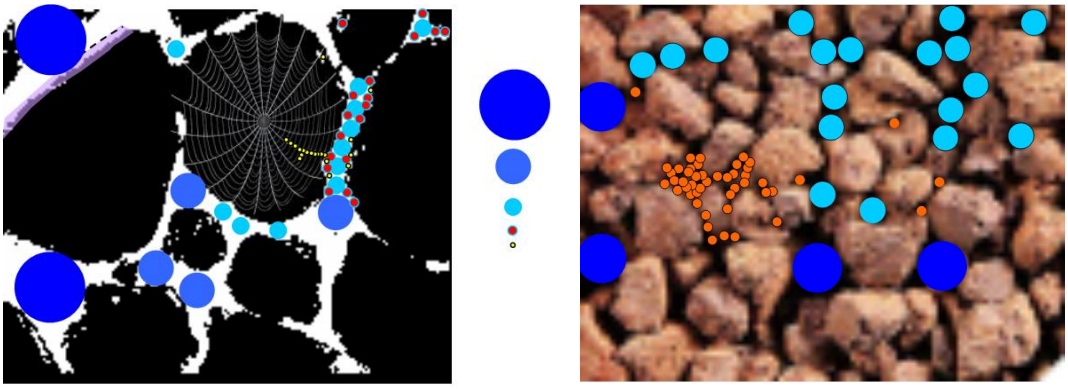

Fig. 4.21: Schematic filling of the pore system with circles/spheres of different diameters. Left: Section Fig. 4.11. Right: Ferrosorp® grain structure (SCHÖPKE & BALKE 2015).

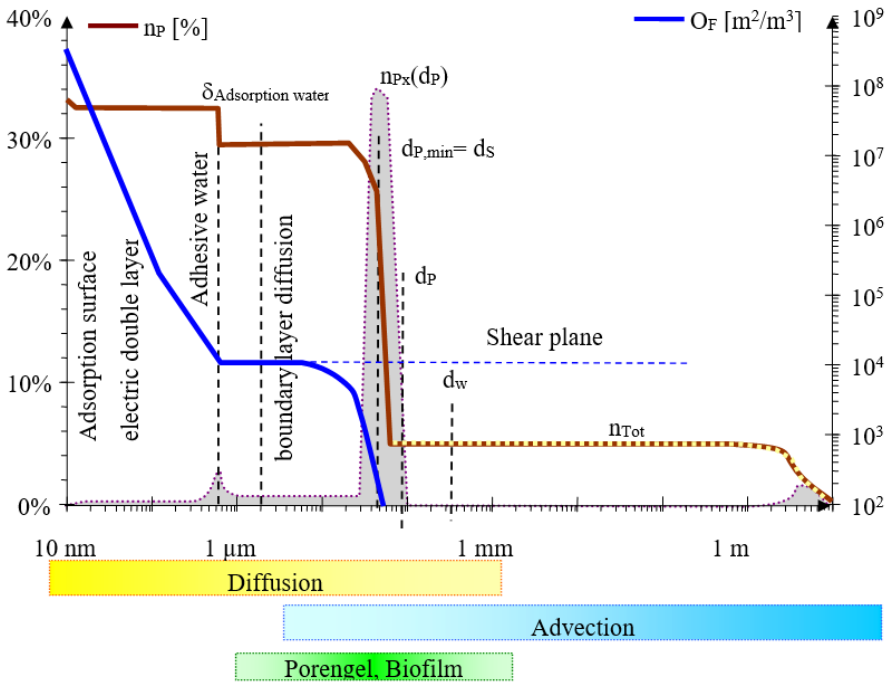

Fig. 4.22: Integral distributions of the accessible pore volume n_P (left) and the associated surface O_F (right) as a function of the diameter of the fitted sphere. The distribution function for the porosity $n_{Px}(d)$ Eq.(4.2-3) is drawn as a gray area not to scale. In it, the definition ranges of characteristic quantities are marked in color. Below this are the areas of action of diffusion and advection and the size range for the pore gel. The dead spaces of macroporosity are dotted.

4.2.1.2 Representative compartments

Operations on a scale level can only be carried out experimentally on volume and time scales that also represent these scales. The lower bound of the spatial and temporal resolution is represented by the representative elementary volume REV and the representative elementary time RET. The REV must be large compared to the characteristic dimensions of the heterogeneities, and small to the range to which the results are to be extrapolated. The REV of a one-dimensional flow through a porous granular medium comprises a bundle of streamlines (streams) that define a representative flow tube. Its flow path L lies above the scale plane of the pore structure, Eq.(4.2-5). In the RET, the adjustment time for local equilibria must be taken into account (BUSCH et al. 1993).

$$\begin{aligned} A_F &>> \left(\frac{d_w}{n_P}\right)^2 \approx d_w^2 \\ L &>> \frac{d_w}{n_P} \approx d_w \end{aligned} \qquad (4.2\text{-}5)$$

Under these minimum conditions for a representative elementary volume, the processes in the pore system can be described as a continuum. The property c(L) then becomes an integral quantity over the flow cross-section at the flow path L.

4.2.1.3 Processes in technology and the environment

In the diagram Fig. 4.22, the relevant effects of water treatment processes in technology and the environment can be classified, Fig. 4.23. The groundwater flow fields determined by hydrogeological models reach up to the kilometre scale. The areas and heterogeneities that constrict the flow cross-section are included as macroporosity n_{Pm}. The electrical tubes are guided around these areas. Filtration in technical water treatment, on the other hand, only reaches up to the metre scale. Dead spaces are minimized technologically, which is why macroporosity plays practically no role. The geometry of the pore system determines, among other things, the particle separation. The pore solution corresponds diffusively to the grain pore system via film kinetics. The pore gel is part of the grain structure. A number of chemical processes, such as adsorption, take place inside the grain. Diffusion dominates in the molecular to the pore area, and from the adhesive water area onwards, transport via the pore solution (advection), Fig. 4.22.

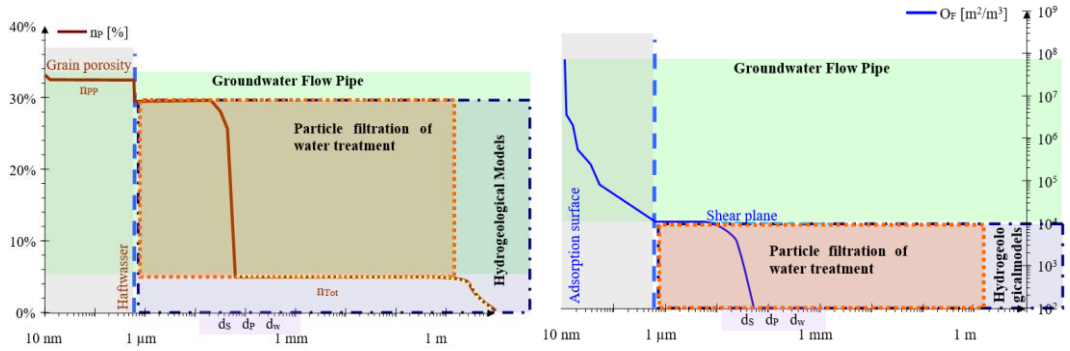

Fig. 4.23: Classification of filtration applications in the size ranges of porosity n_P left and right with respect to the surfaces O_F. A distinction is made between reactions inside the grain, the current tube (particle filtration) and the dead spaces that influence the flow field. The pore gel that is not marked is to be assigned to the stationary scaffolding grain as a peripheral area.

4.2.2 Porous aquifers

Pleistocene sediments are usually present in strata packages with fine-grained components stratification of well-sorted grains, as well as silt or clay lenses (stevedores). Larger stones and possibly lignite particles are also embedded in it. In the structure, smaller particles fill free pore space in relation to homogeneous fills, Fig. 4.24. The grain size distributions are determined from mixed samples of the fine structure recognizable on drill cores and thus show a greater uniformity coefficient than the fine structure layers Fig. 4.25.

In open-cast lignite mining, the overburden is mixed, tipped (crumbled) from materials from different geological formations. The fine-grain aggregates formed from cohesive layers (here boulder clay in stevedores) contain a narrow micropore system with a large adsorption water content and is only diffusively coupled with the mobile pore solution, Fig. 4.26. These *pseudoparticles* consist of the almost impermeable grain structure of the till, which is filled with platelet-shaped (clay) minerals, Fig. 4.28.

No BET surface can be determined for coarse particulate material, Fig. 4.27. The adsorption surfaces can be provisionally estimated by their cation exchange capacity at an adsorption site density of approx. 1.2 nm^{-1} (quartz) and compared with that determined from the grain size distribution.

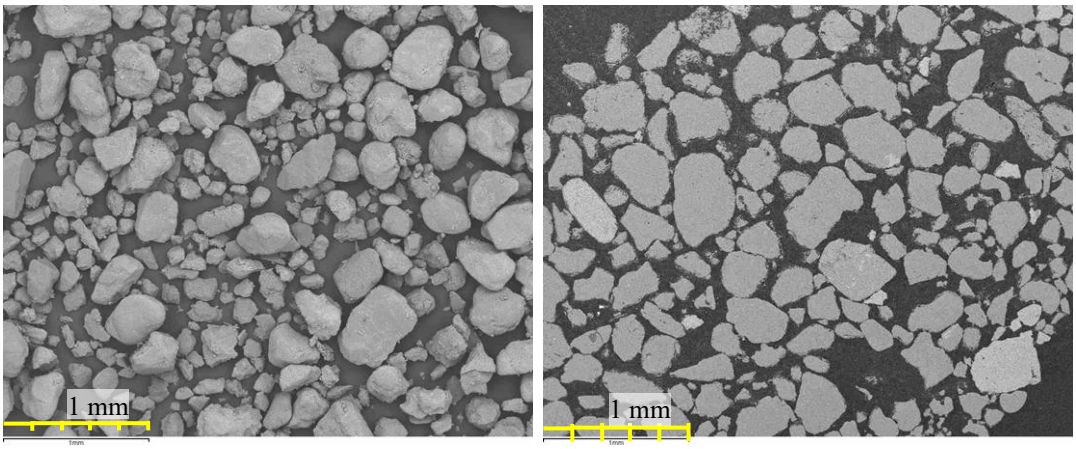

Fig. 4.24: Scatter sample (left) and microstructure section (right) through sample P0_15,4 (SCHÖPKE et al. 2020) of the pleistocene aquifer at the Ruhlmühle.

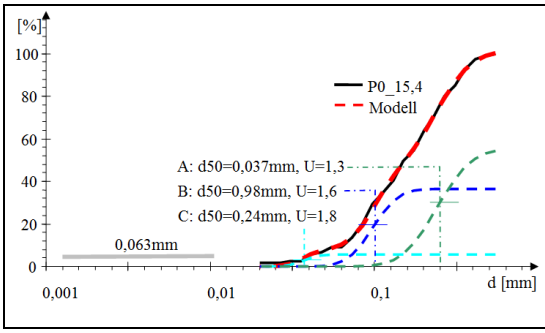

P0_15,4 n_P = 0,34 - 0,39 (SCHÖPKE et al. 2020)

fraction	w	d_{50}	U	d_m
	%	mm	1	mm
< 0,063	5,1			
A	7,9	0,037	1,3	0,04
B	37,4	0,098	1,6	0,111
C	55,6	0,240	1,8	≈ *0,24*
P0_15,4	100	0,200	3,0	0,365

Fig. 4.25: Composition of the grain size distributions of the aquifer P0_15.4 (SCHÖPKE et al. 2020) from the undersize (< 63 µm) of the three logarithmically normally distributed grain sizes A, B, C. (According to chapter 9.1.2.2 calculated distributions dashed, measured solid). The porosity n_P was determined by pixel counting.

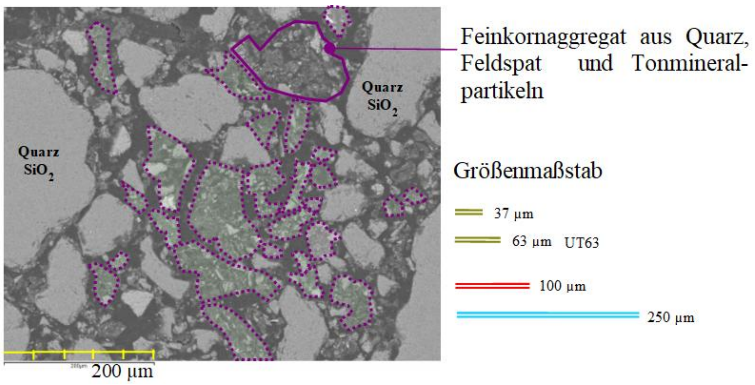

Fig. 4.26: Grinding of a dump aquifer sample from the Skadodam (SB2_17.5m, SCHÖPKE et al. 2011) in which Pleistocene sands were mixed with till. The marl forms the marked fine-grained aggregates (pseudoparticles, dotted outlined). The grain-forming particles are in the size range above 63 µm.

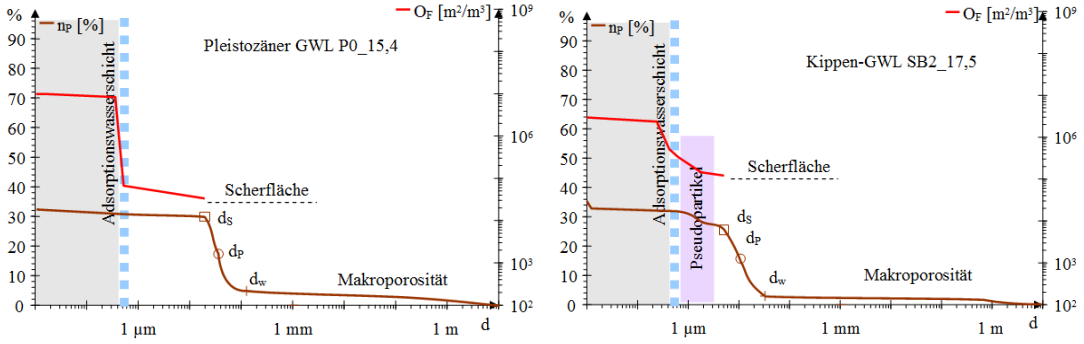

Fig. 4.27: Constructed distributions of pore surface and volume for the Pleistocene P0_15.4 (left) and the dump aquifer SB2_17.5 (right). Below the shear surface, no surfaces can be specified according to SCHÖPKE et al. (2011).

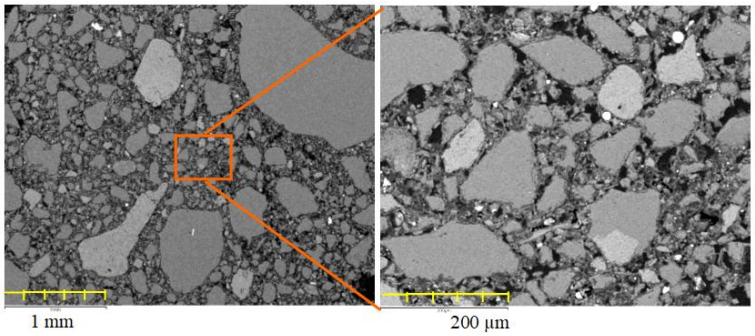

Fig. 4.28: Structural section of tipped boulder chunks (SB1_19.5m) with filled pore system of aluminosilicates and some heavy mineral particles (white dots).

4.2.3 Sandstone quarry flowing through

SCHÖPKE & KOCH* (2007) used sandstone quarry from a former uranium mine, which represented debris fields of leach mining, in filter tests. In these mining-influenced sandstone formations, the fissured pore systems extend over several scales. The particles of the *white sandstone* are composed of sintered fine sand with a continuous inner pore system and are diffusively coupled with the flowing pore solution, Fig. 4.29. The time-dependent penetration depth of substances from the pore solution was modelled, chapter 8.3.4.2. Fig. 8.39. The horizontal filter operated horizontally with this rock fracture could be described by two current tubes flowing through at different filtration velocities, FigFig. 4.210.

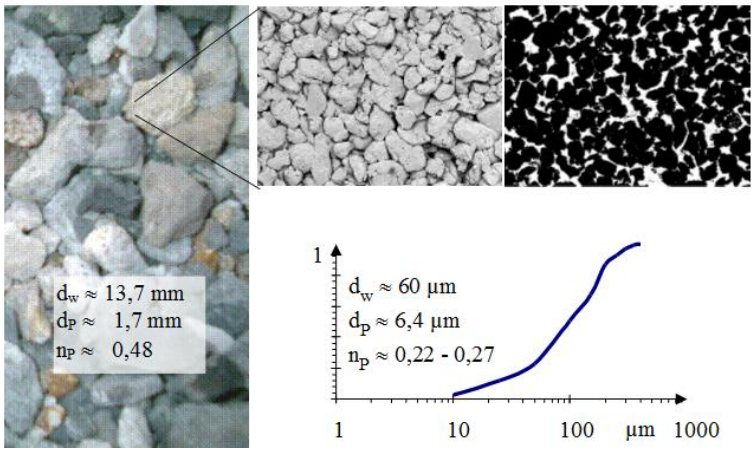

Fig. 4.29: Rock fracture made of sandstone (left), particle section (top center) with pore system (top right) and distribution of the fine sand forming the sandstone (bottom), Schöpke & Koch* (2007).

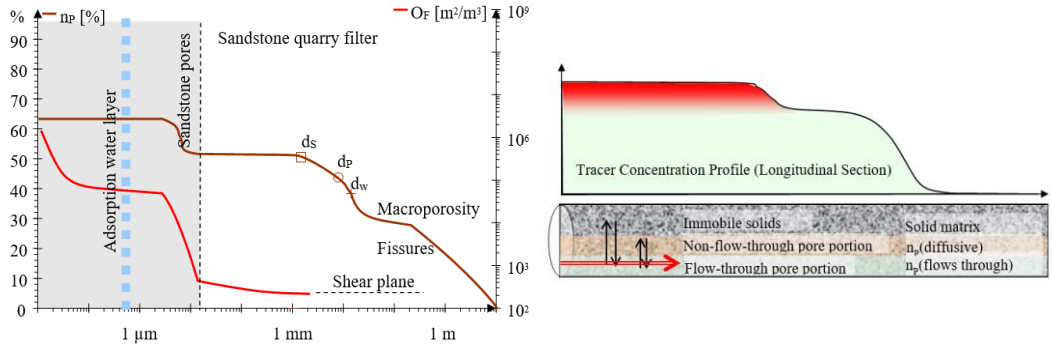

Fig. 4.210: Left: Constructed distribution of pore surface and volume for a flow section from rock fracture (SCHÖPKE & KOCH* 2007). Right: Distribution of the current tube volume into the immobile solid matrix, the diffusively accessible dead spaces (particle porosity) and the part through which the mobile pore solution flows (SCHÖPKE & THÜRMER* 2011a).

4.2.4 Granular Iron Hydroxide Sorbent (Ferrosorp®)

The granular filter material from mine water treatment, consisting mainly of iron hydroxide gel, is used for the adsorption of undesirable water constituents, such as phosphate, arsenate and heavy metals in wastewater treatment and aquaristics, Fig. 4.211. This microporous gel has a high adsorptive inner surface area, Tab. 4.21. Flow-through porosity and adsorptive grain porosity are separated by the stationary adsorption water layer on the grain surface.

Fig. 4.211: Granulated iron hydroxide sorbent (ferrosorp®) and grain cuttings (BALKE & SCHÖPKE* 2009). The dark grain edge in the cut on the right is unrelated to the adsorption properties of the material, and is attributed to the drying process.

Tab. 4.21: Mercury intrusion porosimetry determined pore radius distribution (left) of the material FerroSorp® Plus with the resulting parameters (right) (BALKE & SCHÖPKE* 2009).

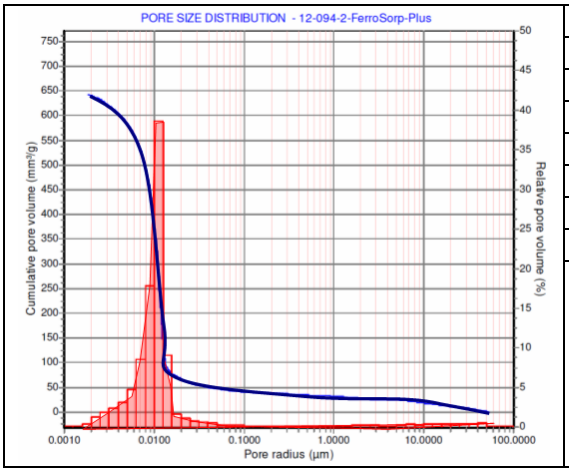

Bulk density	3,0	g/cm³
porosity	66	%
Pore volume	643	mm³/g
Pore surface	144	m²/g
Zylindrical pores radius	9	nm
Medium pore radius (D_{50})	11	nm
Variance of pore distribution	1,5	nm
BET-surface	≈ 300	m²/g

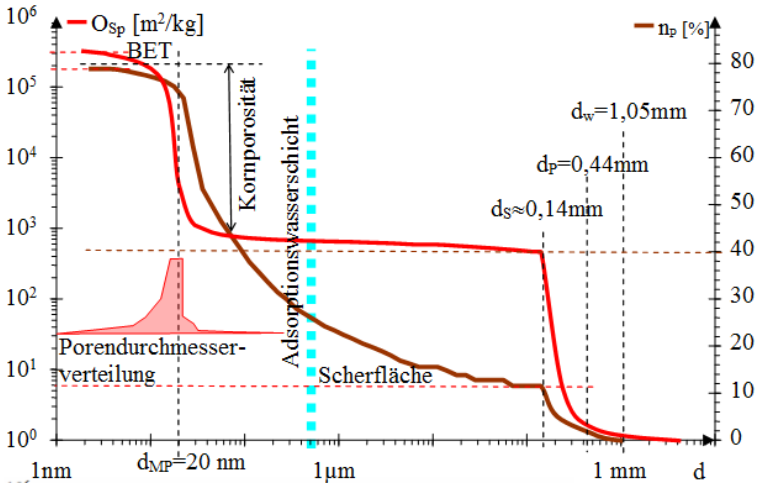

Fig. 4.212: Constructed distribution of pore surface and volume for the granular iron hydroxide gel (BALKE & SCHÖPKE* 2009).

4.2.5 Porenge on inert grain surfaces

4.2.5.1 Structure-forming minerals

Porengel can have different structures. Solid amorphous and crystalline phases form a basic structure in which microorganisms, organic and inorganic phases are embedded. The frequently structure-forming materials of pore gels include:

- Iron and manganeseohydroxides,
- Carbonates of calcium, magnesium and iron,
- Aluminosilicates, including clay minerals,
- organic structures that are difficult to degrade, such as lignite, peat or plant residues, and
- Microorganisms and Biofilms.

Microorganisms and humic substances are embedded in it and react with the pore solution flowing past. The basic structure made of solid materials is usually resistant to small environmental fluctuations (pH, ion composition, redox). Structures consisting of loose compounds of fine particles (clay minerals) with limited soluble humic substances and biofilms, on the other hand, can become unstable with smaller changes in the environment, chapter 10.4. The solid basic structure of these pore gels can be examined by electron microscopy, while the structure elucidation of biofilms and organic coatings requires specific methods.

4.2.5.2 Hydroxide structure

During iron removal and manganese removal of groundwater, the filter material grains are coated by autocatalytic reaction products, FigFig. 4.213. If biological iron removal is preferred, occlusive dendritic structures are formed. The inorganic composition of the chemical and biological precipitates does not differ from each other. In the filling bodies of a mine water treatment plant of Wismut GmbH examined by Koch & Schöpke* (2008), arsenic and traces of uranium were also embedded in the coating, FIG. Fig. 4.214 and Fig. 4.215. Similar coatings can also be found in iron removal filters.

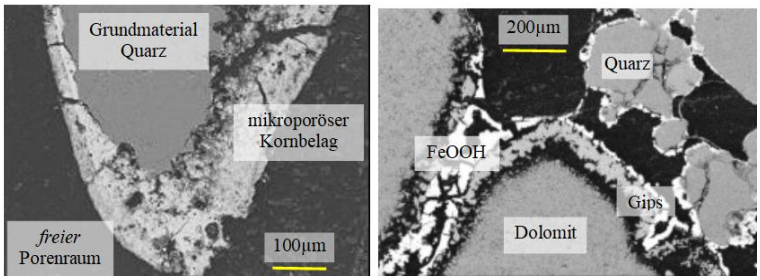

Fig. 4.213: Structural cuts with grain coatings (Porengel). Left: Quartz grain with iron hydroxide coating and sand (quartz)/dolomite mixture after flow of acid acid mine drainage (right), (SCHÖPKE* 2002).

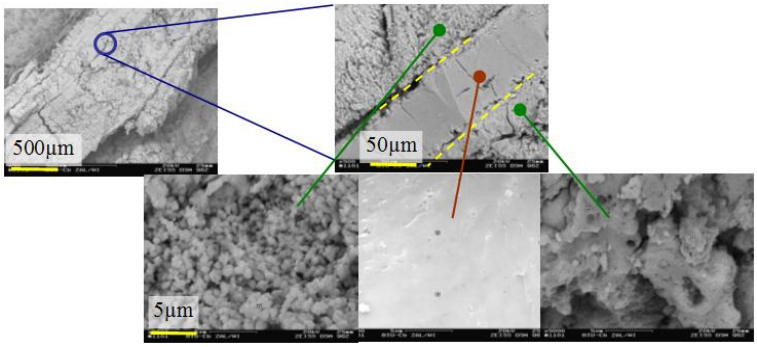

Fig. 4.214: Layering of the Porengel attached to a trickle filler body. (Breaking line with enlarged details, green bacterial deposits, brown autocatalytic reaction products, KOCH & SCHÖPKE* 2008).

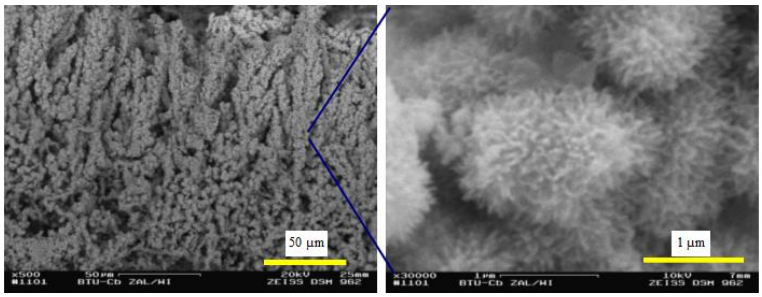

Fig. 4.215: Products of iron oxidizers (*Thiobacillus ferrooxidans,* KOCH & SCHÖPKE* 2008).

4.2.5.3 Carbonate structures

Carbonates form more compact structures than iron and manganese oxide hydrates. Laboratory experiments on the neutralization of mining-acidified acid water (acid mine drainages) in mixtures of dump sand and dolomite or calcite resulted in the formation of carbonate deposits, SCHÖPKE* (2002) and SCHÖPKE (2024). After pH increase by dissolving the material, iron hydroxide precipitated in the aerobic environment and formed the outer light crust around the dolomite grains and covered the quartz particles of the sand in a thinner layer, Fig. 4.216. The calcium released in the process precipitated with the sulphate of the open-cast lake water as gypsum. The material surfaces were passivated by the reaction products iron hydroxide and gypsum. Between the passivating layer and the dolomite/calcite grain, a gap of dissolved material was formed.

4.2.5.4 Biofilms

The extrapolymer substances (EPS) produced by the microorganisms accumulate together with organic water constituents (including humic substances) in the Porengel, Fig. 4.217 below. Their influence on the hydrochemical properties of the material is largely unknown. Estimates assume 60 mg/kg biomass with approx. 20 % organic carbon, chapter 7.5.

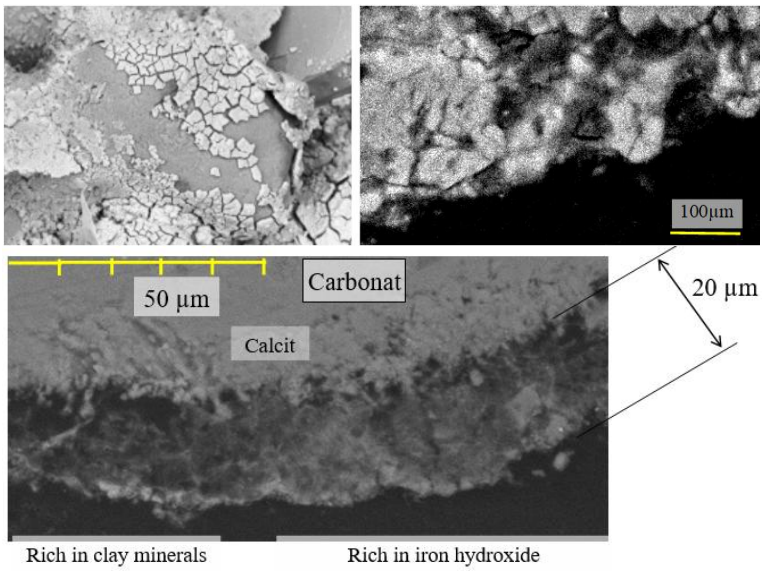

Fig. 4.216: Top: Grain surface with coating burst open during preparation (litter specimen left) and heavily eroded edge of a calcite grain from a reactive wall simulated in the experiment (section on the right) SCHÖPKE* (2002). Bottom: Phase interface (section) formed on a calcite grain during the neutralization of open-pit lake water (SCHÖPKE & THÜRMER* 2012).

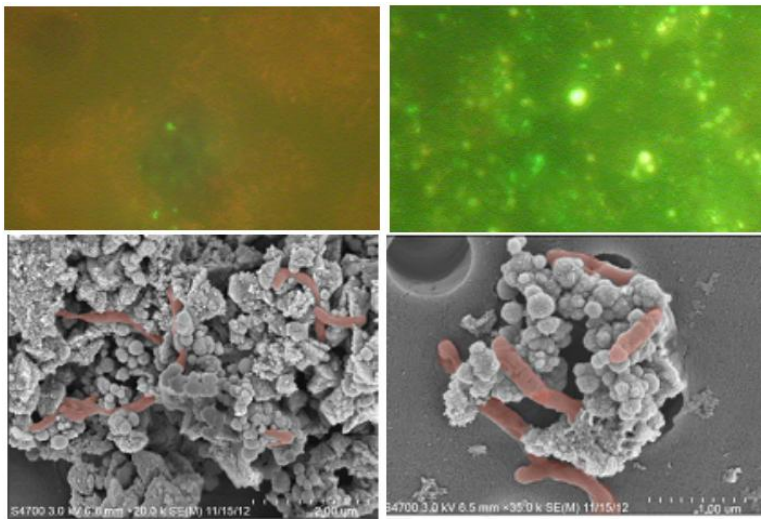

Fig. 4.217: Fluorescence microscopic images of aged biofilm with predominantly dead biomass (top left) and of fresh coating (top right) with living microorganisms, SCHÖPKE et al. (2013). Bottom: Cell-mineral associations (cells false-color orange) according to PERCAK-DENNETT et al. (2017).

4.2.6 Reactive Mixed Grains with Metallic Iron Fe^0

This case study comes from the evaluation of laboratory filter experiments for the removal of As, Cd, Ni from a groundwater contaminated site of a nickel smelter, SCHÖPKE & THÜRMER* (2012) via a reactive wall consisting of $Fe^0/CaCO_3$/gravel. In the

process, metallic iron and calcite were dissolved and metal carbonates were separated. The coating on the carbonate grain consisted mainly of varying proportions of arsenic-containing iron hydroxide and clay minerals, Fig. 4.218. The precipitation products formed diffusion-inhibiting layers on the grain surfaces and also accumulated in pore coils, Fig. 4.219. On the steel particles used, the pavement layer reached thicknesses of between 0.6 µm and 20 µm.

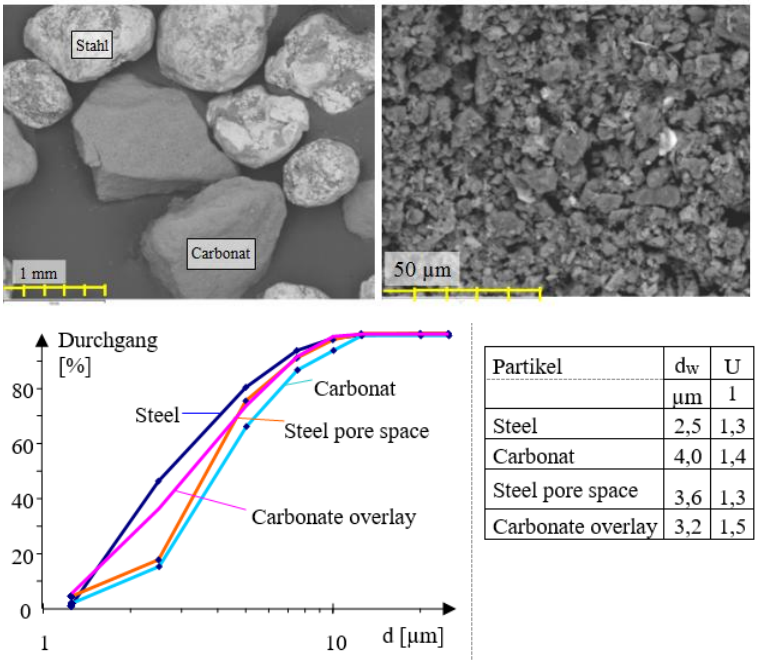

Partikel	d_w	U
	µm	1
Steel	2,5	1,3
Carbonat	4,0	1,4
Steel pore space	3,6	1,3
Carbonate overlay	3,2	1,5

Fig. 4.218: Fe^0/limestone granules from an experimental filter for the simulation of a reactive wall (scatter sample top left) and detail section of the occupied surface (top right), as well as the grain distributions of the separated particles (bottom), (SCHÖPKE & THÜRMER* 2012).

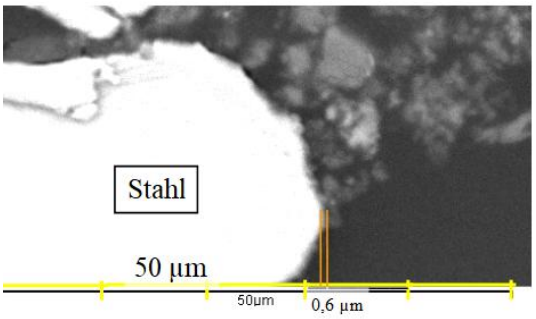

Fig. 4.219: Enlargement of a grain gusset with the boundary layer on the iron grain by 0.6 µm ("Stahl" = steel).

4.2.7 Closure of grain porosity

Bei der Behandlung von bergbauversauertem Sandstein durch Neutralisation der mobilen Porenlösung beobachteten SCHÖPKE & THÜRMER* (2010) den Verschluss der

Kornporosität durch Neubildung von Tonmineralen, Fig. 4.220. Die im Korninneren noch enthaltene saure Lösung wurde dabei konserviert, SCHÖPKE (2024).

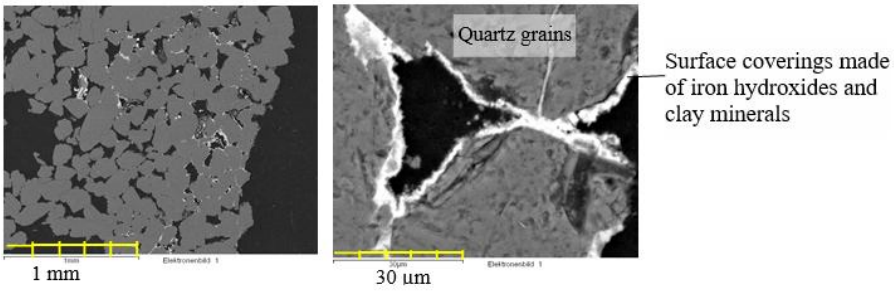

Fig. 4.220: Sections through a grain structure of sandstone particles by mineral formation (SCHÖPKE (2024).

4.3 Filter media flowed through

4.3.1 Calculation methods for the permeability coefficients (k_f) of aquifers

In hydrogeology, a whole series of empirical calculation algorithms are used to determine the permeability coefficients k_f of aquifers over grain size distributions. These calculations are made more precise by evaluating pumping tests and adapting the measured groundwater levels to flow models. The determined permeability coefficients k_f and porosities n_{Pm} represent the part of the aquifer under consideration, including all dead spaces and heterogenities, and thus balance the large-scale groundwater mass transport. The porosities n_{Pm} used are therefore below the values determined from individual drill cores by electron microscopy and/or in cut-out flow cells, chapter 4.2.1.1.

The well-known methods for determining the permeability coefficients k_f [m/s] from grain distributions are described in BUSCH et al. (1993) or SZYMCZAK et al. (2009). The permeability coefficients is determined from a percentile of the grain diameter d_x [mm] and the uniformity coefficient U [1], Eq.(4.3-1) to Eq.(4.3-6).

Hazen's method is applicable to sands $0{,}1 < d_{10} < 0{,}6$ mm, Eq.(4.3-1).

$$k_f = 0{,}0116 \cdot d_{10}^2 \qquad 1 < U < 5 \qquad (4.3\text{-}1)$$

Beyer's method is used:

$2 \cdot 10^{-5}$ m/s $< k_f < 4 \cdot 10^{-3}$ m/s, Eq.(4.3-2)

$$k_f = C(U) \cdot d_{10}^2 \qquad (4.3\text{-}2)$$

with the boundary conditions for the uniformity coefficient U, Eq.(4.3-3) to Eq.(4.3-5).

$$C(U) = 0{,}01 \cdot \begin{pmatrix} 1{,}452405 - 0{,}321185U + 0{,}07894U^2 \\ -0{,}01089U^3 + 0{,}00075U^4 - 0{,}00002U^5 \end{pmatrix} \qquad 1 < U < 12 \qquad (4.3\text{-}3)$$

$$C(U) = 0{,}01 \cdot (0{,}722 + 0{,}0092(12 - U)) \qquad 12 < U < 20 \qquad (4.3\text{-}4)$$

$$C(U) = 0{,}000648 \qquad U > 20 \qquad (4.3\text{-}5)$$

SZYMCZAK et al. (2009) give a useful approximation for till soils, Eq.(4.3-6).

$$k_f = 0{,}0036 \cdot d_{20}^{2{,}3} \qquad \begin{matrix} 10^{-8} < k_f < 10^{-6}\,\text{m/s} \\ d_{10} < 0{,}02\ \text{mm};\ d_{20} > 0{,}002\ \text{mm} \end{matrix} \qquad (4.3\text{-}6)$$

Kaubisch's method (in BILEK 2004) takes into account the strong correlation between the undersize fraction UT < 0.063 mm and the permeability coefficient k_f in dump sediments, Eq.(4.3-7).

$$k_f = 10^{0{,}0005\,UT^2 - 0{,}12\,UT - 3{,}59} \qquad 10\% < UT < 60\% \qquad (4.3\text{-}7)$$

BILEK (2004) uses UT < 63µm for the undersize fraction and SZYMCZAK et al. (2009) refers to the fraction UT < 20 µm as pellit. This can also be determined from the gamma intensity in borehole physicsinvestigations. HOUBEN & BLÜMEL (2017) also offer other methods suitable for the automation of permeability and porosity determination from grain distribution curves.

Methods based on the Kozeny-Carmann equation are also increasingly being used, as well as fractal properties of the pore system (ZHU 2023, PAVÓN-DOMÍNGUEZ & DÍAZ-JIMÉNEZ 2023), as well as Eq.(3.5-16) and Eq.(3.5-18) in chapter 3.5.

The effective grain diameter d_w in the WITTMANN-method corresponds to the surface equivalent sphere diameter. For the determination, the sieve fractions are evaluated according to a discretized form of Eq.(4.1-14) or Eq.(9.8-1) in chapter 9.8.2.

$$k_f = 0{,}0416 \cdot \frac{n_P^3}{(1 - n_P)^2} \cdot d_w^2 \qquad \text{Temp} = 10°C,\ k_f > 10^{-8}\ \text{m/s} \qquad (4.3\text{-}8)$$

Eq.(4.3-8) is identical to Eq.(3.5-18) with the tortuosity $f_L = 1.59$ instead of $f_L = 1.44$ (chapter 3.5.3). By considering the fine-grain fraction as pore *space filling*, its effect on permeability can also be calculated, chapter 5.2.1.3. SCHÖPKE et al. (2011) determined considerable differences between the different methods by means of comparative calculations.

4.3.2 Dispersivity of filters and flow lines

4.3.2.1 Definition of dispersivity α

The remixing in a flow tube (chapter 3.2.2), characterized by the effective axial mixing coefficient (dispersion coefficient) D_L for groundwater flows, APPELO & POSTMA (1993) derive from the *Peclet* number, Eq. (4.3-9) This is formally similar to the Bodenstein number Bo in chemical process engineering, Eq.(3.2-5) or Eq.(3.2-6) RAUSCH et al. (2002) and HAGEN (1993) also formulate D_L for pore channels in the aquifer via the *Peclet number*, Eq.(4.3-9).

$$Pe = \frac{v_{Pore} \cdot d_w}{D_L} = \frac{f_L \cdot v_f \cdot d_w}{n_P \cdot D_L} \qquad (4.3\text{-}9)$$

The pore channel velocity v_{Pore} is related to the filter velocity via the tortuosity f_L and the porosity n_P. The effective axial mixing coefficient D_L is composed of molecular diffusion and macrodispersion α, Eq.(4.3-10).

$$D_L = \frac{D_f}{f_L^2} + \alpha_L v \tag{4.3-10}$$

In relation to the dispersivity, the molecular diffusion D_f can be neglected. Only from $Pe < 0.5$ does molecular diffusion control axial dispersion. At high peclet numbers, dispersion is independent of the flow time or filtration velocity for a given path and is a characteristic property of porous media, Eq.(4.3-11).

$$\alpha_L = \frac{n_P \cdot D_L}{f_L \cdot v_f} \tag{4.3-11}$$

The macrodispersivity of aquifers, on the other hand, is scale-dependent.

4.3.2.2 Scale dependence of dispersivity

Heterogeneities in the grain structure and on the flow section lead to different flow velocities of parallel flow paths and cause macrodispersion on groundwater flow lines. The dispersion processes in the scale range between the pore system and extended aquifers are divided into:

α1) Grain structure-related dispersion

- Velocity profile within a pore.
- Diffusive exchange with the non-flowing Porengel and grain porosity.
- Different spacing velocities due to the pore diameter distribution but with intercoupled current threads.

α2) Small-scale macrodispersion

- Deflection of the flow by small-scale inhomogeneous grain structures, e.g. stones or lenticular stratifications.
- The different current filaments still correspond via transverse dispersion.

α3) Macrodispersion

- Geologically structured flow paths, whereby current tubes with different distance velocities and properties of the solid matrix can be delineated.
- Electrical tubes that are separated from each other can no longer communicate via transverse dispersion.
- The dispersion in demarcated current tubes is lower than the dispersion for the entire flow cross-section, which is averaged via filter wells, for example.

From small-scale dispersion (α2) onwards, the anisotropy of the flow processes plays an increasingly important role. Orthogonal to the direction of flow, transverse dispersivity influences D_T increase, (Fig. 4.31).

4.3.2.3 Empirical guidelines for dispersivity

For hydrodynamic axial dispersion coefficients in water treatment filters, GIMBEL (1984) Eq.(4.3-12).

$$D_L \approx 1{,}8...2{,}2 \cdot v_f \cdot \frac{d_w}{n_P} \qquad (4.3\text{-}12)$$

These are mainly attributed to the grain structure-related dispersion ($\alpha 1$).

Other estimation methods for macro dispersivity are based on the dispersion of the permeability coefficient k_f, Tab. 4.31.

ENZMANN (2000) estimates the longitudinal macrodispersivity from the statistical distribution of the permeability, Eq. (4.3-13) The dispersion of the individual values around the mean values determines the growth of the dispersivity.

$$\alpha_L = \left(\frac{\text{Stabw}\left(\ln\left(k_f\right)\right)}{\text{Mittel}\left(\ln\left(k_f\right)\right)} \right) \cdot \text{const} \qquad (4.3\text{-}13)$$

where const [m] specifies the correlation length for the permeability coefficient distribution. The correlation length, which is certainly meant horizontally, can only be determined from selective exploratory boreholes with great effort.

SCHÖPKE et al. (2020) estimated the longitudinal dispersivity α_L of a pleistocene aquifer over the vertical permeability coefficient distribution, chapter 9.8.5. They determined the following different dispersivities:

- Tracer breakthrough: α_L = 0,2 bis 0,6 m
- k_f-statistics: α_L = 0,21 m
- Flow line simulations α_L = 1 to 2 m

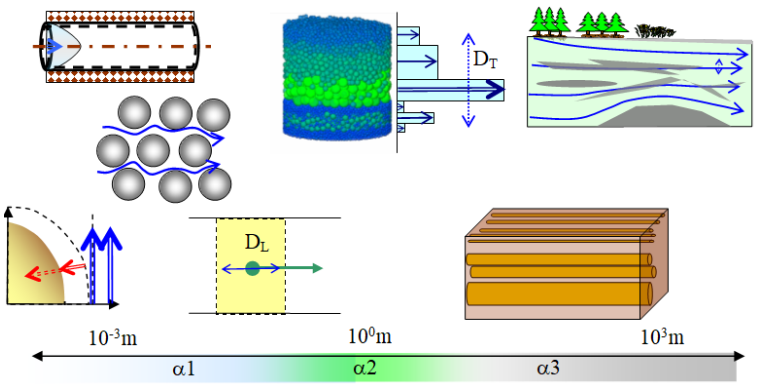

Fig. 4.31: Scale jumps from grain-structure-related dispersion from small-scale to macrodispersion.

Tab. 4.31: Compilation of various dispersivity claims.

Definitionsbereich, Quelle	Definition	Eq.s
Mikrodispersivity (APPELO & POSTMA 1993)	$\alpha_L \approx 3{,}5 \cdot d_{10}$	(4.3-14)
Mikrodispersivity (KOBUS 1992)	$\alpha_L \approx d_{50}$	(4.3-15)
Axial dispersion in water treatment filters according	$\alpha_L \approx 1{,}8...2{,}2 \cdot d_w$	(4.3-12)
Makrodispersivity (APPELO & POSTMA 1993)	$\alpha_L \approx 0{,}1 \cdot L$	(4.3-16)

DAVID et al. (1998) suggest the use of a transverse dispersivity α_T acting transversely to the direction of flow when transitioning to several spatial dimensions, Eq.(4.3-17).

$$\alpha_T \approx \frac{1}{20}\alpha_L \tag{4.3-17}$$

The transverse dispersion is horizontally about 1-2 orders of magnitude smaller than the longitudinal dispersion and is said to lie vertically in the range of molecular diffusion. These estimates must be checked on a case-by-case basis.

5 Reactions in flow-through Filters

5.1 Model approach for particle retention in the pore system

The description of depth filtration GIMBEL (1984) defined boundary conditions for a differential filter layer ∂L:

- a mass or volume balance,
- a kinetic approach that describes the transfer of matter from the flowing phase to the stationary matrix and a
- hydraulic approach to describe the pressure loss.

The separation of particles in pore systems (filters) is based on at least three mechanisms, GIMBEL (1984).

1) Deposition of particles due to the constriction of streamlines and/or finite partial dimensions.

Assuming that a spherical particle moves with its center on a streamline, contact between the particle and the filter grain surface occurs when the distance between the streamline and the grain surface becomes smaller than the particle radius. This mechanism, which is actually only a boundary condition, is usually referred to as the blocking effect or interception.

If a particle is to leave the streamline on which it is located, corresponding forces acting on the particle are required. In particular, the following are taken into account:.

2) The weight force:

The suspended particles can leave the streamline due to their sedimentation capacity. This mechanism is important for particles with a relatively large density difference to the liquid with a diameter of more than 1 µm.

3) The stochastic force due to thermal motion:

With decreasing size, the particles are increasingly subject to Brownian motion. This mechanism is important for particle sizes below approx. 1 µm.

In addition, there are various interactions of the particles with the Porengel (adsorption, adhesion, ...) and their detachment by shear forces in the pore system.

Assuming that there is no mutual influence of the various dispersed particles, a separation efficiency γ is postulated for each elementary filter layer of length $\Delta L = d_w$. This describes the probability with which a particle is retained in the elementary filter layer, Eq.(5.1-1) Strictly speaking, the porosity would have to be included in the distance $\Delta L = d_w/(1-n_P)$.

$$\lambda \approx \frac{\gamma}{d_w} \qquad \text{für } \gamma << 1 \tag{5.1-1}$$

This results in the filter coefficient λ for the exponential decrease in the particle concentration cPi, Eq.(5.1-2).

$$\frac{\partial c_{Pi}}{\partial L} = -\lambda \cdot c_{Pi} \tag{5.1-2}$$

All other influences, summarized in the parameter vector Y, form functions for λ and γ , Eq.(5.1-3).

$$\begin{aligned} \lambda &= \lambda_0\left(\vec{Y}\right) \cdot f_\lambda\left(c_V, \sigma_V, \vec{Y}\right) \\ \gamma &= \gamma_0\left(\vec{Y}\right) \cdot f_\gamma\left(c_V, \sigma_V, \vec{Y}\right) \end{aligned} \tag{5.1-3}$$

λ_0 and γ_0 indicate the filter effectiveness in the initial phase, as long as the filter load c_i does not yet exert any influence on the particle separation. The correction functions Eq.(5.1-4) are initially equal to 1.

$$\begin{aligned} f_\lambda\left(c_V, \sigma_V, \vec{Y}\right) &= 1 \\ f_\gamma\left(c_V, \sigma_V, \vec{Y}\right) &= 1 \end{aligned} \qquad \sigma_V = 0 \tag{5.1-4}$$

Through integration, GIMBEL (1984) obtain the initial profile for the profile distribution, Eq.(5.1-5),

$$c_V = c_{V0} \cdot e^{-\lambda \cdot L} = c_{V0} \cdot \exp\left(-\gamma_0 \cdot \frac{L}{d_w}\right) \tag{5.1-5}$$

with the dimensionless approach for γ_0 Eq.(5.1-6),

$$\gamma_0 = k_0 \cdot N_{Pe}^{k1} \cdot N_R^{k2} \cdot N_G^{k3} \cdot N_I^{k4} \tag{5.1-6}$$

and the dimensionless key figures Eq.(5.1-6) to Eq.(5.1-10) which are linked to the empirical constants k_0 to k_4.

Particle diffusion, Peclet Number $$Pe = N_{Pe} = v_f \cdot \frac{d_w}{D_i} \quad (5.1\text{-}7)$$

With the particle diffusion coefficients D_i, for the particle diameters d_i.

Blocking effect number $$N_R = \frac{d_i}{d_w} \quad (5.1\text{-}8)$$

Sedimentation number $$N_G = (\rho_{SSi} - \rho_W) \cdot g \cdot \frac{d_i^2}{18 \cdot \eta_W \cdot v_f} \quad (5.1\text{-}9)$$

Inertia number $$N_I = (\rho_{SSi} - \rho_W) \cdot v_f \cdot \frac{d_i^2}{\eta_W \cdot d_w} \quad (5.1\text{-}10)$$

The definition of the peclet number Eq.(5.2-3) differs from Eq.(4.3-9) by using the filter velocity instead of the pore channel velocity. For the description of the blocking effect Eq.(5.1-8) the use of the pore channel diameter d_P Eq.(3.4-17) or the minimum pore narrowing diameter $d_{P,min}$ Eq.(3.4-3) instead of the grain diameter d_w. This theoretical approach to particle retention in depth filtration can only be applied to practical problems to an extremely limited extent (special cases).

5.2 Hydraulic effect of particle retention and mineral transformations in the pore system

5.2.1 Porosity and shear plane changes in the pore system due to reactions

5.2.1.1 Description Approach

The retention of suspended particles, new mineral formations or their dissolutions change both the shear plane and the porosity of the filter section. A distinction is made between the scaffolding-forming sphericalfill and the reactive mineral particles, Fig. 5.21. Individual quantities are defined for the inert scaffold-forming ideal sphere packing (index G) and the i reactive phases, Tab. 5.2-1.

The spherical diameter of the reactive phase d_i is a fictitious quantity that indicates the surface-to-volume ratio of the pore space occupancyt:

$d_i >> d_G$ means that the inner surface remains virtually constant, and in the case of

$d_i << d_G$ very small particles are embedded, or the hydrodynamic roughness of the scaffolding-forming spheres increases, which corresponds to an increase in surface area.

$d_i < 0$ applies to a decrease in the inner surface, e.g. by filling in *gussets*.

The change in the flow hydraulics is described via two approximation stages:

1. Change in flowable porosity due to product separation while neglecting shear plane changes.
2. Consideration of shear surface plane as emplacement of particles with defined surface-to-volume ratio, described by d_i.

The initial state is the empty pore structure $m_{Pr0} = m_G$. The precipitated mineral phases are related to the pore water volume [mol/L], e.g. from model calculations. The space requirement of mineral phases follows from their molar volume V_S (Tab. 5.2-2), which is formed from the quotient of the molar mass M_S by the particle density ρ_{SS}, Eq.(5.2-1).

$$V_S = \frac{M_S}{\rho_{SS}} \tag{5.2-1}$$

The relative volume fraction φ of all separations corresponds to the sum of all separated particle volumes per solution volume c_i, Eq.(5.2-2).

$$\varphi = \sum V_{Si} \cdot c_i \ \ [L/L] \tag{5.2-2}$$

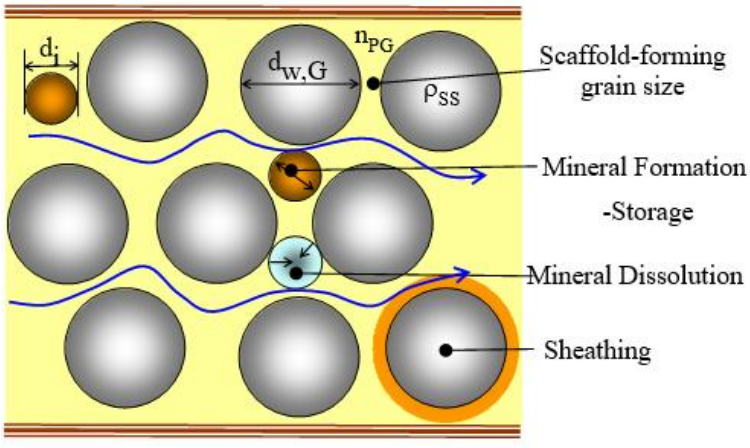

Fig. 5.21: Flow through a sphere packing with new mineral formations and dissolutions, which occur as particle deposits or sheathing in the scaffolding-forming grain.

Tab. 5.2-1: Characteristics of an ideal sphere packing with particle incorporation.

Parameter	Symbol	Unit	Definition	Eq.
Scaffold-forming grain size	G	Index		
Mass	m_G	kg		
Grain density	ρ_{ss}	L/kg		(2.2-9)
Flowable porosity of the framework	n_{PG}	1		
Dry bulk density of the scaffolding	ρ_s	L/kg	$\rho_S = (1 - n_{PG}) \cdot \rho_{SS}$	(5.2-3)
Reactive phases	i	Index		
fictitious spherical diameter of the particle deposits i	d_i	mm		
Molar volume of mineral i	V_{Mi}	L/mol		
Molar mass of the mineral i	M_i	g/mol		
Density of mineral i	ρ_i	L/kg		
Proportion of i in the sample dry matter (m_{Pr})	w_i	mol/kg		
Pore space concentration of i	c_i	mol/L		
mobile mineral concentration	c_{Pi}	mol/L		
hydraulic sphere diameter	d_w	mm		(5.2-15)
Mineral volume deposits related to pore solution	φ	1	$\varphi = \sum V_{Si} \cdot c_i$	(5.2-2)

The mineral deposits are related to the current porosity $n_P(\varphi)$ taking into account the framework porosity n_{PG} (zero state), Eq.(5.2-4) with

$\delta < 0 \quad => \quad \varphi < 0$ Resolution,

$\delta > 0 \quad => \quad \varphi > 0$ Particle storage or sheathing.

$$n_P(\varphi) = n_{PG} \cdot (1 - \varphi) \tag{5.2-4}$$

➢ Mass and porosity balance

For the total sample, the mass balances with respect to the scaffold mass w_i with respect to the pore solution c_i, Eq.(5.2-5) or Eq.(5.2-6).

$$m_{Pr} = m_G \cdot \left(1 + \sum_i M_i \cdot w_i\right) \tag{5.2-5}$$

$$m_{Pr} = m_G \left(1 + \frac{n_{PG}}{\rho_S} \cdot \sum_i M_i \cdot c_i\right) \tag{5.2-6}$$

For the porosity balances, Eq.(5.2-7) and Eq.(5.2-8).

$$n_P = n_{PG} - \frac{m_G}{V_R} \cdot \sum_i V_i \cdot w_i = n_{PG} - \rho_S \cdot \sum_i V_i \cdot w_i \tag{5.2-7}$$

$$n_P = n_{PG} \cdot \left(1 - \sum_i V_i \cdot c_i\right) \tag{5.2-8}$$

From this, the Kozeny-Carmann equation at a constant shear plane (1st approximation) results in the development of the filter resistance Eq.(5.2-9).

$$h_f = \left(72\frac{\nu}{g}\right)\cdot f_L^2 \cdot \frac{\left(1-n_{PG}+n_{PG}\cdot\varphi\right)^2}{n_P^3\cdot\left(1-\varphi\right)^3}\cdot\frac{v_f\cdot L}{d_w^2} \tag{5.2-9}$$

PARBS (2006) derived an analogous relationship for the permeability decrease of Fe^0 walls.

- Shear plane balance

The shear surface of the fill Eq.(3.4-10) is added by the deposited particles surface, Eq.(5.2-10) to Eq.(5.2-12) Their surface/volume ratio describes their fictitious spherical diameter d_i.

$$O_{ges} = 6\cdot m_G\cdot\left(\frac{1}{d_G\cdot\rho_{SS}}+\sum_i V_i\frac{w_i}{d_i}\right) \tag{5.2-10}$$

$$O_{ges} = 6\cdot m_G\cdot\left(\frac{1}{d_G\cdot\rho_{SS}}+\frac{n_{PG}}{\rho_S}\cdot\sum_i V_i\frac{c_i}{d_i}\right) \tag{5.2-11}$$

$$O_{ges} = 6\cdot\frac{m_G}{\rho_{SS}}\cdot\left(\frac{1}{d_G}+\frac{n_{PG}}{1-n_{PG}}\cdot\sum_i\frac{V_i\cdot c_i}{d_i}\right) \tag{5.2-12}$$

This changes the equivalent, hydraulic sphere diameter d_w of the sphere packing, Eq.(5.2-13) to Eq.(5.2-15).

$$d_w \tag{5.2-13}$$

$$\frac{1}{d_K} = \left(\frac{1}{d_G}+\frac{n_{PG}}{1-n_{PG}}\cdot\sum_i V_i\frac{c_i}{d_i}\right) \tag{5.2-14}$$

$$\frac{1}{d_w} = \left(\frac{1}{d_G}+\rho_{SS}\cdot\sum_i V_i\frac{w_i}{d_i}\right) \tag{5.2-15}$$

Used in Eq.(5.2-9) the 2nd approximation Eq. follows for laminar flow conditions and constant particle diameters of the emplacements, Eq.(5.2-16).

$$h_f = \left(72\frac{\nu}{g}\right)\cdot f_L^2\cdot v_f\cdot L\cdot\frac{\left(1-n_{PG}+n_{PG}\cdot\varphi\right)^2}{n_{PG}^3\cdot\left(1-\varphi\right)^3}\cdot\left(\frac{1}{d_G}+\frac{n_{PG}}{1-n_{PG}}\cdot\sum_i\frac{V_i\cdot c_i}{d_i}\right)^2 \tag{5.2-16}$$

Extended to turbulent conditions Eq.(3.5-19) follows Eq.(5.2-17).

$$\frac{h_f}{L} = k_1 \cdot \frac{\nu}{g} \cdot v_f \cdot \frac{(1 - n_{PG} + n_{PG} \cdot \varphi)^2}{n_{PG}^3 \cdot (1-\varphi)^3} \cdot \left(\frac{1}{d_G} + \frac{n_{PG}}{1 - n_{PG}} \cdot \sum_i \frac{V_i \cdot c_i}{d_i} \right)^2 + \frac{k_2}{g} \cdot v_f^2 \cdot \frac{(1 - n_{PG} + n_{PG} \cdot \varphi)}{n_{PG}^3 \cdot (1-\varphi)^3} \cdot \left(\frac{1}{d_G} + \frac{n_{PG}}{1 - n_{PG}} \cdot \sum_i \frac{V_i \cdot c_i}{d_i} \right) \quad (5.2\text{-}17)$$

The tortuosity $f_L = 1.44$ is already contained in $k_1 = 150$, or $k_2 = 1.75$ (Tab. 3.5-1).

Tab. 5.2-2: Mole volumes of mineral deposits. The molar volumes of amorphous ironhydroxides are not exactly known and therefore 5 water molecules are attributed to their molar volume.

Stoff	Formel		M_S [g/mol]	ρ_S [kg/L]	V_S [L/mol]
Water	H_2O		18	1	0,018
Aragonite	$CaCO_3$		100,09	2,95	**0,0339**
Brucite	$Mg(OH)_2$		58,32	2,39	0,0244
Brushite	$CaHPO_4{\cdot}2(H_2O)$	kristallin	172,09	2,328	0,0739
Calcite	$CaCO_3$	kristallin	100,09	2,71	**0,0369**
CO3-Green-Rust (III)	$Fe_6(OH)_{12}CO_3$		599,17	3,5	0,1712
Iron	Fe^0		55,85	7,0	0,00798
Ferroushydroxide	$Fe(OH)_2$	kristallin	90		
Ferroushydroxide (a)	$Fe(OH)_2$(a) * 5 H_2O	amorphous			≈0,15
Ferrichydroxide	$Fe(OH)_3$	kristallin	107	3,1(?)	0,035
Eisen(III)hydroxid (a)	$Fe(OH)_3$(a) * 5 H_2O	amorphous	206		≈0,15
Fe(II)-Carbonat-Hydroxid	$Fe_2(OH)_2CO_3$		205,72	3,65	0,0564
Fe(II)-Hydroxide	$Fe(OH)_2$		89,86	3,4	0,0264
Ferrihydrite	$Fe(OH)_3$		106,87	3,1	0,0345
Gypsum	$CaSO_4{\cdot}2H_2O$	kristallin	172	2,2 - 2,4	**0,075**
Goethite	FeOOH		88,85	4,37	0,0203
Hannebachite	$Ca_2(SO_3)_2{\cdot}H_2O$		258,30	2,52	0,1025
Hannebachite-Freakdef.	$CaSO_3{:}0.5H_2O$		129,15	2,52	**0,05125**
Hydroxyapatite	$Ca_5(PO_4)_3(OH)$	kristallin	502,31	3,2	0,157
Ianthinite	$(UO_2){\cdot}5(UO_3){\cdot}10(H_2O)$		304,04	5,16	0,059
Mackinawite	FeS		87,91	4,1	0,0214
Maghemite	Fe_2O_3		159,69	5,26	0,0304
Magnetite	Fe_3O_4		231,54	5,18	0,0447
Pyrolusite	MnO_2	kristallin	86,94	5,03	0,0173
Metaschoepite	$UO_3{\cdot}n(H_2O)(n<2)$		313,05	4,69	0,067
Paraschoepite	$UO_3{\cdot}2(H_2O)$ (?)		322,06		
Portlandite	$Ca(OH)_2$	kristallin	74	2,23	0,033
Portlandite (a)	$Ca(OH)_2$ * x H_2O	amorphous	74	2,23	**≈0,15**
Pyrite	FeS_2		119,98	5,02	0,0239
Quartz	SiO_2	kristallin	60,1	2,65	**0,044**
Schoepite	$(UO_2)_8O_2(OH)_{12}{\cdot}12(H_2O)$		2612,49	4,8	0,544
Siderite	$FeCO_3$	kristallin	116	3,5-3,9	**0,031**
			115,86	3,96	0,0293
SO4-GR	$Fe_6(OH)_{12}SO_4$		635,23	3,5	0,1815
U_3O_8	U_3O_8	Estimation	842	7	**0,12**
Uraninit	UO_2		270,03	10,8	0,025
DOC	hydratisierte Organik	Estimation			≈ 0,100

5.2.1.2 Filter resistance behavior of water treatment filters

In many water treatments, the filter resistance increases almost linearly with the filter running time (chapter 10.2.2.3). Particle filtrations often show an exponential increase in filter resistance, which is partly due to surface filtration effects (sieves chapter 5.3). The particle separation can be shifted into deeper filter layers, so that room filter effects also have an effect and e.g. Eq.(5.2-16) describe both the linear and the exponential increase in filter resistance. For the sake of simplification, only the laminar flow range will be considered below.

For a grain-independent explanation of these effects, Eq.(5.2-16) with Eq.(3.5-14) to Eq.(5.2-18) reworded.

$$\frac{d_G^2}{k_f} = \left(72\frac{\nu}{g}\right)\cdot f_L^2 \cdot \frac{(1-n_P)^2}{n_P^3} \tag{5.2-18}$$

Taking into account the embedded particles, this results in Eq.(5.2-19) with the physical constants summarized in const and the filter-specific term $F(\varphi, d_i/d_G, n_{PG})$.

$$\begin{aligned} \frac{d_G^2}{k_f} &= \left(72\frac{\nu}{g}\right)\cdot f_L^2 \cdot \frac{(1-n_{PG}+n_{PG}\cdot\varphi)^2}{n_{PG}^3\cdot(1-\varphi)^3}\cdot\left(1+\frac{n_{PG}}{1-n_{PG}}\cdot\frac{d_G}{d_i}\cdot\varphi\right)^2 \\ \frac{d_G^2}{k_f} &= \text{const} \cdot F\left(\varphi, \frac{d_i}{d_G}, n_{PG}\right) \end{aligned} \tag{5.2-19}$$

To exclude the scaffold porosity, the function $F(\varphi, d_i/d_G, n_{PG})$ is normalized to the initial scaffold porosity n_{PG} as a dimensionless function h_{FN}, Eq.(5.2-20).

$$hFN = \frac{F\left(\varphi, \frac{d_i}{d_G}, n_{PG}\right)}{F\left(0, \frac{d_i}{d_G}, n_{PG}\right)} \tag{5.2-20}$$

hFN is only used to illustrate characteristic filter resistance curves. During the phase of stable filtrate quality, the blocking pore volume fraction φ develops proportionally to the filter running time. The function $F(\varphi, d_i/d_G, n_{PG})$ can be appoximated by a 3rd or 4th degree polynomial depending on φ and given d_i/d_G and n_{PG}, which nevertheless does not dispense with numerical integration over the layer length L, Fig. 5.22.

The influence of the embedded fictitious particle diameters is given in relation to the framework grain diameter d_i/d_G. The coating of the framework grain size with reaction products ($d_i/d_G > 1$) manifests itself in the well-known linear filter resistance behavior up to $\varphi < 0.35$, whereas ultrafine particle deposits (($d_i/d_G < 1$) soon turn into an exponential increase in filter resistance. Both effects, known from practice, can be described with the same model.

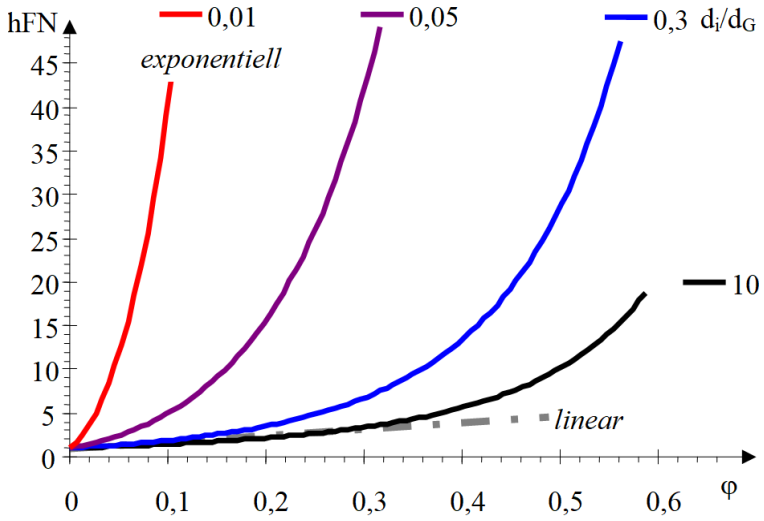

Fig. 5.22: Development of the specific pressure loss as a function hFN as a function of volume deposits φ by particles with different surface ratios d_i/d_G and for n_{PG}=0.3.

5.2.1.3 Hydraulic consideration of fine-grain fractions in sediments (aquifers)

An undersize fraction w_{UT} [mass %] embedded in the pore system of the grain structure occupies the pore space V_{UT}, Eq.(5.2-21).

$$V_{UT} = \frac{m_{Pr}}{\rho_{UT}} \cdot w_{UT} \tag{5.2-21}$$

From Eq.(5.2-2) taking into account the adsorption water layer d_{ads} with regard to the framework porosity, Eq.(5.2-22).

$$\varphi_{UT} = \frac{V_{UT}}{V_{PG}} = \frac{m_{Pr} \cdot \frac{w_{UT}}{\rho_{UT}}}{n_{PG} \cdot V_R} = \frac{w_{UT}}{n_{PG}} \cdot \frac{\rho_S}{\rho_{UT}} = \frac{m_{Pr} \cdot w_{UT}}{V_R \cdot n_{PG}} \cdot \left(\frac{1}{\rho_{UT}} + d_{ads} \cdot O_{sp}(UT) \right) \tag{5.2-22}$$

Assuming that the fine grain is present in units that change little in the shear surface, the hydraulic behaviour is estimated using the 1st approximation, Eq.(5.2-9) There is no empirical evidence yet for its validity.

5.2.2 Reaction-related changes in the stationary solids phase

5.2.2.1 Description Approaches for homogeneous sphere packing

The particulate stationary solid phase changes during the reaction with the pore solution by dissolution or coating with reaction products (Porengel formation) or the penetration of reaction fronts into their grain porosity.

Reaction engineering distinguishes between the

- PCM progressive conversion model

  and the

- SCM shrinking core model

(FARAJI et al. 2020).

In PCM, negligible grain diffusion allows the reaction over the entire volume of solid particles. The discharge is determined by film diffusion with decreasing internal concentration.

In the SCM approaches, the reaction shifts inwards, whereby an increasing mantle layer controls the reaction rate by diffusion as the reaction surface shrinks. The mantle to be diffused through can also consist of reaction products. In dissolution processes, this diffusion obstacle is eliminated except for the aqueous solution film δ (film kinetics), Fig. 5.23.

An idealized spherical reactive material grain with a diameter dw is considered, into which a definable reaction front $\delta > 0$ penetrates to the center of the grain or which is coated by reaction products by $\delta < 0$, Fig. 5.24.

It is agreed:

- The reaction is idealized at the front $0.5 \cdot d_w - \delta$. This describes both the penetration into the grain interior and the formation of the mantle to the outside.
- Starting materials and/or reaction products are in diffusive exchange with the external solution. Depending on the layer/diameter ratio, a spherical diffusion approach applies or an approximate linear approach is sufficient.
  - Separate diffusion coefficients can be attributed to the bulk solution, jacket, reaction layer, and grain.
  - In the special case *of dissolution*, the reaction layer takes on the properties of the external solution.
- When a reaction front penetrates, the remaining volume decreases and the interface of the penetrating front to the original material becomes spherically symmetrically smaller.

The grain concentration c_K in the reaction space remains constant during the reaction, Eq.(3.4-13) The reactive surface O_F depends only on the position of the reaction front, Eq.(5.2-23).

$$O_F = \frac{O_R}{V_R} = \frac{6 \cdot (1 - n_P)}{d_W} = c_K \cdot \pi \cdot d_w^2 \qquad [m^2/m^3] \qquad (5.2\text{-}23)$$

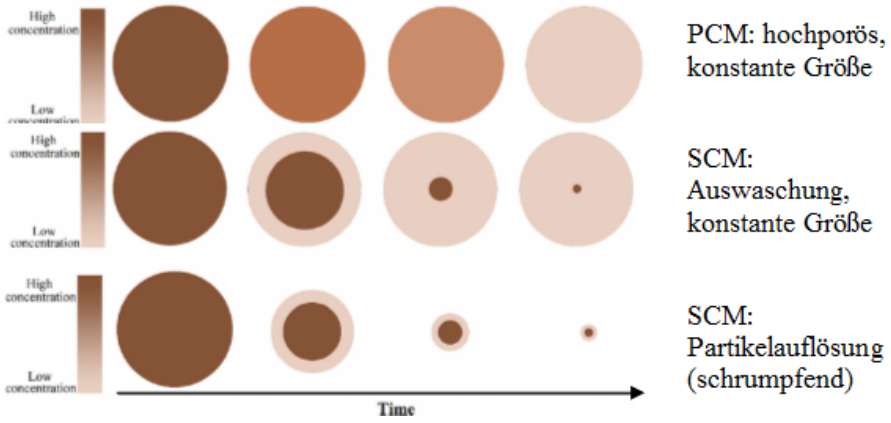

Fig. 5.23: Model approaches for mass discharge from particles, or their solution according to FARAJI et al. (2020).

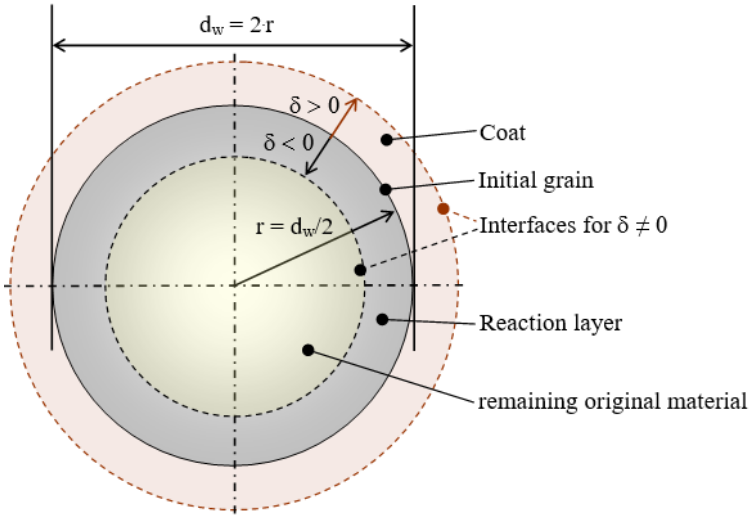

Fig. 5.24: Section through a reactive particle idealized as a sphere with an initial diameter of 2r, the penetrating reaction layer as $\delta > 0$ and the sheathing as $\delta < 0$, as well as the associated varying interfaces.

The grain concentration determines the initial grain structure volume n_{PG}, Eq.(5.2-24),

$$\left(1 - n_{PG}\right) = \frac{\pi}{6} d_{wG}^3 \cdot c_K \tag{5.2-24}$$

and the grain concentration c_{KW}, Eq.(5.2-25).

$$c_{KW} = \frac{\left(1 - n_{PG}\right)}{n_{PG}} \cdot \frac{1}{\frac{\pi}{6} \cdot d_{wG}^3} \tag{5.2-25}$$

Reaction spaces can be dimensioned with the volume fraction φ and the porosity n_P, Eq.(5.2-2).

Bei der Schichtbildung oder Auflösung ändert sich die durchströmte Porosität, während beim Eindringen der Reaktion in das Kornporensystem die Strömungshydraulik unbeeinflusst bleibt.

The following applies, according to Fig. 5.24:

$\delta < 0 \quad => \quad \varphi < 0$ Penetrating reaction front or resolution

$\delta > 0 \quad => \quad \varphi > 0$ Sheathing

For the constant grain concentration, the following applies, taking into account the amount of $2\cdot\delta$ Changing grain diameter Eq.(5.2-26) and

$$c_{KW} = \frac{(1-n_{PG})}{n_{PG}} \cdot \frac{1}{\frac{\pi}{6}\cdot d_{wG}^3} = \frac{(1-n_{PG}\cdot(1-\varphi))}{n_{PG}\cdot(1-\varphi)} \cdot \frac{1}{\frac{\pi}{6}\cdot(d_w+2\cdot\delta)^3} \tag{5.2-26}$$

for the change in diameter as a function of φ Eq.(5.2-27),

$$\frac{(d_{wG}+2\cdot\delta)}{d_{wG}} = \sqrt[3]{\frac{(1-n_{PG}\cdot(1-\varphi))}{(1-n_{PG})\cdot(1-\varphi)}} \tag{5.2-27}$$

or for the layer thickness δ(φ) as a function of the volume difference Eq.(5.2-28).

$$\delta(\varphi) = \frac{d_{wG}}{2}\cdot\left(\sqrt[3]{\frac{(1-n_{PG}\cdot(1-\varphi))}{(1-n_{PG})\cdot(1-\varphi)}}-1\right) \tag{5.2-28}$$

From the grain surface Eq.(3.4-8) follows for the reactive interface Eq.(5.2-29),

$$O_F = \frac{m_{Pr}\cdot O_{Sp}}{V_R} = c_K\cdot\pi\cdot(d_{wG}+2\cdot\delta)^2 \tag{5.2-29}$$

or as a function $O_F(\delta)$ of the layer thickness δ Eq.(5.2-30).

$$O_F(\delta) = 6\cdot(1-n_P)\cdot\frac{(d_{wG}+2\cdot\delta)^2}{d_{wG}^3} \tag{5.2-30}$$

The proportion of the reactive surface with respect to the initial surface is then described by Eq.(5.2-31),

$$\frac{O_F(\delta)}{O_{FG}} = \left(1+2\cdot\frac{\delta}{d_{wG}}\right)^2 \qquad \left| \; d_{wG}+2\cdot\delta > 0 \right. \tag{5.2-31}$$

with the option that original material is still present when reaction fronts penetrate or dissolve. The ratio of the current reactive surface $O_F(\delta)$ to the initial (framework) surface indicates the surface function $F_O(\delta)$, Eq.(5.2-32).

$$F_O = \frac{O_F(\delta)}{O_{FG}} = \left(1+\left(\sqrt[3]{\frac{(1-n_{PG}\cdot(1-\varphi))}{(1-n_{PG})\cdot(1-\varphi)}}-1\right)\right)^2 \left| \; d_{wG}+2\cdot\delta > 0 \right. \tag{5.2-32}$$

5.2.2.2 Transition to discretized grain distributions

In grain distributions, the reaction layer in the fine grain first reaches the center and thus becomes ineffective. The reaction surface/volume ratio is influenced by the grain distribution curve. Thus, the reactivity as a function of the reaction progress is also determined by the grain distribution, Fig. 5.25.

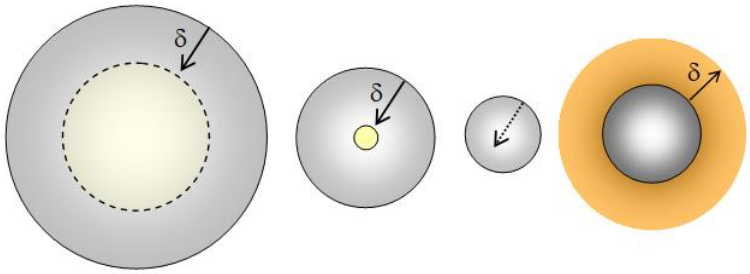

Fig. 5.25: Material grains with different diameters d_w and the same reaction layer thicknesses δ. From left to right: Three grain sizes to the center and coated grain.

Under the boundary condition Eq.(5.2-33)

$$\begin{array}{l|ll} (d_{wi} - 2\cdot\delta) \geq 0 & O_i & V_{Ki} \\ (d_{wi} - 2\cdot\delta) < 0 & O_i = 0 & V_{Ki} = 0 \end{array} \tag{5.2-33}$$

the corresponding grain diameter d_{wi} geometrically averaged from the geometrically averaged sieve boundaries d_i and d_{i+1}, Eq.(5.2-34)

$$d_{wi} = \sqrt{d_i \cdot d_{i+1}} \tag{5.2-34}$$

and above that the number of grains N_i of each fraction is determined, Eq.(5.2-35).

$$N_i = \frac{6}{\pi}\cdot V_{Korn}\cdot\frac{w_i}{d_{wi}^3} = \left(\frac{6}{\pi}\cdot\frac{m_{Pr}}{\rho_{SS}}\right)\cdot V_{Korn}\cdot\frac{w_i(d_i, d_{i+1})}{d_{wi}^3} \tag{5.2-35}$$

If the grain density of the particle collective is the same, its proportion is normalized to its particle volume, Eq.(5.2-36).

$$N_i\cdot\frac{\rho_{SS}}{m_{Pr}} = \frac{6}{\pi}\cdot\frac{w_i(d_i, d_{i+1})}{d_{wi}^3} \quad \left| \; [L^{-1}] \text{ based on particle volume} \right. \tag{5.2-36}$$

By integration via the grain diameter (or from the sum of the screen residues), the surface function $F_O(c_{K,0}, c_{K,\delta})$ is obtained for real grain distributions. Regression calculations with logarithmically normally distributed grain sizes can be used to establish a causal relationship between the initial grain concentration $c_{K,0}$ and the remaining grain concentration $c_{K,\delta}$ after removal of the layer δ, Eq.(5.2-37).

$$\log\left(F_O\left(c_{K,0}, c_{K,\delta}\right)\right) = A\cdot\log\left(\frac{c_{K,\delta}}{c_{K,0}}\right) + B\cdot\left(\log\left(\frac{c_{K,\delta}}{c_{K,0}}\right)\right)^2 \tag{5.2-37}$$

The regression coefficients A and B are functions of uniformity coefficient U, Tab. 5.23. As the uniformity coefficient increases, so does the initial surface area, which is

proportional to the d_{50}/d_w quotient. Around U ≈ 3 there is even a linear relationship between the reactive surface and the remaining grain volume.

Tab. 5.23: Parameters of the function $F_O(c_{K,\delta}, c_{K,0})$ for various uniformity coefficients U, Eq.(5.2-37).

U	d_{50}/d_w	A	B	Remarks
1	mm	1	1	
1,0	1,00	0,67	0	ideal spaeres
1,05	1,00	0,67	-0,006	
1,5	1,04	0,74	-0,046	Fitted to
2,0	1,11	0,85	-0,088	logarithmically
3,0	1,28	1,23	0,015	normally
4,0	1,47	1,49	0,071	distributed
6,0	1,79	1,91	0,199	grain sizes
8,0	1,92	2,21	0,310	

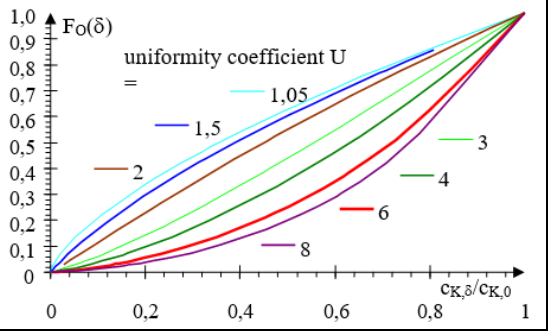

5.2.2.3 Example calculation for reaction layers of a real grain distribution

For demonstration, two sands distributed to different widths and a granular adsorbent (chapter 4.2), Tab. 4.13. The shear surface O_F was calculated for n_P = 0.4 according to Eq.(3.4-21) Fig. 5.26.

Tab. 5.2-4: Comparative grains.

Grains	d_{50}	U	d_K	d_m Eq. (4.1-1)	O_F
	mm	1	mm	mm	m^2/m^3
Filter sand example	1,00	1,25	1,00	1,02	3646
Normal sand example	1,00	6,00	0,52	2,34	6900
Ferrosorp 0,15-2 mm	0,54	4,19	0,68	1,14	5300

In the case of narrowly classified material (U = 1.25), the reaction front ideally penetrates evenly. With a wide distribution, the fine-grained materials react completely first. The reactive surface area and the relative residual volume decrease more slowly with the narrowly classified filter material than with the widely distributed filter material. If the reactive surface determines the reaction rate, then widely distributed grains have a high initial effect, which then quickly decreases.

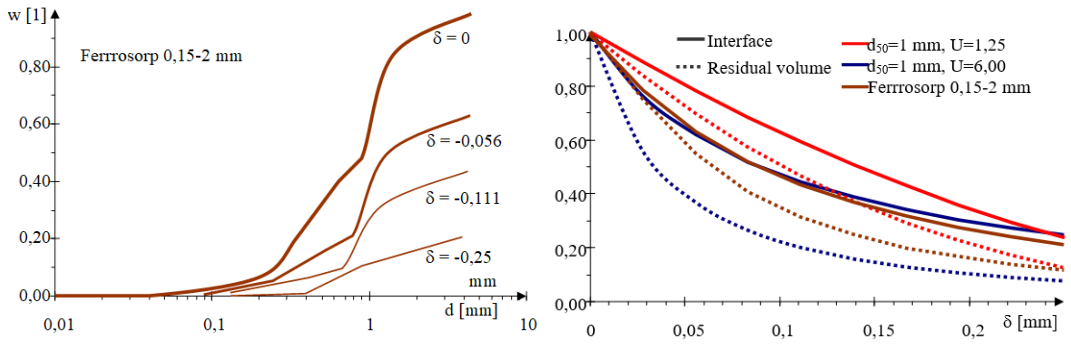

Fig. 5.26: Left: Grain distributions depending on the penetration depth of the reaction front δ into the compound grain Ferrosorp®. The reaction layer formation is considered up to δ = -

0.25 mm. Right: Surfaces of the reaction layer and the remaining grain volumes of the grains in Tab. 5.2-4, based on their initial values as a function of penetration depth δ.

5.3 Hydraulics of surface filtration

5.3.1 Surface filtration layer - Schmutzdecke

Particle separation in surface filtration is mainly carried out by screening, i.e. by mechanical effects when passing through the screen surface. The sieve effect is understood to be the mechanical adhesion of a particle in a pore constriction due to the particle size. For the key figure of the blocking effect Eq.(5.1-8) $N_R > 0.15$ applies. The minimum continuous pore channel diameter $d_{P,min}$ Eq.(3.4-3) Sieve effects also occur in membrane filtration and the *surface filtration* of sand filters, Fig. 5.32.

The prerequisite for the description of the filter/screen resistance and the membrane scaling hf is:

- The pressure loss due to particle retention is due to steric effects on the screen surface, Fig. 5.32.
- Physical and chemical binding forces, as well as changes in the shape of the filter cake (compressibility) due to shear forces are not taken into account.

The flow cross-section is blocked by particles and these, together with precipitated products, form a secondary filter, Fig. 5.32. This partial blockage of the flowcross-section is a two-dimensional process that is determined by the filter/screensurface and the degree of coverage.

The filter cake, which grows from sieved particles, is considered like porous granular media, taking into account its compressibility. The hydraulic effects of screening are relatively large compared to the influence of other particle retentionmechanisms as well as biological effects.

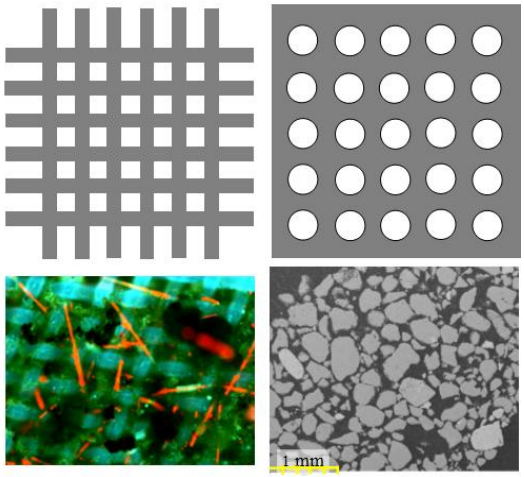

Fig. 5.31: Top: Screens with rectangular and round holes. Bottom: Screen mesh covered with detritus (green, black and algae (red) (left) and microstructure cut by Pleistocene sand, which could also be used for artificial groundwater recharge).

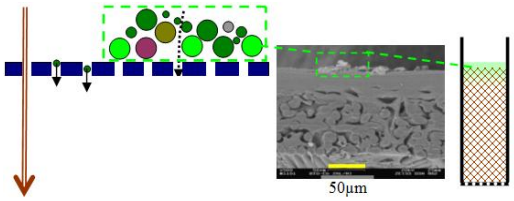

Fig. 5.32: Sieve effects (left) in membrane filtration (middle) and surface filtration on sand filters (right).

5.3.2 Semi-empirical description of the filter (screen) resistance development

5.3.2.1 Exponential approach and two-phase description

From the descriptive approaches of LÖFFLER (1969), VOIGT* et al. (1988) and VOIGT* et al. (1985), SCHÖPKE (2007) developed a description of filtration processes based on sieve effects and filtration processes based on screen effects, which made scale transfers possible. This allows technical design problems to be carried out with sufficient accuracy by means of experiments and analogy considerations:

- Screening and membrane plants,
- Groundwater recharge and slow sand filtration of particulately contaminated unpre-treated surface waters.
- Rapid filtration without the addition of flocculation chemicals.

LÖFFLER (1969) coined two phases for the screening processes in artificial groundwater recharge :

- The *invasion phase*, in which the flow cross-section is reduced by sieved substances, while residual permeability is retained.
- The *colmation phase*, in which the growing secondary filter of sieved materials (Schmutzdecke) determines the hydraulic resistance.

Invasion and colmation phases together as a function of the running time of a filter resulted in an exponential increase in filter resistance, Eq.(5.3-1).

$$h_f = h_0 \cdot e^{\lambda \cdot t} \quad \text{für } v_f = \text{const} \tag{5.3-1}$$

The screening tests and evaluation procedures according to THIELKE* (1972), VOIGT* et al. (1988) and VOIGT* et al. (1985) are based on this model concept. Since the screening effects only take place in the top layer, the filter resistance of the rest of the filter layer remains constant and irrelevant to the process. However, the layer length determines the initial filter resistance Eq.(3.5-16) and influences the exponent λ. Under standardised boundary conditions, design aids could be developed from this. However, since the screening processes are only quantified in general, this model was not very suitable for scale transfers.

An exotic alternative to this approach was described by TANG & MAYS (1998), who used a genetic algorithm to optimize the infiltration of water with strongly fluctuating screening behavior.

5.3.2.2 The invasion phase

Under laminar flow conditions and constant pressure loss (filter resistance), a filter velocity is determined by the flowcross-section that can be flowed through. During sieving, the pores are clogged in proportion to the water column flowing through them, i.e. the filter velocity increases proportionally to the water column flowing through it H Eq.(2.2-4) with a constant filter resistance, Fig. 5.33. The influence of the filter resistance is compensated by the use of the ratio v_f/h_f in the laminar flow range. The closure of the flow cross-section, which increases with the water column H flowing through, is described by the quotient v_f/h_f independent of filter velocity, Eq. (5.3-2) This behavior is identical to the invasion phase of LÖFFLER (1969) and applies to different filter layer lengths L.

$$\frac{v_f}{h_f} = \frac{v_{f0}}{h_{f0}} \cdot \frac{(H_K - H)}{H_K} = \frac{v_{f0}}{h_{f0}} \cdot \left(1 - \frac{H}{H_K}\right) \tag{5.3-2}$$

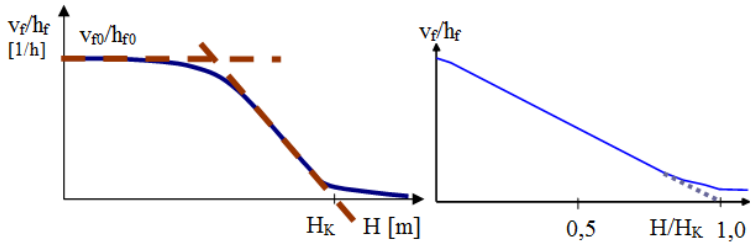

Fig. 5.33: Decrease of the ratio vf/hf during the invasion phase as a function of the suspension water column H until *the complete* pore closure H_K. Left: The hydraulic closure only

takes effect under laminar flow conditions. Right: After normalizing the water column H to H_K, the linear relationship is shown up to a residual permeability before H/ H_K = 1.0.

Theoretically, the flow ends with the complete closure of all pore openings. Under real conditions, Eq.(5.3-2) from the straight line even before complete occultation is reached at H_K. From the consideration that at $H = H_K$ the entire flow cross-section is theoretically covered with sieved substances, a concentration of sievable particles can be derived, Eq.(5.3-3) The quantity $c_P(d_S)$ indicates the concentration of clogging cross-sectional surfaces in the suspension for the sieve diameter d_P, Eq.(5.3-4).

$$n_P \cdot A_F = H_K \cdot A_F \cdot c_P(d_S) \tag{5.3-3}$$

$$c_P(d_S) = \frac{n_P}{H_K} \quad \left[\frac{m^2}{m^3} = m^{-1}\right] \tag{5.3-4}$$

The concentration c_P is a function of the sieve diameter d_S, analogous to a grain size distribution. This relationship, developed from observations, applies approximately to:

- laminar flow,
- seeving zone < Filter layer,
- to H/H_K < 0,8 and
- constant temperature, or corresponding correction.

The concentration of cross-sectional surfaces is comparable to the projection surface, Eq.(4.1-17) If one assumes the shape of a cube for the screened particles, the coverage of the screen surface can be estimated as a function of the screened particle volume φ and its assigned cube edge length d_S, Eq.(5.3-5).

$$\varphi(d_S) = c_P(d_S) \cdot d_S \tag{5.3-5}$$

This can also be used to estimate scaling by mineral precipitation on membranes or, conversely, their colmation point H_K, Eq.(5.3-6).

$$H_K \approx n_P \cdot \frac{d_S}{\varphi(d_S)} \tag{5.3-6}$$

5.3.2.3 The colmation phase

When a pore opening is closed, a residual permeability remains that is lower than the permeability of the sieve or filter system. As the pore openings are covered, the permeability approaches the residual permeability. The sieved particles then build up a secondary filter. The properties of this secondary filter are determined by the sieved substances, the hydraulic conditions and the suspension properties. According to the composition of the water and the grain structure, this secondary filter has a lower permeability than the screen/filter material. In the case of an incompressible filter cake, its layer length and thus the specific filter resistance h_f/v_f increases proportionally to the treated water column H, Fig. 5.34.

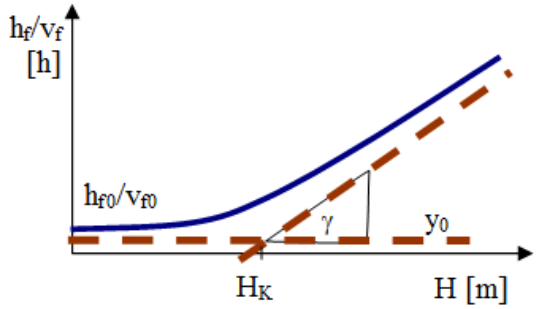

Fig. 5.34: Increase of the filter resistivity h_f/v_f as a function of the water column H flowing through it during the colmation phase. The linear increase of the filter cake resistance γ starts from the colmation point H_K. Before that, the resistivity of the filter rises only marginally above the initial value close to y_0.

This phase corresponds to the colmation phase according to LÖFFLER (1969), Eq.(5.3-7).

$$\frac{h_f}{v_f} = \frac{h_{f0}}{v_{f0}} + \gamma \cdot (H - H_K) \qquad (5.3\text{-}7)$$

with

$$H > 1{,}2\ H_K$$

The quantities describing the colmation cannot be derived from the concentration of the filterable substances or the turbidity. The object-specific relationships between the nature of the water to be infiltrated and the development of colmation can only be determined empirically. Since the colmation coefficient γ is composed of the concentration of colmatating substances and the permeability of the secondary filter formed, the measured values vary greatly. Many technical applications are limited by the onset of the colmation phase. In this process, filter resistances that are no longer acceptable are quickly reached, so that the colmation point H_K is also the dimension relevant for the design.

5.3.3 Summary description of both phases

The measurements in the transition area to both phases are practically impossible to evaluate, but often represent a considerable part of the empirical data material. Therefore, a mathematical common description of both phases was sought and found in a hyperbolic equation with given asymptotes, Fig. 5.35.

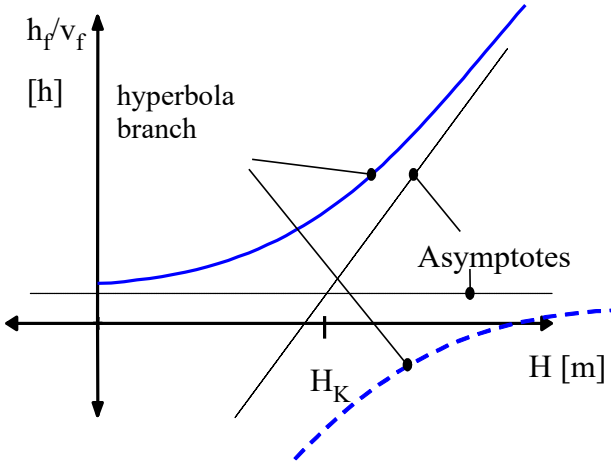

Fig. 5.35: Description of strainer/filter resistance rise by a hyperbola branch.

The asymptote running parallel to the abscissa describes the initial filter resistance, Eq.(5.3-8).

$$H = 0$$

$$\frac{h_f}{v_f} = \frac{h_{f0}}{v_{f0}} \tag{5.3-8}$$

The filter resistance development approaches the linearly increasing asymptote of the colmation phase, Eq.(5.3-9).

$$\frac{h_f}{v_f} = \gamma \cdot (H - H_K) \tag{5.3-9}$$

The intersection of both asymptotes has the coordinates H_K and h_{f0}/v_{f0}. The approach to the asymptot intersection is formally determined by the parameter ε, which otherwise has no practical significance. In the first approximation, the positive solution of the hyperbolic equation satisfies these conditions Eq.(5.3-10).

$$\frac{h_f}{v_f} = y_0 - \frac{\gamma \cdot (H_K - H)}{2} \pm \sqrt{\left(\frac{\gamma \cdot (H - H_K)}{4}\right)^2 + \gamma \cdot \varepsilon} \tag{5.3-10}$$

The parameters of the Eq.(5.3-10) are obtained by adjusting experimental data consisting of pairs of values (H, h_f/v_f).

About the coordinate transformation Eq.(5.3-11)

$$y = \frac{h_f}{v_f} - y0$$
$$x = -H \tag{5.3-11}$$

follows via the asymptotes Eq.(5.3-12)

$$y = 0$$

$$x = x_0 - \frac{y}{\gamma} \tag{5.3-12}$$

the linearized hyperbolic equation Eq.(5.3-13),

$$x = x_0 - \frac{y}{\gamma} + \frac{\varepsilon}{y} \tag{5.3-13}$$

and converted the quadratic equation Eq.(5.3-14).

$$y^2 + \gamma \cdot (x - x_0) \cdot y - \gamma \cdot \varepsilon = 0 \tag{5.3-14}$$

By solving them and transforming them back, a linear multiple regression approach is obtained, from whose regression coefficients $\mathbf{B_1}$, $\mathbf{B_2}$ and $\mathbf{B_3}$ the quantities $\mathbf{H_K}$, $\boldsymbol{\gamma}$ and $\boldsymbol{\varepsilon}$ can be determined, Eq.(5.3-15).

$$H = H_K + \frac{\frac{h_f}{v_f} - y_0}{\gamma} - \frac{\varepsilon}{\frac{h_f}{v_f} - y_0} = B_0 + B_1 \cdot \left(\frac{h_f}{v_f} - y_0\right) + B_2 \cdot \left(\frac{h_f}{v_f} - y_0\right)^{-1} \tag{5.3-15}$$

However, the size $\mathbf{y_0}$ is not known. By iteratively minimizing the sum of the error squares of the regression by varying y_0 (chapter 9.1.3) and taking into account a sensible solution, the parameters of the filter resistance increase can be determined, Eq.(5.3-16).

$$\begin{aligned} H_K &= B_0 \\ \gamma &= \frac{1}{B_1} \\ \varepsilon &= -B_2 \end{aligned} \tag{5.3-16}$$

The confidence intervals of the regression calculations can be used for significance tests if necessary.

5.3.4 Bemessung von Oberflächenfiltern

Screening processes that limit the running time of water treatment plants can be measured using laboratory or small-scale determined screening parameters, dhapter 9.2. With these tests, statistics of screening parameters or screening curves are determined with relatively little effort. Comparisons with some filter tests carried out in parallel could be approximately described by a power function between grain and screen diameter, Eq.(5.3-17).

$$H_K = A \cdot \left(\frac{d_S}{1\text{mm}}\right)^B \tag{5.3-17}$$

For the design, representative, including critical raw water situations are selected to calculate the filter resistance development, Fig. 5.36. The transit time t_L for a constant filter velocity v_f is calculated from the colmation point H_K and the reaching of the limit resistance h_{fG} during the colmation phase, Eq.(5.3-18) The higher the filtration velocity and the colmationcoefficient γ, the smaller the influence of the colmation phase on the totalrunning time. Since the greatest uncertainty lies in the colmation coefficients γ, their shares in the maturity should be regarded as collateral as far as possible.

$$t_L = \frac{H_K}{v_f} + \frac{(h_{fG} - h_{f0})}{\gamma \cdot v_f^2} \qquad (5.3\text{-}18)$$

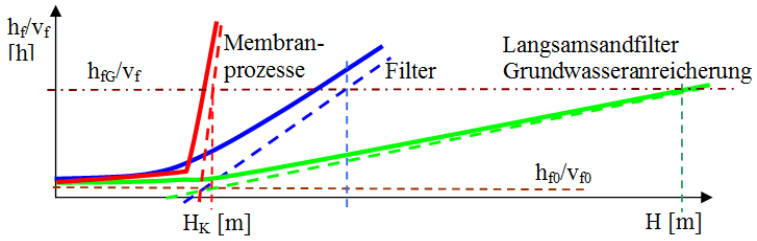

Fig. 5.36: Different curves of sieve/filter resistance in surface filtration.

In membrane processes, the colmation phase is usually very steep, so that the time until the limit resistance is reached can be neglected. In the case of slow sand filters and groundwater recharge plants, the colmation phase largely determines the filter running time, Eq.(5.3-18).

6 Reactions in the pore system

6.1 Reaction Kinetics

6.1.1 Reaction mechanisms

6.1.1.1 Simple reactions

The reaction order determines the potency in which the concentration of a starting substance determines the reaction rate, Eq.(6.1-1).

$$\begin{aligned} r_0 &= k_{(0)} \cdot c^0 = \text{const} && \text{Reaktion nullter Ordnung} \\ r_1 &= k_{(1)} \cdot c^1 && \text{Reaktion erster Ordnung} \\ r_2 &= k_{(2)} \cdot c^2 && \text{Reaktion zweiter Ordnung} \end{aligned} \qquad (6.1\text{-}1)$$

$$\begin{aligned} r_0 &= k_{(0)} \cdot c^0 = const && \text{Zero-order reaction} \\ r_1 &= k_{(1)} \cdot c^1 && \text{First-order reaction} \\ r_2 &= k_{(2)} \cdot c^2 && \text{Second-order reaction} \end{aligned}$$

Broken reaction orders are also possible. The most common reactions are first- and zero-order.

6.1.1.2 Reaction Systems - Follow-on Reactions

In a reaction sequence, the product of a reaction forms a starting component for the next reactions. There may also be equilibria in the reaction chain, Fig. 6.11.

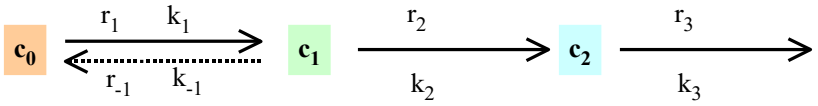

Fig. 6.11: Sequence of reactions, possibly also with equilibria.

The reaction rate may be limited by a rate-determining step, Eq.(6.1-2) in vector notation.

$$k_{ges} = \min\begin{Bmatrix} k_1 \\ k_2 \\ \dots \end{Bmatrix} \tag{6.1-2}$$

For simple systems, analytically controllable solutions can be specified. If an overall reaction takes place in two consecutive subreactions of the first order, the result is again a reaction rate of the first order, the rate constant of which is the harmonic mean of the reaction constant k_i Eq.(6.1-1) provided that both rate constants are of the same order of magnitude. Otherwise, Eq.(6.1-3) in Eq.(6.1-2) about.

$$r = \frac{1}{\frac{1}{k_1} + \frac{1}{k_2}} \cdot c = \frac{k_1 \cdot k_2}{k_1 + k_2} \cdot c = k_{ges} \cdot c \tag{6.1-3}$$

6.1.1.3 Parallel reactions

In the case of parallel reactions, the total reaction rate is the sum of the individual reaction rates. If these are first-order reactions, the addition of the rate constants is sufficient. However, if it is a heterogeneous multi-compartment system, the total reaction rate is formed from the sum of the individual velocities, the concentrations of which must be taken into account in the compartments.

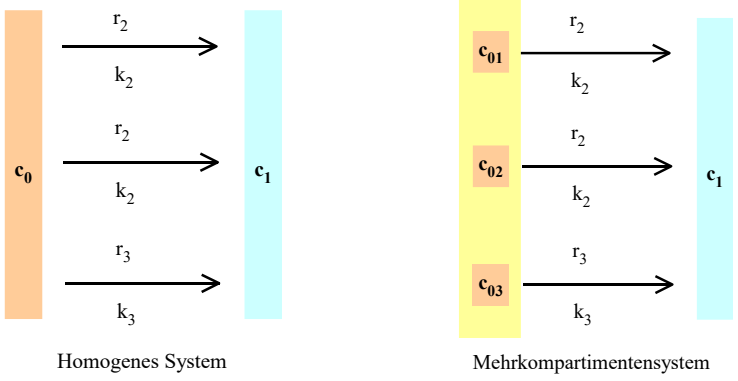

Fig. 6.12: Parallel reactions in a homogeneous and a multicompartment system.

If the solution concentration c_1 is kept close to zero, the compartments can be considered individually and their decrease in concentration can be calculated by separate integration, or their sum, Eq.(6.1-4).

$$r_{ges} = \sum_i \left(c_{0i} \cdot k_{app,i} \cdot \exp\left(- k_{app,i} \cdot t \right) \right) \tag{6.1-4}$$

The constants $k_{app,i}$ contain the respective constant boundary conditions, such as volume and phase interfaces of the compartments, as well as hydraulically determined parameters. This corresponds to a superposition (linear combination) of approach functionsas a function of c_0. The sales can be summarized in vector notation via a stoichiometry matrix, chapter 2.3.2.

6.1.2 Empirical Temperature Functions of Reaction Rate

The reaction rate of simple reactions is described by overcoming the energy barrier E_A, Fig. 2.31. The temperature influence in Eq.(2.3-12) is separated as a temperature term ζ_{Temp}, Eq.(6.1-5) Fig. 6.13.

$$\zeta_{Temp} = e^{-\frac{E_A}{RT}} \tag{6.1-5}$$

In practice, many of the thermodynamic definitions Eq.(6.1-5) divergent empirical temperature functions are applied, Eq.(6.1-6), Eq.(6.1-9) Eq.(6.1-11) and Eq. (6.1-15) These can be compared with each other via approximations via the implicit activation energies. Temp indicates the Celsius temperature [°C]. The temperature function Eq.(6.1-5) is related to a standard temperature $Temp_0$ and calculated for $Temp_1$, Eq.(6.1-6).

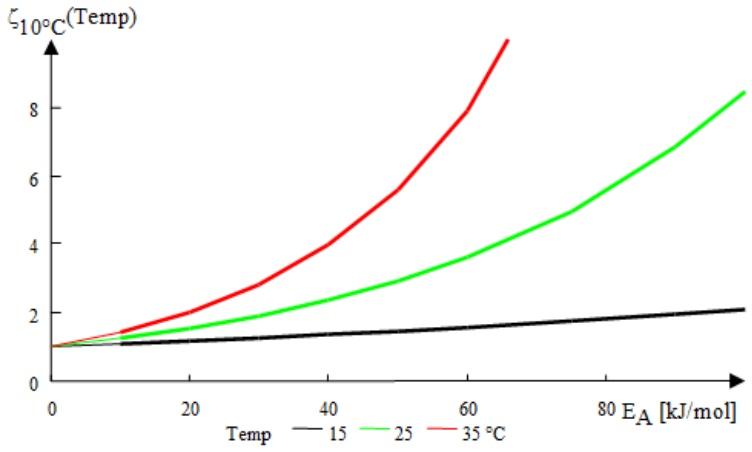

Fig. 6.13: Temperature Functions ζ_{Temp} with respect to Temp0 = 10°C as a function of the activation energy E_A.

$$\zeta_{Temp\,0}(Temp1) = e^{-\frac{E_a}{R(Temp1+273,15)}} \cdot e^{\frac{E_a}{R(Temp0+273,15)}} \tag{6.1-6}$$

Subsequently, an approximate equation for the environment of $T=T_0$ [K] is formulated via Taylor series development (BARTSCH 1972) and the relationship with Eq.(6.1-5) Eq.(6.1.7).

$$\zeta_{Temp}(T_0 + \Delta T) \approx \zeta_{Temp}(T_0) + \frac{\partial \zeta_{Temp}(T_0)}{\partial T} \cdot \Delta T + \frac{\partial^2 \zeta_{Temp}(T_0)}{\partial T^2} \cdot \frac{\Delta T^2}{2!} + \ldots \tag{6.1.7}$$

The series development can be aborted in the applied temperature interval (273K-303K) after the linear term, Eq.(6.1-8).

$$\frac{\partial}{\partial T}\zeta_{Temp}\left(T_0+\Delta T\right)\approx e^{-\frac{E_A}{RT_0}}\cdot\left(1+\frac{E_A}{RT_0^2}\cdot\Delta T\right) \tag{6.1-8}$$

- linear approach Eq.(6.1-9):

$$\zeta_{Temp}\left(T-T_0\right)=1+const\cdot\left(T-T_0\right) \tag{6.1-9}$$

Using constant comparison, *const* is a quantity for the activation energy, Eq.(6.1-10).

$$E_A\approx const\cdot R\cdot T_0^2 \tag{6.1-10}$$

- Potency Approach Eq.(6.1-11).

$$\zeta_{Temp}\left(T-T_0\right)=\left(Temp\right)^{const}\qquad \text{mit } Temp = T-273{,}15 \tag{6.1-11}$$

The approximation is derived from Temp = 10°C = T_0 = 283.15 K,

$$\zeta(Temp)\approx\left(Temp_0\right)^a+a\cdot\left(Temp_0\right)^{const-1}\cdot\left(Temp-Temp_0\right) \tag{6.1-12}$$

or

$$\zeta(Temp)\approx\left(Temp_0\right)^{const}\cdot\left(1+\frac{const}{\left(Temp_0\right)}\cdot\left(Temp-Temp_0\right)\right) \tag{6.1-13}$$

And after comparing coefficients with Eq.(6.1-8) follows Eq.(6.1-14).

$$E_A=\frac{const\cdot RT_0^2}{\left(Temp_0\right)}\cdot\frac{\left(Temp-Temp_0\right)}{\left(T-T_0\right)}=\frac{const\cdot RT_0^2}{\left(Temp_0\right)} \tag{6.1-14}$$

- Exponential approach Eq.(6.1-15):

$$\zeta_{Temp}\left(T-T_0\right)=e^{const\cdot Temp} \tag{6.1-15}$$

The approximation is derived from T_0 = 273.15 K,

$$\zeta(Temp)\approx e^{const0}\cdot\left(1+const\cdot Temp_0\right) \tag{6.1-16}$$

and the activation energy determined, Eq.(6.1-17).

$$E_A\approx const\cdot RT_0^2 \tag{6.1-17}$$

With these functional relationships, the corresponding activation energies can be determined from most of the temperature functions described in the literature, Tab. 6.11.

Tab. 6.11: Transfer of Activation Energy from Empirical Temperature Functions.

Empirical function	Calculation of activation energy E_A	Eq.
$1+\text{const}\cdot(T-T_0)$	$E_A=\text{const}\cdot R\cdot T_0^2$	(6.1-10)
$(\text{Temp})^{\text{const}}$	$E_A=\frac{\text{const}\cdot RT_0^2}{(\text{Temp}_0)}\cdot\frac{(\text{Temp}-\text{Temp}_0)}{(T-T_0)}=\frac{\text{const}\cdot RT_0^2}{(\text{Temp}_0)}$	(6.1-14)
$e^{\text{const}\cdot\text{Temp}}$	$E_A=\text{const}\cdot RT_0^2$	(6.1-17)

6.1.3 Enzyme kinetics

6.1.3.1 Kinetic approach to growth

Under optimal conditions (i.e. in the exponential growth phase), cell growth is determined only by internal factors, such as enzyme concentrations within the cell or their activities, EINSELE et al. (1985). As long as the specific rate of growth μ is constant, the cell concentration c_{cell} increases exponentially, which follows from the first-order law of time, Eq.(6.1-18).

$$r=\frac{\partial c_{cell}}{\partial t}=\mu(\text{Milieu})\cdot c_{cell} \tag{6.1-18}$$

The enzyme kinetics according to Michaelis-Menten describes the substrate dependence of μ attributed to the milieu via a velocity-determining equilibrium of the substrate S with the enzyme X to the complex SX, which then rapidly decays into the product P and the enzyme X, Eq.(6.1-19) The enzyme concentration represents the cell concentration c_{cell}.

$$S+X\xleftarrow{k_1,k_{-1}}SX\xrightarrow{k_2}P+X \tag{6.1-19}$$

This kinetic description of heterogeneous reactions according to LANGMUIR-HINSHELWOOD is based on the idea that the reactants react with each other in an adsorbed phase, Eq.(6.1-20).

$$r=k_2c_{cell}\frac{c_s}{K_S+c_s}=\mu\cdot\frac{c_s}{K_S+c_s} \tag{6.1-20}$$

with the Michaelis constant (Monod constant) K_S, Eq.(6.1-21),

$$K_S=(k_{-1}+k_2)/k_1 \tag{6.1-21}$$

where the enzyme concentration is proportional to the biomass or cell concentration *c* c_{cell} or is optionally related to it. K_S also indicates the substrate concentration for half the maximum growth rate. In the case of carrier-fixed enzymes, phenomena of internal and external mass transport as well as the electrical charge in the microenvironment, as well as the pH gradient in the carrier, may have to be taken into account.

When calculating bacterial growth, the first-order mortality rate with regard to the bacterial concentration must be taken into account, Eq.(6.1-22).

$$r_{cells}=(\mu-b)\cdot c_{cells} \tag{6.1-22}$$

The growth constant μ contains all growth-determining and inhibiting parameters x_i in the milieu, such as temperature, concentrations of substrates, inhibitors, and other factors, approximately as functions $f_i(x_i)$, Eq.(6.1-23).

$$\mu(\text{Milieu}) = \prod_i f_i(x_i) \tag{6.1-23}$$

For substrate and nutrient terms f_{Su}, Eq.(6.1-24)).

$$f_{Su}(c_{Su}) = \frac{c_{Su}}{K_{Su} + c_{Su}} \qquad \text{Substratterm} \tag{6.1-24}$$

The nutrients incorporated into the biomass also influence the growth constant via analogous terms of the Eq.(6.1-24) SCHÖPKE (2024) searched $\{C_5H_7O_2N\}$ or $\{C_{6,625}H_{16,43}O_{2,65}NP_{0,0625}\}$ for the composition of biomass, which are included in the gross reaction equation with the associated stoichiometry coefficients ν. The substrate turnover stoichiometry ν results in the substrate turnover velocity r_S Eq.(6.1-25).

$$r_S = -\nu \cdot \mu \cdot c_{cells} \tag{6.1-25}$$

The substrate consumption r_s is linked to biomass formation, Eq.(6.1-26) In bioengineering, stoichiometry is defined by the yield factor Y.

$$\frac{\partial c_{Su}}{\partial t} = \frac{-1}{Y} \cdot \frac{\partial c_{Biomasse}}{\partial t} \tag{6.1-26}$$

or

$$\frac{\partial c_{Su}}{\partial t} = \frac{\nu_{Su}}{\nu_{Bio}} \cdot \frac{\partial c_{Biomasse}}{\partial t} \tag{6.1-27}$$

The yield factor commonly used among biotechnologists is not suitable for the formulation of stoichiometry matrices and is therefore substituted.(6.1-28).

$$Y = \frac{\nu_{Bio}}{\nu_{Su}} \tag{6.1-28}$$

6.1.3.2 Inhibition

In competitive inhibition (c), an inhibitor I usually competes with the substrate. As a result, the constant K_{Su} seems to increase (EINSELE et al. 1985). The inhibiting effect is formally obtained via the Langmuirisotherm in the notation with c_I as inhibitor concentration and the constant K_I, Eq.(6.1-24).

$$f_{Su}(c_{Su}, c_I) = \frac{c_{Su}}{c_{Su} + K_{Su} \cdot \left(1 + \frac{c_I}{K_I}\right)} \qquad \text{competitive inhibition by } c_I \tag{6.1-29}$$

Product inhibition is mostly competitive.

In non-competitive inhibition (nc), the inhibitor directly attacks the enzyme or enzyme-substrate complex, Eq.(6.1-30).

$$f_{nc}(c_I) = \frac{K_I}{K_I + c_I} = \frac{1}{1 + \frac{c_I}{K_I}} \qquad \text{non-competitive inhibition by } c_I \qquad (6.1\text{-}30)$$

Special forms of substrate inhibition c_{Su} in anaerobic processes are also described according to Haldane's approach, Eq.(6.1-33).

$$f_{Su}(c_{Su}, H1/2) = \frac{c_{Su}}{K_{Su} + c_{Su} + c_{Su}\left(\frac{c_{Su}}{K_I}\right)^n} = \frac{c_{Su}}{K_{Su} + c_{Su} + \frac{c_{Su}^{n+1}}{K_I^*}} \qquad \text{Substrate inhibition by } c_{Su} \qquad (6.1\text{-}31)$$

The exponent n can take the values n = 1 and n = 2. Accordingly, a distinction is made between Haldane 1 (H1) and Haldane 2 (H2).

6.1.3.3 Temperature dependence of different biochemical processes

In addition to the rate constant μ_{max}, the monod constants are also temperature-dependent. If one assumes that these implicitly contain an equilibrium constant, Eq.(6.1-5) with the free binding enthalpy of the enzyme complex, Tab. 6.12. While with increasing temperature μ_{max} increases, the monod constants in the substrate function K_{Sub} usually decrease.

Tab. 6.12: Compilation of researched activation energies of different bacterial groups. Temperature functions of the wastewater treatment of LOPP (2004) were evaluated with Eq.(6.1-17) In addition to the rate constant $_{max}$ the michaelis constant are also temperature-dependent, see KOCH et al. (2006). FER Fermenters ACE Acetogens, MPB Methanogens, SRB Sulfate Reducers.

Bakteriengruppe	E_A kJ/mol	Quelle
Nitrosomonas/Nitratation in wastewater treatment	61	zit. aus LOPP (2004)
Lyse	41	
Chemical ferrous Oxidation	93	MÜLLER (2003)
Biological ferrous Oxidation	59	
Degradation of organic wastewater constituents	24	HIDAKA & TSUNO (2004)
Nitrification	58	
Endogenous respiration with NO_3^-, easily degradable substrate	111	LOPP (2004)
Endogenous respiration with NO_3^-, wastewater treatment	42	
Anaerobes		
FER and some ACE, MPB	50 – 100	ASPE´ et al. (1997)
ACE, MPB, anaerobic sludge	30 – 50	
SRB in marine sediment	23	
E. coli, Anaerobes	14 – 20	

6.1.3.4 pH-Influence

The pH value can already have an effect on the dissociation equilibria of inhibiting components, such as in anaerobic processes, in which hydrogen sulfide and undissociated substrate acids inhibit more strongly than their anions. Empirically

determined pH terms more or less characterize the decrease in reactivity with increasing distance from an optimal value.

For the pH dependence of autotrophic bacteria during the filtration of treated wastewater, HIDAKA & TSUNO (2004) determined three pH ranges, Eq.(6.1-32).

$$f_{pH} = \begin{cases} 0 & pH \le 6 \\ 1 - 0{,}833 \cdot (7{,}2 - pH) & 6 < pH \le 7{,}2 \\ 1 & pH > 7{,}2 \end{cases} \qquad (6.1\text{-}32)$$

The pH dependence of anaerobic processes has been determined by various authors only for pH > 6.8. The functions are not completely symmetrical, but are somewhat steeper in acid. For the data of O'FLAHERTY et al. (1998), a quadratic function with zeros was adapted to pH_o and pH_u. At these points, the influencing factor should be half of the optimum for

$$pH_m = (pH_o + pH_u)/2 \quad \text{or}$$

$$\xi_{pH}(pH_m) = 1$$

From these standardization requirements follows Eq.(6.1-33).

$$\xi_{pH} = 2^{-\left(\frac{4 \cdot (pH - pH_o) \cdot (pH - pH_u)}{(pH_o - pH_u)^2} - 1\right)} \qquad (6.1\text{-}33)$$

SCHÖPKE et al. (2020) separated pH dependence into an essential and an inhibiting term, Eq.(6.1-34) and Eq.(6.1-35).

$$f_{pH}(c_{H+}) = \frac{10^{-pH}}{K_{pH-u} + 10^{-pH}} \qquad \text{H+ essentiell} \qquad (6.1\text{-}34)$$

$$f_{pH-I}(c_{H+}) = \frac{10^{-pH}}{K_{pH-I} + 10^{-pH}} \qquad \text{Inhibition H+} \qquad (6.1\text{-}35)$$

Inhibition by hydrogen ions (pH_u) can be shifted relatively independently of the essential threshold. When the essential threshold (pH_o) is shifted, the behavior changes at low pH values. This means that both pH threshold values have an independent effect on each other, which is advantageous when adjusting them.

The resulting pH function describes a variable optimum. Multiplied by a factor of 1.025, this is good with Eq.(6.1-33) Fig. 6.14. However, since no functional relationship between pH and metabolic activity is known, the literature values can only be applied to similar cases to some extent.

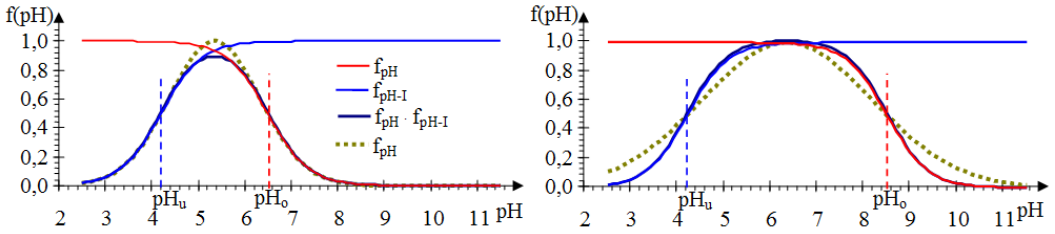

Fig. 6.14: Postulated pH functions for modelling sulphate reduction in groundwater. Left to Eq.(6.1-33) (SCHÖPKE & KOCH 2002) and right to Eq.(6.1-34) and Eq.(6.1-35) (SCHÖPKE et al. 2020).

6.1.3.5 Reaction mechanisms with multiple substrates

Microorganisms can also grow using different carbon sources. BRANDT et al. (2003) developed models for the simultaneous degradation of several substrates. To do this, they defined an enzyme unit SU (synthesizing unit), which forms and degrades complexes with various substrates. A component substrate consisting of A and B that react to C is explained. The enzyme unit can form reactive complexes with any substrate as well as with both at the same time. In this case, four species of SU occur, the proportions of which θι indicates, Fig. 6.15.

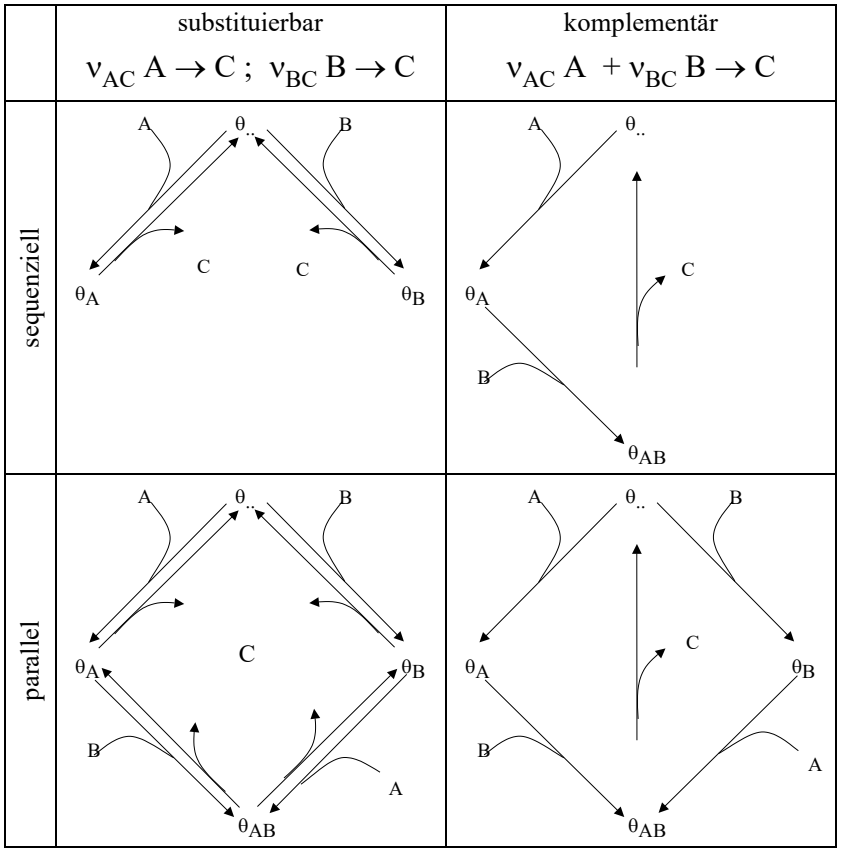

Fig. 6.15: Transformation of two substrates A and B to biomass product C according to BRANDT et al. (2003).

Mining can be divided into four types:

- The substrates are considered substitutable if they can be converted independently of each other to C and
- complementary when both react in a stoichiometric ratio.

These processes can be

- parallel or
- sequentially, Fig. 6.15.

According to the reaction mechanism, the system of differential equations for the reaction rates is to be formulated.

6.1.3.6 Unsteady Growth Kinetics

In biotechnology, it has been observed that when growth conditions change, their influence on the growth rate occurs with a time lag. The transient kinetic approach is second-order (HEKMAT 2002), Eq.(6.1-36).

$$\frac{\partial^2\mu}{\partial t^2} + 2\frac{D_\mu}{T_\mu}\cdot\frac{\partial\mu}{\partial t} = \frac{1}{t^2}\cdot(\mu_S - \mu) \tag{6.1-36}$$

The current value of $\mu(t)$ lags behind the steady-state value μ_S, where T_μ is a characteristic delay time constant and D_μ is a damping constant. The parameters of the Eq.(6.1-36) are adapted from experimental data. In industrial biotechnical reactors, T_μ was in the range of 2 to 6 days and D_μ was less than 0.5. Several days could pass before the new stationary state was adjusted.

IN THIS CONTEXT, HEKMAT (2002) points to the Deborah number, as a quotient of the characteristic relaxation time and the time constant for the change in ambient conditions, Eq.(6.1-37).

$$De = \frac{t_{relax}}{t_{Extern}} \tag{6.1-37}$$

6.1.3.7 Summary aerobic degradation of different organic substances

SCHOENHEINZ & WORCH (2005) describe the first-order summary biochemical degradation c_T of (pseudo-)components (c_{0i}) as the sum of their kinetics, Eq.(6.1-38) Only the biochemically non-degradable substances c_{WWR} (waterworks-relevant chapter 7.1.1.3).

$$c_T(t) = c_{01}e^{-\lambda_1 t} + c_{02}e^{-\lambda 2t} + c_{WWR} \tag{6.1-38}$$

This assumes an excess of active biomass, which is why the growth or lag phase of active biomass can be neglected in this approach. For the biochemical oxygen demand BOD_t calculated from oxygen depletion, this results in Eq.(6.1-39).

$$BSB(t) = BSB_1\left(e^{-\lambda_1 t} - 1\right) + BSB_2\left(e^{-\lambda 2 t} - 1\right) + ... \quad (6.1\text{-}39)$$

6.1.3.8 Die Gibbs-Energy-Dynamic-Yield-Methode (GEDYM)

The metabolism is divided into building metabolism (anabolism) and the breakdown of substances (catabolism). In bioenergetic models, both are stoichiometrically linked by the growth yield. This describes the proportion of the growth-limiting substrate consumed that is converted into cellular biomass. Catabolism is used to obtain the energy for all other metabolic processes in the form of ATP. Their formation from ADP must be secured by the catabolic reactions. SMEATON & VAN CAPELLEN (2018) link biochemical substrate turnover kinetics to ATP gain. This depends on the free reaction enthalpies ΔG_{cat} of the (catabolic) substrate turnover and ΔG_{ATP} of ATP production, Eq.(6.1-40).

$$\frac{\partial c_{Su}}{\partial t} = \mu_0 \cdot f(Milieu) \cdot \left(1 - \exp\left(\frac{\Delta G_{cat} + n \cdot \Delta G_{ATP}}{\chi \cdot RT}\right)\right) \cdot c_{Biomasse} \quad (6.1\text{-}40)$$

n = Number of ATP molecules required for the respective formula turnover.

χ = Average stoichiometry of ATP formation.

With the condition for the sequence of the reaction r, Eq.(6.1-41).

$$\begin{aligned} \Delta G_{cat} + n \cdot \Delta G_{ATP} &< 0 \qquad r > 0 \\ \Delta G_{cat} + n \cdot \Delta G_{ATP} &> 0 \qquad r = 0 \end{aligned} \quad (6.1\text{-}41)$$

This *Gibbs Energy Dynamic Yield (GEDYM) method* can be applied to different biochemical reactions and substrates, such as iron and sulfate reduction in an arsenic-contaminated aquifer (JOHANNESSON et al. 2019). However, this requires many parameters that are still insufficiently known. At present, targeted laboratory experiments are still superior to this.

6.2 Acid-base and complex formation equilibria

6.2.1 Equilibrium definition

Protolysis equilibria of Brønstedt acids are described by the law of mass action (STUMM & MORGAN 1996), Eq.(6.2-1) The activities are summarized as reaction activity coefficients for R, which in turn depend on the ionic strength I [mol/L].(6.2-2).

$$HA = H^+ + A^- \quad (6.2\text{-}1)$$

$$K_S = f_R \cdot \frac{c_A \cdot a_{H+}}{c_{HA}} \text{ with } f_R = \frac{f_A}{f_{HA}} \quad (6.2\text{-}2)$$

With the concentrations of the acid anions c_A and the undissociated acid c_{HA}, as well as their activity coefficients summarized in f_R, the degree of dissociation α is related to total acid concentration c_{ges}, Eq.(6.2-3) and Eq.(6.2-4).

$$c_{ges} = c_{HA} + c_A \tag{6.2-3}$$

$$\alpha = \frac{c_A}{c_{ges}} \tag{6.2-4}$$

In the case of titration of an acid HA with the strong base, e.g. caustic soda NaOH (c_B), the electroneutrality condition for the degree of dissociation α, Eq.(6.2-5) and Eq.(6.2-6),

$$c_{Na+} + c_{H+} = c_{A-} + c_{OH-} \tag{6.2-5}$$

$$c_B = c_{A-} + c_{OH-} - c_{H+} = \alpha \cdot c + c_{OH-} - c_{H+} \tag{6.2-6}$$

and normalized to the total concentration of the acid, Eq.(6.2-7).

$$\frac{c_B}{c_{ges}} = \frac{c_{A-}}{c_{ges}} + \frac{c_{OH-} - c_{H+}}{c_{ges}} = \alpha + \frac{c_{OH-} - c_{H+}}{c_{ges}} \tag{6.2-7}$$

The titration curve is generally understood to be the dilution-corrected pH function as a function of acid or base addition. Thus, the measured titration curve is divided into an *acid* ($c_B < 0$) and a *baseast* ($c_B > 0$) based on the solution used. In the range of $3.5 < pH < 10$, the proton and hydroxylion concentrations can usually be neglected. In this interval, the titration curve depends on the degree of dissociation of the corresponding acid-base pair, Eq.(6.2-8).

$$\begin{aligned} pH &= pH(\alpha) = pK_S + \lg\left(\frac{\alpha}{1+\alpha}\right) \\ \alpha &= \alpha(pH) = \frac{10^{pH-pK_S}}{1+10^{pH-pK_S}} \end{aligned} \tag{6.2-8}$$

At pH = pK_S, acid (HA) and corresponding anion (A^-) are present in equal concentrations. The stabilization of the pH value describes the first derivation of Eq.(6.2-8)whose minimum (turning point of the titration curve) corresponds to a maximum buffering, Eq.(6.2-9).

$$\frac{\partial pH(\alpha)}{\partial \alpha} = \ln(10) \cdot \frac{\partial(\ln(\alpha) - \ln(1-\alpha))}{\partial \alpha} \tag{6.2-9}$$

6.2.2 Interpretation of Titration Curves

If there are several acids ci with different acid constants pK_{Si}, their individual inverse titration curves $c_B(pH)$, Eq.(6.2-10).

$$\begin{aligned} c_B(pH) &= -c_{H+} + c_{OH-} + c_1\alpha_1(pH) + c_2\alpha_2(pH) + ... \\ &= -c_{H+} + c_{OH-} + \sum c_i\alpha_i(pH) \end{aligned} \tag{6.2-10}$$

$c_B(pH)$ is formed from the sum of the $\alpha_i(pH)$ as a linear combination of the individual inverse titration curves and their concentrations of the undissociated acids ci. In the

measured titration curve, the initial pH defines the zero point $c_{B0}(pH_0)$ from which the measurement solutions are added.

In special cases, the overlapping reactions can be separated by adjustment calculation or alternatively as pseudocomponents with characteristic $pK_{S,i}$, chapter 9.1.2.2.

- Acid-base systems with $\Delta pK_{S,i} \approx 1$ appear with widened buffer area.
- From $\Delta pK_S > 2$ onwards, the individual acid components can also be recorded via curve discussion.

Often c_B is also related to the total acidity, as the relative titer Q_{TOT}.

6.2.3 Titration curve of carbonic acid - hydrogen carbonate buffer

The dissolved inorganic carbon (DIC) is composed of the three types of dibasic carbonic acid, apart from cation complexes, which are in two chemical equilibria with each other and form the hydrogen carbonate buffer above them.

1. Dissociation equilibrium

$$\begin{aligned} &CO_2 + H_2O \leftrightarrow HCO_3^- + H^+ \\ &\lg K_1 = \lg a_{HCO_3} - pH - \lg a_{CO2} \approx 6{,}36 \ \ (20°C) \end{aligned} \tag{6.2-11}$$

2. Dissociation equilibrium

$$\begin{aligned} &HCO_3^- \leftrightarrow CO_3^{2-} + H^+ \\ &\lg K_2 = \lg a_{CO_3} - pH - \lg a_{HCO_3} \approx -10{,}33 \ \ (20°C) \end{aligned} \tag{6.2-12}$$

The relative titer Q_{TOT} of carbonic acid H_2CO_3 is defined by Eq.(6.2-13),

$$Q_{TOT} = \frac{c_{HCO3} + 2 \cdot c_{CO3}}{DIC} = 0...2 \tag{6.2-13}$$

which represents a fractional stoichiometry coefficient, Eq.(6.2-14).

$$Q_{TOT} = \frac{c_{HCO3} + 2c_{CO3}}{DIC} \approx \frac{K_{S4,3}}{DIC} \quad \text{mit } H_{(2-Q_{TOT})}CO_3^{-Q_{TOT}} \text{ than carbonic acid} \tag{6.2-14}$$

The temperature- and ion-strength-dependent function $pH(Q_{TOT})$ is also referred to as the general titration curve of carbonic acid, Fig. 6.21. Starting from the dissolved carbon dioxide, it is first converted into hydrogen carbonate and then into carbonate by adding base, or vice versa when acid is added. Due to the difference in the acid constants of four orders of magnitude, the two equilibria do not overlap and the pH jumps between the buffer ranges can be used titrimetrically to determine the carbonic acid species. In the absence of other buffer systems, these are detected by titration with acid and alkali (DIN 38 409-H7-2). This takes advantage of the fact that there is practically no hydrogen carbonate at pH < 4.3 and no dissolved carbon dioxide (carbonic acid) from pH > 8.2 and defines the titration endpoints:

Acid capacity to pH = **4,3**: $K_{S4,3}$ ≈ Hydrogencarbonatkonzentration

Base capacity to pH = **8,2**: $K_{B8,2}$ ≈ Kohlensäurekonzentration

(Note the indices.)

The distance between the transshipment points pH = (4.3...8.2) corresponds to the concentration of inorganic carbon DIC, Eq.(6.2-15).

$$DIC = K_{S4,3} + K_{B8,2} \tag{6.2-15}$$

The addition of acid instead of base is defined as a sign reversal, Eq.(6.2-16).

$$K_{S,pH} = -K_{B,pH} \tag{6.2-16}$$

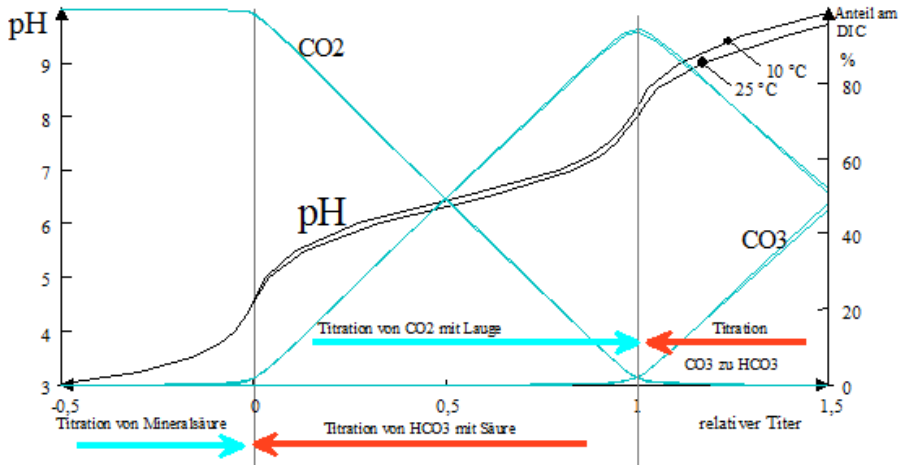

Fig. 6.21: General titration curve of carbonic acid, calculated for ionic strength I = 10 mmol/L at 10°C and 25°C with the proportions [%] of the DIC species CO_2, HCO_3^- and CO_3^{2-}. The carbonate buffer range around pH = 10.5 is incomplete.

6.2.4 Complex Equilibria

Mainly multi-charged ions form complexes with new properties with different counterions present in the solution. This is demonstrated on the Ion Me^{+2} and the compex former X^n, Eq. (6.2-17) Part of the measured total concentration $c_{Me,T}$ is masked by the formation of the complex MeX^{2-n}, which leads to a lower concentration of the free ion c_{Me2}.

$$Me^{2+} + X^{n-} \Leftrightarrow MeX^{2-n} \tag{6.2-17}$$

And the law of mass action Eq.(6.2-18).

$$K_{MeX} = \frac{c_{MeX}}{c_{Me2} \cdot c_X} \tag{6.2-18}$$

with

K_{MeX} Complex stability constant

$c_{X,T}$ Total chelating agent concentration

$c_{Me2,T}$ Total metal concentration.

The total concentration of the complex-forming cation is composed of its free and complex-bound portion, Eq.(6.2-19),

$$c_{Me,T} = c_{MeX} + c_{Me2} = (1 + K_{MeX} \cdot c_X) \cdot c_{Me2} \tag{6.2-19}$$

or Eq.(6.2-20).

$$\begin{aligned} c_{Me} &= \frac{c_{X,T}}{(1 + K_{MeX} \cdot c_X)} \\ c_X &= \frac{c_{X,T}}{(1 + K_{MeX} \cdot c_{Me})} \end{aligned} \tag{6.2-20}$$

In the surplus of the chelating agent X, $c_X \approx c_{X,T}$, Eq.(6.2-21).

$$c_{Me2} = \frac{c_{Me,T}}{(1 + K_{MeX} \cdot c_{X,T})} \tag{6.2-21}$$

or as a quotient Eq.(6.2-22).

$$\frac{c_{Me2}}{c_{Me,T}} = \frac{1}{(1 + K_{MeX} \cdot c_{X,T})} = \frac{1}{\left(1 + 10^{\log(K_{MeX}) + \log(c_{X,T})}\right)} \tag{6.2-22}$$

The logarithmic stability constant $\log K_{MeX}$, supplemented by the chelating agent concentration $c_{X,T}$ is related to the free cation concentration, Fig. 6.22. Since in many cases several chelating agents influence each other, geochemical simulation models are used here (e.g. PHREEQCx).

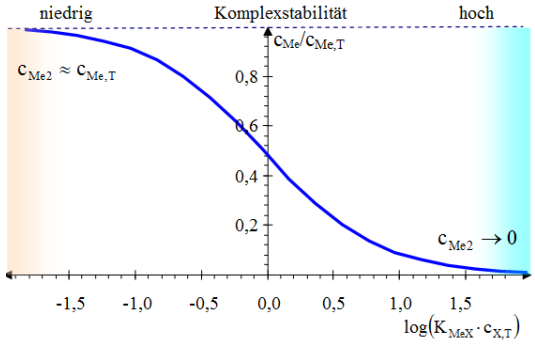

Fig. 6.22: Relationship between complex stability and the proportion of the free ion Me^{2+} in its total concentration $c_{Me2}/c_{Me,T}$.

6.3 Mineral Phase Equilibria and Reactions

6.3.1 Thermodynamic description

The thermodynamic principles, including numerous constants and possible side reactions, are implemented in geochemical computational models (PARKHURST & APPELO 2006 to CRAVOTTA 2021) and specified in SCHÖPKE et al. (2020) for the processes in mining-acidified waters (AMD). Mineral phase equilibriaare described by the solubilityequilibrium, Eq.(6.3-1) and Eq.(6.3-2).

$$A_{\nu A}B_{\nu B} \leftrightarrow \nu_A A + \nu_B B \tag{6.3-1}$$

$$K_L = a_A^{\nu_A} \cdot a_B^{\nu_B} \tag{6.3-2}$$

The activity of pure solid phases is by definition equal to 1. The saturation index SI describes the saturation state of a solution compared to a solid phase and corresponds to the difference of the ion activity fraction IAP Eq.(2.3-17) and the logarithm of the equilibrium constants, Eq.(6.3-3).

$$SI = \lg\left(\frac{a_A^{\nu_A} \cdot a_B^{\nu_B}}{K_L}\right) = \lg\left(f_R \cdot \frac{c_A^{\nu_A} \cdot c_B^{\nu_B}}{K_L}\right) = IAP - \log(K_L) \tag{6.3-3}$$

When transitioning to concentration quantities, the activity coefficients are summarized in a reaction activity coefficient for f_R.

6.3.2 Solid solutions

6.3.2.1 Ideal solid solutions

Mineral phases with variable composition, so-called *solid solutions*, each component is assigned an activity depending on the composition of the mixing phase. In the simplest case, they are proportional to their mole fractions. PARKHURST & APPELO (2013) offer in PHREEQC not only non-ideal binary mixing phases but also the simple linear description approach, Eq.(6.3-4) to Eq.(6.3-10).

It is postulated that the minerals AY and BY form a mixed phase with constant composition, Eq.(6.3-4),

$$(AY)_{\nu A} : (BY)_{\nu B} \leftrightarrow A_{\nu A}B_{\nu B}Y \,|\, \nu_A + \nu_B = 1 \tag{6.3-4}$$

which is described by the solution equilibrium, Eq.(6.3-5),

$$A_{\nu A}B_{\nu B}Y \leftrightarrow \nu_A A + \nu_B B + Y \tag{6.3-5}$$

or rephrased, Eq.(6.3-6).

$$(AY)_{\nu A} : (BY)_{\nu B} \leftrightarrow \nu_A A + \nu_B B + (\nu_A + \nu_B)Y \tag{6.3-6}$$

In the case described, the activities of the *components condensed in the solid solution* correspond to their mole fracture in the condensed phase.

$$a_{AY} = f_{AY} \cdot \nu_A \tag{6.3-7}$$

For the law of mass action taking into account the activities of the solid phase components, Eq.(6.3-8).

$$K_{ABY} = \frac{a_A^{\nu A} \cdot a_B^{\nu B} \cdot a_Y^{\nu A+\nu B}}{a_{AY}^{\nu A} \cdot a_{BY}^{\nu B}} = \frac{K_{AY}^{\nu A}}{(f_{AY} \cdot \nu_A)^{\nu A}} \cdot \left(\frac{K_{BY}}{f_{BY} \cdot \nu_B} \right)^{\nu B} \tag{6.3-8}$$

Logarithmized follows from this Eq.(6.3-9).

$$\log(K_{ABY}) = \nu_A \cdot \log(K_{AY}) + \nu_B \cdot \log(K_{BY}) - \nu_A \cdot \log(f_{AY} \cdot \nu_A) - \nu_B \cdot \log(f_{BY} \cdot \nu_B) \tag{6.3-9}$$

The same is formulated for the ion activity fraction IAP, Eq.(6.3-10).

$$IAP_{ABY} = \nu_A \cdot \log\left(\frac{a_A \cdot a_Y}{f_{AY} \cdot \nu_A} \right) + \nu_B \cdot \log\left(\frac{a_B \cdot a_Y}{f_{BY} \cdot \nu_B} \right) \tag{6.3-10}$$

6.3.2.2 Other solid solutions

The description of non-ideal solubility equilibria with *solidsolutions* (PHREEQCx) requires additional, mostly unknown substance parameters. In the simplest case, the solubility constant KABY resulting from the phase composition differs by the constant amount $\Delta SI_{solidsolutions}$. Inserted into the definition of the saturation index Eq.(6.3-3) the saturation index of the *solid solution is calculated* from the saturation indices of the individual mineral phases. In this case, the activity influences of the solid phases cancel each other out, Eq.(6.3-11) and Eq.(6.3-12).

$$SI_{ABY} = \nu_A \log(a_A \cdot a_Y) + \nu_B \log(a_B \cdot a_Y) - \nu_A \cdot \log(K_{AY}) - \nu_B \cdot \log(K_{BY}) \tag{6.3-11}$$

$$SI_{ABY} = \nu_A SI_{AY} + \nu_B SI_{BY} + \Delta SI_{solidsolution} \tag{6.3-12}$$

where $\Delta SI_{solidsolutions}$ is to be determined empirically, e.g. according to chapter 9.1.2.2 SCHÖPKE et al. (2020) used this approach to hypothetically explain the tendency to determine siderite supersaturation in groundwaters.

For non-ideal binary mixing phases, PARKHURST & APPELO (1999) include so-called Guggenheim expressions for calculating the activity coefficients, Eq.(6.3-13) and Eq.(6.3-14).

$$f_1 = \exp\left(a_0 - a_1(4x_1 - 1) \cdot x_1^2\right) \tag{6.3-13}$$

$$f_2 = \exp\left(a_0 + a_1(4x_2 - 1) \cdot x_1^2\right) \tag{6.3-14}$$

The dimensionless Guggenheim parameters are calculated from so-called free excess enthalpies.

6.3.2.3 Example of the mixed carbonate calcium/manganese carbonate

APPELO & POSTMA (1993) explain these relationships using the Calcite/Rhodochrosite system, Eq.(6.3-15) and Eq.(6.3-16).

$$CaCO_3 = Ca^{2+} + CO_3^{2-} \qquad \text{Calcite} \tag{6.3-15}$$

$MnCO_3 = Mn^{2+} + CO_3^{2-}$ Rhodochrosite (6.3-16)

For both solubility equilibria the laws of mass action Eq.(6.3-17) and Eq.(6.3-18).

$$K_{L,Ca} = \frac{a_{Ca} \cdot a_{CO3}}{a_{Calcite}} \tag{6.3-17}$$

$$K_{L,Mn} = \frac{a_{Mn} \cdot a_{CO3}}{a_{Rhodochrosite}} \tag{6.3-18}$$

This means that for the activity break in the solution Eq.(6.3-19).

$$\frac{a_{Mn}}{a_{Ca}} = \frac{a_{Rhodochrosite}}{a_{Calcite}} = \frac{K_{L,Mn}}{K_{L,Ca}} \tag{6.3-19}$$

The activities of the phase components are calculated from their mole fraction x_i, Eq.(6.3-20)

$$a_i = f_i \cdot x_i \quad \text{mit } i = Ca^{2+}, Mn^{2+} \tag{6.3-20}$$

$$\text{with } \sum_i x_i = 1$$

Inserted and rearranged follows Eq.(6.3-21).

$$\frac{K_{L,Mn}}{K_{L,Ca}} \cdot \frac{f_{Ca} \cdot f_{Rhodochrosite}}{f_{Mn} \cdot f_{Calcite}} = K_{sol} = \frac{c_{Mn}}{c_{Ca}} \cdot \frac{x_{Calcite}}{x_{Rhodochrosite}} \tag{6.3-21}$$

IIn the simplest case, the constants and activity coefficients are summarized in the distribution coefficient K_{sol}. Multiphase systems can also be described in the same way.

6.3.3 Mineral solution/precipitation kinetics

6.3.3.1 Reaction mechanisms at phase interfaces

The formation and degradation of mineral phases is usually referred to as the dissolution or precipitation process, which also includes weathering. VOIGT (1989) distinguishes three mechanisms that determine reaction kinetics:

1. The surface reaction (reaction-controlled),
2. dhe diffusion of the reactants through a boundary layer to the phase interface **(**transport-controlled, chapter 3.6) and
3. the diffusion of elements in the mineral phase (leaching, grain diffusion, chapter 3.7).

The diffusion-controlled mechanisms are first-order with regard to the concentration gradient between the phase interface and the free solution (bulk) and first-order with regard to the phase interface. The reaction-controlled mechanism (1) is based on the respective chemical reaction.

6.3.3.2 General reaction-controlled solution kinetics

The geochemical calculation model PHREEQC (from PARKHURST & APPELO 2006) contains reaction-controlled solution kinetics for various inorganic mineral phases. From the theory of the transition complex, it follows for the surface-related reaction rate rK [mol/(m2.s)] in general for super- and undersaturated solutions, even far from chemical equilibrium, Eq.(6.3-22).

$$r_k = k_k \left(1 - \left(\frac{IAP}{K_k} \right)^{\sigma} \right) \text{ mit } \frac{IAP}{K_k} = 10^{SI} \tag{6.3-22}$$

and with

k_k empirical constant

σ Stoichiometry ratio for the activated complex. In most cases, $\sigma = 1$.

Another approximation is described by Eq.(6.3-23).

$$r_k = k_k \cdot \sigma \cdot \log\left(\frac{IAP}{K_k} \right) = k_k \cdot \sigma \cdot SI \tag{6.3-23}$$

6.3.3.3 Solution kinetics of individual minerals

The solution reactions take place at the phase interface and are determined by its charge and the various surface complexes (adsorbed phases).

- Calcite

From the sum of different reaction mechanisms, the PHREEQC programs contain a time law for solution and precipitation, Eq.(6.3-24).

$$r_{Calcite} = k_1 \cdot a_{H+} + k_2 \cdot a_{CO2} + k_3 \cdot a_{H2O} - k_4 \cdot a_{Ca} \cdot a_{HCO3} \tag{6.3-24}$$

with the temperature-dependent constants Eq.(6.3-25).

$$\begin{aligned} \lg k_1 &= 0{,}198 - \frac{444}{T} \\ \lg k_2 &= 2{,}84 - \frac{2177}{T} \\ \lg k_3 &= -5{,}86 - \frac{317}{T} \text{ (bis 25°C)} \end{aligned} \tag{6.3-25}$$

In the base dataset wateq4f, the k_4 term is replaced by the saturation, Eq.(6.3-26).

$$r_{Calcite} = \left(k_1 \cdot a_{H+} + k_2 \cdot a_{CO2} + k_3 \cdot a_{H2O} \right) \cdot \left(1 - \left(\frac{IAP}{K_{Calcite}} \right)^{\frac{2}{3}} \right) = r_h \cdot \left(1 - 10^{\left(\frac{2}{3} \cdot SI \right)} \right) \tag{6.3-26}$$

STUMM & MORGAN (1996) give an order of magnitude lower solution rate for the solution of dolomite and a 3 orders of magnesite solution as a guideline.

➢ Calcium hydroxide

JOHANNSEN & RADEMACHER (1999) investigated the dissolving kinetics of calcium hydroxide.

$$Ca(OH)_2(s) \xleftrightarrow[k_f,-k_b]{} Ca^{2+} + 2OH^- \qquad (6.3\text{-}27)$$

Backward and backward reactions must be taken into account. The reverse reaction depends on the activities of the hydroxyl and calcium ions.

$$r_{CaO} = \frac{1}{O}\frac{\partial c_{Ca}}{\partial t} = k_f - k_b \cdot a_{Ca} \cdot a_{OH}^2 \qquad (6.3\text{-}28)$$

with

k_f = $2{,}2 \cdot 10^5 \pm 1{,}3 \cdot 10^5$ mmol/(L·s·cm^2)

k_b = $2{,}1 \cdot 10^9$ L^2/(mmol^2·s·cm^2)

at 25°C.

6.3.3.4 Nucleation from supersaturated solutions as an initial or induction phase

The spontaneous equilibrium adjustment of metastable supersaturated solutions by mineral phase formation takes place via several intermediate steps that delay precipitation. First, crystal nuclei in chemical equilibrium form in the solution, which only irreversibly grow into crystals once they reach a critical size, FigFig. 6.31. The induction time tind indicates the time interval after which nucleation begins and marks the start time of the nucleation rate Eq.(6.3-29).

$$\ln t_{ind} = A \cdot \frac{1}{T^3 \cdot SI^2} - B \quad | \; SI > 0 \qquad (6.3\text{-}29)$$

In this process, the molar volume and the surface energy of the critical nucleus are incorporated into A. B contains the diffusion coefficient of the solution and the diameter of the critical germ. From a supersaturation SI > 0.6, for example, in supersaturated gypsum solutions, homogeneous nucleation begins parallel to crystal growth, in which many finely crystalline crystal nuclei spontaneously form (NIEMANN 2004). Conversely, low supersaturation tends to produce coarse crystalline precipitation. Mineral phases (seed crystals) already present in the solution circumvent the slower nucleation that takes place via nucleation.

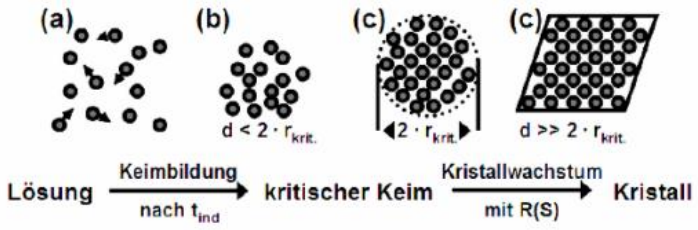

Fig. 6.31: Individual steps up to the formation of a critical nucleus from a supersaturated solution. a: Agglomeration of specific species in solution; b: Structural disorder, formation and dissolution of clusters in chemical equilibrium c: Formation of stable nuclei after the

induction time t_{ind}; d: Structural order, crystal nucleus grows as a function of supersaturation and forms crystal surfaces (gypsum precipitation according to NIEMANN 2004).

6.4 Redox equilibria

6.4.1 Thermodynamic basics

Redox equilibria are electron exchange processes as a result of which the oxidation state of elements changes. The redox reaction is described as the transfer of z electrons, Eq.(6.4-1).

$$\mathrm{Ox} + z\,e^- \leftrightarrow \mathrm{Red} \tag{6.4-1}$$

or generally Eq.(6.4-2).

$$z \cdot e^- + \sum \nu_i \cdot X_i = 0 \tag{6.4-2}$$

Electron release is defined as oxidation and electron uptake as reduction. The free molar standard reaction enthalpy $\Delta_R G$ Eq.(2.3-13) is defined as a standard for the reduction of hydrogen ions to hydrogen gas, Eq.(6.4-3),

$$H^+ + e^- \leftrightarrow 0{,}5H_2(g) \tag{6.4-3}$$

with the free molar reaction enthalpy Eq.(6.4-4).

$$\Delta_R G = \Delta_R G^\circ + RT \cdot \ln\left(\frac{a_{H+}}{p_{H2}^{0,5}}\right) \tag{6.4-4}$$

On the free molar standard reaction enthalpy $\Delta_R G°$ of the hydrogen electrode, all redox reactions are performed as a voltage difference with ion activitiesProduct IAP Eq.(2.3-17) Eq.(6.4-5).

$$U_H = \frac{\Delta_R G^\circ - \Delta_R G}{z \cdot F} = \frac{\Delta_R G^\circ - RT \cdot \ln(IAP)}{z \cdot F} \qquad \left[\frac{J}{mol}\frac{mol}{As} = \frac{VAs}{As} = V\right] \tag{6.4-5}$$

This corresponds to Nernst's equation, Eq.(6.4-6) in Tab. 6.41. To measure the RedOx environment, the redox potential and with regard to the standard hydrogenelectrode EH [mV] are measured (KÜMMEL & PAPP 1990). The measured value is pH-dependent, Eq.(6.4-8) Based on the definition of the pH value, the negative decadal logarithm of electron activity is given as a pε or pE value, Eq.(6.4-9) or Eq.(6.4-10).

Tab. 6.41: Definitions of redox parameters.

Parameter	Symbol	Units	Definition	Eq.
Redox potential	U_H	V	$U_H = U_H^\circ + \frac{RT}{z \cdot F} \ln\left(\frac{a_{ox}}{a_{red}}\right)$	(6.4-6)
			$U_H = U_H^\circ - \frac{RT}{zF} \ln \prod_i a_{X_i}^{\nu_i}$	(6.4-7)
Standard potential related to the standard hydrogen electrode	U_H^0	V	$U^\varnothing = -2{,}303 \cdot \frac{RT}{F} \lg(K)$	(6.4-8)
Negative decadal logarithm of electron activity	pE	1	$pE = p\varepsilon = -\lg(a_{e^-})$	(6.4-9)
	or pε		$p\varepsilon = -\lg(a_{e^-}) = \frac{F}{\ln(10) \cdot RT} \cdot U_H$ $p\varepsilon \approx \frac{U_H}{0{,}059V}$ bei 25°C	(6.4-10)
Ideal gas constant	R	J/(mol·K)	8,314	
Faraday constant	F	A·s/mol	96490	
Temperature	T	K	-273,15 °C	

6.4.2 The electrochemical voltage series

In the electrochemical voltage series, redox half-reactions are listed as a reduction according to their standard electrode potential against the standard hydrogen electrode. The more electropositive half-reaction is reduced and the more electronegative is oxidized. In the usual tabulating, the half-reactions from the top are listed with decreasing standard potential downwards. The equilibria possible from the potential differences can only be achieved under the condition of undisturbed kinetics. The redox reactions compiled by PARKHURST & APPELO (2013) can be converted into pH-dependent standard potentials UH and compared with biochemical redox potentials KÜMMEL & PAPP (1990), Tab. 6.42 and Fig. 6.41.

For the oxidizing agent oxygen, the dataset *wateq4f* contains two slightly different values. The potential of hydrogen refers to dissolved hydrogen at the given pH values, whereas the zero potential of the hydrogen electrode for hydrogen gas is defined at pH = 7.0. Manganese in groundwater can only be reductively dissolved from mineral phases, analogous to pyrolusite, manganite or hausmannite. Ferric iron is a strong oxidizing agent that is pH-independent, but only sufficiently available in acids. Amorphous ferric hydroxide is reductively highly soluble. The reduction of nitrate, sulphate and methane formation are only catalyzed by microbiology.

Tab. 6.42: Redox potentials for different pH values and in comparison with the data of KÜMMEL & PAPP (1990) for biochemical reactions in the Bio column. The half-reactions are sorted by descending EH for pH = 7.0. In this process, the more electropositive half-reaction is reduced as an oxidizing agent, for which an underlying electronegative reaction provides the electrons, whereby it is oxidized as a reducing agent. The potential difference is proportional to the standard free enthalpy of reaction, Eq.(6.4-7) with Eq.(6.4-5).

Reaktion → / ←	Description in Fig. 6.41	lgK	E_H [mV] für pH					Bio
			2,5	**4,3**	**6,0**	**7,0**	**7,5**	**≈ 7**
MnO2 + 4H+ + 2e- = Mn+2 + 2H2O	Birnessite	43,6	1142	1035	935	876	846	
O2 + 4H+ + 4e- = 2H2O	O2-Ox	86,1	1125	1019	918	859	829	810
MnO2 + 4H+ + 2e- = Mn+2 + 2H2O	Nsutite	42,6	1111	1005	904	845	815	460
0,25O2 + H+ + e- = 0,5H2O	O2-Ox	20,8	1081	975	874	815	786	810
Ag+ + e- = Ag	Ag	13,5	799	799	799	799	799	
Fe+3 + e- = Fe+2	Fe(2)/Fe(3)	13,0	770	770	770	770	770	
2 NO3- + 12 H+ + 10e- = N2 + 6H2O	NO3/N2	207,1	1048	920	799	728	693	750
Cu+ + e- = Cu	Cu	8,8	518	518	518	518	518	
MnO2 + 4H+ + 2e- = Mn+2 + 2H2O	Pyrolusite	41,4	928	715	514	396	337	460
NO3- + 10H+ + 8e- = NH4+ + 3H2O	NO3/NH4	119,1	696	563	437	363	326	
MnOOH + 3H+ + e- = Mn+2 + 2H2O	Manganite	25,3	1055	736	434	257	168	460
Mn3O4 + 8H+ + 2e- = 3Mn+2 + 4H2O	Hausmannite	61,0	1214	788	385	149	30	460
Fe(OH)3 + 3H+ + e- = Fe+2 + 3H2O	Fe(OH)3(a)	17,9	616	296	-5	-183	-271	-100
CO3-2 + 10 H+ + 8e- = CH4 + 3 H2O	CO3/CH4	41,1	119	-14	-140	-214	-251	-240
SO4-2 + 10H+ + 8e- = H2S + 4H2O	SO4/H2S	40,6	116	-17	-143	-217	-254	-240
S + 2e- = S-2	Sulfur	-15,0	-444	-444	-444	-444	-444	
Fe+2 + 2e- = Fe	Fe	-15,3	-453	-453	-453	-453	-453	
2 H+ + 2 e- = H2	H2aq	-3,2	-241	-348	-448	-507	-537	-430
FeOOH + 3H+ + e- = Fe+2 + 2H2O	Goethite	12,0	267	-52	-354	-531	-620	-100
Zn+2 + 2e- = Zn	Zn	-25,8	-762	-762	-762	-762	-762	
FeS2 + 2H+ + 2e- = Fe+2 + 2HS-	Pyrit/Fe(2)	-18,5	-694	-801	-902	-961	-990	
CO2+4H+ +4e- =1/6{C6H12O6}+H2O	org							-670

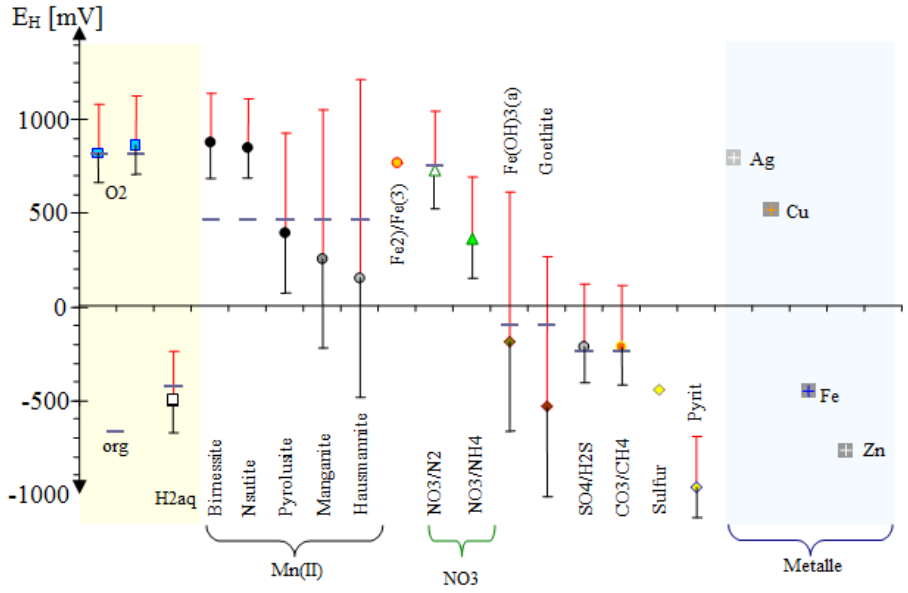

Fig. 6.41: Standard redox potentials E_H of TabTab. 6.42 for pH = 7.0 (pH = 4.3 black bars and pH = 2.5 red bars). The gray lines indicate associated biochemical E_H (bio). Oxygen, hydrogen and biomass are highlighted in yellow as glucose, as well as metals in blue (voltage series).

6.4.3 Biochemical redox series

Metabolism is usually divided into building metabolism (anabolism) and the breakdown of substances (catabolism). In bioenergetic models, both are stoichiometrically linked by the growth yield. This describes the proportion of the growth-limiting substrate consumed that is converted into cellular biomass. Catabolism provides the energy for all other metabolic processes in the form of ATP. Their formation from ADP must be secured by the catabolic reaction. In heterotrophic energy production, an organic substrate (C source) is usually oxidized to carbon dioxide and water. The highest energy gain is achieved by oxygen as an oxidizing agent (electron acceptor). With decreasing energy gain, this is followed by nitrate, brownstone (MnO_2), iron oxide hydrates and finally sulphate, Tab. 6.42. The standard energy gain per exchanged electron follows from the standard voltage difference between the two partial reactions. Hydrogen can also be formed biochemically, e.g. from acetate. The (very low) hydrogen partial pressure then characterizes the redox potential. To characterize the redox conditions of a habitat of microorganisms, KÖHLER & VÖLSGEN (1998) proposed the pH-independent parameter rH_2 value, Eq.(6.4-11) and Tab. 6.43.

$$rH_2 = \frac{E_H}{0{,}029V} + 2pH = 2pE + 2pH \qquad (6.4\text{-}11)$$

Tab. 6.43: rH_2 areas of anaerobic processes according to KÖHLER & VÖLSGEN (1998). Biochemical redox reactions usually take place within these ranges.

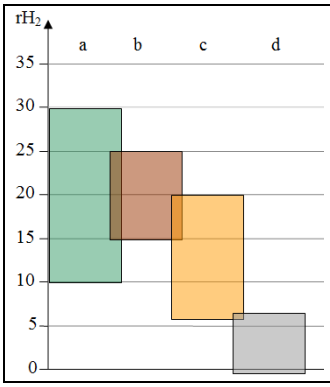

a Denitrifikation
Pseudomonas

b Fe-/Mn-Reduction
Pseudomonas, Alteromonas

c Desulfurication
Desulfovibrio

d Methanogenesis

Other applications:

- Experimental investigation of the iron(II) oxidation kinetics of groundwater after aeration in chapter 9.3.
- Homogeneous and heterogeneous ferrous iron oxidation in water treatment via filtration, chapter 10.1.

6.5 Phase and distribution equilibria

6.5.1 Differentiation of distributional equilibria

A distribution equilibrium describes the concentrations between two different phases, e.g. between the pore solution and the pore gel in the filter or gases (chapter 6.5.2.3), Fig. 6.51. Classically, a distinction is made between absorption (homogeneous in phase) and adsorption on a surface. Extraction and gas-phase equilibria are classical absorption processes, including solid solutions, chapter 6.3.2. Adsorption is the accumulation of substances at a phase interface via the interaction of active centers with atoms, molecules and/or ions of the neighboring phase (KÜMMEL & WORCH 1990). In the case of non-specific interactions (van der Waals), several adsorbate layers can form (multilayer adsorption).

The transition between adsorption and absorption is fluid. The atoms, molecules and ions that interact in complex complexities at the interface to the pore solution are defined as a separate *surface phase*, in which forms of absorption can also occur, Fig. 6.51.

Models of surface complexation with and without electrical potential specify different bonding sites under competing solution components. The electrical potential at the surface, which has a retroactive effect on the equilibrium position, can be planar, spherical or stratified. Macromolecules can condense into gels (Donnan phases, chapter 6.5.6) with external surfaces and internal mixing phases. In the complex mixing phases (Porengels), classical absorption and adsorption processes are superimposed.

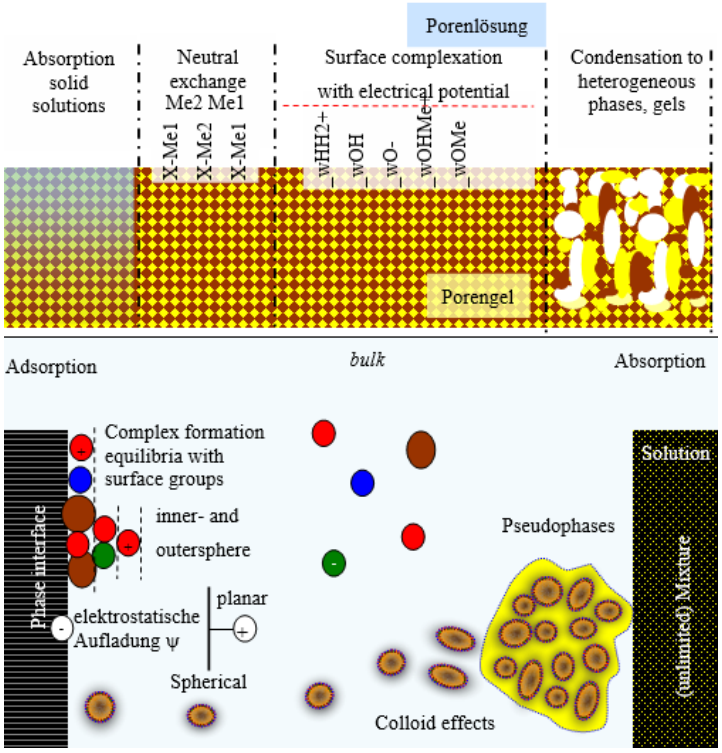

Fig. 6.51: Forms of phase equilibria between pore gel with a textured surface and the pore solution (top) and transition forms between adsorption and absorption (bottom).

6.5.2 Absorption Equilibria

6.5.2.1 Thermodynamics of extraction equilibria

A binary system is considered, consisting of the phases W (e.g. water) and O (e.g. organics), which cannot be mixed with each other. The system is in phase equilibrium if the chemical potentials μi of a substance i are the same in both phases, Eq.(6.5-1) or Eq.(6.5-2).

$$\mu_{i,W} = \mu^*_{i,W} + RT \cdot \ln\left(f_{i,W} \cdot x_{i,W}\right) = \mu_{i,O} = \mu^*_{i,O} + RT \cdot \ln\left(f_{i,O} \cdot x_{i,O}\right) \qquad (6.5\text{-}1)$$

mit

j	=	Phase W or O,
$x_{i,j}$	=	Mole fracture of the substance i in the phase j,
$f_{i,j}$	=	Activity coefficient of the substance i in the phase j
$\mu_{i,j}^*$	=	Standard potential of the substance i in the phase j

$$RT \cdot \ln\left(f_{i,O} \cdot x_{i,O}\right) - RT \cdot \ln\left(f_{i,W} \cdot x_{X,W}\right) = \mu^*_{i,W} - \mu^*_{i,O} \qquad (6.5\text{-}2)$$

The difference between the standard potentials determines the equilibrium constant $K_{i,O/W}$, Eq.(6.5-3).

$$\ln\left(K_{i,O/W}\right) = \ln\left(\frac{f_{i,O} \cdot x_{i,O}}{f_{i,W} \cdot x_{i,W}}\right) = -\frac{\Delta_R G^*_{i,O/W}}{RT} \tag{6.5-3}$$

Under ideal (diluted, $f_i \approx 1$) conditions, a constant concentration ratio of the substance i in the phases is derived, the distribution coefficient K_d Eq.(6.5-4).

$$K_d(i,O/i,W) = \frac{c_{i,O}}{c_{i,W}} \tag{6.5-4}$$

6.5.2.2 Distribution Equilibria Water/Organics log $K_{O/W}$

n-octanol has similar absorption properties to biological cell wall structures. Therefore, the distribution coefficient log $K_{O/W}$ indicates the possible accumulation of a substance i in the biomass, Eq.(6.5-5).

$$\log K_{OW} = \frac{c_{i,Octanol}}{c_{i,Wasser}} \tag{6.5-5}$$

Due to different standard chemical potentials μ^* of substances in the phases, a linear relationship between the distribution coefficients of phase O2 and phase O1 with the constants a and b can be defined as a first approximation, (GEORGI 1998), Eq.(6.5-6).

$$\log K_{O2/W} = a \cdot \log K_{O1/W} + b \tag{6.5-6}$$

The soil organic substances, which consist mainly of humic substances, contain hydrophobic and aromatic structures with similar binding properties as organic solvents. If the dissolved natural organic substances (DOM) are also considered as humic colloid phases, Eq.(6.5-6) can also be applied to these (seechapter 7.3.2.1).

Tab. 6.5-1: Constants of the Eq.(6.5-6) with OC = organic carbon. (GEORGI 1998).

{C}	a	b	case under consideration
OC	0,3...0,8	0,3...1,9	range
OC	0,903	0,094	General
OC	0,81	0,1	chlorinated hydrocarbons
DOC	1	-0,18	PAK of humic substances
DOC	0,67	1,85	PAK and DDT at humic substances
DOC	0,93	-0,35	PAK and PCB at humic substances
DOC	0,97	-0,75	PAK and PCB at pore water colloids
DOC	1,44	-2	PAK at pore water colloids
DOC	0,24	2,78	PAK, DDT, HCB and PCB at DOM

6.5.2.3 Thermodynamics of gas-phase equilibria

Gas-phase equilibria describe the absorption of a gas component with the partial pressure p_i in a solution. In ideal gases, the partial pressure is calculated from the product of the molar fraction of the gaseous substance x_i and the total pressure p_{ges}, Eq.(6.5-7).

$$p_i = x_i \cdot p_{ges} \tag{6.5-7}$$

The activity of gas components is related to the pressure of 1 atm and the activity coefficient is called fugacity $f_{i,g}$, Eq.(6.5-8).

$$\mu_i(g) = \mu_{i,g}^* + RT \cdot \ln\left(\frac{p_i}{1\,atm}\right) = \mu_{i,g}^* + RT \cdot \ln\left(f_{i,g} \cdot x_i \cdot \frac{p_{ges}}{1\,atm}\right) \tag{6.5-8}$$

By equating the chemical potentials μ_g and μ_W, the temperature-dependent Henry constant K_H, follows for the gas phase equilibrium Eq.(6.5-9),

$$\ln\left(\frac{c_i}{p_i/1atm}\right) = \ln(K_H) = \frac{\left(\mu_{i,g}^* - \mu_{i,W}^*\right)}{RT} - \log f_{W/g} \tag{6.5-9}$$

also known as HENRY's Law, Eq.(6.5-10) and Eq.(6.5-11).

$$c_i = K_H \cdot p_i \tag{6.5-10}$$

The Henry constant $H_{g/W}$ is the concentration ratio between the phases.

$$H_{i,g/W} = \frac{c_{i,g}}{c_{i,W}} \tag{6.5-11}$$

In the partial pressure calculation of aqueous media from the mole fracture (x = volume fraction of ideal gases) and the total gas pressure p_{ges}, the vapor pressure of the water must be subtracted, Eq.(6.5-12).

$$p_i = x_i \cdot \left(p_{ges} - p_{H_2O}\right) \tag{6.5-12}$$

If the sum of the partial pressures in the aqueous phase exceeds the total pressure in the gas phase pges, the aqueous phase is supersaturated with gases. The equilibrium can be restored by the formation of new gas phases, the composition of which is derived from the partial pressures (beading).

- Downstream equilibria in the solution increase its overall concentration. For example, in the solution of carbon dioxide, hydrogen sulfide, ammonia ... Consider acid-base equilibria and dissolved ion complexes.
- SCHÖPKE (2024) describes the limitation of hydrogen carbonate buffering by high calcium concentrations.
- For the experimental determination of gas-phase equilibria, the following information is given in pt. 9.3 a methodology is presented.

6.5.2.4 Constants for calculating gas phase equilibria

The Henry or equilibrium constants given in the references differ slightly, Tab. 6.5-2.

Tab. 6.5-2: Compilation of Henry coefficients and equilibrium constants. [a)]MERKEL & PLANER-FRIEDRICH (200), [b)]PARKHURST & APPELO (2006), [c)]HANCKE (1991), [d)] wikipedia 30.09.2010.

Species i	K_{25}	**log_K**			
Reference	a	a	b	c	d
	mol/(kg·kPa)				
N2	6,40E-06	-3,188	-3,260	-3,192	-3,215
O2	1,26E-05	-2,894	-2,898	-2,896	-2,886
CO2	3,39E-04	-1,464	-1,468	-1,471	-1,469
CO					-3,022
CH4	1,29E-05	-2,884	-2,86	-2,873	
NH3	5,70E-01	1,761	1,770	1,756	
N2O	2,54E-04	-1,590			
NO	1,90E-05	-2,716			
NO2	1,00E-04	-1,994			
H2S			-0,997	-0,997	
SO2	1,25E-02	0,103		0,097	
H2			-3,15		-3,108
O3	9,40E-05	-2,021			
He	3,76E-06	-3,419			-3,469
Ne	4,49E-06	-3,342			-3,347
Ar	1,37E-05	-2,858			-2,854
H2O			1,510		

Tab. 6.5-3: Compilation of Henry coefficients of organic components.

Species	$\log\_K_H$	ΔH	Reference
1,1-Dichlorethen	-1,173		http://www.fachdokumente.lubw.baden-wuerttemberg.de/servlet/is/10039/gwr0023.html
Chlormethan	-1,504		
Benzol	-0,744		
Toluol	-0,773		
Xylol	-0,724		
Naphthalin	0,315		
Phenol	1,892		
MTBE	-0,140	37,8 kJ/mol	SCHIRMER et al. (2008)

SCHWARDT et al. (2021) supplemented the available database with volatile organic compounds typical of contaminated sites in a wide temperature range, Eq.(6.5-13) with Tab. 6.54.

$$\ln(K_H) = A - \frac{B}{T} + C \cdot \ln(T) \tag{6.5-13}$$

Tab. 6.54: Logarihmian Henry constants and the distribution coefficient octanol/water lg K_{OW} for 25°C and constants of the Eq.(6.5-13) for the specified temperature range and molar mass M.

Species	log_K_H	lg K_{OW}	Temp °C	A	B	C	M g/mol
Chloromethane			0 - 93	164,514	9538,1	-23,426	
Dichloromethane	-0,99	1,50	5 - 93	137,31	8923,3	-19,246	84,9
Trichloromethane	-0,82	1,52	2 - 93	164,981	10720	-22,979	119,4
Tetrachloromethane	0,08	2,80	2 - 93	373,715	19941,3	-53,821	153,8
Chloroethane			8 - 93	212,454	11752,3	-30,493	
1,1-Dichloroethane			2 - 93	232,792	13489,4	-33,172	
1,2-Dichloroethane		1,83	2 - 93	367,459	19937,2	-53,27	99,0
1,1,1-Trichloroethane	-0,17	2,40	2 - 93	459,803	23465,6	-66,958	133,4
1,1,2-Trichloroethane	-1,42	1,90	2 - 50	196,111	12330	-27,737	133,4
1,1,2-Trichloroethane	-1,43	1,90	2 - 90	111,318	8598,1	-15,053	133,4
1,1,1,2-Tetrachloroethane	-1,02	2,70	20 - 40	-627,459	-24549,8	95,262	167,9
1,1,1,2-Tetrachloroethane	-1,10	2,70	10 - 90	643,414	34195,7	-93,24	167,9
1,1,2,2-Tetrachloroethane		2,40	10 - 40	-1526,119	-64857,6	228,96	167,9
Vinylchloride	0,00	1,50	8 - 91	-17,713	1196,2	3,813	62,5
Vinylchloride	0,00	1,50	8 - 91	-16,658	1145,5	3,597	62,5
1,1-Dichloroethylene	0,05	1,94	2 - 40	357,062	18641,4	-51,677	96,9
1,1-Dichloroethylene	0,03	1,94	2 - 90	272,503	14818,7	-39,091	96,9
1,2-cis-Dichloroethylene	-0,76	1,90	1,8 - 91	39,763	4457,4	-4,664	96,9
1,2-trans-Dichloroethylene	-0,40	1,90	1.8 - 70	49,275	5027,6	-5,85	96,9
1,2-trans-Dichloroethylene	-0,39	1,90	1,8 - 90	177,76	10748,7	-25,03	96,9
Trichloroethylene	-0,43	2,60	1,8 - 95	88,308	7242	-11,411	131,4
Trichloroethylene	-0,43	2,60	1,8 - 95	110,411	8218	-14,715	131,4
Tetrachloroethylene	-0,15	3,40	1,8 - 91	269,309	15787,9	-38,035	165,8
Tetrachloroethylene	-0,15	3,40	1,8 - 91	306,515	17408,7	-43,611	165,8
1,2-Dichloropropane	-0,96	1,80	2 - 70	177,116	11180,7	-24,893	113,0
Benzene	-0,65	1,99	0 - 89	246,963	14043	-35,34	78,1
Ethylbenzene	-0,51	3,03	2 - 70	571,229	29076,8	-83,347	106,2
Ethylbenzene	-0,53	3,03	2 - 90	220,665	13454,3	-31,024	106,2
Propylbenzene	-0,35	3,70	10 - 30	-103,29	-1594,1	17,05	120,2
Chlorobenzene	-0,78	2,90	2 - 70	322,326	17338,1	-46,683	112,6
Chlorobenzene		2,90	2 - 90	190,288	11451,5	-45,382	112,6
1,2-Dichlorobenzene (o)			10 - 30	-2848,646	-123827,5	426,617	
1,3-Dichlorobenzene (m)			10 - 30	-1.475.902	-62683,5	221,782	
1,4-Dichlorobenzene (p)			10 - 30	-1396,419	-59065,8	209,956	
1,2,4-Trichlorobenzene			2 - 30	-691,61	-28320,2	104,319	
Pentachlorobenzene	-1,54	5,20	14,8 - 50,5	192,339	13042,3	-26,701	250,3
Toluene	-0,60	2,54	0 - 89	322,281	17633,4	-46,425	92,1
2,4-Dichlorotoluene	-0,84	4,20	7,8 - 50	51,72	6354,8	-5,677	161,0
p-Xylene	-0,55	3,09	0 - 50	690,635	34608,8	-101,065	106,2
p-Xylene	-0,57	3,09	0 - 90	325,315	18501,7	-46,436	106,2
o-Xylene	-0,70	3,09	0 - 70	565,741	28883,6	-82,576	106,2
m-Xylene	-0,53	3,09	0 - 70	432,9	22590,2	-62,896	106,2
Anthracene		4,35	4,1 - 35,3	-203,722	-4966,5	31,759	178,2
Phenanthrene		4,35	4,1 - 34,7	447,075	23724,2	-65,603	178,2

Species	log_K_H	lg K_{OW}	Temp °C	A	B	C	M g/mol
Pyrene	-3,16	4,93	4,1 - 31	7,922	5078,8	0,321	202,3
Naphthalene		3,17	2 - 35,5	-551,765	-20877,5	83,86	128,2
Acenaphthene	-2,13	4,33	4,1 - 31	30,841	6909	-2,205	154,2
Fluoranthene		5,20	4,1 - 50,5	38,789	6855,4	-4,047	202,3
2,4,5-Trichlorobiphenyl			4 - 31	-1723,949	-71259,7	259,866	
MTBE			3 - 70	258,241	15697,9	-36,674	
Phenol		1,51	4 - 29	1069,045	50360,9	-159,859	93,1

The data of TabTab. 6.54 can be converted to the notation in PHREEQCx, Eq.(6.5-14),

$$\begin{aligned} \lg(K_H) &= A_1 + A_2 \cdot T + \frac{A_3}{T} + A_4 \cdot T + \frac{A_5}{T^2} + A_6 \cdot T^2 \\ \lg(K_H) &= \frac{A}{\ln(10)} + 0 \cdot T - \frac{B}{\ln(10) \cdot T} + \frac{C}{\ln(10)} \cdot T + \frac{0}{T^2} + 0 \cdot T^2 \end{aligned} \tag{6.5-14}$$

bzw. Eq.(6.5-15).

$$\begin{aligned} A_1 &= \frac{A}{\ln(10)} \\ A_2 &= 0 \\ A_3 &= -\frac{B}{\ln(10)} \\ A_4 &= C \\ A_5 &= 0 \\ A_6 &= 0 \end{aligned} \tag{6.5-15}$$

6.5.3 Adsorption isotherms and kinetics of individual substances

If a sorptive solution is brought into contact with a defined amount of an adsorbent in a closed system, a stable state will be established after a sufficiently long time if only adsorption processes are taking place. This is characterized by a residual concentration of sorptive in the solution and an associated loading of the adsorbent. This steady state is commonly referred to as adsorption equilibrium, although it is not always a true equilibrium in the sense of the strict definition of thermodynamics, since in some cases the final state that occurs can also depend on the path by which it is reached and on changes in the sorbent structure that occur in the process. This stable state is generally described by adsorption isotherms for a single substance. According to its name, each isotherm is only valid for a constant temperature (SONTHEIMER et al. 1985).

The single-substance isotherms developed on various theoretical and empirical foundations were first characterized according to their progression from linear to sigmoid (LIMOUSIN et al. 2007). Single-substance isotherms describe the loading of the adsorbent q_i [mol/kg] in equilibrium with the solution concentration c_i [mol/L] over one or more constants.

The linear isotherm follows from Eq.(6.5-4) by reference to the mass of the adsorbent, Eq.(6.5-16) This K_d concept is applied to migration processes of trace substances, Eq.(6.5-4).

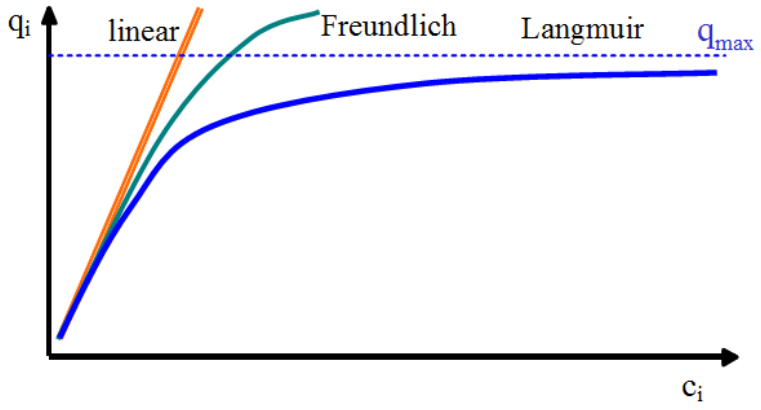

Fig. 6.52: Single-material isotherms: linear, without loading limit according to Freundlich and with limited loading qmax,i according to Langmuir (Sigmoid not shown).

On an empirical basis, the Freundlich isotherm was derived from the linear relationship for low loads, Eq.(6.5-19) The friendly isotherm is related to a logarithmically decreasing affinity of the binding sites with increasing loading. Therefore, there is no maximum load. For many technical applications within limited concentration ranges, this description has proven itself (SONTHEIMER et al. 1985).

From the definition of a chemical equilibrium at the surface, the isothermal equation according to Langmuir is derived via the law of mass action Eq.(6.5-17) An ideal homogeneous surface with binding sites of the same affinity is required, which is rarely the case.

For better adaptation to empirical processes, numerous isothermal equations, some of which are based on theoretical concepts, have been developed.(6.5-21) Eq.(6.5-22) to Eq.(6.5-25) Simple cases of competing adsorption are also quantified, Eq.(6.5-18) Eq.(6.5-20) (SONTHEIMER et al. 1985 and LIMOUSIN et al. 2007), as well as for the neutral exchange Eq.(6.5-26).

Tab. 6.5-5: Compilation of frequently used single-substance isotherms qi(ci) (SONTHEIMER et al. 1985 and LIMOUSIN et al. 2007).

Isothermenbezeichnung	Definition $q_i(c_i)$	Eq.
lineare Isotherme	$q_i = K_{d,i} \cdot c_i$	(6.5-16)
Langmuir	$q_i = q_{max,i} \frac{K_i \cdot c_i}{1 + K_i \cdot c_i}$	(6.5-17)
Langmuir, extended for competing adsorption	$\frac{q_i}{q_{max}} = \frac{K_i \cdot c_i}{1 + \sum_{i,j} K \cdot c_j}$	(6.5-18)
Freundlich	$q_i = K_{F,i} \cdot c^{n_i}$	(6.5-19)

Isothermenbezeichnung	Definition $q_i(c_i)$	Eq.
Freundlich for competing adsorption	$q_i = K_{F,i} \cdot c_i \cdot \left(\sum_j a_{i,j} \cdot c_j \right)^{n_i - 1}$	(6.5-20)
Langmuir-Freundlich	$\frac{q}{q_{max}} = \frac{K \cdot c^n}{1 + (K \cdot c)^n}$	(6.5-21)
Generalized Langmuir	$\frac{q}{q_{max}} = \left(\frac{K \cdot c}{1 + K \cdot c} \right)^n$	(6.5-22)
Sigmoidal Langmuir	$\frac{q}{q_{max}} = \frac{K \cdot c}{1 + K \cdot c + \frac{S}{c}}$	(6.5-23)
Toth	$\frac{q}{q_{max}} = \frac{K \cdot c}{\left(1 + (K \cdot c)^n\right)^{\frac{1}{n}}}$	(6.5-24)
Temkin	$q_i = K_1 \cdot \ln(c) + K_2$	(6.5-25)
Exchange equilibrium according to Rothmund–Kornfeld	$\frac{q_i}{q_j} = K_{ex} \cdot \left(\frac{c_i}{c_j} \right)$	(6.5-26)
Isotherms via Neural Networks and AI	MORSE et al. (2011)	

Competing adsorption based on changes in surfacetension (IAS theory, SONTHEIMER et al. 1985) is described by, among other things: BURWIG et al. (1995) and (KÜMMEL & WORCH 1990). The IAS theory is applied to adsorption analysis, in which an adsorption isotherm determined from a multi-substance mixture is decomposed into several competing Freundlich isotherms as pseudocomponents with predetermined Freundlich parameters.

Adsorption kinetics is often described according to empirical models, Tab. 6.5-6, from which the respective proportions of grain and film diffusion (chapter **Fehler! Verweisquelle konnte nicht gefunden werden.**) should not be disclosed.

Tab. 6.5-6: Compilation of frequently used adsorption kinetics for individual substances (LIMOUSIN et al. 2007).

Isothermenbezeichnung	Definition $q_i(c_i)$	Eq.
First-order kinetics	$\frac{\partial q}{\partial t} = k_1 \cdot c - k_{-1} \cdot q$	(6.5-27)
n-th order kinetics	$\frac{\partial q}{\partial t} = k_1 \cdot c^n - k_{-1} \cdot q$	(6.5-28)
Elovich	$\frac{\partial q_i}{\partial t} = k \cdot \exp(-P \cdot q)$	(6.5-29)
Power	$\frac{\partial q_i}{\partial t} = k \cdot c^m \cdot q^n$	(6.5-30)

6.5.4 Surface complex equilibria of different stoichiometry

The ion exchange equilibrium is the simplest description of competing adsorption. By definition, there are no free adsorption sites in neutral exchanges. Stoichiometry is determined by the charges of the ions to be exchanged. For the exchange of the cation $Me^{\nu+}$ with ν anionic adsorption sites XH loaded with hydrogen ions, Eq.(6.5-31),

$$\nu XH + Me^{\nu+} = X_\nu Me + \nu H^+ \tag{6.5-31}$$

with the law of mass action Eq.(6.5-32).

$$K_{Me} = \frac{a_{XMe} \cdot a_{H+}^{\nu}}{a_{XH}^{\nu} \cdot a_{Me}} \tag{6.5-32}$$

The same applies to the anion exchange for hydroxyl ions.

In an extended formulation of specific adsorption, a component from the solution reacts with a functional group of the surface to form a surfacecomplex. This binding of dissolved species on the solid surface is considered in *surface complexation models,* analogous to the formation of complexes in solution, as a surface complexity of ν_i molecules of the substance X_i with a binding site R, Eq.(6.5-33),

$$R + \nu_i X_i + \Leftrightarrow \left[RX_{i,\nu}\right] \tag{6.5-33}$$

with the relative surface activity/concentration θ [1, %] and the corresponding law of mass action Eq.(6.5-34).

$$K_{RXi\nu} = \frac{\theta_{RXi\nu}}{\theta_R \cdot a_{Xi}^{\nu}} \tag{6.5-34}$$

For n adsorbing substances, the proportion of free binding sites is Eq.(6.5-36).

$$\theta_R + \sum_n \nu_i \cdot \theta_{RXi\nu} = 1 \tag{6.5-35}$$

$$\theta_R = 1 - \nu_i \cdot \theta_{RXi\nu} - \sum_{j \neq i} \nu_j \cdot \theta_{RXj\nu} \tag{6.5-36}$$

And for the adsorption of X_i in a mixture of X_j, further components with the equilibrium constants K_{RXj} and the stoichiometries νφ follow for loading with X_i Eq.(6.5-37) to Eq.(6.5-39).

$$\theta_{RXi} = K_{RXi} \cdot \theta_R \cdot a_{Xi}^{\nu} = K_{RXi} \cdot \left(1 - \nu_i \cdot \theta_{RXi} - \sum_{j \neq i} \nu_j \cdot \theta_{RXj}\right) \cdot a_{Xi}^{\nu} \tag{6.5-37}$$

$$\theta_{RXi}\left(1 + K_{RXi} \cdot \nu_i \cdot a_{Xi}^{\nu}\right) = K_{RXi} \cdot a_{Xi}^{\nu} \cdot \left(1 - \sum_{j \neq i} \nu_j \cdot \theta_{RXj}\right) \tag{6.5-38}$$

$$\theta_{RXi} = \left(1 - \sum_{j \neq i} \nu_j \cdot \theta_{RXj}\right) \cdot \frac{K_{RXi} \cdot a_{Xi}^{\nu}}{\left(1 + K_{RXi} \cdot \nu_i \cdot a_{Xi}^{\nu}\right)} \tag{6.5-39}$$

Eq. (6.5-39) forms a numerically almost insoluble system of equations for X_i and all X_j. Under the conditions ($i \neq j$) and Eq.(6.5-40)

$$\begin{aligned} a_j &= \text{const} \\ \theta_{RXj} &= \text{const} \Rightarrow \\ 1-\sum_{j\neq i}\nu_j\cdot\theta_{RXj} &= \text{const} \end{aligned} \tag{6.5-40}$$

multiplied by the maximum load $q_{max,i}$, the empirical Sips isotherms (quoted in MORSE et al. 2011), Eq.(6.5-41).

$$\begin{aligned} q_i &= q_{max}\cdot\left(\frac{1-\sum_{j\neq i}\nu_j\cdot\theta_{RXj}}{\nu_i}\right)\cdot \frac{\nu_i\cdot K_{RXi}\cdot a_{Xi}^{\nu}}{\left(1+\nu_i\cdot K_{RXi}\cdot a_{Xi}^{\nu}\right)} \\ q_i &= \overline{q_{max}}\cdot \frac{b\cdot c_i^{1/n}}{\left(1+b\cdot c_i^{1/n}\right)} \end{aligned} \tag{6.5-41}$$

Their parameters are determined from adsorption tests.

$$\begin{aligned} \overline{q_{max}} &= \left(\frac{1-\sum_{j\neq i}\nu_j\cdot\theta_{RXj}}{\nu_i}\right) \\ b &= \nu_i\cdot K_{RXi} \\ n &= \frac{1}{\nu_i} \end{aligned} \tag{6.5-42}$$

With $\nu_i = 1$, Eq.(6.5-39) into the well-known Langmuir expression Eq.(6.5-17) applied over and to competing systems follows the extended Langmuir isotherm Eq.(6.5-43) or Eq.(6.5-18).

$$q_i = q_{max,i}\cdot\frac{K_i\cdot c_{Xi}}{\left(1+K_i\cdot c_{Xi}+\sum_{j\neq i}K_j\cdot c_{Xj}\right)} \tag{6.5-43}$$

The Sips Model for Competing Systems Eq.(6.5-44) was developed from the combination of Langmuir and Freundlich isotherms (quoted in ABDULAZIZ & MUSAYEV 2017) with the empirically determined parameters K_i and n. These only approximate thermodynamic constants.

$$q_i = q_{max}\frac{\left(K_i\cdot c_i\right)^{1/n}}{1+\sum_i\left(K_i\cdot c_i\right)^{1/n}} \tag{6.5-44}$$

6.5.5 Surface complexes on oxide surfaces

Oxide surfaces represent two-dimensional polyelectrolytes. The BET surface represents the adsorption surface on which different acid functions (binding sites) are distributed. For iron hydroxide surfaces, DZOMBAK & MOREL (1990) defined two different sites,

Hfo_sOH strong binding for approx. 2,5% and

Hfo_wOH weak binding for the rest

of adsorption capacity.

The amphoteric hydroxyl groups of the sites can be protonated as well as dissociated under proton release (surface acidity, PHREEQC wateq4f), Eq.(6.5-45) and Eq.(6.5-46).

$$Hfo\_s/wOH + H^+ \Leftrightarrow Hfo\_s/wOH_2^+ \qquad \log\_K_1 = 7{,}29 \qquad (6.5\text{-}45)$$

$$Hfo\_s/wOH \Leftrightarrow Hfo\_s/wO^- + H^+ \qquad \log\_K_2 = -8{,}93 \qquad (6.5\text{-}46)$$

The different surface groups also form complexes defined with solution species, which describe adsorption or ion exchange, Eq.(6.5-47) and Eq.(6.5-48) for calcium, Tab. 6.57.

$$Hfo\_sOH + Ca^{2+} \Leftrightarrow Hfo\_sOHCa^{2+} \qquad \log\_K_1 = 4{,}97 \qquad (6.5\text{-}47)$$

$$Hfo\_wOH + Ca^{+2} \Leftrightarrow Hfo\_wOCa^+ + H^+ \qquad \log\_K_2 = -8{,}85 \qquad (6.5\text{-}48)$$

Adsorption stoichiometry is usually $\nu = 1$.

Tab. 6.57: Compilation of surface parameters of oxide adsorbents. Adjustment results are marked with "x" instead of the molar mass. The sites concentration Γ is related to the adsorbent mass and the sorption surface, and the space requirement of a "sites" and the two acid constants are also given. Sources: [a)]DZOMBAK & MOREL (1990), [b)]PARKHURST & APPELO (1999), [c)]CRAVOTTA (2022), [d)]STEINER (2003), [e)]quoted in HADELER (1999), [f)]SCHÖPKE et al. (2020), [g)]SCHÖPKE et al. (2011), [h)]Space requirement of adsorbed gases SONTHEIMER et al. (1985).

Adsorbent	M	O_{sp}(ads)	c_{sites}	Γ	$1/\Gamma$	lgK_1	lgK_2	Quelle
	g/mol	m^2/g	mmol/g	nm^{-2}	nm^2			
Goethit				1,5 - 7	0,67 - 0,14			e
Fe(OH)3(a)	89	600	2,26	2,30	0,45	7,29	-8,93	a, b
Fe(OH)3	107	600	1,92	1,92	0,52			c
Hfo_sOH	107	600	0,047	0,05	21,32	7,29	-8,93	c
Hfo_wOH	107	600	1,869	1,88	0,53	7,29	-8,93	c
Fe(OH)3 - Ferrosorp	x	300	1,146	2,30	0,43			d
Hfe_sOH	x	300	0,029	0,06	17,39	7,29	-8,93	d
Hfe_wOH	x	300	1,117	2,24	0,45	7,29	-8,93	d
Fe(OH)2	107	600	1,92	1,92	0,52			c
Hfn_sOH	107	600	0,047	0,05	21,32	7,29	-8,93	c
Hfn_wOH	107	600	1,869	1,88	0,53	7,29	-8,93	c
MnOOH	105	746	2,10	1,69	0,59			c
Hmo_xOH	105	746	1,343	1,08	0,92	2,35	-6,06	c
Hmo_yOH	105	746	0,752	0,61	1,65	2,35	-6,06	c
Gibbsite (Al2O3)				2 - 3	035 - 0,3			e
Al(OH)3	78	32	0,42	7,96	0,13			e

Adsorbent	M	O_{sp}(ads)	c_{sites}	Γ	1/Γ	lgK_1	lgK_2	Quelle
	g/mol	m^2/g	mmol/g	nm^{-2}	nm^2			
Hao_OH	78	32	0,42	7,96	0,13	7,17	-11,18	c
Quarz				4,5 - 10	0,2 - 0,1			e
Montmorillonit				0,6 - 1,0	1,7 - 1			a
GWL-SiO2	x	12,165	0,01212	0,60	1,67			f
Sand_wOH	x	12,165	0,01212	0,60	1,67	5,50	-8,20	f
Sand_o	x	12,165	0,15	7,43	0,13			f
Kippen-GWL								g
Sand_wOH	x	0,75	0,0125	10,04	0,10			g
pH> 9								
Sand_lOH	x	0,75	0,15	120,44	0,01		-6,0	g
N_2-BET	28			6,2	0,162			h
Ne	20			7,2	0,138			h
Ar	40			5,0	0,202			h

Depending on the surface occupancy of the surface with charged species, the charge balance, a surface potential is formed compared to the free solution (bulk) depending on site density. The sites density (Γ [nm^{-2}]) calculated from the maximum adsorption capacity and the BET surface can also be used to check the plausibility of the measured values. The repercussions of the surface potential on the chemical equilibria are described by different model approaches, chapter 6.5.6.

6.5.6 The surface potential

6.5.6.1 Model presentations

The charged surface groups form a potential difference to the free solution, which reacts on the complex formation equilibria, Fig. 6.53 and Tab. 6.5-8. The different models differ in the structure of the electrochemical bilayer, in particular through the assignment of the sorbed species within different sorption layers and the definition of the surface compexes (HADELER 1999). The equilibrium constants of one model cannot therefore be easily transferred to other models. There are various approaches to the distribution of charges depending on the distance. STUMM & MORGAN (1996) distinguish between *constant capacitance* model (CCM), *diffuse double layer* model (DLM) and *triple layer* model (TLM), Fig. 6.54.

- The *constant capacitance model* (CCM) considers the surfaces between the solid and liquid phases as a plate capacitor (capacitor model).

The excess charge at the solid surface is linearly balanced by a number of countercharges from the liquid phase corresponding to the surface charge up to the distance δ .

- The *diffuse double layer model* (DLM) takes into account the thermal molecular motion of the ions.

All ions in aqueous solution therefore also possess kinetic energy as a result of the disordered heat movement, which counteracts the attractive effect of the Coulomb forces. The distribution of the freely movable charge carriers (counterions) therefore

takes place in a disordered manner in space in a so-called *diffuse double layer*. Within the boundary layer, the potential is exponential from the distance to the solid surface.

- In the *triple layer model* , the electrochemical double layer is divided into an immobile adsorption layer and a mobile diffusion layer.

In the mobile layer, the ions are loosely bound, and the influence of the charges on the solid surface decreases with increasing distance.

- The ***NICA-Donnan*** model combines adsorption in a homogeneous charged gel phase with diffuse layer transitions into the solution.

For nanoparticles and macromolecules, the electric bilayer with spherical geometry (spherical symmetry) is used.

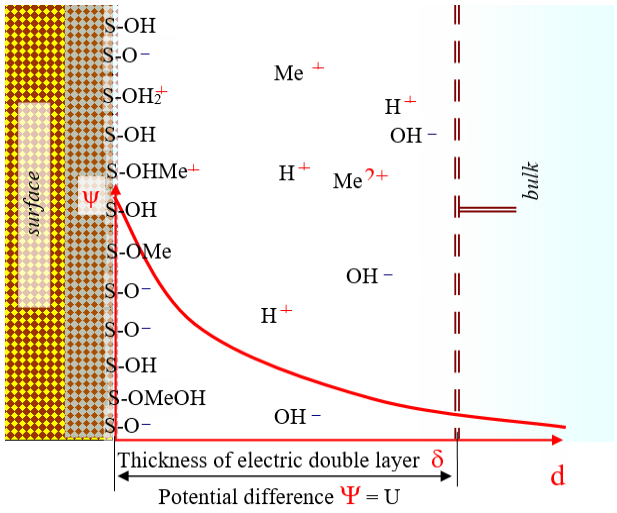

Fig. 6.53: Diffuse layer - Two-layer model with different charged surface complexes and the potential distribution Ψ(d) as a function of the distance d of the electric bilayer. The electric double layer has the thickness δ.

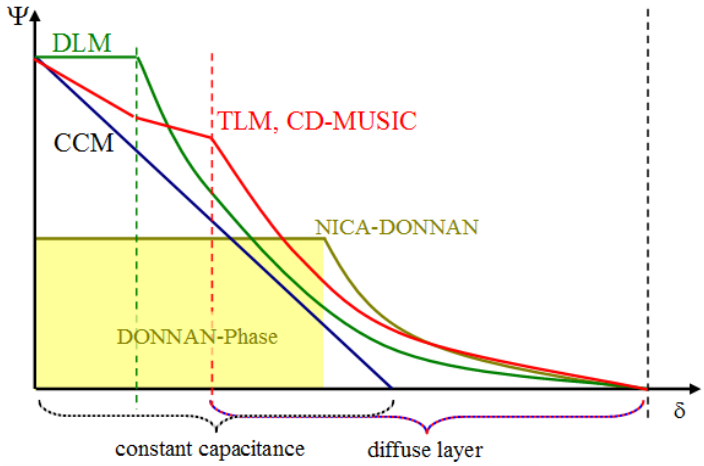

Fig. 6.54: Postulated charge distributions as a function of the distance δ from the surface. CCM-constant capacitance, DLM-diffuse layer, TLM-triple layer and CD-MUSIC, as well as the DONNAN phase. In the NICA-DONNAN model, the constant charge in the DONNA phase is combined with a subsequent *diffuse layer* .

6.5.6.2 Influence of surface charge on equilibrium constants

The surface charge is calculated from the charge balance, related to the specific sorption surface. Its influence on the complex formation equilibria at the surface is investigated in PHREEQC using the two-layer model (DZOMBAK & MOREL 1990, Fig. 6.53). The free enthalpy of the reaction of the surface equilibria is split into a chemical and an electrostatic term, Eq.(6.5-45) to Eq.(6.5-48) The apparent (or apparent, app) equilibriumconstants contain both terms, from which the chemical term (intrinsic, int) is derived.

Tab. 6.5-8: Dimensioning of the electrical double layer Fig. 6.53 with constants, Tab. 6.59.

Parameter	Symbol	Einheiten	Definition	Eq.
c_{ads}	Concentration of sites (≈ KAK)	mol/kg		
$O_{sp}(ads)$	specific adsorption surface, BET	m^2/g		
w_i	relativer Anteil der Oberflächenspecies	1		
c_{surf}	Oberflächenspecies bezüglich Lösungsvolumen	mol/L		
Δc_e	Charge balance	mol/kg	$\Delta c_e = z \cdot \sum_i z_{ei} \cdot c_i$	(6.5-49)
σ	Surface Charge from the charge Balance	As/m^2	$\sigma = \frac{\Delta c_e}{O_{sp}(ads)}$	(6.5-50)
δ	Electric double-layer	m	10^{-8}m	Standard
Ψ_S	Surface potential from the charge balance	V	$\Psi_S = \frac{F \cdot \text{Ladungsbil anz}}{\text{Kapazität}}$	(6.5-51)

Tab. 6.59: Constants Used.

F	Faraday constant according to Tab. 2.1-2	96493,5	J/(V·mol) = As/mol
ε_0	Dielectric constant for vacuum	$8{,}854 \cdot 10^{-12}$	As/(Vm)
ε	relative dielectric constant for water	78,54	(25°C)

The charge balance indicates PHREEQCx with respect to the solution phase, Eq.(6.5-52).

$$\sum_i z_{ei} \cdot c_i = c_{ads} \cdot \sum_i z_{ei} \cdot w_i \qquad (6.5\text{-}52)$$

The laws of mass action are each composed of an activity fraction and an electrostatic term, Eq.(6.5-53)

$$K^{int}_{Hfo\_wO-} = \frac{a_{Hfo\_wO-} \cdot a_{H+}}{a_{Hfo\_wOH}} \cdot e^{-\frac{F \cdot \Psi_S}{2 \cdot RT}} \qquad (6.5\text{-}53)$$

and with the apparent equilibrium constant $K_{S,app}$ for planar bilayers, Eq.(6.5-54).

$$K_{S,app} = K_{S,int} \cdot \exp\left(\frac{F \cdot \Psi_S}{RT}\right) \qquad (6.5\text{-}54)$$

In addition, there are approaches for spherical (spherically symmetrical) surface charges of colloids.

6.5.6.3 Diffuse double layer model in PHREEQC

PHREEQC calculates the charge balance for a cell with V_W = 1 liter. The surface phase (standard 1 kg sorbent material, PARKHURST & APPELO 1999) is already fully dimensioned with the concentration of the surface sites cads [mol/L], the adsorption surface O_{sp}(ads) [m^2/g] and the defined surface reactions, and the thickness of the diffuse electric bilayer δ is already determined, Eq.(6.5-55) to Eq.(6.5-64)

For the associated surface potential Ψ_S , Eq.(6.5-55),

$$\Psi_S = F \cdot \frac{\Delta c_e}{\frac{O_{sp}}{\delta} \cdot \varepsilon \cdot \varepsilon_0} \tag{6.5-55}$$

with the dimension consideration Eq.(6.5-56) and Eq.(6.5-57).

$$\Psi_S = \frac{96496\,{}^{As}/_{mol}}{\frac{O_{sp}}{\delta} \cdot 78{,}54 \cdot 8{,}854 \cdot 10^{-12}\,{}^{As}/_{V \cdot m}} \cdot \Delta c_e[mol/kg] \tag{6.5-56}$$

$$\Psi_S = 1{,}388 \cdot 10^{14}\,\frac{V \cdot m}{mol} \cdot \frac{\delta[m]}{O_{sp}[m^2/kg]} \cdot \Delta c_e[mol/kg] \tag{6.5-57}$$

After the insertion of the charge balance Eq.(6.5-49) taking into account the phase ratio z follows Eq.(6.5-58),

$$\Psi_S = F \cdot \frac{\delta \cdot z \cdot \sum_i z_{ei} \cdot c_i}{O_{sp} \cdot \varepsilon \cdot \varepsilon_0} \tag{6.5-58}$$

and for the apparent equilibrium constant $K_{S,app}$ Eq.(6.5-59) and Eq.(6.5-60).

$$\lg K_{S,app} = \lg K_{S,int} + \frac{1}{\ln 10} \cdot \left(\frac{\delta \cdot z}{O_{sp}} \cdot \frac{F^2 \cdot \sum_i z_{ei} \cdot c_i}{RT \cdot \varepsilon \cdot \varepsilon_0} \right) \tag{6.5-59}$$

$$\lg K_{S,app} = \lg K_{S,int} + \frac{1}{\ln 10} \cdot \left(\frac{F^2 \cdot \sum_i z_{ei} \cdot c_i}{RT \cdot \varepsilon \cdot \varepsilon_0} \right) \cdot \left(\frac{\delta \cdot z}{O_{sp}} \right) \tag{6.5-60}$$

After the insertion of Eq.(6.5-52) you get Eq.(6.5-61).

$$\lg K_{S,app} = \lg K_{S,int} + \frac{1}{\ln 10} \cdot \left(\frac{F^2 \cdot \sum_i z_{ei} \cdot w_i}{RT \cdot \varepsilon \cdot \varepsilon_0} \right) \cdot \left(\frac{c_{ads} \cdot \delta \cdot z}{O_{sp}} \right) \tag{6.5-61}$$

All surface phases with the size const are equivalent, Eq.(6.5-62) and Eq.(6.5-64).

$$\frac{c_{ads} \cdot \delta \cdot z}{O_{sp}} = \text{const} \tag{6.5-62}$$

Eq. (6.5-62) is reformulated to the material-related quantities c_{ads} [mol/kg], O_{sp} [m^2/kg] and z [L/kg], Eq.(6.5-63) and Eq.(6.5-64).

$$c_{surf} = \frac{c_{ads} \cdot m_{Pr}}{V_W} = \frac{c_{ads}}{z} \tag{6.5-63}$$

$$\frac{c_{surf} \cdot \delta}{O_{sp}} = const \tag{6.5-64}$$

In model calculations, therefore, the standard value for the layer thickness $\delta = 10^{-8}$ m does not need to be varied. The concentration of the surface groups cads and the specific surface area O_{sp} of the adsorbent influence the thermodynamic boundary conditions, while the phase ratio z does not play a role.

6.5.6.4 The Donnan gel

Colloidal macromolecules with surface potentials can condense into gel phases with a constant electrical potential inside and separated from the outside by an electric double layer, Fig. 6.51. This model, known as Donnan gel, is applied to humic substances with the binding types carboxyl and phenyl (e.g. BASSER & GRODZINSKY 1993, SAITO et al. 2004). The volume of the respective Donnan phase V_D [L/kg] to be considered is given by an empirical relationship, Eq.(6.5-65).

$$\log(V_D) = \alpha + \beta \log(I) \qquad [L/kg] \tag{6.5-65}$$

With the empirical parameters α, β, which describe the influence of the ionic strength I [mol/L].

The charging of the gel aggregates and thus the potential difference to the solution - the Donnan potential ψ_D - follows from the charge balance. This affects the concentrations of the ions c_i dissolved in the Donnan volume, Eq.(6.5-66).

$$c_{D,i} = c_{0,i} \cdot \exp\left(-\frac{z_i \cdot F \cdot \psi_D}{RT}\right) \tag{6.5-66}$$

The concentrations in the Donnan volume are in equilibrium with the adsorbed phase and are used in combination in the NICA-Donnan model.

6.5.6.5 Non-Ideal Competitive Adsorption (NICA)-model

The Non-Ideal Competitive Adsorption (NICA) model describes the binding of cations to macromolecules with multiple bond types for wide concentration ranges and over a wide range of environmental conditions (pH, ionic strength). For this purpose, it is defined:

Index i:	Kation	H^+, Me^{2+}, ...
Index j:	Binding sites type	1 = Carboxyl, 2 = Phenyl

The individual bond types are given stoichiometries.

$\nu_{i,j}$ Stoichiometry numbers for binding i to j

The surface complex is formed for a doubly charged cation and the binding site Rj, Eq.(6.5-67).

$$\nu_{i,j}Me_i^{2+} + RjOH \Leftrightarrow \left[RjOH_{(1-\nu_{i,j})}Me_{\nu_{i,j}}\right]^{\nu_{i,j}} + (1-\nu_{i,j})H^+ \tag{6.5-67}$$

The proportion of bound binding places in each case is calculated as

$\theta_{i,j}$ Proportion of j posts occupied by species i

The equilibrium constants at the sites of the bond types are calculated from Eq.(2.3-32) according to Eq.(6.5-1) around $K_{m,i,j}$ normally distributed, Eq.(6.5-68).

$$\left(\frac{\partial\theta_{i,j}}{\partial\log(K_{i,j})}\right)_j = \frac{1}{\sigma_j\cdot\sqrt{2\pi}}\cdot\exp\left(-\frac{1}{2}\left(\frac{\log(K_i)-\log(K_{m,i,j})}{\sigma_j}\right)^2\right) \tag{6.5-68}$$

If the adsorption capacity $_{max,j}$ [mol/kg] of each of the two binding site types j is related to the dissociable protons, Eq.(6.5-69) indicates the load q_i [mol/kg] with the ion i. The stoichiometry of the protolysis is entered as $\nu_{H,j}$. The composition of the adsorption surface is called the Donnan phase, the composition of which is described by the electrostatic Donnan submodel.

$c_{D,i}$ concentration of species i in the Donnan phase

$$\begin{aligned} q_i &= \frac{\nu_{i,1}}{\nu_{H,1}}\cdot q_{max,1}\frac{\left(K_{m,i,1}c_{D,i}\right)^{\nu_{i,1}}}{\sum_i\left(K_{m,i,1}c_{D,i}\right)^{\nu_{i,1}}}\cdot\frac{\left[\sum_i\left(K_{m,i,1}c_{D,i}\right)^{\nu_{i,1}}\right]^{p_1}}{1+\left[\sum_i\left(K_{m,i,1}c_{D,i}\right)^{\nu_{i,1}}\right]^{p_1}} \\ &+ \frac{\nu_{i,2}}{\nu_{H,2}}\cdot q_{max,1}\frac{\left(K_{m,i,2}c_{D,i}\right)^{\nu_{i,2}}}{\sum_i\left(K_{m,i,2}c_{D,i}\right)^{\nu_{i,2}}}\cdot\frac{\left[\sum_i\left(K_{m,i,2}c_{D,i}\right)^{\nu_{i,1}}\right]^{p_2}}{1+\left[\sum_i\left(K_{m,i,2}c_{D,i}\right)^{\nu_{i,2}}\right]^{p_2}} \end{aligned} \tag{6.5-69}$$

The distribution of the equilibrium constants for each bond type, which is based on the Sips isotherm, is determined by two parameters.

$K_{m,i,j}$ Median value of equilibrium constant of species i to bond type j,

p_j Parameters for the width of the affinity distribution according to Eq.(6.5-70) based on Eq.(2.3-32).

$$p_j = \frac{\sigma_j}{\ln(10)} \tag{6.5-70}$$

This so-called *intrinsic affinity distribution* characterizes the chemical heterogeneity of the respective bond type in the molecular structure. In a constantly composed milieu, Eq.(6.5-69) formally to a combination of Langmuir expressions as a function of a few cation concentrations.

6.6 Transfer of reactions to a representative elementary volume (REV, batch)

When modeling filters and flow sections with the mixed cell model, all reactions and stationary phases are implemented in a series of cells that are only gradually flowed through by the mobile solution phase, chapter 3.2.3. The geochemical calculation program PHREEQC version 3 (PARKHURST & APPELO 2013) or later is recommended. The extensive basic data set *wateq4f.dat* can be problem-related, even with pseudo-components (chapter 2.3.5.3). The *interactive tool* PHREEQ-N-AMD (CRAVOTTA 2021) for passive mine water treatment (AMD) includes extensive extensions for groundwater problems, heavy metals and rare earths.

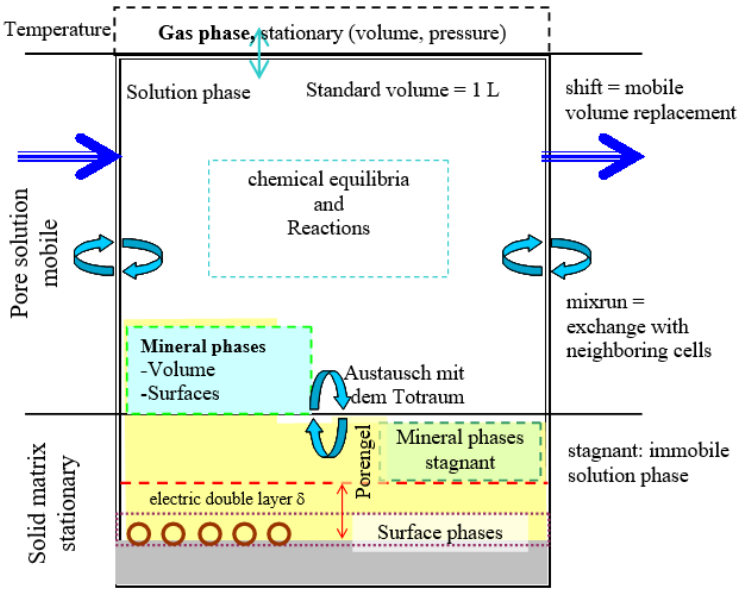

Fig. 6.61: Extended volume element (mixed cell) with phases and interactions to be considered.

The following operations can be implemented in each cell:

- Chemical equilibria in the solution (water),
- Complex formation,
- Dissolution and precipitation of minerals and solid solutions, chapter 6.3,
- Gas exchange, chapter 6.5.2.3,
- Redox reactions, chapter 6.4,
- Ion exchange as a special case of adsorption, chapter 6.5.3,
- Sorption reactions of defined surface complexes, chapter 6.5.5,
- Solid solutions, chapter 6.3.2
- irreversible chemical reactions kinetics, chapter 6.1,

as well as in the *mixed cell* tube

- Mixture
- Transport with longitudinal dispersion
- Immobile solution phases, chapter **Fehler! Verweisquelle konnte nicht gefunden werden.**,
- Diffusion

The cell configured in this way forms the smallest element of a current tube formulated as a *mixed cell*. Mass transfer is carried out by mixing with the mobile volume.

7 Complex material systems

7.1 Summary Quantification

7.1.1 Quantification using sum parameters

7.1.1.1 Overview

Summary pseudocomponents represent subsets of the substance inventory with common properties despite variable composition. These can be dissolved and paricular inorganic and organic substances.

These include:

- Summary concentrations of substances (reference to quantities of substances [g, L, mol]:
  - Salinity as a mass concentration,
  - Evaporation residue as mass concentration,
  - Ion concentration, molar,
  - Total Element Concentrations as mass or molar Concentrations,
  - Water hardness as the sum of alkaline earth concentrations,

and

- Common characteristics:

- Electrical conductivity,
- Ionic strength,
- Partial pressure,
- Elemental concentration (carbon, halogen, ...)
- Oxidizability, biochemically or with strong oxidizing agents,
- MPU- **m**ost **p**robable **u**nites of defined elements, e.g. colony-forming units (CFU),
- Particle size and shape.

These summary properties of the subsets should be measured largely with SI-compliant units. Characteristic properties can be assigned to these subsets as ratios between sum parameters analogous to the partial molar quantities, Eq.(2.3-35) in chapter 2.3.5. The formal mathematical forms of description must be specified to the respective special features.

7.1.1.2 Inorganic Sum Parameters

Numerous methods are presented for the estimation of *electrical conductivity* from water analysis (e.g. COURY 1999, MCCLESKEY et al. 2012, SCHÖPKE). As the ion concentration increases, the catalytic and anions migrating in the electric field hinder each other. Therefore, only in diluted solutions is there an approximately linear relationship between the ionic strength and the electrical conductivity. DIN 38 404 Part 10, Draft 3/93, which is no longer valid, specifies the relationship between ionic strength I and the electrical conductivity LF in the drinking water sector Eq.(7.1-1).

$$I \approx LF \cdot \frac{mmol/L}{62\mu S/cm} \quad \text{für } 25°C \tag{7.1-1}$$

The *total hardness GH* is defined as the sum of the alkaline earth ions of the second main group from magnesium onwards, i.e. Mg^{2+}, Ca^{2+}, Sr^{2+}, Ba^{2+} and Ra^{2}, which is practically only composed of calcium and magnesium.

Other inorganic substance complexes are:

- Grain distributions, chapter 3.4,
- clay minerals (aluminosilicates) in combination with quartz surfaces, chapter **Fehler! Verweisquelle konnte nicht gefunden werden.**,
- Zeolites as a special subgroup of aluminosilicates, chapter 7.6.1.

7.1.1.3 Organic Sum Parameters

A systematic presentation of organic substances can be found in every classic textbook of organic chemistry. Structure and characteristic functional groups form the criteria here. The index number serves as an ordering and labelling criterion and is assigned to substances in legislation (Directive 67/548/EEC and listed substances according to the

Hazardous Substances Ordinance). In it, the affiliation to chemically defined substance groups is stated in encrypted form (e.g. 601 for hydrocarbons, 602 for halogenated hydrocarbons, etc.). The ELINCS/EINECS (EC number) and CAS (Chemical Abstracts Service identification number) are used for registration. Within these categories, the practice-relevant properties of the substances vary so strongly that chemically different species fall into problem-oriented categories, such as: *pesticides*, *surfactants* or *environmental toxins* have been reclassified. However, these lists of substances contain only those substances that are important for human civilization in some form, while all other substances are often only summarily given via sum parameters.

The DOC (Dissolved Organic Carbon) is defined as the concentration of carbon contained in all dissolved organic compounds. The TOC (Total Organic Carbon) also records the particulate portion of carbon.

The concentration of organic carbon in natural groundwater and surface waters, which consists mainly of humic and fulvic compounds, is also referred to as NOM (Natural Organic Matter) or DNOM (Dissolved NOM, VOGT et al. 2024). The biochemically irreducible, refractory part of this is sometimes listed as ROM, whereby its internal substance conversions are omitted in the definition of the term at a constant total organic carbon concentration.

The concentrations of organically bound heteroelements are given in terms of mass as

- DON (Nitrogen),
- DOS (Sulfur) or
- DOX (Halogen), ...,

The suspended portion is again taken into account in the total concentrations. The organic halogens are adsorbed from the water to activated carbon, enriched and detected. The adsorption is not complete, so the measured AOX is not the same as the DOX (total-dissolved)). The situation is similar with EOX, which represents the organic halogen compounds that can usually be extracted from solids or soils with an organic solvent, as well as POX, which indicates the blow-out fraction.

The chemical oxygen demand CSB is a measure of the concentration of oxidizable substances in water. Oxidizing agents of different strengths are used.

- potassium dichromate for the CSB, which almost completely oxidizes over 90% of the organic matter, or
- Potassium permanganate as a less frequently used oxidizability, which only covers up to 60% of natural organic matter (NOM).
- With the biochemical oxygen demand BSB_t, only those organic substances that are biochemically easily degradable (putrefactive) in a given time are oxidatively recorded. This meant that BSB should apply ≤ CSB.

The complete chemical oxidation of an organic substance produces defined reaction products, Eq.(7.1-2).

$$C_{\nu C}H_{\nu H}O_{\nu O}N_{\nu N}P_{\nu P}S_{\nu S}X_{\nu x}Na_{\nu Na} + 0{,}5\nu_{Ox}O_2 \Rightarrow$$
$$\nu_C CO_2 + 0{,}5\nu_H H_2O + \nu_N NO_3^- + \nu_P PO_4^{3-} + \nu_S SO_4^{2-} + \nu_X X^- + \nu_{Na} Na^+ \quad (7.1\text{-}2)$$
$$+ \left(\nu_N + 3\nu_P + \nu_X + 2\nu_S - \nu_{Na}\right) \cdot \nu_{Ox} H^+$$

with Na := Na + K + Ca/2 + Mg/2

and X := F + Cl + Br + J

From this, stoichiometry for oxygen demand is derived, Eq.(7.1-3),

$$\nu_{Ox} = 2\nu_C + 0{,}5\nu_H - \nu_O + 2{,}5\nu_N + 2{,}5\nu_P + 3\nu_S - 0{,}5\nu_X + 0{,}5\nu_{Na} \quad (7.1\text{-}3)$$

or as CSB on oxygen mass-related Eq.(7.1-4).

$$CSB(\text{stöch}) = \nu_{Ox} \cdot M_O = \frac{\nu_{Ox}}{2} \cdot M_{O2} \text{ [mg } O_2\text{/mol]} \quad (7.1\text{-}4)$$

The CSB (stoch) forms the upper limit for the maximum reduction capacity of a given organic matter.

The numerous representatives of toxic trace substance groups are also standardised to a typical representative according to their individual toxicity. The proportions of polycyclic aromatics, chlorinated biphenyls, plant protection products, polychlorinated dibenzodioxins and furans, ... of total dissolved organic carbon DOC is usually negligible.

The property of many organic substances to absorb electromagnetic radiation is used by colorimetric sum parameters by measuring the entire UV/VIS spectrum or only the spectral absorption coefficient at λ = 254 nm (SAK_{254}), as well as different color extinctions in the visible wavelength range, chapter 7.1.2. Their share of the DOC is also called CDOM (colored dissolved organic matter) .

Other organic matter complexes as Natural Organic Matter (NOM) and anthropogenic analogues:

- Huminstoffe, chapterHumic substances 7.4,
- Metabolites and extrapolymeric substances (EPS), chapter 7.5,
- anthropogenic trace substances,
- Substances typical of mineral oil and gas works, chapter 10.3.4.1,
- Biofilms and coatings in the form of Porengels chapter 10.4.

7.1.2 Electron Spectroscopy (UV/VIS)

7.1.2.1 Absorption of electromagnetic radiation from substances dissolved in water

In the visible and ultraviolet spectral range, the electron systems of many organic molecules can absorb them by interacting with electromagnetic radiation. The prerequisite for this is that the molecules have π-electrons or, in the presence of

heteroatoms, non-bonding electron pairs. During light absorption, electrons are then transferred from the ground state to an excited state (π–π* or n-π* transitions, FRIMMEL & KUMKE 1998).

After the absorption of a photon, a molecule is in an electronically excited state. Deactivation can be carried out both radiation-free and radiating by emission of a light quantum. In this context, radiative processes that are allowed to spin are called fluorescence and processes that are forbidden to spin are called phosphorescence.

The transition of the electron state occurs at defined energies. The resulting absorption line is widened by superposition with oscillation and rotation states to a absorption band around the absorption maximum with the frequency ν_{max}. The molar free enthalpy for an absorption line is proportional to the radiation frequency with Planck's quantum of action h as a factor Eq.(2.1-6) and Eq.(2.1-7) From this, the absorption wavelength λ_{max} derived, where c indicates the speed of light in a vacuum.

$$\Delta G = h \cdot \nu_{max} = h \cdot \frac{c}{\lambda_{max}} \tag{2.1-6}$$

$$\Delta G = 6{,}625 \cdot 10^{-34}\ \mathrm{Ws}^2 \frac{2{,}998 \cdot 10^{8}\ \mathrm{m}}{10^{-9}\ \frac{\mathrm{m}}{\mathrm{nm}} \cdot \lambda_{max}\ \mathrm{s}} = \frac{1{,}986 \cdot 10^{-16}}{\frac{1}{\mathrm{nm}} \cdot \lambda_{max}}\ \mathrm{J} = \frac{1{,}196 \cdot 10^{5}}{\lambda_{max}} \frac{\mathrm{nm} \cdot \mathrm{kJ}}{\mathrm{mol}} \tag{2.1-7}$$

When a light quantum is absorbed, the electron state is changed in a molecular region. This electron structure, which is delimited in the molecule and has a defined absorption capacity (λ_{max}), is also known as the chromophore.

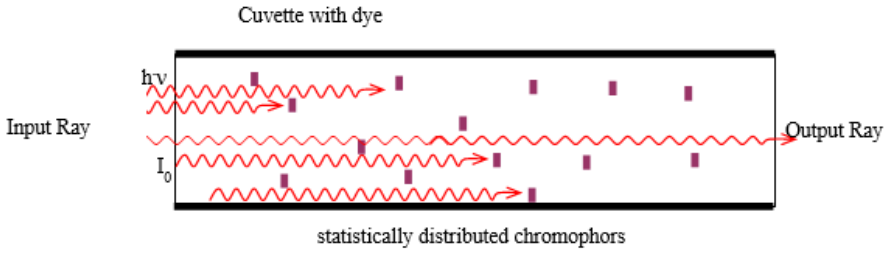

Fig. 7.11: Interpretation of the concentration of absorption units (~areas).

The probability of absorption ΔI/I on the way ΔL is proportional to the chromophore concentration c with the transition-specific proportionality factor ε_λ, Eq.(7.1-5).

$$\partial I = -\varepsilon_\lambda \cdot c \cdot I \cdot \partial L \tag{7.1-5}$$

Integrated in dilute solutions, this results in an exponential decrease in radiation intensity with the layer length, Lambert-Beer's law, Eq.(7.1-6).

$$I = I_0 \cdot \exp(-\varepsilon_\lambda \cdot c \cdot L) \tag{7.1-6}$$

The negative decadal logarithm of the quotient I/I_0 is called the extinction E_L, Eq.(7.1-7),

$$E_L = -\lg \frac{I}{I_0} = \varepsilon_\lambda \cdot c \cdot L \tag{7.1-7}$$

or as an extinction coefficient independent of layer length E_λ, Eq.(7.1-8).

$$E_\lambda = \frac{E_L}{L} \tag{7.1-8}$$

The spectral absorption coefficient at $\lambda = 254$ nm, SAK_{254} corresponds to the extinction coefficient E254 used here. In the range of validity of Lambert-Beer's law, the specific extinction coefficient ε_λ is a substance constant dependent on the wavelength λ, which is determined by absorbance measurements of solutions of defined concentrations, Eq.(7.1-9).

$$\varepsilon_\lambda = \frac{E_\lambda}{c} \left[\frac{m^2}{mol}\right] \tag{7.1-9}$$

The extinction coefficient is a measure of concentration. The "quantity of substance" is formally derived from the product *concentration* * *volume*, Eq.(7.1-10).

$$\begin{array}{lcll} \text{Quantity of absorption units} & E_{n,\lambda} & = E_\lambda \cdot V & \frac{m^3}{m} = m^2 \\ \text{Quantity of substance} & n & = c \cdot V & mol = 10^3 mmol \end{array} \tag{7.1-10}$$

For the amount of light-absorbing units, this results in the dimension m^2. This quantity can be imagined as absorption surfaces statistically distributed in the beam path, which correspond at the molecular level to the cross-section, expressed in the unit Barn b, Fig. 7.11.

$1\ b = 10^{-28}\ m^2 = 100\ fm^2 = 60{,}2\ mm^2/mol$ or

$1\ m^2/mol = 1{,}7 \cdot 10^4\ b$

The set of absorption units is an extensive state quantity. The wavelength-dependent specific extinction coefficient ε_λ, on the other hand, is a partial molar quantity (SCHÖPKE 2007). The total measured value is composed of the components of the individual substances, regardless of whether the extensive absorption units or directly the extinction coefficients are considered Eq.(7.1-3).

$$\begin{aligned} c &= \frac{E_\lambda}{\varepsilon_\lambda} \\ n &= \frac{E_{n,\lambda}}{\varepsilon_\lambda} \end{aligned} \tag{7.1-11}$$

The superposition of spectra of different substances can be mathematically separated, chapter 9.6.

7.1.2.2 Absorption bands

Due to superpositions with resonances and oscillation states, an absorption band appears instead of a sharp absorption line. The measured absorption spectrum is represented as a function of the wavelength λ or occasionally also the frequency ν as a spectrum, Eq.(7.1-12).

$$\text{Spektrum} : E(\lambda) = E(\nu) \tag{7.1-12}$$

Various absorption bands overlap in it. The extinction function of an absorption band according to the absorption energy can be represented approximately as a Gaussian distribution, Eq.(7.1-13). The energy indirectly proportional to the wavelength λ is substituted by the wavelength of the extinction maximum λ_{max}, Eq.(7.1-13).

$$E_\lambda = E_{max} \cdot \exp\left(- diff^2 \cdot \left(\frac{\lambda_{max}}{\lambda} - 1 \right)^2 \right) \tag{7.1-13}$$

with

diff = Band width as a reciprocal value of the relative standard deviation.

Yan ET AL. (2013) AND Yan et al. (2016) also use this band formulation to describe humic substance spectra. Applied to the specific extinction coefficient, Eq.(7.1-14).

$$\varepsilon_\lambda = \varepsilon_{max} \cdot \exp\left(- diff^2 \cdot \left(\frac{\lambda_{max}}{\lambda} - 1 \right)^2 \right) \tag{7.1-14}$$

Equivalent band definitions are often used, which use the excitation energy or the bandwidth in electron volts W [eV] instead of the wavelength λ or use the latter as the half-width (YAN et al. 2023), Eq.(7.1-19).

$$\varepsilon_\lambda = \frac{eps}{\sqrt{2} \cdot \pi \cdot W} \cdot \exp\left(- \left(\frac{\frac{const}{\lambda} - \frac{const}{\lambda_{max}}}{\sqrt{2} \cdot W} \right)^2 \right) \text{ mit const = 1240 nm·eV} \tag{7.1-15}$$

The conversions of the parameters are obtained via constant comparison, Eq.(7.1-16),

$$diff = \frac{const}{\sqrt{2} \cdot W \cdot \lambda_{max}} \text{ bzw. } W = \frac{const}{\sqrt{2} \cdot diff \cdot \lambda_{max}} \tag{7.1-16}$$

and for the molar extinction coefficients Eq.(7.1-17).

$$\varepsilon_{max} = \frac{diff \cdot \lambda_{max}}{\pi \cdot const} \cdot eps \text{ bzw. } eps = \frac{\pi \cdot const \cdot}{diff \cdot \lambda_{max}} \varepsilon_{max} \tag{7.1-17}$$

From the half-value width $\Delta\lambda$ used by ZENG et al. (2023), the conversion Eq.(7.1-18).

$$diff = \frac{\sqrt{\ln(2)}}{\left(\frac{\lambda_{max}}{\lambda_{max} - \Delta\lambda} - 1 \right)} \tag{7.1-18}$$

7.1.2.3 Integral absorption coefficients

The effective excitation energy is slightly altered by thermal kinetic energy and interaction with the medium, among other things, which is expressed in the Gaussian extinction dependence on the photon energy. The concentration of the respective

chromophore is therefore proportional to the integral of the absorption of the entire band. The extinction maximum εμαξ decreases with the width of the absorption band. The concentration of chromophores does not correlate with the maximum extinction coefficient Emax, but with the area of the band under the energy axis. The analysis of individual substances is not affected by this, but sums of many substances with overlapping absorption bands of different widths can be quantitatively compared by their integral absorption. The integral molar extinction coefficient of the absorption band follows from Eq.(7.1-14) by conversion to the normal form of the Gaussian distribution, Eq.(7.1-19) to Eq.(7.1-21).

$$\varepsilon = \varepsilon_{max} \cdot \exp\left(- \mathrm{diff}^2 \cdot \lambda_{max}^2 \left(\frac{1}{\lambda} - \frac{1}{\lambda_{max}} \right)^2 \right) \tag{7.1-19}$$

Substitution of wavelength by frequency, Eq.(7.1-20).

$$\varepsilon = \varepsilon_{max} \cdot \exp\left(- \mathrm{diff}^2 \cdot \frac{c^{*2}}{\nu_{max}^2} \left(\frac{\nu}{c^*} - \frac{\nu_{max}}{c^*} \right)^2 \right) \qquad \text{with the vacuum speed of light } c^* \tag{7.1-20}$$

Extension obtains the standard form of Gaussian distribution,

$$\varepsilon = \varepsilon_{max} \cdot \sqrt{\pi \left(\frac{\nu_{max}}{\mathrm{diff}} \right)^2} \cdot \frac{1}{\sqrt{\pi \left(\frac{\nu_{max}}{\mathrm{diff}} \right)^2}} \cdot \exp\left(- \frac{(\nu - \nu_{max})^2}{\left(\frac{\nu_{max}}{\mathrm{diff}} \right)^2} \right) \tag{7.1-21}$$

whose integral for ν between -∞ and +∞ is equal to one, Eq.(7.1-22).

$$\int_{-\infty}^{+\infty} \left[\frac{1}{\sqrt{\pi \left(\frac{\nu_{max}}{\mathrm{diff}} \right)^2}} \cdot \exp\left(- \frac{(\nu - \nu_{max})^2}{\left(\frac{\nu_{max}}{\mathrm{diff}} \right)^2} \right) \right] \partial\nu = 1 \tag{7.1-22}$$

After the integration of Eq.(7.1-21) taking into account Eq.(7.1-22) follows for the integral molar extinction coefficient Eq.(7.1-23):

$$\int_{-\infty}^{+\infty} \varepsilon \, \partial\nu = \varepsilon_{max} \cdot \sqrt{\pi} \cdot \frac{\nu_{max}}{\mathrm{diff}} = \varepsilon_{max} \cdot \sqrt{\pi} \cdot \frac{c^*}{\lambda_{max} \cdot \mathrm{diff}} \tag{7.1-23}$$

By substituting the constants and taking into account the molar extinction coefficient defined as a decadal logarithm, the working equation Eq.(7.1-24).

$$\int_{-\infty}^{+\infty} \varepsilon \, \partial\nu = 5{,}31 \cdot 10^{17} \cdot \ln(10) \cdot \frac{\varepsilon_{max}}{m^2/mol} \cdot \frac{1\,nm}{\lambda_{max} \cdot \mathrm{diff}} \cdot \frac{m^2}{s \cdot mol} \tag{7.1-24}$$

The integral extinction coefficient of a band is proportional to the energy absorption, Eq.(7.1-25).

$$h \cdot \nu = h \cdot \int_{-\infty}^{+\infty} E_\nu \, \partial\nu \tag{7.1-25}$$

According to Lambert-Beer's law, the concentration dependence Eq.(7.1-26).

$$\int_{-\infty}^{+\infty} E_\nu \, \partial\nu = c \cdot \int_{-\infty}^{+\infty} \varepsilon \, \partial\nu \tag{7.1-26}$$

and from this it follows for concentration Eq.(7.1-27).

$$c = \frac{\int_{-\infty}^{+\infty} E_\nu \, \partial\nu}{\int_{-\infty}^{+\infty} \varepsilon \, \partial\nu} \tag{7.1-27}$$

The integration of the extinction coefficient yields analogous to Eq.(7.1-23) and Eq.(7.1-24) the expression Eq.(7.1-28).

$$\int_{-\infty}^{+\infty} E_\nu \, \partial\nu = \frac{E_{max}}{\ln(10)} \cdot \sqrt{\pi} \cdot \frac{c^*}{\lambda_{max} \cdot diff} = 1{,}22 \cdot 10^{18} \cdot \frac{E_{max}}{m^{-1}} \frac{1\,nm}{\lambda_{max} \cdot diff} (m \cdot s)^{-1} \tag{7.1-28}$$

For reasons of better handling, Eq.(7.1-28) derived the working parameters of the integral extinction E_{int} and ε_{int} for the molar extinction coefficient, in which the natural constants are not taken into account as a factor, Eq.(7.1-29).

$$\int_{-\infty}^{+\infty} E_\nu \, \partial\nu = \left(\frac{c^*}{\ln(10)} \cdot \sqrt{\pi} \right) \cdot \left(\frac{E_{max}}{\lambda_{max} \cdot diff} \right) = 1{,}22 \cdot 10^{18} \, \frac{nm}{s} \cdot E_{int}$$

$$E_{int} = \frac{E_{max}}{\lambda_{max} \cdot diff} \left[\frac{1}{nm \cdot m} \right] \tag{7.1-29}$$

$$\varepsilon_{int} = \frac{\varepsilon_{max}}{\lambda_{max} \cdot diff} \left[\frac{m^2}{nm \cdot mol} \right]$$

According to the definition of an elementary absorption unit ε_{def} Eq.(7.1-27) can be used to determine the concentration of known substances, Eq.(7.1-30).

$$\varepsilon_{def} = \frac{\varepsilon_{max}}{diff} = \varepsilon_{int} \cdot \lambda_{max} = 1{,}0 \, \frac{m^2}{mol} \tag{7.1-30}$$

Thus, the integral extinction coefficient can also be given as the concentration of these absorption units,

$$c_{def} = \frac{E_{int}}{\varepsilon_{def}} \cdot \lambda_{max} = \frac{E_{max}}{diff \cdot \varepsilon_{def}} \left[\frac{mol}{m^3} \right] \tag{7.1-31}$$

whereby the measures remain the same when the unit of measurement is changed.

7.1.2.4 UV/VIS spectra of organic substances

Covalent single bonds (sp hybrid electrons) require a high excitation energy, so that their absorption maxima are usually below $\lambda_{max} < 200$ nm. Isolated double bonds also absorb only around $\lambda_{max} \approx 180$ nm. Aromatics show at least two absorption bands in the measuring range $\lambda > 200$ nm. The more intense is between $\lambda\mu\alpha\xi = 200$ and 230 nm and the weaker one in the range $\lambda_{max} = 250$ to 290 nm. Mesomerism-stabilizing substituents shift the absorption bands to the longer wavelength (bathochromic shift). In more complex π, n-electron systems, further bands appear, e.g. around $\lambda = 230$ nm and $\lambda >$ 300 nm, which overlap in the NOM to form a largely continuous extinction course, Fig. 7.12. In the context of satellite remote sensing of the oceans, YAN et al. (2023) formulated three types of compounds:

Type 1: Aliphatic compounds (e.g., acetic acid and alanine).

Type 2: Simple aromatic compounds with substitution groups linked directly to the benzene ring by σ bond (e.g., phenol and benzoic acid) or an equivalent structure (e.g., pyridine and its derivatives).

Type 3: Aromatic compounds with carbon-carbon double bonds bonded to the benzene ring, such as styrene (e.g. caffeic acid and rosmarinic acid), or those that exhibit condensed aromatic structures (e.g. naphthalene).

The continuous spectral curve is often also described by exponential or linear adjustments. The determined parameters are then correlated with regionally or problem-specific CDOMs, e.g. in remote sensing of oceanic carbon turnover (LI & HUR 2017).

In the case of waters dominated by humic substances (Natural Organic Matter NOM) with a continuous spectral progression, there is a correlation between the spectral absorptioncoefficient at $\lambda = 254$ nm (SAK_{254}) and the DOC, which provides additional information, chapter 7.4.3. SAK_{254} (E_{254}) is determined by the concentration of aromatic and unsaturated organic chromophores in the humic substances. Both sum parameters are combined to form the molar extinctioncoefficient or aromaticity ε_{254}, Eq.(7.1-32).

$$\varepsilon_{254} = \frac{E_{254}}{c_{DOC}} = \frac{E_{254}}{DOC} \cdot M_C \qquad [m^2/mol] \qquad (7.1\text{-}32)$$

M_C = Molar mass of carbon (12 g/mol).

In practice, the indication of aromaticity is related to the carbon mass.

$$\text{Aromatizität } \varepsilon_{254}\left[\frac{1/m}{\frac{mg}{L}DOC} = \frac{m^2}{g\,C} = \frac{1}{12} \cdot \frac{m^2}{mol}\right] \qquad (7.1\text{-}33)$$

This molar extinction coefficient can be extended to the entire wavelength range ε_λ .

The pseudo-components determined from the spectral analysis do not represent independent material fractions, but describe the elementary bands or mathematically expressed Eq.(7.1-34).

$$B_i \cap B_j \neq 0 \,|\, i \neq j \qquad (7.1\text{-}34)$$

Material fractions can only be specified in connection with material separations.

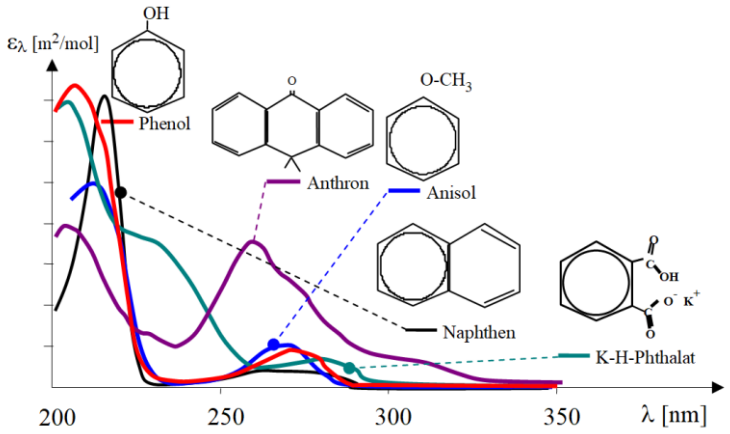

Fig. 7.12: Spectra of different aromatics (non-scale).

7.1.2.5 Decomposition into elementary absorption bands

SCHÖPKE (2024), as well as YAN et al. (2013) and YAN et al. (2016) determined by decomposing UV/VIS spectra into several elementary bands according to Eq.(7.1-14) Additional substance- and reaction-specific properties of the systems under investigation, chapter 9.6.2. As a rule, no clear adaptation can be determined, but only different possible perimeter ensembles with different interpretations, FigFig. 7.13.

The groundwaters in the trial area of the Ruhlmühle (SCHÖPKE et al. 2020) were broken down into process-technically sensible pseudo-components by combining a short-wave band short with a longer-wave wide band HumKont and two narrow bands (*Spez1*, *Spez2*) in between. The chromophores ($\lambda < 200$ nm), which also contain inorganic substances (NO_3 ...) but are incompletely recorded, were excluded as *disorders*. The maxima and shoulders that occasionally occur in the continuous course of the spectra could be represented by the absorption bands *Spez1* and *Spets2*. *Spez1* was fixed and *Spez2* varied in the specified wavelength range, Tab. 7.11. This band ensemble IV can be applied to many regional groundwater and even process waters, Fig. 7.14 and Tab. 7.12.

YAN et al. (2013) interpreted the UV/VIS spectra of a river fulvic acid and its copper complexes into the elementary absorption bands A0 to A5. The spectra of the metal complexes differed markedly from those of the dissolved fulvic acid, which probably also characterize spectra of (ground) waters rich in iron and hardness.

Sampling and preparation must also be taken into account when interpreting the spectra. For example, small oxygen inputs in groundwater samples could already form detectable ferric complexes, which has not yet been noticed.

Tab. 7.11: Perimeter ensembles for the adaptation of UV/VIS spectra of CDOM. [I)]SCHÖPKE (2007), [II)]YAN et al. (2013) and YAN et al. (2016, *diff graphically estimated) for a river water fulvic acid, SCHÖPKE et al. (2011) and [IV)]SCHÖPKE (2024).

Ensemble			Definition of elementary bands					
I			**B0**	**B1**	**B2**	**B3**	**B4**	
various waters	λ_{max}	nm	210	229	250	275	324	
	diff	1	18	18	15	13	7	
II			**A0**	**A1**	**A2**	**A3**	**A4**	**A5**
Suwannee River	λ_{max}	nm	210	240	273	314	375	540
(SRFA)	diff*	1	12,4	12	14	10	5,5	6
III			**B0**	**B1**	**B2**	**B3**	**B4**	
Dump groundwater	λ_{max}	nm	190	225	244	278	358	
Skadodamm	diff	1	7	9	11	6	4,6	
IV			Kurz	Spez1	Spez2	Humkont		
Groundwater	λ_{max}	nm	194	221	*238 ... **243** ... 248*	229		
IVa			194	221	265	229		
	diff	1	10	17	17	3,5		

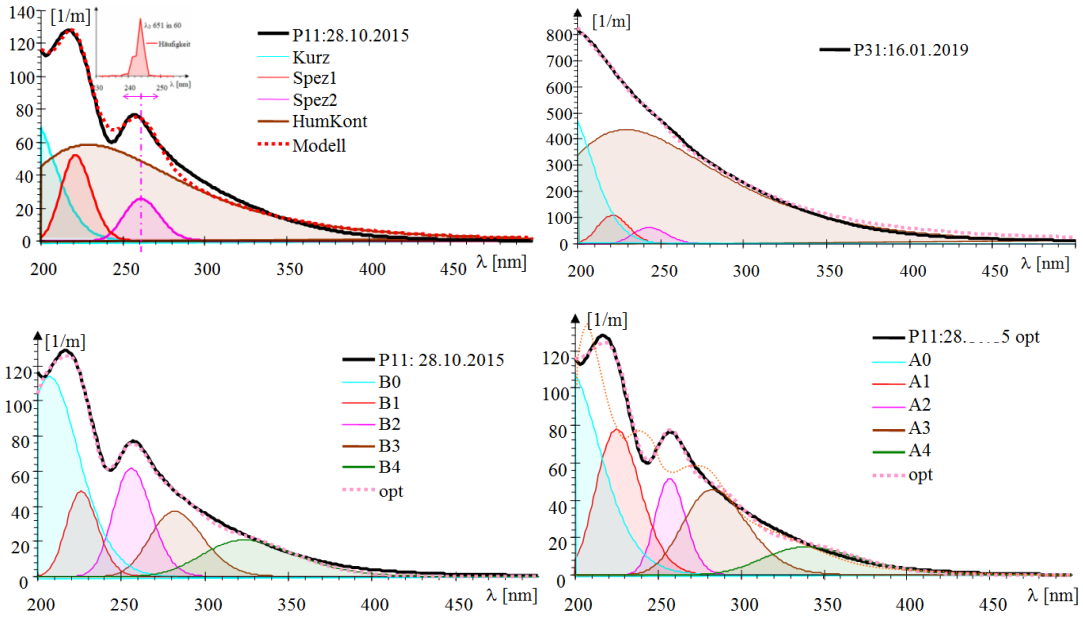

Fig. 7.13: Top: Decomposition of two groundwater spectra at the Ruhlmühle site (SCHÖPKE et al. 2020) into four elementary bands with local maxima (left) and a continuous course (right). Bottom: Adjustments of the groundwater spectrum P11 to the ensembles of SCHÖPKE (2007) (left) and according to YAN et al. (2013) slightly optimized, or dotted according to original parameterization (right).

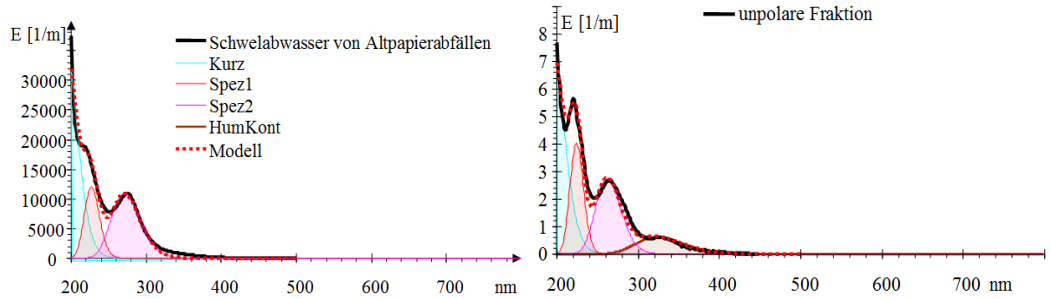

Fig. 7.14: Spectra of a mixture of low-molecular aromatics (left) and their non-polar trace fraction (right). There *is no humic substance* behind the trace nonpolar elemental absorption band Humkont.

Tab. 7.12: Parameters of the Eq.(7.1-13) for the elementary bands *Kurz*, *Spez1*, *Spez2* and *Humkont*. [a)]SCHÖPKE et al. (2020), [b), c)] SCHÖPKE* et al. (2011), [d)] KOCH et al. (2007), [e)] SIEBER (2001) and SCHÖPKE & KOCH (2002), [f)] STRAUB (2008), [g)] SCHÖPKE & KOCH (2002). For color coding, see Tab. 7.11. *Italics*: Deviations from the standard definition of *HumKont*.

	Banden	*Kurz*		*Spez1*		*Spez2*		*Humkont*	
	Sample	λ_1	$diff_1$	λ_2	$diff_2$	λ_3 variabel	$diff_3$	λ_4	$diff_4$
a	Groundwater Ruhlmühle	194	10	221	17	*238 ... 243 ... 248*	17	229	3,5
b	Grundwasser Bad Muskau	194	10	221	17	247	17	259	3,5
c	Groundwater Gaswerksaltlast	194	10	221	17	256... 259 ... 264		259	3,5
d	Pyrolysis wastewater according to Intensive Biology	194	10	221	17	240	12	*276*	*5*
	non-polar component	194	10	221	17	241	12	*271*	*4*
e	Smoldering wastewater from waste paper recycling waste	194	10	227	16	271	10		
	non-polar component	194	10	224	19	262	12	*323*	*8*
f	Small wastewater treatment plant effluents	194	10	221	17	244	17	*259*	*3,5*
g	Hemp digestion wastewater	194	10	221	17	271	10	*277*	*3,5*

7.2 Pseudo-component definitions via separation methods

7.2.1 Separation of substances by adsorption

Mixtures of substances with different affinities to a phase can be separated ad-/absorptively at it (adsorption, extraction, stripping). If affinity differences are sufficiently large, the separation into at least two different fractions takes place, according to the condition Eq.(2.3-34) Using suitable equilibrium models, pseudo-components can be mathematically separated from empirical data, from overlapping sorption processes (chapter 9.5.2). Each pseudo-component makes a different contribution to the respective measured sum parameters.

Vobach et al. (1977) *introduced* the concept of *substance continuum* for the characterization of organic substances in water analysis. Using the *Eliminierungs-analyse* (EA), a special case of the frontal method of column chromatography, they

separated the organic matter complex into two fractions each (coarse separation). In practice, the elimination analysis was mainly reduced to the separation of acidically modified alumina into a polar and a non-polar fraction with detection via oxidation with potassium dichromate (COD). This made it possible to make statements about the main substance groups (AMW 1981). Based on the elimination analysis, a *house method* was developed for the differentiated determination of the distribution of dissolved non-polar substances via enrichment and selective elution with organic solvents on *C18* and *phenyl* surfaces (KOCH et al. 2002, SCHÖPKE 2007). Detection was carried out exclusively using the UV/VIS spectra, Tab. 7.12.

The *Adsorptionsanalyse* according to SONTHEIMER et al. (1985) divides a measured activated carbon isotherm into several pseudocomponents of different affinity. The adsorption model is based on Freundlich isotherms, which are linked to a competing system via the IAS theory (KÜMMEL and WORCH 1990). However, this empirically and technically complex adsorption analysis in its original form only allows a statement about the DOC for given Freundlich parameters of the pseudocomponents.

7.2.2 Molar mass separation via gel chromatography

The LC-OCD (***Liquid Chromatography - O****rganic* ***Carbon Detection***, HUBER et al. 2011) is a gel chromatography in combination with highly sensitive downstream detection of organic carbon, the spectral absorption coefficient SAK254 (E_{254}) and the total nitrogen concentration. Additional investigations, such as UV/VIS spectra of the individual fractions, can also be carried out. In the chromatography column, the organic ingredients are separated according to their molecular size. Depending on their molecular size, the organic ingredients diffuse deeply into the molecule-scale porous gel. The low-molecular components thus have a larger flow cross-section at their disposal than higher-molecular pseudocomponents, which appear first in the column sequence, Fig. 7.21. This interaction is superimposed by ionic, hydrophobic interactions.

The molar masses are calibrated with dextran standards and/or based on the lower limit for aromatics (MP0 = 78 g/mol, retention time t_{P0}) the molar masses M_i of the other fractions are interpolated over the retention times t_{Pi}, Eq.(7.2-1).

$$M_i \approx M_{P0} \cdot \left(\frac{t_{P0}}{t_{Pi}} \right)^{1,9} \tag{7.2-1}$$

The hydrophobic substances (HOC) are calculated from the difference between sample DOC and detected C. They usually have a high C:O ratio. The biopolymers can alternatively be identified after hydrolysis by ion chromatography. They often come from the bacterial cell wall or from dead bacteria and algae, as well as biofilms.

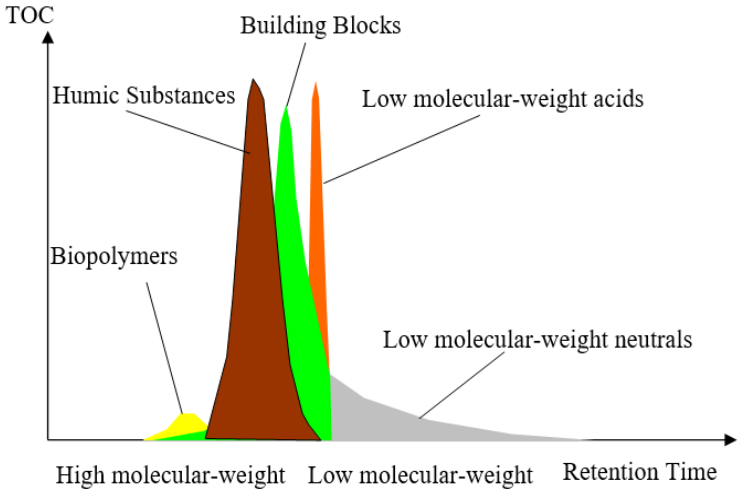

Fig. 7.21: Interpretation of an LC-OCD chromatogram.

Tab. 7.21: Pseudocomponents of the LC-OCD chromatogram (HUBER et al. 2011).

Parameter	Description	Unit
HOC	Non-chromatographically detectable organic carbon (hydrophobic fraction of the DOC)	mg/L C
CDOC	Chromatographically detectable organic carbon (hydrophilic fraction of the DOC)	mg/L C
POC	particulate organic carbon	mg/L C
Humic Substances	Polycarboxylic acids and substituted phenols, M = 500-1500 g/mol	µg/L C, m^{-1}
Building Blocks	low molecular weight humic acid precursors, Polycarboxylic acids, M = 350-500 g/mol	
Biopolymers (polysaccharides, amino sugars, polypeptides and proteins)	High molecular weight, M > 20 000 g/mol	
Low molecular-weight neutrals	amino acids, alcohols, aldehydes, ketones, M < 350 g/mol	
Acids	einbasische Säuren, M <350 g/mol	

7.2.3 Parameter für spezifisches Umwelt- und Behandlungsverhalten

With regard to environmental behaviour, a distinction is made between conservative, persistent and refractory organic substances. This classification is helpful for assessing the treatment behaviour of a water. The concentrations of the pseudo-components defined according to their environmental and treatment behavior are given by sum parameters (DFG 1993).

- Conservative substances are not subject to any material conversion and exchange processes.
- Persistent substances are not subject to any biochemical processes.
- Refractory organic substances are those organic substances whose conversion or degradation rate in the ecosystem is relatively low and therefore have a correspondingly long residence or lifespan in a given system. Humic substances are usually understood to be humic substances.

For drinking water treatment from water-contaminated flowing waters via groundwater recharge and activated carbon treatment, the pseudo-components are defined according to waterworks and drinking water relevance. The type and quantity of wastewater constituents discharged determine the necessary treatment effort, which is estimated using these criteria.

VÖLKER & SONTHEIMER (1988) distinguish between:

- Biodegradable substances, i.e. substances that are eliminated during biologically active groundwater recharge.
- Watertreatment-related substances (**WWR**) that are biologically resistant.
- Drinking water-related substances (**TWR**) that are biologically resistant and that have been classified by adsorption analysis as non-adsorbable and poorly adsorbable to activated carbon (GIMBEL & SONTHEIMER 1987).

For the classification according to biodegradability, test filter systems weredesigned to simulate long-term biological depletion, chapter 9.4. As an alternative to adsorption analysis (chapter 7.2.1), GIMBEL et al. (1996) suggested using the equilibrium concentrations in the batch test for two cans of activated carbon to determine the substances relevant to drinking water. The substance content for a dose of 20 mg/L activated carbon (TWR20) is estimated to be not or only very poorly adsorbable to activated carbon and would therefore pass through an adsorber relatively easily. The proportion of substances that is in equilibrium with 500 mg/L (TWR500) breaks through very early, Fig. 7.22.

The detection of these pseudo-components, defined according to treatment criteria, is carried out using the sum parameters DOC, COD, SAK_{254}, UV/VIS spectrum, AOX and, if necessary, additionally via LC-OCD chromatograms (chapter7.2.2) and/or relevant individual substances.

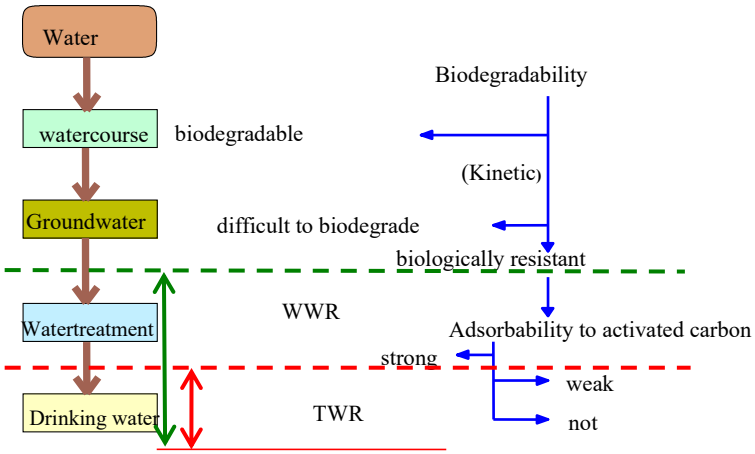

Fig. 7.22: Classification of the organic matter complex into watertratment-related substances (WWR) and drinking water-related substances (TWR) according to their treatment via groundwater recharge and activated carbon treatment.

7.3 Pseudo-component evaluations

7.3.1 Partial (molar, characteristic) sizes of pseudocomponents

Analogous to the *partial molar quantities*, which are related to the amount of substance [mol] (chapter 2.3.5.3), pseudo-components are characterized by relations between sum parameters and a selected base parameter, Eq.(2.3-35) In contrast to the partial molar quantities, these relations are called *characteristic properties*. The dissolved organic carbon DOC is preferred as the basic parameter, which does not indicate the amount of substance, but the carbon bound in the pseudocomponent, Tab. 7.31.

Tab. 7.31: Characteristic Properties of Pseudocomponents (Selection).

Parameter	Description	Unit
M	Molar mass of equivalent of pseudocomponent	g/mol
ν_c	Number of carbon atoms in an equivalent of pseudocomponent	1
M_{eq}	Molmasse eines Äquivalentes bezogen auf deren organischen Kohlenstoff	g C/mol
ε_λ	specific extinction coefficient at wavelength λ	m^2/mol
$\varepsilon(\lambda)$	specific UV/VIS spectrum for $\lambda_1 \le \lambda \le \lambda_2$	m^2/mol
ε_{254}	specific extinction coefficient at λ = 254 nm, aromaticity	m^2/mol m^2/g C
$\varepsilon_{int}(i)$	Integral specific absorbance coefficient of absorption band i	m^2/(mol·nm)
Γ	Adsorption site density	sites/nm^2

7.3.2 Graphical representations of material systems with pseudo-components

7.3.2.1 Physicochemical classification of substances

Analysis tables and chromatograms are not very clear. For this reason, basic properties are presented in diagrams in a problem-oriented manner for a better understanding:

- Molecule/aggregate size, volume, preferably as **molar mass**,
- Dipole moment,
- Volatility, vapor pressure, boiling point,
- Solubility in water and organic solvents (**partition coefficient**),
- Reactivity, e.g. as acid (pK_S) electron excitability, redox behavior (E_H),
- Absorption spectra in the UV/VIS range or **aromaticity** ε_{254}.

The molecular size influences diffusion, volatility and colloidal effects. With regard to the accumulation behaviour of organic substances, n-octanol (n-C_8H_{18}) is used as a model substance. The distribution coefficient log K_{OW} (n-octanol/water) corresponds approximately to that of cell membranes, Eq.(6.5-5) Non-polar substances with high distribution coefficients log K_{OW} are preferentially absorbed by the cell membrane, stored in fat cells and accumulated in the food chain. This means that the non-polar substances, which are usually only dissolved in traces, are of great ecotoxicological importance. The affinity to the activated carbon surface and humus components also correlates with the log K_{OW}.

Thus, it seems to make sense to represent the log K_{OW} against the molar mass (KOCH et al. 2002 and SCHÖPKE 2007). Various properties of humic substances correlate with their aromaticity ε_{254}, which suggests their representation according to the molar mass.

7.3.2.2 Classification scheme with regard to the log K_{OW}

In the two-dimensional representation log K_{OW}(M), known groups of substances form characteristic areas, Fig. 7.31. The respective log K_{OW} can be calculated using various calculation methods from the molecular structure and physical data and is available for most relevant substances. Depending on the approach or measurement method used, the values given in the literature may differ slightly.

Due to the decreasing water solubility, only the substances up to log $K_{OW} < 8$ need to be taken into account in water analysis. Accumulation in adipose tissue occurs mainly in the range log $K_{OW} = 3 - 6$ (STENZ 2001). According to SKARK & ZULLEI-SEIBERT (1994), the transport of non-polar substances with the leachate from the soil zone into the groundwater is only possible as far as log $K_{OW} < 5$.

Reactions and changes within the organic matter complex can also be traced in this scheme, Fig. 7.32. With aliphates, the log K_{OW} grows with increasing chain length. In the homologous series of alkanes, each inserted CH_2 group increases log K_{OW} by 0.54. The polarity increases from saturated cyclohexane to aromatic benzene. Polar substituents lower the log K_{OW}, non-polar substituents increase it. The result depends on the respective position and mutual interactions. Any chlorination leads to an increase in the log K_{OW} compared to the unchlorinated compound. (BIENERT et al. 1993).

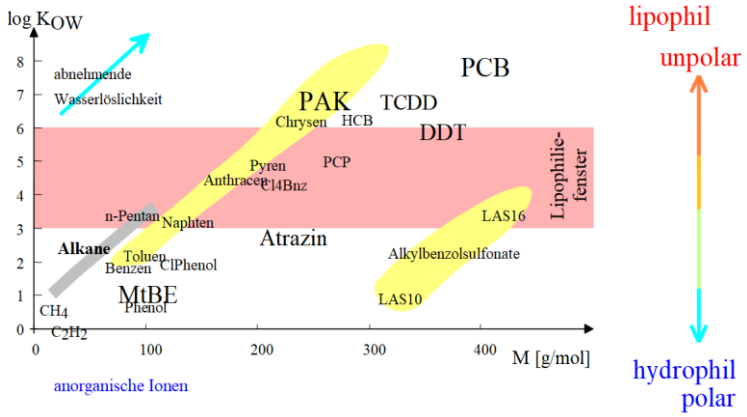

Fig. 7.31: Characterization of low molecular weight nonpolar organic substances by representation in the log K_{OW} molar mass plane, with PAH = polycyclic aromatics, PCB = polychlorinated biphenyls, HCB = hexachlorobenzene, TCDD = dioxin representative. The ecotoxicologically relevant lipophilicity window is highlighted in red (SCHÖPKE 2007).

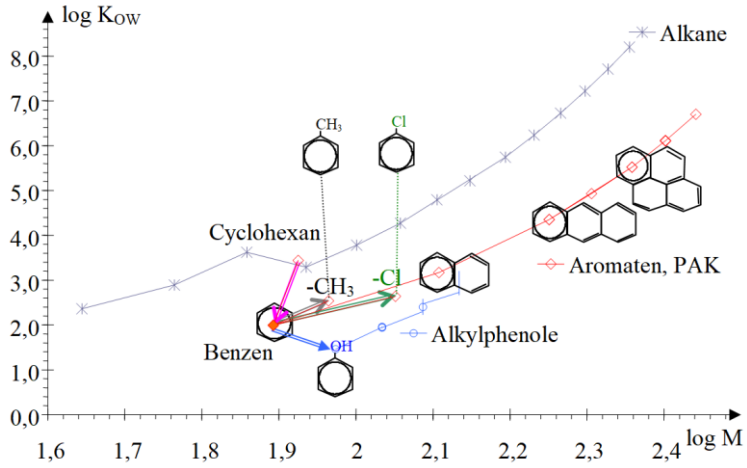

Fig. 7.32: Molar mass log K_{OW} representation of hydrocarbon series and the influence of different substituents on benzene.

7.4 Humic substances as part of the Natural Organic Matter

7.4.1 Definitions and compositions of humic substances

Humic substances are pigmented, high-molecular polyelectrolytes as part of the Natural Organic Matter (NOM). The division into three groups is based on the traditional fractionation of soil humic substances, the fulvic acids, humic acids and humins.

The treatment of soil humic substances with diluted bases dissolves fulvic and humic acids and leaves the insoluble humines as residues. If this alkaline extract is acidified, the humic acids precipitate and the fulvic acids remain in solution. The humic acids can be further separated into hymatomelic, grau and brown humic acids by extraction with alcohol or re-dissolving in alkalis with the addition of electrolytes (STEINBERG 2002).

Numerous studies deal with the composition of humic substance fractions and isolates. For this study, the humic substances first had to be enriched and fractionated from natural waters. In addition to their elementary compositions, the proportions of determining structural elements and functional groups were also determined (STEINBERG 2002), Tab. 7.4-1.

Tab. 7.4-1: Elemental composition of humic (HS) and fulvic acids (FS) and functional units according to research by STEINBERG (2002), as well as stoichiometries derived from them (ν_C).

		HS		FS		HS	FS	HS	FS
Element		mol/kg				Mol- %		ν_C	[1]
Carbon	C	46,8		38,04		39,5%	31,2%	1	1
Hydrogen	H	47		54		39,7%	44,2%	1,01	1,42
Oxygen	O	22,2		27,97		18,7%	22,9%	0,05	0,04
Nitrogen	N	2,25		1,5		1,90%	1,23%	0,47	0,73
Sulfur	S	0,25		0,578		0,21%	0,47%	0,0053	0,0151
Phosphorus	P	0,0371		0,0371		0,03%	0,03%	0,0008	0,0010
Chlorine	Cl	0,0085		0,0085		0,01%	0,01%	0,00025	0,00032
Structural Units		von	bis	von	bis				
aromatic π pairs	2π(Ar)							0,23	0,25
Carboxylic-	COOH	1,5	5,7	5,2	11,2			0,077	0,220
Phenyl-	OH	2,1	5,7	0,3	5,7			0,083	0,079
Alcoholic-	OH	0,2	4,9	2,6	9,5			0,054	0,160
Quinoid/Keto	C=O	0,1	5,6	0,3	3,1			0,061	0,045
Methoxy	OCH_3	0,3	0,8	0,3	1,2			0,012	0,020
Sum of acidic groups		5,3	8,9	6,4	14,2			0,155	0,270

From the mean compositions, representative molecular formulas of humic and fulvic acid units can be constructed, Fig. 7.41:

Humic acids: $\{C_{100}\ H_{100}\ O_{48}\ N_{4,8}\ S_{0,53}\ P_{0,08}\ Cl_{0,02}\}$ or

M = 2148 g/mol $\{C_{100}\ (2Ar\text{-}\pi)_{25}\ (COO\text{-}H)_{22}\ (ArO\text{-}H)_{7,9}\ (RO\text{-}H)_{16}(C{=}O)_{6,1}\ (OCH_3)_{4,5}\}$

Fulvic acids: $\{C_{25}\ H_{35}O_{18}\ N_1\ S_{0,38}\ S_{0,53}\ P_{0,024}\ Cl_{0,006}\}$ or

M = 657 g/mol $\{C_{25}\ (2Ar\text{-}\pi)_{6,25}\ (COO\text{-}H)_{5,5}\ (ArO\text{-}H)_2\ (RO\text{-}H)_{4,0}\ (C{=}O)_{1,3}\ (OCH_3)_{0,5}\}$

In the past, various authors have tried to develop structural formulas from which the physicochemical behavior of these substances can also be explained, Tab. 7.42.

The high-molecular molecular structures are partly formed from subunits linked by hydrogen bonds and metal complexes, which react sensitively to changes in pH value and ionic composition (ionic strength, Fe, Ca, Mg, heavy metals). This means that they already change during the analytical recording. In addition, carbohydrate units, peptides, heterocycles and other structures are associated. ZIECHMANN (1996) points to flexible molar mass distributions under mechanical stress, among other things. Bonds in humic molecule associates can break loose when passing through narrow pores and then re-establish themselves. The differently delocalized π electron systems occurring in the structural proposals form the continuous UV/VIS spectrum of the humic substances by superposition, Fig. 7.13.

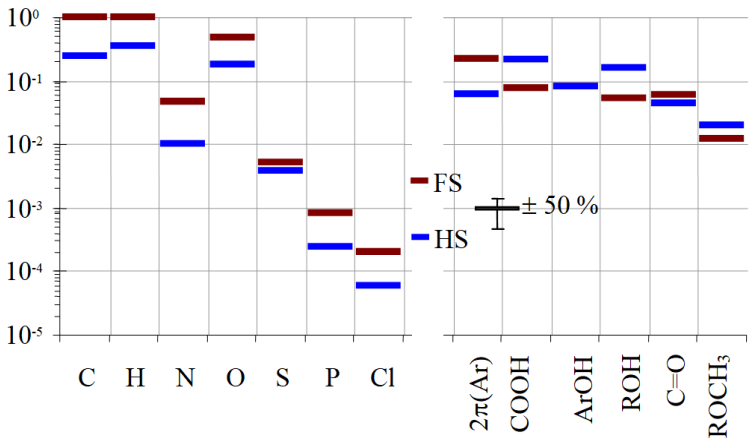

Fig. 7.41: Illustrations of the average composition of humic and fulvic acids on a logarithmic scale, with a description of the range of ± 50 % in the order of magnitude of which the individual parameters vary at least.

Tab. 7.42: Examples of postulated humic acid and two biopolymer structural formulas. The aromatic π electrons are marked by orange rings, aromatic carboxyl groups red, aromatic hydroxyl groups blue and nitrogen-containing groups green.

Postulated structure	Explanation
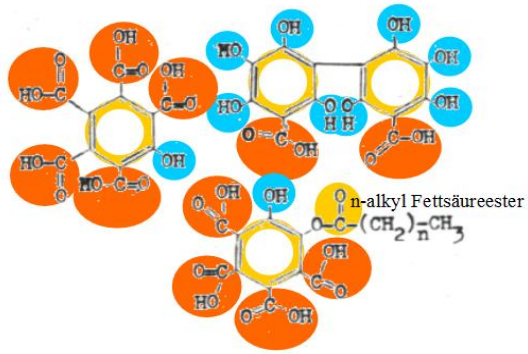	Fulvic acid consists of three subunits linked by hydrogen bonds in the molar mass range of the Building Blocs. A humic acid associate postulated from 6 subunits has a molar mass > 2000 g/mol (cited BIRKEL 2001).
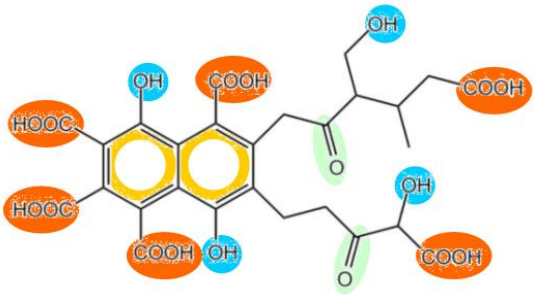	Fulvic acid, $C_{27}H_{26}O_{18}$ M = 638 g/mol (cited MADHAV et al. 2017)
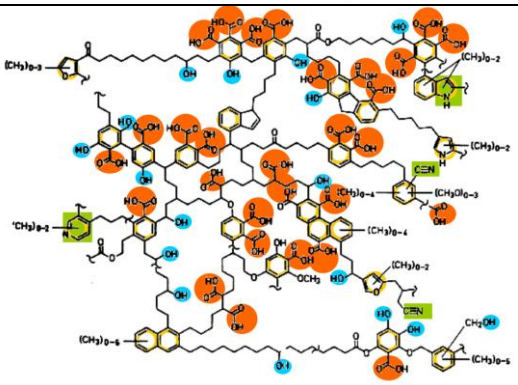	Structural proposal of a nitrogenous (green) humic acid $C_{293}H_{232}O_{85}N_4$, M = 5164 g/mol (cited BIRKEL 2001)
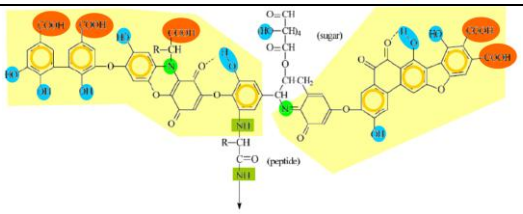	Structural proposal with two delocalized π electron systems, $C_{63}H_{44}O_{36}N_4$, M = 11432 g/mol (cited BAUER 2008 nach Stevenson 1994)

Postulated structure	Explanation
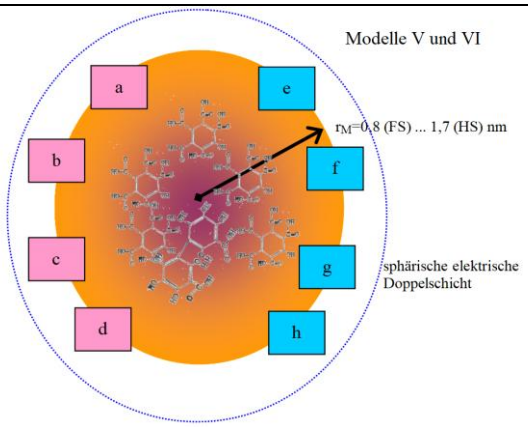	Postulate of humic colloids with cation binding sites M = 1500 g/mol Fulvic acid M = 5100 g/mol Humic acid Density 1,5 g/cm³ a - d: COO-H e - f: ArO-H (TIPPING 1998)
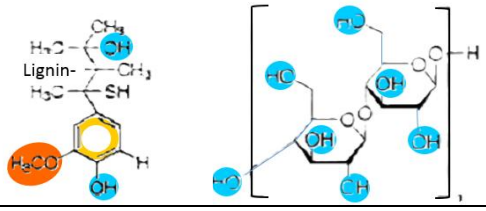	A possible section of the lignin structure (left) and section of the cellulose structure without chromophore groups. Hydroxylic groups in blue (ZENG et al. 2023).

7.4.2 Acidity and complex formation behavior

7.4.2.1 Description by two pseudo-components

The pseudocomponents of *fulvate* and *humates* are assigned acid and complex formation constants in PHREEQC, Tab. 7.4-3. The different humic/fulvic acid isolates used by the authors to determine the complex stabilities lead to contradictory information, which severely limits their usability. For cations, the following order of binding strength is known:

$$Mg^{2+} < Ca^{2+} < Mn^{2+} < Cd^{2+} < Co^{2+} < Ni^{2+} \approx Zn^{2+} < Pb^{2+} < Cu^{2+} < VO^{2+}$$

Tab. 7.4-3: Complex formation constants [a] *wateq4f.dat* (PARKHURST & APPELLO 1999, [b] PHREEQ-N-AMD.dat, Iron(II) mit copper(II) equated (CRAVOTTA 2022), [c] BOSIRE & NGILA (2017).

Definition equation		log K	Reference
H+ + Fulvate-2 = HFulvate-	H+ + Humate-2 = HHumate-	4,27	a
Fe+3 + Fulvate-2 = FeFulvate+	Fe+3 + Humate-2 = FeHumate+	9,4	a
Fe+3 + Fulvate-2 = FeFulvate+		-1,1	c
Fe+2 + Fulvate-2 = FeFulvate	Fe+2 + Humate-2 = FeHumate	6,2	b
Cu+2 + Fulvate-2 = CuFulvate	Cu+2 + Humate-2 = CuHumate	6,2	a
Cd+2 + Fulvate-2 = CdFulvate	Cd+2 + Humate-2 = CdHumate	3,5	a
Ag+ + Fulvate-2 = AgFulvate-	Ag+ + Humate-2 = AgHumate-	2,4	a
Ca+2 + Fulvate-2 = CaFulvate		-3	c
Mg+2 + Fulvate-2 = MgFulvate		-2,4	c
Ba+2 + Fulvate-2 = BaFulvate		-4,8	c
Al+3 + Fulvate-2 = AlFulvate+		12,16	c
Cu+2 + Fulvate-2 = CuFulvate		8,26	c
Zn+2 + Fulvate-2 = ZnFulvate		-0,73	c

7.4.2.2 Surface complexation on colloids

TIPPING et al. (1991) described the protolysis and complex formation of humic substances via colloidal macromolecules with a diameter of more than 1 nm and active functional groups on their outer surface of the molecule, which is electrically charged and connected to the solution by a spherical electric bilayer, Tab. 7.42. The inner functional groups stabilize the molecule or the association via hydrogen bonds. The charge density of the molecule determines the electrical term of a two-layer model for surface complex formation, chapter 6.5.6. Based on TIPPING (1998), the humic acid models V, VI and VII were developed and parameterized for defined humic and fulvic acid isolates (BOSIRE & NGILA 2017, GUSTAVSON & VAN SCHAIK 2003, TIPPING et al. 2011, GUSTAFSSON 2020, etc.) and in PHREEQC version 3 (PARKHURST & APPELO 2013) with an interchangeable set of constants.

The fulvic and humic acid macromolecules are each assigned four carboxylic (a, b, c, d) and four phenolic (e, f, g, h) acid groups. The multitude of possible combinations is reduced to eight representative bidentate binding sites for polyvalent cations, Fig Fig. 7.47 and Tab. 7.45.

The individual acid and complex formation constants are defined by series developments, whereby the constants $pK_{A/B}$ and $\Delta pK_{A/B}$ must be known for each cation, Eq.(7.4-1) and Eq.(7.4-2).

$$pK_i = pK_A + \frac{2i-5}{6}\Delta pK_A \quad \text{für } i = 1..4 \text{ bzw. a, b, c, d} \tag{7.4-1}$$

$$pK_i = pK_B + \frac{2i-13}{6}\Delta pK_B \quad \text{für } i = 5..8 \text{ bzw. e, f, g, h} \tag{7.4-2}$$

Tab. 7.4-4: Steric parameters of humic molecules of models V and VI according to TIPPING & HURLEY (1992) and TIPPING (1998).

Parameter			Model V	Model VI	
			Humic acid	Fulvic acids	Humic acids
Molar mass	M	g/mol	1500	1500	5100
Density	ρ	g/cm³	1,5		
Molecular radius	r_M	nm	0,8	0,8	1,72
Specific surface	O_{sp}	m²/g	2500	2500	1200
Sites	n_A	mol/kg	7,05	7,05	3,1

Tab. 7.45: Simplified definition of acid groups on humic and fulvic colloids according to TIPPING (1998, model VI) with selected monodentate and bidentate sites for multiply charged cations and a spherical electric bilayer (not shown).

SURFACE_SPECIES	
Carboxylisch -CO-OH	
einzähnig	zweizähnig
Hs_aOH	Hs_abOH2
Hs_bOH	Hs_cdOH2
Hs_cOH	Hs_aeOH2
Hs_dOH	Hs_bfOH2
Phenolisch Ar-OH	
Hs_eOH	Hs_cgOH2
Hs_fOH	Hs_dhOH2
Hs_gOH	Hs_efOH2
Hs_hOH	Hs_ghOH2
Hs_aOH = Hs_aO- + H+ Hs_abOH2 = Hs_abOH- + H+ Hs_aOH + Me+2 = Hs_aOMe+ + H+ Hs_adOH2 + Me+2 = Hs_adOMe + 2H+	

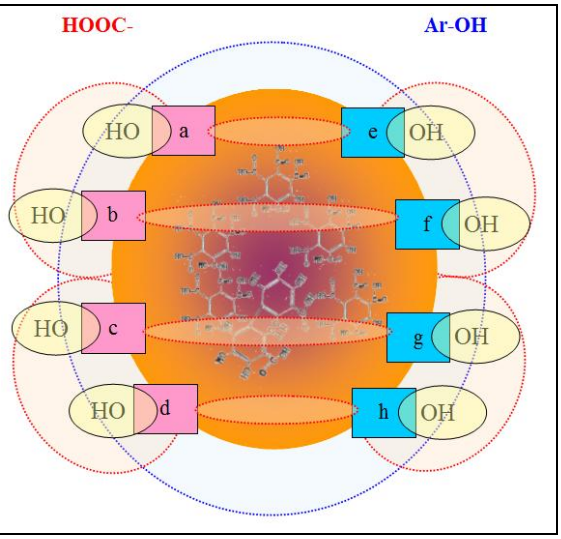

7.4.2.3 PHREEQC3 orientation calculations with the humic acid model VII

SCHÖPKE (2024) carried out orientating model calculations on the complex formation of humic substances with real waters using constant theorems from the literature and estimation of humic concentration. In proportion, the humin-komplex content of iron was higher than that of calcium. The (apparent) siderite supersaturation measured in some groundwaters can also be traced back in part to humic complexes. After the iron removal of the Spreewald groundwater (Fig. 7.42 left), a residual iron concentration remained that even survived cooking (SCHÖPKE* 1984). Only after several years of operation of the filter system did biological effects (probably) cause the decline in this residual iron concentration. Impairments of groundwater treatment cannot be predicted with the model approaches presented and can only be explained empirically (SCHÖPKE* 1986).

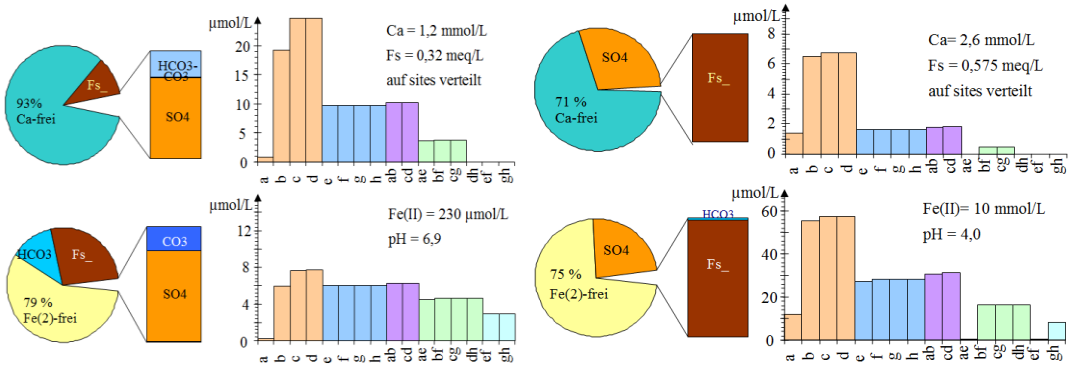

Fig. 7.42: Modelled distributions of komplexed calcium (top) and iron (bottom) at the dentate and bidentate sites of *mean* fulvic acid (Fs_ TIPPING 1998). Left: Humin-contaminated groundwater from the Spreewald. Right: Mine-acidified groundwater in the stream to the Spree.

7.4.2.4 The Stockholm Humic Model (SHM)

GUSTAFSSON (2020) expands the Model VI into the Stockholm Humic Model (SHM), which also includes solid humin phases as Donnangel (chapter 6.5.6.4) in the software Visual MINTEQ version 3.1. It is believed that the humic substances in the solid phase are a mixture of humic acid and fulvic acid. The proton binding parameters and the metal complexation constants are estimated using simple weighted averages. The dissolved humic substances are assigned a spherical geometry and the solid phases a planar geometry.

7.4.2.5 Description with the NICA-Donnan model (Visual MINTEQ)

The NICA-Donnan model, a combination of the NICA isotherm with a Donnan model, is also used to describe interfacial reactions of other types of organic matter (i.e., lignin, algae, etc., KINNIBURGH et al. 1999). The organic matter is considered Donnan gel. The use of the NICA equation (chapter 6.5.6.5) allows the simulation of cation complexation with components that are very heterogeneous in terms of binding site affinity, Eq.(6.5-69) The binding strength of an ion with stoichiometry ν to a carboxyl or phenolic site is normally distributed over the parameters log_K and p. The system is divided into two phases, both containing water, the *bulk solution phase and the humingel phase (Donnan*). The distribution of ions between the two phases is determined by a Donnan equilibrium. It is assumed that the amount of bound cation is in equilibrium with the concentration of the cation in the Donnan phase.

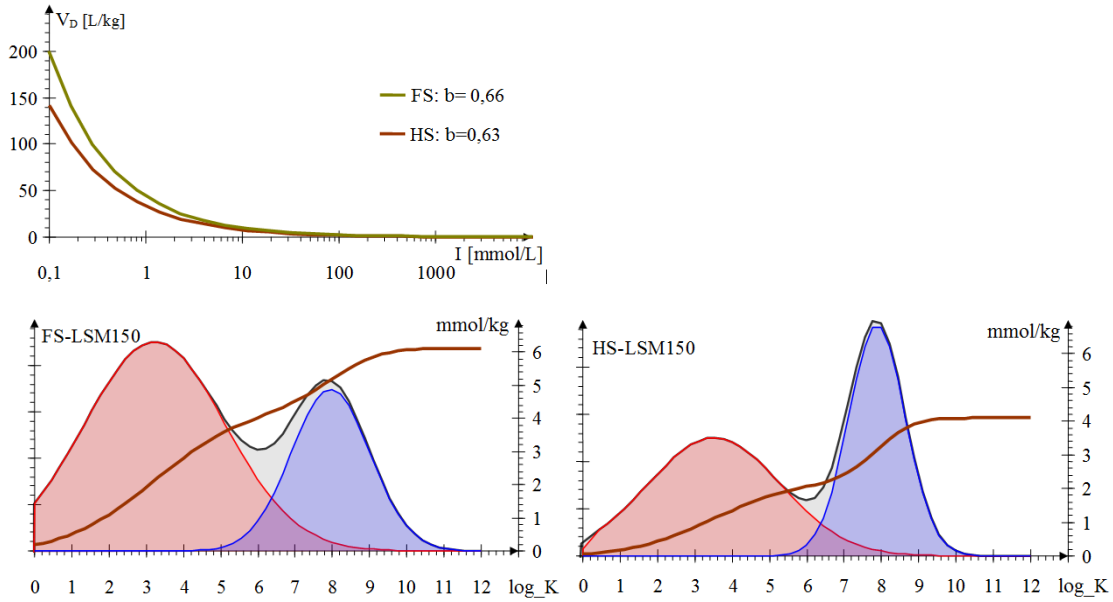

Fig. 7.43: Top: Donnan volume as a function of ionic strength. Bottom: Distribution of the carboxylic (RCOOH red) and aromatic (ArOH, blue) acid groups for the fulvic and humic acid isolates FS/HS-LSM150, as well as their sum abundance (brown, right axis) (PLAZA et al. 2006).

Tab. 7.4-6: Compilation of humic properties according to the NICA-Donnan model. [a)]SAITO et al. (2004), [b)]XU et al. (2016), [c)]MILNE et al. (2003), [d)]KINNIBURGH et al. (1996), [e)]KINNIBURGH et al.(1999), [f)]PLAZA et al. (2006).

Isolate or representative average	Quelle	RCOOH				ArOH				Donnan		
		c	p	log_K	ν	c	p	log_K	ν	b	α	β
		mol/kg	1	1	1	mol/kg	1	1	1	L/kg		
HS Aldrich	a	2,99	0,89	3,53	0,66	2,66	0,375	7,95	0,66	0,63	-0,37	-0,63
HS soil	b	8,72	0,72	2,18	0,74	3,90	0,66	8,19	0,89	0,81	-0,19	-0,81
FS average		5,88	0,59	2,34	0,66	1,86	0,70	8,6	0,76	0,57	-0,43	-0,57
HS lignite		2,97	0,90	3,52	0,72	2,86	0,44	7,99	0,59	0,60	-0,40	-0,60
HS soil		2,35	0,80	3,27	0,87	3,48	0,53	8,33	0,59	0,48	-0,52	-0,48
HS soil		4,46	0,53	2,95	0,78	1,38	0,82	7,52	0,82	0,47	-0,53	-0,47
HS average		3,15	0,62	2,93	0,81	2,55	0,41	8,00	0,63	0,49	-0,51	-0,49
FS average	c	5,88	0,59			1,86	0,70			0,57	-0,43	-0,57
HS average		3,15	0,62			2,55	0,41			0,49	-0,51	-0,49
HS peat	d	2,74	0,54	2,98	0,86	3,54	0,54	8,73	0,57	0,43	-0,57	-0,43
HS optimum	e	2,30	0,63	2,89	0,87	4,32	0,42	8,83	0,59	0,33	-0,66	-0,33
HS-LSM	f	1,36	0,82	4,44	0,58	1,58	0,41	8,11	0,73	0,70	-0,30	-0,70
HS-LSM0		3,59	0,63	3,06	0,76	2,28	0,31	7,58	0,67	0,56	-0,44	-0,56
HS-LSM90		2,75	0,64	3,34	0,70	1,89	0,31	7,87	0,74	0,59	-0,41	-0,59
HS-LSM150		2,23	0,77	3,52	0,62	1,86	0,33	7,88	0,70	0,63	-0,37	-0,63
FS-LSM		3,94	0,96	3,33	0,63	1,46	0,45	8,13	0,90	0,76	-0,24	-0,76
FS-LSM0		4,89	0,60	2,88	0,69	1,91	0,45	7,80	0,90	0,63	-0,37	-0,63
FS-LSM90		4,75	0,77	2,96	0,70	1,87	0,43	7,82	0,86	0,66	-0,34	-0,66
FS-LSM150		4,27	0,82	3,23	0,64	1,85	0,46	7,95	0,82	0,66	-0,34	-0,66

Humic and fulvic acids have proven to be good examples of such complex-forming ligands. Das Donnan volume of humic substances converges to I = 10 mol/L to V_D = 0.1 L/kg. From Eq.(6.5-65) follows the simplified relationship Eq.(7.4-3),

$$\log(V_D) = b \cdot (1 - \log(I)) - 1 \qquad (7.4\text{-}3)$$

with the empirical parameter b for the influence of the ionic strength I [mol/L], which *characterizes the* swelling capacity.

The complex humic substance models can only be used to a limited extent and with considerable effort for the determination of the constants, Tab. 7.4-6. The investigated fulvic and humic acid isolates differ in the distribution of the acid constants, FigFig. 7.43. It becomes even more complicated when concurrent cation complex formation is included.

7.4.2.6 Empirical Titration Curves

Theoretically, the humic substance models presented can also be used to calculate titration curves in advance, which rarely agree with empirical results. SCHÖPKE (2007) therefore proposed to describe the measured titration curves by several acid pseudocomponents as substitute functions, chapter 9.1.2.2 Using the example of a titration curve of humic acid in drinking water calculated according to Model VI, SCHÖPKE (2007) replaced it with five acid pseudocomponents, Fig. 7.44. The majority

of the acidic groups are firmly bound to hardeners, although calcium and magnesium form less stable complexes compared to transition metals.

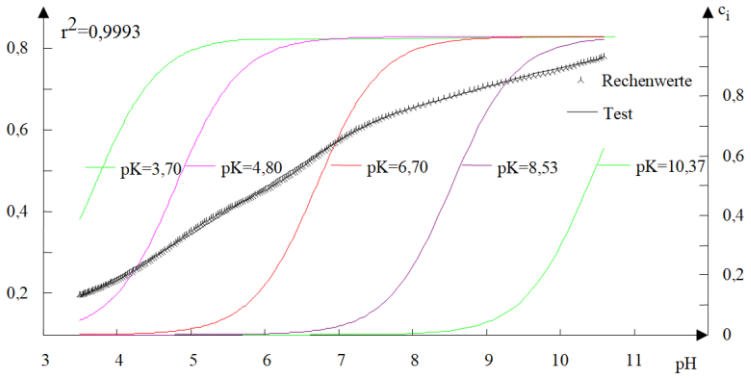

Fig. 7.44: Description of a modeled titration curve by an adapted replacement system of 5 acids (SCHÖPKE 2007).

7.4.3 Spectroscopic properties

7.4.3.1 Influence of trial pretreatment

The UV/VIS spectra of Natural Organic Matter (NOM), which consists mainly of humic substances, are influenced by the chemical environment of the sample being examined, which includes different complex formations. Changes in the pH value, the redox ratios or the concentration of complex-forming cations must be taken into account when interpreting measured spectra, chapter 7.1.2. The spectra should be determined from the turbidity-free (centrifuged or filtered) sample that is as unaerated as possible. The DOC and the inorganic parameters are to be determined from the same sample.

Standardisation on the proportion of groundwater relevant to drinking water has not proven successful. As part of the pre-treatment, the sample was aerated and the precipitated ferric hydroxide was separated before the measurement. The aim was to simulate iron removal and to create a composition corresponding to the later pure water. In this case, all humic substances precipitated with it elude the measurement. The conditions of the sample pre-treatment do not necessarily have to be the same as the conditions for ferrous iron filtration. At high iron concentrations, e.g. in mining-influenced waters, ferric iron precipitation is delayed, while the pH value must be corrected several times. Subsequent re-felling can render the measurement unusable due to clouding. In addition, the proportion of the organic matter complex precipitated with the ferric hydroxide is missing.

7.4.3.2 Classification scheme of humic pseudocomponents with regard to aromaticity

Humic substances have an almost continuous spectral pattern, which makes characterization by aromaticity useful. The pseudo-components of LC-OCD chromatography with the spectral absorption coefficients SAK_{254} (E_{254}) can be entered as fuzzy surfaces in an aromaticity-molar mass diagram, in which they occupy characteristic areas, Fig. 7.45.

7.4.3.3 Interpretation der UV/VIS-Spektren

In many cases, the UV/VIS spectra of the humic-NOM or CDOM can be composed of the elementary bands Spez1, Spez2 and HuminKont, whereby the incompletely recorded short is eliminated as *an interference band*, chapter 7.1.2.5. By comparing their integral extinctions with each other, regionally typical spectra can be compiled and deviations from them can be identified, FigFig. 7.46. Further interpretation is carried out in the context of the respective boundary conditions.

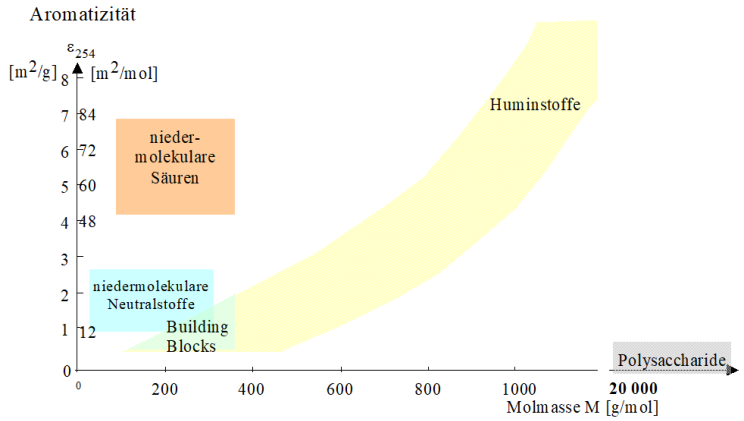

Fig. 7.45: Orienting regions of pseudocomponents of LC-OCD chromatograms from groundwater and surface water as a representation of aromaticity ε_{254} against the molar mass (KOCH et al. 2006 and SCHÖPKE 2007). The area known for humic substances is highlighted in yellow. In each specific case, the location of the areas is specified and assigned to the measured DOC.

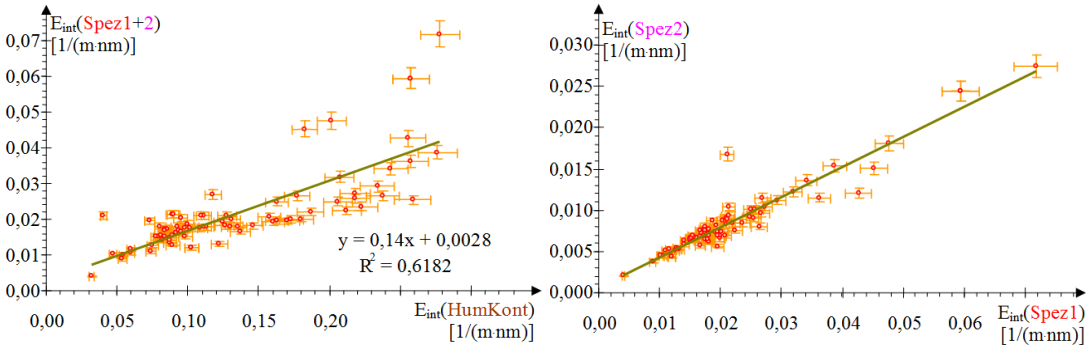

Fig. 7.46: Relationships between the integral extinctions E_{int} Eq.(7.1-29) of the sum (Spez1 + Spez2) and those of the HuminKont (left) as well as the one between Spez1 and Spez2 (right) at the measuring point P31 in the sulfate-reducing underground reactor of the Ruhlmühle (SCHÖPKE et al. 2020). The error bars indicate the standard deviations of the spectral adjustment.

7.4.3.4 Pseudo-component definition via aromaticity ε_{254}

If a mixture contains groups of substances with strongly differing aromaticities ε_{254} , e.g. aliphates ($\varepsilon_1 \approx 0$) and humic substances (ε_2), they can be mathematically separated

by their different aromatics. The dissolved organic carbon of a sample DOC(Pr) is mathematically separated into pseudo1 and pseudo2 using the different aromaticities of the predefined pseudocomponents (SCHÖPKE et al. 2011).

$$\mathrm{DOC(Pseudo\ 1)} = \frac{(\varepsilon_{Pr} - \varepsilon_1)}{(\varepsilon_2 - \varepsilon_1)} \cdot \mathrm{DOC(Pr)}\ \mathrm{[mg/L\ C]} \qquad (7.4\text{-}4)$$

$$\mathrm{DOC(Pseudo\ 2)} = \mathrm{DOC(Pr)} - \mathrm{DOC(Pseudo\ 2)}\ \mathrm{[mg/L\ C]} \qquad (7.4\text{-}5)$$

The marginal aromaticities ε_1 and ε_2 are selected from the parameters of the determined frequency distribution of aromaticity ε_{254}, Fig. 7.47.

SCHÖPKE et al. (2020) applied this evaluation to sulfate-reducing groundwater at the Ruhlmühle site for the mathematical separation of the DOC into a substrate/metabolite (Met) and a natural DOC fraction (NOM). Although the added substrate does not absorb *glycerol* and its main metabolites at λ = 254 nm (ε_{254} = 0 m²/mol), ε_{Met} = 6 m²/mol was chosen for the substrate residues and metabolites at the edge of the distribution. By setting the aromaticity for groundwater humic substances (NOM) at ε_{NOM} = 60 m²/mol, negative calculation values for NOM and mead in Eq.(7.4-4) and Eq.(7.4-5) This does not completely rule out the possibility that the NOM fraction also contains variable aliphate components. The limit aromaticities must be adapted to the respective problem under consideration, Tab. 7.47. The further classification of the DOC into three pseudocomponents with separate humic and fulvice fractions has not yet yielded any applicable results.

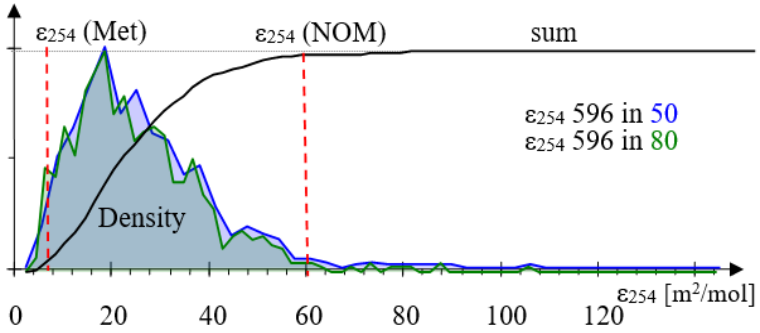

Fig. 7.47: Frequency distributions of the aromaticity of the groundwaters enriched with glycerol substrate for the microbial sulphate reduction and the limit aromaticities. Pseudocomponent Met = substrate+metabolites, pseudocomponent NOM ≈ humic substances (SCHÖPKE et al. 2020).

Tab. 7.47: Applied aromaticities of predominantly aliphatic substances (Met) and groundwater humic substances (NOM) in comparison empirical values. [a)]SCHÖPKE et al. (2011), [b)]SCHÖPKE et al. (2020), [c)]FRIMMEL & KUMKE (1998).

Standort	ε_{254}(Met)	ε_{254}(NOM)	Reference
	m²/mol	m²/mol	
Microbial sulfate reduction: tip groundwater Skadodamm	0	110	a
Microbial sulfate reduction: groundwater Ruhlmühle	6	60	b
Groundwater		54	c
Fulvic acid fractions		64	

7.4.4 Reactions in the humic substance system

7.4.4.1 Formation and degradation processes in the humic substance system

Humic substances can be formed in two ways, by degradation of complex organic matter or by polymerization/condensation of low-molecular starting materials. During the microbial degradation of organisms and their metabolites, the biochemically available macromolecules are crushed and metabolized. More resistant components or biopolymers, such as lignin, cutine, suberine, N-containing paraffinic macromolecules, melanins and other biopolymers are selectively preserved to later become part of what is operationally called *humin*. As a result of the increased degradation, the structure of the resulting macromolecules becomes more variable and begins to lose their chemical similarity to the starting material. This way of humification takes place, for example, in composting (CHEFETZ et al. 1998).

The other metabolic pathway involves condensation and polymerization reactions from low-molecular reactive starting materials, Fig. 7.48. This autochthonous formation of humic substances is oxidatively enzyme-catalyzed, e.g. via phenolases and peroxidases or abiotic via autooxidation. Colloidal complexes, gel-like and solid phases are then formed by aggregation of the resulting macromolecules. The macromolecules created in this way are also increasingly losing their similarity to their starting materials (VOGT et al. 2002). Thus, substances of anthropogenic origin, e.g. from contaminated sites, can also form humic substances, Fig. 7.49. The chemically similar lignins are formed biochemically, whose degradation products integrate into the humic substance complex via the humification process.

The low-molecular starting materials still have individual spectral curves, but their superposition can already result in a continuous course, FigFig. 7.48. Humification begins in the low molecular weight range of the log_K_{OW}-log_M diagram, Fig. 7.49 left. Measured over the total carbon DOC, the humic substances appear chemically inert as so-called **R**efractory **O**rganic **M**atter **(ROM).** The individual components are constantly reacting with and with each other. In the molar mass-aromaticity diagram, the humic components are in a characteristic range, Fig. 7.49 right. Humic substances are also formed spontaneously during wastewater treatment, composting, contaminated sites and other natural and technical processes.

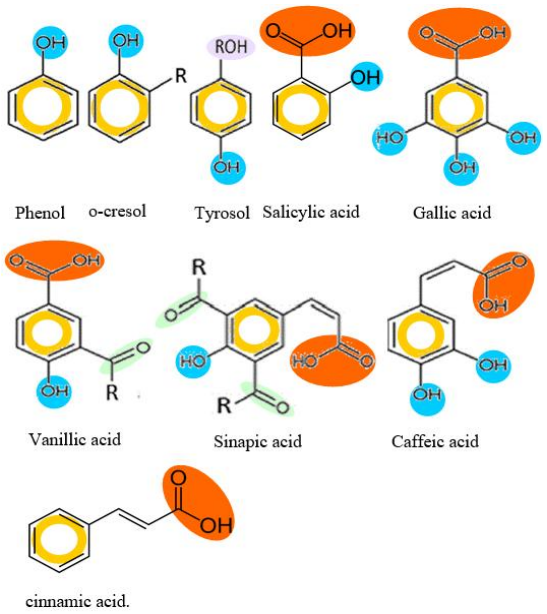

Fig. 7.48: Selected starting materials of humification with marking of the structuralelements: aromatic π systems (2Ar-π) yellow rings, carboxyl groups (COO-H) red, phenolic hydroxyl groups (ArO-H) blue, carbonyl groups (C=O) green, alcoholic hydroxyl groups (RO-H) violet. Methoxy (OCH3) and heteroatoms not included.

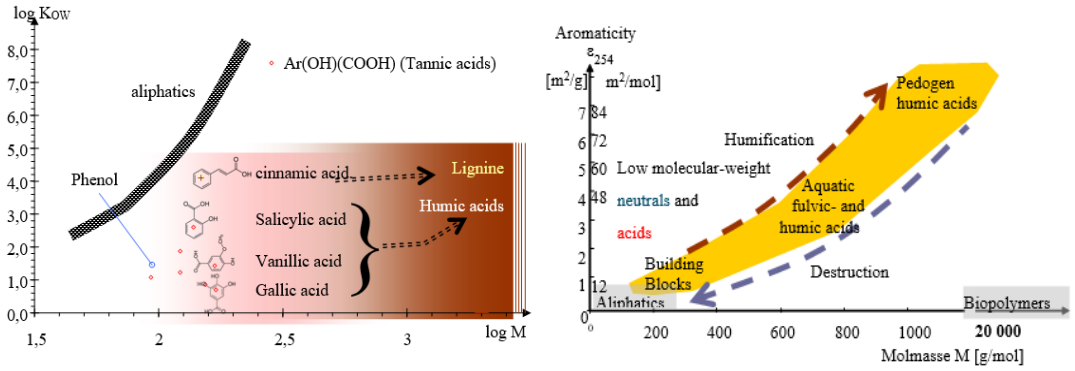

Fig. 7.49: Left: Statistical polymerization of low-molecular phenylcarboxylic acids to humic substances in addition to the ordered biosynthesis of lignins. Right: Presentation of the processes in the system of aquatic humic substances according to HUBER (2003).

7.4.4.2 Redox reactions of humic substances

The RedOx properties of humic substances are often explained by those of quinoid structures, Tab. 7.48.

Tab. 7.48: Chinonoid redox systems converted to BAUER (2008).

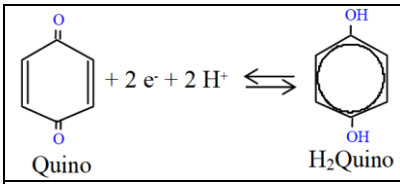

Quino + 2H+ + 2e- = H2Quino mit Quino =	log K	
Chinon	10,26	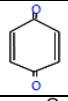
Juglon (5-Hydroxy-[1,4]naphthochinon)	6,31	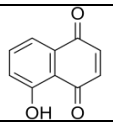
Lawsone (2-Hydroxy-1,4-naphthoquinone)	5,14	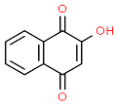
Dissolved Organic Matter DOM	3,35 to 7,75	

The electron exchange capacity of humic substances by 0.02 to 6 mmol/g C corresponds to the equivalent of 0.24 to 72 mmol/mol C, i.e. just below the concentration of aromatic π electron pairs (2Ar-π), or as a stoichiometry factor:

$\nu_e = 0{,}24 \cdot 10^{-3}$ bis $72 \cdot 10^{-3}$

This redox behavior can be used in geochemical calculations (PHREEQCx).

7.4.4.3 Explanation of the oxidative decolorization of humic substances

During the discoloration of humin-contaminated waters by means of oxidants, double bonds in delocalized π electron systems are probably formed according to Eq.(7.4-6) causing their absorption bands to shift to the shorter-wavelength range. This corresponds to a decrease in coloration in the visible range.

Postulierte Oxidation von C=C Doppelbindungen:

$$\begin{matrix}R_1\\R_2\end{matrix}\!>\!C=C\!<\!\begin{matrix}R_3\\R_4\end{matrix} + 2OH^- \rightarrow \begin{matrix}R_1\\R_2\end{matrix}\!>\!C(OH)-C(OH)\!<\!\begin{matrix}R_3\\R_4\end{matrix} + 2e^- \rightarrow \ldots \qquad (7.4\text{-}6)$$

The subsequent reactions can be very different. For potassium permanganate, the oxidation reaction in the neutral range is relevant.

$$KMnO_4 + 4H^+ + 3e^- \rightarrow MnO_2 + K^+ + 2H_2O \qquad (7.4\text{-}7)$$

somit gilt für die Wegoxidation einer Doppelbindung Eq.(7.4-8)

$$\begin{matrix}R_1\\R_2\end{matrix}\!>\!C=C\!<\!\begin{matrix}R_3\\R_4\end{matrix} + \tfrac{2}{3}MnO_4^- + \tfrac{2}{3}H^+ + \tfrac{2}{3}H_2O \rightarrow \begin{matrix}R_1\\R_2\end{matrix}\!>\!C(OH)-C(OH)\!<\!\begin{matrix}R_3\\R_4\end{matrix} + \tfrac{2}{3}MnO_2 \qquad (7.4\text{-}8)$$

- 1mg/L $KMnO_4$ = 3,55 µmol π-Electron pairs (>C=C<)

Only a relatively small number of double bonds need to be oxidized for decolorization. Therefore, even the use of low doses of potassium permanganate achieves a discoloration effect, while the DOC and the UV spectrum hardly change overall.

7.5 Biofilm with extrapolymer substances (EPS)

7.5.1 Occurrence and significance

In biofilms, the microorganisms live in a self-produced matrix of hydrated extracellular polymeric substances (EPS). EPS is mainly composed of polysaccharides, proteins, nucleic acids and lipids. They ensure the mechanical stability of biofilms, mediate their adhesion to surfaces and form a cohesive, three-dimensional polymer network that connects biofilm cells and transiently immobilizes them. In addition, the biofilm matrix acts as an external digestive system by holding extracellular enzymes close to the cells, allowing them to metabolize dissolved, colloidal, and solid biopolymers (FLEMMING & WINGENDER 2010). The retention of extracellular enzymes creates a versatile external digestive system that binds dissolved and particulate nutrients from the water phase and utilises them as a source of nutrients and energy.

The mechanical properties *of pure* biofilms are largely determined by the environment of the aqueous solvent (pH value, ionic strength, type of mono- and bivalent counterions), such as: LATTNER (2003) on model materials of *Pseudomonas aeruginosa* and its isolates (EPS, alginate).

Under turbulent flow conditions, the biofilm undergoes cycles between colonization-growth and (partial) detachment. In granular media with a largely laminar flow through it, an equilibrium between growth and decomposition (after death) is more likely to occur, or it leads to the suppression of the flow through pore clogging. Biofilm phases stored in the pore gel are stabilized by mineral and organic phases, such as iron oxide hydrates, clay minerals, plant residues, coal and humic substances.

Biofilms as part of the Porengel are of particular importance in water supply systems for the recontamination of drinking water. However, they also eliminate biochemically degradable substances in water treatment and substances that can be absorbed in the biofilm, Fig. 7.51.

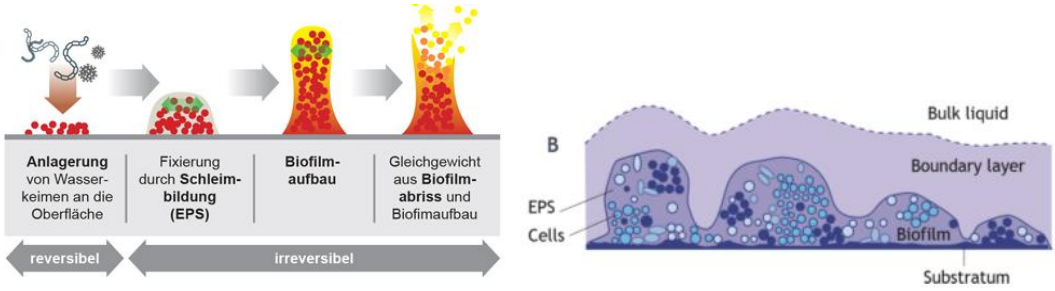

Fig. 7.51: Left: Developmental stages of a biofilm in turbulent flow (FLEMMING 1991). Right: Schematic representation of the different components of a biofilmsystem: bulk liquid, boundary layer, biofilm and substrate (B) (Wanner et al. 2006 cited CHEN et al. 2023).

7.5.2 Composition of Extra Polymeric Substances

Pure cultures of *Pseudomonas aeruginosa,* which are mainly composed of polysaccharides and proteins up to M > 100 000 g/mol, are often used as a model for the aerobic bacterial extracellular polymer substance, Fig. 7.52 and Tab. 7.5-1. In contrast, no generalizable data were obtained for anthropogenically unaffected anoxic aquifers.

In sludge and water sediments examined by Rode (2004), the colony numbers fluctuated from 10^7 to 10^8 CFU/g DM (colony-forming units per g dry matter). The total cell counts were two to three orders of magnitude higher.

All cells are made from the same types of polymeric building materials. CHEN et al. (2023) give the mean composition of biofilms (biomass + EPS) with

$$\{C_{100}H_{180}O_{50}N_{20}P_3S_2Mg_1K_{0.8}....\} \quad M = 262 \text{ g/mol}$$

independent of prokaryotes or eukaryotes (in comparison: Eukaryotic algae $\{C_{106}H_{263}O_{110}N_{16}\}$). The EPS gel lying on the solid matrix forms a diffusion barrier to underlying reactive phases,

.

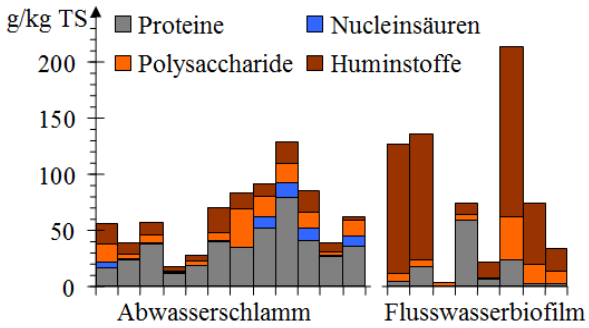

Fig. 7.52: Composition of biomaterial from wastewater sludge (*Abwasserschlamm*) and river water biofilm (*Flusswasserbiofilm* without nucleic acids) according to RODE (2004).

Tab. 7.5-1: Composition of biofilms: [a)]Activated sludge CHEN et al. (Hg.) (2023), [b)]Extrapolymeric substances of *Bacillus subtilis* in interaction with ferrichydroxide (adsorbed and as coprecipitate, ZHANG et al. 2021), [c)]Sewage sludge from trickling filter, [d)]River water biofilm, [e)]EPS (RODE 2004) (Minimum ... Maximum).

Quelle	a	b	c	d	e
Substance group	%	mg/mol C	%	%	%
Protein	30-60	5,36	1,10 ... 7,9	0,26 ... 5,9	... 0,19
Polysaccharide	5-30	7,75	0,17 ... 3,3	0,13 ... 3,9	... 0,06
Humic substances			0,34 ... 2,3	0,98 ... 15,2	... 0,21
Lipids	5-10				
Nucleic acids	5-15 (RNA) 1 (DNA)	0,67	0,10 ... 1,3		

Tab. 7.52: Reference values for diffusion coefficients of EPS of biofilms.

Medium	D_F [m²/s]	Reference
Aerobic biofilms D_W	$0{,}8 \cdot D_W$ Eq.(2.3-42), Eq.(2.3-44)	CHEN et al. (2023)
	$9{,}3 \cdot 10^{-10}$	
Natural aquatic DOM	$2{,}48\ 10^{-10}$ bis $5{,}31\ 10^{-10}$	adopted as an analogy
Humic substances	$3{,}48\ 10^{-10}$ bis $6{,}05\ 10^{-10}$	BALCH & GUÉGUEN (2015)

7.5.3 Acidity and complex formation with metal ions

The biofilm surfaces contain carboxyl (-COOH), phosphoryl (-PO4 or -POH), amino (-NH3+) and aromatic hydroxyl groups (ArOH). Their acidities are described as protolysis and the metal bond as complex formation reactions. Tab. 7.53. Dentate and multi-dentate complexes with different surface groups are organism-specific. Since the microorganisms are mostly embedded in extracellular polymeric substance (including Porengel), the dielectric properties of the bilayer also differ from those of the aqueous solution. The specified constants can only be used as initial values for the adjustment of experimental results. EPS pore gels can also be described as thunder angels, chapter 6.5.6.4 and chapter 6.5.6.5.

For a biomass with an estimated particle density of

ρ_{SS} = 1,1 kg/dm³

and a characteristic rod shape of

L_{Bakt} = 3,835 µm und d_{Bakt} = 0,6 µm

d_K = 5,45 µm for the equivalent sphere, Eq.(4.1-16)

and the associated specific surface

O_{sp} = 10^6 m²/kg, Eq.(3.4-10).

And this results in the lower surface density of

Γ = 0,3 sites/nm² (HA et al. 2010, Tab. 7.53)

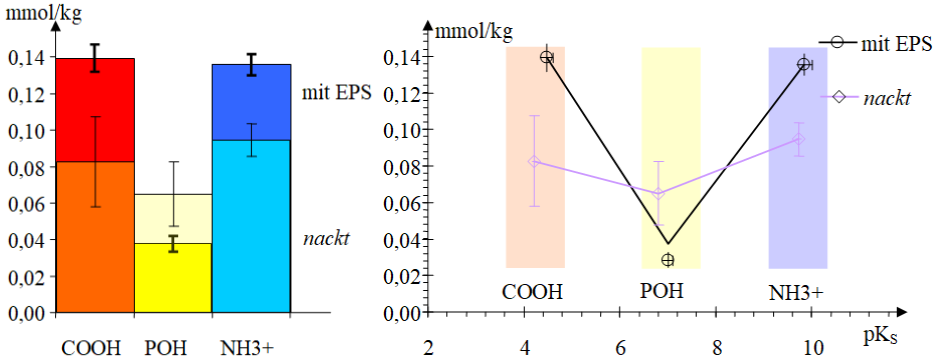

Fig. 7.53: Left: Acidity capacities of carboxyl (-COOH), phosphoryl (-POH) and Amino (-NH3+) sites of *Shewanella oneidensis* with and without (naked) EPS. Right: Acidity capacities and their acid constants (simplified according to HA et al. 2010).

Tab. 7.53: Selected surface complexes of bacterial biomass. [a)]*Bacillus subtilis* in the temperature range 30 ... 75°C and TOR-39 for 50°C according to WIGHTMAN et al. (2001), [b)]*Bacillus subtilis* und *Bacillus licheniformis* according to DAVID (1998), [c)]*Shewanella oneidensis* according to HA et al. (2010), [d)]PHREEQC *wateq4f.dat* und *minteq.dat*, rewritten (PARKHURST & APPELO 2013). Since the microorganisms are mostly embedded in extracellular polymeric substance (including Porengel), the dielectric properties of the bilayer also differ from those of the aqueous solution.

Kation	Complexation equation	Group	log_k	Temp	c_{ads}	Reference
				°C	mol/kg	
H+	HAcetate = Acetate- + H+	**COOH**	**-4,76**	25	-	d
H+	Bsubtil_COOH = Bsubtil_COO- + H+	COOH	-4,40	30		a
H+	TOR_COOH = TOR_COO- + H+	COOH	-4,40	50		a
H+	Shewo_COOH = Shewo_COO- + H+	COOH	-4,48	30	0,139	c
H+	H2PO4- = HPO4-2 + H+	**PO4**	**-7,21**	25	-	d
H+	Bsubtil_PO4H = Bsubtil_CPO4- + H+	PO4	-6,10	30		a
H+	TOR_PO4H = TOR_CPO4- + H+	PO4	-6,10	50		a
H+	Shewo_POH = Shewo_PO- + H+	POH	-7,00	30	0,038	c
H+	Bsubtil_OH = Bsubtil_O- + H+	ArOH	-8,30	30		a
H+	TOR_OH = TOR_O- + H+	ArOH	-8,30	50		a
H+	NH4+ = NH3 + H+	**NH3+**	**-9,25**	25	-	d
H+	Shewo_NH3+ = Shewo_NH2 + H+	NH3+	-9,85	30	0,136	c

Kation	Complexation equation	Group	log_k	Temp	c_{ads}	Reference
				°C	mol/kg	
Ca	Bsubtil_COO- + Ca+2 = Bsubtil_COO-Ca+	COOH	2,80			b
Zn	Acetate- + Zn+2 = ZnAcetate+	**COOH**	**1,57**	25	-	d
Zn	Shewo_COOH + Zn+2 = Shewo_COOZn+	COOH	3,70	30	0,138	c
Cu	Acetate- + Cu+2 = CuAcetate+	**COOH**	**2,22**	25	-	d
Cu	Bsubtil_COO- + CuOH+ = Bsubtil_COOCuOH	COOH	6,40			b
Cu	Blich_COO- + CuOH+ = Blich_COO-CuOH	COOH	6,10			b
Pb	Acetate- + Pb+2 = PbAcetate+	**COOH**	**2,87**	25	-	d
Pb	Bsubtil_COO- + PbOH+ = Bsubtil_COOPbOH	COOH	5,80			b
Pb	Blich_COO- + PbOH+ = Blich_COOPbOH	COOH	6,60			b
Pb	Shewo_COOH + Pb+2 = Shewo_COOPb+	COOH	4,57	30	0,138	c
Zn	Shewo_POH + Zn+2 = Shewo_POZn+	POH	3,73	30	0,037	c
Zn	Shewo_POH + Pb+2 = Shewo_POPb+	POH	4,07	30	0,037	c

7.6 Aluminosilicates as inorganic systems

7.6.1 Zeolithe

Zeolites are crystalline aluminosilicates, of which about 60 naturally occurring ones are known, and more than 150 different types have been synthesized. Mineralogically, they are summarized under the term zeolite group. (https://de.wikipedia.org/wiki/Zeolithe_(Stoffgruppe) They consist of a microporous framework structure of AlO4 and SiO4 tetrahedrons (Tab. 7.61). The aluminum and silicon atoms are connected to each other by oxygen atoms. Depending on the type of structure, this results in a structure of uniform regular pores and/or channels in which substances can adsorb (Fig. 7.61). In nature, water is usually adsorbed there, which can be removed from the pores by heating it without changing the zeolite structure.

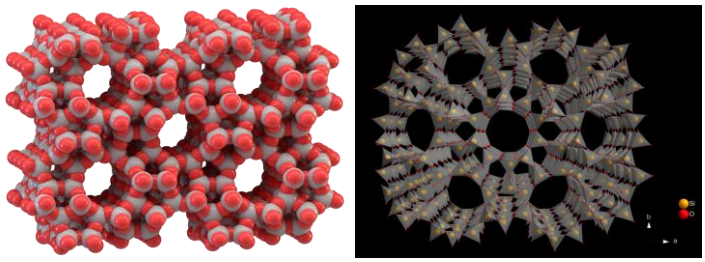

Fig. 7.61: Structure of a ZSM-5 (left) and representation of the coordination tetrahedrons.

Since only molecules that have a smaller kinetic diameter than the pore openings of the zeolite structure adsorb in the pores, these are also referred to as *molecular sieves* . Due to trivalent aluminum atoms, to which two divalent oxygen atoms are formally assigned, zeolites have an anionic scaffold charge. Therefore, there are cations on the inner and outer surface of aluminum-containing zeolites. In water-containing zeolite, these cations are often present in dissolved form in the channel systems of the zeolites, so they are relatively easily accessible and therefore interchangeable. Common cations are Na^+, K^+, Ca^{2+} and Mg^{2+}. The inner surface is well over 1000 m^2/g. Generally transferable complex formation constants are not known due to their different structures

and must be determined for the respective concrete boundary conditions. Zeolites can absorb water and other low-molecular substances and release them again when heated without destroying their crystal structure. $y/x > 1$ in the molecular formula indicates the molar ratio of SiO_2 to AlO_2.

Tab. 7.61: General composition of different zeolites in formulas. n is the charge of the cation (1 or 2). These cations are required for the electrical charge equalization of the negatively charged aluminum tetrahedrons and are not built into the main lattice of the crystal, but reside in cavities of the lattice – and are therefore easily movable or exchangeable within the lattice. z indicates how many water molecules have been absorbed by the crystal.

Zeolith	Composition of the elementary cell
General	$Me^{n+}_{x/n}\,[(AlO_2)^-_x\,(SiO_2)_y] \cdot z\,H_2O$
Zeolith A	$Na_{12}[(AlO_2)_{12}(SiO_2)_{12}] \cdot 27\,H_2O$
Zeolith X	$Na_{86}[(AlO_2)_{86}(SiO_2)_{106}] \cdot 264\,H_2O$
Zeolith Y	$Na_{56}[(AlO_2)_{56}(SiO2)_{136}] \cdot 250\,H_2O$
Zeolith L	$K_9[(AlO_2)_9(SiO_2)_{27}] \cdot 22\,H_2O$
Mordenit	$Na_{8,7}[(AlO_2)_{8,7}(SiO_2)_{39,3}] \cdot 24\,H_2O$
ZSM 5	$Na_{0,3}H_{3,8}[(AlO_2)_{4,1}(SiO_2)_{91,9}]$
ZSM 11	$Na_{0,1}H_{1,7}[(AlO_2)_{1,8}(SiO_2)_{94,2}]$

7.6.2 Clay minerals

Clay minerals as weathering products of mica or new weathering formations of potash feldspars consist of layers of densely packed O and OH ligands, in whose interstices cations (Si, Al, Fe) are embedded. Due to the smaller size of central cations, such as silicon or partly aluminum, they are surrounded by four oxygen atoms (coordination number 4), while the larger cations, such as Al, Fe and Mg, are surrounded by six oxygen or OH ligands (coordination number 6). This different coordination results in tetrahedron (Si,AlO_4) and octahedron $[(Al,Mg,Fe)(O,OH)_6]$. The tetrahedrons are linked to layers via common oxygen ions. In the plane, the tetrahedrons are connected to form a network of six-point rings. The tetrahedral layer is condensed to an octahedral layer, BIRKEL (2001).

- A clay mineral made up of a sequence of tetrahedrons and octahedrons is called a two-layer mineral, which includes kaolinites.
- The minerals, on the other hand, which are made up of a sequence of tetrahedron-octahedron-tetrahedron, are called three-layer minerals, which include smectites with montmorillonite.

The actual clay mineral leaflet is formed by about 10 - 40 such silicate layers, Fig. 7.62. The cations between layers can be exchanged. Larger molecules, including organic material (NOM), are adsorbently bound to the particle surface and in aggregate spaces. The water molecules within the aggregates are associated with the surfaces, lie within the adsorption water layer and thus do not follow the Darcy law of filter flow. Apart from pure clay mineral deposits, these are continuous substances.

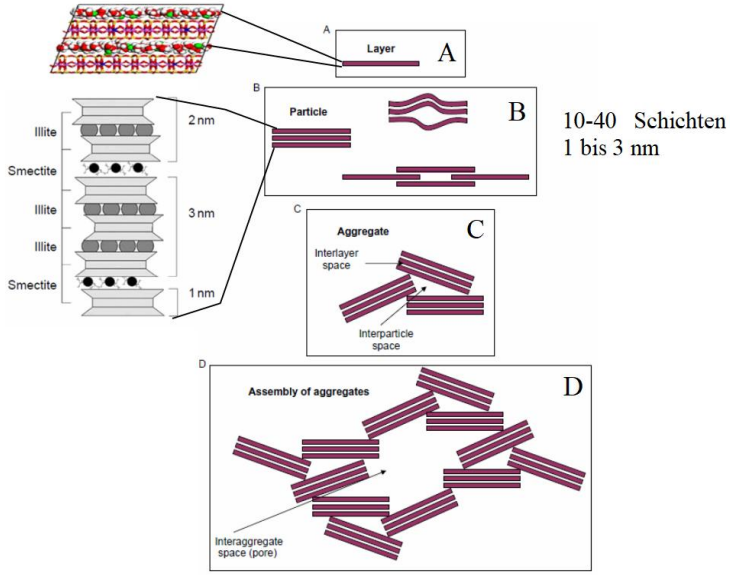

Fig. 7.62: Clay mineral layers (A); Particles from layer packages (B); their aggregates (C) and ensembles of aggregates (D) (according to BERGAYA & LAGALY 2013 and BIRKEL 2001).

7.6.3 Physikochemische Eigenschaften

The PHREEQCx data set *wateq4f.dat* compiles the solubility equilibria of numerous clay minerals. The surface acidity is compared with the SiOH surface.

Tab. 7.62: Adsorptive surface parameters derived for the three-layer mineral montmorillonite, BIRKEL (2001).

Parameter			average	
KAK	mmol/kg	1200	1000	800
O_{ads}	m^2/g	700	750	800
	m^2/kg	700000	750000	800000
KAK/O_{ads}	$\mu mol/m^2$	1,7	1,3	1,0
Γ	nm^{-2}	1,03	0,80	0,60

The dominant surface complex equilibria occur very differently in natural systems, Tab. 7.63.

Tab. 7.63: Calculated Parameters of Ensembles (Fig. 7.62) consisting of clay mineral aggregates of various sizes compared to a *filter sand* with ρ_{SS} = 2,5 kg/dm³ n_P = 20% and δ = 0,5 µm.

Unit diameter	d_K	**µm**	**0,5**	**1**	**5**	**10**	**50**	***1000***
Diameter of a cylinder pore	d_p	µm	0,083	0,17	0,83	1,67	8,33	*167*
Still passable pore narrowing	d_S	µm	0,077	0,15	0,77	1,55	7,74	*155*
Fixed porosity	Δn_P	%	20	20	20	20	4,8	*0,24*
Specific surface area of the fill	O_{sp}	m^2/g	4,8	2,4	0,48	0,24	0,048	*0,0024*
Surface	O_F	m^2/cm^3	9600	4800	960	480	96	*4,8*

The water in the inner pore system is adsorptively bound, i.e. only accessible diffusively. This means that the pore solution flows around clay mineral aggregates.

The chemical adsorption surface (BET) is several orders of magnitude higher. The chemical properties vary greatly depending on the mineral type, conditioning and environmental conditions and must be researched or determined in an application-oriented manner.

8 Special particulate solutions

8.1 Balance adjustment with 1st order kinetics

The approach to an equilibrium or stationary state, characterized by the concentration c_S, in many cases proceeds according to a reaction kinetics of the first order, Eq.(8.1-1) This includes transport-controlled processes at phase interfaces (solution, precipitation, ...). The c_S concentration can also be a function of other parameters.

$$r = k \cdot (c_S - c) \tag{8.1-1}$$

The equilibrium function $c_S(...)$ is included in the transformation X, Eq.(8.1-2),

$$X = (c_S(...) - c) \tag{8.1-2}$$

differentiated, Eq.(8.1-3)

$$\frac{\partial X}{\partial t} = -\frac{\partial c}{\partial t} \tag{8.1-3}$$

and in Eq.(8.1-1) Eq.(8.1-4).

$$\frac{\partial X}{\partial t} = -k \cdot X \tag{8.1-4}$$

This results in the exponential approximation to the equilibrium state, Eq.(8.1-5).

$$\partial \ln(X) = -k \cdot \partial t \tag{8.1-5}$$

The differential equation Eq.(8.1-5) is solved by certain integration in the boundaries t=0 to t, or X_0 to X, Eq.(8.1-6).

$$\int_{X0}^{X} \partial \ln(X) = -k \cdot \int_{t=0}^{t} \partial t \tag{8.1-6}$$

The retransformation of X, Eq.(8.1-2) between c_{S0} and c_S gives the exponential expression Eq.(8.1-7).

$$\ln\left(\frac{(c - c_S(...))}{(c_0 - c_{S0}(...))} \right) = -k \cdot t \tag{8.1-7}$$

Instead of t, in Eq.(8.1-7) also the spatial coordinate x, L or the Filtration Parameter FP Eq.(3.3-23)) with the mass transfer coefficient β Eq.(3.6-17) for sphere packing, Eq.(8.1-8).

$$\ln\left(\frac{(c - c_S(...))}{(c_0 - c_{S0}(...))}\right) = -\beta \cdot FP = \lambda_t \cdot t = \lambda_L \cdot L \tag{8.1-8}$$

After disturbance of a solution-solid equilibrium and transport-controlled compensatory reaction of the 1st order, a new equilibriumstate with exponential approximation subsequently occurs. For these, the time constant λ_t can be specified and for constant filtration velocity the filter length coefficient λ_L can be specified, Eq.(8.1-9).

$$\begin{aligned} \lambda_t &= \frac{O_{ges}}{n_P \cdot V_R} \cdot \beta = \frac{6 \cdot (1 - n_P)}{d_w \cdot n_P} \cdot \beta \\ \lambda_L &= \frac{O_{ges}}{V_R} \cdot \frac{\beta}{v_f} = \frac{6 \cdot (1 - n_P)}{d_w \cdot v_f} \cdot \beta \end{aligned} \tag{8.1-9}$$

To illustrate this, the coefficients can be given as half-lives $t_{1/2}$ or half lengths $L_{1/2}$, Eq.(8.1-10).

$$\begin{aligned} t_{1/2} &= \frac{\ln(2)}{\lambda_t} \\ L_{1/2} &= \frac{\ln(2)}{\lambda_L} \end{aligned} \tag{8.1-10}$$

The proportion of the reactive surface φ in circulating filters with porous materials can be corrected by the ratio of λ_t (measured) and λ_t (calculated) Eq.(8.1-11).

$$\varphi = \frac{O_{reaktiv}}{O_{ges}} = \frac{\lambda_t(\text{gemessen})}{\lambda_t(\text{berechnet})} \tag{8.1-11}$$

8.2 Stationäre eindimensionale Filtrationsprozesse

8.2.1 Influence of dispersivity α on concentration profiles of 1st order kinetics

In a filter with exponential concentration decrease on the flow path, caused by film kinetics at the phase interface, this is also influenced by the dispersivity α. The steady-state balance equation for the one-dimensional case Eq.(2.2-7) in relation to the distance velocity v_A is simplified to Eq.(8.2-1).

$$\dot{c} = \left(\frac{\partial}{\partial t} c\right)_L = v_A \cdot \frac{\partial c}{\partial L} + D \cdot \frac{\partial^2 c}{\partial L^2} + r = 0 \tag{8.2-1}$$

The reaction takes place on the surface of the solids. The flow path L and the residence (flow) time are determined by the filtration parameter FP Eq.(3.3-23) and the surface/pore solution ratio is substituted over the pore channel diameter dP of the shell and tube model, Eq.(8.2-2).

$$FP = \frac{4}{d_P} t = \frac{4 \cdot L}{d_P \cdot v_A} = \int_{c_0}^{c} \frac{\partial c}{r_O} \left[\frac{h}{m}\right] \tag{8.2-2}$$

From this the substituents of the Eq. (8.2-3) and Eq.(8.2-4) from.

$$L = \frac{d_P \cdot v_A}{4} FP \tag{8.2-3}$$

$$\partial L = \frac{d_P \cdot v_A}{4} \partial FP \text{ bzw. } \frac{1}{\partial L} = \frac{4}{d_P \cdot v_A} \frac{1}{\partial FP} \tag{8.2-4}$$

The reaction term is determined by the mass transfer coefficient β, Eq.(8.2-5)

$$r = \frac{O_{ges}}{V_W} r_O = \frac{4}{d_P} r_O = \frac{4}{d_P} \cdot \beta \cdot c \tag{8.2-5}$$

The longitudinal diffusion coefficient $D = D_L$ is replaced by the dispersivity α and the distance velocity v_A, Eq.(9.7-14) and used in Eq.(8.2-1) follows Eq(8.2-6).

$$\alpha_L \cdot \frac{16}{{d_P}^2 \cdot v_A} \cdot \frac{\partial^2 c}{\partial FP^2} + \frac{4}{d_P} \cdot \frac{\partial c}{\partial FP} + \frac{4}{d_P} \cdot \beta \cdot c = 0 \tag{8.2-6}$$

For the ideal piston flow α = 0 as a reference, Eq.(8.2-6) to Eq.(8.2-7) with the solution Eq.(8.2-8).

$$\frac{4}{d_P} \cdot \frac{\partial c}{\partial FP} + \frac{4}{d_P} \cdot \beta \cdot c = 0 \tag{8.2-7}$$

$$c = c_0 \cdot e^{-\beta \cdot FP} \tag{8.2-8}$$

Eq.(8.2-6) converted into the normal form of an inhomogeneous differential equation of the 2nd degree by summarizing the parameters in the constant γ, Eq.(8.2-9) and Eq.(8.2-10).

$$\gamma = \frac{v_A \cdot d_P}{4 \cdot \alpha_L} \text{ [m/s]} \tag{8.2-9}$$

$$\frac{\partial^2 c}{\partial FP^2} + \gamma \cdot \frac{\partial c}{\partial FP} + \gamma \cdot \beta \cdot c = 0 \tag{8.2-10}$$

From Eq.(8.2-8) a homogeneous differential equation of the 2nd order, Eq.(8.2-11),

$$\alpha \cdot \frac{\partial^2 c}{\partial FP^2} + \frac{\partial c}{\partial FP} + \beta \cdot c = 0 \tag{8.2-11}$$

with the general solution (BARTSCH 1972), Eq. (8.2-12) and Eq.(8.2-13).

$$c = C_1 \cdot e^{\lambda_1 FP} + C_2 \cdot e^{\lambda_2 FP} \text{ mit } c(FP = 0) = c_0 \tag{8.2-12}$$

$$\lambda_{1/2} = -\frac{\gamma}{2} \pm \sqrt{\frac{\gamma^2}{4} - \beta \cdot \gamma} = -\frac{v_A \cdot d_P}{8 \cdot \alpha_L} \pm \sqrt{\frac{v_A^2 \cdot {d^2}_P}{64 \cdot {\alpha^2}_L} - \beta \cdot \frac{v_A \cdot d_P}{4 \cdot \alpha_L}} \tag{8.2-13}$$

For the boundary condition of diffusion $c_{Surface} = 0$, $\lambda < 0$ and $r < 0$ apply, from which the positive term $\beta \cdot \gamma > 0$ follows, Eq.(8.2-14).

$$\lambda_{FP} = -\frac{\gamma}{2} + \sqrt{\frac{\gamma^2}{4} + \beta \cdot \gamma} = -\frac{v_A \cdot d_P}{8 \cdot \alpha_L} + \sqrt{\frac{v_A^2 \cdot d^2{}_P}{64 \cdot \alpha^2{}_L} + \beta \cdot \frac{v_A \cdot d_P}{4 \cdot \alpha_L}} \tag{8.2-14}$$

By constant comparison, one obtains the flowpath, and -time-dependent exponents, Eq.(8.2-15).

$$\begin{aligned} \lambda_L &= \lambda_{FP} \cdot \frac{4}{d_P \cdot v_A} \\ \lambda_{VWZ} &= \lambda_{FP} \cdot \frac{4}{d_P} \end{aligned} \tag{8.2-15}$$

Die theoretische Mikrodispersivität α von Filterschichten liegt knapp über der der idealen Kolbenströmung ($\alpha = 0$), Tab. 4.31. In der Realität treten in Stromröhren höhere Werte auf, die bei der Prozessmodellierungzu beachten sind, Fig. 8.21.

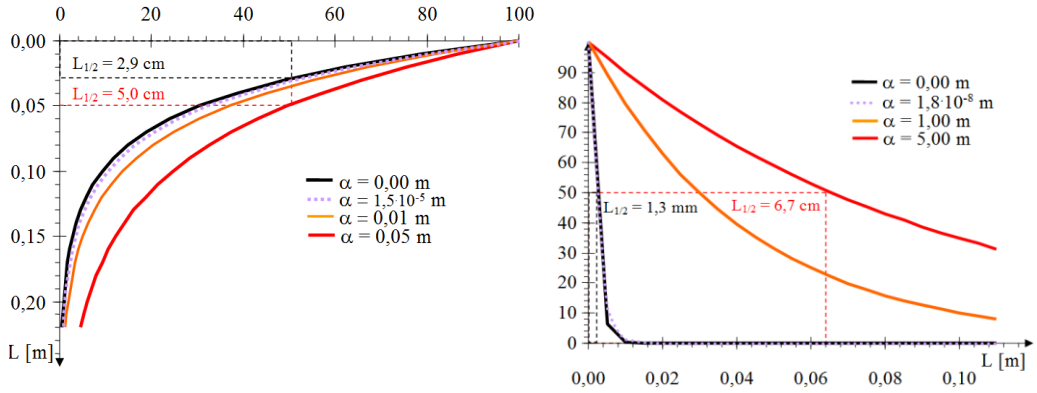

Filter	L	d_W	v_f	β	$L_{1/2}(\alpha=0\ m)$
Iron removal (a)	2 m	1,00 mm	10 m/h	$1{,}6 \cdot 10^{-05}$ m/s	0,0292 m
Groundwater flow section (b)	200 m	0,38 mm	2,1 m/d	$3{,}0 \cdot 10^{-07}$ m/s	0,0013 m

Fig. 8.21: Concentration flow section profiles with $c_0 = 100$ for an iron removal filter (vertical, left) and a groundwater flow tube (horizontal, right) with differentdispersives α. The half-value lengths are shown for $\alpha = 0$ m (black) and the maximum value shown (red) (examples a and b in chapter 10.1).

8.2.2 1st order steady-state reaction in a *mixed cell* model

HAGEN (1993) gives for the stationary concentration of a stirring stage cascade with ncell *mixed cells,* in which a first-order reaction takes place, Eq.(8.2-16)).

$$\frac{c_i}{c_0} = \frac{1}{(1 + k \cdot t_F)^{n_{cell}}} \tag{8.2-16}$$

For a surface reaction, the spacetime t_F is determined by the filtration parameter FP Eq.(8.2-2) and the reactionconstant k by the mass transfer coefficient β Eq.(3.6-6) or Eq.(3.6-17) Eq.(8.2-17).

$$\frac{c_i}{c_0} = \frac{1}{\left(1+\frac{4}{d_P}\beta\cdot\frac{d_P}{4}FP\right)^{n_{cell}}} = \frac{1}{(1+\beta\cdot FP)^{n_{cell}}} \tag{8.2-17}$$

The product of space-time and velocity constant, or β·FP, corresponds to the first Damköhler number Da_1 in process engineering, Eq.(8.2-18).

$$Da_1 = \beta\cdot FP = k\cdot t_F \tag{8.2-18}$$

8.3 Migration of ideal concentration jumps (retardation) through the aquifer

8.3.1 Problem description

In the pore aquifer, laminar flow processes predominate. The current paths of the water particles, also known as current threads, run parallel, can be bundled into *current tubes* and described as filters, Fig. 8.31. Under the mostly slow flow and the associated long contact times between the pore solution and the pore gel lining the solid matrix, chemical equilibria is established between the two, which can extend over entire groundwater bodies. Ideally, groundwater bodies of different sizes with the same pore solution/pore yellow properties can be defined. When the mobile pore solution of one groundwater body penetrates (migrates) into another, a new equilibrium is established at the transition point with a different solution/Porengel configuration. Between this new configuration and that of the original one, a transitional front with successive equilibrium states is formed.

These situations arise during massive interventions in the groundwater system, such as contamination and subsequent remediation measures or as a result of mining. In the course of dewatering in active mining, formerly anaerobic aquifers are oxidized by atmospheric oxygen. As a result acid mise drainage bodies are formed, which also occur intips. Due to technology-related changes in the flow field, these water bodies can then penetrate into surrounding unaffected aquifers, whereby migrating transition and displacement fronts form through the aquifer, Fig. 8.31. These move at a slower distance velocity than the pore solution (retardation). Under these conditions, the modelling effort is reduced to the structural description of the displacement front and the calculation of its migration velocity. Without irreversible reactions, the mathematical description is independent of direction and time, i.e. the time t can be determined by the water column H Eq.(2.2-4) Fig. 8.32. The processes to be considered are comparable to those in chromatography.

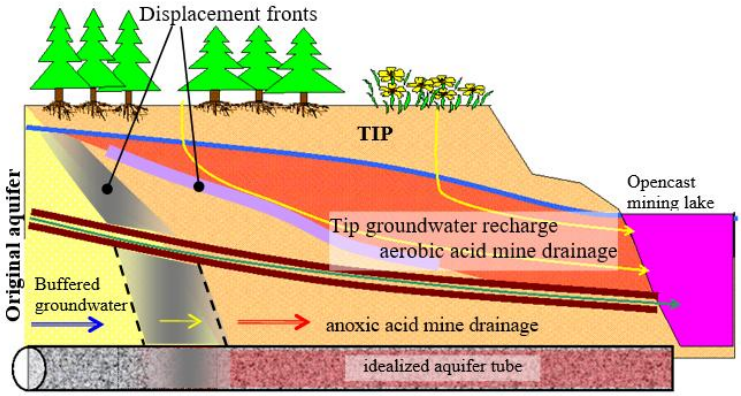

Fig. 8.31: Section through the aquifers of an abandoned opencast mine, consisting of the aquifers at the edge of the tip, the tip and the water body of the forming opencast mining lake. From the groundwater recharge, the tip groundwater lamella of *aerobic acid mine drainage* has formed, which is displaced by the inflow of unaffected groundwater. In the process, the pore water quality changes from tip groundwater to the groundwater in the grey displacement front. This *envelope* can be described as a filter process in a current tube. Another displacement front (purple) forms during the transition from oxic leachate to anoxic state, SCHÖPKE, PREUß & THÜRMER (2011).

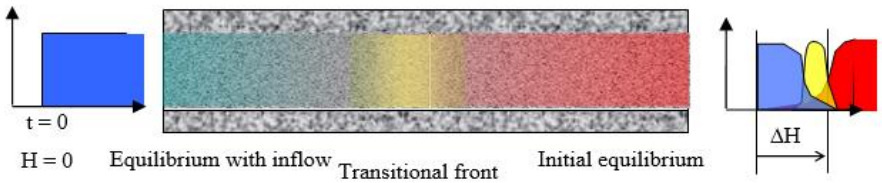

Fig. 8.32: Diagram of the displacement of a water body in a filter tube by an inlet water of a different quality with the formation of a transition front, as well as the changes in the quality of the output as a function of the water column H flowing through it.

8.3.2 Migration in phase equilibrium (retardation)

8.3.2.1 Accounting and retardation

The material balance is considered in a filter without remixing and without irreversible reactions, FigFig. 3.11. The one about Eq.(3.1-17) is reduced to a rectangular function for balancing. The leap in concentration supplied at the *input* migrates unchanged through the flow section, balanced by the water column H Eq.(2.2-4) flowing through it with the initial conditions:

$t = 0 \quad => \quad H = 0, c = c_1$

And for the flow section L in equilibrium with the stationary stock of matter q_0:

$t = 0 \quad => \quad c = c_0(q_0)$

With the volume V_t at a constant filtration velocity v_f, the amount of substance n_{zu} is fed into the system, Eq.(8.3-1),

$$n_{zu}(t) = c_1 \cdot H(t) \cdot A_F = c_1 \cdot v_f \cdot t = c_1 \cdot V_t \qquad (8.3\text{-}1)$$

and led away by the drain n_{ab}, Eq.(8.3-2).

$$n_{ab}(t) = -c_0 \cdot H(t) \cdot A_F = c_0 \cdot v_f \cdot t = c_0 \cdot V_t \tag{8.3-2}$$

Without taking into account the amount of substance stored at the station (q = 0), the material balance is calculated from the difference between the inlet and outflow, Eq.(8.3-3).

$$\Delta n = (c_1 - c_0) \cdot H(t) \cdot A_F \tag{8.3-3}$$

The storage capacity of the reactor, taking into account the stationary stored quantity of substance q, is composed of the

- Solution volume calculated from reactor length L, cross-sectional area A_F and porosity n_P

  and the

- volume-related capacities of the stationary phase $q_V(c_0)$ and $q_V(c_1)$,

which expands the material balance, Eq.(8.3-4).

$$\Delta n = (c_1 - c_0) \cdot L \cdot n_P \cdot A_F + (q_V(c_1) - q_V(c_0)) \cdot L \cdot A_F \tag{8.3-4}$$

Integrated via the concentration jump, when the storage capacity is exhausted according to the flow path L, the delayed breakthrough (Durchbruch) $c_0 \Rightarrow c_1$ occurs as a concentration jump, with the distance velocity v_A for the concentration breakthrough, Eq.(8.3-5) and Eq.(8.3-6).

$$H(\text{Durchbruch}) = L \cdot n_P + \left(\frac{q_V(c_1) - q_V(c_0)}{(c_1 - c_0)} \right) \cdot L = v_f \cdot t \tag{8.3-5}$$

$$\frac{H(\text{Durchbruch})}{t} = v_A \cdot \left(n_P + \left(\frac{q_V(c_0) - q_V(c_1)}{(c_0 - c_1)} \right) \right) = v_f \tag{8.3-6}$$

The quotient between the distance velocity of the mobile phase and the distance velocity of the breakthrough front is generally defined as the retardation R_F^* . The amount of substance stored in the solution fraction n_P of the reactor volume is not taken into account.

Since the porosities n_P of flow sections are rarely known with certainty, the retardation R_F is related to the reactor empty volume. From the observedjumps in concentration, the capacity variables can be determined, Eq.(8.3-7).

$$\frac{\Delta q_V}{\Delta c} = \left(\frac{q_V(c_1) - q_V(c_0)}{(c_1 - c_0)} \right) = R_F - n_P \tag{8.3-7}$$

This R_F value, determined from residence time evaluations for individual current tubes, is composed of the porosity and storage capacity of the stationary phase, Eq.(8.3-8).

$$R_F = \frac{v_f}{v_A} = n_P + \left(\frac{q_V(c_1) - q_V(c_0)}{(c_1 - c_0)} \right) = \frac{H(\text{Durchbruch})}{L} \tag{8.3-8}$$

$$R_F = \frac{v_f}{v_A} = n_P + \frac{\partial q_V}{\partial c} = \frac{H(\text{Durchbruch})}{L} \tag{8.3-9}$$

Occasionally (e.g. in KOß 1997) retardation R_F^* is defined for a known porosity n_P and bulk density ρ_S. (SHENG & SMITH 1999)

$$R_F^* = 1 + \frac{\rho_S}{n_P} K_d \tag{8.3-10}$$

Mass-related capacitance functions Δq_m are calculated with the phase ratio z Eq.(2.2-10) Eq.(8.3-11).

$$\frac{\Delta q_m}{z \cdot \Delta c} = \left(\frac{q_m(c_1) - q_m(c_0)}{z \cdot (c_1 - c_0)} \right) = R_F - n_P \tag{8.3-11}$$

Eq.(8.3-12) links the mass reference q_m with the reactor volume reference q_V and the pore solution reference $q_{PHREEQC}$.

$$\Delta q_m = \frac{\Delta q_V}{\rho_S} = z \cdot \Delta q_{PhreeqC} \tag{8.3-12}$$

Substances that do not interact with the stationary phase (*non-reactive tracers) are used* to determine the residence time from which the porosity n_P of the flow section can be determined.

8.3.2.2 Migration of loading fronts in adsorption filters

In an adsorption filter, the loaded and unloaded areas of the stationary phase are in equilibrium with the inlet solution, or with the treated solution, separate from the displacement front (breakthrough). Under equilibrium conditions, the adsorption problem is reduced to the migration of the reaction front, FigFig. 8.33 with the material balance Eq.(8.3-7).

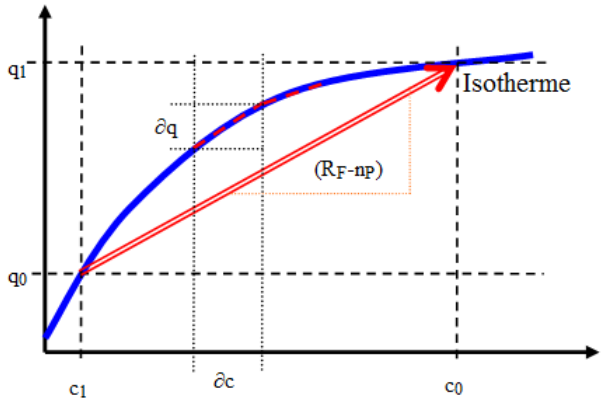

Fig. 8.33: In the advancing loaded zone, the inlet concentration c_0 is in equilibrium with the loaded adsorber q_1, while the effluent concentration c_1 is in equilibrium with the unloaded adsorber q_0. Both states lie on the adsorption isotherm q(c) (blue). The change in the material balance due to displacement is represented by the red arrow, the increase of which is indicated by Eq.(8.3-7) or Eq.(8.3-11) The course of the breakthrough front is determined by the differentiated isotherm dq/dc, Eq.(8.3-9).

Within the displacement front, the concentration runs along the adsorption isotherm. The material balance between the displacement front follows from the difference between the two states, the integral of the differentiated isotherms, Eq.(8.3-13).

$$q_V(c_0) = q_V(c_1) + (R_F - n_P) \cdot (c_0 - c_1) \tag{8.3-13}$$

Until the reaction front arrives at the end of the flow section L, the water column H (breakthrough, Durchbruch) flows through the filter, Eq.(8.3-14),

$$H(\text{Durchbruch}) = R_F \cdot L = v_f \cdot t_L \tag{8.3-14}$$

which corresponds to the corresponding transit time t_L at steady state flow v_f, Eq.(8.3-15).

$$t_L = \frac{R_F \cdot L}{v_f} \tag{8.3-15}$$

For example, for ion exchange resins, the usable volume capacity NVK is defined as the amount of ions exchanged that is absorbed to the selected breakthrough point after normal regeneration. The actual volume capacitance q_V under ideal conditions (reaction front as a rectangular transition) is greater than the NVK, Eq.(8.3-16).

$$q_V = (c_0 - c_1) \cdot \frac{H}{L} = R_F \cdot \Delta c > NVK(c_0, c_1, L, v_{f,\ldots}) \tag{8.3-16}$$

The transit time estimation is therefore based on the retardation R_F. In the technical use of adsorption, the filter bed used is intended to be replaced many times. Therefore, n_P is small compared to R_F and thus usually negligible.

8.3.2.3 Retardation for Linear Isotherms (K_d)

From Eq.(8.3-9) R_F definitions are derived for different isotherms. The linear sorption isotherm Eq.(6.5-16) applies only to low loads q with the distributioncoefficient K_d, Eq.(8.3-17).

$$K_d = \frac{q(c)}{c} = \text{const} \tag{8.3-17}$$

From the isothermal equation Eq.(8.3-18)

$$q_V(c) = \rho_S \cdot K_d \cdot c \tag{8.3-18}$$

follows in conjunction with Eq.(8.3-7) the substance intake Eq.(8.3-19),

$$\frac{\Delta q_V}{\Delta c} = \left(\frac{\rho_S \cdot K_d \cdot c_0 - \rho_S \cdot K_d \cdot c_1}{(c_0 - c_1)} \right) = \rho_S \cdot K_d = R_F - n_P \tag{8.3-19}$$

and vice versa for the retardation Eq.(8.3-20).

$$R_F = n_P + \frac{\Delta q_V}{\Delta c} = n_P + \rho_S \cdot K_d \tag{8.3-20}$$

A maximum volume capacity $q_{V,max}$ (saturation) cannot be specified.

8.3.2.4 Retardation for the Langmuir-isotherm

Starting from Eq.(6.5-18) all constantly competing influences (constant milieu) are summarized in K_I. Without competitive adsorption, $K_I = 1$, Eq.(8.3-21),

$$q_V = \rho_S \cdot q_{max} \cdot \frac{K \cdot c}{K_I + K \cdot c} \tag{8.3-21}$$

and differentiated Eq.(8.3-22),

$$\frac{\partial q_V}{\partial c} = \rho_S \cdot q_{max} \cdot K \cdot \frac{K_I}{(K_I + K \cdot c)^2} \tag{8.3-22}$$

from which R_F follows, Eq.(8.3-23).

$$R_F = n_P + \rho_S \cdot q_{max} \cdot K \cdot \frac{K_I}{(K_I + K \cdot c)^2} = n_P + \rho_S \cdot q_{max} \cdot \frac{K_I / K}{\left(K_I / K + c\right)^2} \tag{8.3-23}$$

For $c << K_I/K$, Eq.(8.3-21) into the linear form of Eq.(8.3-20)

At very high concentrations, the breakthrough front approaches the water front ($R_F \approx 1$). The volume capacity q_V depends on the concentration at the inlet, Eq.(8.3-24).

$$q_V \approx \rho_S \cdot q_{max} \cdot \frac{K \cdot K_I \cdot c}{(K_I + K \cdot c)^2} \tag{8.3-24}$$

8.3.2.5 Retardation for the Freundlich isotherm

With the parameters K_f and n, Eq.(8.3-25) to Eq.(8.3-28) from.

$$q = K_f \cdot c^n \quad \text{or differentiated} \tag{8.3-25}$$

$$\partial q = K_f \cdot n \cdot c^{n-1} \cdot \partial c \tag{8.3-26}$$

From this follows the derivation for the friendly isotherm Eq.(8.3-27).

$$R_F = 1 + \frac{\rho_S}{n_P} \cdot K_f \cdot n \cdot c^{n-1} \tag{8.3-27}$$

The maximum volume capacity q_V also depends on the concentration at the inlet.

$$q_V \approx \frac{\rho_S}{n_P} \cdot K_f \cdot n \cdot c^n \tag{8.3-28}$$

8.3.3 Comparison of complex reaction fronts over the phase ratio z

8.3.3.1 Description Approach

The distribution system in a filter section or in a batch approach can be described by the vectors of the loads with the elements q_X and the concentrations with the elements c_X with $X \in$ dissolved components, Eq.(8.3-29).

$$\begin{aligned} \vec{c} &= (c_A, c_B, ..., c_X)^T \quad \text{mit} \quad X \in \{\text{Komponente n}\} \\ \vec{q} &= (q_A, q_B, ..., q_X)^T \quad \text{z.B.} \quad X \in \{A, B, Na^+, ..., Z\} \end{aligned} \tag{8.3-29}$$

Adsorption equilibria are formed between the solution components and the stationary material, Eq.(8.3-30).

$$Ads + \nu_X X \leftrightarrow AdsX_{\nu X} \tag{8.3-30}$$

ν_X indicates the adsorption stoichiometry of each component X. The generalization is made for equilibrium-related processes by:

- Concentration of a conservative tracer in the inlet as a reaction coordinate.
- Water-solid ratio (phase ratio z) for all (L, t) or (L, BV) as reaction coordinate.

The breakthrough curve is a particulate solution to the reversible transport problem. The scale transfer can be carried out independently of time and flow (t, H) via the phase ratio z [L/kg] of the filter.

For a *mixed cell* flow section of n_{cell}, the corresponding phaseratio z(ncell) is calculated from the phase ratio of a cell z_{cell}[L/kg] and the transport steps n_{shift}, Eq.(8.3-31) The phase ratio $z_{cell}(n_{cell})$ is defined in filter mode for the water column H flowing through Eq.(2.2-15).

$$z(n_{cell}) = \frac{n_{shift}}{n_{cell}} \cdot z_{cell} \tag{8.3-31}$$

The equilibrium between stationary and mobile phase determines the source/sink term. The breakthrough curve for the ideal piston flow consists of a sequence of state jumps, each of which occurs at z = z_{Di}, Eq.(8.3-32) and Fig. 8.34.

$$\vec{c}\,(z) = \vec{c}_i \quad \text{für} \quad z_{Di} \le z \le z_{Di+1} \quad | i = 0 \ldots n \tag{8.3-32}$$

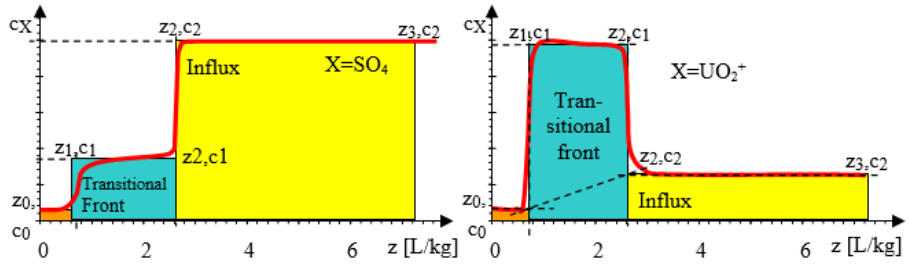

Fig. 8.34: Displacement of low-mineralized pore water by highly mineralized inlet water (acid mine drainage, amd) in a filter section with adsorbed uranylion. Between the original pore water (z_0,c_0) and the state in equilibrium with the inlet (amd z_3,c_2), a transitional or displacement front c_1 forms between z_1 and z_2. All states are in chemical equilibrium, so that the displacement appears as a square curve under the assumption of piston flow.

The results in the example Fig. 8.34, which is composed of three loading states, can be expressed as a polygon (rectangular curve) with the vertices (z_0,c_0); (z_1,c_0); (z_1,c_1); (z_2,c_2); (z_3,c_2) (with c_i as concentration vectors). The loading of the individual equilibrium phases is composed of the difference between the inlet and outlet, Eq.(8.3-33) and Eq.(8.3-34).

$$\vec{q}_{Zulauf} = \vec{c}_{Zulauf} \cdot z \tag{8.3-33}$$

$$\vec{q}_{ablauf} = \sum_{i=0}^{n-1} \vec{c}_i \cdot \left(z_{Di} - z_{Di+1}\right) \tag{8.3-34}$$

This results in the total load for the states i, under constant inflow composition. Eq.(8.3-35).

$$\vec{q}(i) = \vec{q}(z_0) + \vec{c}_{Zulauf} \cdot z_{Di} + \sum_{i=1}^{n} \vec{c}_{i-1} \cdot \left(z_{Di-1} - z_{Di}\right) \tag{8.3-35}$$

The specific mobilization is calculated from the area of the transition front minus the direct concentration transition. This corresponds to the area of the polygon above the z-axis. The loading in the example Fig. 8.34 is calculated up to i=3, Eq.(8.3-36).

$$\vec{q}(3) = \vec{q}(0) + \vec{c}_{Zulauf} \cdot z_3 + \vec{c}_0 \cdot (0 - z_1) + \vec{c}_1 \cdot (z_2 - z_1) + \vec{c}_2 \cdot (z_3 - z_2) \tag{8.3-36}$$

Between the states, the loads change linearly with regard to the phase ratio, e.g. The sum of all loads is constant, Eq.(8.3-37).

$$q(ads, max) = \sum_{X \in Komponenten} \nu_X \cdot q_X = const \tag{8.3-37}$$

If you combine for the jump i Eq.(8.3-8) with Eq.(2.2-15) the link between retardation and phase ratio is obtained, Eq.(8.3-38),

$$R_F(i) = \frac{v_f}{v_A(i)} = n_P + \rho_S \cdot \left(\frac{q(c_{i-1}) - q(c_i)}{(c_{i-1} - c_i)} \right) = \frac{H(i)}{L} = \rho_S \cdot z_{Di} \tag{8.3-38}$$

and for calculating the filter breakthrough after the flow section LF Eq.(8.3-39)

$$H_D = v_f \cdot t_D = R_F(i) \cdot L_F = \left(n_P + \rho_S \cdot \left(\frac{q(c_{i-1}) - q(c_i)}{(c_{i-1} - c_i)} \right) \right) \cdot L_F = \rho_S \cdot z_{Di} \cdot L_F \tag{8.3-39}$$

The quotient of load and concentration change is likely to be flawed in practical applications due to incomplete measurements and the idealization of the breakthrough curve.

8.3.3.2 Application example

During the flushing of power plant ash into a Pleistocene aquifer, neutral calcium sulphate-containing infiltrate displaced weakly acidic groundwater in a Pleistocene aquifer (KOCH & SCHÖPKE* 1996 und SCHÖPKE 2024). In the process, calcium displaced adsorbed cations at the solid matrix and formed a displacement front with a strongly increased iron concentration between the two water bodies, Fig. 8.35.

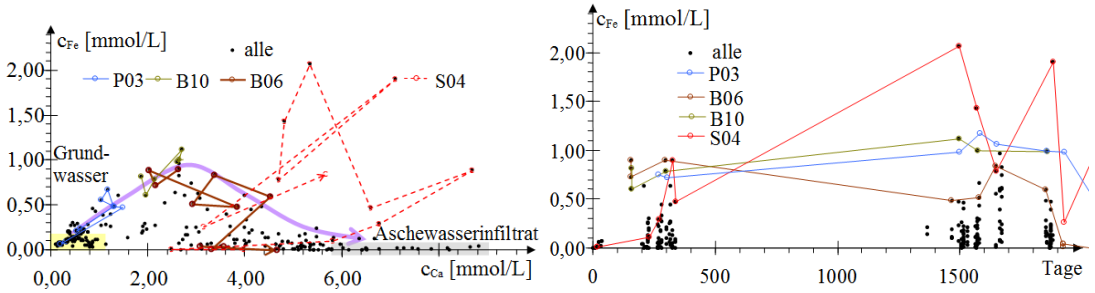

Fig. 8.35: Characteristics in the environment of ash water infiltration into a Pleistocene aquifer. Left: Iron and calcium concentration in the study area (alle) at selected measuring points (P03,B10,B06, S04). The displacement front of the groundwater (highlighted in yellow) by the infiltrate (Aschewasserinfiltrat, highlighted in grey) is characterised by increased iron concentrations. Right: Temporal courses of the iron concentration (days from 20.04.1991). The measuring point S04 has been flowed through several times with changing temperatures and thus shows an unusual course. The relationship determined by modelling can only be seen statistically in the courses of the marked measuring points (purple arrow, left).

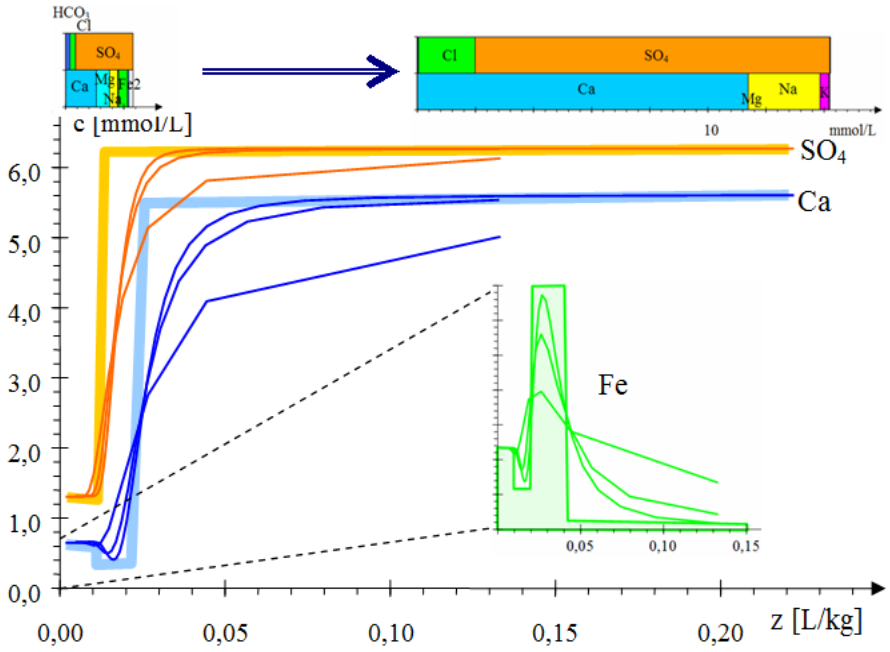

Fig. 8.36: Modelled displacement of groundwater in equilibrium with the Pleistocene solid matrix by neutral ash water as a function of the phase ratio z and the rectangular functions resulting for $D_L \rightarrow 0$. The breakthrough front of iron (green), which is also analogous to magnesium and manganese, is prominent.

The displacement process could not be fully observed at any measuring point. Rather, the analyses only showed momentary situations which, taken together, suggested a statistical distribution of concentrations in the displacement front.

The causal relationship only became apparent during modelling (SCHÖPKE & PREUß 2013 und SCHÖPKE* 2014). Sulfat is only slightly adsorbed and appears as a non-reactive tracer. The calcium breakthrough, on the other hand, is delayed. During the increase in calcium concentration, the concentrations of other cations, especially ferrous iron, temporarily increase.

In the representation of modelled iron and calcium concentrations, individual measuring points of the transition front can be classified.

8.3.4 Dual-porosity model

8.3.4.1 Numerical Simulation in PHREEQCx

PHREEQC offers an exchange of the mobile solution with dead spaces as *double porosity*, Fig. 8.37. The coupled dead spaces represent only diffusively accessible particle interiors (grain porosity) in which phase equilibria and/or irreversible reactions can be defined. With the discretization of the material flows via exchange steps between cell and dead volumes, modeling via PHREEQC is limited to individual cases in which the connection with the physical constants must first be established via adjustment calculations.

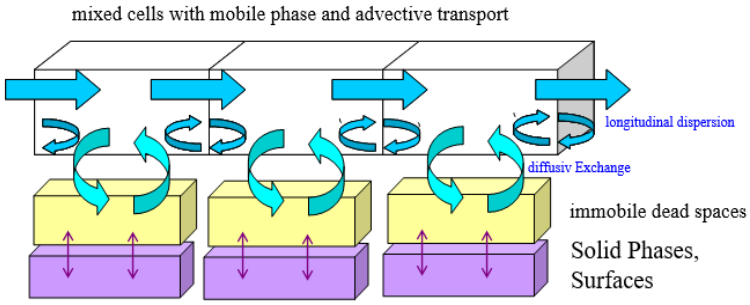

Fig. 8.37: Mixed-cell model with diffusively coupled dead spaces, surfaces and phases in PHREEQCx.

8.3.4.2 Transient diffusion profiles in dead spaces orthogonal to pore flow

In the transient observation of reactions in flow-through sandstone grains and fractures by means of *dual porosity*, the question of the interaction between the flowing pore solution (*bulk*) and the solution bound in the grain porosity arose (SCHÖPKE & KOCH* 2008). This problem is reduced to a flow-through cylindrical pore with a diameter d_P. Perpendicular to the direction of flow are diffusively coupled dead spaces with depth Δx, whose concentration profiles describe the flow path and time-dependent *penetration depth* of substances of the mobile pore solution into the porous stationary solid phase, Fig. 8.38.

The diffusively coupled dead space has its own porosity n_{PM}. If granular media are thus converted into a current tube (chapter 3.4.1), this diffusion layer should not exceed its grain radius (plausibility check). It is better to reduce the penetration depth to a fraction of the grain diameter, e.g. $\Delta x < 0{,}1 \cdot d_w$. There is an analytical solution for this problem, which has to be adapted to the respective boundary conditions, FigFig. 8.39.

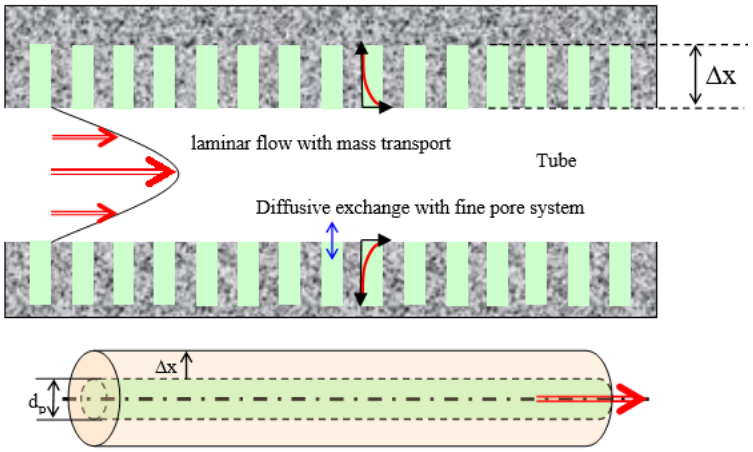

Fig. 8.38: Current tube with diffusively coupled finr pore system (dead space).

The concentration profile when diffusing into the dead space pore describes Fick's 2nd law, Eq.(8.3-40).

$$c(x) = 2 \cdot c_0 \cdot \left(1 - \operatorname{erf}\left(\frac{x}{\sqrt{2 \cdot D \cdot t}}\right)\right) \qquad u(x) = \frac{x}{\sqrt{2 \cdot D \cdot t}} \tag{8.3-40}$$

x is substituted by the function u(x), Eq.(8.3-41),

$$\operatorname{erf}(u) = \frac{2}{\sqrt{\pi}} \cdot \int_0^u e^{-u^2} \partial u \tag{8.3-41}$$

differentiated and used, Eq.(8.3-42) to Eq.(8.3-46).

$$\frac{\partial}{\partial u}(\operatorname{erf}(u)) = \frac{2}{\sqrt{\pi}} \cdot e^{-u^2} \tag{8.3-42}$$

$$\frac{\partial}{\partial x} u(x) = \frac{2}{\sqrt{2 \cdot D \cdot t}} \tag{8.3-43}$$

$$\frac{\partial}{\partial t} u(t) = -\frac{3}{2} \cdot \frac{x}{\sqrt{2 \cdot D}} \cdot t^{-3/2} \tag{8.3-44}$$

$$\frac{\partial}{\partial x}(\operatorname{erf}(u(x))) = \frac{2}{\sqrt{2\pi \cdot D \cdot t}} \cdot e^{-u^2} \tag{8.3-45}$$

$$\frac{\partial}{\partial t}(\operatorname{erf}(u)) = -\frac{3 \cdot x}{\sqrt{2 \cdot \pi \cdot D}} \cdot t^{-3/2} \cdot e^{-u^2} \tag{8.3-46}$$

The derivatives to x are converted into Eq.(8.3-40) is substituted by functions of u, Eq.(8.3-47) to Eq.(8.3-49).

1.Derivation of

$$\frac{\partial}{\partial x}(c(x)) = -c_0 \cdot \frac{4}{\sqrt{2 \cdot \pi \cdot D \cdot t}} \cdot e^{-u^2} \tag{8.3-47}$$

2.Derivative to x:

$$\frac{\partial^2}{\partial x^2} c(x) = -c_0 \cdot \frac{4}{\sqrt{2 \cdot \pi \cdot D \cdot t}} \cdot (-2u) \cdot \frac{1}{\sqrt{2 \cdot D \cdot t}} \cdot e^{-u^2} \tag{8.3-48}$$

$$\frac{\partial^2}{\partial x^2} c(x) = c_0 \cdot \frac{4x}{\sqrt{2 \cdot \pi}} \cdot (D \cdot t)^{-3/2} \cdot e^{-u^2} \tag{8.3-49}$$

1.Derivation according to t:

$$\frac{\partial}{\partial t} c(t) = c_0 \cdot \frac{6 \cdot x}{\sqrt{2 \cdot \pi \cdot D}} \cdot t^{-3/2} \cdot e^{-u^2} \tag{8.3-50}$$

This is followed by the insertion into diffusion equation, Eq.(8.3-50) Eq.(8.3-51).

$$\frac{\partial}{\partial t} c(x,t) = D \frac{\partial^2}{\partial t^2} c(x,t) \tag{8.3-51}$$

$$\frac{6}{\sqrt{2 \cdot \pi}} = \frac{4}{\sqrt{2 \cdot \pi}} \tag{8.3-52}$$

After solving the boundary value problems:

x=0 => $c=c_0$

x->00 => $c=c_1$

the function for the time-dependent concentration profile is obtained, Eq.(8.3-53).

$$c(x,t) = c_0 + 2 \cdot (c_1 - c_0) \cdot \operatorname{erf}\left(\frac{x}{\sqrt{2 \cdot D \cdot t}} \right) \tag{8.3-53}$$

From this, the diffusion velocity Eq.(8.3-54) or Eq.(8.3-55),

$$j = D \cdot \frac{\partial}{\partial x} (c(x,t)) = (c_1 - c_0) \cdot \frac{2D}{\sqrt{2\pi \cdot D \cdot t}} \cdot \exp\left(-\left(\frac{x}{\sqrt{2 \cdot D \cdot t}} \right)^2 \right) \tag{8.3-54}$$

$$j = (c_1 - c_0) \cdot \sqrt{\frac{2 \cdot D}{\pi \cdot t}} \cdot \exp\left(-\left(\frac{x}{\sqrt{2 \cdot D \cdot t}} \right)^2 \right) \tag{8.3-55}$$

and converted for the calculation with EXCEL, Eq.(8.3-56).

$$j = (c_1 - c_0) \cdot 2 \cdot D \cdot \mathrm{NORM.VERT}(x;0;\sigma;0) \tag{8.3-56}$$

For the pore opening to the mobile phase x=0, Eq.(8.3-57).

$$j(x=0) = (c_1 - c_0) \cdot \sqrt{\frac{2 \cdot D}{\pi \cdot t}} \tag{8.3-57}$$

With Eq.(8.3-57) the temporal decrease of diffusion from a layer under constant conditions can be described.

Diffusive replenishment from the solution of a porous particle.

The depth of penetration is defined as x(by α less flow)

$$\alpha = \frac{j(x_\alpha)}{j(x=0)} \tag{8.3-58}$$

so that

$$\alpha = \frac{(c_1 - c_0)\cdot\frac{2D}{\sqrt{2\pi\cdot D\cdot t}}\cdot\exp\left(-\left(\frac{x_\alpha}{\sqrt{2\cdot D\cdot t}}\right)^2\right)}{(c_1 - c_0)\cdot\sqrt{\frac{2\cdot D}{\pi\cdot t}}} \tag{8.3-59}$$

and

$$\alpha = \exp\left(-\left(\frac{x_\alpha}{\sqrt{2\cdot D\cdot t_\alpha}}\right)^2\right) \tag{8.3-60}$$

and vice versa, the penetration depth is calculated for given α and t_α.

$$x_\alpha = \sqrt{-2\cdot D\cdot t_\alpha\cdot\ln\alpha} \tag{8.3-61}$$

The penetration velocity decreases with the square root of time, Eq.(8.3-62).

$$v_\alpha = \sqrt{\frac{-2\cdot D\cdot\ln\alpha}{t_\alpha}} \tag{8.3-62}$$

Fig. 8.39 illustrates an application.

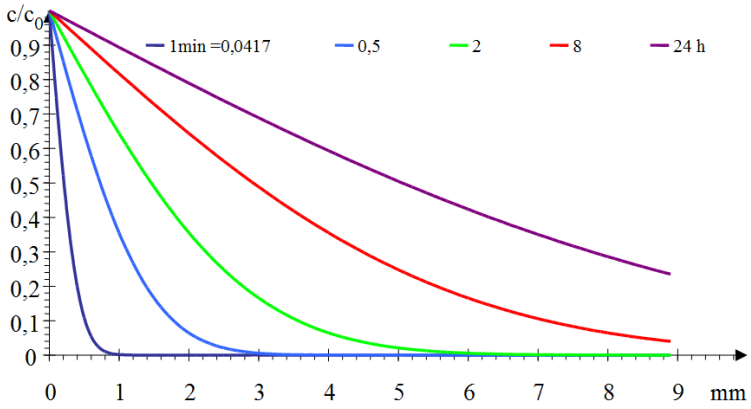

Fig. 8.39: Indentation profiles for D = $6.5\cdot10^{-10}$ m^2/s and different diffusion times [h].

8.3.4.3 Filtration parameters FP for stationary conditions in heterogeneous flow sections

Stationary concentration profiles based on surface reactions can be described by the filtration parameter FP, Eq.(3.3-23). A flow section is considered that is composed of

differently permeable current tubes with the same potential gradient (h_f/L). Each of these current tubes forms its own concentration profile depending on FP. From the volume of a current tube Eq.(4.1-10) and their surface Eq.(4.1-9) the respective filtration parameter FP, Eq.(8.3-63).

$$FP = \frac{1}{v_A} \cdot \frac{L \cdot \pi \cdot d_P}{L \cdot \frac{\pi}{4} \cdot d_P^2} \cdot L = \frac{4}{v_A \cdot d_P} \cdot L \tag{8.3-63}$$

And about Eq.(3.5-15) a relationship to h_f, Eq.(8.3-64),

$$FP = 72 \cdot \frac{8}{3} \cdot \frac{\nu \cdot f_L^2}{g} \cdot \frac{L^2}{h_f \cdot d_P^3} \tag{8.3-64}$$

and switched to the flow path Eq.(8.3-65),

$$L = \sqrt{\frac{FP}{\left(72 \cdot \frac{8}{3} \cdot \frac{\nu \cdot f_L^2}{g}\right)} \cdot h_f \cdot d_P^3} \tag{8.3-65}$$

or as a working equation for 10°C (SCHÖPKE 2008), Eq.(8.3-66).

$$L = \sqrt{0{,}141 \cdot \frac{FP}{h/m} \cdot \frac{h_f}{m} \cdot \frac{d_P^3}{mm^3} \cdot \frac{1}{f_L^2} \cdot m^2} \tag{8.3-66}$$

For the same flow path L, the filtration parameter depends on the cylinder pore diameter assigned to the respective current tube, Eq.(8.3-67).

$$FP = 192 \cdot \frac{\nu \cdot f_L^2}{g} \cdot \frac{L^2}{h_f \cdot d_P^3} \cdot \tag{8.3-67}$$

This means that the flow path for the same surface reaction progress increases with the power 1.5 of the pore diameter.

$$L(FP) = \text{const} \cdot d_P^{\frac{3}{2}} \tag{8.3-68}$$

For the evaluation, the cross-section distributions as a function of the porediameter must be taken into account. With Eq.(8.3-67) and Eq.(8.3-68) the results of defined experimental filters can be transferred to flow sections of heterogeneous current tubes, SCHÖPKE (2008).

9 Parameter determination

9.1 Mathematical methods of data evaluation

9.1.1 Bilanzierung über integrale Outputfunktionen

In the cumulative (integral) *output* function, e.g. the amount of substance n(H), statistical fluctuations, such as measurement errors, are smoothed out, Eq.(2.2-12). Concentration peaks appear integrally as a jump *smeared* by the dispersion D and constant concentration curves as straight line sections depending on the water column H, Eq.(2.2-4) The respective slope corresponds to their concentration, Fig. 9.11.

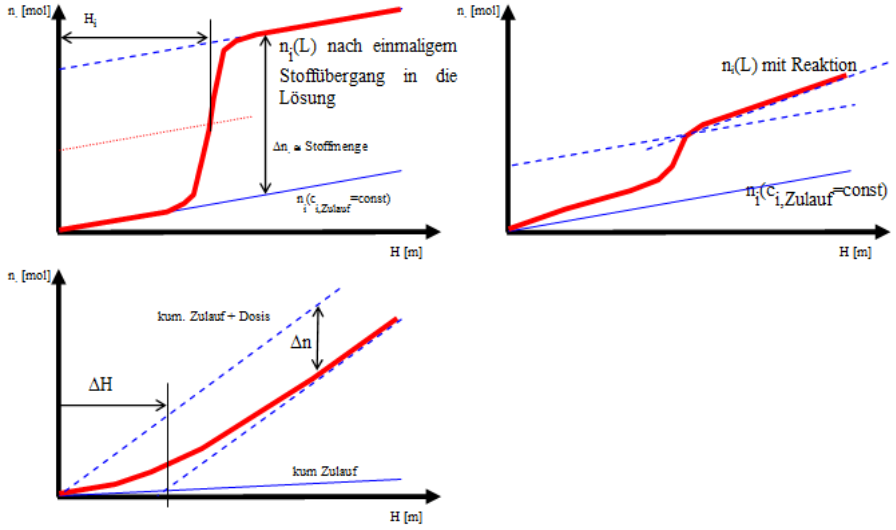

Fig. 9.11: Cumulative amount of substance ni as a function of the water column H flowing through it during the mobilization of substances (top) and when a conservative tracer breaks through (bottom).

Mass storage becomes visible when the input concentration changes, because the change appears in the output system with a delay. The storage takes place

- in the pore solution as porosity n_P and
- reactive, e.g. by (reversible) sorption, solution or precipitation,

and can be determined via curve discussion, Eq.(8.3-5).

Reactions usually lead to a constant change in the output nature. Individual components can provide indications of stoichiometric ratios.

9.1.2 Frequency evaluations

9.1.2.1 Method

To determine a frequency distribution, the measured values are divided into classes of a selected criterion. The root of the sample size provides an initial orientation for the optimal number of classes. However, it is recommended to check different class classifications. As the number of classes increases, the distinction between frequencies increases, but with increasing statistical noise.

The absolute frequencies of the measured values belonging to these classes are cumulated in ascending order and the *sum frequency function is* constructed from this (chapter 2.3.5.2). The first derivative according to the criterion represents the *frequency density* ρ(x) Eq.(2.3-31) which is normalized to the maximum distribution $\rho_{norm}(x)$, Eq.(9.1-1) The normalized density has a dimension of 1, in contrast to the often cumbersome dimension resulting from data evaluation.

$$\rho_{norm}(x) = \frac{\rho(x)}{\max(\rho)} \tag{9.1-1}$$

Only after superimposing the density functions of different class divisions do the essential properties of the investigated parameter collective become clearer, frequency density distributions composed of individual normal distributions can be mathematically separated into them, chapter 9.1.2.2.

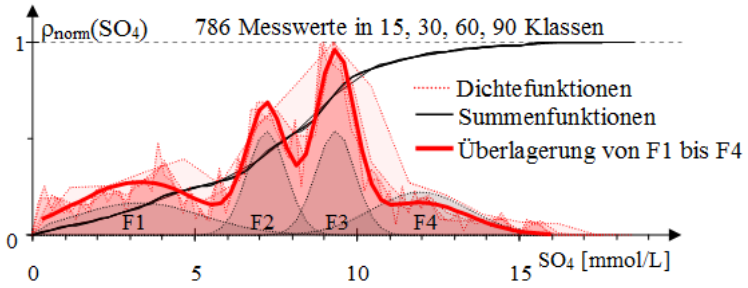

F1	F2	F3	F4	R²	KRT	Schritt
3,30±1,95	7,20±0,61	9,30±0,61	11,9±1,46	0,917	7,7%	0,1

Fig. 9.12: Superposition of density functions of all sulphate concentrations of a groundwater body (SCHÖPKE et al. 2020), which were determined with different class classifications (red areas). While all sum frequency curves run almost on top of each other, the density functions show at least four groupings. The density function of 60 classes has been adapted to four overlapping Gaussian functions (gray areas F1 to F4).

9.1.2.2 Statistical identification of phase equilibria

If the largely variable nature of a water body is limited by a phase equilibrium, the frequency distribution of the saturation indices breaks off above the saturation (*breaking edge*) or a frequency maximum around the saturation equilibrium is observed. Unaccounted for and unknown influences often shift the observed saturation compared to the thermodynamically justified value by ΔSI, Fig. 9.13. The variation around the saturation is at least equal to the value derived from the analysis errors $\pm\sigma_{Analysenfehler}$ (analysis error) in the form of a Gaussian distribution, chapter 2.3.3.3 The values around SI = 0 ± ΔSI are in the saturation equilibrium. Their dispersion should be greater than the estimated analysis error, Fig. 9.13. In the undersaturated, distributions transformed from the nature statistics often appear that have no further meaning.

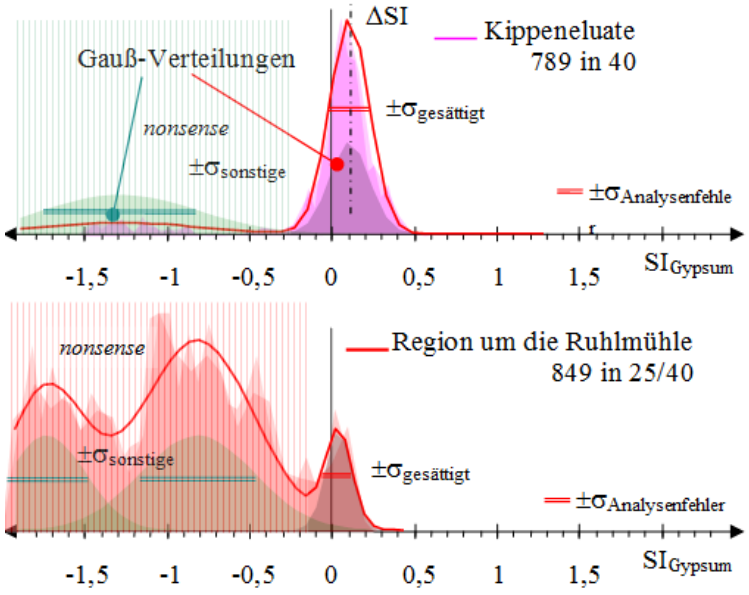

Fig. 9.13: Frequency distributions of gypsum saturations SI_{Gypsum} for acidic dump eluates (top) and a mining-influenced groundwater body with adapted Gaussian distributions ΔSI, $\sigma_{saturated}$ of the saturation maximum, the analytical error $\sigma_{Analysenfehler}$ and *barred* non-relevant distributions (SCHÖPKE et al. 2020). The determined distributions can be represented from the sum of the elementary Gaussian distributions highlighted in gray or green.

9.1.3 Algorithm for Fitting to Sums of Nonlinear Models

Measured and simulated quantities y, which are composed of the sum of many individual effects, can often be described by a linear system of equations whose elements are linked to nonlinear process or state variables. Significant correlations can then be recorded via a linear multiple regression with a regression coefficient that tends towards one if possible, Eq.(9.1-2).

$$y = A \cdot f(x_1) + B \cdot f(x_2) + C \cdot f(x_3) + ... \left| R^2 \rightarrow 1 \right. \tag{9.1-2}$$

For individual problems, the respective coefficients are usually marked with the capital letters A, B, ... may refer to:.

SCHÖPKE (2007) proposed a two-step fitting algorithm with indexed $f_i(x,x_{m,i}, const_i)$ approach functions with the corresponding constant sets $x_{m,i}$, consti, Eq.(9.1-3) A starting mixture is described by the concentrations of its n (pseudo-) components, summarized in the column vector $\vec{c}_0$. The measured value y of the sum parameter is composed of the sum of the components c_{0i} (measured with this sum parameter). For arbitrary mixtures, their contributions to the total measured value are described by the approach functions f_i, Eq.(9.1-3).

$$y(x) = \sum_{i=1}^{n} c_{0,i} \cdot f_i(x, x_m, const_i) \tag{9.1-3}$$

For the source mix selected as a reference, all functions $f_i()$ have a value of one. If one considers the changes in defined reactions in the mixture, e.g. by adsorption as a

function of the adsorbent dose x, the approach functions can be calculated using a mostly nonlinear process model.

In order to adapt the model via the regression approach, there must then be more data sets (m) than approach functions. The system of equations overdetermined from m > n equations is solved by minimizing the squares of error, i.e. a linear multiple regression.

The measured values y_j are summarized in the column vector consisting of m rows $\vec{y}$. The regression approach is described by the vector product Eq.(9.1-4).

$$\vec{y} = \underline{G} \times \vec{c} \tag{9.1-4}$$

The approach functions $f(x_i)$ calculated from the model form the coefficient matrix $\underline{G}$, Eq.(9.1-5).

$$\begin{array}{lcl} \text{Spaltenvektor der Pseudokomponenten} & \vec{c} & = \left(c_1, \ldots c_i \ldots c_n\right)^T \\ \text{Spaltenvektor der Messwerte} & \vec{y} & = \left(y_1, \ldots y_j, \ldots y_m\right)^T \\ \text{Matrix der Ansatzfunktionen} & \underline{G} & = \begin{pmatrix} f_{1,1} & . & f_{n,1} \\ . & f_{i,j} & . \\ f_{1,m} & . & f_{n,m} \end{pmatrix} \end{array} \tag{9.1-5}$$

The column vector of the initial concentrations $\vec{c}_0$ is the result of the regression-analysis, Eq.(9.1-4) The regression coefficient R^2 indicates the degree of agreement of the given model with the experimental data. The calculated initial concentrations $c_{i.0}$ are assigned their standard deviations $\sigma_{0,i}$ from the inverted regression matrix. The calculated relative errors of the pseudocomponent concentrationsare much more sensitive to the accuracy of the fitting. From this, the adjustment criterion KRT is derived, which corresponds to the mean value of the relative errors, Eq.(9.1-6).

$$\mathrm{KRT} = \left(\frac{1}{n} \sum_{i=1}^{n} \frac{\sigma_i}{c_i} \right) \rightarrow \min \tag{9.1-6}$$

In the following nonlinear adjustment steps, all constant sets are varied to the best match with the given function y(x), where the regression coefficients $c_{0,i}$ indicate the respective share of the function $f_i(x, \mathrm{consti})$ in the value y(x) for the entire range of values. The optimization of the constant sets for $R^2 \rightarrow 1$ often results in implausible progressions of the selected approach functions, e.g. alternating positive and negative c0,i. Therefore, the non-linear adjustment steps are carried out manually under graphical control and minimization of the adjustment criterion KRT. Changing the value pairs (xm, const) in discrete steps has proven to be effective. The step size *step* is adapted to the respective concentration curves.

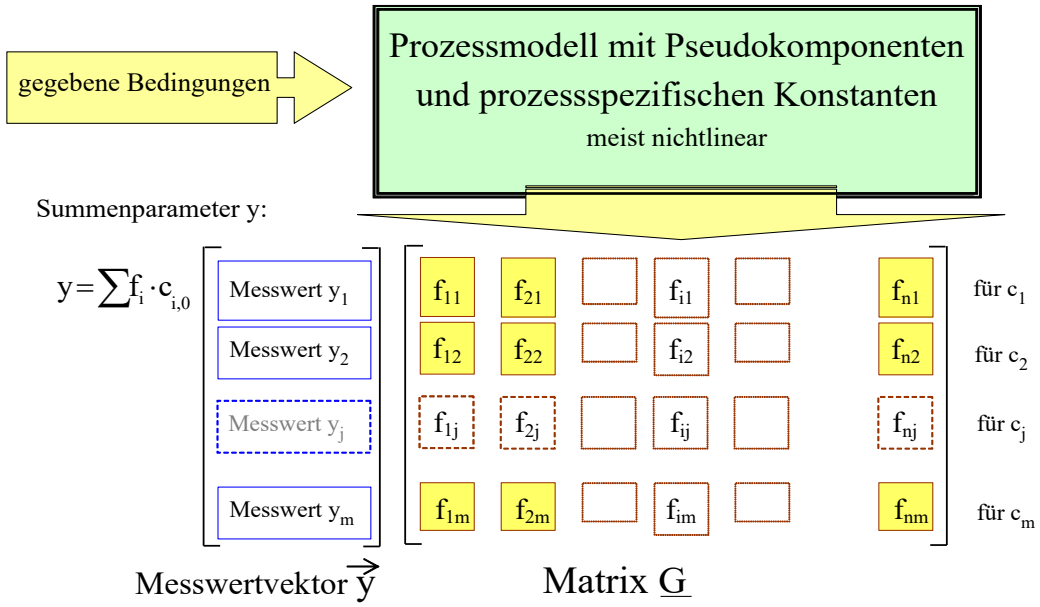

Fig. 9.14: Linear Process Model with Nonlinear Approach Functions.

For this adaptation, an EXCEL spreadsheet was developed for a maximum of 10 different approach functions and a maximum of 10000 records y(x, const). Optionally, an absolute term can also be admitted.

Sometimes there is an implausible result (e.g. with negative concentrations) at a local minimum. Therefore, automating the nonlinear adjustment stage is not advisable. The graphical comparison between the measurement data and the modeled data is used to check the plausibility of the adjustment results during the optimization process. This procedure can be applied to a whole range of problems, Tab. 9.11.

Tab. 9.11: Approach functions for determining pseudo-components and process parameters and references to their applications. The boolean variable wf determines whether the Gaussian distribution (wf = false) or its integral (wf = true) is output.

Anwendung	y	x	const	Ansatzfunktionen $f_i(x)$	chapter.
Häufigkeitsverteilungen	$y_{0,i}$	x	σ_x	$\mathrm{NORM.VERT}\left(x; x_m; \left(\sigma_{x,\mathrm{Excel}}\right); \mathrm{falsch}\right)$	9.1.2
Häufigkeitssumme	$y_{0,i}$	x	σ_x	$\mathrm{NORM.VERT}\left(x; x_m; \left(\sigma_{x,\mathrm{Excel}}\right); \mathrm{wahr}\right)$	
Frontendurchbruch	$y_{0,i}$	t	σ_t	$\mathrm{NORM.VERT}\left(t; t_0; \left(\sigma_{t,\mathrm{Excel}} \cdot \sqrt{t}\right); \mathrm{wahr}\right)$	9.7
Sauerstoffzehrung	BSB_i	t	λ	$\left(e^{-\lambda_i t} - 1\right)$	9.4.2
Titration	c_S	pH	K_S	$1/\left(1 + 10^{(K_{Si} - pH)}\right)$	9.5.1
Elementarspektren	$E_{max,i}$	λ	λ	$\exp\left(-\mathrm{diff}_i^2 \cdot \left(\frac{\lambda_{max,i}}{\lambda} - 1\right)^2\right)$	9.6.2
Sigmoid	$y_{0,i}$	x_m	K	$1 \Big/ \left(\exp\left(\frac{(x - x_m)}{K_i}\right) + 1\right)$	
Sinusperiode	y_i	x_m		$\sin\left(2\pi \cdot (x - x_m)\right) + 1$	9.5.3
Exponentiell	y_i	t, x	λ	$e^{-\lambda_i t}$	

9.2 Experimental recording of screening parameters

9.2.1 Selection of hydraulic data

Aus zuverlässigen Wertepaaren (h_f/v_f, H) von Siebprozessen lassen sich über grafische oder numerische Auswertungsverfahren die den Siebprozess beschreibenden Größen (H, h_f/v_f) ermitteln, chapter 5.3. Vorher müssen diese Daten mit möglichst geringem Aufwand und hoher Repräsentanz ermittelt werden.

Häufig ist eine kombinierte Vorgehensweise von Vorteil:

- Auswertung von Daten vorhandener Anlagen.
- Häufige Durchführung von Vor-Ort-Tests über eine längere Zeitspanne und statistische Bearbeitung des gewonnenen Datenmaterials (KOCH et al. 2002).
- Durchführung von kleintechnischen Versuchen oder Betrieb von Pilotanlagen mit einer repräsentativen Rohwasserqualität.

Durch die längerfristig angelegten Tests ist eine statistische Bewertung der aufwendigen Versuche möglich, bei denen nicht alle möglichen Rohwasserzustände erfasst wurden, chapter 5.3.4.

9.2.2 Filter test

9.2.2.1 Experimental set-up

This test was further developed from the filter test according to THIELKE (1972), which assumes an exponential increase in filter resistance. This rapid test is used to determine the colmation point HK of the current water condition for specified mesh sizes or grain sizes. The test is frequent and can be carried out with little effort compared to small-scale experiments. The colmation coefficient γ can only be determined with little certainty.

The apparatus consists of a calibrated clear 1 inch tube with a test sieve or a test filter before the drain and accessories, Fig. 9.21. This allows the filter resistance-flow rate behavior to be determined in a wide range of permeability.

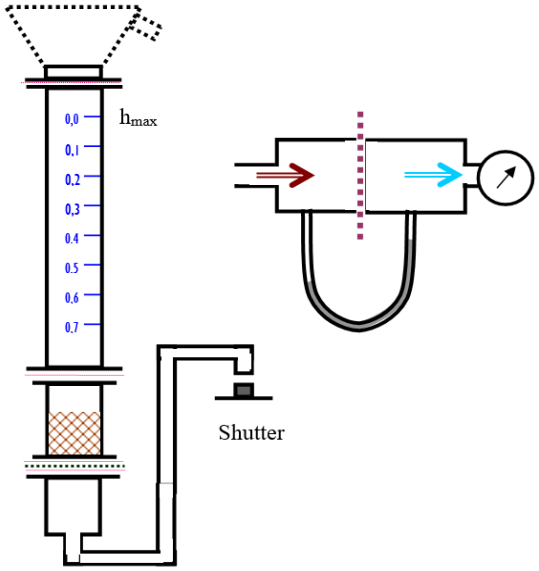

Fig. 9.21: Experimental set-up of the sieve/filter test, KOCH et al. (2002).

9.2.2.2 Experimental Procedure

In the test filter, narrowly classified filter sands, glass beads or even original filter materials are filled without air bubbles. It must be taken into account that even in the case of narrowly classified test sands, there is a risk of classification during filling. Fine-grained layers can be removed by careful stirring or suction. An equivalent mesh size of $d_S \approx d_w/5$ is assumed for the filter materials. The measuring range of screens can be adjusted by using suitable cross-sectional surfaces (mask).

- Before the measurements, the water level h_{max} is determined with clear water when the overflow is open and then the drain is closed.
- The apparatus is filled up to the 0 mark with well-mixed sample water.
- After the drain has been released, the lowering of the water level is measured, also possible with computer support.

Tab. 9.21: Example of a Measurement Protocol of the Sieve/Filter Test.

H m	t s	Note
0,050	2	Timekeeping at the marks
0,100	11	
0,150	21	
0,200	34	
0,232	60	H-measurement at specific times
0,241	90	
0,262	210	

The measurement is adapted to the respective situation.

If the colmation point is not reached, a defined amount of sample water should be refilled. The added volume is logged and charged as an additional water column during the evaluation.

- Extension of the measuring range

The h_f/v_f behavior is determined in the described way only when the flow is open. In the case of coarse sieves and filter materials, the initial values are disturbed by turbulent conditions and it is advisable to discard these measurements.

Sample water is refilled until a measurable colmation effect occurs.

In the case of fast throughput, the drain can be used throttled with the firmly attached hopper as a storage container. Under no circumstances should the screened material be stirred up.

The quantities of water added must be accurately balanced. For very long tests with a throughput of a few 10 litres, it is advisable to collect the run-off water in a calibrated bucket. In between, the hf/vf behavior is determined several times. As the throughput decreases, the measurement accuracy must be gradually increased.

9.2.3 Experimental set-ups for small-scale tests

Investigations with variable filtration velocity can also be carried out on small-scale filter systems. The test arrangements described above are also suitable for investigating quality and other processengineering problems. The filter hydraulics are only one aspect of the test execution.

For investigations on the infiltration of road surface water, e.g. by KOCH et al. (2002), liners were used for the extraction of drill cores from soft rock aquifers and converted into experimental filters. At the outlet there is a so-called liner end cap with a sieve plate that prevents the discharge of material.

Tab. 9.22: Dimensions of Test Filters from Drill Core Liners (KOCH et al. 2002).

Inner diameter	1,05	dm
Cross-sectional area	0,87	dm^2
Length	10,00	dm
Recommended layer length of the material	8,00	dm
Bed volume	6,93	dm^3

It follows from this:

1 m water column	are	8,66 L	Water	or
1 L Water	are	115 mm	Water column	

The effluent level must be above the top edge of the fill in order to prevent the apparatus from running dry.

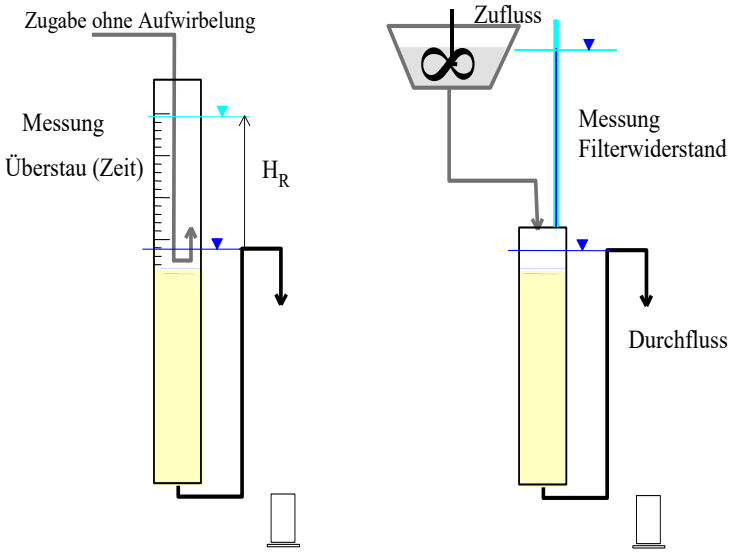

Fig. 9.22: Test Arrangements for Filter Tests with Low Concentration of Sievable Substances.

The tests can be operated as an open filter or as a pressure filter.

- In the case of a variable overflow (open arrangement) and discontinuous addition, the filter velocity and colmation resistance are determined directly from the overflow height-time behavior. Turbulence at the colmation layer can have a disadvantageous effect.
- In the case of a closed arrangement, flow and pressure loss must be measured separately. On the other hand, larger flows are achieved at higher congestion.

Both driving styles can also be combined with each other. In the case of infiltration basins with impoundment heights of more than 0.5 m, the pool water levels and the amount of water applied can also be evaluated.

9.2.4 Evaluation

9.2.4.1 Evaluation of the filter test at constant filter resistance

The filter test developed by LÖFFLER (1969) for the preparation of groundwater recharge systems measures the decrease in filtration velocity under constant filter resistance. Temperature fluctuations during the runtime must be taken into account via the viscosity. From Eq.(5.3-2) follows for the parameter H_K, Eq.(9.2-1).

$$v_f = v_{f0} \cdot \exp\left(-\frac{v_{f0}}{H_K}\right) \tag{9.2-1}$$

This relationship given by LÖFFLER (1969) follows from the equation of determination of the invasion phase after the separation of the sieve zone length L_{SB} from the total filter length L, Eq.(9.2-2):

$$\frac{h_f}{v_f} = \frac{L_{SB}}{k_f \cdot \left(1 - \frac{H}{H_K}\right)} + \frac{L - L_{SB}}{k_f} = \frac{1}{k_f} \cdot \left(\frac{L_{SB}}{\left(1 - \frac{H}{H_K}\right)} + L - L_{SB} \right) \tag{9.2-2}$$

The L_{SB} calculated by the hydraulics are usually larger than the penetration depths determined visually or from the filter pressure diagrams and can be simplified, Eq.(9.2-3) to Eq.(9.2-5).

$$\frac{h_f}{v_f} = A + \frac{B}{1 - H/H_K} \tag{9.2-3}$$

with

$$A \approx \frac{L - L_{SB}}{k_f} \tag{9.2-4}$$

and

$$B \approx \frac{L_{SB}}{k_f} \tag{9.2-5}$$

and $H < 0.8 \cdot H_K$

9.2.4.2 Evaluation of the colmation at variable water level

Between the screen resistance and the water level in the measuring tube H_R, Eq.(9.2-6),

$$h_S = h_{max} - H_R \tag{9.2-6}$$

or Eq.(9.2-7),

$$\frac{v_f}{h_f} = \frac{\frac{\partial H_R}{\partial t}}{h_{max} - H_R} = -\frac{\partial}{\partial t} \ln\left(h_{max} - H_R\right) \tag{9.2-7}$$

and simplifies Eq.(9.2-8).

$$\frac{v_f}{h_f} \approx -\frac{\Delta \ln\left(h_{max} - H_R\right)}{\Delta t} \tag{9.2-8}$$

The h_f/v_f are formed from the sinking of the water column in the apparatus Fig. 9.21 and assigned the corresponding H from the balancing of the water column flowing through it, Eq.(9.2-8).

9.2.4.3 Filter test for the determination of the SDI index according to D 4189-95 (2002)

The SDI = Sludge Density Index was developed for particulate material in water with turbidity Tr < 1.0 NTU (test D 1129). The indices determined by this method are not compatible with the theoretical description presented here.

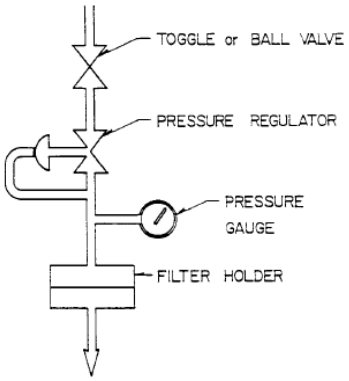

Fig. 9.23: Apparatus for measuring the SDI index.

9.3 Determination of the gas-phase equilibrium during aeration and subsequent investigation of homogeneous ferrous-iron oxidation kinetics

9.3.1 Test principle

The gas-phase equilibrium is set with a defined gas volume after sampling. Pressure and temperature correspond to the sampling ratios. By varying the phase ratio z, conditions between pressure ventilation (low air/water ratio) and an intensive stripping process (high air surplus) can be simulated. The parameters typical of equilibrium (pH, CO_2, O_2 and other volatile constituents) must be determined before and after equilibrium adjustment. The determined phase equilibria are compared with model calculations. The ferrous-iron oxidation kinetics can then be followed for several hours, ZAHN (2020).

9.3.2 Experimental apparatus and adjustment of the gas-phase equilibrium

Two laboratory glass bottles are connected to a T-piece via a screw thread. Two taps are attached to these connectors, from each of which a hose reaches into the bottles for sampling. The calibrated water bottles are filled with the sample water up to overflow and connected to the air bottle (volume known) via the T-piece. The empty cylinders must be blown out with (compressed) air or, if necessary, with a defined gas mixture before the start of the test.

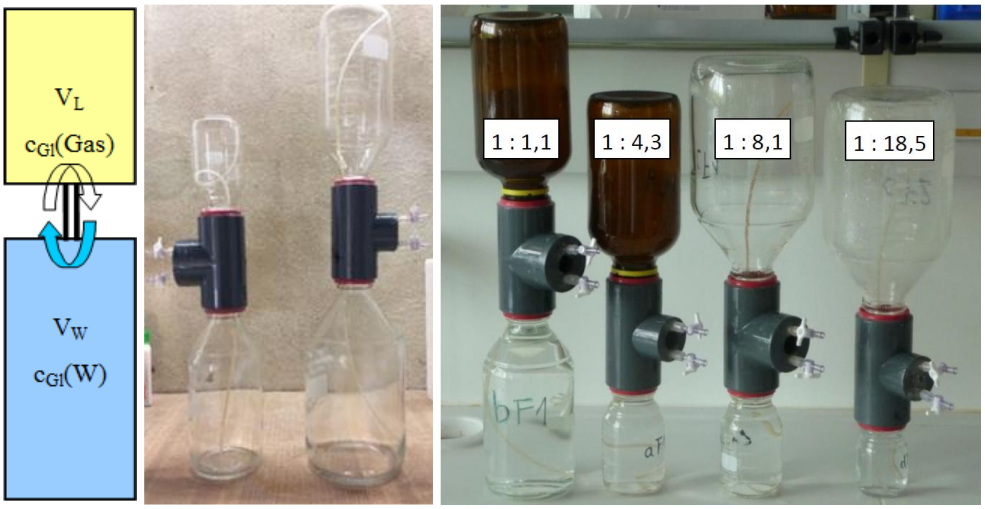

Fig. 9.31: Test configurations with different water-to-air ratios.

The phase equilibrium is adjusted by turning the apparatus over about 20 times, during which the water content changes the bottle. The temperature should not change as much as possible. After the first opening of the apparatus, e.g. for a pH measurement, the experiment can no longer be continued.

9.3.3 Tracking ferrous iron Oxidation

In roughly staggered time steps, small volumes are taken from the sample tubes for photometric ferrous iron determination, if necessary, turbidity must be taken into account. After completion of the experiment, at least pH value, oxygen, RedOx potential, $K_{S4.3}$ are determined after opening the bottle. In addition, the carbonic acid buffering can also be checked via the TIC (avoiding outgassing). A representative full analysis of the sample water should be available for each sample water. With well-buffered water and low ferrous iron concentrations, stable pH conditions can be expected. Otherwise, the changes in the chemistry (pH, hydrogen carbonate) must be interpolated between the initial and final state with the help of geochemical simulation.

9.3.4 Evaluation

By combining bottles of different sizes, different water-air phase ratios z can be set (Fig. 9.31). The simulated effect can be compared with the technical performance parameters of the plants. The boundary conditions used only serve as orientation. The required discharge effect or efficiency E [1, %] is used to determine the required efficiency of mechanical deacidification, Eq.(9.3-1).

$$E(z) = \frac{c_0 - c_E}{c_0} \tag{9.3-1}$$

In aerated, well-buffered groundwater, the oxidation reaction generally proceeds according to pseudo-first-order Eq. (9.3-2) if there is sufficient excess oxygen (>1mg/L).

$$\frac{\partial c_{Fe^{2+}}}{\partial t} = k_{Feox} \cdot c_{Fe^{2+}} \tag{9.3-2}$$

The observed oxidation rate depends on other factors:

- The reaction product ferric hydroxide, which initially precipitated colloidally, catalyzes oxidation heterogeneously.
- Inorganic and organic chelating agents (e.g. humic substances) delay the oxidation reaction.
- In the case of insufficiently buffered water, oxidation can practically come to a standstill after pH value drop.

The reactions (pseudo) of the first order are described in Eq.(9.3-3).

$$c_t = c_0 \cdot \exp(\lambda \cdot t) \tag{9.3-3}$$

All other influencing variables are contained in the coefficient λ, including the temperature function with the activation energy E_A, Eq.(9.3-4).

$$\lg\left(\zeta_{Temp0}(Temp1)\right) = \frac{1}{\ln(10)} \cdot \frac{E_A}{R}\left(\frac{1}{(Temp0 + 273{,}15)} - \frac{1}{(Temp1 + 273{,}15)}\right) \tag{9.3-4}$$

Taking into account pH value, temperature and oxygen concentration, the regression approach Eq.(9.3-5) .

$$\log(\lambda) = const + A_{pH} \cdot pH - B \cdot \left(\frac{1}{(298{,}15)} - \frac{1}{(Temp1 + 273{,}15)}\right) + C \cdot \log(c_{O2}) \tag{9.3-5}$$

The determined reaction rates often deviate from the theoretical specifications.

9.4 Determination of watertreatment-related substances WWR

9.4.1 Consumption experiments derived from the test filter principle

For the testing of water for biodegradability, GIMBEL et al. (1996) developed an apparatus- and time-consuming test filter methodology that represents a model representation of a ground passage. Alternatively, a sample that has been depleted for the determination of the biochemical oxygen demand (BSB_t) is proposed here as relevant to the waterworks, Fig. 9.41. After a correspondingly long treatment time in the integrated test filter, the waterworks-relevant substances remain in the circulating water.

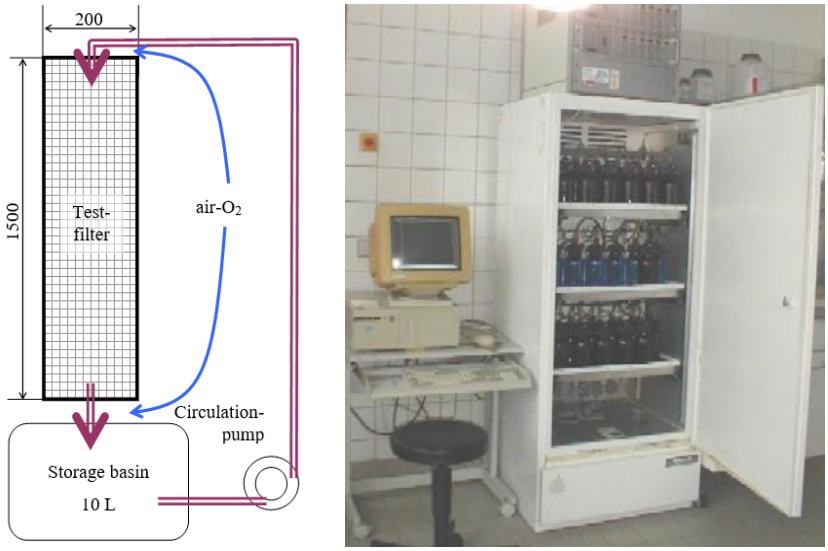

Fig. 9.41: Principle of a circulating filter system as a test filter (left) and long-term consuming apparatus with an open thermostat (Sapromat).

In principle, all apparatus with which the biodegradable substances can be separated from a sample water should be suitable for determining substances relevant to the watertreatment (SCHÖPKE 2007). For example, equipment for continuously measuring the depletion behavior of water samples can also be used for this purpose. In contrast to the test filters, there is not always an incorporated biomass, so that lag phases and successive degradation stages can determine the process of consumption. In wastewater technology, the consumption of the biomass and inorganic substances formed (NH_3, H_2S) is prevented by suitable measures or an inoculum is added to accelerate the depletion. These measures must be critically questioned if the substances relevant to the waterworks are also to be determined from the depleted samples.

9.4.2 Adaptation of oxygen consumption to a sum of individual reactions

HOBBY & GIMBEL (1988) described the degradation kinetics in the cycle according to a 1st order time law. SCHOENHEINZ & WORCH (2005) extended this approach to several overlapping pseudo-components, Eq.(9.4-1) for three components.

$$c(t) = c_{01} e^{-\lambda_1 t} + c_{02} e^{-\lambda_2 t} + c_{03} \tag{9.4-1}$$

The residual concentration of organic substances c_{03} corresponds to the watertreatment-relevant substances WWR. Integrated follows BOD(t) for oxygen depletion Eq.(9.4-2).

$$BSB(t) = BSB_1 \left(e^{-\lambda_1 t} - 1\right) + BSB_2 \left(e^{-\lambda_2 t} - 1\right) \tag{9.4-2}$$

The biochemical processes can also be delayed one after the other. This is taken into account by the lag times t_{0i}. The exponential initial phase is not taken into account, Eq.(9.4-3) for consuming components.

$$BSB(t) = \sum_i BSB_{0i} \begin{cases} t > t_{i0} & \left(e^{-\lambda i \cdot (t - t_{0i})} - 1\right) \\ t < t_{i0} & 0 \end{cases} \tag{9.4-3}$$

This results in the approach function Eq.(9.4-4).

$$f_i(\lambda_i, t_{0i}, t) = \begin{cases} t > t_{i0} & \left(e^{-\lambda i \cdot (t - t_{0i})} - 1\right) \\ t < t_{i0} & 0 \end{cases} \qquad (9.4\text{-}4)$$

T0i and □i are to be adjusted nonlinearly for each pseudo-component. From the results, the maximum consumption can be predicted even before the end of the test.

9.4.3 Application

As an example, the process of consumption after the first intensive biology treatment of a smoldering wastewater is presented, FigFig. 9.42 and Tab. 9.41. The graphical interpretation of the degradation kinetics from linear sections of the measured r(BSB) function cannot separate overlapping degradation processes and can therefore be misinterpreted. The consumption curve occasionally turns into a linear increase. Then it must be clarified whether bacterial biomass is being exhaled or whether there is a systematic drift of the apparatus. The oxidation of groundwater with high ferrous iron concentrations often leads to strong pH reductions. Nutrient deficiencies can also inhibit degradation. For these cases, the experimental apparatus should be supplemented with a continuous pH measurement and a dosing device into the closed system.

Tab. 9.41: Parameters of the Adjustment Functions Eq.(9.4-3) for the effluent of a smoldering wastewater after intensive biology (KOCH* et al. 2007).

Pseudocomponent		Bio(1)			Bio(2)		
i		1	2	3	1	2	3
lag_i	d	0	3,5	7,3	0	3,2	5,9
λ_i	1/d	0,83	0,160	0,046	1,09	0,1925	0,0063
BSB_i	mg/L O_2	241	1784	1494	214	1203	3494
	±	0,01	6		0,01	2	5,7
Customization		R^2 = 0,9999 KRT = 0,7 %			R^2 =1,0 KRT = 0,3 %		

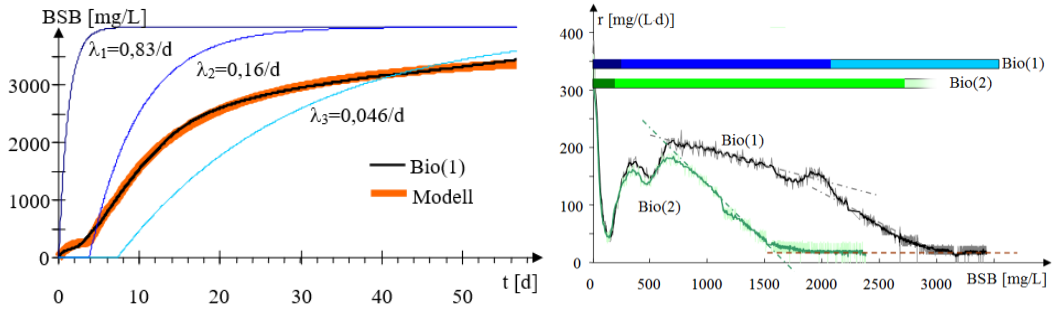

Fig. 9.42: Left: Decomposition of a depletion curve from the course of intensive care biology into three overlapping pseudocomponents (shades of blue) of different degradability (measured black, calculated red), KOCH* et al. (2007). Right: Oxygen depletion rates r [mg/(L·d)] as a function of the BSB [mg/L] for the left sample Bio(1) and the parallel sample Bio(2) (shades of green). The concentrations of the pseudocomponents given as BSB are shown as bars. The reaction rates calculated from difference coefficients were smoothed out.

9.5 Adaptation of empirical data to sums of nonlinear approach functions

9.5.1 Titration curves of different buffer systems

The dissociation equilibrium of a weak acid and its description by the law of mass action can be used to define the approach functions for the respective acid constants pK_{Si}, Eq.(6.2-1) and Eq.(6.2-2).

$$f_i\left(pK_{Si}, pH\right) = \frac{1}{1 + 10^{pK_{Si} - pH}} \tag{9.5-1}$$

The algorithm is used when dissociation equilibria overlap. This allows e.g. hydrogen carbonate ($pK_{S,1}$ = 6.4) and low-molecular organic acids ($pK_{S,2} \approx 4.5$) to be mathematically separated from each other from titration curves, SCHÖPKE (2007).

9.5.2 Adsorption isotherms as the sum of Langmuir expressions

Adsorption equilibria as a pair of values of the load and the dissolved component (c, q) are described by the two-step adjustment algorithm as overlapping Langmuir isotherms, Eq.(9.5-2) and Eq.(9.5-3).

$$q = q_{max} \cdot \frac{K_L \cdot c}{\left(1 + K_L \cdot c\right)} \tag{9.5-2}$$

$$f_i\left(K_L, c\right) = \frac{K_L \cdot c}{\left(1 + K_L \cdot c\right)} \tag{9.5-3}$$

However, the results are only a stopgap if no causal description of the sorption processes (surface complexation, ...) is available.

9.5.3 Periodic oscillations

Harmonic oscillations, i.e. sine or cosine functions of various parameters, are generated in nature by annual and daily periods. These fluctuations are sometimes suitable as natural tracers in which the change in the oscillation parameters amplitude and phase shift can be interpreted (SCHÖPKE 2007). The fluctuation frequency must already be known, otherwise software solutions for Fourier analysis must be used.

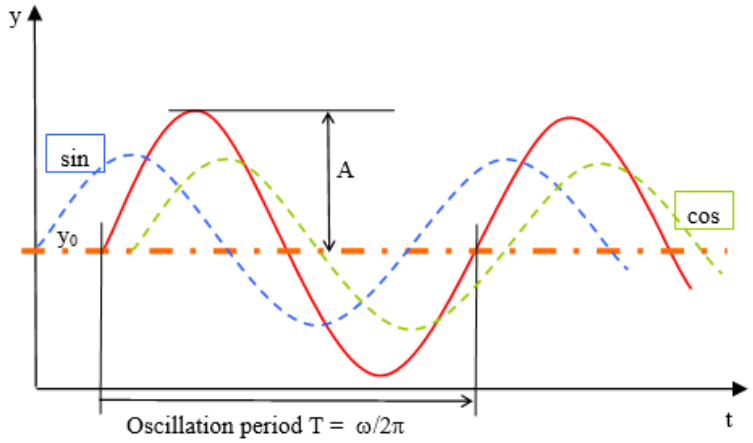

Fig. 9.51: Periodically oscillating parameter y and surrogate functions.

The change of a harmonically oscillating parameter y(t) is described in the first approximation by a sine function, possibly with a linear trend γ_T, Eq.(9.5-4).

$$y(t) = y_0 + A \cdot \sin(\omega \cdot (t - t_0 + \tau)) + \gamma_T \cdot (t - t_0) \qquad (9.5\text{-}4)$$

It contains:

y Periodically fluctuating value

y_0 Mean

A half amplitude

t_0 Reference date

T Oscillation period (e.g. T = 1 a)

τ Time difference

2πω Circular frequency

γ_T constant trend factor

$$\omega = \frac{2\pi}{T} \qquad (9.5\text{-}5)$$

1 Year period corresponds to ω = 2π/365,25 d = 0,0172 d^{-1},

1 Day period corresponds to ω = 2π/1 d = 6,28 d^{-1}.

The calculation of the coefficients in Eq.(9.5-4) is carried out via linear regression, after this has been converted into a sum expression via an addition theorem for the calculation of angular sums (BARTSCH 1972), Eq.(9.5-6).

$$y(t) = y_0 + A \cdot \cos(\omega \cdot \tau) \cdot \sin(\omega \cdot t) + A \cdot \sin(\omega\tau) \cdot \cos(\omega \cdot t) + \gamma_T \cdot (t - t_0) \qquad (9.5\text{-}6)$$

The time is normalized to the beginning of the measurements, t_0 = 0. All constant quantities (τ, A) for a measuring point are summarized in the coefficients of the regression approach, Eq.(9.5-7):

$$y(t) = b_0 + b_1 \sin(\omega(t)) + b_{-1} \cos(\omega(t)) + \gamma_T \cdot (t) \tag{9.5-7}$$

With

y(t) = linear trend approach

sin(ωt) = 1. regression analysis approach function

cos(ωt) = -1. regression analysis approach function

The trend is faded out. The coefficient comparison with Eq.(9.5-6) yields Eq.(9.5-8).

$$\begin{aligned} b_0 &= y_0 \\ b_1 &= A \cdot \cos(\omega \cdot \tau) \\ b_{-1} &= A \cdot \sin(\omega \cdot \tau) \end{aligned} \tag{9.5-8}$$

This results in the time difference τ, Eq.(9.5-9).

$$\tau = \frac{1}{\omega} \cdot \arctan\left(\frac{b_{-1}}{b_1}\right) \tag{9.5-9}$$

and half the amplitude A follows from the calculated τ, Eq.(9.5-10).

$$A = \frac{b_1}{\cos(\omega \cdot \tau)} \tag{9.5-10}$$

The time shift τ indicates the phase difference with respect to the selected time reference t_0. The phase shifts between two measuring points (0 and 1) are obtained by forming differences, Eq.(9.5-11).

$$\Delta t = \tau(1) - \tau(0) \tag{9.5-11}$$

A time lead time (Δt > 0) can also be interpreted as a delay because of the periodicity (365.25 d + Δτ for annual periodics). A calculated negative amplitude would therefore correspond to a shift of π/2 on the time axis.

9.6 Interpretation of UV/VIS spectra

9.6.1 Equalization of spectra by merging measurements from dilutions

The concentration of light-absorbing substances in diluted solutions (chapter 7.1.2) is linearly linked to light absorption via Lambert-Beer's law, Eq.(9.6-1).

$$E_\lambda = -\frac{1}{L} \cdot \lg \frac{I}{I_0} = \varepsilon_\lambda \cdot c \tag{9.6-1}$$

with

I, I_0 =Intensity of the outgoing or entering light beam,

ε_λ =Specific extinction coefficient as solvent-specific substance constant and function of wavelength λ.

The extinction coefficients of absorption bands usually extend over several orders of magnitude, which means that the range of validity of the Lambert-Beerschen law is not observed for all wavelengths λ . The linear relationship between the concentration and the extinction coefficient can be established by:

- Equalization via nonlinear calibration curves,
- Dilution and reference to undiluted solution.

The equalization of the nonlinear range is only possible to a limited extent, which is why a dilution series is preferred. In the overlapping measurements, the measured values in the optimal measuring range are weighted more strongly than those at the edge of the respective measuring range via the measuring device-specific function g(E). The weighting function g(E) takes into account the accuracy of the respective measured value. A Gaussian function is used, which strives towards zero in the nonlinear range and evaluates even small values low, Eq.(9.6-2).

$$g(E) = \exp\left(-8\frac{(E-E_0)\cdot(E-E_U)}{(E_o-E_U)^2}\right) \tag{9.6-2}$$

With the parameters proven in practice:

E_U = 0,1 cm^{-1}

E_O = 1,8 cm^{-1}

The weighting Eq.(9.6-2) has been chosen in such a way that it takes a value of one at the specified measurement range limits. This function reaches the maximum between the two limits with a value of 7.4. The lower limit E_U also takes into account values close to the detection limit, Fig. 9.61.

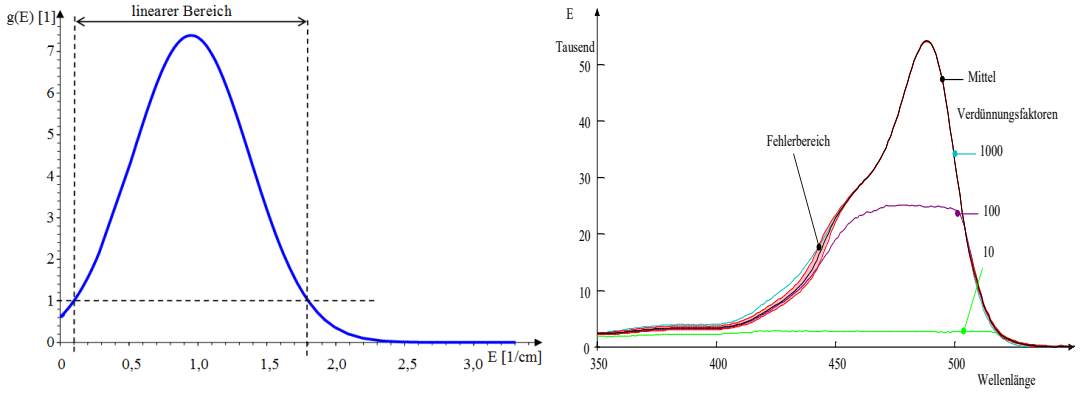

Fig. 9.61: Applied weighting function on the left and construction of the spectrum of rhodamine B from measurements of different dilution (KOCH et al. 2002).

The compound extinction $E_{m,\lambda}$ is then calculated using the weighted mean, Eq.(9.6-3).

$$E_{m,\lambda} = \frac{\sum g(E\ ) \cdot E_{\lambda}}{\sum g(E)} \tag{9.6-3}$$

The accuracy of the weighting indicates the modified standard deviation $\sigma\mu,\lambda$ wavelength-dependent, Eq.(9.6-4).

$$\sigma_{m,\lambda} = \frac{\sum \left(g(E_{\lambda}) \cdot (E_{\lambda} - E_{m,\lambda})^2 \right)}{\sum g(E_{\lambda})} \tag{9.6-4}$$

This error range can only be specified where at least two measurements are in the evaluable range and serves the analyst as a decision-making aid on the usability of the measurements.

9.6.2 Decomposition of spectral curves into elementary bands

The UV/VIS spectrum E(λ) Eq.(7.1-12) is converted into a sum of elementary bands of type Eq.(7.1-14) disassembled, Eq.(9.6-5).

$$E(\lambda) = \sum_{i=1}^{n} E_{\lambda}(i) = \sum_{i=1}^{n} \left[E_{max,i} \cdot \exp\left(-diff_i^2 \cdot \left(\frac{\lambda_{max,i}}{\lambda} - 1 \right)^2 \right) \right] \tag{9.6-5}$$

The nonlinear elementary bands form the approach functions for given $\lambda_{max,i}$ and $diff_i$, Eq.(9.6-6).

$$f_i(\lambda_{max,i}, diff_i, \lambda) = E_{max,i} \cdot \exp\left(-diff_i^2 \cdot \left(\frac{\lambda_{max,i}}{\lambda} - 1 \right)^2 \right) \tag{9.6-6}$$

When adjusting the elementary spectra to the measured and equalized and smoothed spectrum, the $E_{max,i}$ are obtained via the regression step. In the nonlinear adjustment step, the two parameters $\lambda_{max,i}$ and $diff_i$ are varied. The adjustment of overlapping elementary bands is specified by extending the data set by the 1st derivatives as difference coefficients (derivative or differential spectroscopy). In practice, a weighting of the 1st derivatives with a factor of 10 has proven to be effective. In any case, the plausibility must be checked graphically and, if necessary, also deviate slightly from the KRT minimum.

As a result of the adjustment, the integral extinction coefficients are given as concentration synonyms, Eq.(7.1-29).

9.7 Adaptation of breakthrough curves to determine reactor parameters

9.7.1 Adjustment of the residence time of the filter tubes (EXCEL)

Starting from the approach function Eq.(3.1-17) the breakthrough behavior of a tracer after the flow section L is described using the normal distribution function available in EXCEL, Eq.(9.7-1).

$$c(L,t) = A_0 \cdot \text{NORM.VERT}\left(v_A \cdot t; L; \sqrt{D_L \cdot t}; wf\right) \tag{9.7-1}$$

This function provides the integrated normal distribution with the option wf = *true* and alternatively the density function (option wf = *false*), Fig. 9.71.

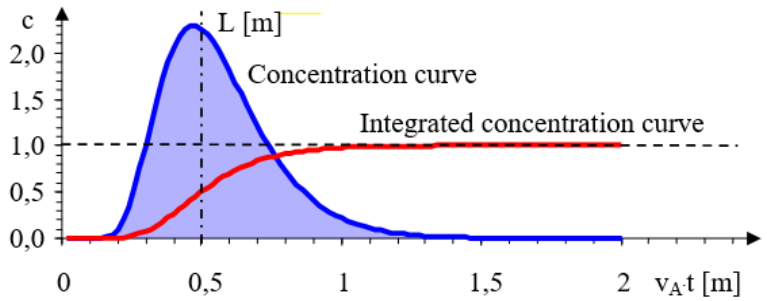

Fig. 9.71: Concentration curves of a Dirac pulse after the flow path L=0.5m (wf = false) and its integral (wf = true) or D = 0.25 m²/d, $\Delta n/A_F$ = 1 mol/m², v_A = 1 m/d.

After replacing the flow section L in Eq.(3.1-20) the breakthrough time t_0 is followed by the concentration curves Eq.(9.7-2) or Eq.(9.7-3).

$$c\left(\frac{L}{v_A}, t\right) = c(t_0, t) = \frac{\frac{\Delta n}{A_F}}{\sqrt{2 \cdot \pi \cdot D \cdot t}} \cdot \exp\left(-\frac{v_A^2 \cdot (t_0 - t)^2}{2 \cdot D \cdot t}\right) \tag{9.7-2}$$

$$c(t_0, t) = \frac{\frac{\Delta n}{A_F}}{\sqrt{2 \cdot \pi} \cdot \sqrt{D \cdot t}} \cdot \exp\left(-\frac{(t_0 - \cdot t)^2}{2 \cdot \frac{D}{v_A^2} \cdot t}\right) \tag{9.7-3}$$

To convert to the Excel function, Eq.(9.7-3) transformed into Eq.(9.7-4),

$$c(t_0, t) = \frac{\frac{\Delta n}{A_F}}{\sqrt{2 \cdot \pi} \cdot v_A \cdot \sigma_{t,Excel} \sqrt{t}} \cdot \exp\left(-\frac{(t_0 - \cdot t)^2}{2 \cdot \sigma_{t,Excel}^2 \cdot t}\right) \tag{9.7-4}$$

with $\sigma_{t,Excel}$, Eq.(9.7-5).

$$\sigma_{t,Excel} = \frac{\sqrt{D_L}}{v_A} \qquad \left[\sqrt{\text{Zeit}}\right] \tag{9.7-5}$$

The density function (wf = false) takes over the unit of time used, e.g. [1/d], Eq.(9.7-6).

$$c(t_0,t) = A_0 \cdot \text{NORM.VERT}\left(t; t_0; \left(\sigma_{t,\text{Excel}} \cdot \sqrt{t}\right); \text{wf} = \text{falsch}\right) \tag{9.7-6}$$

The concentration A_0 describes the cross-sectional area-standardised amount of substance addition Δn, Eq.(9.7-7),

$$A_0(\text{wf} = \text{falsch}) = \frac{\Delta n}{A_F \cdot v_A} \cdot \left[\frac{1}{\text{Zeiteinhei t, d}}\right] \tag{9.7-7}$$

or Eq.(9.7-8).

$$\frac{\Delta n}{A_F} = A_0(\text{wf} = \text{falsch}) \cdot v_A \cdot [\text{Zeiteinhei t, d}] \tag{9.7-8}$$

The corresponding integral function (wf = true) is dimensionless, Eq.(9.7-9).

$$\int_0^t c(t_0,t) \cdot \partial t = A_0 \cdot \text{NORMVERT}\left(t; t_0; \left(\sigma_{t,\text{Excel}} \cdot \sqrt{t}\right); \text{wf} = \text{wahr}\right) \tag{9.7-9}$$

The same value of A_0 results from the time integral (wf = *true*) and can be calculated according to Eq.(9.7-8) without taking into account the unit of time. The concentration integral has the unit concentration·Time.

9.7.2 Transfer to the flowing water column H

For an empty conduit $n_P = 1$, or $v_A = v_f$, the concentration curve Eq.(9.7-10).

$$c\left(L, \frac{H}{v_A}\right) = \frac{\frac{\Delta c}{A_F}}{\sqrt{2 \cdot \pi} \cdot \sqrt{H \cdot \frac{D}{v_A}}} \cdot \exp\left(-\frac{(L-H)^2}{2 \cdot H \cdot \frac{D}{v_A}}\right) \tag{9.7-10}$$

Rewritten to real filter sections ($n_P < 1$), their porosity must also be taken into account, Eq.(9.7-11),

$$c\left(L, \frac{H}{v_f}\right) = \frac{\frac{\Delta c}{A_F}}{\sqrt{2 \cdot \pi} \cdot \sqrt{H \cdot \frac{D}{v_f}}} \cdot \exp\left(-\frac{\left(L - \frac{H}{n_P}\right)^2}{2 \cdot H \cdot \frac{D}{v_f}}\right) \tag{9.7-11}$$

with the variance for the Excel function $\sigma_{H,\text{Excel}}$, Eq.(9.7-12).

$$\sigma_{H,\text{Excel}} = \sqrt{\frac{D_L}{v_f}} \tag{9.7-12}$$

From this follows the concentration function Eq.(9.7-13).

$$c(L,H) = A_0 \cdot \text{NORM.VERT}\left(H; L; \sigma_{H,\text{Excel}} \cdot \sqrt{H}; \text{wf}\right) \tag{9.7-13}$$

9.7.3 Relationships between functional and process parameters

9.7.3.1 Dispersivity

The function parameters are related to the process parameters, Eq.(9.7-14).

$$\begin{aligned} L &= v_A \cdot t_0 = n_P \cdot v_f \cdot t_0 \\ D_L &= \alpha_L \cdot v_A \end{aligned} \tag{9.7-14}$$

This results in the longitudinal diffusion coefficient D_L Eq.(9.7-15),

$$D_L = \alpha_L \cdot v_A = v_A^2 \cdot \sigma_{t,Excel}^2 = v_A \cdot \sigma_{H,Excel}^2 \tag{9.7-15}$$

and for the dispersivity α_L Eq.(9.7-16).

$$\alpha_L = v_A \cdot \sigma_{t,Excel}^2 = \sigma_{H,Excel}^2 \tag{9.7-16}$$

9.7.3.2 Addition of substances

The integral approach results in the substance addition Eq.(9.7-17).

$$\frac{\Delta n(L,t)}{A_F} = \int_0^t c(L,H) \cdot \partial H = \int_0^t (v_f \cdot c(L,t)) \cdot \partial t \tag{9.7-17}$$

Converted to the time-integrated values of the adjustment, Eq.(9.7-18) and Eq.(9.7-19),

$$\int_0^t (c(L,t)) \cdot \partial t = \frac{\Delta n}{A_F \cdot v_A} \cdot \text{NORM.VERT}\left(t; t_0; \sigma_{t,Excel} \cdot \sqrt{t}; wf = wahr\right) \tag{9.7-18}$$

$$\int_0^t (c(L,t)) \cdot \partial t = A_0 \cdot \text{NORM.VERT}\left(t; t_0; \sigma_{t,Excel} \cdot \sqrt{t}; wf\right) \tag{9.7-19}$$

and for the flow cross-section-related material addition Eq.(9.7-20).

$$\frac{\Delta n}{A_F} = A_0 \cdot v_A \tag{9.7-20}$$

The addition of substance refers to the entire flow cross-section, regardless of porosity.

9.7.3.3 Concentration Peak

In the asymmetrical course of the concentration, the maximum is reached just before H=L or t = t_0. For the maximum concentration at t = t_0 or H/n_P = L, Eq.(9.7-21) or Eq.(9.7-22).

$$c(L,t_0) = \frac{\frac{\Delta n}{A_F}}{\sqrt{2 \cdot \pi \cdot t_0} \cdot v_A \cdot \sigma_{t,Excel}} \tag{9.7-21}$$

oder

$$c(L, n_P \cdot H = L) = \frac{A_0}{\sqrt{2 \cdot \pi \cdot \frac{L}{v_A}} \cdot \sigma_{H,Excel}} = \frac{A_0}{\sqrt{2 \cdot \pi \cdot t_0} \cdot \sigma_{H,Excel}} \qquad (9.7\text{-}22)$$

9.7.4 Overlay of breakthroughs

A complicated breakthrough course is composed of the sum of several individual breakthroughs, Eq.(9.7-23) and Fig. 9.72 for three events. The same approach can be applied to the time-integrated concentrations (wf = true) and/or the water column H flowing through it. The parameters of the attachment functionscan be determined using the adjustment algorithm chapter 9.1.2.2 .

$$\begin{aligned} c(L,t) = c_0 + & A_1 \cdot \text{NORMVERT}\left(t; t_{01}; \left(\sigma_{t,Excel,1} \cdot \sqrt{t}\right); wf = falsch\right) \\ & + A_2 \cdot \text{NORMVERT}\left(t; t_{02}; \left(\sigma_{t,Excel,2} \cdot \sqrt{t}\right); wf = falsch\right) \\ & + A_3 \cdot \text{NORMVERT}\left(t; t_{03}; \left(\sigma_{t,Excel,3} \cdot \sqrt{t}\right); wf = falsch\right) \end{aligned} \qquad (9.7\text{-}23)$$

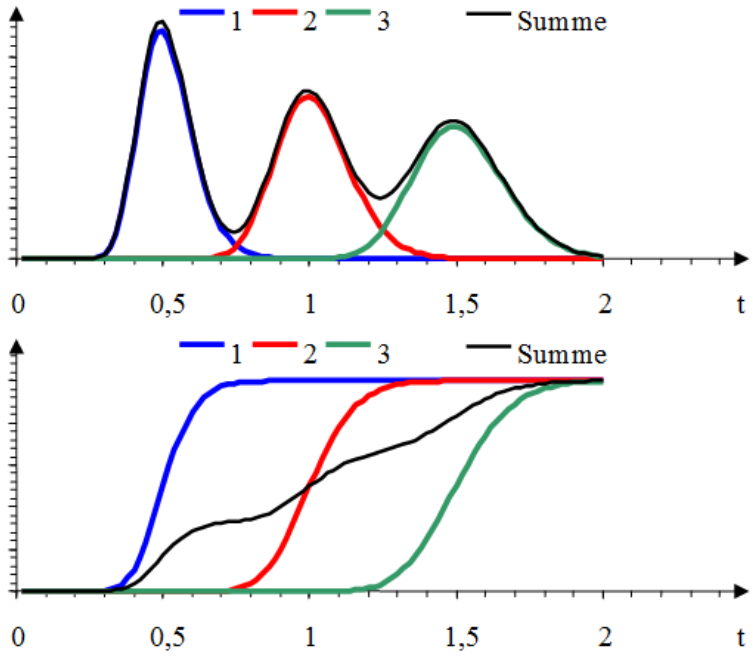

Fig. 9.72: Overlay of Three Consecutive Breakthrough Functions (Non-Scale).

A distinction between two concentration jumps is practically only possible after the occurrence of two turning points, or two concentration maxima of the density function, Fig. 9.73.

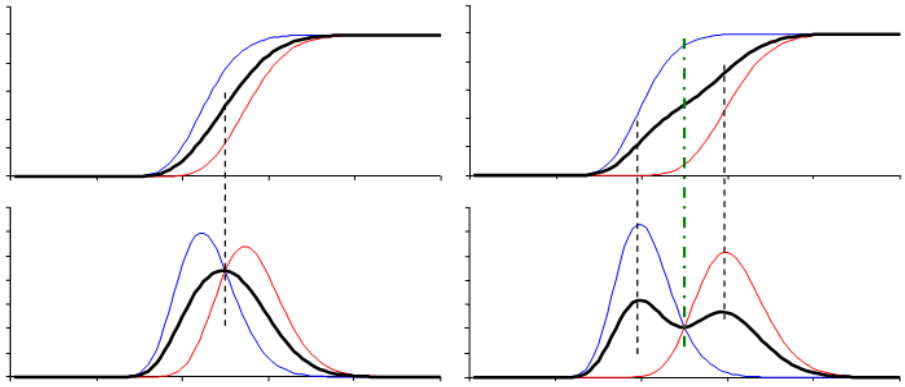

Fig. 9.73: Superposition of two concentration jumps with different retardations (non-scale).

Before that, the superposition appears as a concentration leap with greater dispersion.

9.8 Parameterization of the aquifer

9.8.1 Grain Size Analyses

The particle size distribution of technical filter materials is determined by dry screening (usually according to DVGW Worksheet W113, DVGW Regulations 1983). The sieve towers used contain up to 10 sieves with mesh size decreasing from top to bottom. Vibrations cause the material to be classified to be thrown into motion, whereby smaller particles are transported to the screen openings and fall through them until the screen size is reache $d < d_{particles}$. For the duration of the screening process, optimal values are specified in the respective operating instructions.

The calculation of the equivalent diameter is carried out by numerically integrating the grain distribution with the screen passages as support points. The accuracy can be increased if the integration method optimally interpolates the curve between the support points, chapter 4.1.2. The fine grain $w(d_{min})$ must first be hidden from the surface calculation.

9.8.2 Parameterization of the sphere packing from grain size analyses

9.8.2.1 Integration of the particle size distribution curve

The equivalent grain diameter d_K is calculated by integrating the size distribution curve in the specified sieve range [d_{min}, d_{max}], Eq.(4.1-6) With d_{min}, fine-grained areas that do not have a flow effect are likely to be excluded. d_{max} is chosen above the largest sieve fraction.

$$\frac{1}{d_K} = \int_{d\,min}^{d\,max} \frac{\partial w(d)}{d} \qquad (4.1\text{-}6)$$

The lower sieve limit d_{min} has a sensitive effect on the equivalent sphere diameter, while the upper limit d_{max} usually has little effect. The numerical integration is based on the diameters of the sieve set used. The wider the distances between the screen diameters (mesh sizes) used, the less accurate the numerical integration becomes.

9.8.2.2 Linear interpolation using the trapezoidal method

The undersize $d < d_{min}$ which is not defined in its diameter, is first faded out and the rest is set to 100%, Eq.(9.8-1).

$$\frac{1}{d_K} = \left(\frac{1}{1 - w(d_{min})} \right) \cdot \sum \frac{w(d_i) - w(d_{i-1})}{0{,}5 \cdot (d_i + d_{i-1})} \tag{9.8-1}$$

The more the curve between the support points deviates from the straight, the higher the integration error. This also increases with increasing interval width.

9.8.2.3 Geometric Interpolation

Geometric interpolation assumes that the size distribution curves in the fine-grained range can often be linearized in a double logarithmic representation, Eq.(9.8-2).

$$\frac{1}{d_K} = \left(\frac{1}{1 - w(d_{min})} \right) \cdot \sum \frac{w(d_i) - w(d_{i-1})}{(d_i \cdot d_{i-1})^{0,5}} \tag{9.8-2}$$

9.8.2.4 Exponential Interpolation

This interpolation is based on the approximate similarity to exponential progression, Eq.(9.8-3).

$$\frac{1}{d_K} = \left(\frac{1}{1 - w(d_{min})} \right) \cdot \sum \frac{w(d_i) - w(d_{i-1})}{\ln\left(\frac{d_i}{d_{i-1}} \right)} \tag{9.8-3}$$

9.8.2.5 Using data from the size distribution curve

SCHÖPKE (2007) recommended a procedure for the multiple application of Kepler's barrel rule with ten support points to be taken from the grain distribution curve, Eq.(9.8-4).

$$\frac{6}{d_K} = \frac{0{,}4}{d_{95}} + \frac{0{,}5}{d_{90}} + \frac{1{,}6}{d_{70}} + \frac{0{,}8}{d_{50}} + \frac{1{,}6}{d_{30}} + \frac{0{,}44}{d_{10}} + \frac{0{,}16}{d_8} + \frac{0{,}09}{d_6} + \frac{0{,}2}{d_{3,5}} + \frac{0{,}05}{d_1} \tag{9.8-4}$$

Eq. (9.8-4) pays particular attention to the fine-grain content with a high surface area of up to 1 % sieve passage for filter materials filters.

9.8.3 Decomposition of compound grain distributions into several normal distributions

Complex grain distributions can be calculated according to the algorithm chapter 9.1.2.2 over a sum of distribution functions Eq.(4.1-20) In contrast to the adjustment of concentration breakthroughs (chapter 9.7), the variance σ is a variable characteristic of the distribution, which is linked to the uniformity coefficient U, chapter 4.1.2.3.

9.8.4 Determination of porosity from electron microscopic sections and tomographic examinations

A number of sophisticated methods are available for the characterization of pore structures, such as microfocus X-ray CT systems with connected image processing software. In most cases, however, simpler electron microscopy methods have to be used. When determining porosity from electron microscopic sections, the pore space is delineated from the matrix. This is done by defining a threshold value that assigns the gray tones to the solid matrix or the pore space. Due to the fact that each image is different in terms of contrast and brightness, this threshold (Treshold, numerical parameter of the grayscale in image evaluation) must be determined individually between the grain and pore space, Fig. 9.81.

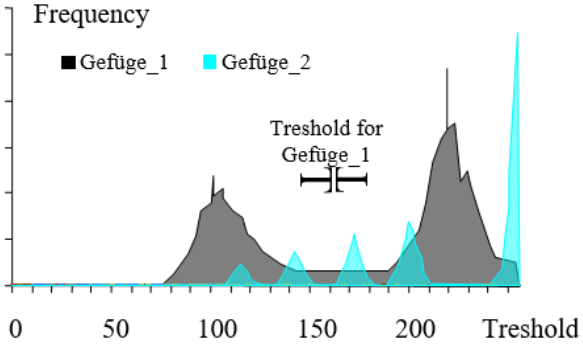

Fig. 9.81: Histogram of two structural sectional images with the selection of the threshold (treshold) for the Gefüge_1. No porosity can be determined from the intake of Gefüge_2, consisting of different materials (quartz, aluminosilicates, etc.).

The porosity is then determined by pixel counting of the evaluable image transferred to a binary file, Fig. 9.82.

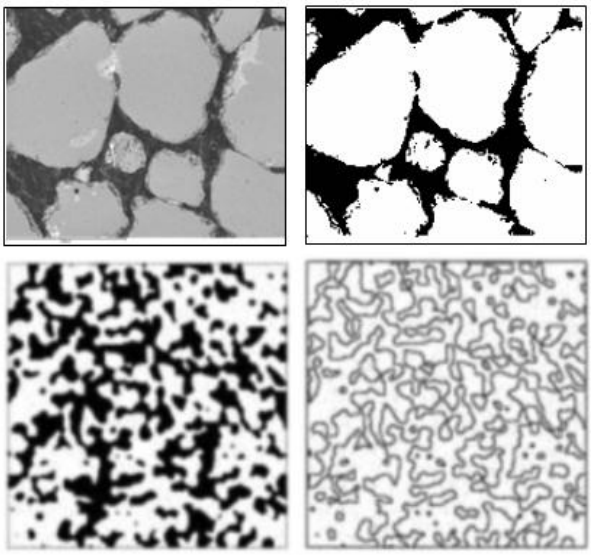

Fig. 9.82: Top: Structural section (left) and sectional image prepared for pixel counting with black pore spaces (right, SCHÖPKE et al. 2020). Bottom: Inverted binary image and extracted pore space profile of a sintered sandstone-analog glass bead fill (HAN et al. 2019). The specific phase interface can be determined from the interfacial length in the section.

In most cases, there is a wide distance between the two phases, which allows for a clear transfer into black or white pixels. Grinding of various minerals does not allow this, Tab. 9.81. The distinction between different minerals (quartz, aluminosilicate, pyrite) on the basis of their shades of gray does not yield reproducible results. Only in individual cases can different phases be quantified. In the example of Gefüge_2, it is not possible to assign different minerals to defined grayscales.

Tab. 9.81: Gefüge_2 with different thresholds (treshold) for the distinction between matrix and pore space. The aluminosilicate appears optically heterogeneous, which means that it cannot be quantified in a limited brightness range. (schwarz = black).

Treshold	230-254	100-254	190-211	188-208	164-179
schwarz	66,3%	54,3	7,5%	7,0	5,9%
Bild	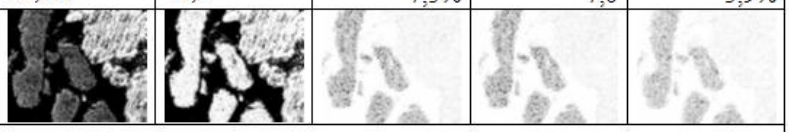				
	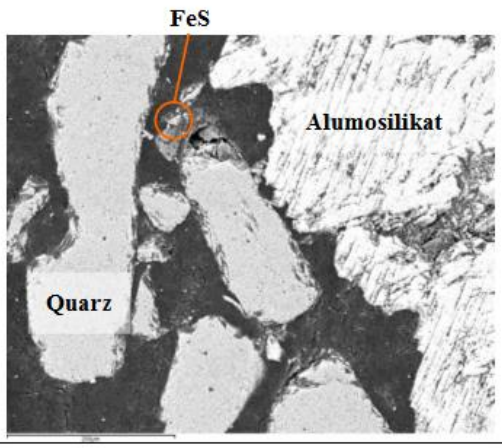				

9.8.5 Ermittlung von Anisotropien aus Bohrkernen von Porengrundwasserleitern

On groundwater flow sections, the flow cross-section is blocked by rock silt lenses, so-called dead spaces, which do not contain the current tubes inscribed for transport modelling, Fig. 2.2-1. Information about the storage and texture of aquifers can be provided by strata lists and drill cores, supplemented by particle size analyses carried out at selected depths, electron microscopic microstructure analysis (chapter 9.8.4), chemical properties and further investigations. The determined porosities, possibly with grain shape and mineralogical compositions, are then extrapolated to the entire depth profile. The frequently encountered fine layering in areas of a few millimeters appears in the sieve curves as an increased uniformity coefficient. These well-sorted grain structure structures are often self-similar to a large extent independent of the particle diameter, whereby the porosity determined by electron microscopy can be transferred to the macroscopic layer. The information contained in the strata lists about dead spaces or less permeable layers is subtracted from the cross-section through which it flows, Fig. 9.83. This porosity related to the depth range through which the flow corresponds to the macroporosity n_{Pm}.

SCHÖPKE et al. (2020) thus transferred the longitudinal dispersion α_L from k_f depth profiles of an exploratory borehole, which could be confirmed by tracer tests, Fig. 9.83.

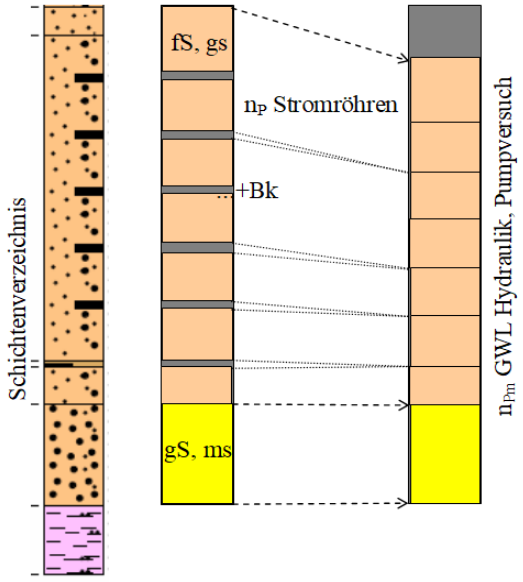

Fig. 9.83: Macroporosity n_{Pm} transferred from the list of strata with individual current tubes. The well-sorted grain sizes (right) usually have a higher porosity than the grain mixtures made from them (left), SCHÖPKE et al. (2020).

9.8.6 Kationenaustausch von Lockergesteinen und Böden

Soil science refers to the rootable mixture of mineral particles (sand, clay minerals, sesquioxides, ...) and organic substances (humus) as a substrate. This is assigned to cation exchange processes that run as neutral exchanges, Eq.(6.5-31) and Eq.(6.5-32) The sum of the exchangeable cations is determined experimentally by exchange with a neutralsalt solution (e.g. KCl or NH_4Cl). The cation exchange capacity (CAC, T-value, [mmol/kg]) is a measure of the exchangeable cations and thus the number of negative binding sites of cation exchangers in the soil.

The *potential cation exchange capacity*, as the maximum number of free cation binding sites, refers to the cation exchange capacity at a *neutral* pH value (pH = 8.1) of the soil (DIN ISO 13536). International classifications (FAO-UNESCO, US-Soil-Taxonomy) determine the potential cation exchange capacity at pH = 7.

The *effective cation exchange capacity* refers to the number of actual free cation binding sites depending on the corresponding pH value of the soil (SCHEFFER & SCHACHTSCHABEL 1992). The effective cation exchange capacity is determined by the-concentrations of the cation charges and hydrogen ions displaced by ammonium ions.

These ideas of neutral exchange of ions of the pore solution with ions bound to the solid matrix cannot be completely transferred to filters and aquifers. The transfer of cation exchange capacity (CC) to adsorption capacity provides only one orientation, SCHÖPKE et al. (2020).

9.9 Plausibility of analysis and test data

9.9.1 Correction of the measured redox state during analysis plausibility checks via PHREEQC

Before geochemical modelling, the analyses used should be checked for plausibility. Anoxic groundwater in particular is sensitive to predetermined redox potentials. The measured redox potential is composed of the sum of redox reactions, the average potential of which is tapped with the platinum electrode against a reference electrode. The reference is converted to the normal hydrogen electrode. The redox equilibria at the platinum electrode is very slow and the measured value does not always correspond to the equilibrium state. For this reason, the electron activity (pE value) calculated from the measured redox voltage often deviates from the hydrochemical conditions, as a result of which mathematically unstable compositions are calculated. This manifests itself in implausible simulation results, such as the oxidation of ferrous iron, the supersaturation of ferric hydroxide or a calculated sulphur formation from sulphate. To avoid this, PHREEQC offers the possibility to correct the redox state according to measured redox pairs, Tab. 9.9-1.

Tab. 9.9-1: Boundary conditions for the determination of the redox state. [1)]Redox measurement, [2)]anoxic groundwater with traces of ferroic hydroxide, [3)]sulphate-reducing groundwaters, [4)]surface waters with oxygen.

Nr.	Redox pair		Boundary condition
1)	#	pE	Measured redox voltage
2)	redox	Fe(2)/Fe(3)	Equilinbrium with ferroic and pH-value
3)	redox	S(-2)/S(6)	Analytical data from sulfate-reducing milieu
4)	redox	O(-2)/O(0)	Analytical data from the oxic environment

9.9.2 Equilibrium adjustment in batch approach (isotherm)

Phase equilibria can be produced and investigated using various methods. The easiest way is to examine an already established equilibrium state. The disadvantage: Functional dependencies, such as isotherms, can rarely be determined from a few measured states.

In several batch approaches, increasing doses of adsorbent are added to a starting solution or, alternatively, different starting solutions with an adsorbent dose are used. The difference in concentration and the adsorbent dose are used to calculate the equilibrium load, which is opposed to the equilibrium concentration.

In most cases, the equilibrium between the solution and solid phases is only possible by intensive shaking or stirring. Disturbing structural disturbances can be circumvented by using circulatory filters. Especially when investigating adsorption equilibria, it is important to consider:

- The adsorption (or desorption) isotherm does not necessarily provide information about the reactions involved in the sorption phenomenon.
- The reaction time until the equilibrium is adjusted must be carefully selected. Superimposed irreversible reactions can lead to misinterpretations.
- The concentration range of the substance to be retained must be chosen in such a way that the concentration and loading differences can be determined with acceptable uncertainties.
- The chemical environment, in particular competing processes, must be included in measurement.

10 Applications

10.1 Filter dimensioning

10.1.1 Grain structure

With the basics compiled here, filter configurations can be evaluated from a procedural point of view. The different configurations of filter flow sections are demonstrated below using three examples.

a) Rapid filter for groundwater treatment

b) Aquifer flow tube

c) Differential filter with aquifer material b

The dimensioning of the rapid filter is in the range of the usual technology for groundwater treatment. Near-natural applications can be reduced to filter reactors by defining aquifer flow tubes. The groundwater flow tube selected for the comparison describes a flow cross-section of 4 m deep and 10 m wide, which can be assigned to a groundwater measuring point, Tab. 10.1-1.

Tab. 10.1-1: Reactor dimensions and filter material. (Specified dimensions **bold** and quantities derived from it according to the given equations blue, implausible red).

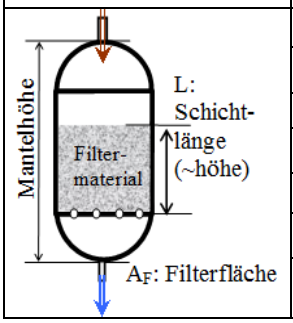

Parameter		Unit	Eq.	a	b	c
Diameter	d_F	m		**2,0**	7,14	**0,081**
Area	A_F	m^2		3,1	**40**	0,0052
Length	L	m		**2,0**	**200**	**0,108**
Volume = 1 BV	V_R	m^3	(2.2-1)	6,3	8000	0,00056
Mass, dry	m_{Pr}	kg		10053	$14{,}4 \cdot 10^6$	1,00
Bulk density	ρ_S	kg/dm^3	(2.2-5)	**1,6**	**1,8**	**1,8**

Porous aquifers made of material with wide grain distributions usually also have a lower porosity, Tab. 10.12.

Tab. 10.12: Specifications for the grain structure.

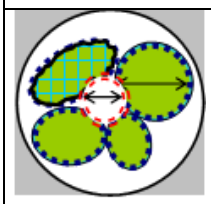

Parameter		Unit	Eq.	a	b	c
Grain density	ρ_{SS}	kg/dm³	(2.2-9)	**2,5**	2,5	2,5
Porosity (bulk)	n_{PG}	%	(2.2-6)	36	**28**	**28**
Pore volume	V_P	m³		2,3	2240	0,00016
Phase Ratio, Saturated	z	L/kg	(2.2-10)	0,23	0,16	0,16

Aus den Kornverteilungen wird eine repräsentative Kugelschüttung konstruiert, Tab. 10.1-3.

Tab. 10.1-3: Parameter des Modells einer idealen Kugelschüttung.

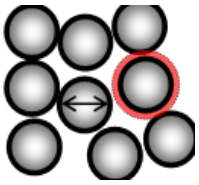

Parameter		Unit	Eq.	a	b	c
Grain diameter	d_K	mm		**1,0**	**0,38**	**0,38**
Form Factor	f_O	1	(3.4-19)	**0,95**	**0,95**	**0,95**
Effective grain diameter	d_w	mm		0,95	0,36	0,36
Specific interface	O_{sp}	m²/kg	(3.4-10)	2,53	6,65	6,65
Specific surface area of the fill	O_F	m²/m³	(3.4-12)	4040	11900	12000
Grain surface of a fill	O_R	m²	(3.4-11)	$25 \cdot 10^3$	$96 \cdot 10^6$	6,6
Still passable pore narrowing	$d_{P,min}$	mm	(3.4-3)	0,15	0,056	0,056
Adsorpted water layer	d_{ads}	µm	cpt. 4.1.1	**0,5**	**0,5**	**0,5**
Fixed porosity	Δn_P	%		0,2	0,6	0,6

The adsorption water layer d_{ads} was investigated by BUSCH et al. (1993) as a guideline. Equivalent to the ideal sphere packing is the tube bundle model, Tab. 10.1-4.

Tab. 10.1-4: Equivalent tube bundle

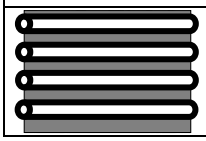

Parameter		Unit	Eq.	a	b, c
d(Zylinderpore)	d_p	mm	(3.4-17)	0,36	0,094
Tortuosity	f_L	1	(3.5-20)	**1,44**	**1,44**

The tortuosity for the equivalent tube bundle is given as $f_L = 1.44$.

Die Fließeigenschaften der Porenlösung werden hauptsächlich von der Temperatur bestimmt, während gelöste anorganische Ionen eine untergeordnete Rolle spielen, Tab. 10.1-5.

Tab. 10.1-5: Flowing medium (water).

Parameter		Unit	Eq.	a	b, c
Temperature	Temp	°C		**10,0**	**10,0**
Gravitational acceleration	g	m/s²		**9,81**	**9,81**
Kinematic viscosity	ν	m²/s	(2.3-40)	$1{,}3 \cdot 10^{-6}$	$1{,}3 \cdot 10^{-6}$
Dynamic viscosity	η	kg/(s·m)	(2.3-39)	0,0013	0,0013
Dissolved salts		g/kg		0,5	1,5
Density	ρ_W	kg/L	(2.3-37)	1,0001	1,0009

The flow properties of the pore solution and the size of the shear surface are used to derive the process-technically relevant and hydraulic properties of the filter fill, Tab. 10.1-6.

Tab. 10.1-6: Flow-through filter.

	Parameter		Unit	Eq.	a	b	c
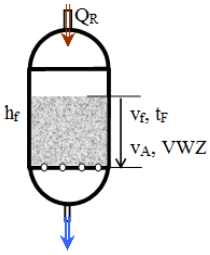	Flow-through porosity	n_{PG}	1		0,36	0,27	0,27
	Volume flow	Q_R	m^3/h		31,4	0,94	0,0008
	Filtration velocity	**v_f**	m/h	(2.2-2)	**10**	**0,024**	**0,16**
	Distance velocity	v_A	m/h	(2.2-7)	27,9	0,086	0,57
	Space-time	t_F	h	(2.2-3)	0,2	8470	0,70
	Residence time	VWZ	h	(2.2-8)	0,072	2320	0,19
			d			96,7	
	Reynolds number	Re	1	(3.5-3)	3,2	0,0025	0,016
	Permeability coefficient	k_f	m/s	(3.5-17)	$5{,}0 \cdot 10^{-3}$	$2{,}56 \cdot 10^{-4}$	$2{,}56 \cdot 10^{-4}$
	Filter resistance	h_{f0}	m	(3.5-19)	1,14	5,13	0,018
	Filtration parameter	FP	h/m	(3.3-25)	808	$101 \cdot 10^{6}$	8324
	Filter resistance, loaded	h_f	m	(5.2-16)			
	Diffusion coefficient	D	m^2/s	cpt. 2.3.6.3	$\mathbf{9{,}2 \cdot 10^{-10}}$	$\mathbf{6{,}5 \cdot 10^{-10}}$	$\mathbf{6{,}5 \cdot 10^{-10}}$

From the selection of diffusion coefficients, a value for the molar mass of the iron M = 56 g/mol is assigned to the iron removal filter (a), Eq.(2.3-42) while the mean (10°C) for dissolved ions is used for the groundwater flow tube. This shows the orienting character of these calculations. The mass transfer kinetics via diffusion through film kinetics, which are determined by the flow state and the diffusion coefficient, can only be given for orientation, Tab. 10.17.

Tab. 10.17: Calculating Film Diffusion.

	Parameter		Unit	Eq.	a	b	c
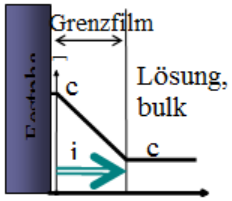	Schmidt number	Sc	1	(3.6-8)	1402	2000	2000
	Sh(eff) number	Sh	1	(3.6-7)	30	0,4	0,8
	Mass transfer coefficient	β	m/s	(3.6-17)	$1{,}6 \cdot 10^{-5}$	$2{,}5 \cdot 10^{-7}$	$5{,}6 \cdot 10^{-7}$
	boundary layer	δ	µm	(3.6-6)	57	*2631*	*1168*
	Length coefficient	λ_L	1/m	(8.1-9)	24	450	150
	Time constant	λ_t	1/h	(8.1-9)	660	39	87
	Half lengths	L(1/2)	mm	(8.1-10)	29	1,5	4,5
	Half-lives	t(1/2)	s	(8.1-10)	3,8	64	29

The boundary layer thickness δ is a fictitious quantity that follows from the model concept of film kinetics and is sometimes calculated to be larger than the cylinder pore diameter d_P, which has no relevance. The length and time exponents λ_L and λ_t given for $D_L = 0$ are increased by dispersion, chapter 8.2.1, Eq.(8.2-15).

10.1.2 Residence time behavior

The residence time behavior of filters is estimated using mixed cell models. From this, specifications for tracer tests can be derived and/or flow section models (PHREEQCx, n_{cell}, mixrun) can be designed. For this purpose, three scenarios are considered in each case, Tab. 10.18, Fig. 10.11 and Fig. 10.11. Die Dispersivitätsschätzung nach dem Korngerüst (GIMBEL 1984), Eq.(4.3-12) is unrealistic because macrodispersion processes are already at work on longer flow lines. Realistic dispersivities can be set via the number of stirring stages. Small cells have the disadvantage of low length and temporal resolution. PHREEQCx compensates for this with intermediate mixing steps *mixrun*. However, the desired dispersivity can only be approximated, Tab. 10.18 cells.

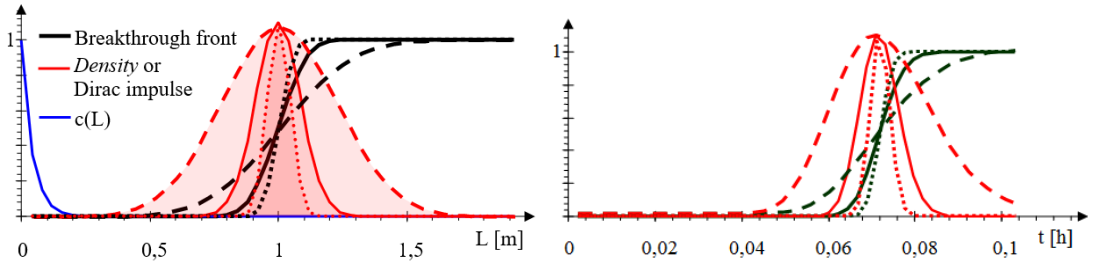

Fig. 10.11: Residence time scenarios for rapid filters. Dirac impulse red and breakthrough front **black**. Left: Longitudinal profiles of the tracer concentration after 50 % of the residence time, and the scenarios a1 dotted, a2 solid and a3 dashed. The decrease in concentration at film kinetics, a grain surface concentration zero and $D_L = 0$ for the length exponent λ_L, Tab. 10.17 is shown in blue. Right: Breakthrough curves at L= 2 m.

Tab. 10.18: Transport behavior with parameter determination for a *mixed cell* model. Scenarios a1 and b1 use the axial dispersion coefficients D_L of water treatment filters (GIMBEL 1984), Eq.(4.3-12) The other scenarios calculate D_L according to the number of *mixed cells*.

Parameter			Eq.	a1	a2	a3	b1	b2	b3
Number of cells	n_{cell}	1	(3.2-8)	526	**100**	**20**	139000	**100**	**20**
Cell length	L_{cell}	m	(3.2-10)	0,0038	0,02	0,1	0,0014	2,0	10
Time step	t_{cell}	h	(3.2-11)	0,000136	0,000716	0,00358	0,017	23,2	116
Bodenstein-, Peclet number (>20)	Bo=Pe	1	(3.2-6)	1053	200	40	277000	200	40
Dispersivity	α_L	m	(4.3-11)	0,0019	0,01	0,05	0,00072	1	5
Axial dispersion coefficients	D_L	m^2/s	(4.3-10)		$7{,}8\cdot10^{-5}$	$3{,}9\cdot10^{-4}$		$2{,}4\cdot10^{-5}$	$1{,}2\cdot10^{-4}$
			(4.3-12)	**$1{,}5\cdot10^{-5}$**			**$1{,}8\cdot10^{-8}$**		
mixed cells	mixrun	1	(3.3-2)	**1**	**2**	**2**	**2**	**2**	**2**
PHREEQCx	α_L	m	(3.3-3)	0,0013	0,013	0,067	0,048	1,33	6,7

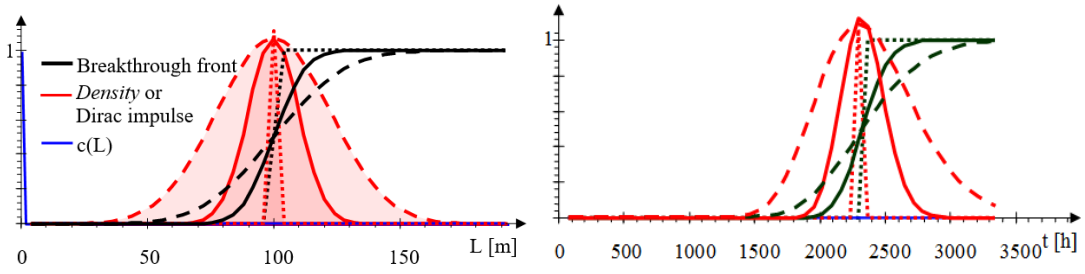

Fig. 10.12: Residence time scenarios for the groundwater flow tube. Dirac impulse red and breakthrough front **black**. Left: Longitudinal profiles of the tracer concentration after 50 % of the residence time t, the concentration decrease according to λ_L blue and the scenarios b1 dotted, b2 solid, b3 dashed. Right: Breakthrough curves at L= 200 m.

10.1.3 Continuous loop reactor

Kreislaufreaktoren mit Differenzialfiltern eignen sich für die zeitliche Spreizung schnell ablaufender Reaktionen. SCHÖPKE (2024) beschreibt Methoden zur Herstellung von Gleichgewichten zwischen Porenlösung und nahezu ungestörter Feststoffmatrix aus Filtern und Porengrundwasserleitersedimenten.

Fig. 10.13: Parameters for closed-loop reactors without partial passage of dimensioning c with material a and b according to chapter 3.3.2.

	Parameter		unit	Eq.	**a**		**b**	
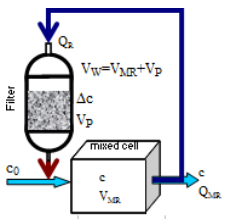	Flow ratio	α	%		**0**	**0**	**0**	**0**
	Pore volume of filter	V_P	L		0,20		0, 156	
	Volume mixing reactor	V_{MR}	L		**1**	**2**	**1**	**2**
	Partial flow in the circuit	Q_R	L/h		52		0, 8	
	System flow	Q_{MR}	mL/h		0		0	
	residence time of filter	VWZ	h		0,04		0,19	
	spacetime mixing reactor	t_{MR}	h	(2.2-8)	0,02		1,25	
	Time spread	t_{MR}/VWZ	1		5,02	10	6,56	13

10.2 Groundwater treatment, iron and manganese removal

10.2.1 Differentiation of iron removal filtrations

Iron turnover in the environment usually takes place in the border area between anoxic and oxic milieu. Various iron minerals interact with other species in the solution, often present in traces, via adsorption and/or the formation of solid solutions. Iron and its compounds are thus among the core elements of important global material cycles. These processes also determine the conventional groundwater deferrization in the oxidizing environment. A distinction is made between:

- Homogeneous ferrous iron oxidation

After oxygen is added to the anaerobic groundwater, homogeneous ferrous iron oxidation begins. The ferric iron formed in this process is colloidal to particulate (flakes). Autocatalytic processes at the formed phase interfaces accelerate the process. Observations have shown that siderite particles that precipitate after gas exchange are oxidized particularly quickly. Technologically, the proportion of colloid-particulate ferric iron after aeration is significant.

- Ferrous iron filtration

Ferrous iron oxidation is catalyzed on iron hydroxide surfaces. The reaction rate is far higher than that of homogeneous oxidation. In this process, adsorbed ferrous iron reacts with atmospheric oxygen and forms catalytically active ferrichydroxide again. Since the filtration performance increases with increasing pH value, an upstream intensive CO_2 discharge through aeration has a positive effect.

- Iron(III) and Iron(II,III) oxide filtration

According to observations, up to 80% colloidal content of the total iron concentration, i.e. at least 20% ferrous iron, is removed by ferrous iron filtration in a time-stable and pressure-resistant manner. At higher ferric iron contents, the process changes to an unstable flocculation filtration, the so-called iron(III) filtration.

Colloidal ferric iron binds to adsorbed ferrous iron, which is determined by the ferrous iron concentration. The oxidation of ferrous iron and the retention of ferric iron run in parallel, which also results in the limitation by the ferrous iron content.

- Biological iron removal

Below pH < 6.5, iron bacteria (*Gallionella*) are able to oxidize ferrous iron to a large extent and store it as ferrichydroxide. As the pH value decreases, the biological proportion of the iron removal performance increases. The oxygen may only be added in the stoichiometric ratio, which is achieved by recirculating oxygen-enriched pure water. Accordingly, the filters are only regenerated by high-voltage water flushing with raw water. Although biological iron removal has much more favourable performance parameters than autocatalytic processing, there is still a lack of practicable design bases, which severely limits its use.

The principles of action and areas of application of the autocatalytic iron removal and manganese removal processes are compiled in the Technical Rule, Worksheet W223-: Iron Removal and Manganese Removal of the DVGW (2005), Tab. 10.21.

Tab. 10.21: Comparison of biochemical and autocatalytic filtration according to DVGW worksheets W223-1 to 3 and HANCKE (1991). [1)]Upper grain in multilayer filters.

Kriterium		Autocatalytic	Biochemical
Raw water parameters			
Oxygen concentration	mg/L	> 0,14·c_{Fe}	0,14·c_{Fe}
pH	1	6,7...8	6...7,2
Iron concentration	mg/L	0,2...15 (...>20)	0,2...>30
Filter design			
Length	m	1...2,5	1...>2,5
Grain diameter	mm	0,75...4[1)]	>2
Filtration velocity	m/h	3...20	20...>50
Filter area loading	kg/m^{2}Fe	< 5	< 13
Order of oxidation reactions		Methane Iron, Ammonium Manganese	Iron Methane Ammonium Manganese

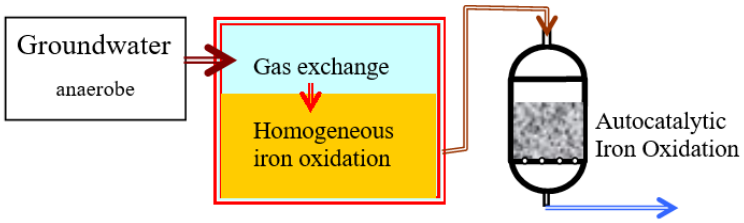

Fig. 10.21: Treatment by aeration and filtration of iron-contaminated groundwater.

10.2.2 Design bases for the removal iron, manganese and carbon dioxide of groundwater by filtration

10.2.2.1 Standard procedures on an empirical basis

For groundwater treatment, empirical design equations have been developed in the past, in which the chemical and flow-related influences are implicitly included. Parameters relevant to the design are specified, such as the permissible filtration velocity when specifying the filter dimensioning, the inlet and the effluent condition to be observed. KITTNER et al. (1975) stated for the permissible iron removal rate of the ferrous iron filtration v_E, Eq. (10.2-1) f_H is a hardness-dependent safety factor (0.8...1.8) which is not explained further here. The safety factor f_H = 0.7 originally used resulted in numerous *capacityreserves* in the application.

$$v_E = f_H \left[\frac{3 \cdot (pH - 6{,}2) \cdot Temp^{0{,}8}}{c_0^{0{,}1} \cdot \ln\left(\frac{c_0}{c_L}\right)} \cdot \frac{L}{d_w} \right]^{1{,}28} \qquad (10.2\text{-}1)$$

Rathsack (1996) revised the design of ferrous iron filtration, describing the temperature dependence by the activation energy E_A. He added the ionic strength influence I as an additive quantity, Eq.(10.2-2).

$$\ln\left(\frac{c_{FeL}}{c_{Fe0}}\right)=\frac{k_0\cdot(pH_0-6{,}2)}{\exp\left(\frac{E_A}{RT}+2{,}04\cdot\sqrt{\frac{I}{1\,mol/L}}\right)}\frac{L}{v_f^{0,7}\cdot d_w} \qquad (10.2\text{-}2)$$

The removal of manganese was described by LAMM (quoted in KITTNER et al. 1975) and BOHM (1992), Eq.(10.2-3).

$$Mn^{2+} + {}^1/_2\ O_2 + H_2O \rightarrow MnO_2 + 2H^+ \qquad (10.2\text{-}3)$$

Lamm's older design equation takes into account the competing adsorption of manganese with the other cations on the catalytic surface, Eq.(10.2-4),

$$v_f=\eta\cdot\left[\frac{A_{Mn}\cdot(pH-6{,}2)\cdot(28\cdot c_{HCO3}+50)\cdot(1+0{,}206\cdot Temp)}{10\cdot\ln\left(\frac{c_0}{c_L}\right)\cdot c_0^{0,72}\cdot e^{Kat}}\frac{L}{d_w}\right]^{0,91} \qquad (10.2\text{-}4)$$

with the term Kat, Eq.(10.2-5).

$$Kat=0{,}042(5{,}6\cdot c_{GH}-2{,}8\cdot c_{HCO3})+0{,}097\cdot\frac{c_{NH4}}{mg/L}+0{,}0042\frac{c_{Na}}{mg/L} \qquad (10.2\text{-}5)$$

The design equation developed by BOHM (1992) and BOHM (1992A) can also be used for half-fired dolomites, Eq.(10.2-6).

$$v_{Mn}=\eta\left[\frac{k_{Mn}}{\exp\left(\frac{5280}{T}\right)}\cdot\frac{n_P\cdot B\cdot(pH-5{,}6)\cdot c_{HCO3}^{0,2}\cdot\left(12{,}5\,\frac{mmol}{L}-c_{Ca}-c_{Mg}\right)^{0,3}}{\ln\left(\frac{c_0}{c_L}\right)}\frac{L}{d_w}\right]^{1,6} \qquad (10.2\text{-}6)$$

The activity of the surface is described by the degree of coverage B.

Chemical removal of carbon dioxide via half-fired dolomite represents a mineral dissolution process (WIEGLEB, quoted in KITTNER et al. 1975), Eq. (10.2-7) The reaction is not limited by calcite saturation.

$$CaCO_3\cdot MgO + 3CO_2 + 2H_2O \rightarrow Ca^{2+} + Mg^{2+} + 4HCO_3^- \qquad (10.2\text{-}7)$$

Parallel to removal of carbon dioxide, iron and manganese can also be removed in lower concentrations, whereby the activity A_{CO2} takes into account the formation of deposits on the surface, Eq.(10.2-2) The design equation converted to the filter velocity v_f for the required carbon dioxide removal effect is usually far below the iron removal velocity v_E and cannot be specified with certainty due to the periodic additions to the material. Limescale separating properties in the filter can cause considerable operational disruptions due to material bonding. For this reason, decarbolite filtration was usually only used for iron removal/manganese removal Eq.(10.2-9).

$$c_L = c_0 \cdot \exp\left(-\frac{A_{CO2} \cdot e^{0,05 \cdot Temp}}{\left(1 + 2,8 \cdot K_{S4,3}\right) \cdot c_0^{0,5} \left(\frac{c_{Ca}}{c_{Mg}} \right)^{0,1}} \cdot \frac{L}{v_f \cdot d_w} \right) \tag{10.2-8}$$

$$v_E = \left[A_{Fe} \frac{e^{0,04 \cdot Temp} \ln\left(0,22 \cdot pH\right)}{\left(1 + 2,8 \cdot K_{S4,3}\right)^{0,3} c_0^{0,25} \cdot \ln\left(\frac{c_0}{c_L} \right)} \cdot \frac{L}{d_w} \right]^{1,5} \tag{10.2-9}$$

All design equations are based on a temporally stable, stationary concentration profile and apply within specified limits of use, Tab. 10.21.

Tab. 10.21: Areas of application of the designs Eq.(10.2-1) to Eq.(10.2-9).

Removal of			Fe		Mn	CO_2
Materialof filtration			Sand	Decarbolith	Sand	Decarbolith
Permissible filter velocity	v_f	m/h	< 30	< 30	3... 20	< 30
Length	L	m	0,5 ... 3	0,5... 3	0,5... 3	0,5... 3
sphere diameter	d_w	mm	1... 2	1... 3	1... 3	1... 3
Temperature	Temp	°C	6 ... 18	3... 17	8... 14	3... 17
pH	pH	1	6,8 ... 7,3	5... 7,3	6,6 ... KKGl*).	> 5,9
Concentration, inflow	c_0	mg/L	0,5... 10	< 20	< 2	
Concentration, outflow	c_L	mg/L	0,1	0,1	0,05	KKGl.
*) Calcite saturation						

10.2.2.2 Process Engineering Evaluation of Empirical Design Equations

The processing processes described above take place on the shear surface of the granular material used. Different filter designs can be compared with the same mass transfer conditions using the filtration parameter FP, Eq.(3.3-25) The exponential concentration curve according to the layer length L refers to a transport-controlled reaction of 1st order. Accordingly, the empirical design equations can be split into a chemical, a mass transfer and a filter-specific term FP, Eq.(10.2-10).

$$\ln\left(\frac{c_X}{c_{X0}} \right) = f\left(Temp, pH, ...\right) \cdot FP \cdot v_f^{const} \tag{10.2-10}$$

The chemical term f(pH, Temp, ...) summarizes the reaction-specific quantities. The layer length and grain diameter in the filter-specific term FP determine the grain surface. The filter velocity stands for the residence time. The additional filter velocity term is used to formulate its influence on the mass transfer. The term describing the filter design in the design equations is replaced by the filtration parameter under simplifying assumptions:

- The equivalent grain diameter d_K is transferred from the effective grain diameter d_w determined by screening with the form factor $f_O = 0.85$ and the pore volume of flushable filter sheets is assumed to be $n_P \approx 0.35$.
- The quantities with specified dimensions are to be inserted into the design equations. This results in a factor of 10^{-3} for the grain diameter in millimeters.
- The flow state that determines the mass transport to the grain surface depends mainly on the filter velocity, as the grain diameters of the filter materials used are in a narrow range. For the limits of application of the filtration processes (Tab. 10.21) follows their Reynolds number range:
  - $Re \approx 3$ for $d_w = 3$ mm, $v_f = 30$ m/h and
  - $Re \approx 90$ for $d_w = 1$ mm, $v_f = 3$ m/h.

The flow dependence of the mass transfer coefficient β describes approximately Eq.(10.2-11) in the given Reynolds number range.

$$\beta \sim v_f^{0,5} \tag{10.2-11}$$

The design equations can be reformulated accordingly, Eq.(10.2-12) and Tab. 10.24.

$$\frac{L}{d_w \cdot v_f} = \frac{f_O}{6 \cdot (1 - n_P)} \cdot FP \approx \frac{0,85}{6 \cdot (1 - 0,35)} \cdot FP \approx 0,2 \cdot 10^{-3} \cdot FP \tag{10.2-12}$$

Tab. 10.2-2: Design equations converted to the concentration ratio and substituted by FP.

$\ln\left(\frac{c_L}{c_0}\right) = -\frac{6\cdot10^{-4}\left(pH-6{,}2\right)\cdot Temp^{\,0{,}8}}{c_0^{0{,}1}} v_f^{0{,}22}\cdot FP$	Iron removal, KITTNER	(10.2-13)
$\ln\left(\frac{c_L}{c_0}\right) = -\frac{2\cdot10^{-4}\cdot k_0\cdot\left(pH_0-6{,}2\right)}{\exp\left(\frac{E_A}{RT}+2{,}04\cdot\sqrt{\frac{I}{1\,mol/L}}\right)}\cdot v_f^{0{,}3}\cdot FP$	Iron removal, RATHSACK	(10.2-14)
$\ln\left(\frac{c_L}{c_0}\right) = -\frac{2\cdot10^{-4}\cdot A_{Mn}\cdot\left(pH-6{,}2\right)\cdot\left(2{,}8\cdot c_{HCO3}+5{,}0\right)}{c_0^{0{,}72}\cdot e^{Kat}}\cdot\left(1+0{,}206\cdot Temp\right)\cdot v_f^{-0{,}1}\cdot FP$	Manganese removal, LAMM	(10.2-15)
$\ln\left(\frac{c_0}{c_L}\right) = \frac{2\cdot10^{-4}\cdot k_{Mn}}{\exp\left(\frac{5280}{T}\right)}\frac{n_P\cdot B\cdot\left(pH-5{,}6\right)\cdot c_{HCO3}^{0{,}2}}{\cdot\left(12{,}5\,\frac{mmol}{L}-c_{Ca}-c_{Mg}\right)^{0{,}3}\cdot v_f^{0{,}375}\cdot FP}$	Manganese removal, BOHM	(10.2-16)
$\ln\left(\frac{c_L}{c_0}\right) = -\frac{2\cdot10^{-4}\cdot A_{CO2}\cdot e^{0{,}05\cdot Temp}}{\left(1+2{,}8\cdot K_{S4,3}\right)\cdot c_{CO2-0}^{0{,}5}\left(\frac{c_{Ca}}{c_{Mg}}\right)^{0{,}1}}\cdot FP$	Carbon dioxide removal, WIEGLEB	(10.2.17)
$\ln\left(\frac{c_L}{c_0}\right) = -2\cdot10^{-4}\,A_{Fe}\frac{e^{0{,}04\cdot Temp}\ln\left(0{,}22\cdot pH\right)}{\left(1+2{,}8\cdot K_{S4,3}\right)^{0{,}3}c_{Fe0}^{0{,}25}}\cdot v_E^{\,1/3}\cdot FP$	Iron removal, WIEGLEB	(10.2-18)

The temperature functions are defined in activation energies E_A (chapter 6.1.2), Tab. 10.2-3.

Tab. 10.2-3: Activation energies E_A and flow influence of the filtration processes (SCHÖPKE 2007).

Verfahren		Bemessung	E_A	Strömung
			kJ/mol	
Autokatalytische Enteisenung	Sand	KITTNER et al. (1975)	50	$v_f^{0,22}$
		RATHSACK (1996)	12 ... < 10	$v_f^{0,3}$
	Decarbolith	KITTNER et al. (1975)	25	$v_f^{0,333}$
Autokatalytische Entmanganung	Sand	Lamm zit. KITTNER et. al (1975)	128	$v_f^{0,1}$
		BOHM (1992)	44	$v_f^{0,375}$
Entsäuerung	Decarbolith	zit. KITTNER et al. (1975)	31	v_f^{0}

The flow term can be used to assess whether the reaction at the grain surface or the transport through the diffusion layer determines the reaction rate. For the transition area, Eq.(6.1-3).

In the design formulas, the influence of the filter velocity by $v_f^{0.3}$ is somewhat lower than theoretically expected in the case of iron removal/manganese removal, Eq.(10.2-11) This is also confirmed by the results of SCHÖPKE* (1984), who found practically no usable treatment effects during the shutdown of iron removal filters.

The solution of semi-calcined dolomite is not flow-dependent in the defined area, i.e. the solution reaction on the surface controls the reaction rate.

The activation energies converted via the temperature terms fluctuate considerably, as was to be expected from empirical approaches. The temperature and ionic strength dependence summarized in one term by RATHSACK (1996) represents the activation energy very inaccurately. In transport-controlled reactions, the temperature dependence of the viscosity and the diffusion coefficients is implicit in the converted (apparent) activation energy. The design formulas transformed in this way can be used in the scale transfer of test results.

10.2.2.3 Filter resistance development of iron removal filters

In the iron removal standards of the GDR (WAPRO), nomograms were given to estimate the average filter running time. IN his revision, Wingrich (2002) states the relationship between the filter running time t_L [h] to a maximum pressure head loss $h_{f,max}$ [m] at a drain iron concentration of Fe_L = 0.1 mg/L, Eq.(10.2-19).

$$t_L = \left(\frac{370}{v_f} \cdot \frac{h_{f,max}^{0,8} \cdot d_w^{1,3}}{L^{0,4} \cdot c_{Fe0}^{0,8} \cdot (pH - 5,6)} \right)^{1/0,92} \tag{10.2-19}$$

From this, an approximate linear increase in filter resistance can be derived, Eq.(10.2-20).

$$h_f = \left(\frac{v_f \cdot L^{0,4} \cdot c_{Fe0}^{0,8} \cdot (pH - 5,6)}{370 \cdot d_w^{1,3}} \cdot t_L^{0,92} \right)^{1,25} \tag{10.2-20}$$

In Eq.(10.2-20) the exponential concentration profile is implemented. This empirical correlation also shows the positive influence of the filter velocity and the dependence on the water column $H = v_f \cdot t_L$. For practical application Eq.(10.2-20) not accuratly.

10.2.3 Reaction model of iron removal

10.2.3.1 Homogeneous ferrous iron oxidation

After the addition of the oxidant, the chemical oxidation processes take place in a series of mostly radical sub-steps, Eq.(10.2-21).

$$Fe^{2+} + 0,25O_{2(aq)} + H^+ \rightarrow Fe^{3+} + H_2O \tag{10.2-21}$$

In further steps, iron(III) first hydrolyzes to amorphous iron hydroxide, Eq.(10.2-22).

$$Fe^{3+} + 3H_2O \rightarrow Fe(OH)_3(a) + 3H^+ \tag{10.2-22}$$

After exceeding the critical germ size, they grow over the colloid size to micro- and later macroflakes, chapter 6.3.3.4.

SINGER & STUMM (1970) determined the law of time, Eq.(10.2-23).

$$-\frac{\partial c_{Fe^{2+}}}{\partial t} = \left(k' + k \cdot c_{OH}^2 \cdot pO_2 \right) \cdot c_{Fe^{2+}} \tag{10.2-23}$$

From Eq.(10.2-21) combined with Eq.(10.2-22) follows the reaction kinetics of the first order with regard to ferrous iron and oxygen, as well as the second order reaction kinetics after the hydroxyl ion concentration with the reaction constant $k = 1.33 \cdot 10^{12}$ $L^2/(mol^2 \cdot atm \cdot s)$, 25°C). Because at pH < 3.5 the reaction only proceeds according to the first order with regard to ferrous iron, occasionally (e.g. JONES et al. 2014) the constant $k' << k$ in the time law Eq.(10.2-23) The hydroxylion concentration is substituted by the pH value and the oxygen partial pressure is substituted by the concentration of dissolved oxygen (e.g. DAVISON & SEED 1983), Eq.(10.2-24).

$$-\frac{\partial c_{Fe^{2+}}}{\partial t} = k \cdot c_{Fe^{2+}} \cdot c_{O2} \cdot 10^{-2 \cdot pH} \qquad | \; k = 2{,}53 \cdot 10^{-14}\ L/(mol \cdot s) \qquad (10.2\text{-}24)$$

10.2.3.2 Precipitation of ferrichydroxide phases

In the neutral range, a process chain begins after oxidation that leads to the formation of stable freeichydroxide phases, GRUNDL & DELWICHE (1993). The surface of the colloid and flake phases catalyze the oxidation reaction that continues to take place. SHENG et al. (2020) refer to ferric iron, which is in equilibrium with the solution and can also be measured analytically, as *labile iron*. The transition of *the labile iron* and amorphous ferrichydroxide into the more stable (usually) goethite phase is summarized together with the water separation under the term sludge aging, Eq.(10.2-25).

$$Fe^{2+} \xrightarrow{k_{ox}} Fe^{3+}_{aq} \xleftrightarrow{K_{hydrilys}} Fe(OH)^{3-x}_{x} \xrightarrow{k_{am}} Fe(OH)_3(a) \xrightarrow{k_{alt}} \text{Goethite} \qquad (10.2\text{-}25)$$

k_{ox} Oxidation of ferrous iron to dissolved ferric iron

$K_{hydrolys}$ Ferrichydroxide nucleation equilibrium in supersaturated solution

k_{am} Autocatalytic colloidal and (micro)flocculation

k_{alt} Sludge aging

Depending on the examination, the concentration of colloidal and microcrystalline iron phases is considered suspended iron

c_{susp} and/or c_{Fe3}

The formation of ferrichydroxide nuclei, from which iron colloids and flakes arise, proceeds according to the mechanisms known from gypsum setting,chapter 6.3.3.4. As a result of an increase in pH due to carbon dioxide outgassing, this process begins after the induction time Eq.(6.3-29) With alkalis, blue-green ferrouscarbonate and -hydroxide phases spontaneously precipitate at the addition site at high supersaturation and determine the further, predominantly heterogeneous oxidation process. In intermediate tanks (mixing reactor), catalytic iron hydroxide particles (colloids and flakes) accumulate during operation, which make it difficult to predict the ferrous iron concentration in the tank effluent.

10.2.3.3 Influence of ferrous iron complexes

Ferrous iron complexes exhibit different oxidation behavior. Many organic complexes reduce the oxidation rate by *masking* the concentration of reactive ferrous iron

complexes. The simple inorganic complexes react differently, Tab. 10.24. In addition, there are numerous organic complexes, chapter 6.2.4. SCHÖPKE (2024) demonstrated the complexation of ferrous iron and calcium by fulvic and humic acid using model calculations. Oxidation-stable, i.e. masked, iron remains as residual iron during oxidation tests, chapter 9.3.3.

SALMON & MALMSTRÖM (2002) and SALMON & MALMSTRÖM (2004) investigated the oxidation of ferrous iron formed during pyrite oxidation by atmospheric oxygen and concluded from the pH dependence of the oxidation kinetics that the ferrous iron species present in homogeneous solution react according to different time laws Eq.(10.2-26).

$$r_{hom} = -\frac{\partial c_{Fe2}}{\partial t} = -\left(k_{Fe} \cdot c_{Fe2+} + k_{FeOH} \cdot c_{FeOH+} + k_{FeOH2} \cdot c_{Fe(OH)2}\right) \cdot c_{O2} \qquad (10.2\text{-}26)$$

However, different, contradictory values are given for the individual rate constants. PHAM & WAITE (2008) determined the kinetics in the pH range from pH = 6.0 to 8.0. Overall, Eq.(10.2-24) SANTANA-CASIANO et al. (2006) investigated the oxidation of ferrous iron in the nanomolar concentration range with O_2, H_2O_2 and their mixtures, while SALMON & MALMSTRÖM (2004) focused on the acidic leachate in mining dumps. Up to pH < 8, the contribution of the $FeOH^+$ ion dominates alongside the $FeCO_3$ neutral complex. At pH values above 8, the $Fe(OH)_2$ and $Fe(CO3)_2^{2-}$ species contribute more than 20% to the rates. These investigations cannot be generalized, Tab. 10.24.

Tab. 10.24: Inorganic complex formation equilibria of ferrous iron. [a)]PARKHURST & APPELO (2006), [b)]PHAM & WAITE (2008) and logarithmic rate constants (log_k_i) of relevant ferrous species. [c)]PHAM & WAITE (2008), cited in [d)]King (1998), [e)]Santana-Casiano et al. (2004), [f)]SALMON & MALMSTRÖM (2004), [g)]SANTANA-CASIANO et al. (2006). Negligible rate constants are marked in red.

Bildungsgleichungen der Komplexspecies	log_K		log_$k_{ox,i}$ [-log(mol·s)]				
	a	b	c	d	e	f	g
Fe+2			-0.90	-6.40	-2.35	-5.10	-1.23
Fe+2 +H2O = FeOH+ + H+	-9.50	-9.51	1.6	0.48	1.05	1.4	0.60
Fe+2 + 2H2O = Fe(OH)2 + 2H+	-20.57	-20.60	5.4	5.58	7.24	6.9	7.84
Fe+2 + CO3-2 = FeCO3	4.38	5.69		-1	-2.13		2.38
Fe+2 + H+ + CO3-2 = FeHCO3+	12.30	11.80		-1	-2.13		-2.78
Fe+2 +2CO3-2 = Fe(CO3)2-2		7.45	3.6	3.68	4.35		1.91
Fe(OH)CO3-	?		2.3	1.86	2.53		0.092
Fe+2 + Cl- = FeCl+	1.48	0.30	-3	-3	-2.35		
Fe+2 + SO4-2 = FeSO4	4.04	2.42	-3	-3	-2.35		

10.2.3.4 Microbiological and heterogeneous oxidation

For acidic leachate in mining dumps, SALMON & MALMSTRÖM (2002) added another term for microbial iron(II) oxidation, Eq.(10.2-27).

$$r_{bio} = -k_{bio} \cdot c_{bakt} \cdot c_{Fe2+} \cdot c_{O2} \cdot c_{H+} \qquad c_{bakt}\ [g/L],\ pH > 2 \qquad (10.2\text{-}27)$$

Ferrous iron adsorbed on mineral phases (lepidocrocites, γ-FeOOH(s) or labile iron) is oxidized heterogeneously. The oxidation process is preceded by an adsorption equilibrium, Eq.(10.2-28).

$$Fe^{2+}_{aq} \xleftrightarrow{K_{ads}} Fe^{2+}_{ads} \xrightarrow{+0{,}25O_2 + 2{,}5H_2O;\ r_{ox}} Fe(OH)_3 + 2H^+ \qquad (10.2\text{-}28)$$

The heterogeneous oxidation rate k_{surf} is normalized to the phase surface. When transferring to the solution, the respective surface/solution volume ratio O/V must be taken into account. The strongly binding sites (strong: Hfo_sOH, around 0.06 mmol/g, PARKHURST & APPELO 2006) play a negligible role in ferrous iron oxidation compared to the weak: Hfo_wOH, around 2 mmol/g). The surface complexes react differently, Eq.(10.2-29) and Tab. 10.25.

$$r_{surf} = \frac{O}{V} \cdot k_{surf} \cdot \left(c_{FeO\_Fe+} + c_{FeO\_FeOH}\right) \cdot c_{O2} \qquad (10.2\text{-}29)$$

DZOMBAK & MOREL (1990) attribute a sorption area of around 600 m^2/g to the amorphous ferrichydroxide, which initially precipitates .

Tab. 10.25: Adsorption equilibria and their equilibrium constants (logK) for lepidocrocite (γ-FeOOH) compared to those of amorphous ferrichydroxide (Fe(OH)3(a)) (PARKHURST & APPELO 2006).

Reaktion	logK		Eq.
	Lepidocrocit	Fe(OH)3(a)	
Hfe_OH = Hfe_O- + H+	-8.27	-8.93	(10.2-30)
Hfe_OH + H+ = Hfe_OH+2	6.45	7.29	(10.2-31)
Hfe_OH + Fe+2 = Hfe_OFe+ + H+	-2.00	sOH: -0.95 wOH: -2.98	(10.2-32)
Hfe_OH + Fe+2 + H2O = Hfe_OFeOH + 3H+	-8.39	wOH: -11.55	(10.2-33)

10.2.3.5 Ferrichydroxide *Porengel* in the treatment filter

The reaction products in various modifications of ferrichydroxide are deposited at the phase interface of the grain structure and form the autocatalytically active mineral *Porengel*, Fig. 10.22 (see also chapter 4.2.5.2). During aging under water release, the deposits become more compact (KITTNER et al. 1975) and form a compact ferric oxide hydrate layer about 10 µm thick. A solid porous layer of hydroxide particles smaller than 5 µm lies on top. The particles are diffusively accessible and do not form a smooth interface to the laminar pore flow. The loosely bound layers are partially removed with filter regeneration.

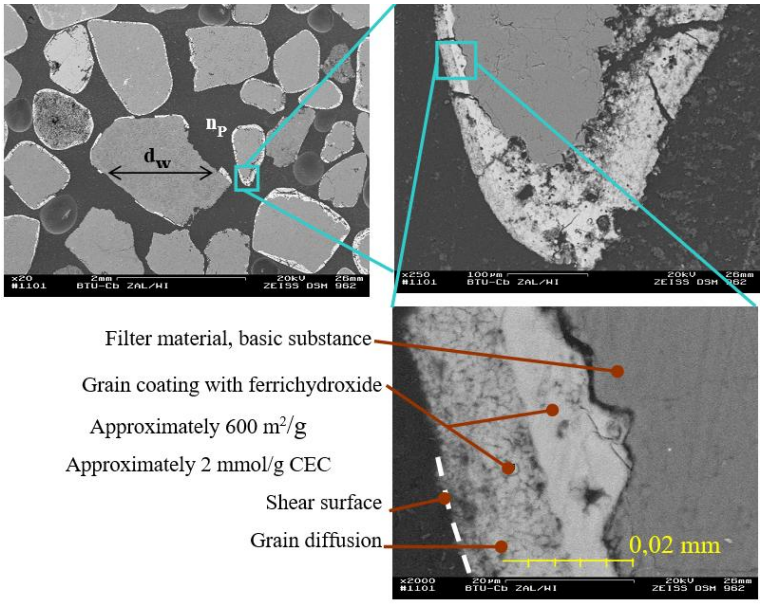

Fig. 10.22: Section through a filter material with the fine structure of the ferric hydroxide coating (detail from Fig. 4.213 left, cracks probably due to preparation).

10.2.4 Modelling of autocatalytic iron removal filtration

10.2.4.1 Model approach

The decrease of the ferrous iron concentration before entering the pore system below the critical value of the ferrous iron filtration can be checked by the homogeneous oxidation rate r_{hom}, Eq.(10.2-34).

$$r_{susp} = -k_{susp} \cdot \left(c_{FeO\_Fe+} + c_{FeO\_FeOH}\right) \cdot c_{Fe\_susp} \qquad (10.2\text{-}34)$$

The rate constant k_{surf} was estimated using model calculations.

The heterogeneous reaction r_{surf} takes place on the reactive surface, which is generally expressed as the surface/pore volume ratio (O/V), Eq.(10.2-29) For the rate of iron removal, only the layer of deposits limited by grain diffusion is effective (middle effective layer), Fig. 10.23. Part of the surface of the pavement is blocked hydraulically or by other mineral formations. This means that only a part of the hydraulic shear surface is also involved in the mass transfer. The microorganisms embedded in the microporous grain coating contribute to the iron removal, Eq.(10.2-27).

Properties of the active *Porengel*:

- Reactive surface O_{sp} (reakt) [m²/g]
- Concentration of binding sites c_{ads} [mol/kg]

with the mass fraction of the effective layer

- on the shear surface w_{reakt} [g/m²]

From this, the specifications for the dimensioning of the *mixed cells i*n a transport model are calculated *(*Fig. 6.61) as a concentration with respect to the pore solution, Eq.(10.2-35) and Eq.(10.2-36).

$$c(\text{reakt}) = \frac{O_{spG} \cdot w_{reakt}}{z} \tag{10.2-35}$$

$$c(\text{surf}) = c_{ads} \cdot c(\text{reakt}) \tag{10.2-36}$$

The material transfer to the flowing pore solution takes place via a diffusion layer on the hydraulically effective shear surface. The boundary layer δ is determined by the flow state (Reynolds number, Re). The molecular diffusion coefficient and the film thickness are calculated in the mass transfer coefficient β in Eq.(3.6-6) The mass transfer velocities are also derived from the diffusion coefficient (contained in the Sherwood number Sh) and the individual concentration gradients according to Eq.(3.3-18).

The total reactions at the shear surface r_O consists of two subreactions of the first order of the film and surface reaction and is formed from their harmonic mean of the rate constants. These are k_{surf} for the surface reaction and β for the transport-controlled mass transfer, Eq.(10.2-37).

$$r_O = \frac{1}{\frac{1}{k_{surf}} + \frac{1}{\beta}} \cdot c = \frac{1}{\frac{1}{k_{surf} \cdot c} + \frac{1}{\beta \cdot c}} = \frac{1}{\frac{1}{r_{surf}} + \frac{1}{\beta \cdot c}} \tag{10.2-37}$$

The surface reaction is related to the entire shear surface, but only takes place on one x_{frei}-st part. At these points, the reaction must be faster. However, this increase must be taken into account when referring to the total area (surface blockage), Eq. (10.2-38) Effectively, the change in the reactive surface has an effect on the limiting effect of the transport. Since the calculation of the mass transfer coefficient also contains uncertainties, these are calculated freely by the fictitious factor x.

$$r_O = \frac{x_{frei}}{\frac{x_{frei}}{r_{surf}} + \frac{1}{\beta \cdot c}} \tag{10.2-38}$$

Tab. 10.2-6: Constants of the laws of time according to SALMON & MALMSTRÖM (2002).

Symbol	Einheit	Wert	Eq.
k_{Fe}	L/(mol·s)	$7.9 \cdot 10^{-6}$	(10.2-26)
k_{FeOH}	L/(mol·s)	25	
$k_{Fe(OH)2}$	L/(mol·s)	$7.9 \cdot 10^{6}$	
k_{surf}	$L^{2} \cdot mol^{-1} \cdot m^{-2} \cdot s^{-1}$	5.0	(10.2-29)
k_{bio}	$L^{3} \cdot mol^{-2} \cdot g^{-1} \cdot s^{-1}$	2 900	(10.2-27)
k_{susp}	$L^{2} \cdot mol^{-1} \cdot m^{-2} \cdot s^{-1}$	≈ 10· k_{surf} nach Modellrechnungen	

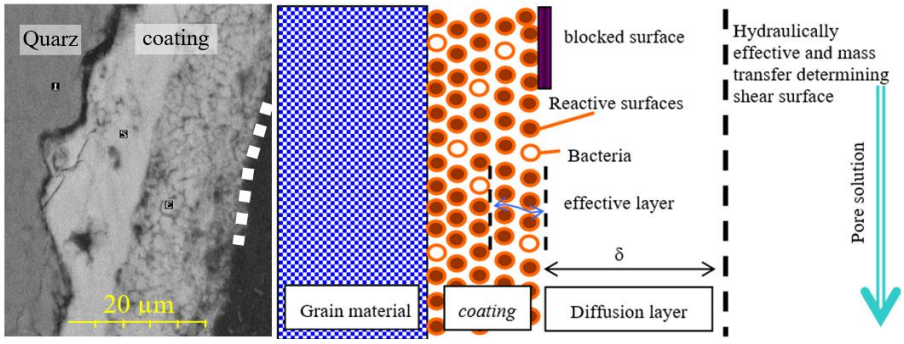

Fig. 10.23: Diagram of the reactive interfaces on the iron removal grain. Left: Detail Fig. 4.213, right: Scheme.

10.2.4.2 Calculation via a *mixed cell* modell

In autocatalytic oxidation reactions, the oxidation states must be defined as separate master variables (Fe_di and Fe_tri). This prevents the spontaneous adjustment of the redox equilibrium. Subsequently, all iron species are also reformulated and a suspended ferric iron phase (Fe_susp) is defined.

```
SOLUTION_MASTER_SPECIES
Fe_di     Fe_di+2        0.0     55.847              55.847
Fe_tri    Fe_tri+3       0.0     55.847              55.847
Fe_susp Fe_susp     0 1 1

SOLUTION_SPECIES
Fe_di+2  = Fe_di+2: log_k   0
Fe_tri+3  = Fe_tri+3; log_k   0
Fe_di+2 + H2O = Fe_diOH+ + H+; log_k -9.5; delta_h 13.2 kcal
...
PHASES
Fe(OH)3(a)
Fe_tri(OH)3 + 3H+ = Fe_tri+3 + 3H2O; log_k 4.891
...
```

The *mixed cell* reactor with a layer length of L = 2 m was divided into n_{cell} = 50 cells and different dispersives α_L. The specified discretization resulted in α_L = 0.01 m. This was increased to α_L = 0.11 m by inserting mixing steps (mixrun = 8).

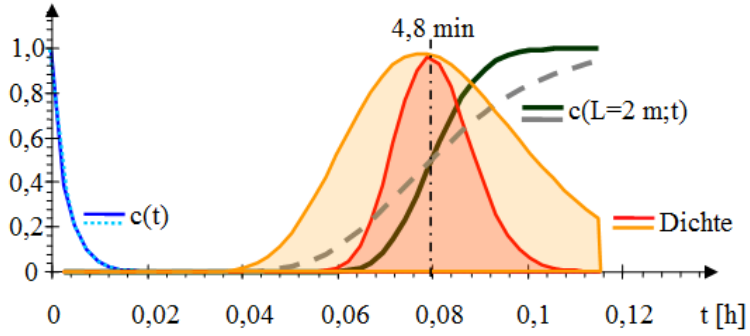

Fig. 10.24: Influence of different dispersivities on calculated breakthrough curves for n_{cell} = 50 and α_T = 0.01 m and α_T = 0.11 m, normalized to 1.0, according to chapter 10.1.2.

The reaction mechanisms describe a pseudo-first-order reaction to iron with hydraulic and pore-specific rate constants, the quantities of which must be empirically corrected. In comparison with the assessment approaches (chapter 10.2.2.1) according to KITTNER et al. (1975) Eq.(10.2-1) and RATHSACK (1996) Eq. (10.2-2) the following factors were chosen:

k_{Fe} Faktor = 1,5

k_{bio} Faktor = 10

Simulated deviations from the exponential concentration curve are based on changes in the pH value with insufficient buffering and slightly varying adsorption behavior. With the cell length of $\Delta L = 4$ cm, half-life lengths $L_{1/2}$ cannot be resolved in the case of the dispersives α_L relevant for water treatment filters, Fig. 10.25.

α_L ($\Delta L = 4$ cm)	cm	0,3	1,0	11	20
$L_{1/2}$ simulated	cm		3,5	3,5	
$L_{1/2}$ calculated	cm	3,7	4,1	7,2	8,9

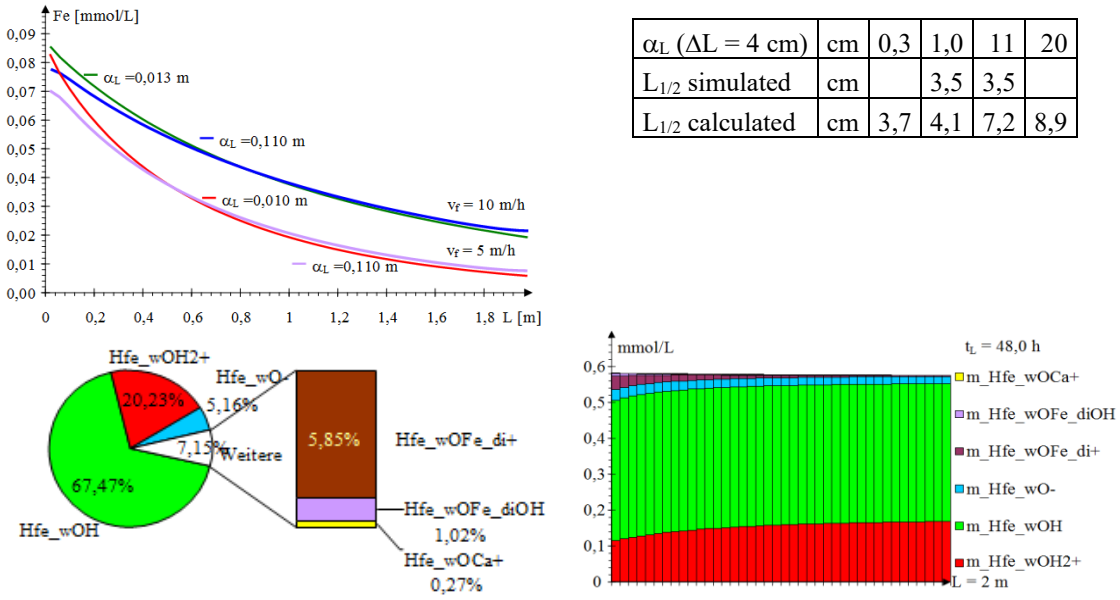

Fig. 10.25: Top: Exponential concentration profiles for v_f = 10 m/h and v_f = 5 m/h, as well as different dispersivities. The dispersivity of the filter section slightly dampens the exponential decrease (left). Comparison of simulated half-life lengths $L_{1/2}$ with those calculated according to chapter 8.2.1 (right) Bottom: Composition of the surface species [%] at the filter surface (left) and in the flow section profile with respect to the water phase [mmol/L] (right) for Fe_0 = 10 mg/L, pH = 6.8 and v_f = 5 m/h.

10.2.4.3 Filter resistance behavior

The filter resistance follows from the (numerical) integration of Eq.(5.2-16) for laminar, or Eq.(5.2-17) for turbulent flow conditions (chapter 5.2) and filling of the pore space with reaction products φ_{int} the particle diameter d_i, Eq.(10.2-39).

$$h_f(\varphi_{int}, L) = \int_0^L k_1 \cdot \frac{\nu}{g} \cdot v_f \cdot \frac{(1 - n_{PG} + n_{PG} \cdot \varphi_{int})^2}{n_{PG}^3 \cdot (1 - \varphi_{int})^3} \cdot \left(\frac{1}{d_G} + \frac{n_{PG}}{1 - n_{PG}} \cdot \frac{\varphi_{int}}{d_i} \right)^2 \cdot dL \qquad (10.2\text{-}39)$$

φ_{int} follows from the simulation calculation of place L and time t in the filter. The precipitated products are already ascribed a representative particle diameter d_i. With a

temporally constant flow profile and filtration conditions (c_X, v_f, ...), $\varphi_{int}(L)$ proportionally flowed water column H, or Eq.(10.2-40).

$$\left(\frac{\partial \varphi}{\partial t}\right)_L = -\frac{V_{FeOH}}{n_{PG}} \cdot \left(\frac{\partial c_{Fe}}{\partial t}\right)_L \qquad \left[\frac{m^3}{mol}\frac{mol}{m^3 \cdot h} = \frac{1}{h}\right] \qquad (10.2\text{-}40)$$

With Molvolume V_{FeOH}, possibly deviating from Tab. 5.2-2 ($Fe(OH)_3(a) * 5\ H_2O$).

For a steady-state concentration profile, the filter resistance increase can be approximated using a *mixed cell* approach using a spreadsheet (EXCEL). A simplified analytical solution for the exponential concentration profile has not yet been found. In addition, the filter resistance can be superimposed by sieving iron hydroxide flakes formed after aeration, chapter 5.3.

Unfortunately, the measurement results of related iron filtration tests are no longer available. Alternatively, for the calibration of the hydraulically relevant deposited particle diameters d_{FeOH} and their fictitious molar volume V_{FeOH} to Eq.(10.2-20)), Fig. 10.26. The particle diameter and molar volume behave in opposite directions, i.e. the grain structure is not smoothly coated.

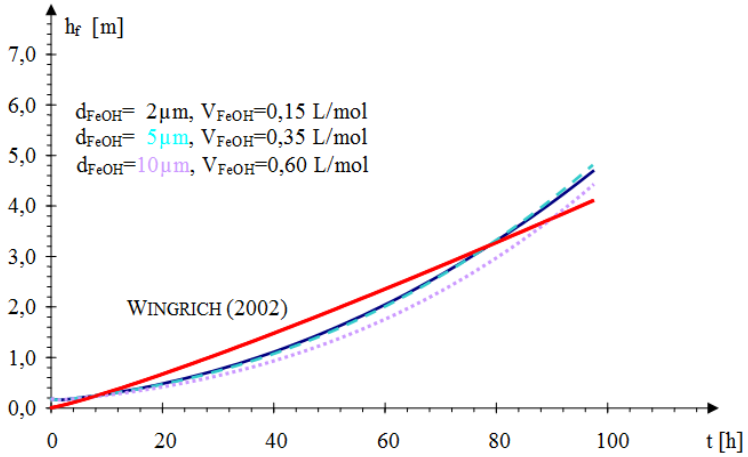

Fig. 10.26: Filter resistance behavior for Fe_0 = 5 mg/L, v_f = 10 m/h, L = 2 m (λ_L = 1.33/m, ncell = 50, α_L = 0.01 m), different iron hydroxide particle configurations compared to WINGRICH (2002, red) Eq.(10.2-20).

10.3 Reactions and balances between the *Porengel* and the pore solution

10.3.1 Stability of complex composed *Porengel*s

The *Porengel* in filter sections of water treatment or in the aquifer is formed when the solid phase interface interacts with the mobile solution. It is generally known that solid humic acids increase in solubility with increasing pH and decreasing ion concentration. In the event of a change of milieu, the resulting instabilities can lead to the mobilization of parts of the *Porengel*. With the exception of stable minerals (iron, manganese hydroxide), this *Porengel* can be imagined as colloid particles held together by weak

interactions (electrostatic and van der Waals forces, hydrogen bonds) that have to withstand the shear forces of the mobile solution phase. The soil pH value is determined in a potassium or magnesium chloride suspension because colloids mobilized in pure water cloud the supernatant solution.

The stability is based on the reactions (chapter **Fehler! Verweisquelle konnte nicht gefunden werden.**) with the complex material systems (chapter 7). The aggregation of low-molecular organic substances into insoluble humic substances, as well as adapted biofilms (with EPS) and inorganic aggregates, such as clay minerals and hydroxide deposits, play a major role in this, Fig. 10.31. GUSTAFSSON (2020) describes solid humic phases as a mixture of humic and fulvic acids in the form of thunder rods, chapter 7.4.2.4. It can also contain various particles, such as clay minerals, etc. Negative charges on the particle surfaces stabilize aggregates by complexing with (usually) multiply charged cations or they are destabilized if they are absent. The volume of Donnan gel phases shrinks with increasing ionic strength, increasing their stability against shear forces, Eq.(6.5-65).

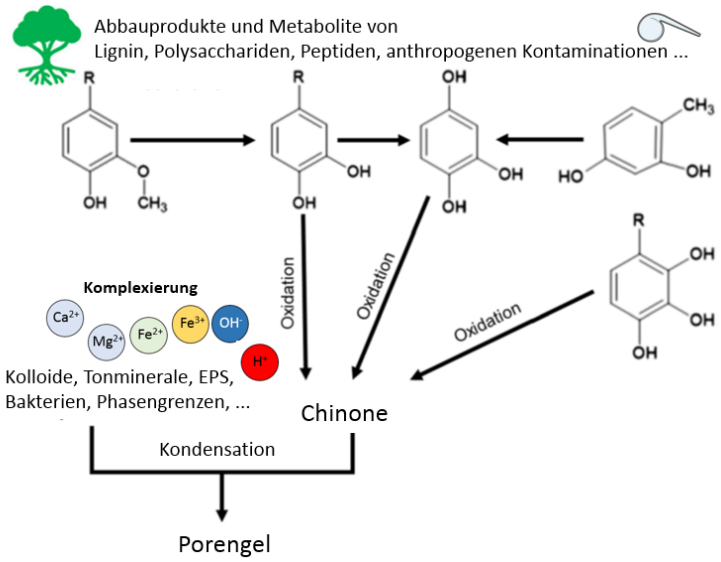

Fig. 10.31: Reaction scheme for the formation of humic substances and *Porengel*s from different starting materials. The reversal of the reaction pathways causes the mobilization of substances fixed in the pore gel. (Revised according to SUTRADHAR et al. 2023).

10.3.2 Mobilization of *Porengel*s from dump aquifers

In various laboratory and pilot tests, the mobilization of organic (humic) substances was observed even at low pH increases. As expected, the mobilized substances had a higher aromaticity and higher molar masses, FigFig. 10.32. KOCH et al. (2006), SCHÖPKE et al. (2007) and SCHÖPKE (2024) developed models based on experimental results for the stability of humic aggregates at increasing pH, which could be used to construct substance distributions according to a solubility constant. However, the results do not yet have any practical relevance.

In the case of drastic pH increases due to the addition of alkalis, the bonds between clay mineral particles are also loosened and these are discharged with the pore solution

stream, Fig. 10.33. Since the affinity of polyvalent cations to acid residues (silicate, aluminate, ...) is greater than to monovalent cations, these colloids can be destabilized by adding magnesium ions ($MgCl_2$) and weighed after separation. The mobilized humic substances (DOC, UV spectra) remain in the solution..

The electron microscopic examination of the discharged solids (4g/kg Dry Solids, Loss on ignition = 69.9%) showed platelet-shaped particles with a maximum edge length of 600 µm and clear erosion phenomena on their surfaces. The composition of the mineral particles (microbeam analyses EDX) came close to the clay mineral illite, Fig. 10.33.

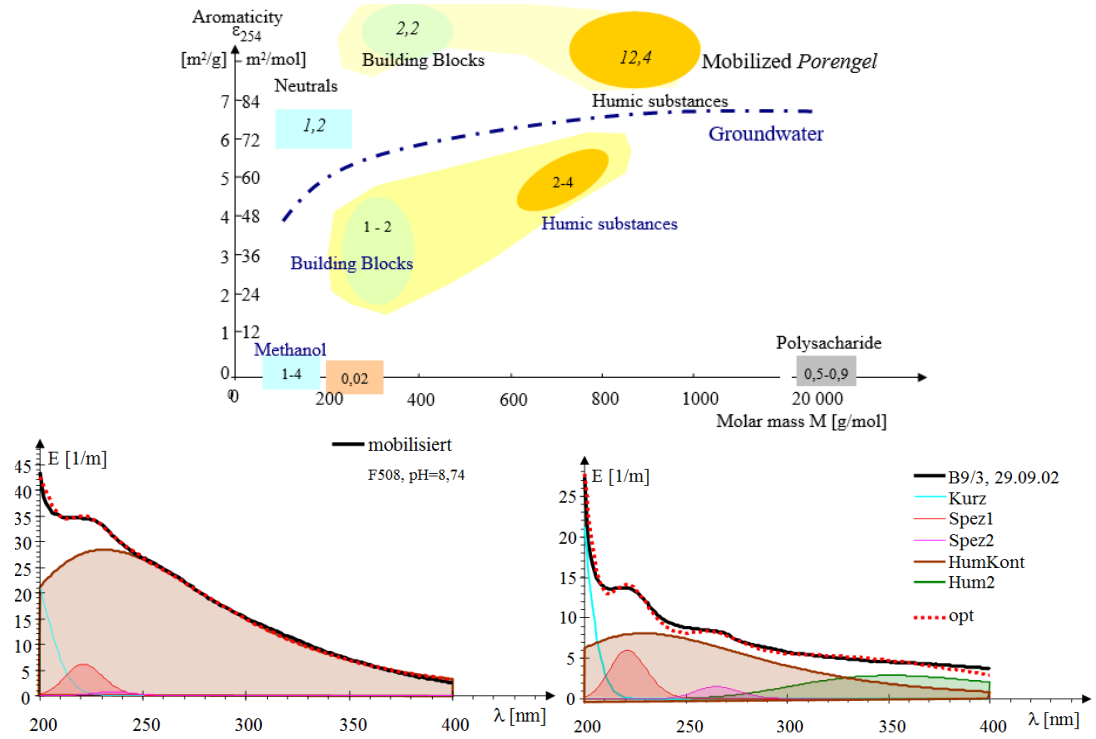

Fig. 10.32: Top: Comparison of the LC-OCD investigations of a sulfate-reduced groundwater (methanol = residual substrate) with the alkaline soluble fraction of the corresponding *Porengel* (indication of the DOC in mg/L). Bottom: UV spectra of mobilized humic substances (left) and a dump groundwater (right: KOCH et al. 2006).

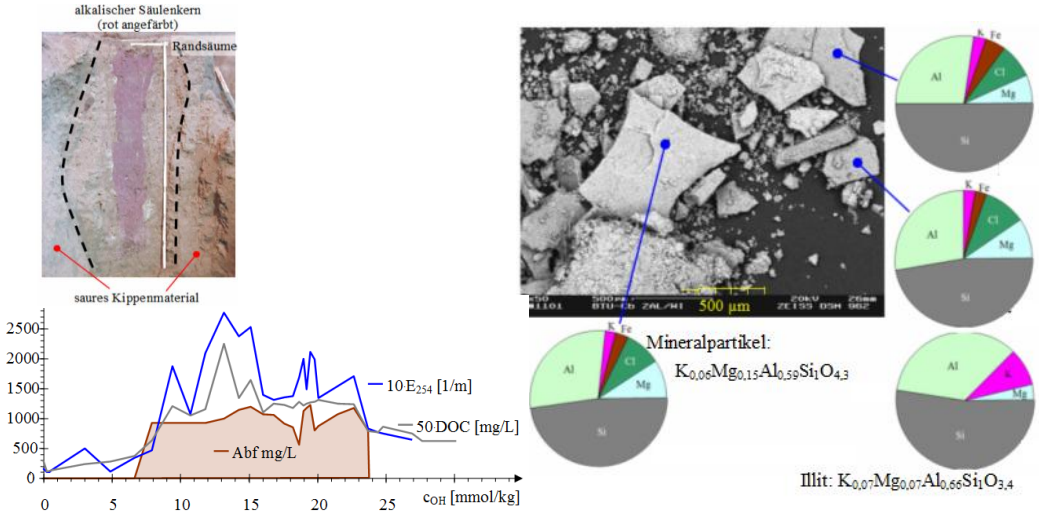

Fig. 10.33: Top left: Profile cutting surface of an ash column produced in the pilot plant and produced by injection of a fly ash suspension. The alkaline remaining area was stained red with phenolphthalein. In the marginal edges, the alkaline mobilized fine grain was deposited again after neutralization. Bottom left: Mass discharge from a dump sand filter by adding alkaline [mmol/kg] as E_{254} and DOC (humic substances), as well as magnesium chloride precipitable mobilized solids (Abf). Bottom right: Electron microscopic view of the mineral particles precipitated with magnesium chloride and their inorganic composition compared to illite. Organic components were not recorded due to preparation. The effluent pH value of the column between pH = 4 to 7 does not represent the mobilization pH value on the flow path, SCHÖPKE et al. (2007).

10.3.3 Plaque formation (*Porengel*) due to contaminants typical of gasworks

Water-soluble pyrolysis products, which include substances typical of gasworks, contain substituted aromatic and phenolic substances that tend to polymerize under oxygen consumption, similar to the humification process.Fig. 10.31. Here, too, water-insoluble phases - *Porengel*s - form together with inorganic precipitated products. SCHÖPKE* et al. (2011) investigated such a *Porengel* in the laboratory, which caused malfunctions in pump and treat groundwater remediation plants on the Schwarze Pumpe plant site in the form of deposits.

Das anaerobe Grundwasser enthielt anorganischen und organisch gebundenen Sulfidschwefel. BEERBALK (2011) formulierte einen Bindungmechanismus zwischen Eisensulfiden-, Schwefel (S_8) und Heterocyclen als Arbeitshypothese. Elektronen-mikroskopisch zeigten sich filigrane Strukturen aus Eisensulfiden, -carbonaten und -hydroxiden, zwischen denen sich organische Gele befanden, wahrscheinlich huminanaloge Polymere, Fig. 10.34. Diese wurden aus den nachgewiesenen leichtflüchtigen Alkylpyridinen und -phenolen, sowie weiteren Heterocyclen mit mikrobieller Unterstützung gebildet.

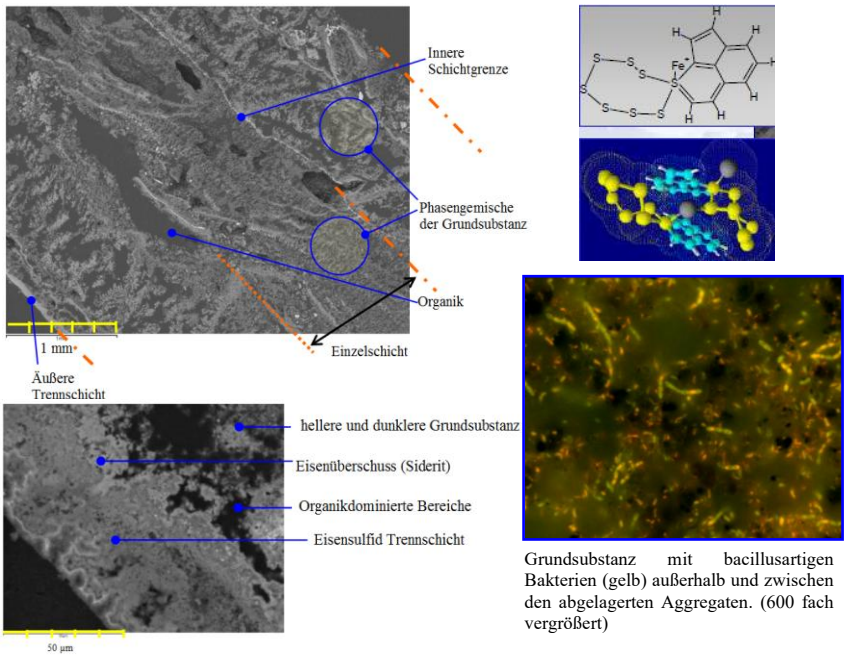

Fig. 10.34: Top left: Ground crustal particles (coating, *Porengels*) with a filigree structure recognizable by electron microscopy. The fine-grained phase mixture is referred to as the basic substance. Top right: Bond between iron sulphide, sulfur (S8) and heterocycles postulated by BEERBALK (2011). Bottom right: Bacteria stained by light microscopy (yellow) in the crustal particle.

Das an der Belagskruste (Porengel) strömende Grundwasser wurde LC-OCD- und gaschromatografisch untersucht. Dabei konnten den Neutralstoffpeaks X1 bis X6 des LC-OCD-Chromatogramms gaschromatografische ermittelte Stoffe und Stoffgruppen zugeordnet und im Molmasse-Aromatizitäts-Diagramm zusammengeführt werden, Fig. 10.35. Diesen enthielten auch Stickstoff. Den LMW-acids, Huminstoffen und deren Vorstufen (HS+BB) ließen sich keine gaschromatografisch identifizierten Stoffgruppen zuordnen. Sie sind wahrscheinlich mit aromatischen und heterocyclischen Kontaminanten Verbindungen eingegangen. Beiden Analysenverfahren entging allerdings ein erheblicher Anteil des höhermolekularen organischen Kohlenstoffs (HOC).

Das im Kontakt mit den Belägen stehende kontaminierte Grundwasser trübte sich nach geringer Sauerstoffzufuhr innerhalb weniger Tage ein, interpretiert als Beginn mikrobiologischer Gelphasenbildung. Diese nach Sauerstoffzufuhr einsetzenden biochemisch unterstützten Polymerisationsreaktionen wurden durch Zugabe von Kondensationskeimen in Form pulverisiertem Eisenhydroxid (Ferrosorp®), Zeolith und Aktivkohle unterstützt. Die UV/VIS-Spektren ließen sich mit geringfügig nachjustierten Elementarbanden Kurz, Spez1, Spez2 und in Spuren Humkont anpassen. Während der kurzen Beobachtungszeit von vier Tagen wurde der DOC im Grundwasser und den ferrosorp- und zeolithangereicherten Proben von 160 mg/L auf ca. 90 mg/L gesenkt. Adsorption an polaren Oberflächen spielte keine Rolle. Anders bei der Aktivkohle. Dort wurden die unpolaren Aromaten adsorbiert und es verblieben die polaren Anteile von DOC ≈ 7 mg/L, wodurch die Bande Humkont erst nachweisbar wurde. Die experimentelle Aufklärung dieser Prozesse war nicht vorgesehen.

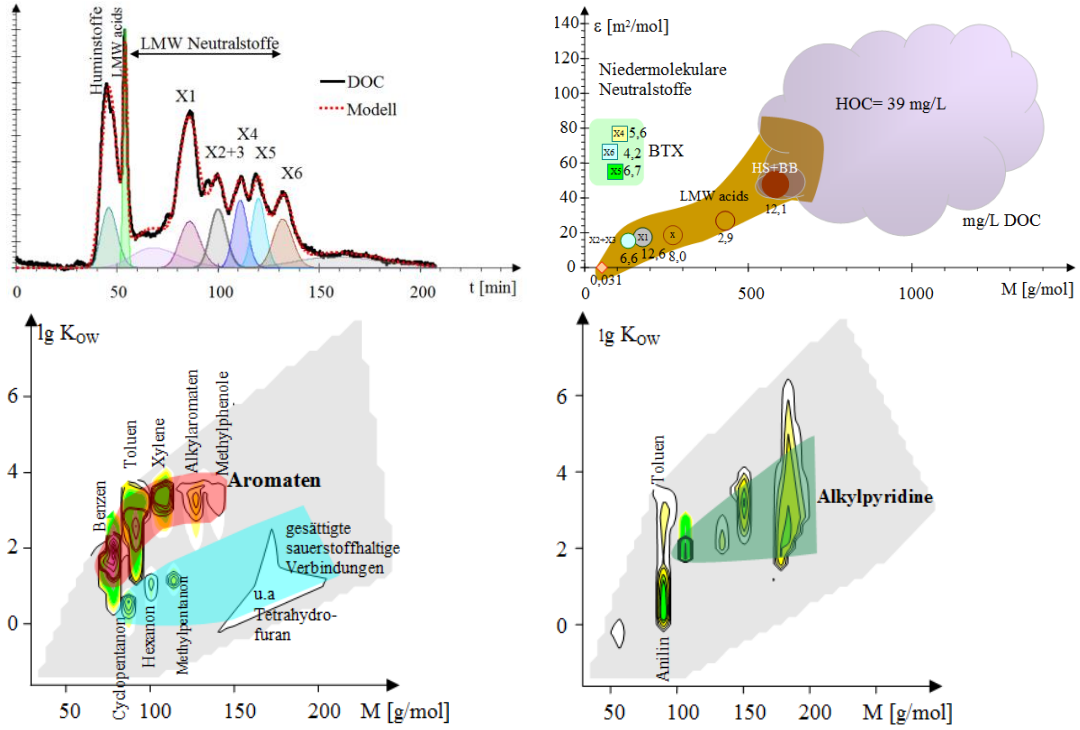

Fig. 10.35: Top: Merge of LC-OCD and gas chromatography. Evaluation of the LC-OCD chromatogram (left) and interpretation in the aromaticity-molar mass diagram (right). The one in the HOC (hydrophobic LC-OCD- nonchromatographable organic carbon) is shown as a higher molecular weight *cloud* with greater aromaticity. Bottom: log K_{OW} molar mass diagram of low-boiling substances in groundwater (left) and (volatile) substances distilled from the solid (right).

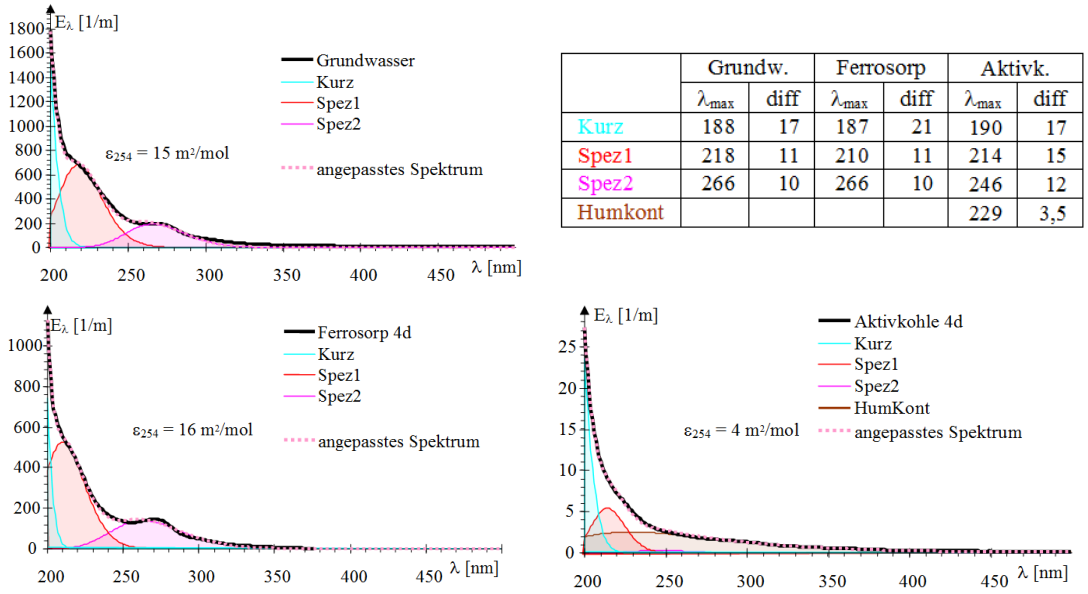

	Grundw.		Ferrosorp		Aktivk.	
	λ_{max}	diff	λ_{max}	diff	λ_{max}	diff
Kurz	188	17	187	21	190	17
Spez1	218	11	210	11	214	15
Spez2	266	10	266	10	246	12
Humkont					229	3,5

Fig. 10.36: UV/VIS spectral measurements of groundwater. Top: Groundwater (left) and readjusted elementary bands. Bottom: Humification-analogous processes initiated after aeration with condensation particles. Ferrosorp Iron Hydroxide Powder and Activated Carbon Powder.

10.3.4 Treatment of wastewater containing aromatics by stimulating humification processes

10.3.4.1 Pyrolysis Wastewater

SCHÖPKE (2007) already investigated the question of whether the humification processes of nature initiated by the oxidative polymerization of different aromatics can be transferred to similarly constituted wastewater. The tests with wastewater from residue smoldering and cellulose digestion yielded no results. The latter mainly contained lignin fragments.

KOCH et al.* (2007) investigated the inadequate COD degradation of pyrolysis wastewater (SVZ-Schwarze Pumpe) also from the point of view of the use of humification processes. The condensation water produced during the entrained flow gasification of waste was pre-cleaned, then the phenol was extracted and ammonium was expelled. The remaining highly contaminated organic pyrolysis wastewater, which was pre-cleaned in an intensive biology laboratory with the addition of oxygen and then treated in a wastewater treatment plant together with municipal wastewater, nevertheless still contained a refractory residual COD (> 210 mg/L O_2) above the legally prescribed discharge value. Already in GDR times, the Schwarze Pumpe gas combine was held responsible for part of the organic base load of the Spree near Berlin, SCHÖPKE et al.* (1985).

Together with previous investigations, a concentration pattern typical of biologically stabilized pyrolysis wastewater emerges. The problematic refractory substances (Watertreatment-related substances, WWR) consist of aliphatic components, presumably branched hydrocarbon chains in the molar mass range between 250 and 750 g/mol, which are linked to each other via ester and ether bonds and are only partially biodegradable. They cannot be assigned to humic substances, but to non-ionic surfactants (indication: foaming). This is also indicated by the low proportion of acid functions, Tab. 10.32. Screening analyses of the operator were combined with LC-OCD studies, UV/VIS spectra, titrations, biodegradation and treatment trials in the laboratory, Tab. 10.31. The remaining consumption behaviour BOD(t) after intensive biology has already been described, chapter 9.4.3 with Fig. 9.42 and Tab. 9.41.

Tab. 10.31: Test results: Pyrolysis (waste) water (Pyr) after dephenolization, after intensive biology (I-Bio), double determination of watertreatment-related substances (WWR1/2) and after treatment together with municipal wastewater in the sewage treatment plant (GKA).

Parameter		Pyr	I-Bio	WWR(1)	WWR(2)	GKA
Temp	°C	34	28	20	20	25
pH	1	7.83	6.66	7.05	6.97	7.65
LF	mS/cm	14.24	14.28	15.31	15.19	7.54
TOC	mg/L		3013	2024	2226	211
DOC	mg/L	5422	2678	2016	1876	207
DIC	mg/L		190	465	390	173
DIC	mmol/L		15.8	38.8	32.5	14.4
DN	mg/L		572	433	385	40.2
DN	mmol/L		31.8	24.1	21.4	2.2
CSB-uf	mg/L	13850	8505	5150	6010	615
CSB-f	mg/L	13600	8295	4885	5215	545
E_{254}	1/m	3990	3982	4162	3911	502

Tab. 10.32: Derived parameters: Pyrolysis (waste) water (Pyr) after dephenolation, after intensive biology (I-Bio), double determination of watertreatment-related substances (WWR1/2) and after treatment together with municipal wastewater in the wastewater treatment plant (GKA).

Parameter		Pyr	I-Bio	WWR(1)	WWR(2)	GKA
CSB/DOC	1	1,88	2,32	1,82	2,08	1,97
ε_{254}	m^2/mol	8,8	17,8	24,8	25,0	29,1
Titrations						
DIC	mmol/L	13	13	30	31	8
	mg/L	151	156	360	374	96
R-COOH	pK	5,7	5,4	5,7	5,6	6,1
	mmol/L	4,3	18	18,5	18,6	8,4
NH3+ArOH	pK	9,5	9,2			9,5
	mmol/L	13	28			15
DIC-titrated	%		82	77	96	55
NH3+ArOH-tititized	%		88			672
R-COOH/DOC	1		0,024	0,034	0,036	0,354
NH3+ArOH/DOC	1		0,125			0,870

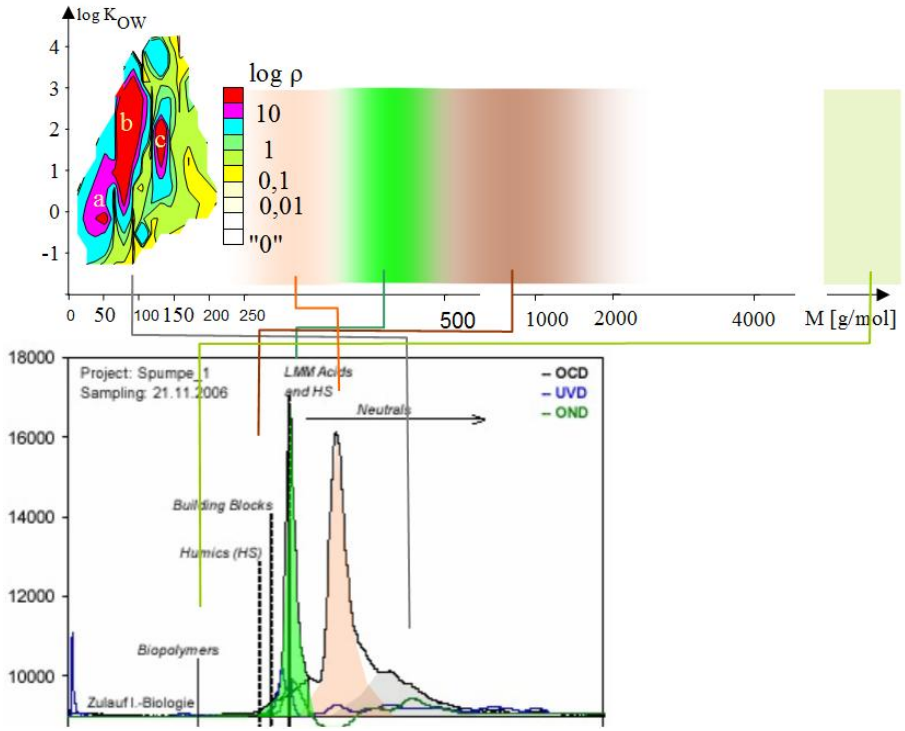

Fig. 10.37: Interpretation of the composition of pyrolysis wastewater. Top: Two-dimensional COD distribution ($\log K_{OW}$-M) of 80 to 90% of the substances detected by gas chromatography in the boiling range C5 to C18. The density shown in color ($\log \rho$ chapter 9.1.2) in the selected grid ($\Delta M = 13{,}2$ g/mol; $\Delta \log K_{OW} = 0.37$) marks their concentration distribution (left). (a) acetone, acetonitrile, (b) simple aromatics of various polarities, (c) pyrrole, phenol, benzene, toluene, pyridine, pyrazine, 2-methylpyrazine, n-butanol (hydrolysis product of the phenol extractor used) and alkylphenols with M > 100 g/mol. The maximum around M = 144 g/mol is formed by naphthol and derivatives. Higher polycyclic alcohols were no longer recorded. To the right of them are the higher molar mass ranges of unknown polarity. Bottom: LC-OCD chromatogram of the pyrolysis water after dephenolization with reference to the molar mass ranges shown above.

The proportions of carboxyl functions in the DOC (R-COOH/DOC) determined by titration are much smaller in the treated pyrolysis wastewater than those of humic substances (≈ 0.22 chapter 7.4.1), in contrast to the one treated with urban wastewater, Tab. 10.32. It is likely that the refractory fraction (WWR) consists of higher molecular weight polar condensates with a high aliphate content and is therefore not accessible to humification processes. The molecules are too large to penetrate the activated carbon pore system, do not bind to hyroxide surfaces via hydrogen bonds due to a lack of acid functions, and are not yet large enough for coagulation (flocculation). The results can probably be generalized to pyrolysis wastewater and gas plant contamination.

A condensation wastewater from the smoldering of paper residues (*Spuckstoffe*) had a high consumption potential due to biologically available phenols, which appeared in the UV spectrum by a local maximum of $\lambda = 278$ nm. Here, too, the substances in the range of M < 400 g/mol could not be stimulated to humification, Tab. 10.33.

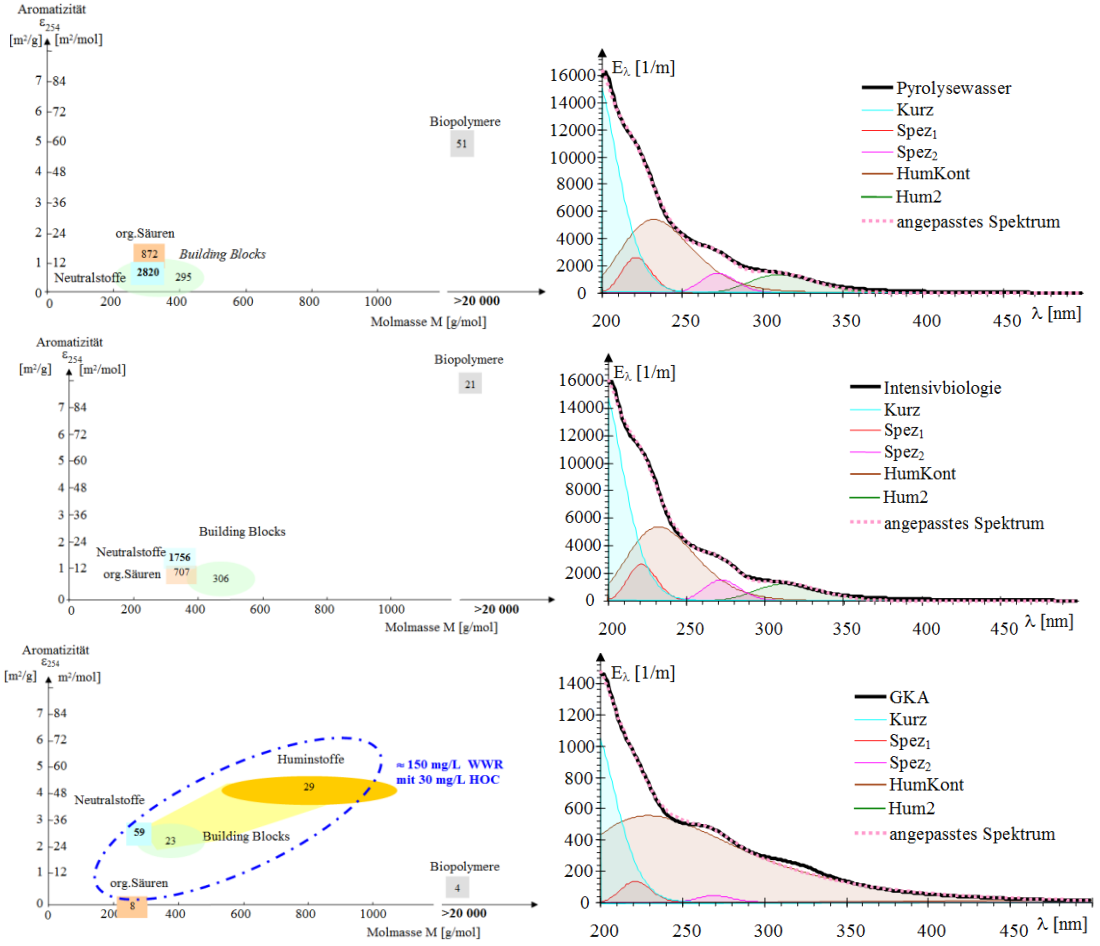

Fig. 10.38: Left column: Aromaticity molar mass representations of LC-OCD chromatograms (DOC [mg/L]). For the effluent of the community wastewater treatment plant (GKA), the DOC of watertreatment-related substances (WWR) and that of non-chromatographable hydrophobic substances (HOC) is given. Right column: UV/VIS spectra with elementary band decomposition. Top: Pyrolysis (waste) water after dephenolation and before intensive biology treatment. Middle: after intensive biology. Bottom: after treatment with municipal wastewater in the wastewater treatment plant (GKA).

Tab. 10.33: Smoldering wastewater from residues of paper applications (*Spuckstoffe*) with phenols. Left: Organic sum parameters with LC-OCD evaluation. Right: UV spectrum with adapted elementary band decomposition, SIEBER* (2001).

Organic Sum parameter	mg/L	UV- Spectra KRT = 3,5 %	λ_{max} nm	diff 1	E_{max} 1/m	E_{int} 1/(m²·nm)
TOC	32600	Kurz	194	18	41085	12
CSB	93000	Spez1	219	18	10475	3
BSB_5	32600	Spez2	278	16	5901	1,3
Phenolindex	900	Humkont	229	4,3	8378	8,5

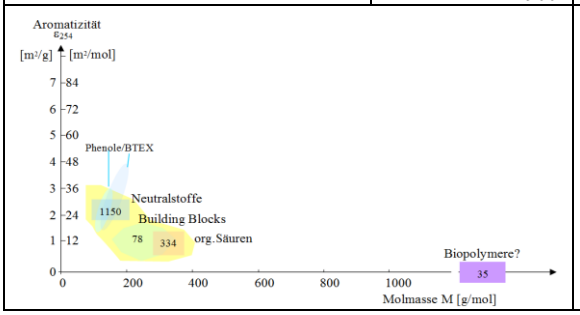

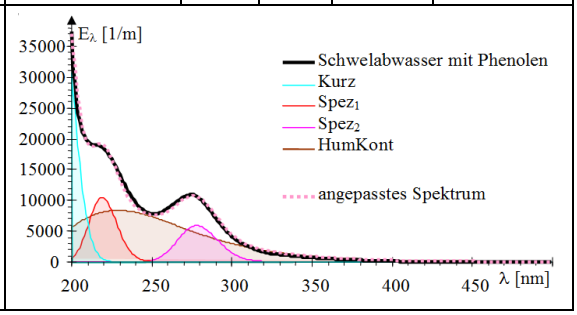

10.3.4.2 Lignin-containing wastewater

The alkaline digestion of textile hemp produces a dark-coloured alkaline wastewater, *Schwarzlauge,* during the production process. SCHÖPKE et al. (2002) and KOCH et al. (2006) tested their application as a substrate for microbial sulfate reduction. For this purpose, the colouring lignin fragments would have had to be removed beforehand, e.g. by incorporation into the chemically similar humic substances. Here, too, the substances in the range of M < 400 g/mol could not be stimulated to humification, Tab. 10.3-4.

Tab. 10.3-4: Hemp digestion water (*Schwarzlauge*). Left: Organic sum parameters with LC-OCD evaluation. The depletion attempt was faulty and other parameters could no longer be found. Right: UV spectrum with adapted elementary band decomposition, SCHÖPKE et al. (2002) and KOCH et al. (2006).

Organic Sum parameter	mg/L	UV- Spektren KRT = 1,3 %	λ_{max} nm	diff 1	E_{max} 1/m	E_{int} 1/(m²·nm)
TOC	12551	Kurz	194	10	73976	38
CSB	nicht mehr auffindbar	Spez1	223	17	9651	2,5
BSB_5	> 1000	Spez2	245	12	8859	3,0
Phenolindex		Humkont	287	4,5	10007	7,7

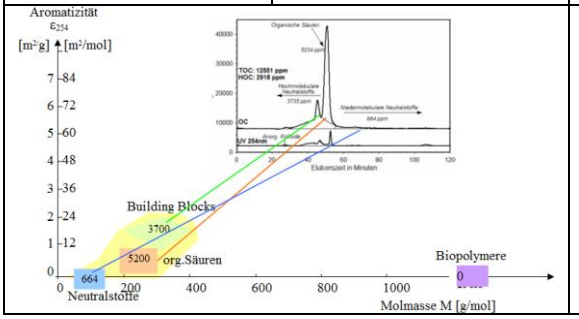

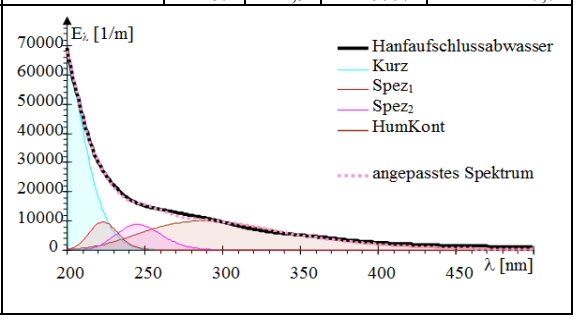

10.3.4.3 Evaluation of the attempts to stimulate humification

The use of humification processes under near-natural conditions was unsuccessful overall. Near-natural means the temperature range of drinking water and municipal wastewater, atmospheric pressure and no drastic changes in the environment, i.e.:

- pH changes in the range pH = 3 - 10,
- Oxidation with oxygen, hydrogen peroxide and ozone far below total oxidation,
- electrochemically via a diamond electrode,
- conventional flocculation and adsorption,
- Stimulation of polymerization reactions, e.g. by formaldehyde, etc.,
- Biodegradation.

Only the highly concentrated contaminants typical of the gasworks tended to condense into mechanically stable deposits, chapter 10.3.3. Some of the non-chromophore components were able to condense on hydroxide surfaces (iron hydroxide, zeolite) under microbiological influence. The components causing the continuous UV spectra remained in the solution and were partially activated carbon adsorbable. The treatment effect remained unsatisfactory and humification reactions could not be detected. The formation of traces of mucus-like products, which is not relevant to the process, makes the untested application of membrane processes appear pessimistic.

10.3.5 DOC oxidation in mine-acidified Lusatian open-cast mining lakes

FRIESE et al. (2002) attributed the low DOC concentrations in mining-acidified Lusatian opencast lakes, which are fed by humin-contaminated dump groundwaters, to photochemical oxidation according to the Fenton mechanism, FigFig.10.39. In the acidic oxic water layers, up to more than 90 % of the total iron (around 1 mmol/L) is present as ferric iron. The oxidative attack on π-electron systems also leads to a reduction in aromaticity.

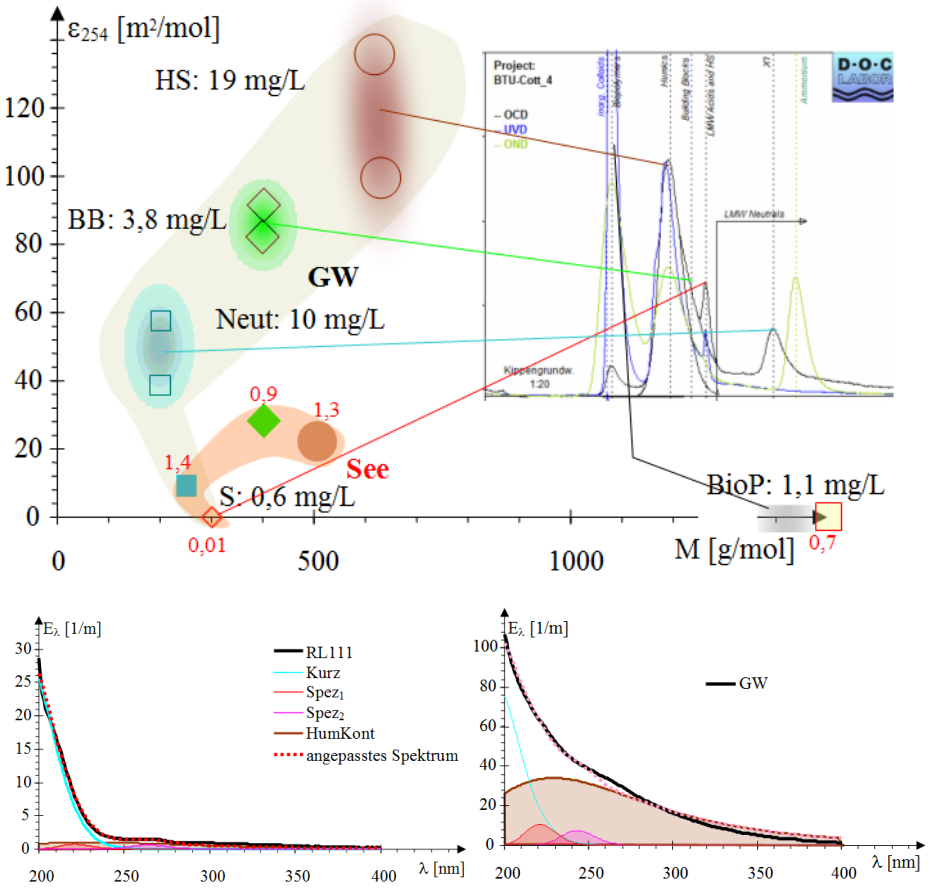

Probe	Kurz			Spez1			Spez2			Humkont		
	λ	diff	$10^3 \cdot E_{int}$	λ	diff	$10^3 \cdot E_{int}$	λ	diff	$10^3 \cdot E_{int}$	λ	diff	$10^3 \cdot E_{int}$
	nm	1	$(nm \cdot m)^{-1}$	nm	1	$(nm \cdot m)^{-1}$	nm	1	$(nm \cdot m)^{-1}$	nm	1	$(nm \cdot m)^{-1}$
RL111	194	10	14,4	221	17	0,2	264	17	0,1	229	3,5	1,3
GW	194	10	42,6	221	17	2,8	243	17	1,8	229	3,5	42,5

Fig.10.39: Photochemical DOC degradation. Top: The LCOCD chromatogram of the dump groundwater (GW: AN2–2 SCHÖPKE et al. 2007) converted into the ε_{254} molar mass diagram in comparison with that of the lake water (Lake/*See*: RL111, PREUß 2004). Both samples do not correspond with each other, but illustrate the degradation of high-molecular humic substances to lower molecular weight acids (S red), building blocks (BB green), neutrals (Neut blue) and humic acids (HS brown) with lower aromaticity. The DOC proportions are indicated in black for groundwater and red in red for acidic seawater. Among them are the associated band decompositions of the UV spectra.

10.4 Porengels of Biofiltration

10.4.1 Artificial groundwater recharge and slow sand filter

Slow sand bank filtration and artificial groundwater recharge for water treatment, as well as trickling filters and constructed wetlands in wastewater treatment represent biochemical filtration processes. If there is insufficient groundwater supply, well galleries are often built near the banks of bodies of water with the aim of obtaining

additional bank filtrate. Shore filtrate is groundwater that forms through natural processes after infiltration of surface water by the river bed. In the case of artificial groundwater recharge, additional infiltration systems will be installed. In the infiltration area of these near-natural processes, processes analogous to those in the slow sand filters, which also have a biological effect, take place, Fig. 10.41.

The formation of groundwater from the infiltrate takes place in several phases:

1. *Filtering* (sieve and filter effects) of particulate matter on the basin surface or the water bed.

The filtered substances form an increasingly less permeable filter cake on the filter surface. The colmation layer that forms at the bottom of the water is cleared away by occasional floods. On the seepage basins, this so-called *Schmutzdecke* must be cleared away using various regeneration processes. In the case of planted seepage basins for drinking water and wastewater treatment, one relies on the natural degradation of the predominantly organic deposits.

The sum parameters watertreatment-related substances WWR for the rest after soil passage and drinking water-related substances after activated carbon treatment were defined with regard to these technologies, chapter 7.1.1.

2. Vertical passage or seepage section or aeration zone (gas exchange with soil air).

This is where the essential aerobic degradation processes take place, right down to the substances relevant to the waterworks. In the process, biomass is formed as well as *respired*.

3. Transition to the anoxic environment with the reductive solution of manganese and iron oxide hydrates and the horizontal passage to the production wells.

If the remaining waterworks-relevant substances do not comply with the required quality criteria, further treatment steps (ozonation, flocculation, activated carbon, ...) are required.

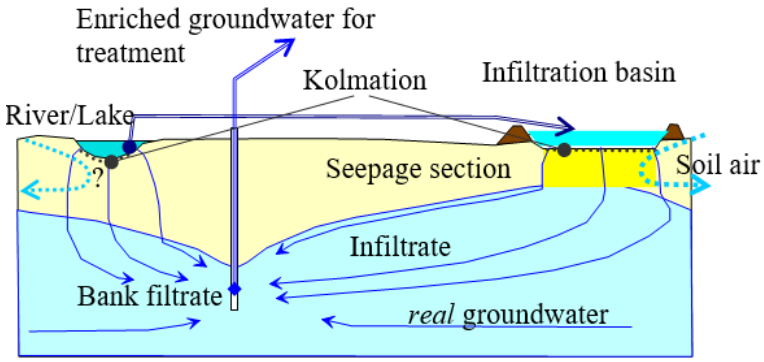

Fig. 10.41: Bank filtration (left) and artificial groundwater recharge (GWA, right).

10.4.2 Influence of oxygen concentration on infiltrate composition

The decisive treatment reactions take place in the slow sand filter under the *Schmutzdecke*. The biologically active biofilms in this zone metabolize biodegradable

substances and adsorb colloids and dissolved trace substances. This biofilm feeds on the dissolved and colloidal substances of the flowing pore solution, including wastewater-borne microorganisms. Inorganic particles such as clay minerals, humic substances and iron hydroxide colloids are embedded in it and stabilize the EPS gels. In contrast to wastewater treatment, biomass build-up and degradation processes stabilize its low layer thickness with negligible hydraulic effect.

At high water temperatures, the biomass formed is quickly metabolized again and accumulated under colder winter temperatures. As temperatures rise again, this leads to an increased demand for oxygen, which must be covered by the flowing pore solution. Under oxygen deficiency, the aerobic *Porengel* loses its stability as a result of reductive dissolution of iron and manganese oxide hydrates and the death of aerobes, releasing the substances trapped in the *Porengel* and microorganisms that are still active.

The quality breakthroughs summarized by SCHÖPKE (2007) consisted of increased concentrations of ferrous iron, manganese, organic substances, including humic substances, as well as bacteria (colony-forming unit CFU, *Coliforms*) and probably also viruses. Once mobilized, they were transported with the pore solution to the production well. To ensure the operational safety of these plants, anaerobies must therefore be avoided in the biochemically active slow sand filter layer.

10.4.3 Oxygen depletion in the aerobic zone

The biologically active layer must be completely oxygenated by the pore solution. For the oxygen consumption on the biofilm/*Porengel* surface, a film kinetics (1st order) is postulated and the flow time or the flow path of different filter configurations is replaced by the filtration parameter FP. SCHÖPKE* et al. (1985) formulated boundary conditions for the avoidance of anaerobic filter processes, which can be transferred to different filter configurations via the integral oxygen depletion rate R_{O2}, Eq.(10.4-1):

- aerobic flow $c_{O2} > 1$mg/L: Stable drain quality
- Oxygen deficiency $c_{O2} < 1$mg/L: Texture breakthrough

Die integrale Sauerstoffzehrungsgeschwindigkeit eines Filters R_{O2} wird aus seiner Sauerstoffzehrung und dem zugehörigen Filtrationsparameter FP als R_{O2} [mg/(m²·h)] in Versuchen bestimmt, Eq.(10.4-1).

$$R_{O2} = \frac{\Delta c_{O2}}{FP} \qquad \text{für } c_{O2} > 1 \text{ mg/L} \qquad (10.4\text{-}1)$$

Experimental slow filters required at least six months of training for the accumulation of a reproducibly stable biofilm (*Porengel*) compared to technical systems. Rapid filters had a higher integral oxygen consumption (up to 12 mg/(m²·h)) compared to parallel slow filters (up to 1 mg/(m²·h)).

From the integral oxygen depletion rates R_{O2}, minimum filtration velocity $v_{f,min}$ were derived for different filter configurations, up to which anaerobic states are not to be expected, Eq.(10.4-2).

$$v_{f,min} > R_{O2} \cdot \frac{6 \cdot (1 - n_p) \cdot L}{(c_{O2} - 1 mg/L) \cdot d_w} \qquad (10.4\text{-}2)$$

10.4.4 Application examples

10.4.4.1 Quality problems in the slow sand filtration of water from Müggelsee

In the 1980s, the filtration velocity in the slow sand filters of the Müggelsee water treatment (Berlin/Friedrichshagen) fell below the minimum filtration velocity $v_{f,min}$ at high plankton concentrations, with subsequent severe impairments of the filtrate quality (SCHÖPKE* et al. 1980). Schöpke et al. (1990) demonstrated the reductive mobilization of humic substances from the filter sand after three weeks of incubation with methanol and sucrose as substrate. First, manganese went into solution, followed by humic substances, qualitatively proven by their UV spectra. The problem was temporarily solved by pre-filtration via sand filters for hydraulic relief of the slow sand filters. Direct seawater treatment was completely shut down after 1990.

10.4.4.2 Formation of organically highly polluted water bodies (*Huminwolken*)

SCHÖPKE* et al. (1985) documented the transfer of mobilized *Porengel* components into the aquifer and their subsequent migration as so-called humic clouds in experiments on the groundwater recharge of Spree water near Berlin. Under high water temperatures, anaerobic conditions developed in the infiltration area after a short flow time (< 1 d), as a result of which the pH value dropped and the infiltrate temporarily enriched with iron, manganese, humic substances and bacteria (colony-forming unit increase). The so-called *Huminwolken* migrated with the infiltrate stream to the catchment over the course of months. The different migration of the individual parameters was due to dispersion and chromatography effects.

These processes, which are only documented at great expense, usually go unnoticed under the conditions mentioned in bank filtration and artificial groundwater recharge. This was indicated by the short-term exceedances of the bacteriological findings of the bank filtrate wells observed during the same period.

10.4.4.3 Recommendations for the use of biofilters with soil passage for water treatment

Prowa Cottbus* (1989) summarised the experiences from several groundwater recharge trials in an unpublished draft of the WAPRO 1.17 groundwater recharge:

The colmation of the upper sand layer limits the operating time of sand basins, chapter 5.3. Most elimination processes take place under aerobic conditions, whereas remobilization processes are possible under anaerobic conditions. The quality of the enriched groundwater, in particular its hygienic load, is determined by the oxygen supply of the slow sand filter-analogue infiltration area. Accordingly, pre-treatment steps must be provided. Peatty aquifers are not suitable for soil passage because of their oxygen-depleting potential and with their high content of mobilizable humic substances.

10.5 Adsorption Filtration

10.5.1 Adsorbent

10.5.1.1 Activated carbon

Adsorption of activated carbon has been used technically in drinking water treatment since the 1920s. Originally, the goal was only to remove odor- and taste-impairing substances. Today, adsorption is used to separate dissolved organic substances (KÜMMEL & WORCH 1990). In addition, activated carbon is also used for dechlorination.

The size of the sorption surface and its accessibility to water constituents are determined by the pore radius distribution. Depending on the activated carbon, the maximum pore radius distribution is between 0.2 and 0.8 nm. Macromolecular humic substances or the like can sometimes compete with micropollutants or impair the treatment performance of the activated carbon by blocking the micropores.

Special abrasion-resistant activated carbons with high adsorption capacities are used for activated carbon filtration. In practice, filters are operated with layer lengths of 1 - 3 m and fictitious contact times of 10 - 30 minutes. The filtration velocities are therefore in the range of 5 - 20 m/h. Oxygen consumption must be taken into account, especially at low filtration velocities (DVGW W239). Due to the unavoidable colonization of the grain surfaces, activated carbon filtration in drinking water treatment must always be followed by disinfection. The microorganisms can extend the filter running time (operating time between two coal changes) through biochemical degradation of adsorbed substances.

Tab. 10.5-1: Characteristics of activated carbons.

Particle size distribution curve, effective grain diameter, uniformity coefficient
Density of grain
Bulk density
Flowable porosity
BET-surface
Pore radius distribution (Hg-Porosimetrie)
Iodine number [mg/g für 20 mmol/L concentration of equilibrium]
Phenolaufnahme [mass-% for 1 mg/L Gleichgewichtskonzentration]
Adsorption isotherms
Diffusion constants for Film and grain

10.5.2 Concentration breakthrough

The first occurrence of a substance to be adsorbed at a specific location on the filter bed or in the effluent is called a breakthrough, Fig. 10.51. The breakthrough curves of mixtures of substances are determined by their different isotherms and their adsorption kinetics and form complex breakthrough fronts that migrate through the filter layer, chapter 8.3. The moderately adsorbing substances initially penetrate into deeper layers. The highly adsorbable substances, which advance more slowly, displace the moderately

adsorbable substances, which means that they appear in the filter outlet even in higher concentrations than in the inlet, Fig. 10.51.

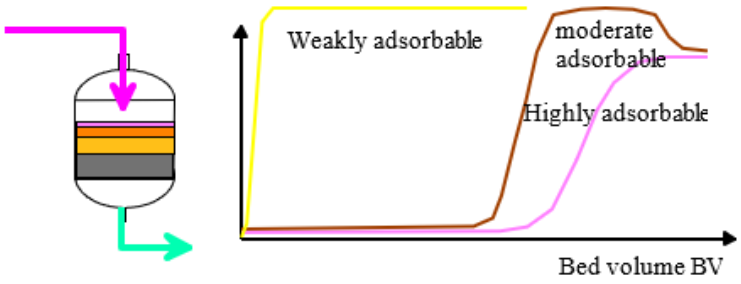

Fig. 10.51: Diagram of activated carbon filtration and breakthrough curves of water constituents with different levels of adsorbability.

The filter breakthrough is defined differently:

- Stoichiometric breakthrough

Assuming the adsorption equilibrium, the filter reaches the stoichiometric load $q(c_0)$ with respect to the inlet concentration. In simple cases, this is reached after $c = c_0/2$ in the sequence.

- Complete breakthrough

The complete breakthrough of the adsorber is achieved when the entire adsorption material is in equilibrium with the inlet concentration in terms of loading. ($c = c_0$).

- Target value breakthrough

In this process, a specified target value is reached as a termination criterion in the process.

10.5.3 Adsorption filtration modeling

10.5.3.1 Basics

Adsorption kinetics are determined by the following processes:

- External mass transport: Transport of the adsorptive from the free solution to the edge of the boundary layer of the adsorbent grain, chapter 3.3,
- Film diffusion: Diffusion velocity from the solution to the grain surface through the flow-dependent boundary layer, chapter **Fehler! Verweisquelle konnte nicht gefunden werden.**.
- Surface complex formation (adsorption reaction often negligible),
- Grain diffusion: Diffusion rate of the surface complex into the grain interior to still free adsorption sites, chapter **Fehler! Verweisquelle konnte nicht gefunden werden.**.

The modelling of these processes is difficult despite various simplifications. In the case of negligible grain porosity, e.g. granular iron hydroxides (ferrosorp®), the *mixed cell* equilibrium model can be applied while neglecting the kinetics, SCHÖPKE et al. (2013). Calibration is carried out via filter tests.

10.5.3.2 Use of dimensionless numbers

Another possibility is the scale transfer of filter tests to technical systems via dimensionless numbers, chapter **Fehler! Verweisquelle konnte nicht gefunden werden.**. SONTHEIMER et al. (1985) and BAHR (2012) thus reduced the number of parameters to be taken into account for the design, Tab. 10.52.

Tab. 10.52: Dimensionless quantities of an adsorption filter according to SONTHEIMER et al. (1985) and BAHR (2012).

Kapazitätsfaktor	C_F	$C_F = \frac{\rho_S}{n_P} \cdot \frac{q_0(c_0)}{c_0}$	(10.5-1)
Reduzierte Filterlaufzeit	T	$T = \frac{t}{t_F \cdot C_F} = \frac{v_f \cdot t}{L \cdot C_F} = \frac{H}{L \cdot C_F}$	(10.5-2)
Reduzierte Lösungskonzentration	X	$X = \frac{c}{c_0}$	(10.5-3)
Reduzierte Beladung	Y	$Y = \frac{q}{q_0}$	(10.5-4)
Axialkoordinate des Filters	Z	$Z = \frac{L}{L_F}$	(10.5-5)
Radialkoordinate (Korn)	R	$R = \frac{2 \cdot r}{d_w}$	(10.5-6)
Diffusionsmodul Ed	Ed	$Ed = \frac{4 \cdot D_S \cdot C_F \cdot t_F}{d_w^2}$	(10.5-7)
modifiziert STANTON-Zahl	ST^*	$ST^* = \frac{2 \cdot (1 - n_P) \cdot t_F \cdot \beta}{n_P \cdot d_w}$	(10.5-8)
BIOT-Zahl	Bi	$Bi = \frac{St^*}{Ed} = \frac{(1 - n_P) \cdot d_w \cdot c_0}{2 \cdot \rho_S \cdot q_0(c_0)} \cdot \frac{\beta}{D_S}$	(3.7-10)
FREUNDLICH-Exponent	n	$q = K_{Freundlich} \cdot c^n$	(10.5-9)

The difference between Eq.(3.7-10) and Eq.(3.7-11) consists in the use of bulk density instead of grain density, which is converted by $(1-n_P)^{-1}$

In the dimensionless form, the breakthrough curve is described by a function of dimensionless quantities, Eq.(10.5-10).

$$X = f(T, C_F, St^*, Bi, n) \tag{10.5-10}$$

This is based on a friendly isotherm for a single substance. BAHR (2012) recommends the software *FAST - Fixed-bed Adsorption Simulation Tool*.

10.5.3.3 Influence of adsorption on longitudinal dispersion α_L

According to the transport model of WORCH (2004), adsorption processes lead to an increase in the dispersivity of concentration fronts. To this end, he extends the balance equation Eq.(3.1-9) on the loading of the filter material q, Eq.(10.5-11),

$$v_f \cdot \frac{\partial c}{\partial L} + n_P \cdot \frac{\partial c}{\partial t} + \rho_S \cdot \frac{\partial q}{\partial t} = D_L \cdot n_P \cdot \frac{\partial^2 c}{\partial L^2} \tag{10.5-11}$$

and the linear adsorption isotherm Eq. (6.5-16) Used Eq.(8.3-10).

$$R_F^* = \frac{R_F}{n_P} = \frac{v_f}{n_P \cdot v_A} = 1 + \frac{\rho_S}{n_P} \cdot K_d = 1 + \frac{q(c)}{c} \tag{10.5-12}$$

This is described in Eq.(10.5-11) Eq.(10.5-13) to Eq.(10.5-16).

$$\frac{v_f}{n_P} \cdot \frac{\partial c}{\partial L} + \frac{\partial c}{\partial t}\left(1 + \frac{\rho_S}{n_P} \cdot K_d\right) = D_L \cdot \frac{\partial^2 c}{\partial L^2} \tag{10.5-13}$$

$$\frac{v_f}{n_P} \cdot \frac{\partial c}{\partial L} + \frac{R_F}{n_P} \cdot \frac{\partial c}{\partial t} = D_L \cdot \frac{\partial^2 c}{\partial L^2} \tag{10.5-14}$$

thus

$$v_A \cdot \frac{\partial c}{\partial L} + \frac{\partial c}{\partial t} = n_P \cdot \frac{D_L}{R_F} \cdot \frac{\partial^2 c}{\partial L^2} \tag{10.5-15}$$

with

$$D^* = n_P \cdot \frac{D_L}{R_F} \tag{10.5-16}$$

Rewritten from Eq.(3.1-19) follows Eq.(10.5-17).

$$\frac{c(H_D, v_f \cdot t)}{c_0} = \frac{1}{2}\operatorname{erfc}\left(\frac{H_D - v_f \cdot t}{2 \cdot \sqrt{D \cdot t}}\right) \tag{10.5-17}$$

WORCH (2004) and SCHOENHEINZ & WORCH (2005) adopt analytical solutions from the literature, Eq.(10.5-18) and Eq.(10.5-19).

$$\frac{c}{c_0} = \frac{1}{2}\left(\operatorname{erfc}\left(\frac{L - v_A \cdot t}{2 \cdot \sqrt{D^* \cdot t}}\right) + \exp\left(\frac{v_A \cdot L}{D^*}\right) \cdot \operatorname{erfc}\left(\frac{L + v_A \cdot t}{2 \cdot \sqrt{D^* \cdot t}}\right)\right) \tag{10.5-18}$$

For the increase in dispersivity by the distribution equilibrium Eq.(10.5-20),

$$\alpha_{eff} = \alpha_L + \frac{n_P \cdot v_f}{k_S \cdot O_{sp} \cdot \rho_S \cdot R_F} = \alpha_L + \frac{v_f}{k_S \cdot O_{sp} \cdot \rho_S \cdot \left(1 + \frac{\rho_S}{n_P} \cdot K_d\right)} \tag{10.5-19}$$

and with k_L Eq.(3.7-8) follows simplified Eq.(10.5-20).

$$\alpha_{eff} = \alpha_L + \frac{d_w^2 \cdot v_f}{60 \cdot D_S \cdot R_F} \tag{10.5-20}$$

Tab. 10.53: Surface diffusion coefficients of chelated exchangers and granulated iron hydroxide (GEZ). [a)]BAHR (2012), [b)]GENZ (2005).

Water	Adssorbent	Versuch	D_S	Zitat	M
			m^2/s		g/mol
Modellwasser	Chelataustauscher	DKR		a	
Berliner TW	Chelataustauscher	DKR		a	
GW Eisenberg	Chelataustauscher	DKR		a	
GW Eisenberg	Chelataustauscher			a	
NOM GW-Berlin	GEH	KFA	9.6E-15	b	1000
NOM GW-Berlin	GEH	KFA	4.8E-14	b	3000
NOM (GW Füchtenfeld)	GEH	KFA	4.8E-15	b	1000
	GEH	KFA	6.7E-14	b	3000
SRNOM	GEH	KFA	4.8E-14	b	1000
	GEH	KFA	5.4E-14	b	3000
Salicylsäure	GEH	KFA	4.9E-13	b	
Arsenat	GEH	KFA	3.5E-14	b	
Phosphat	GEH	KFA	1.6E-14	b	

10.6 Applications of surface filtration

10.6.1 Artificial groundwater recharge

On the surface of infiltration basins of artificial groundwater recharge or slow sand filters with surface water, its sieved particles form a colmation layer, the so-called *Schmutzdecke*. The particle load of surface water can fluctuate greatly within hours.

The planning of infiltration basins, their regeneration effort and the necessary pre-treatment require lengthy pilot tests. Their effort can be statistically secured by frequent filter tests in all condition situations, chapter 9.2.

During ongoing treatment experiments for artificial groundwater recharge with *Spree* and *Neisse* water, the colmation points determined on individual test days were combined into sieve curves, Fig. 10.61. At that time, the Neisse was heavily contaminated with suspended coal and ash particles, as well as fibers from *Sphaerotilus* colonies (bacterial colonies. referred to as *Abwasserpilz*). The inorganic particles occurred especially during floods and the bacterial colonies in the cold season. The *Spree* was affected by algal blooms.

From the determined colmation points H_K, minimum operating times for the planned infiltration basins were derived. The determined colmation coefficients γ, on the other hand, could only be transferred with a high degree of uncertainty, as they were influenced by the compression behavior of the *Schmutzdecke* and/or biochemical long-time effects. Only the results from the Spree near Neuzittau (SCHÖPKE et al. 1985) were specified by parallel pilot tests.

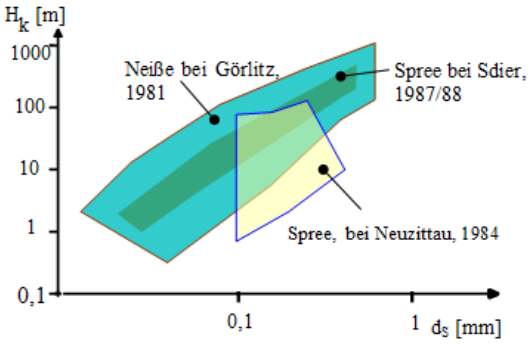

Fig. 10.61: Sieve curves $H_K(d_S)$ of river waters intended for infiltration. Neisse near Görlitz, (SCHÖPKE* et al. 1982 and SCHÖPKE* 1989a), Spree near Berlin near Neuzittau, (SCHÖPKE* et al. 1985) and the Spree below Bautzen near Sdier (SCHÖPKE* 1989).

10.6.2 Municipal wastewater

In Vorbereitung einer Filtration gereingten Abwassers bestimmten BALKE & SCHÖPKE* (2009) orientierend das Siebverhalten von vier Kläranlagenablaufproben. Die Kolmationsbeiwerte γ zeigten insgesamt eine stark streuende potenziell-abnehmende Tendenz, die die Einzelmessungen nicht repräsentierten.

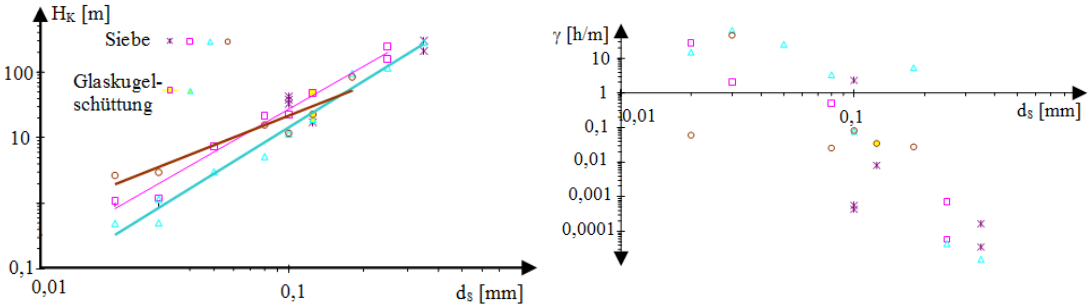

Fig. 10.62: Four samples of the effluent of the Cottbus wastewater treatment plant with the double logarithmic-linear dependence between the colmation point and the sieve diameter.

Tab. 10.61: Parameters of the Eq.(5.3-17) for screening curves of the wastewater treatment plant effluent in Cottbus.

Datum	A	B	R^2
	m	1	1
06.03.2009	1310	1,65	0,83
19.03.2009	4010	2,17	0,98
14.04.2009	3190	2,35	0,98
07.07.2009	681	1,50	0,91

Initially, it is not possible to assign an exact screen diameter d_S to technical filter materials. The few tests with surface and treated municipal wastewater have shown a relatively close relationship between the screen diameter and the effective grain diameter. The determined ratios are just above the theoretical grain spacing of the densest spherical fill (chapter **Fehler! Verweisquelle konnte nicht gefunden werden.**) between 4 balls of 0.14 (BUSCH et al. 1993), Tab. 10.62.

Tab. 10.62: Determined ratios between screen diameter and effective grain diameter with equivalent hydraulic action.

Wasser	d_S/d_w	Quelle
Neiße/Görlitz	0,27	SCHÖPKE* (1989a)
Spree/Sdier	0,19	SCHÖPKE* (1989)
Kläranlagenablauf Cottbus	0,25	BALKE & SCHÖPKE* (2009)

10.6.3 Colmation of swallowing wells

The water level in a wetland was stabilised by means of infiltration wells, among other things, whose output fell relatively quickly below the target value and required regular regeneration, SCHÖPKE & PREUß* (2010). For practical reasons, the specific colmation resistance was related to the volume flow Q_{Br} for the structurally identical wells, Eq.(10.6-1)

$$\text{Kolmationswiderstand} = \frac{h_f}{A_F \cdot v_{inf}} = \frac{\Delta h}{Q_{Br}} \left[\frac{h}{m^2} \right] \qquad (10.6\text{-}1)$$

with the well filter area A_F and Δh of the water level increase compared to the ground state. The colmation course $\Delta h/Q_{Br}$ was evaluated with regard to the water volume V [m^3] infiltrated after regeneration with the colmation volume V_K. The colmation behaviour of the 20 infiltration wells over a longer period of time was statistically evaluated, Fig. 10.63.

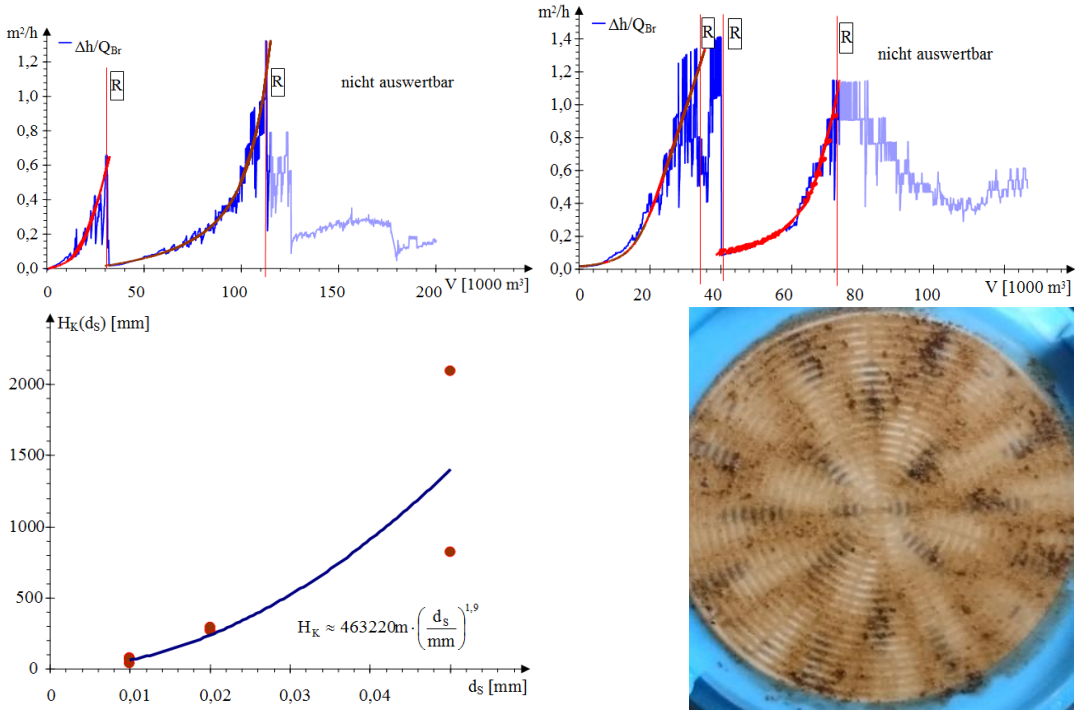

Fig. 10.63: Top: Colmation course of two wells marked with regeneration [R]. The adjusted colmation curves are marked in red and non-evaluable phases are covered. Bottom: Screen curve of the inlet water (left) and screen dS = 0.02 mm after a test (in the background the *carrier screen*).

10.6.4 Membrane filtration

The various membrane processes use very large surfaces in relation to filters at high transmembrane pressures (1 bar = 10.2 m WS). The low filtrate capacities in the range of 150 L/(h·m²) is compensated by the large, usually coiled membrane area, MELIN & RAUTENBACH (2007).

In experiments by KOCH et al. (2009) with a nanofiltration system, gypsum scaling limited its performance according to HK ≈ 9 m. The evaluation of screening processes made the process optimisation more precise, Fig. 10.64 and Fig. 10.65.

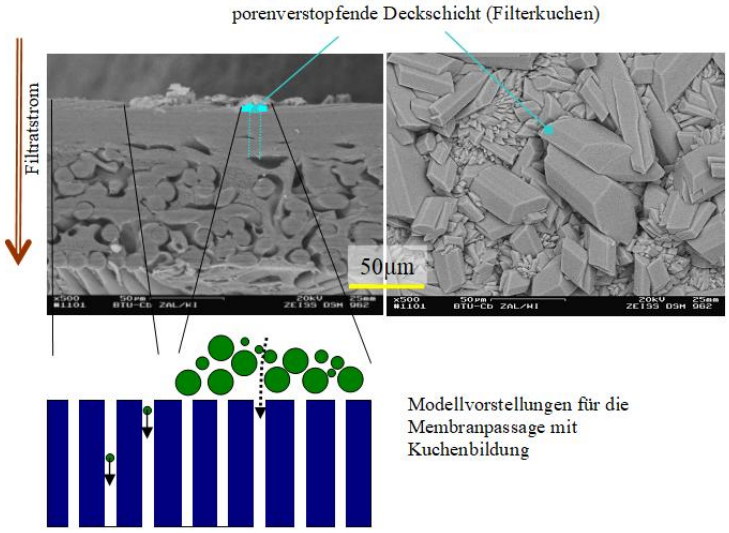

Fig. 10.64: Cross-section through a membrane with surface layer particles that restrict the cross-sectional area flowing through.

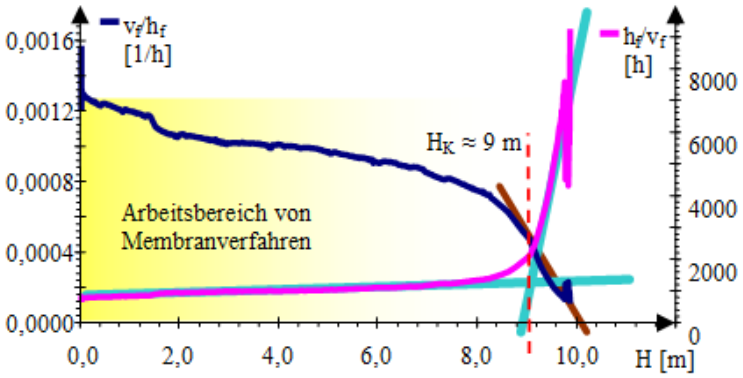

Fig. 10.65: Colmation behavior of a nanofilter membrane KOCH et al. (2009).

11 Directories

11.1 List of abbreviations and symbols

Multiple assignments of symbols in different subject areas cannot always be avoided. However, there is no risk of confusion within the subject areas. This avoids unnecessarily confusing indexing.

Symbol	Parameter	Unit	Reference/Eq.
A_F	Area of the flow cross-section	m^2, dm^2	Tab. 2.2-1
Bo	Bodenstein number	1	(3.2-5)
b	molecular cross-section, Barn	100 fm^2	Cpt. 7.1.2.1
c	Concentration	mmol/L	
c_K	Grain (number) concentration	m^{-3}	Tab. 3.4-1
d_F	Diameter of filter	m	Tab. 10.1-1
diff	Reciprocal value of absorption band width	1	(9.6-5)
d_K	Ball diameter, grain diameter	mm	Tab. 3.4-1
D_L	Axial diffusion coefficient	m^2/s	(3.1-9)
d_m	Average grain diameter	mm	(4.1-1)
$D_{O/V}$	Fractional dimension of the distribution	1	Cpt. 4.1.2.5
d_P	Diameter of the cylinder pore	mm	(3.4-17)
$d_{P,min}$	Still passable pore narrowing	mm	(3.4-3)
d_w	Effective grain diameter	mm	Tab. 3.4-1
E_λ	Extinction at λ (=SAK_λ)	m^{-1}	(7.1-8)
EPS	Extracellular polymeric substances		Cpt. 7.5
F	Faraday constant	J/(V·mol)	Tab. 2.1-2
$F_O(\delta)$	Surface function	1	(5.2-32)
f_L	Tortuosity	1	(4.3-10)
f_{LL}	Tortuosity of the pore system	1	(3.7-1)
f_O	Form factor	1	Tab. 3.4-1
FP	Filtration parameter	h/m	(3.3-23)
g	Gravitational acceleration	m/s^2	
g	Free Enthalpy	J	Cpt. 2.3.1
G	Molar free Enthalpy	kJ/mol	Cpt. 2.3.1
H	Water column flowing through	m	(2.2-4)
H	Henry constant	atm·m^3/mol	(6.5-11)
h_f	Filter resistance	m	(3.5-14)
h	Enthalpy	J	Cpt. 2.3.1
H	Molar enthalpy	kJ/mol	Cpt. 2.3.1
Hfo_wOH	weak binding site		Cpt. 6.5.5
I	Ionic strength	mol/L	(2.3-47)
IAP	Ion Activity Product		(2.3-17)
L	Length	m, dm	Tab. 2.2-1
m_{Pr}	Solids (sample) mass	kg	Tab. 2.22
n	Amount of substance, cumulative material passage	mol	(2.2-12)
n_{BV}	Number of bed volumes flowed through (BV)	1	(2.2-13)
n_{cell}	Number of mixed cells	1	(3.2-8)
n_P	Porosity of bulk	1	(2.2-6)
n_{PP}	Porosity of the particle	1	Tab. 2.22
n_{PV}	Number of pore volumes flowed through	1	(2.2-14)
n_{shift}	Number of transport steps	1	(3.2-12)
O_F	Surface-to-reactor volume ratio	m^2/m^3	(3.4-21)

Symbol	Parameter	Unit	Reference/Eq.
O_R	Interface between mobile and immobile phase (shear surface)	m^2	Tab. 2.22
O_{sp}	Specific interface	dm^2/kg	(3.4-10)
$O_{sp}(ads)$	Sorption adsorption surface	m^2/g	Tab. 6.57
Pe	Peclet number	1	(3.2-5)
Q_R	Volume flow	m^3/s, m/h	Tab. 2.2-1
$q_V(c)$	Volume-related capacities of the stationary phase	mmol/L	(8.3-4)
$q_O(c)$	Surface-related capacities of the stationary phase	$mmol/m^2$	
r	Rate of reaction	mmol/(L·h)	(3.3-18)
R	Ideal gas constant	J/(mol·K)	Tab. 2.1-2
Re	Reynolds number	1	(3.5-3)
R_F	Retardation	1	(8.3-8)
s	Entropy	J/K	Cpt. 2.3.1
S	molar Entropy	J/(K·mol)	Cpt. 2.3.1
SAK_λ	Spectral absorption coefficient at λ (=E_λ)	m^{-1}	Cpt. 7.1.2.1
Sc	Schmidt number	1	(7.3-28)
Sh_{eff}	effektive Sherwood number	1	(7.3-34)
t	Time	s, h, d	
Temp	Temperature	°C	
TWR	Trinkwasserrelevante Stoffe		Cpt. 7.2.3
t_F	Space-time	d, h	(2.2-3)
v_A	Distance velocity	m/d, m/h	(2.2-7)
v_A	Fortpflanzungsgeschwindigkeit des Konzentrationssprunges	m/h	(3.1-8)
v_f	Filtration velocity	m/d, m/h	(2.2-1)
$V_P = V_W$	Pore volume	m^3, dm^3	Tab. 2.22
V_R	Reactor volume	m^3, dm^3	(2.2-1)
VWZ	Residence time	d, h	(2.2-8)
WWR	Watertreatment-related substances		Cpt. 7.2.3
Y	Yield factor	-	(6.1-28)
z	Phase Ratio	dm^3/kg	(2.2-10)
z	Spatial coordinate	m	
z	Number of charges		Cpt. 2.3.6.4
Δx	Cell length	m	(3.2-10)

α	Dispersivity	m	(4.3-11)
β	Mass transfer coefficient	m/s	(3.6-6)
Γ	Sites concentration	nm^{-2}	Cpt. 6.5.5
δ	Boundary layer	mm	(3.6-2)
δ	Thickness of the diffuse electric bilayer	$\approx 10^{-8}$m	(6.5-55)
ε	Relative dielectric constant for water	1	Tab. 6.59
ε_0	Dielectric constant for vacuum	As/(Vm)	Tab. 6.59
φ	Proportion of the reactive surface	1, %	(8.1-11)
φ	Sum of all particle volumes per solution volume	1, %	(5.2-2)
η	Dynamic viscosity	Ps·s, kg/(m·s)	Cpt. 0
λ_L	Length coefficient	1/m	(8.1-9)
λ_t	Time constant	1/h	(8.1-9)
μ	Rate of growth constant	1/d	(6.1-18)
ν_A	Stoichiometric coefficient of A	1	Cpt. 2.3.2
ν	Kinematic viscosity	m^2/s	Cpt. 0
$\rho(t)$	Residence time density function		(3.1-12)
ρ_S	Bulk density	kg/dm^3	(2.2-5)

ρ_{SS}	Solids (grain) density	kg/dm^3	(2.2-9)
σ	Varianz		
σ	Surface Charge from the charge Balance	As/m^2	Tab. 6.5-8
Ψ	Surface potential from the charge balance	V	(6.5-55)
ξ	Reaction run number	mol, mol/L	Cpt. 2.3.2

11.2 References

11.2.1 Published references

ABDULAZIZ, F.; MUSAYEV, S. (2017): Multicomponent biosorption of heavy metals from aqueous solutions: A Review; Pol. J. Environ. Stud. Vol. 26, No. 4, 1433-1441.

AMW (1981): Autorenkollektiv Ausgewählte Methoden der Wasseruntersuchung (AMW) Bd1; Jena.

APPELO, C.A.J.; POSTMA, D. (1993): Geochemistrry, groundwater and pollution; A:A:BALKEMA/ROTTERDAM/BROOKFIELD.

ASPE´, E.; MARTI, M., C.; ROECKEL, M. (1997): Anaerobic treatment of fishery wastewater using a marine sediment inoculum; Water Research Volume 31, No.9, pp. 2147-2160.

Autorenkollektiv (1971): Komplexes Lehrwerk Grundstudium Chemie; VEB Deutscher Verlag für Grundstoffindustrie Leipzig.

BAHR, C. (2012): Entfernung von Uran aus Trinkwasser durch Adsorption an Granuliertem Eisenhydroxid (GEH): Dissertation, Fakultät III - Prozesswissenschaften der Technischen Universität Berlin.

BALCH, J.; GUÉGUEN, C. (2015): Effects of molecular weight on the diffusion coefficient of aquatic dissolved organic matter and humic substances; Chemosphere 119 pp.498-503.

BARTSCH, H.-J. (1972): Mathematische Formeln; VEB Fachbuchverlag Leipzig.

BASSER, P. J.; GRODZINSKY, A. J. (1993): The Donnan model derived from microstructure; Biophysical Chemistry, 46 pp.57-68.

BAUER, M. (2008): Influence of natural organic matter on the mobility of arsenic in aquatic systems, soils ans sediments; Dissertation, Universität Bayreuth.

BEERBALK, H.-D. (2011): Sanierung komplex kontaminierter Veredlungsstandorte am Beispiel der ehem. BHT Kokerei Lauchhammer;Aktive und passive Grundwassersanierung; Büro Dr. Beerbalk; 19. Bodenschutzforum Sanierung der ehemaligen Kokerei Lauchhammer 21.09.2011; Lauchhammer.

BERGAYA, F.; LAGALY, G. (Hg.) (2013): Handbook of Clay Science; 2006 Elsevier Ltd. Amsterdam; ISBN: 978-0-08-098258-8 ISSN: 1572-4352 sowie ISBN: 978-0-08-098259-5 ISSN: 1572-4352.

BIENERT,K.; KLAMT, A.; KROCKENBERGER (1993): Zum Bioakkumulationspotential von Chlororganika; UWSF-Z. Umweltchem. Ökotox.5(4).

BILEK, F. (2004): Beschaffenheitsprognose für den Grundwasser-Abstrom aus Braunkohle-Tagebaukippen auf der Basis von experimentell bestimmten Parametern und geochemisch charakterisierten Sedimenten; Dissertation, Christian-Albrechts-Universität Kiel; DGFZ Proceedings Heft 26.

BIRKEL, U. (2001): Transformation organischer Schadstoffe und abiotische Bildung von Huminstoffen in Böden durch oberflächeninduzierte Reaktionen an Tonmineralen; Dissertation der Georg-August-Universität zu Göttingen.

BOHM, L. (1992): Optimierung der chemikalienlosen Entmanganungsfiltration; Dissertation, TU Dresden.

BOHM, L. (1992): Modell der chemikalienlosen Entmanganungsfiltration; Vom Wasser, 79, S.249-257.

BOLLRICH und Autorenkollektiv (1989): Technische Hydromechanik Band 2; Verlag für Bauwesen Berlin.

BOSIRE, G. O.; NGILA, J. C. (2017): Effect of Natural Organic Matter on Scale reduction in Cooling Water Circuits: A Comprehensive assessment based on Empirical Characterization and Theoretical PHREEQCI Model computations; Water and Desalination Research Journal Vol. 1, No. 1 pp.73-91.

BRANDT, G. (2015): Produktivkräfte für eine ökosoziale Gesellschaft; Beiträge zur Umweltpolitik; Ökologische Plattform bei der Partei DIE LINKE; bzu_2015-01_Produktivkräfte.pdf.

BRANDT, B.W.; VAN LEEUWEN, I.M.M.; KOOIJMAN, S. A. L. M. (2003): A general model for multiple substrate biodegradation. Application to co-metabolism of structurally non-analogous compounds; Water Research Volume 37, Issue 20, Pages 4843-4854.

BUFFLE, J.; ZHANG, Z.; STARTCHEV, K. (2007): Metal Flux and Dynamic Speciation at (Bio)interfaces. Part I: Critical Evaluation and Compilation of Physicochemical Parameters for Complexes with Simple Ligands and Fulvic/Humic Substances; ENVIRONMENTAL SCIENCE & TECHNOLOGY VOL. 41, NO. 22, pp.7609-7620.

BURWIG, G.; WORCH, E.; SONTHEIMER, H. (1995): Eine neue Methode zur Berechnung des Adsorptionsverhaltens von organischen Spurenstoffen in Gemischen; Vom Wasser, 84, 237-249.

BUSCH,K.F.; LUCKNER, L.; TIEMER, K. (1993): Geohydraulik; 3. neubearbeitete Auflage; Gebr.Bornträger Berlin Stuttgart.

CHEFETZ, B.; HADAR, Y.; CHEN, Y. (1998): Dissolved Organic Carbon Fractions Formed during Composting of Municipal Solid Waste: Properties and Significance; Acta hydrochem. hydrobiol. 26, 3 S.152f.

CHEN, G.; VAN LOOSDRECHT, M. C. M.; EKAMA, G. A.; BRDJANOVIC, D. (Hg.) (2023): Biological Wastewater Treatment. Principles, Modelling and Design. 2nd edition. IWA Publishing; ISBN: 9781789060362 (eBook); Doi: 10.2166/9781789060362.

COURY, L. (1999): Conductance Measurements. Part 1: Theory; Current Separations 18:3 pp.91-96.

CRAVOTTA III, C. A. (2021): Interactive PHREEQ-N-AMD Treat water-quality modeling tools to evaluate performance and design of treatment systems for acid mine drainage; Applied Geochemistry 126 104845.

CRAVOTTA, C.A. III (2022): Interactive PHREEQ-N-AMDTreat+REYs water-quality modeling tools to evaluate potential attenuation of rare-earth elements and associated dissolved constituents by aqueous-solid equilibrium processes (software download); U.S. Geological Survey Software Release (https://doi.org/10.5066/P9M5QVK0) https://code.usgs.gov/water/phreeq-n/phreeq-n-amdtreat-reys/-/release.

D 4189-95 (Reapproved 2002) (2002): Standard Test Method for Silt Density Index (SDI) of Water; ASTM International, 100 Barr Harbor Drive, PO Box, West Conshohocken. PA 19428-2959, United States.

DAVID A. FOWLE, D. A.; FEIN, J.B. (1999): Competitive adsorption of metal cations onto two gram positive bacteria: testing the chemical equilibrium model; Geochimica et Cosmochimica Acta, Volume 63, Issues 19-20 (October 1999), Pages 3059-3067.

DAVID, R.; SAUCEZ, P.; VASEL, J.-L.; VANDE WOUWER, A. (2009): Modeling and numerical simulation of secondary settlers: A Method of Lines strategy; Water Research, Volume 43, Issue 2, Pages 319-330.

DAVID, I. (1998): Grundwasserhydraulik; Strömungs- und Transportvorgänge; Braunschweig; Wiesbaden Vieweg.

DAVISON, W.; SEED, G. (1983): The kinetics of the oxidation of ferrous iron in synthetic and natural waters; Geochim. Cosmochim. Acta 47, 67-79.

DFG Deutsche Forschungsgemeinschaft (1993): Refraktäre organische Säuren in Gewässern; VCH Weinheim 1993.

DVGW (2005): Technische Regel, Arbeitsblatt W223-: Enteisenung und Entmanganung; Teil 1: Grundsätze und Verfahren, Teil 2: Planung und Betrieb von Filteranlagen; Teil3: Planung und Betrieb von Anlagen zur unterirdischen Aufbereitung; DVGW Regelwerk.

DZOMBAK, D. A.; MOREL, F. M. M. (1990): Surface complexation modelling; New York: Wiley-Interscience.

EINSELE, A.; FINN, R. K.; SAMHABER, W.(1985): Mikrobiologische und biochemische Verfahrenstechnik; Eine Einführung; VCH Verlagsgesellschaft Weinheim.

ENZMANN, F. H. (2000): Modellierung von Porenraumgeometrien und Transport in korngestützten porösen Medien; Dissertation Uni Mainz, FB Geowissenschaft.

EVANGELOU, V. P. (1995): Pyrite oxidation and its control; CRC Press Boca Raton New York London Tokio.

FARAJI, F.; ALIZADEH, A.; RASHCHI, F.; MOSTOUFI, N. (2020): Kinetics of leaching: a review; Rev Chem Eng aop https://doi.org/10.1515/revce-2019-0073; Received October 26, 2019; accepted April 29, 2020; published online.

FLEMMING, H.-C.; WINGENDER, J. (2010): The biofilm; matrixNaturereviews|Microbiology pp.623-633.

FLEMMING H.-C. Biofilme und Wassertechnologie; Teil 1: Entstehen, Aufbau, Zusammensetzung und Eigenschaften von Biofilmen; gwf Wasser Abwasser 132(1991)Nr.4, https://www.aqua-free.com/de/magazin/biofilm-in-wassersystemen.

FRIESE, K., HERZSPRUNG, P.; WITTER, B. (2002): Photochemical Degradation of Organic Carbon in Acidic Mining Lakes; Acta hydrochimica et hydrobiologica Volume 30, Issue 2-3.

FRIMMEL, F. H.; KUMKE, M. U. (1998): Optische Parameter zur Stoffcharakterisierung vom Trinkwasser bis zum Abwasser; Postprints der Universität Potsdam Mathematisch-Naturwissenschaftliche Reihe 25.

FUCHS, S.; ZIESCHE, M.; NILLERT, P. (2017): Empirische Verfahren zur Ableitung verschiedener Porositätsarten aus Durchlässigkeitsbeiwert und Ungleichkörnigkeitszahl - ein Überblick; Grundwasser, Volume 22, Issue 2, pp.81-82; DOI 10.1007/s00767-017-0355-2.

GENZ, A. (2005): Entwicklung einer neuen Adsorptionstechnik zur Entfernung natürlicher Organika mit granuliertem Eisenhydroxid; Dissertation, TU Berlin.

GEORGI, A. (1998): Sorption von hydrophoben organischen Verbindungen an gelösten Huminstoffen; Dissertation 1998; UFZ-Bericht Nr.4/1998, ISSN 0948-9452.

GIMBEL, R; NAHRSTEDT, A. (2004): Grundlagen der Tiefenfiltration; In: GIMBEL, R.; JEKEL, M.; LIEßFELD, R. (Hrsg.): Wasseraufbereitung - Grundlagen und Verfahren; DVGW Lehr- und Handbuch Wasserversorgung Bd. 6; DVGW Deutsche Vereinigung des Gas- und Wasserfaches e.V.; Oldenbourg Industrieverlag München Wien.

GIMBEL, R.; SONTHEIMER, H. (1987): Erprobung und Weiterentwicklung eines Testfilters zur frühzeitigen Erkennung von unerwünschten Qualitätsbeeinträchtigungen bei Uferfiltratwasserwerken; BMFT-Schlußbericht 02 WT 86290, Karlsruhe.

GIMBEL, R. (1984): Abscheidung von Trübstoffen aus Flüssigkeiten in Tiefenfiltern; Veröffentlichungen des Bereichs und des Lehrstuhls für Wasserchemie und der DVGWForschungsstelle am Engler-Bunte-Institut der Universität Karlsruhe, ZfGW-Verlag Frankfurt.

GIMBEL, R.; GERLACH, M.; NAHRSTEDT, M.; ROHN, A. (1996): Bewertung der Gewässergüte von Saale und Havel hinsichtlich der Trinkwassernutzung; Teilprojekt 9: Uferfiltration; Abschlußbericht für das Forschungsvorhaben 02 WT9265/7; Duisburg.

GRÖSCHKE, A. (2007): Eisenhaltige Schlämme aus Grubenwasserreinigungsanlagen des Lausitzer Braunkohlereviers; Dissertation BTU Cottbus, LS Hydrologie und Wasserwirtschaft.

GRUNDL, T.; DELWICHE, J. (1993): Kinetics of ferric oxyhydroxide precipitation; Journal of Contaminant Hydrology, 14 pp.71 -97.

GUSTAFSSON, J. P. (2020): Visual MINTEQ ver. 3.1; KTH Stockholm, Sweden; https://vminteq.lwr.kth.se/.

GUSTAVSON, J. P.; VAN SCHAIK (2003): Cation binding in a mor layer: batch experiments and modelling; European Journal of Soil Science, 54, pp.295-310.

HA, J.; GELABERT, A.; SPORMANN, A. M.; BROWN JR., G. E. (2010): Role of extracellular polymeric substances in metal ion complexation on Shewanella oneidensis: Batch uptake, thermodynamic modeling, ATR-FTIR, and EXAFS study; Geochimica et Cosmochimica Acta 74, pp. 1-15.

HADELER, A. (1999): Sorptionsreaktionen im Grundwasser: Unterschiedliche Aspekte bei der ModelIierung des Transportverhaltens von Zink; Berichte aus dem Fachbereich Geowissenschaften der Universität Bremen Nr.145.

HAGEN, J (1993): Chemische Reaktionstechnik; Eine Einführung mit Übungen; Weinheim.

HAN, D.; WANG, Z.; WANG, Q.; WU, B.; WANG, D. (2019): Analysis of the Kozeny-Carman model based on pore networks; Journal of Geophysics and Engineering 16, 1191-1199; doi:10.1093/jge/gxz089.

HANCKE,K. (1991): Wasseraufbereitung; Chemie und chemische Verfahrenstechnik; VDI-Verlag Düsseldorf.

HEKMAT, D. (2002): Reaktionstechnik von instationären biologischen Prozessen; Habilitation TU München, Berichte aus der Biotechnologie, Garching.

HIDAKA, T.; TSUNO, H. (2004): Development of a biological filtration model applied for advanced treatment of sewage;Water Research Volume 38, Issue 2 Pages 335-346.

HOBBY, R.; GIMBEL, R. (1988): Bisherige Ergebnisse von Testfilteruntersuchungen an Abwässern aus Kommunen und der Zellstoffindustrie; In: Wasserwerks- und trinkwasserrelevante Stoffe; Kolloquium des DVGW-Fachausschusses am 12.April 1988 in Karlsruhe DVGW-Schriftenreihe Wasser Nr. 60, Eschborn.

HONG, Y.-S; KIM, G.-I.; ZHANG, J.-X.; RI, C.-J.; SON, G.-C.; KIM, B.-S.; PAEK, M.-U.; KIM, I.-H.; RIM, H.-M.; LIU, B.-S. (2018): Which model should be selected to analyze the experimental data among many adsorption kinetic models? ORCID: Yong-Son Hong: 0000-0002-0566-6632, Bing-Si Liu: 0000-0001-7119-8614, https://ndownloader.figshare.com/files/10011505.

HOUBEN, G.J.; BLÜMEL, M. (2017): Automatisierung des Verfahrens nach Beyer & Schweiger (1969) zur Bestimmung von Durchlässigkeit und Porosität aus Kornverteilungskurven; Grundwasser, Volume 22, Issue 4, pp.309-312.

HUBER, S. (2003): LC- OCD : Method and Applications; v. 8 (1/ 2003); DOC- LABOR DR. HUBER, Karlsruhe, Germany; www.doc-labor.de.

HUBER , S. A.; BALZ, A.; ABERT, M.; PRONK, W. (2011): Characterisation of aquatic humic and non-humic matter with size-exclusion chromatography e organic carbon detection e organic nitrogen detection (LC-OCD-OND); Water Research Volume 45, pp. 879 -885.

JOHANNESSON, K. H.; YANG, N.; TRAHAN, A. S.; TELFEYAN, K.; MOHAJERIN, T.; ADEBAYO, S. B.; AKINTOMIDE, O. A.; CHEVIS, D. A.; DATTA, S.; WHITE, C. D. (2019): Biogeochemical and reactive transport modeling of arsenic in groundwaters from the Mississippi River delta plain: An analog for the As-affected aquifers of South and Southeast Asia; Geochimica et Cosmochimica Acta 264, pp.245-272.

JOHANNSEN, K.; RADEMACHER, S. (1999): Modelling the Kinetics of Calcium Hydroxide Dissolution in Water; Acta hydrochim. hydrobiol. 27 (1999)2.

JONES, A. M.; GRIFFIN, P. J.; COLLINS, R. N.; WAITE, T. D. (2014): Ferrous iron oxidation under acidic conditions - The effect of ferric oxide surfaces; Geochimica et Cosmochimica Acta 145, pp. 1-12.

KINNIBURGH, D. G.; MILNE, C. J.; BENEDETTI, M. F.; PINHEIRO, J. P.; FILIUS, J.; KOOPAL, L. K.; VAN RIMSDIJK, W. H. (1996): Metal Ion Binding by Humic Acid: Application of the NICA-Donnan Model; Environ. Sci. Technol. 30, 1687-1698.

KINNIBURGH, D. G.; VAN RIEMSDIJK, W. H.; KOOPAL, L. K.; BORKOVEC, M.; BENEDETTI, M. F.; AVENA, M. J. (1999): Ion binding to natural organic matter: competition, heterogeneity, stoichiometry and thermodynamic consistency; Colloids Surfaces A: Physicochem. Eng. Aspects 151pp.147-166.

KITTNER, H.; STARKE, W.; WISSEL,D. (1975): Wasserversorgung; Verlag für Bauwesen, Berlin.

KOBUS, H. (1992): Stofftransport im Untergrund, Forschungsbericht; DFG Schadstoffe im Grundwasser Bd.1; VCH-Verlagsgesellschaft.

KOCH, R.; SCHÖPKE, R.; PREUß, V.; MANGOLD, S.; STRIEMANN, A.(2002): Erarbeitung einer Methodik zur Bestimmung der Eigenschaften und Leistungsfähigkeit von natürlichen Böden für die Behandlung schwach belasteter Abwässer; Schriftenreihe Siedlungswasserwirtschaft und Umwelt, Bd.6/2002; ISBN 3-934294-06-5.

KOCH, R.; SCHÖPKE, R.; MANGOLD, S.; REGEL, R.; STRIEMANN A. (2006): Entwicklung und Erprobung eines Verfahrens zur Untergrundentsäuerung von Kippengrundwässern; Schriftenreihe Siedlungswasserwirtschaft und Umwelt, Bd.11.

KOCH, R.; PREUß, V.; KOCH, TH.; SCHÖPKE, R. (2009): Verminderung der Sulfatbelastung neutralisierter Grubenwässer mittels Nanofiltration - Laborversuche zur Verfahrensentwicklung -; Schriftenreihe Siedlungswasserwirtschaft und Umwelt Bd.16; ISBN 3-934294-25-1.

KÖHLER, M.; VÖLSGEN, F. (1998): Geomikrobiologie; Grundlagen und Anwendungen; WILEY-VCH Weinheim Berlin New York ...

KOSOBUCKI, P.; BUSZEWSKI, B. (2014): Natural Organic Matter in Ecosystems - a Review; Nova Biotechnologica et Chimica 13-2: DOI 10.1515/nbec-2015-0002.

KOß, V. (1997): Umweltchemie - Eine Einführung für Studium und Praxis; Springer Berlin ...

KREIß, C. (2020): Gekaufte Wissenschaft. Wie uns manipulierte Hochschulforschung schadet und was wir dagegen tun können. tredition GmbH, Halenreie 40-44, 22359 Hamburg.

KÜMMEL,R.; PAPP,S. (1990): Umweltchemie; VEB Dt.Verlag f.Grundstoffindustrie.

KÜMMEL, R.; WORCH, E. (1990): Adsorption aus wässrigen Lösungen; Leipzig.

KUNTZMANN, J. (1970): Systeme von Differentialgleichungen; Wissenschaftliche Taschenbücher Bd. 71; Akademieverlag Berlin, Vieweg+Sohn, Braunschweig.

LATTNER, D. (2003): Untersuchung schwacher Wechselwirkungen innerhalb von Biofilmen mittels 13 C-NMR - Spektroskopie; Dissertation, Fakultät für Naturwissenschaften der Universität Duisburg-Essen.

LI, P.; HUR, J. (2017): Utilization of UV-Vis spectroscopy and related data analyses for dissolved organic matter (DOM) studies: A review; Environmental Science and Technology, 47:3, 131-154, DOI: 10.1080/10643389.2017.1309186.

LIMOUSIN, G.; GAUDET, J.-P.; CHARLET, L.; SZENKNECT, S.; BARTHES, V.; KRIMISSA, M. (2007): Sorption isotherms: A review on physical bases, modeling and measurement; Applied Geochemistry 22 pp.249-275.

LÖFFLER, H. (1969): Zur Technologie und Bemessung offener Infiltrationsanlagen für Grundwasser-anreicherung; Dissertation TU Dresden.

LOPP, M.(2004): Optimierung der biologischen Klärschlammbehandlung durch die Aerob-Anoxische Nachbehandlung (AAN); Grundlagen, Anwendung und Wechselwirkungen mit der Faulung; Schriftenreihe des LS Abfallwirtschaft und Siedlungswasserwirtschaft der Bauhaus-Universität Weimar, Berlin.

LUCKNER; SCHESTAKOW (1986): Migrationsprozesse im Boden und Grundwasserbereich; Leipzig.

MADHAV, H.; GERICKE, G.; MISHRA, S.; NGILA, J. C.; BOSIRE, O. (2017): Comparative Simulative Studies Using PHREEQC-Interactive and Visual MINTEQ Model for Understanding Metal-NOM Complexation Occurring in Cooling and Raw Water and the Effects on Saturation Indices; Sustainability Department, Applied Chemistry and Microbiology, Eskom, Private Bag X40175, Cleveland, 2022, South Africa.

MCCLESKEY, R. B.; NORDSTROM, D. K.; RYAN, J. R. (2012): Comparison of electrical conductivity calculation methods for natural waters; Limnol. Oceanogr.: Methods 10, pp.952-967.

MELIN, T.; RAUTENBACH, R. (2007): Membranverfahren, Grundlagen der Modul- und Anlagenauslegung; VDI-Buch, Springer Berlin Heidelberg.

MERKEL, B. J.; PLANER-FRIEDRICH, B. (2002): Grundwasserchemie; Praxisorientierter Leitfaden zur numerischen Modellierung von Beschaffenheit, Kontamination und Sanierung aquatischer Systeme; Springer Berlin Heidelberg.

MILNE, C.; KINNIBURGH, D. G.; VAN RIEMSDIJK; TIPPING, E. (2003): Generic NICA-Donnan Model Parameters for Metal-Ion Binding by Humic Substances; Environ. Sci. Technol. 37 pp.958-971.

MORSE, G.; JONES, R.; THIBAULT, J.; TEZEL, F. (2011): Neural network modelling of adsorption ISOTHERMS; Adsorption Volume 17, Number 2, 303-309.

NIEMANN, L. (2004): Die Reaktionskinetik des Gipsabbindens: Makroskopische Reaktionsraten und Mechanismen in molekularem Maßstab; Karlsruher Mineralogische und Geochemische Hefte; Schriftenreihe des Instituts für Mineralogie und Geochemie 28.

NOMURA, S.; YAMAMOTO, Y.; SAKAGUCHI, H. (2018): Modified expression of Kozeny–Carman equation based on semilog–sigmoid function; Soils and Foundations 58 pp. 1350-1357.

O'FLAHERTY, MAHONY, T.; O'KENNEDY, R.; COLLERAN, E. (1998): Effect of pH on growth kinetics and sulphide toxicity thresholds of range of methanogenic syntrophic and sulphate-reducing bacteria Process; Biochemistry 33, No. 5, pp. 555-569.

OKABE, S.; NIELSEN, P.H.; CHARACKLIS, W.G. (1992): Factors affecting microbial sulfate reduction by Desufovibrio desulfuricans in continuosing culture: Limiting nutrients and sulfide concentration; Biotechnology and Bioengineering, Vol 40, pp 725-734.

OKABE, S.; CHARACKLIS, W.G. (1992):EFFECTS OF TEMPERATURE AND PHOSPHOROUS CONCENTRATIon on microbial sulfate reduction by Desulfovibrio desulfuricans; Biotechnology and Bioengineering, Vol 39, pp 1031-1042 (1992).

PARBS, A. (2006): Langzeiteffektivität und Funktionalität von Fe0-Reaktionswänden Untersuchung von Einflussfaktoren und Beurteilung der Leistungsfähigkeit durch den Einsatz reaktiver Tracer; Dissertation, Christian-Albrechts-Universität Kiel.

PARKHURST, D. L.; APPELO, C. A. J. (1999): User's guide to PHREEQC; (Version 2)--a computer program for speciation, batch-reaction, one-dimensional transport, and inverse geochemical calculations U.S. Geological Survey Water-Resources Investigations Report 99-4259, 312 p.

PARKHURST, D. L.; APPELO, C.A.J. (2006): USER'S GUIDE TO PHREEQC (VERSION 2) - A COMPUTER PROGRAM FOR SPECIATION,BATCH-REACTION, ONE-DIMENSIONAL TRANSPORT, AND INVERSE GEOCHEMICAL CALCULATIONS; Water-Resources Investigations Report 99-4259.

PARKHURST, D. L.; APPELO, C. A. J. (2013): Description of Input and Examples for PHREEQC Version 3—A Computer Program for Speciation, Batch-Reaction, One-Dimensional Transport, and Inverse Geochemical Calculations; U.S. Geological Survey, Denver, Colorado; Chapter 43 of Section A, Groundwater Book 6, Modeling Techniques; PHREEQC_3_2013_manual.pdf.

PAVÓN-DOMÍNGUEZ, P.; DÍAZ-JIMÉNEZ, M. (2023): Characterization of synthetic porousmedia images by using fractal and multifractal analysis; GEM - International Journal on Geomathematics (2023) 14:27; https://doi.org/10.1007/s13137-023-00237-6.

PERCAK-DENNETT, E.; HE, S.; CONVERSE, B.; KONISHI, H.; XU. H.; CORCORAN, A.; NOGUERA, D.; CHAN, C.; BHATTACHARYYA, A.; BORCH, T.; BOYD, E.; RODEN, E. E. (2017): Microbial acceleration of aerobic pyrite oxidation at circumneutral pH; Geobiology. pp.1-14.

PHAM, A. N.; WAITE, T. D. (2008): Oxygenation of Fe(II) in natural waters revisited: Kinetic modeling approaches, rate constant estimation and the importance of various reaction pathways; Geochimica et Cosmochimica Acta 72; 3616-3630.

PLAZA, C.; HERNÁNDEZ, D.; FERNÁNDEZ, J. M.; POLO, A. (2006): Long-term effects of amendment with liquid swine manure on proton binding behavior of soil humic substances; Chemosphere 65 pp.1321-1329.

PREUß, V. (1999): Laboruntersuchungen von Stoffübergangsvorgängen in Modellsystemen Kippsand – Grundwasser; Schriftenreihe Siedlungswasserwirtschaft und Umwelt Bd. 3/1999; ISBN 3-934294-02-2.

PREUß, V. (2004): Entwicklung eines biochemischen Verfahrens zur Aufbereitung sulfathaltiger Wässer am Beispiel der Entsäuerung schwefelsaurer Tagebaurestseen; Dissertation BTU Cottbus, LS Siedlungswasserwirtschaft und Siedlungswasserbau; Schriftenreihe Siedlungswasserwirtschaft und Umwelt, Bd. 9.

RATHSACK, U. (1996): Untersuchungen zur Eisen-(II)-Filtration; Wissenschaftliche Schriftenreihe Umwelttechnik Band 6; Köster, Berlin; ISSN 1431-0481.

RAUSCH, R.; SCHÄFER, W.; WAGNER, C. (2002): Einführung in die Transportmodellierung im Grundwasser; Gebrüder Bornträger Berlin Stuttgart.

RODE, A. (2004): Isolierung und Charakterisierung von bakteriellen extrazellulären polymeren Substanzen aus Biofilmen; (http://www.ub.uni-duisburg.de/ETD-db/theses/available/duett-09132004-102114/unrestricted/Rode_Dissertation_2004.pdf); Dissertation; Fakultät für Naturwissenschaften der Universität Duisburg-Essen.

SAITO, T.; NAGASAKI, S.; TANAKA, S.; KOOPAL, L. K. (2004): Application of the NICA-Donnan model for proton, copper and uranyl binding to humic acid; Radiochim. Acta 92, 567-574.

SALEM, H. S. (2001): Application of the Kozeny-Carman Equation to Permeability Determination for a Glacial Outwash Aquifer, Using Grain-size Analysis; Energy Sources, 23:5, 461-473, DOI: 10.1080/009083101300058480; http://dx.doi.org/10.1080/009083101300058480.

SALMON, S. U.; MALMSTRÖM, M. E (2002): MiMi - Steady state, geochemical box model of a tailings impoundment: Application to Impoundment 1, Kristineberg, Sweden, and prediction of effect of remediation; MiMi 2002:2; Engineering Hydrology and Hydrogeochemistry, Department of Land and Water Resources Engineering, Royal Institute of Technology,Brinellvägen 32, S-100 44 Stockholm, Sweden; ISSN 1403-9478 ISBN 91-89350-22-7.

SALMON, S. U.; MALMSTRÖM, M. E (2004): Geochemical processes in mill tailings deposits: modelling of groundwater composition; Applied Geochemistry 19 pp. 1 - 17.

SANTANA-CASIANO, J. M.;GONZÁLEZ-DÁVILA, M.; MILLERO, F. J. (2006): The role of Fe(II) species on the oxidation of Fe(II) in natural waters in the presence of O_2 and H_2O_2; Marine Chemistry 99, pp. 70-82.

SCHEFFER, SCHACHTSCHABEL (1992): Lehrbuch der Bodenkunde; Stuttgart.

SCHIRMER, M.; MARTIENSSEN, M.; STOTTMEISTER, U.; WENDLANDT; WEIß,H.; WERNER, P.; FISCHER, A.; DAHMKE, A.; GRATHWOHL, P.; BITTENS, M. (2008): KORA: TV1, Projektverbund Methyltertiärbutylether (MTBE); Leuna als Referenzstandort zur Implementierung des Enhanced-Natural-Attenuation Ansatzes (METLEN) -Abschlussbericht-; CD-Anlage zu /R3614/ bis /R3616/ DECHEMA e.V. Exportorientierte Forschung und Entwicklung auf dem Gebiet der Wasserver- und -entsorgung; Teil I: Trinkwasser: Uferfiltration Schlussbericht Teilprojekt B4:DOC-Entfernung bei der Uferfiltration unter Berücksichtigung extremer Temperaturbedingungen und Belastungsschwankungen; BMBF 02WT0277; TU Dresden, Institut für Wasserchemie.

SCHÖPKE, R.; BALKE, S.; OTTO, A.; THÜRMER, K. (2013): Entwicklung eines Verfahrens zur Adsorption von Phosphor an körnigem Eisenhydroxid und Regeneration des Adsorptionsmittels zur Phosphorrückgewinnung; Schriftenreihe Siedlungswasserwirtschaft und Umwelt Bd. 22; ISBN 3-934294-29-4.

SCHÖPKE, R.; BALKE, S. (2015): Entwicklung von Bemessungsansätzen für den von Adsorptionsfiltern auf der Basis von gekörntem Eisenhydroxid zur Phosphorrückgewinnung oder zur Schadstoffelimination in diskontinuierlich betriebenen Filtern. In: PINNEKAMP, J.; WESSLING, M. (Hg.): Verfahren der Wasseraufbereitung und Abwasserbehandlung. Begleitbuch zur 11. Aachener Tagung Wassertechnologie 27.-28. Oktober; Aachener; Verfahrenstechnik, RWTH Aachen.

SCHÖPKE, R.; KOCH, R. (2002): Experimentelle und modellgestützte Entwicklung von Verfahren der geochemischen Grundwasser- und Untergrundbehandlung zur Gefahrenabwehr im Nordraum des Senftenberger Sees; In: Deneke, R.; Nixdorf, B.(Hrsg): Gewässerreport(Nr.7) Tagungsband; Aktuelle Reihe 3/2002 der BTU Cottbus Fak. Umweltwissenschaften und Verfahrenstechnik.

SCHÖPKE, R.; PREUß, V. (2013): Beschreibung der Hydrochemie von potenziell saurem Kippengrundwasser bei der Migration durch unterschiedlich beschaffene Grundwasserleiter. In: MERKEL, B.; WOLOSZYN, I.; SIELAND, R.: Mine Water Symposium; Wissenschaftliche Mitteilungen der TU Bergakademie Freiberg, Institut für Geologie Heft 44.

SCHÖPKE, R. (2007): Vielkomponentensysteme in der Wasserbehandlung - Erfassung und Anwendung bei der Bemessung von Aufbereitungsanlagen; Schriftenreihe Siedlungswasserwirtschaft und Umwelt, Bd.14.

SCHÖPKE, R. (2008): Nutzung der Ergebnisse von Labor- und kleintechnischen Versuchen zur Vorbereitung und Durchführung von in-situ Sanierungsmaßnahmen; In: MERKEL, B. SCHAEBEN, H.; HASCHE-BERGER, A. (Hrsg.): Behandlungstechnologien für bergbaubeeinflusste Wässer; Proceedingband zum 59. BHT, Wissenschaftliche Mitteilungen 37, Freiberg.

SCHÖPKE, R. (2024): Hydrochemische Aspekte der Erkundung und Behandlung von bergbaubürtigen Sauerwässern (AMD) - Ergebnisse von 25 Jahren Forschung und Entwicklung; Schriftenreihe Siedlungswasserwirtschaft und Umwelt Heft 32; ISBN 934294-39-1.

SCHÖPKE, R.; KOCH, R.; PREUß, V.; STRIEMANN, A. (2002): Anwendung von Testfiltern nach Sontheimer zur Auswahl von Substraten für eine anaerobe Wasserbehandlung; gwf-Wasser/Abwasser 143 Nr.7-8, 586-591.

SCHÖPKE, R.; KOCH, R.; MANGOLD, S.; REGEL, R.; STRIEMANN, A. (2007): Herstellung passiver reaktiver Wände (PRW) aus Braunkohlefilterasche mittels Rütteldruckverfahren im Skadodamm; Schriftenreihe Siedlungswasserwirtschaft und Umwelt Bd.15; ISBN 3-934294-21-9.

SCHÖPKE, R.; GAST, M.; WALKO, M.; REGEL, R.; KOCH, R.; THÜRMER, K. (2011): Wissenschaftliche Auswertung von Sanierungsversuchen zur Untergrundsulfatreduktion im ehemaligen Lausitzer Bergbaurevier; Schriftenreihe Siedlungswasserwirtschaft und Umwelt Bd.21; https://www-docs.b-tu.de/fg-wassertechnik/public/Publikationen/Schriftenreihe/Heft21.pdf ISBN 3-934294-28-6.

SCHÖPKE, R.; WALKO, M.; REGEL, R.; THÜRMER, K. (2020): Bemessung der mikrobiellen Sulfatreduktion zur Behandlung von pyritverwitterungsbeeinträchtigten Grundwasserströmen - Ergebnis eines Demonstrationsversuches am Standort Ruhlmühle; Schriftenreihe Siedlungswasserwirtschaft und Umwelt, Bd.27.

SCHÖPKE, R.; PREUß, V.; THÜRMER, K. (2011): Prognosetools für Maßnahmen der Untergrund-wasserbehandlung in GW-Wiederanstiegsgebieten von Bergbaufolgelandschaften; Dresdner Grundwassertage 2011; Proceedings des Dresdner Grundwasserforschungszentrums e.V. Heft 45; ISSN 1430 0176.

SCHWARDT, A.; DAHMKE, A.; KÖBER, R. (2021): Henry's law constants of volatile organic compounds between 0 and 95 °C - Data compilation and complementation in context of urban temperature increases of the subsurface; Chemosphere 272: 129858.

SHENG, D.; SMITH, D.W. (1999): Analytic solutions to the advective contaminant transport equation with non-linear sorption; Int. J. Numer. Anal. Meth. Geomech., 23, 853-879.

SHENG, A.; LIU, J.; LI, X.; QAFOKU, O.;COLLINS, R. N.; JONES, A. M.; PEARCE, C. I.; WANG, C.; NI, J.; LU, A.; ROSSO, K. M. (2020): Labile Fe(III) from sorbed Fe(II) oxidation is the key intermediate in Fe(II)-catalyzed ferrihydrite transformation; Geochimica et Cosmochimica Acta (272) pp.105-120.

SINGER, P.C.; STUMM, W (1970).: Acid mine drainage, The rate determinating step; Science, 167(1970) S.1121-1123.

SIRIPINYANOND, A.; WORAPANYANOND, S.; SHIOWATANA, J. (2005): Field-Flow Fractionation-Inductively Coupled Plasma Mass Spectrometry: An Alternative Approach to Investigate Metal-Humic Substances Interaction; Environ. Sci. Technol. 39, pp. 3295-3301.

SKARK, CH.; ZULLEI-SEIBERT, N. (1994): Auftreten von Pflanzenschutzmitteln in Grundwässern unter Berücksichtigung diffuser Stoffeinträge von Totalherbiziden; Vom Wasser,82, 91-105.

SMEATON, C. M.; VAN CAPELLEN, P. (2018): Gibbs Energy Dynamic Yield Method (GEDYM): Predicting microbial growth yields under energy-limiting conditions; Geochimica et Cosmochimica Acta 241 pp.1-16.

SONTHEIMER, FRICK, FETTIG, HÖRNER, HUBELE, ZIMMER (1985): Adsorptionsverfahren zur Wasserreinigung; DVGW Karlsruhe.

STEINBERG, C. (2002): Zur ökologischen Bedeutung von Huminstoffen; Leibniz-Institut für Gewässerökologie und Binnenfischerei, http://www.igb-berlin.de.

STEINER, M. (2003): Adsorption von Kupfer aus Niederschlagsabflüssen an granuliertes Eisenhydroxid; Dissertation der Eidgenössischen Technischen Hochschule Zürich.

STENZ, G. (2001): Entwicklung eines Summenparameters für potenziell bioakkumulierbare Stoffe (PBS)im Abwasser; Dissertation der Fakultät für Chemie und Pharmazie der Eberhard-Karls-Universität Tübingen.

STETTER, D. (2004): Dimensionierung von Chelat-Ionenaustauschern bei der Trinkwasseraufbereitung; Dissertation, Universiversität Duisburg-Essen, Fachbereich Chemie.

STRAUB, A. (2008): Einfache Messmethoden zur Charakterisierung sowie Maßnahmen zur Erhöhung der Zuverlässigkeit und Leistungsfähigkeit biologischer Kleinkläranlagen; Dissertation, Fakultät für Umweltwissenschaften und Verfahrenstechnik der Brandenburgischen Technischen Universität Cottbus.

STUMM, W.; MORGAN, J. J. (1996): Aquatic chemistry - Chemical Equilibria and Rates in Natural Waters; third edition John Wiley, New York.

SUTRADHAR, S.; FATEHI, P. (2023): Latest development in the fabrication and use of lignin‐derived humic acid; Biotechnology for Biofuels and Bioproducts (2023) 16:38; https://doi.org/10.1186/s13068-023-02278-3.

SZYMCZAK, P.; WASSILIEW, M.; BEHNKE, A. (2009): Bedienhinweise zum Programm für die Auswertung von Korngrößenanalysen im Fachinformationssystem Hydrogeologie: Programm UK32; Version 1.1; G.E.O.S. Freiberg und HGC Hydro-Geo-Consult GmbH, Freiberg für das Sächsische Landesamt für Umwelt, Landwirtschaft und Geologie.

TANG, A.; MAYS, L.W. (1998): Genetic Algorithms for Optimal Operation of Soil Aquifer Treatment Systems; Water Resources Management 12 (5):375-396, October 1998.

TIPPING, E.; LOFTS, S.; SONKE, J. E. (2011): Humic Ion-Binding Model VII: a revised parameterisation of cation-binding by humic substances; Environmental Chemistry 8(3) pp.225-235; https://doi.org/10.1071/EN11016.

TIPPING, E.; HURLEY, M.A. (1992): A unifying model of cation binding by humic substances; Geochimica et Cosmochimica Acta, Vol. 56, Pages 3627-3641.

TIPPING, E. (1998): Humic Ion-Binding Model VI: An Improved Description of the Interactions of Protons and Metal Ions with Humic Substances; Aquatic Geochemistry 4: 3–48.

TIPPING, E.; WOOF, C.; HURLEY, M.A. (1991): Humic substances in acid waters; modelling aluminium binding contribution to ionic charge balance, and control of pH; Water Research Volume 25, Issue 18, Pages 425-435.

VAUCK, R. A.; MÜLLER, H. A. (2000): Grundoperationen chemischer Verfahrenstechnik; Deutscher Verlag für Grundstoffindustrie Leipzig Stuttgart.

VOBACH, V.; GOTTSCHALDT, N.; BEER, A.; KLAUS, R. (1977): Ergebnisse der Eliminierungsanalyse Teil 2: Ein Beitrag zur Theorie des organischen Stoffkomplexes; Acta hydrochemica et hydrobiologica 5(1977)4 S337-349.

VOGT, C.; ALFREIDER, A.; LORBEER, H.; WÜNSCHE, L.; BABEL, W. (2002): Optimierter mikrobiologischer Abbau von Chlorbenzen in In situ-Grundwasserreaktoren (SAFIRA); Grundwasser 7 (2002) 3, S.156-164.

VOGT, R. D.; GARMO, Ø.A.; AUSTNES, K.; KASTE, Ø.; HAALAND, S.; SAMPLE, J.E.; THRANE, J.-E.; SKANCKE, L.B.; GUNDERSEN, C.B.; DEWIT, H.A. (2024): Factors Governing Site and Charge Density of Dissolved Natural Organic Matter; Water 2024, 16, 1716. https://doi.org/10.3390/w16121716.

VOIGT, H.-J. (1989): Hydrogeochemie; VEB Deutscher Verlag für Grundstoffindustrie; Leipzig.

VÖLKER, E.; SONTHEIMER, H. (1988): Charakterisierung und Beurteilung von Kläranlagenabläufen aus der Sicht der Trinkwasserversorgung; gwf Wasser Abwasser 192 (1988) H.3.

WETZLER, H. (1985): Kennzahlen der Verfahrenstechnik; Heidelberg.

WIGHTMAN, P.,G.; FEIN, J.,B.; WESOLOWSKI, D., J.; PHELPS, T., J.; BÉNÉZETH, P.; PALMER, D., A. (2001): Measurement of bacterial surface protonation constants for two species at elevated temperatures; Geochimica et Cosmochimica Acta, Volume 65, Issue 19, (1. November 2001), Pages 3657-3669.

WINGRICH, H. (2002): Bemessung und Betrieb von Anlagen zur Grundwasseraufbereitung; Dresdner Berichte 20; Institut für Siedlungs- und Industriewasserwirtschaft der TU Dresden.

WORCH, E. (1993): Eine neue Gleichung zur Berechnung von Diffusionskoeffizienten gelöster Stoffe; Vom Wasser, 81, 289-297.

WORCH, E. (2004): Modelling the solute transport under nonequilibrium conditions on the basis of mass transfer equations; Journal of Contaminant Hydrology 68, pp.97-120.

WORKBENCH (2016): The Geochemist's WORKBENCH; The Geochemist's WORKBENCH; software for Generation Earth; https://www.gwb.com/.

XU, J.; TAN, W.; XIONG, J.; WANG, M.; FANG, L.; KOOPAL, L. K. (2016): Copper binding to soil fulvic and humic acids: NICA-Donnan modeling and conditional affinity spectra; Journal of Colloid and Interface Science 473 pp.141-151.

YAN, M.; DRYER, D.; KORSHIN, G.V.; BENEDETTI, M.F. (2013): In situ study of binding of copper by fulvic acid: Comparison of differential absorbance data and model predictions; Water Research Volume 47, Pages 588-596.

YAN, M.; DRYER, D.; KORSHIN, G. W. (2016): Spectroscopic characterization of changes of DOM deprotonationeprotonation properties in water treatment processes; Chemosphere 148 pp. 426-435.

YAN, M.; LIU, Z.; MO, S.; ZHANG, C.; LIU, F.; KORSHIN, G. (2023): A Novel Method to Dynamically Observe the Threedimensional Global Oceanic Dissolved Organic Carbon Reservoir; Earth and environmental sciences/Environmental sciences/Environmental impact; DOI: 10.21203/rs.3.rs-2357170/v1.

ZAHN, L. (2020): Untersuchungen zur Eisen(II)-Oxidation in belüftetem Grundwasser; Schriftenreihe Siedlungswasserwirtschaft und Umwelt, Bd.26; ISBN 3-934294-32-4; https://www-docs.b-tu.de/fg-wassertechnik/public/Publikationen/Schriftenreihe/Heft26.pdf

ZENG, R.; MANNAERTS,C. M.; LIEVENS, C. (**2023**): Assessment of UV-VIS spectra analysis methods for quantifying the absorption properties of chromophoric dissolved organic matter (CDOM); Front. Environ. Sci. 11:1152536. doi: 10.3389/fenvs.2023.1152536.

ZHANG, M.; PEACOCK, C. L.; XIAO, K.-Q.; QU, C.; WU, Y.; HUANG, Q. (2021): Selective retention of extracellular polymeric substances induced by adsorption to and coprecipitation with ferrihydrite; Geochimica et Cosmochimica Acta (299) 15-34.

ZHU, J. (2023): Uncertainty of Kozeny-Carman Permeability Model for Fractal Heterogeneous Porous Media; Hydrology 2023, 10, 21. https://doi.org/10.3390/hydrology10010021.

ZIECHMANN, W. (1996): Huminstoffe und ihre Wirkungen; Spektrum Verlag Heidelberg Berlin Oxford.

11.2.2 Unpublished References

Unpublished references are marked with a "*".

BALKE, S.; SCHÖPKE, R.* (2009): Entwicklung eines neuen Verfahrens zur Adsorption von Phosphor an körnigem Eisenhydroxid und Regeneration des Adsorptionsmittels bei gleichzeitiger Phosphorrückgewinnung; Ermittlung der chemischen Wirkungsmechanismen; Sachbericht zum Meilenstein 1/2009; Bericht für Arbeitsgemeinschaft industrieller Forschungsvereinigungen (AiF) von BTU Cottbus und HeGo Biotec GmbH Berlin.

KOCH, R.; SCHÖPKE, R.* (1996): Ermittlung der Gefährdung der Wasserfassung Spremberg durch die Aschehalde Trattendorf; Gutachten des LS Wassertechnik der BTU Cottbus für den Spremberger Wasser- und Abwasserzweckverband.

KOCH, R.; SCHÖPKE, R.; AY, P.; WALASZEK, W.* (2007): Bewertung der einzelnen Verfahrensstufen der Abwasserbehandlungsanlagen unter Einbeziehung aller Abwasserteilströme und Herausarbeitung von Optimierungsansätzen sowie Maßnahmen zur Verbesserung des CSB-Abbaus im SVZ-Schwarze Pumpe; Prof.Dr.-Ing.habil.R.Koch, Bad Muskau für SUSTEC Schwarze Pumpe.

Prowa BT Cottbus* (1989): Entwurf WAPRO 1.17; Projektierung Technologie, Bemessung und Regenerierung von Sandbecken; Wasserwirtschaft Werkstandard 5. Entwurf 02/88 WAPRO 1.17 02/88.

SCHÖPKE, R.; KOCH, R.* (2007): Wissenschaftliche Begleitung des Pilotversuchs zum Sulfiteinsatz - Jahresbericht 2007-; Dokumentation für die Wismut GmbH, Chemnitz.

SCHÖPKE, R.; KOCH, R.* (2008): Auswertung Pilotversuch Sulfiteinsatz für die Grube Königstein (Laufzeit März 2007 bis Februar 2008) -Abschlussbericht-; Dokumentation für die Wismut GmbH, Chemnitz; Bearbeitungsnummer: 1093010-409.

SCHÖPKE, R.; PREUß, V.* (2010): Erarbeitung von Maßnahmevorschlägen zur Ermittlung der Ursachen der Infiltrationsbrunnenkolmation für das Vorhaben Laßzinswiesen¸ Zuarbeit für DGC, Dresdner Grundwasser Consulting GmbH; (Vattenfall).

SCHÖPKE, R.; THÜRMER, K.* (2010): Pilotversuch zum Sulfiteinsatz in der Grube Königstein, Versuchsphase 3 (Laufzeit März 2009 bis Februar 2010); Institut für Wasserwirtschaft, Siedlungswasserbau und Ökologie (IWSÖ) GmbH für Wismut GmbH.

SCHÖPKE, R.; THÜRMER, K.* (2011): Bericht: Auswertung eines begleitenden Säulenversuches zum Feldversuch "Injektion von Pufferfluiden am Standort Königstein"; Institut für Wasserwirtschaft, Siedlungswasserbau und Ökologie (IWSÖ) GmbH für Wismut GmbH; Bearbeitungsnummer 3137392-U09.

SCHÖPKE, R.; THÜRMER, K.* (2012): Bewertung der Verhältnisse in einer reaktiven Wand zur Grundwassersanierung über Datenauswertung, elektronenmikroskopische Untersuchungen und Modellierung für den Standort Nickelhütte Aue; IWSÖ GmbH / BTU Cottbus, LS Wassertechnik & Siedlungswasserbau für G.E.O.S. Ingenieurgesellschaft mbH.

SCHÖPKE, R.* (1984): Dokumentation über die Erfahrungen eines einjährigen Versuchsbetriebes der Hauswasserversorgungsanlage "Typ Spreewald" in Burg; Dokumentation; Prowa Cottbus.

SCHÖPKE, R.* (1986): PWT Bericht Hauswasserversorgung Typ Spreewald; Dokumentation; Prowa Cottbus.

SCHÖPKE, R.* (1989): Laborversuche zum Vorbereitung der GWA Sdier; Bericht Prowa Cottbus.

SCHÖPKE, R.* (1989a): Verfahrenstechnische Untersuchungen zum Investitionsvorhaben WW-Görlitz/Weinhübel; Bericht Prowa Cottbus 1989.

SCHÖPKE, R.* (2002): Untersuchungen zum Einsatz von Seereaktions- / Seekolmationswänden in sauren Tagebaurestseen mit ausgewählten Alkalisierungsmitteln im Seeböschungs- / Seebodenbereich; BTU Cottbus LS Wassertechnik, Zuarbeit für eta-AG.

SCHÖPKE, R.* (2014): Auswerteprotokolle zur Modellierung Invasion von Wasser in Grundwasserleiter, Invasionsprotokoll.

SCHÖPKE, R.* (2020): Eisenoxidationskinetik, Entwurfsfassung.

SCHÖPKE, R.* (2024): Sammlung von Spektrenprotokollen (Baustein: Spektrenauswertung).

SCHÖPKE, R.; WOLF, R.; BAUER, W.; WÜNSCHE, H.* (1980): Aufbereitungsversuche zur Vorfiltration im WW Friedrichshagen -Versuchsbericht-; VEB Projektierung Wasserwirtschaft (Prowa) BT Cottbus.

SCHÖPKE, R.; WOLF, R.; BAUER, W.; WÜNSCHE, H.* (1982): Grundsätzliche Aufbereitungsmöglichkeiten von Neißewasser im Raum Görlitz zur Schaffung von Bemessungsparametern des WW Görlitz und des VEB Landskron-brauerei/Weinhübel; -Versuchsbericht- VEB Projektierung Wasserwirtschaft (Prowa) BT Cottbus.

SCHÖPKE, R.; WOLF, R.; BAUER, W.; WÜNSCHE, H.* (1985): Versuchsbetrieb der GWA-Pilotanlage Neuzittau; VEB Projektierung Wasserwirtschaft (Prowa) BT Cottbus.

SCHÖPKE, R.; BAUER, W.; WÜNSCHE,H.* (1990): Verfahrenstechnische Untersuchungen im WW Frankfurt/O -Versuchsberichte; Ingenieurbüro PROWA Cottbus.

SCHÖPKE, R.; MARTIENSSEN, M.; THÜRMER, T.* (2011): Erarbeitung von Vorschlägen für verfahrenstechnische Maßnahmen, die Ablagerungen in Rohrleitungen und Armaturen von Grundwassersanierungsanlagen auf dem Werksgelände Schwarze Pumpe verhindern können; IWSÖ GmbH, BTU Cottbus für Büro Dr. Beerbalk, Berlin.

SIEBER, H.* (2001): Erarbeitung eines Lösungsvorschlages für den Aufbau einer biologischen Kultur zur Behandlung von Abwässern einer Schwelanlage; Diplomarbeit BTU Cottbus, LS Aufbereitungstechnik.

THIELKE* (1972): Entwicklung leistungsfähiger Grobfilter; PWT V5 VEB Projektierung Wasserwirtschaft (Prowa) BT Dresden.

VOIGT et al.* (1985): Lösungsvorschlag für ein Siebtestgerät; NVe 51/80/85/III/14; VEB Projektierung Wasserwirtschaft (Prowa) BT Dresden.

VOIGT; WINKLER, SCZIBILINSKI, THIELKE* (1988): Arbeitsvorschrift und technische Dokumentation für Filtersiebtestgerät; NVe 51/80/86/III/16; VEB Projektierung Wasserwirtschaft (Prowa) BT Dresden.

11.3 List of figures

11.4 Table index